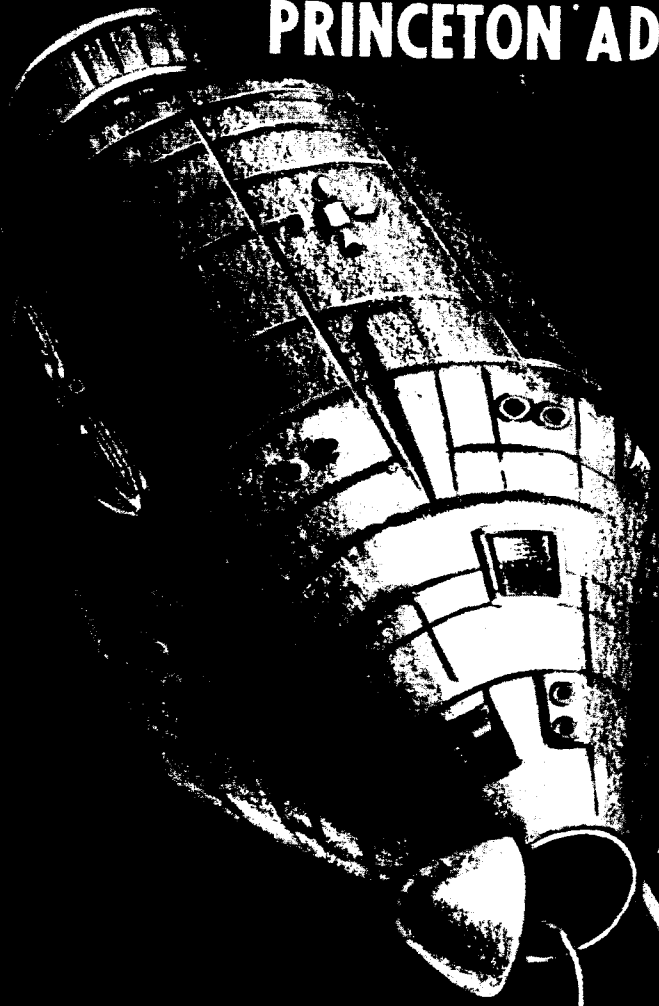


# PRINCETON ADVANCED SATELLITE STUDY



GPO PRICE \$ \_\_\_\_\_  
 CFSTI PRICE(S) \$ \_\_\_\_\_  
 Hard copy (HC) 6.22  
 Microfiche (MF) 2.75  
 ff 653 July 65



FACILITY FORM 808

N66 34368	N66 34372
(ACCESSION NUMBER)	(THRU)
373	1
(PAGES)	(CODE)
CR-75294	3
(NASA CR OR TMX OR AD NUMBER)	(CATEGORY)

PERKIN-ELMER

PRINCETON ADVANCED SATELLITE STUDY

FINAL REPORT

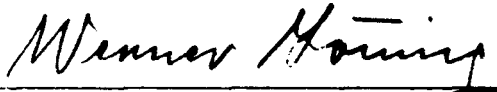
SUBCONTRACT NO. 1, NASA GRANT

NGR-31-001-044

8 MARCH 1965 TO 15 MAY 1966

PREPARED FOR:

PRINCETON UNIVERSITY OBSERVATORY  
PRINCETON, NEW JERSEY

  
W. F. Loening,  
Engineering Program Manager

  
H. S. Hemstreet, Manager,  
Space Optics Department

THE PERKIN-ELMER CORPORATION  
ELECTRO-OPTICAL DIVISION  
NORWALK, CONNECTICUT 06852

PRINCETON ADVANCED SATELLITE STUDY

Contributors:

C.R. Fencil

H.S. Hemstreet

W. Loening

D.A. Markle

H.W. Marshall, Jr.

E.R. Schlesinger

L.B. Scott

R.M. Scott

I. Steiner

A.B. Wissinger

**PERKIN-ELMER**

**N66 34369**

Report No. 8346(I)

VOLUME I

PRINCETON ADVANCED SATELLITE STUDY

## TABLE OF CONTENTS

<u>Section</u>	<u>Title</u>	<u>Page</u>
I	Introduction	1
II	General Problems Associated with Spaceborne Telescopes	3
III	40-Inch System Description	11
IV	OAO/APEP in Association with AAP	29
V	Recommendations for Additional Effort	33
VI	Selected Design Parameters	35

PRINCETON ADVANCED SATELLITE STUDY

## LIST OF ILLUSTRATIONS

<u>Figure</u>	<u>Title</u>	<u>Page</u>
1	Reflectance of Aluminum Based Reflective Coatings	4
2	Orbital Variation in Total Heat Flux	5
3	Thermal Behavior of a 40 Pound Aluminum Telescope Tube (40" Dia. x 80" Long)	6
4	Instantaneous Temperature Distribution in a Semi-Fused Silica Slab ( $f = 0.566/\text{Hr.}$ )	7
5	Guide Star Two Field-of View Optical Sensor Principle (Single Axis-Schematic)	8
6	Minimum RMS Pointing Error ( $E_p$ ) Versus Stellar Magnitude	9
7	Tracking Error Versus Bandwidth ( $D = 1$ Meter)	10
8	OA0 Vehicle and Advanced Princeton Experiment Package (APEP)	11
9	Optical Package	12
10	Cassegrain Telescope and Corrector	13
11	Telescope Field Corrector Details	14
12	Imaging System	15
13	Wide Field Microscope Objective ( $f/3.7, 0.2\mu-0.6\mu$ )	16
14	Spectrograph System	17
15	Image Mover Assembly	18
16	Image Mover in Skewed Position	19
17	Coarse Guidance System	20

## LIST OF ILLUSTRATIONS (Continued)

<u>Figure</u>	<u>Title</u>	<u>Page</u>
18	Fine Guidance System	21
19	Instrument Package Optical Layout	22
20	Pointing Errors Versus Disturbance Torques (Final Tracking Mode - Pitch and Yaw Axes)	23
21	Pointing Error Versus Star Magnitudes (Pitch and Yaw Axes)	24
22	Roll Axis Pointing Errors Versus Disturbance Torques	25
23	Echelle Spectrograph Format	26
24	Four-Element Spectrograph	27
25	Two-Element Spectrograph Design	28
26	Shielding Weight Needed to Shield a Cylindrical Volume (8 Inch Diameter by 4 Inches) From Doses Exceeding One Radian as a Function of Days Exposure	29
27	Shielding Requirements as a Function of Number of Days Exposure	31

PRINCETON ADVANCED SATELLITE STUDYI. Introduction

Perkin-Elmer was awarded a feasibility study program by Princeton University Observatory on March 8, 1965 under Subcontract No. 1, NASA Grant NGR-31-001-044. The purpose of this program was to study general problems of large high resolution optical instruments with an aperture between 30" and 120" diameter in space, and the specific problems associated with a high resolution, UV spectrometer photometry, imaging telescope of 40" diameter aperture on board an OAO. Work through August 1965 resulted in a concept for a telescope magnetically suspended inside an OAO spacecraft which can be used for high resolution (0.1 $\lambda$ ) spectral investigations down to approximately 1000 $\text{\AA}$  wavelength, and high resolution star imagery with close to diffraction-limited performance. The progress of the effort through the end of August 1965 was documented in the Semi-annual Progress Report submitted to PUO.

The original scope of the study effort (Phase I) was increased on September 24, 1965 by Phase II which broadened the program to study also the merits accruing from a combined manned vehicle and astronomical package payload, specifically the use of an Apollo Extension System in combination with the OAO spacecraft equipped with the high resolution instrument. With the award of Phase II the Grumman Aircraft Engineering Corporation entered a subcontract with the Perkin-Elmer Corporation to assist in the specific aspects of associating an OAO with a manned space station, an area GAEC investigated on previous occasions.

The results of both phases of this study are included in the final report which is comprised of four volumes as defined below.

- Volume I - Summary.
- Volume II - General Problems Associated with Spaceborne Telescopes.
- Volume III - 40-inch System Description.
- Volume IV - OAO/APEP in Association with AAP.



**Page intentionally left blank**

II. General Problems Associated With Spaceborne Telescopes

The general portion of the study was directed towards exploring the factors most likely to compromise the resolution capability of a large aperture telescope. This is described in Volume II which includes a comparison of the relative susceptibility of various mirror-materials and configurations to elastic strain during test, plastic strain during launch, and thermal strain and long-term dimensional changes during operation. Also considered is the temporal variation in heat flux and the effect of this on the optical system. Finally, the theoretical pointing accuracy determined by stellar magnitude, aperture diameter, and system bandwidth is derived.

The following table and illustrations summarize the more important findings of this general portion of the study.

TABLE 1  
PHYSICAL PROPERTIES OF MIRROR MATERIALS

Material	$\frac{K/C\alpha\rho}{\text{°C cm}^{-2} \text{ sec}}$	Coefficient of Expansion ( $\alpha$ ) $\text{°C}^{-1}$	$\frac{E/\rho}{\text{Newton-cm gm}}$
Fused Silica	$14.50 \times 10^3$	$0.55 \times 10^{-6}$	$3.18 \times 10^6$
Pyrex — 7740	$1.44 \times 10^3$	$3.20 \times 10^{-6}$	$2.89 \times 10^6$
Aluminum	$38.20 \times 10^3$	$23.90 \times 10^{-6}$	$2.56 \times 10^6$
Beryllium	$37.50 \times 10^3$	$12.40 \times 10^{-6}$	$15.40 \times 10^6$
Invar (36% Ni)	$26.30 \times 10^3$	$1.30 \times 10^{-6}$	$1.85 \times 10^6$
Silicon	$230.00 \times 10^3$	$4.15 \times 10^{-6}$	$5.56 \times 10^6$

Three figures of merit for selection of a mirror material are presented here. These are: the ratio of thermal diffusivity to coefficient of expansion,  $K/C\alpha\rho$  (important in the determining temperature distribution and resulting thermal distortions), the coefficient of expansion,  $\alpha$  (important in glasses when thermal environment determines temperature distribution), and the ratio of modulus of elasticity to density,  $E/\rho$  (important in determining deflections during working and testing in gravity environment).

- Best Figure of Merit for Temperature Distribution - Silicon
- Best Figure of Merit for Coefficient of Expansion - Fused Silica
- Best Figure of Merit for Rigidity - Beryllium

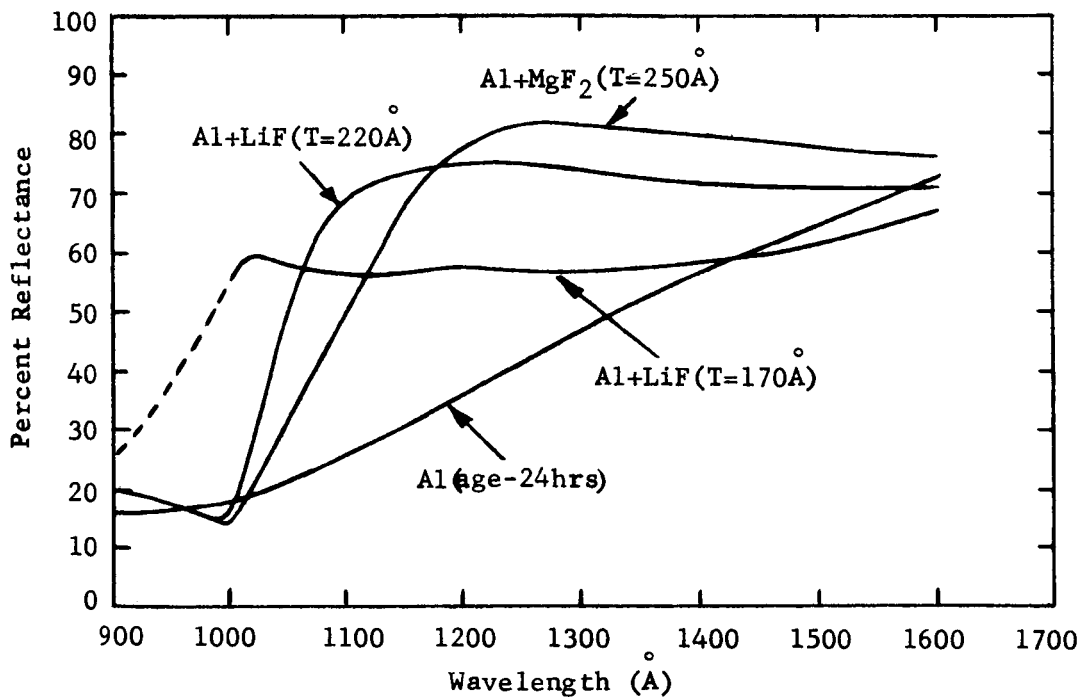


Figure 1. Reflectance of Aluminum Based Reflective Coatings

Below 1600Å, the formation of a thin oxide coating drops the reflectivity of aluminum from above 80% to very low values. LiF and MgF<sub>2</sub> can be used to inhibit oxide formation but also begin to absorb below 1200Å. No good reflective coating is apparent for the 900Å to 1000Å region.

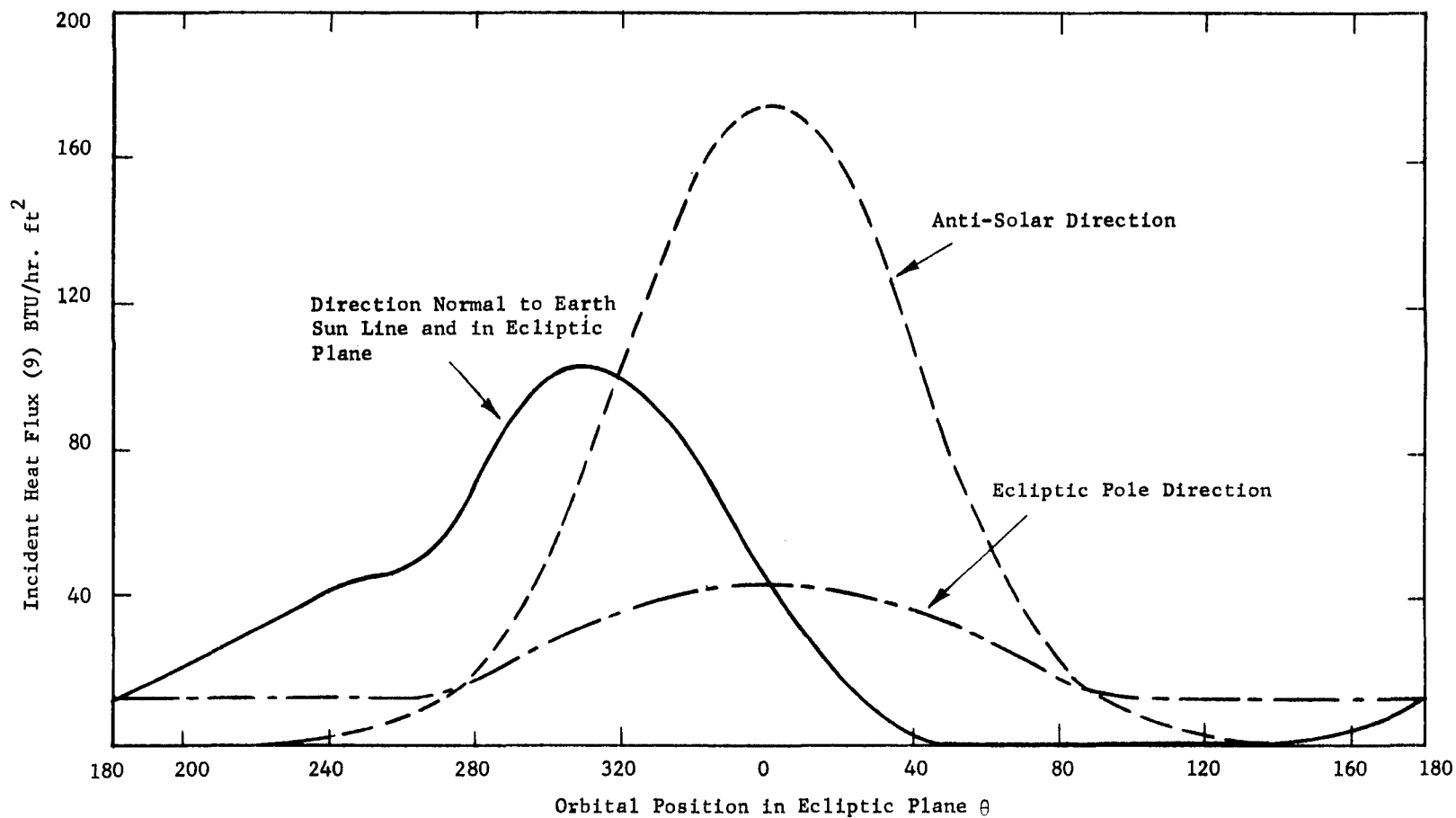


Figure 2. Orbital Variation in Total Heat Flux

The total heat flux due to earth reflected sunlight and direct earth emission is shown for three telescope pointing directions assuming a 600 n.m. orbit in the ecliptic plane. A 20% increase can be expected for the worst case anti-solar direction with a 300 n.m. orbit.

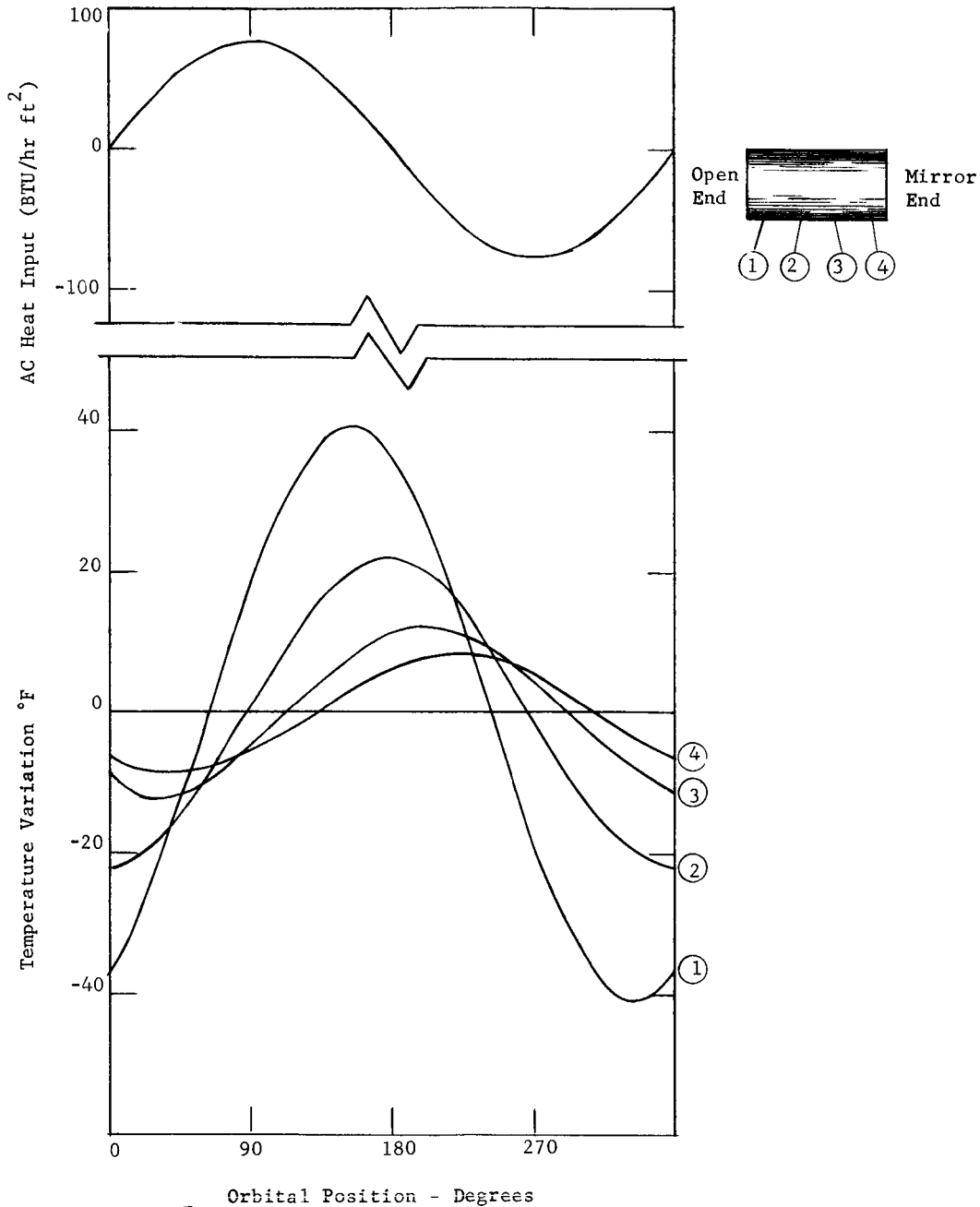


Figure 3. Thermal Behavior of a 40 Pound Aluminum Telescope Tube (40" Dia. x 80" Long)

Numbered curves show the temperature variation for various parts of the telescope tube as a function of position in the ecliptic orbital plane. A sinusoidal, isotropic heat flux is assumed to exist at the open end of the telescope tube. This is shown in the top curve.

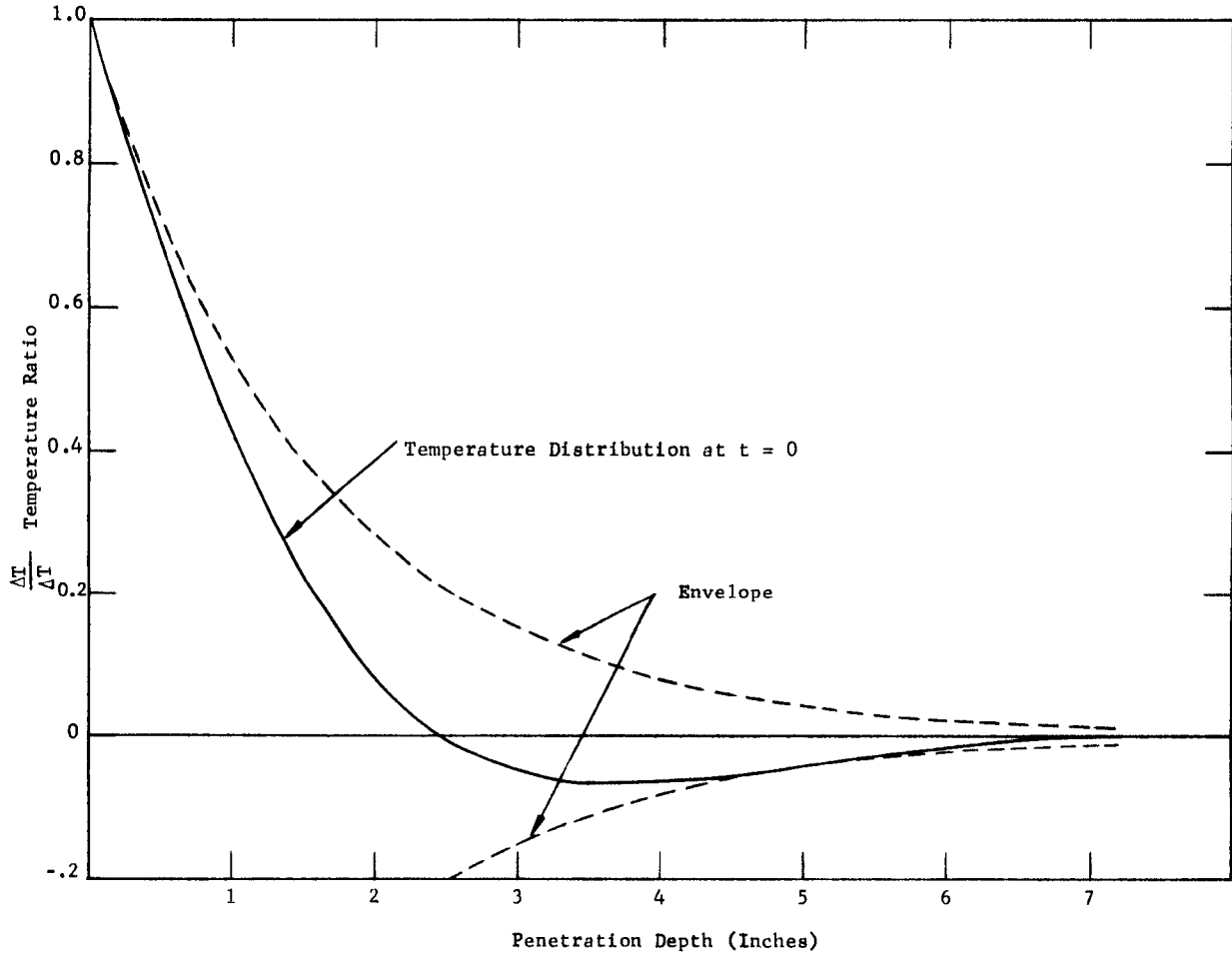


Figure 4. Instantaneous Temperature Distribution in a Semi-Infinite Fused Silica Slab ( $f = 0.566/\text{Hr.}$ )

The orbital variation in heat flux reaching the front surface of the primary mirror causes a thermal wave to propagate into the mirror material. As it propagates, the wave is attenuated logarithmically. The figure illustrates that about 90% attenuation of an orbital period wave occurs in the first 3.5 inches of a fused silica mirror.

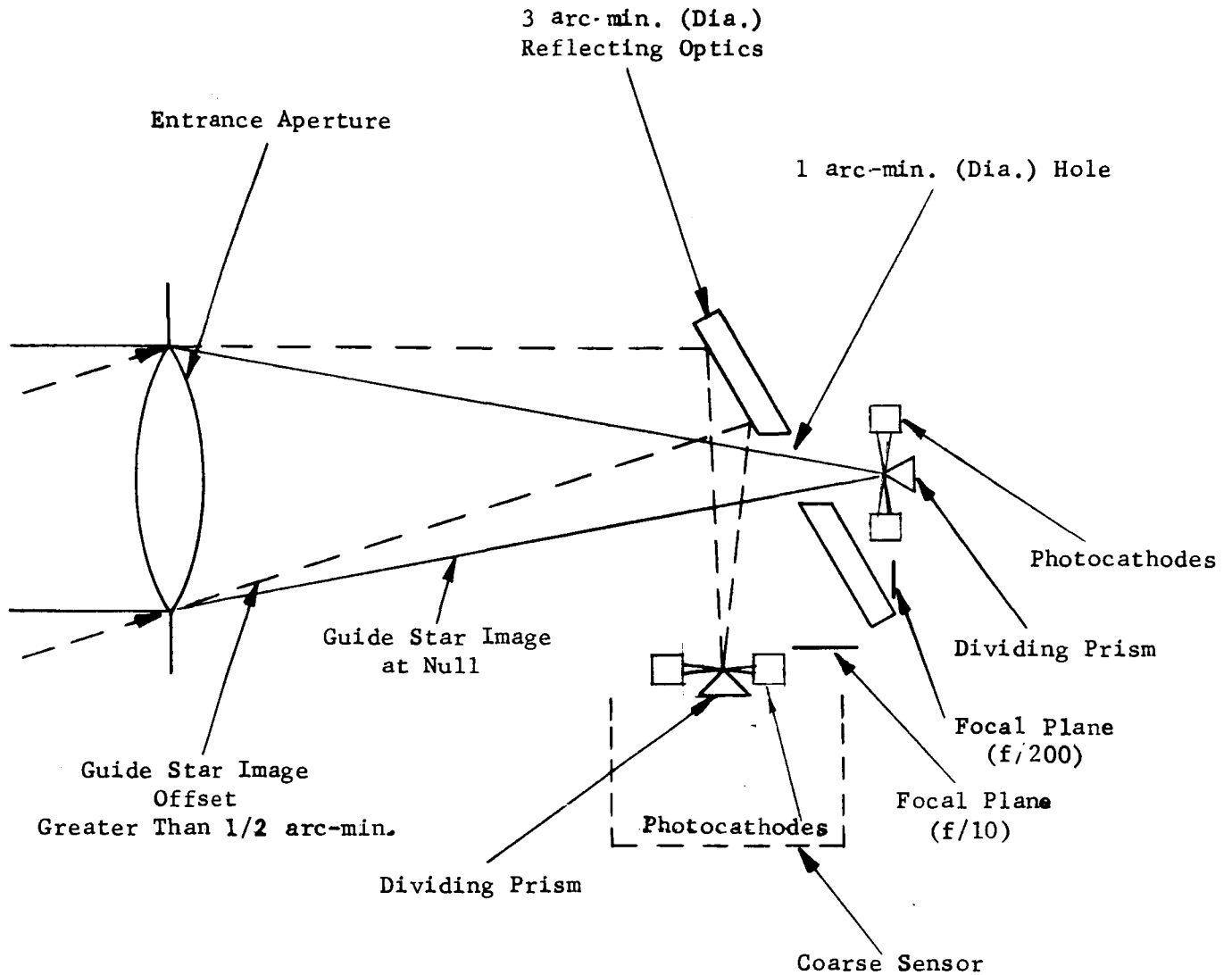


Figure 5. Guide Star Two Field-of-View Optical Sensor Principle (Single Axis-Schematic)

The telescope pointing system error analysis was based on the above optical sensor principle which operates in the following manner. For angular pointing errors greater than  $\pm 1/2$  arc-minute, the star light is reflected to the coarse sensor dividing prism in the  $f/10$  focal plane. For errors less than  $\pm 1/2$  arc-minute, the light proceeds directly to the fine sensor prism in the  $f/200$  focal plane.

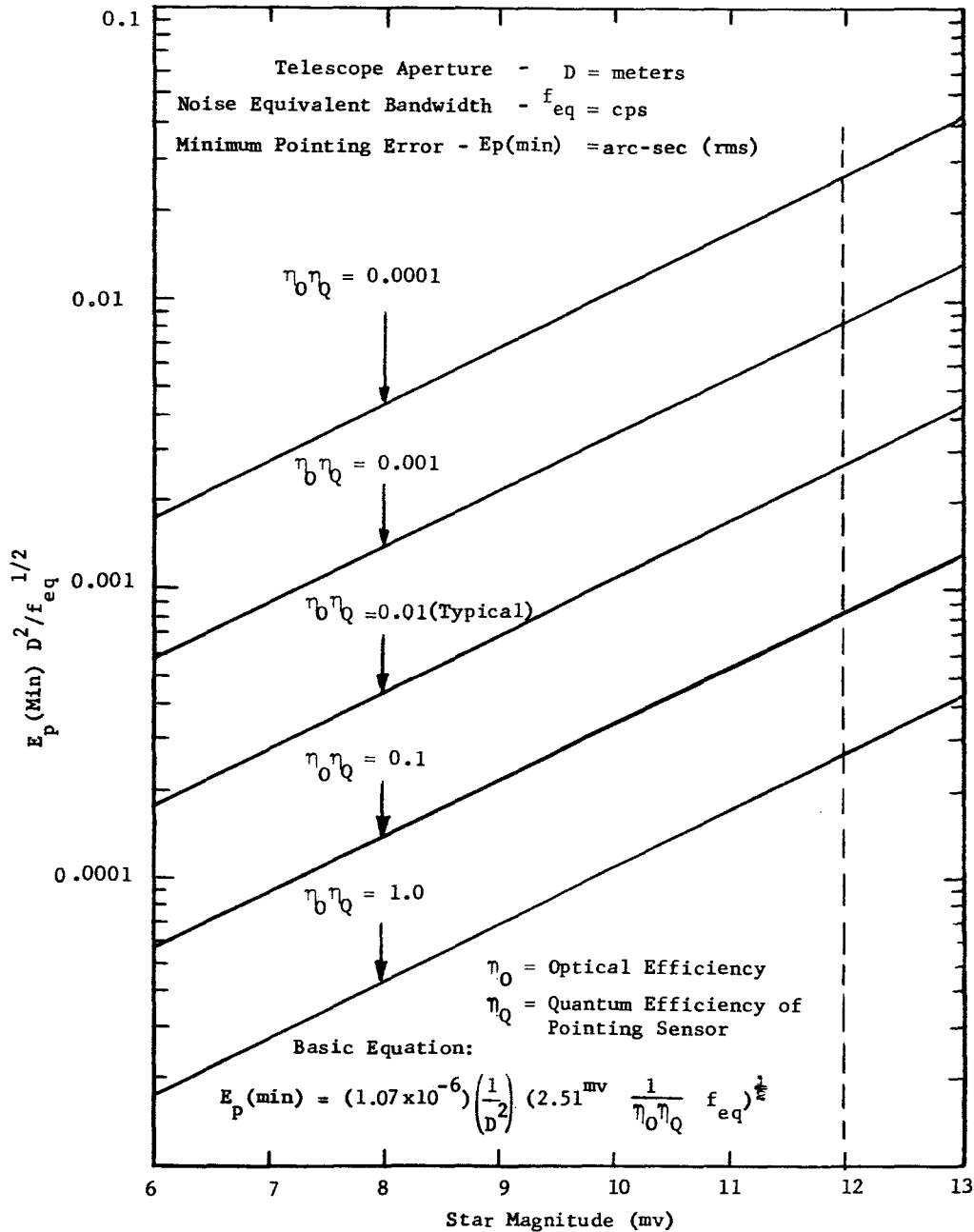


Figure 6. Minimum RMS Pointing Error ( $E_p$ ) Versus Stellar Magnitude

Using the optical sensor principle of Figure 5, and zero background and dark current noise conditions, the above minimum pointing errors can be realized.



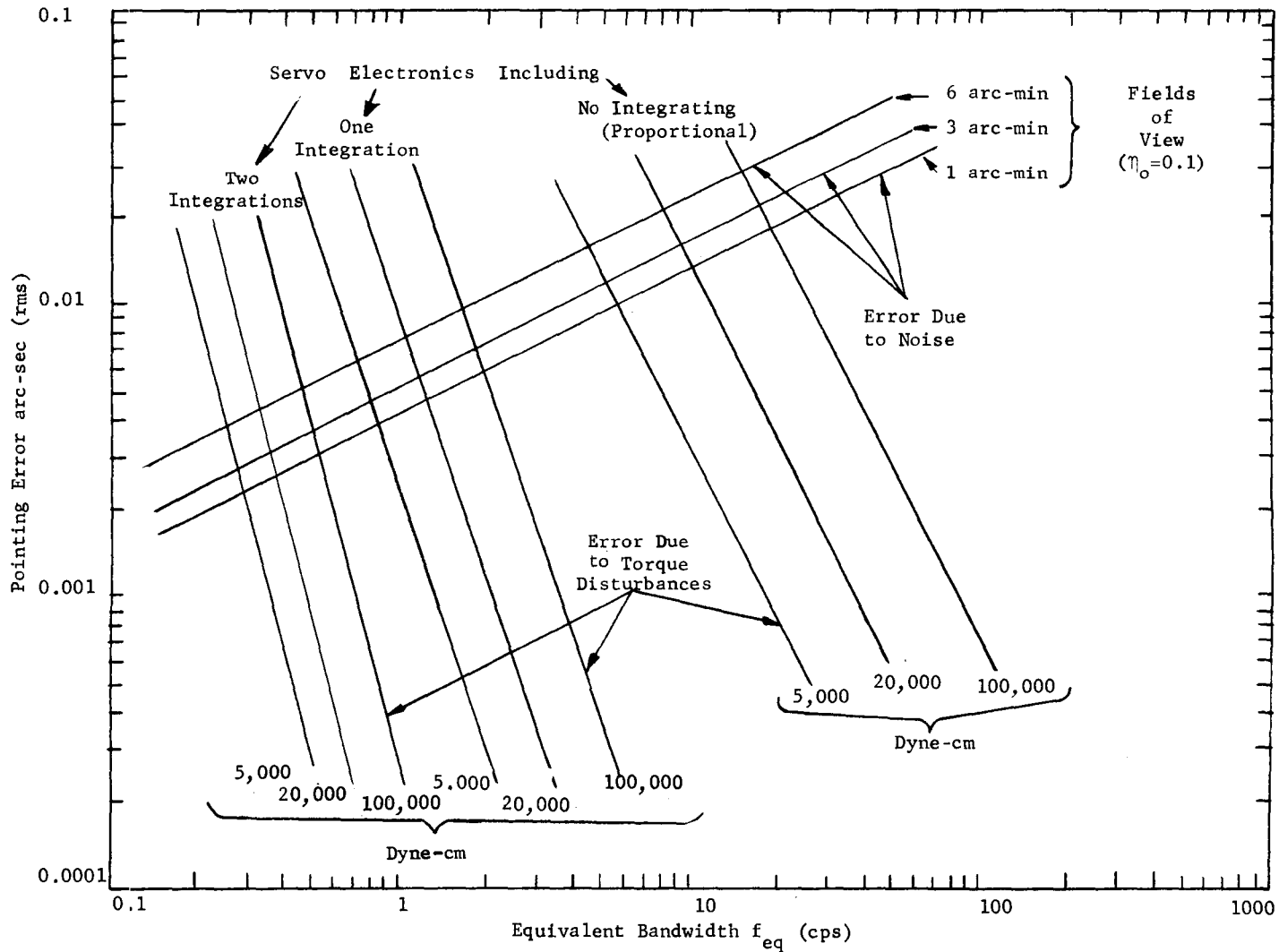


Figure 7. Tracking Error Versus Bandwidth ( $D = 1$  Meter)

For pointing servo systems employing various levels of signal integrator, the pointing errors due to noise and the pointing errors due to disturbing torques will vary as shown as a function of equivalent bandwidths.

### III. 40-Inch System Description

Volume III describes an Advanced Princeton Experiment Package (APEP) which has been tailored to fit into the same outer vehicle used for the Orbiting Astronomical Observatory (OAO) series of satellites. The experiment package contains a 40-inch diameter Cassegrain telescope which is used in conjunction with two SEC Vidicons for high-resolution spectrophotometry and diffraction-limited imagery in the visible and UV spectral regions. The optical system allows either vidicon to be used for spectrography or imagery so that failure of one vidicon does not compromise the experiment objectives.

The major innovation incorporated into the design is a suspension system which allows the experiment package to float with respect to the outer OAO vehicle. This minimizes the effect of disturbances arising from the momentum wheels and gas jets in the outer vehicle and permits the telescope to use the entire OAO vehicle as a momentum wheel. Long term pointing stability is obtained by fixing the orientation of the telescope with respect to two guide stars located within its field of view. The guidance system is designed to handle the relatively high angular displacements and displacement rates encountered during acquisition. It is also capable of minimizing high frequency disturbances due to statistical variations in photon arrival rates as well as low frequency disturbances due to magnetic and gravity gradient torques.

A detailed mechanical analysis taking into account the effect of the launch environment has not been performed on any part of the experiment package. The structures shown in many of the following figures are intended to indicate the design concept only, and are not meant to convey a completed design. Graphs are also included to depict the pointing system performance.

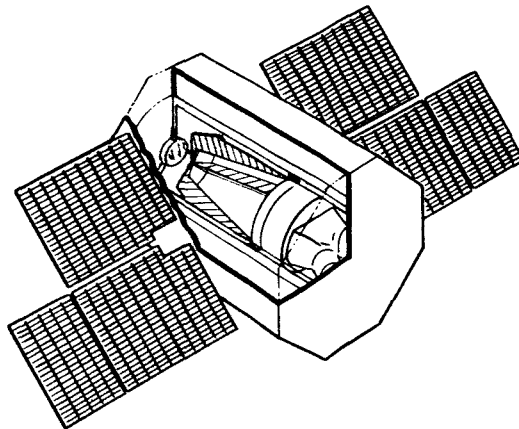


Figure 8. OAO Vehicle and Advanced Princeton Experiment Package (APEP)

During normal operation, the experiment package floats within the OAO vehicle and uses it for a momentum wheel.

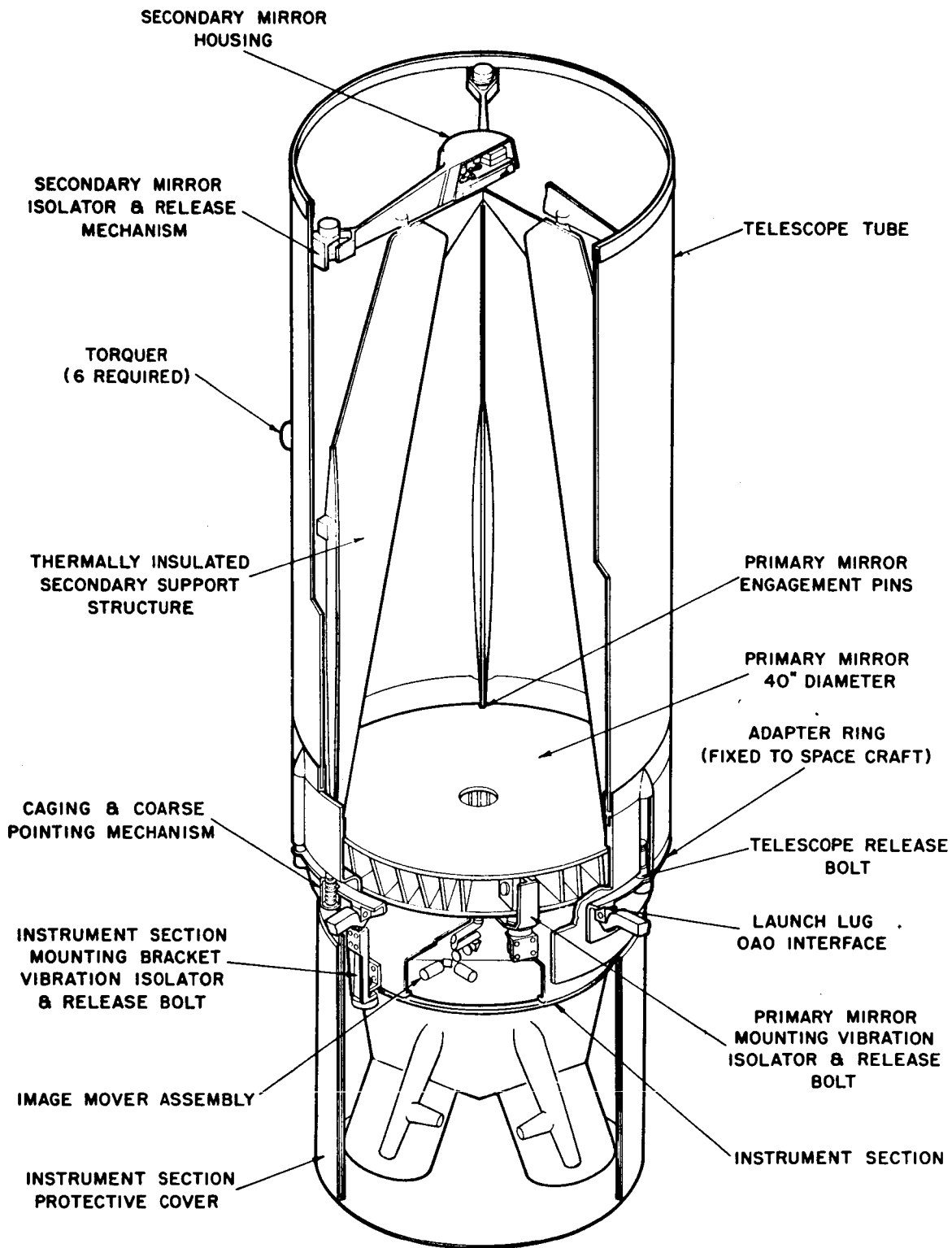


Figure 9. Optical Package

13

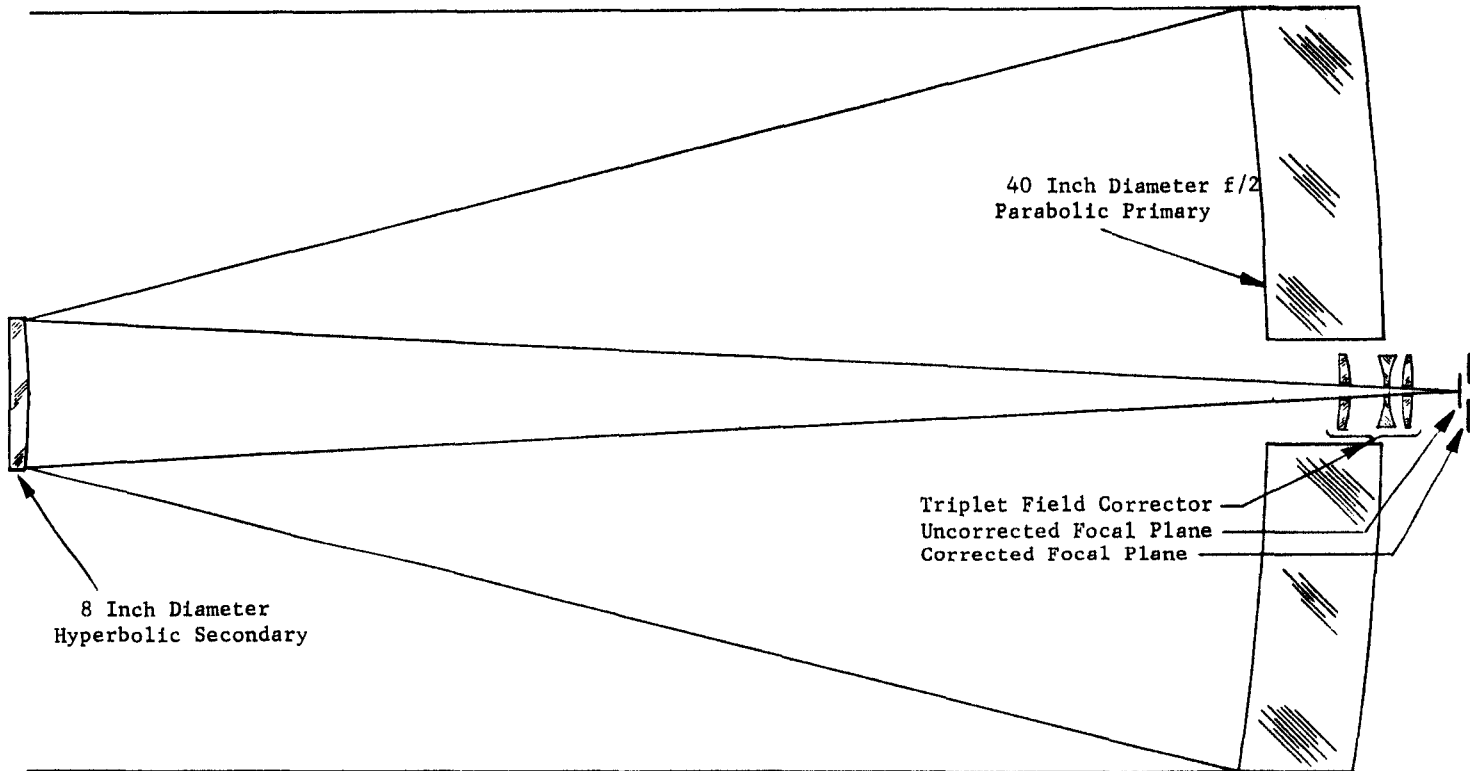
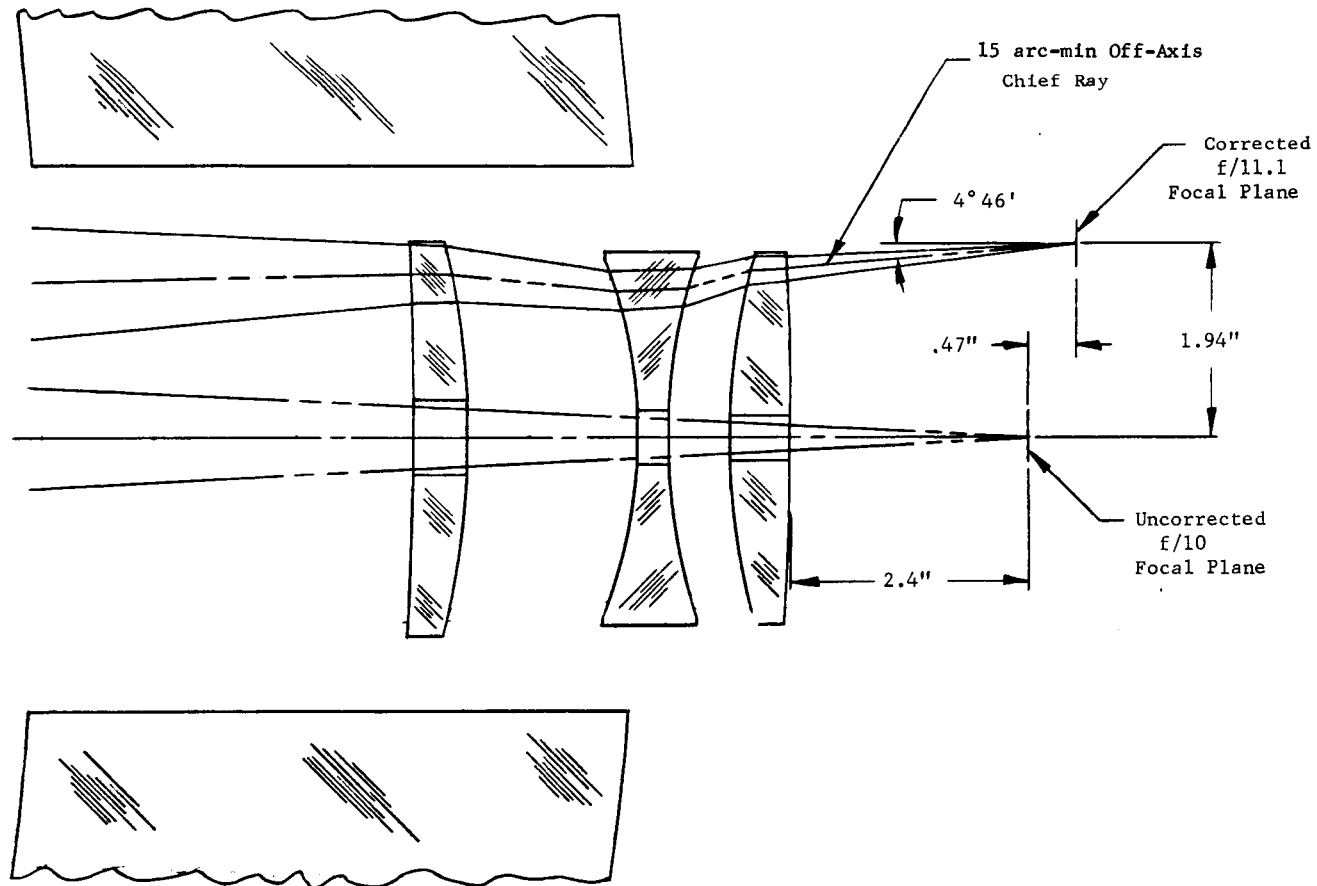


Figure 10. Cassegrain Telescope and Corrector

A fast,  $f/2$  primary, and a secondary with 5X magnification form a  $f/10$  optical system with only a 65" separation between them.



14

Figure 11. Telescope Field Corrector Details

The corrector provides a flat, well corrected field 30 minutes of arc in diameter at the f/11.1 focal plane. A very small field a few arc-minutes in extent and containing no refractive components is provided by a hole through each refractive component.

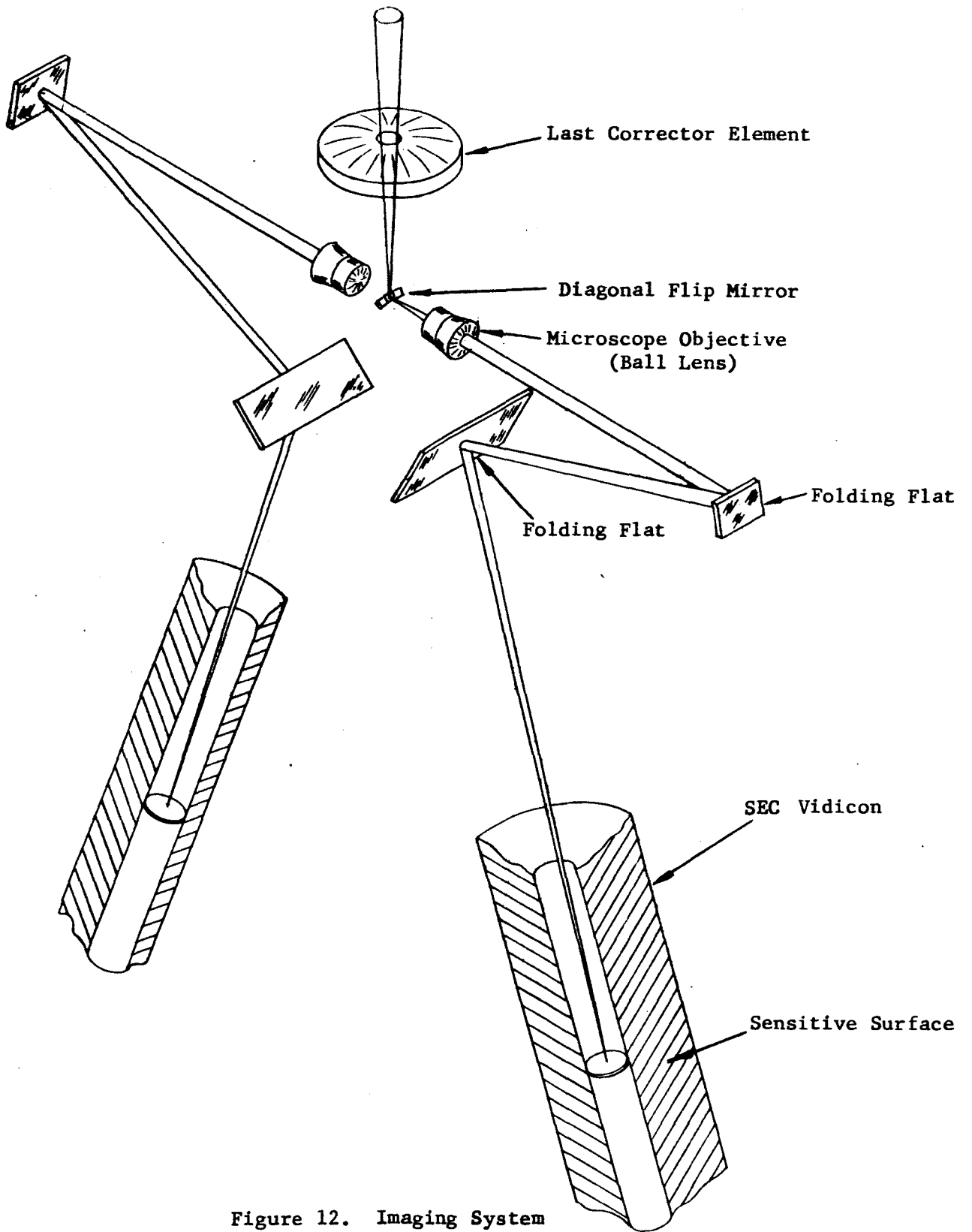


Figure 12. Imaging System

The small diagonal flip mirror situated under the last telescope field corrector and in the  $f/10$  focal plane rotates about the optical axis to direct the image beam to one or the other identical imaging system associated with each vidicon.

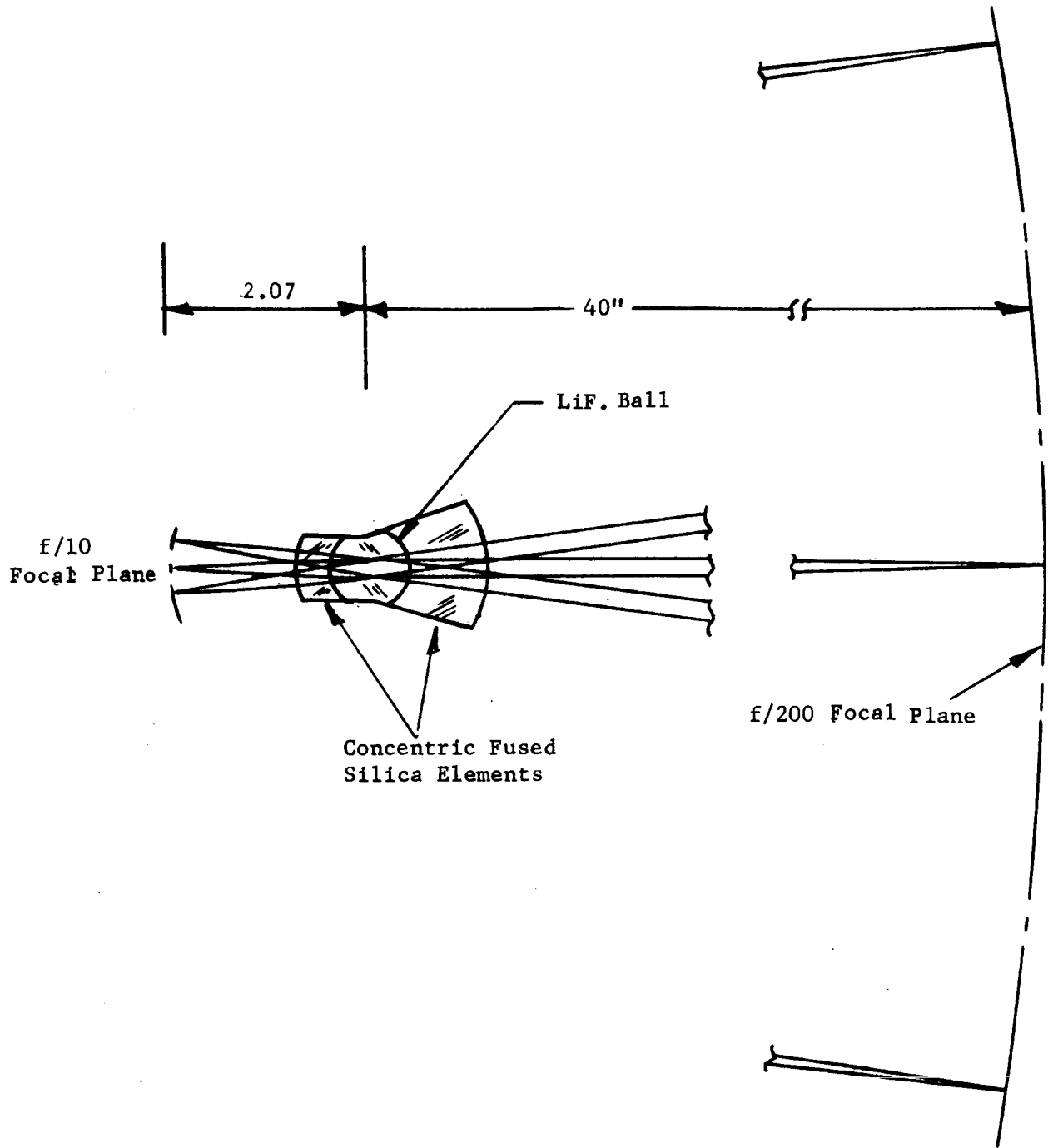


Figure 13. Wide Field Microscope Objective ( $f/3.7$ ,  $0.2\mu - 0.6\mu$ )

This is a "ball lens" type of design. Since all surfaces are concentric, there is no optical axis and, therefore, no off-axis aberrations which normally restrict the field of more conventional lens types.

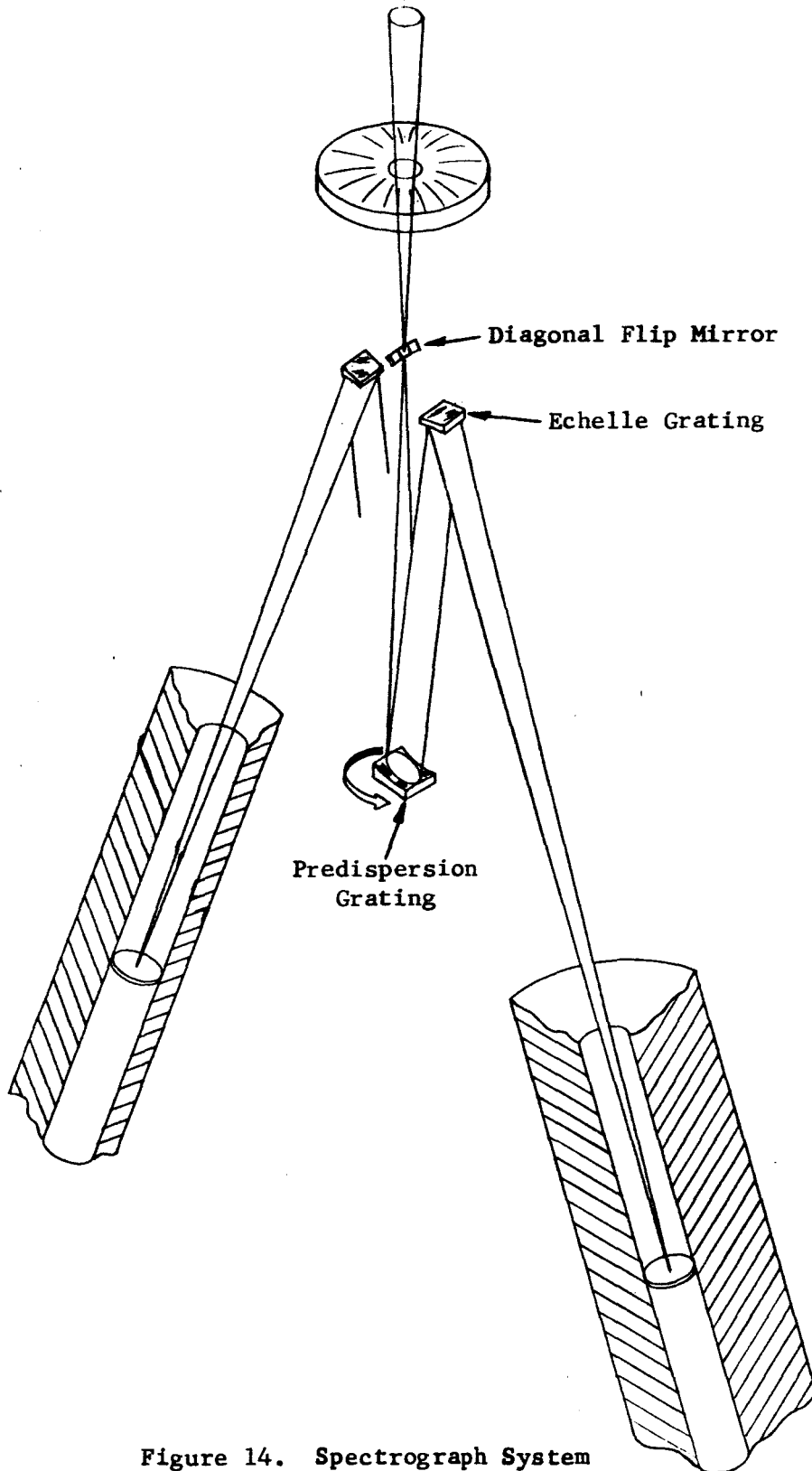


Figure 14. Spectrograph System

Energy enters the spectrograph through a small slit in the diagonal flip mirror and strikes a spherical predispersion grating. Rotation of the predispersion about the optical axis directs the energy into one or the other of a pair of echelle gratings associated with each vidicon.



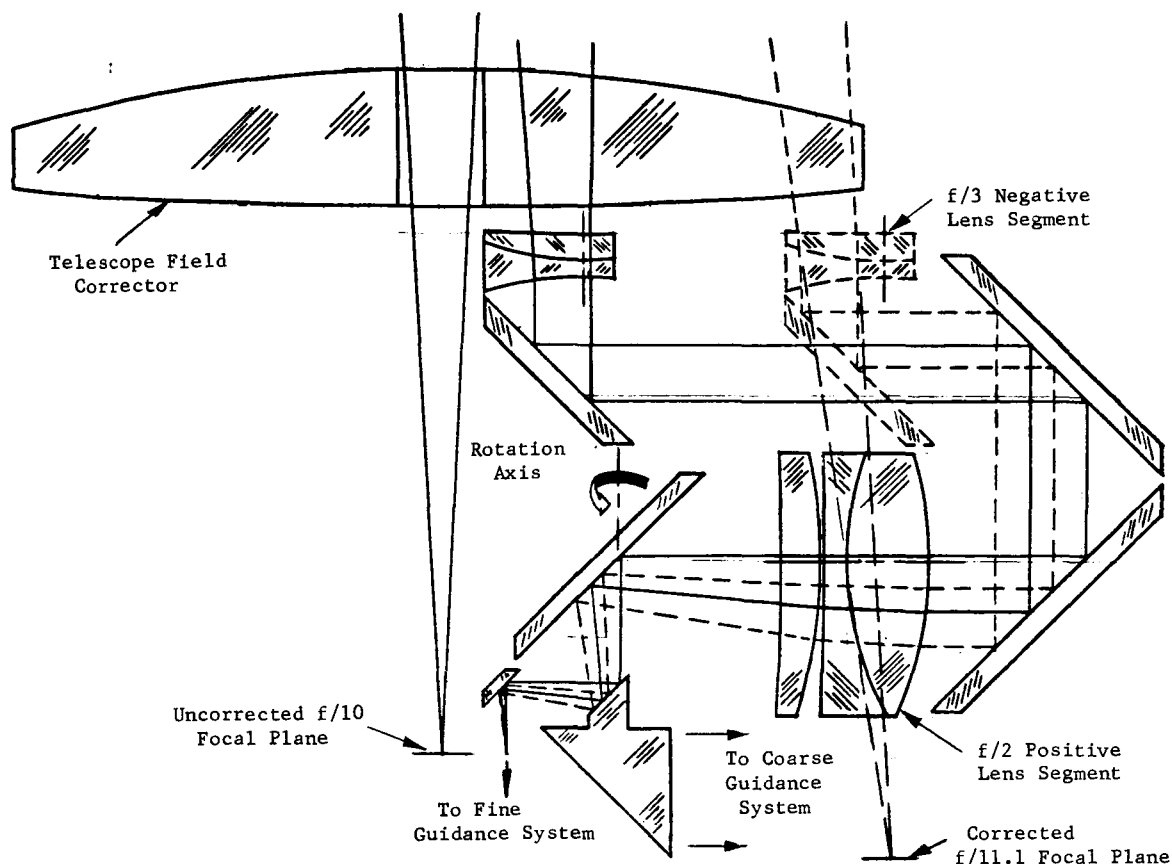


Figure 15. Image Mover Assembly

The image mover assembly relays a guide star image from its normal position in the telescope field to a position close to the telescope optical axis. The portion of the telescope field to be relayed by the image mover is selected by sliding the negative lens and diagonal mirror assembly in and out as shown by the bold and phantom views and by rotating the entire image mover assembly about an axis through the positive lens diagonal mirror. The coarse guidance prism and the small mirror immediately above the  $f/10$  focal plane do not rotate but remain fixed.

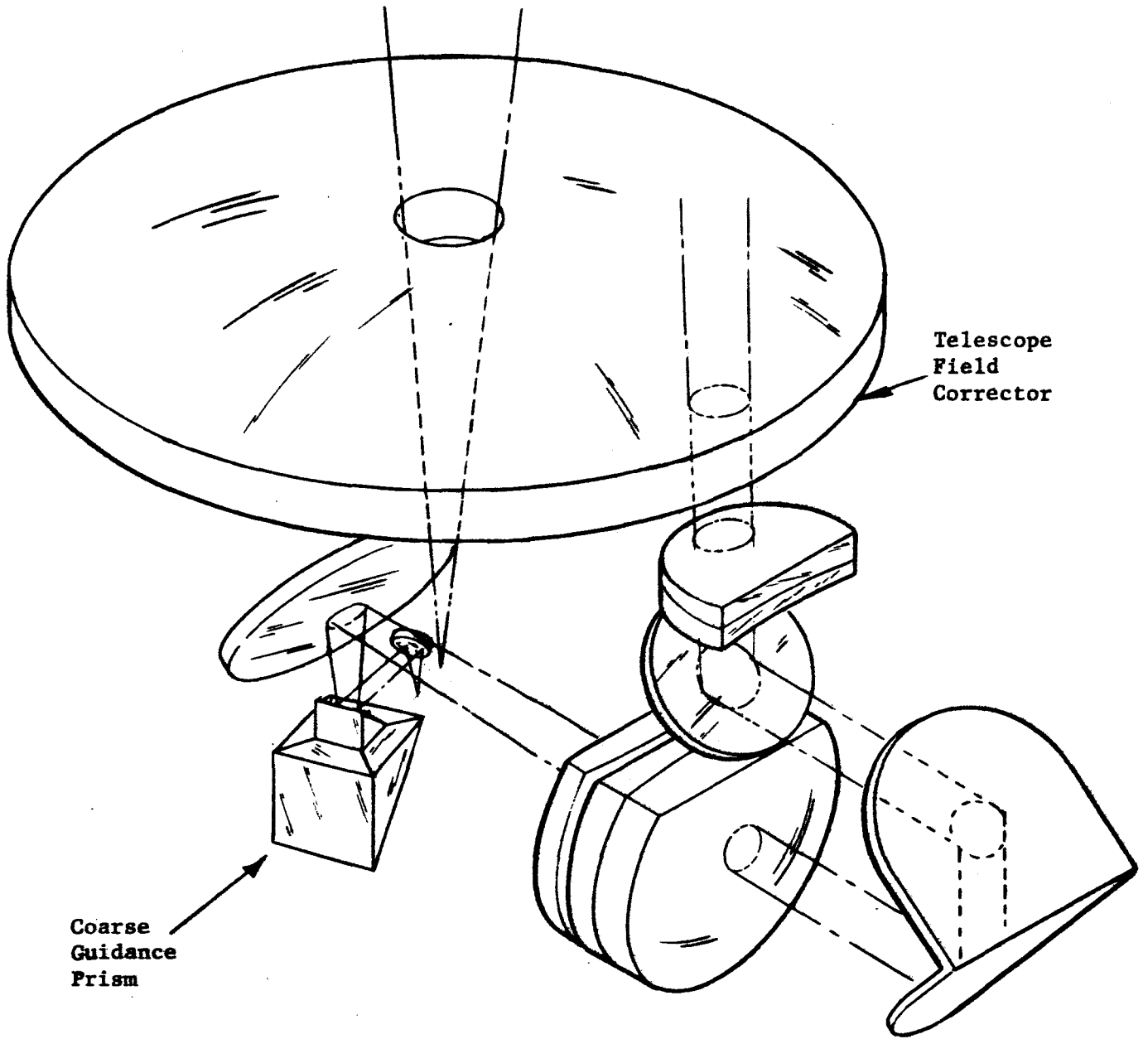


Figure 16. Image Mover in Skewed Position

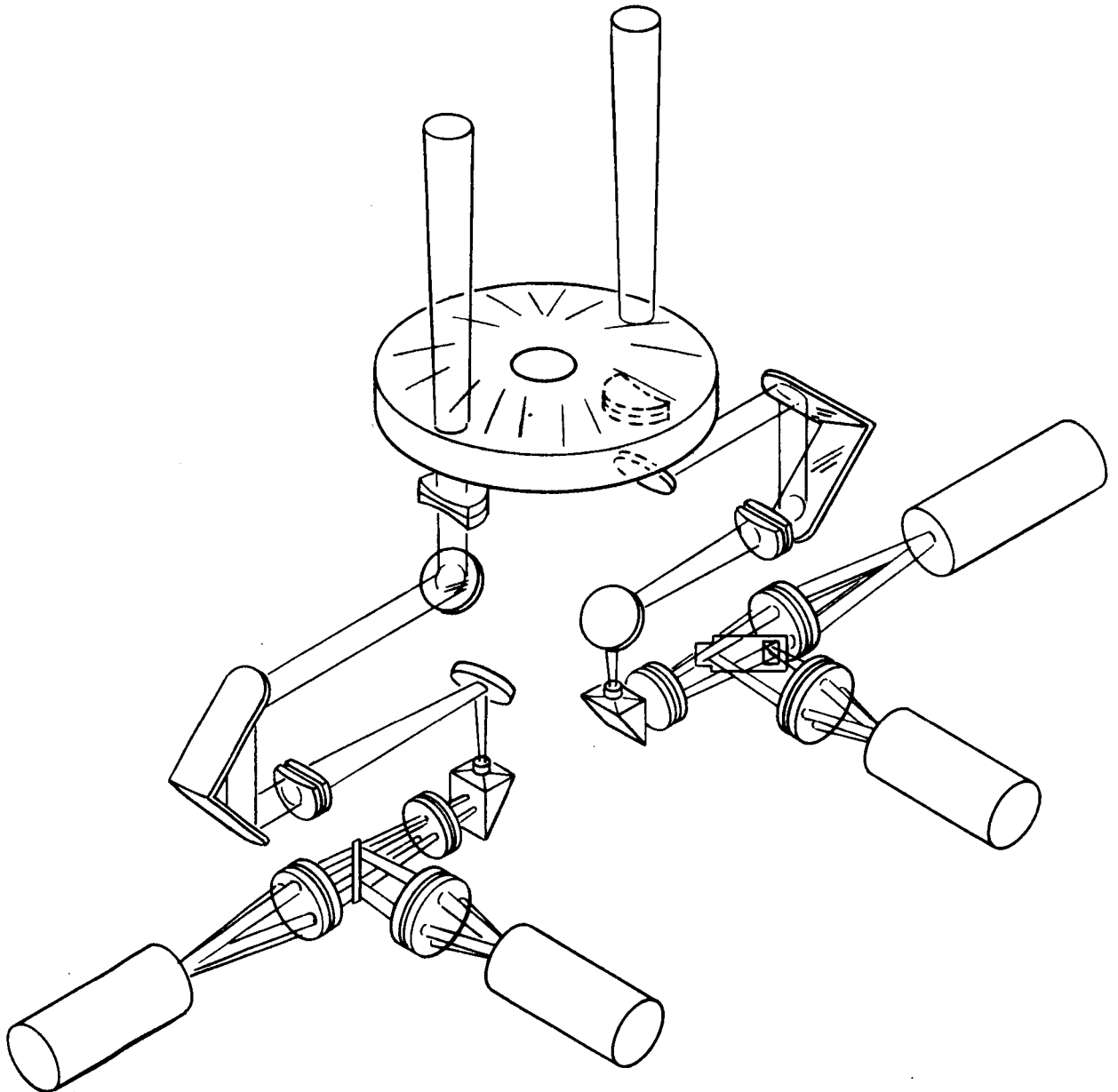


Figure 17. Coarse Pointing System

Guide star images which fall outside of the fine guidance field of view intercept the bevelled top of the coarse guidance prism. This directs the image beam to one of four positions on an optical encoder which causes the various quadrants to be seen alternately by two phototubes. The phase of the resultant signal provides guidance error signals.

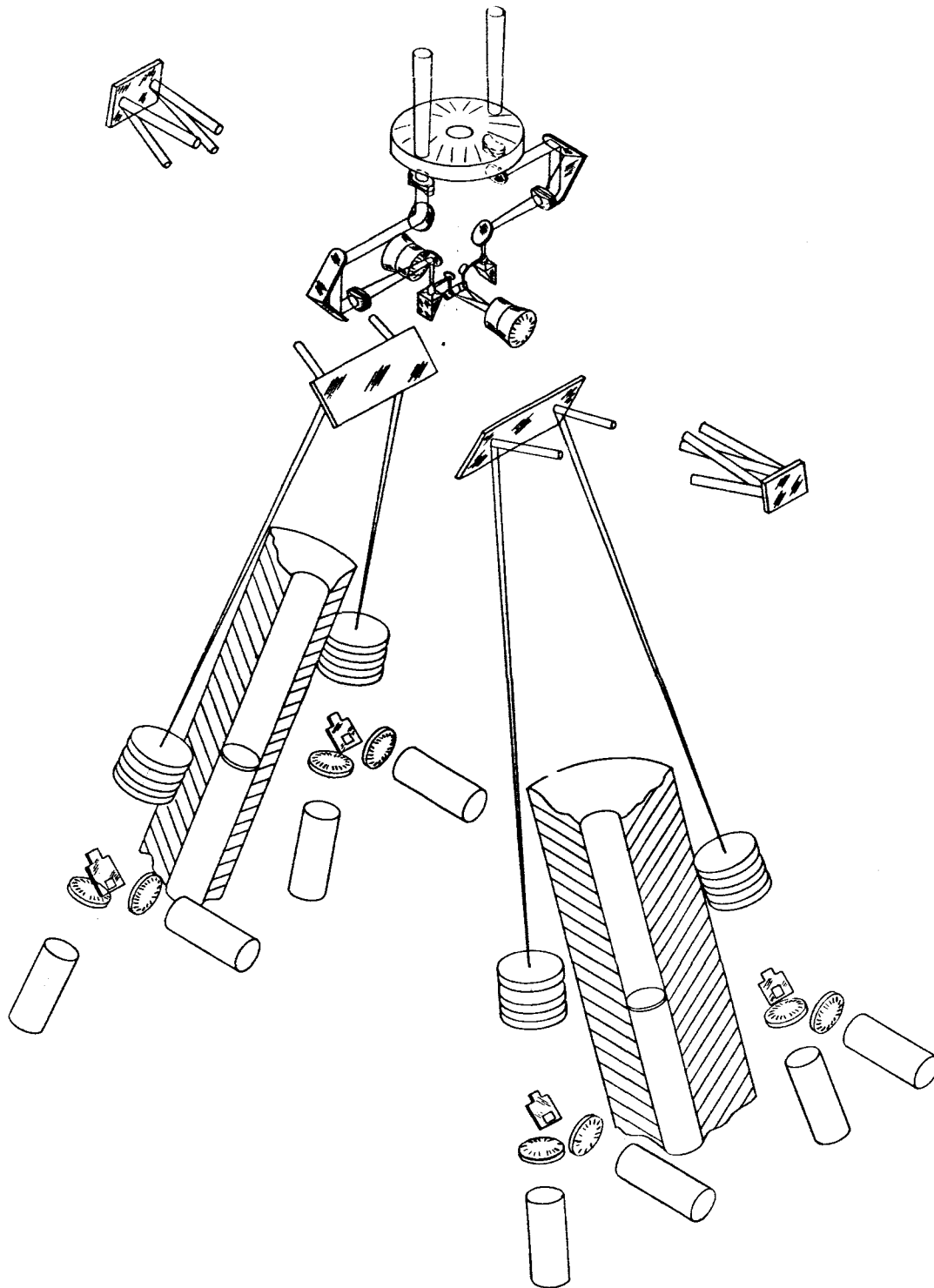
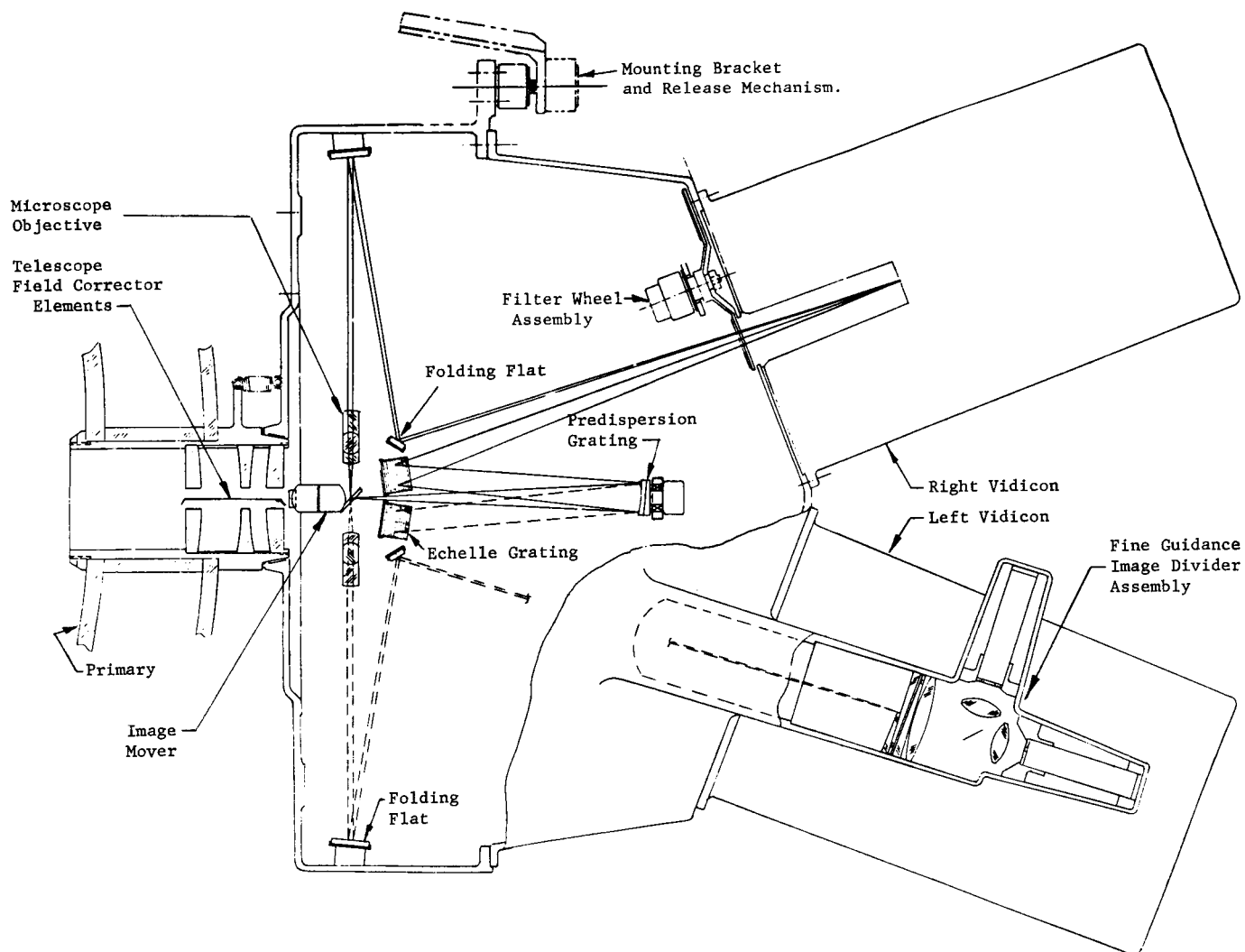


Figure 18. Fine Guidance System

Guide star images are relayed by the image movers to positions close to the optical axis. From here, they follow a path similar to the image beam until intercepting a pair of image dividers in the  $f/200$  image plane.



22

Figure 19. Instrument Package Optical Layout

The section through the fine guidance assembly is out of the plane of this main cross-section.

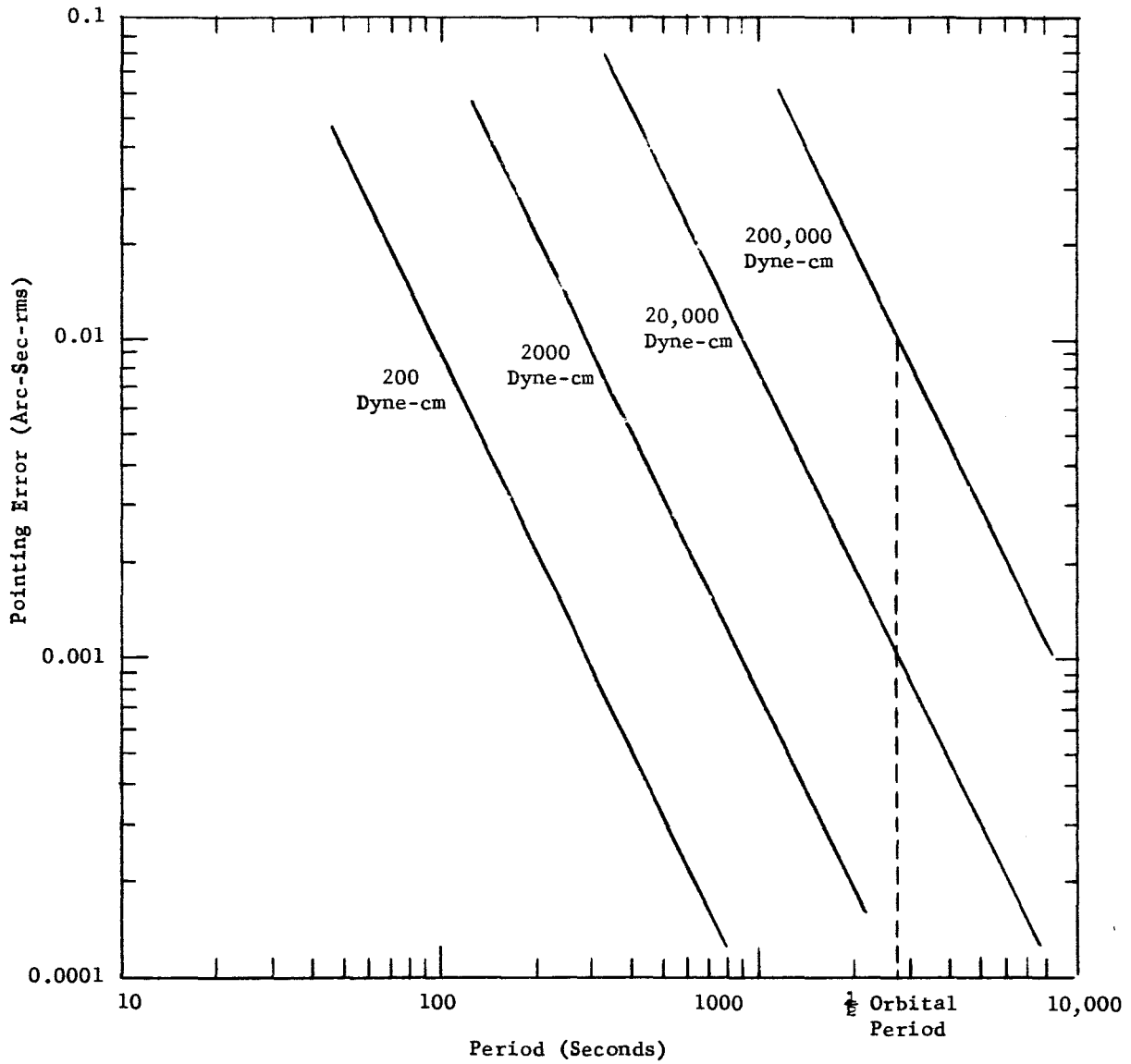


Figure 20. Pointing Errors Versus Disturbance Torques (Final Tracking Mode - Pitch and Yaw Axes)

If various magnitudes and periods of sinusoidal disturbing torques are applied to the telescope pitch and yaw axes, the resulting pointing errors occur for a servo system employing low bandpass techniques.

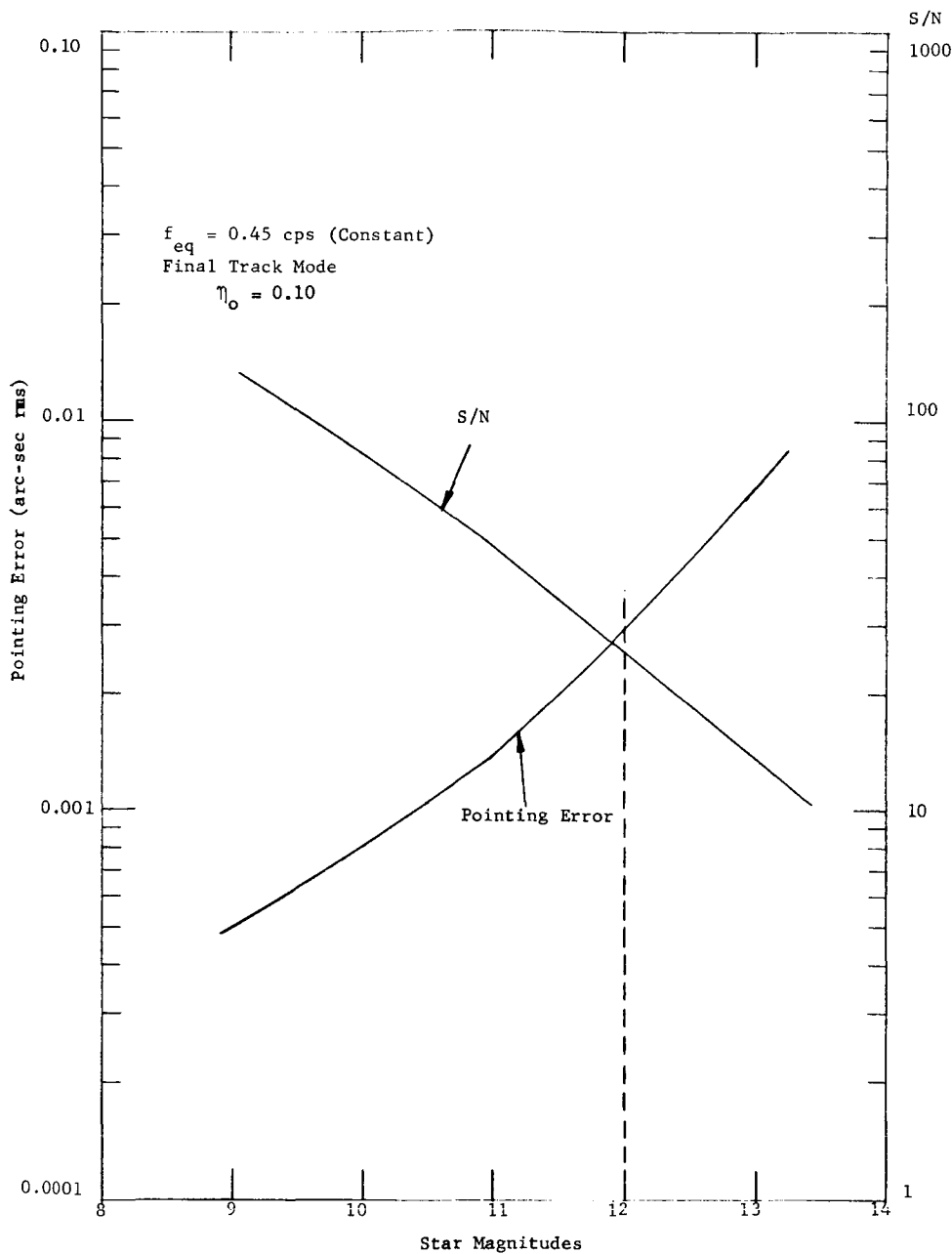


Figure 21. Pointing Error Versus Star Magnitudes (Pitch and Yaw Axes)

The telescope pointing errors due to noise (random) vary as a function of stellar magnitude as shown for a servo system with a constant bandwidth.

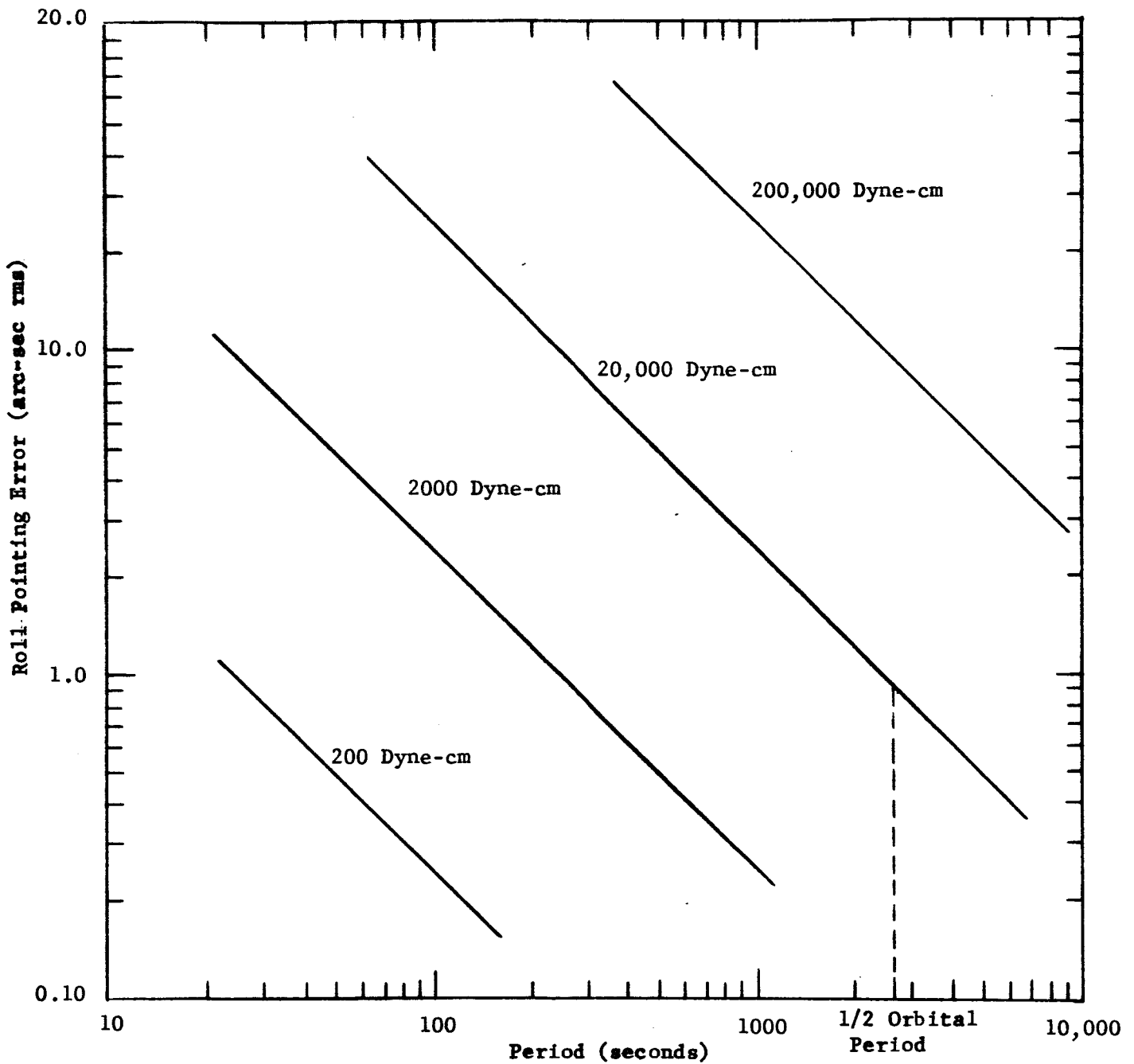


Figure 22. Roll Axis Pointing Errors Versus Disturbance Torques

If various magnitudes and periods of sinusoidal disturbing torques are applied to the telescope roll axis, the resulting pointing errors occur for a servo system employing low bandpass techniques.



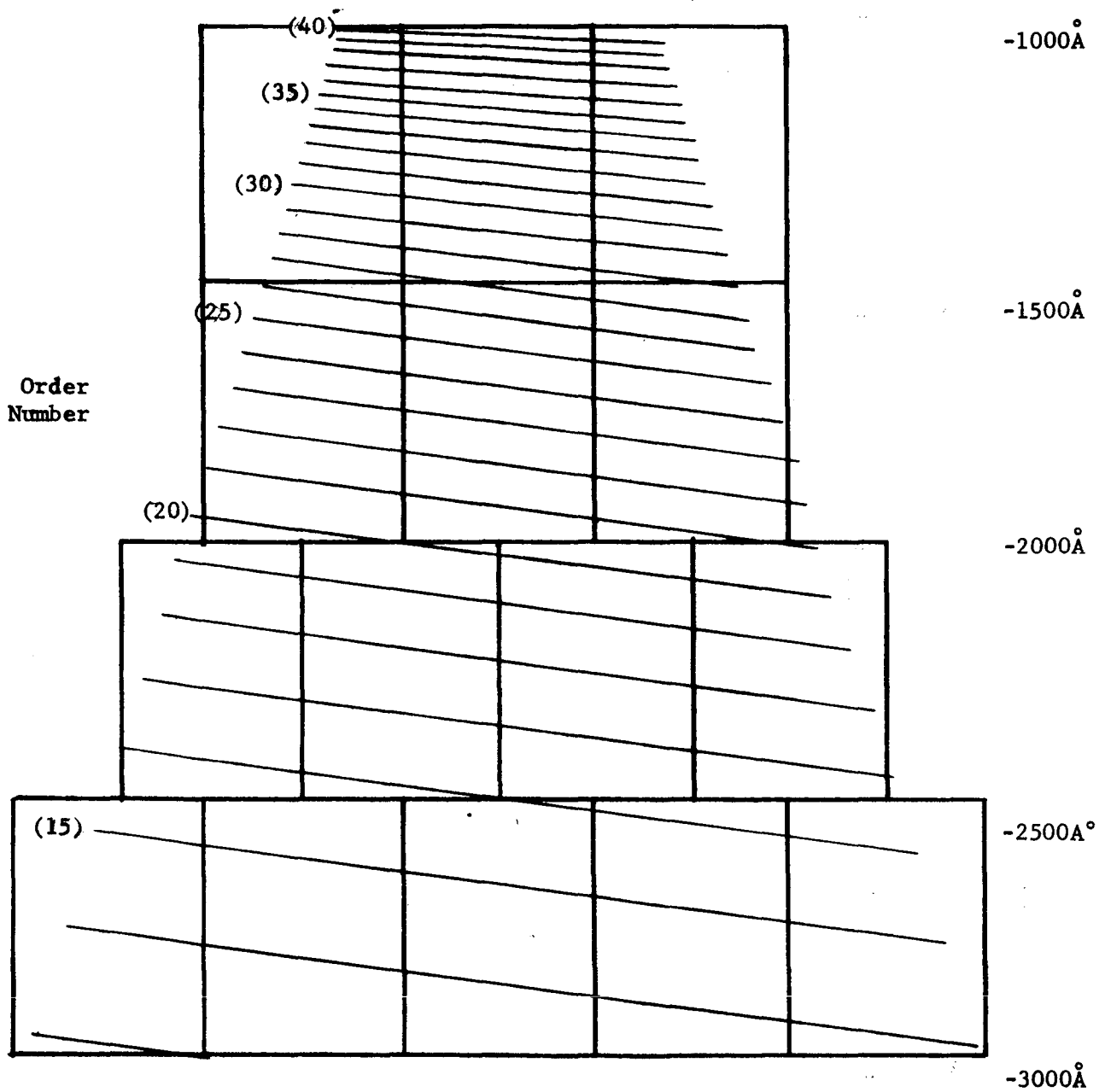


Figure 23. Echelle Spectrograph Format

Lines corresponding to longer wavelengths and lower diffraction orders become longer and the space between them increases rapidly. With a 20 x 15 mm vidicon sensitive surface, a number of steps will be required to cover the complete spectrum.

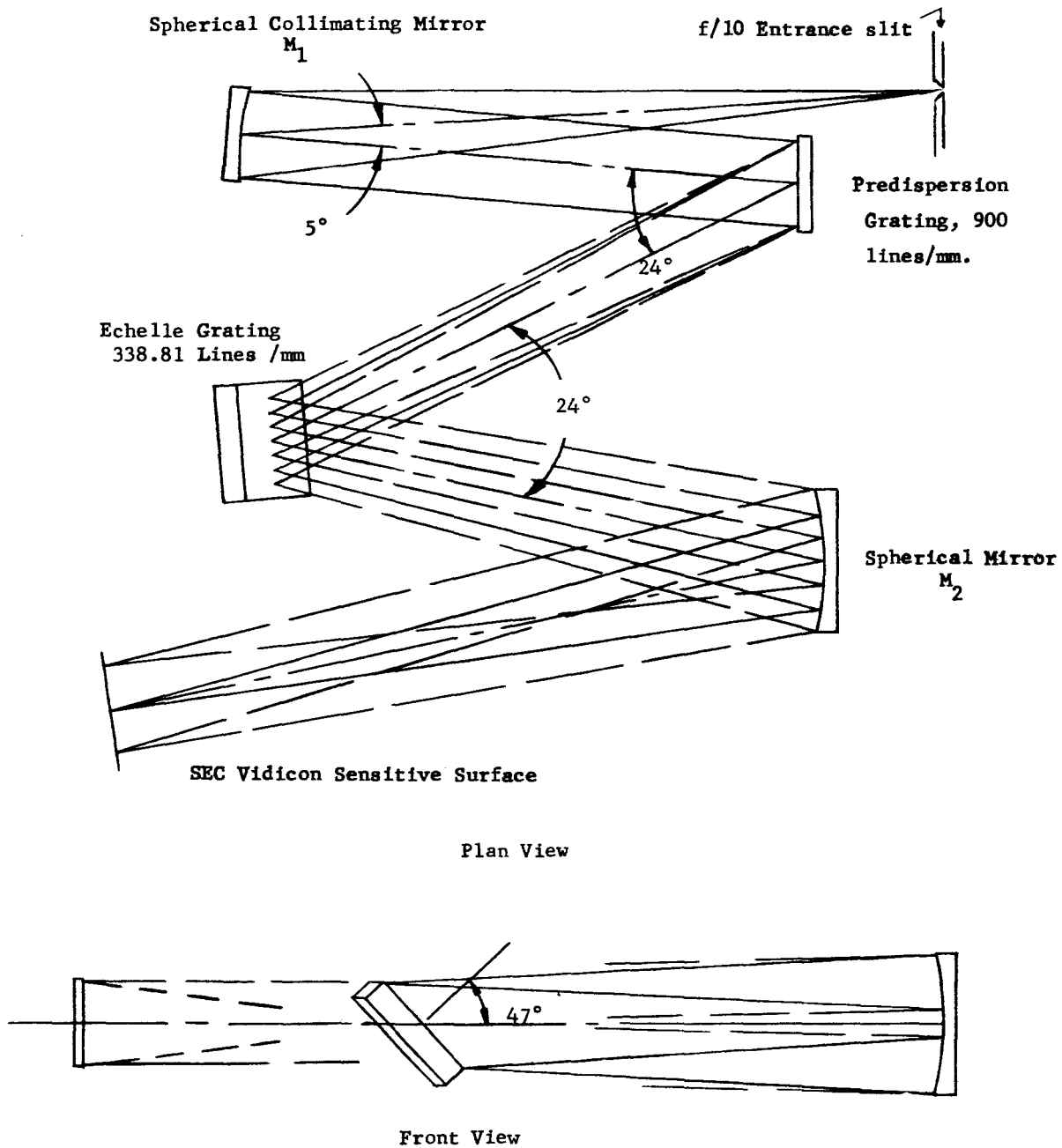


Figure 24. Four-Element Spectrograph

A spherical collimating mirror directs energy onto a flat, low dispersion, predisperser and then onto a flat high dispersion echelle grating. The predisperser and echelle gratings are arranged so that their dispersion directions are crossed. A second spherical mirror focuses the resulting two-dimensional spectrum on the sensitive surface of the vidicon.

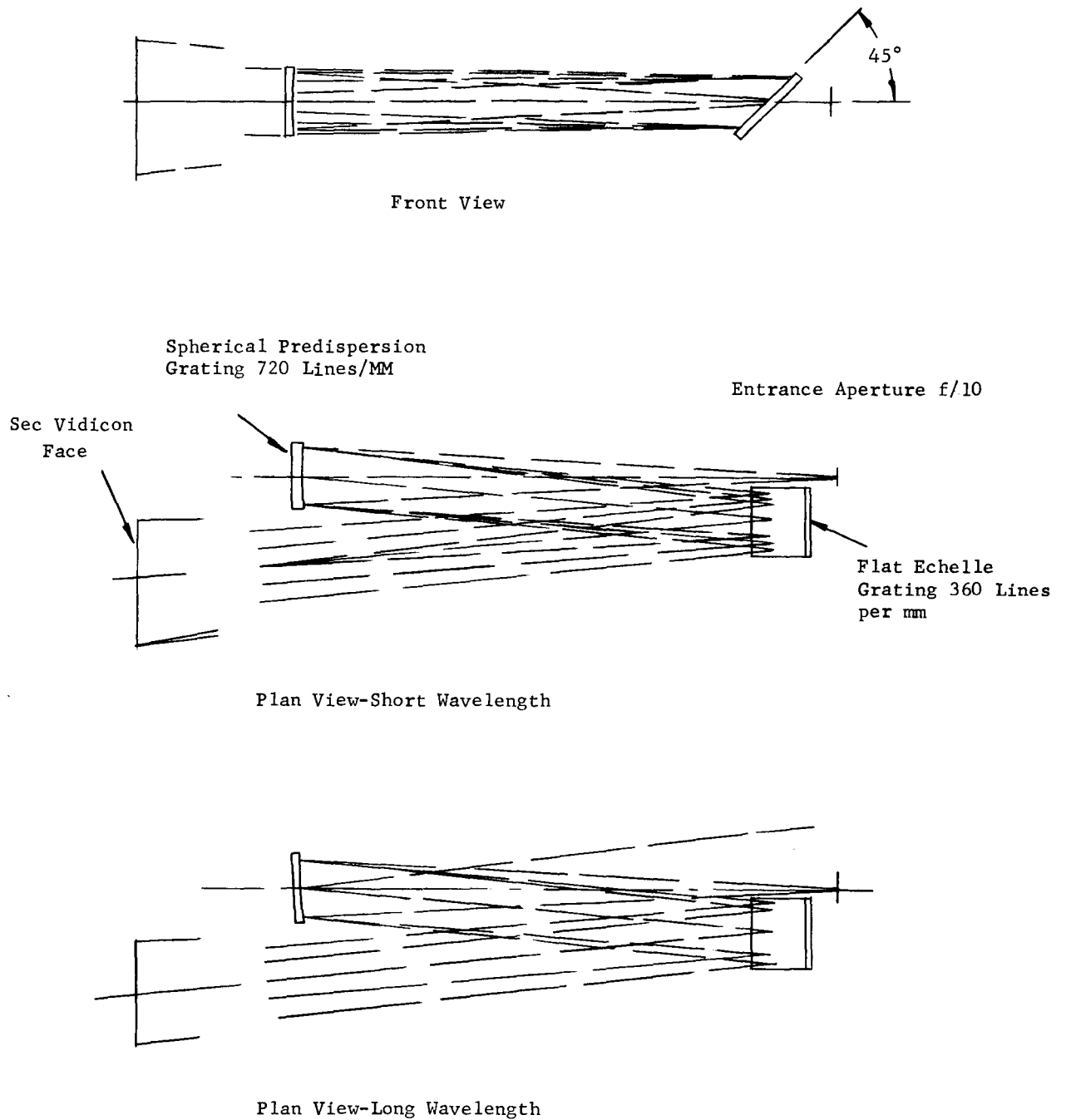


Figure 25. Two-Element Spectrograph Design

A spherical predisperser is arranged so as to direct a converging beam on a flat echelle grating which folds the beam so that it focuses on the vidicon face. The spectral region seen by the vidicon is varied by changes in the orientation of both gratings.

IV. OAQ/APEP in Association with AAP

The benefits and design criteria arising from associating an advanced OAQ experiment with a manned Apollo mission are explored in Volume IV. The study assumes that man-assisted operation of the OAQ occurs during the first 30 days in orbit, but that the OAQ is capable of remote operation during the remainder of its one year expected life. Wherever possible, existing systems and technology are contemplated in order to facilitate a 1972 launch. The results of the study indicate that a gimballed connection between the command module and OAQ vehicle is feasible. A 300 mile orbit appears to be the best compromise to ensure a one-year operational life for the OAQ vehicle and a tolerable radiation hazard to man. Radiation induced fogging and graininess appears to be a significant problem even with very thin photographic emulsions such as those of the Schumann type. Possible means of alleviating this problem include a heavily shielded (using low-z material) film storage container, an extra-vehicular activity (EVA) schedule which avoids photographic exposures during passage through the South Atlantic anomaly, and photographic development immediately following exposure. Limitations and considerations pertaining to the use of film by the astronauts in orbit are shown in the following table and graphs. Indications are that 100 pounds of shielding will permit film survival for eight days.

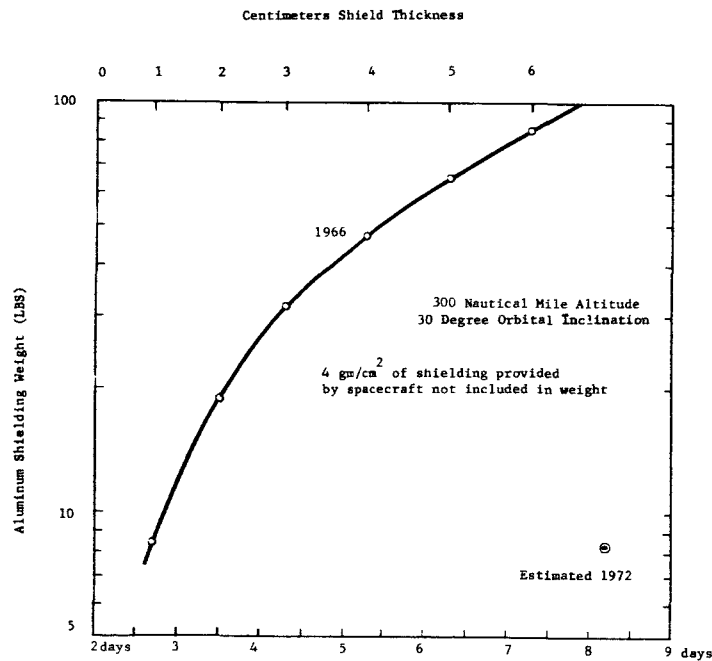


Figure 26. Shielding Weight Needed to Shield a Cylindrical Volume (8 Inch Diameter by 4 Inches) From Doses Exceeding One Radian as a Function of Days Exposure

TABLE 2

ADVANTAGES AND DISADVANTAGES OF SPECTROSCOPIC PLATES AND FILMS (103a AND IIa)

<u>Advantages</u>	<u>Disadvantages</u>
Relatively low reciprocity failure	Relatively high sensitivity to Van Allen Belt radiation.
Relatively high abrasion tolerance	Diminishing spectral sensitivity below 2500Å.
Available in quite convenient forms	Bimat processing not recommended.
Good spectral sensitivity available between 2500Å and 7000Å	Should not be in hard vacuum environment for long time periods.
Acceptable resolving power	

ADVANTAGES AND DISADVANTAGES OF UV COATED SPECTROSCOPIC PLATES AND FILMS (103a AND IIa)

<u>Advantages</u>	<u>Disadvantages</u>
Uniform spectral response possible between 800Å and 3000Å	Plates are not supplied coated. Customer must apply.
May be used in hard vacuum	Some coatings must be removed with a special solution prior to processing.
Relatively high abrasion tolerance	Bimat processing not recommended.
Relatively low reciprocity failure	Spectral sensitivity relatively low.
Coatings do not appreciably reduce inherent film resolving powers	Resolving power relatively low.
Available in quite convenient forms	

ADVANTAGES AND DISADVANTAGES OF "SCHUMANN" EMULSIONS (SWR, DC-3, SC-5, AND SC-7)

<u>Advantages</u>	<u>Disadvantages</u>
Relatively low sensitivity to Van Allen Belt radiation	Resolving power may be slightly lower than desired.
Higher tolerance to vacuum	Reciprocity failure at long exposures.
Relatively high sensitivity in UV	Very low abrasion tolerance. Handling is very difficult. Bimat processing not recommended.
	Available in very limited forms.

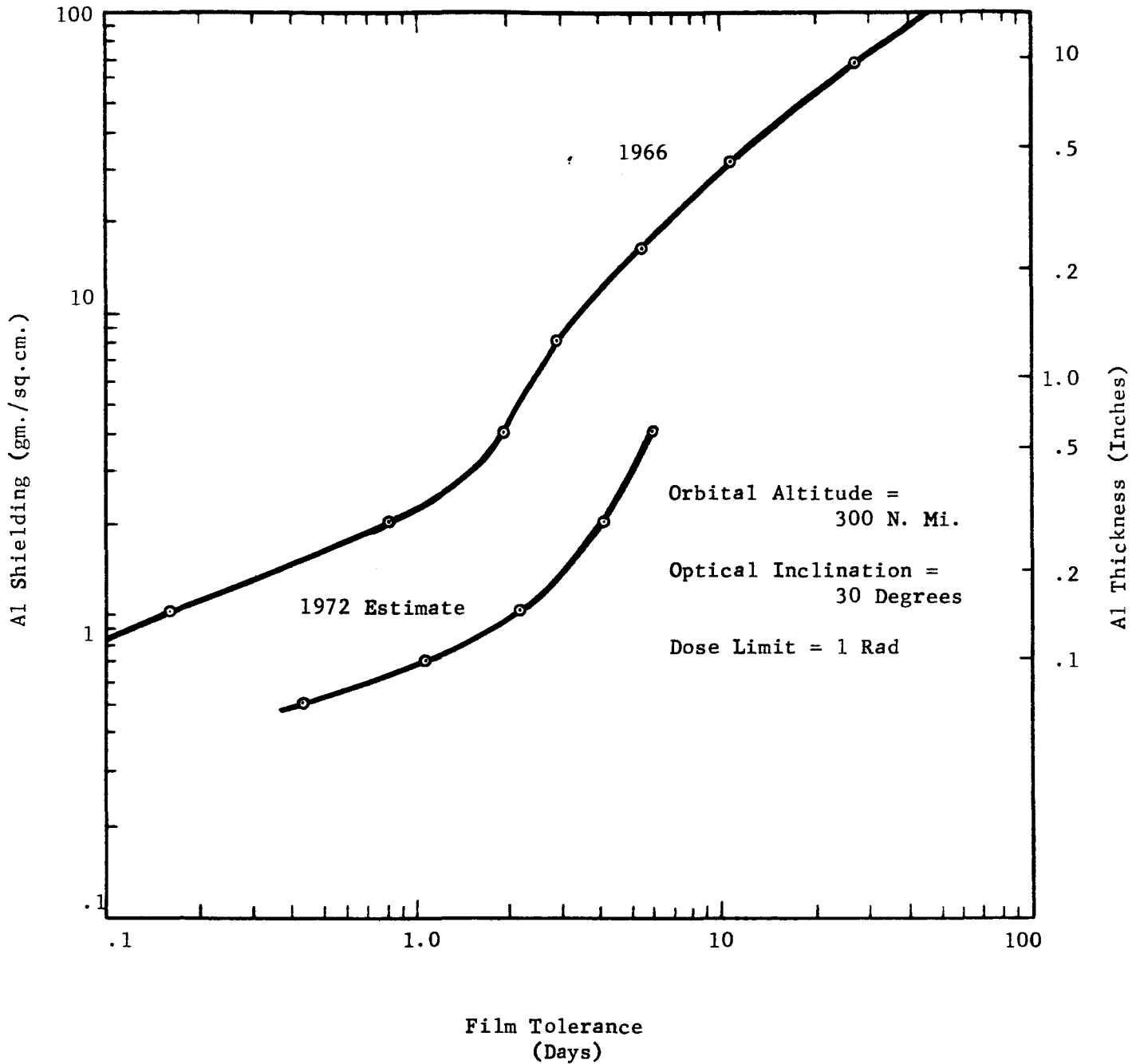


Figure 27. Shielding Requirements as a Function of Number of Days Exposure

#### V. Recommendations for Additional Effort

The following table lists recommendations for future effort and consideration so that the system concept developed in the study can be advanced from a general feasible approach to that of optimization:

TABLE 3

1. The possibility of silicon as a mirror material.
2. Study of radiation effects and hard vacuum on mirror materials and coatings.
3. The possibility of composite mirror structures (quartz egg-crate structure stuffed with aluminum wool).
4. Optimization of radiation coupling of optical elements.
5. Complete thermal analysis (including effect of internal heat sources).
6. Keeping full-scale mock-up current.
7. Design of a breadboard image mover.
8. Optimization of primary optics and relaying microscope design.
9. Selection of a two versus four-element spectrograph through computer analysis.
10. Completion of spectrograph optical design.
11. Further analysis of interlacing the spectrum on the vidicons.
12. Grating development and efficiency measurements of the finally selected gratings. Optical bench setup to verify spectrometer design using visual wavelength model.
13. Allocation of optical element figure tolerance.
14. Further investigation of an optical system with the exit pupil at infinity.
15. Further investigation of coma, and design of a coma detector breadboard.
16. The effect of temperature reduction on reciprocity failure of UV film (particularly on Schumann type emulsions).
17. Further study of processing UV type film in zero-g gravity.
18. Optimization of film shielding including design and configuration.
19. Multiple-axis computer simulation of pointing and magnetic centering servo system. Further study of expected torque disturbance, mechanical resonances, rigid body cross-coupling, and system simplification would compliment this simulation.
20. Further study and implementation of pulse-processing techniques to reduce cosmic ray noise.
21. Electronics systems optimization to reduce power requirements and information system (telemetry) preliminary design.
22. Study of system reliability, failure modes, and modularization for replacement by astronaut.

VI. Selected Design Parameters

Optics: Cassegrain Telescope  
 Primary Mirror 40 Inch Dia, f/2  
 Secondary Mirror 8 Inch Dia, 5X  
 Field of View, Uncorrected approx. 2 arc-minutes  
 Corrected 30 arc-minutes  
 Relaying Microscope 20X  
 Spectrograph (Echelle Type) f/10  
 Wavelength Range 900 to 3000Å  
 Resolution 10,000 (at 1000Å)  
 Recording Sensor SEC Vidicon (nominal)  
 UV Film (during manned portion)

Guidance: Magnetically Suspended Telescope in Spacecraft  
 Guidestar Field 30 arc-minutes  
 Guidestars 1 arc-minutes  
 Initial Position Error for Acquisition  
 Pitch and Yaw Axes ±1 arc-minute  
 Roll ±2 degrees  
 Initial Rate Error for Acquisition 1 arc-min/sec  
 Acquisition Time 2 minutes  
 R.M.S. Pointing Jitter (12th Magnitude Guidestar plus 11th Magnitude star/16 arc-minutes<sup>2</sup> - background) 0.01 arc-second

Spacecraft: Objective High Resolution (Diffraction Limited Performance) Visual and Spectrographic Observation of Stars  
 Orbital Altitude 300 naut. miles  
 Lifetime 1 year  
 Man's Participation OAO Gimbal-connected to AAP  
 Duration - - - - - approx. 30 days  
 Tasks - - - - - Initial Checkout, Malfunction Correction, Photographic Operation of Telescope. Possible Rendezvous at Later Time With Gimbal Re-connection.  
 Earliest Possible Launch - - - - - 1972



**PERKIN-ELMER**

**N66 34370**

Report No. 8346(II)

VOLUME II

## TABLE OF CONTENTS

<u>Section</u>	<u>Title</u>	<u>Page</u>
1.0	INTRODUCTION	1-1
2.0	PRIMARY MIRROR DESIGN CONSIDERATIONS	2-1
	2.1 Present State-of-the-Art	2-1
	2.2 Mirror Materials	2-2
	2.3 Dimensional Stability	2-7
	2.4 Configuration	2-15
	2.5 A Composite Mirror Structure	2-18
	2.6 Active Optical Systems	2-18
	2.7 Coatings for the UV Spectral Region	2-20
3.0	THERMAL CONTROL	3-1
	3.1 The Thermal Environment	3-1
	3.2 Critical Component Temperature Distributions	3-9
	3.3 Thermal Tolerances	3-15
4.0	POINTING SERVO	4-1
	4.1 Theoretical Considerations	4-1
	4.2 Signal-to-Noise Calculations	4-2
	4.3 System Response	4-12
	4.4 Acquisition Considerations	4-26
	4.5 Summary and Conclusions	4-34

## LIST OF ILLUSTRATIONS

<u>Figure</u>	<u>Title</u>	<u>Page</u>
2.1	Fused Silica Coefficient of Expansion Variation With Temperature	2-6
2.2	Mirror Cross-Sections	2-16
2.3	Possible Ribbed Mirror Configuration	2-18
2.4	Active Optics Telescope Systems	2-19
2.5	Refractance of Aluminum Based Reflective Coatings	2-20
3.1	Satellite Geometry	3-1
3.2	Heat Flux Variation in Anti-Solar Direction	3-2
3.3	Heat Flux Variation in Direction Normal to Earth-Sun Line and in Ecliptic Plane	3-2
3.4	Heat Flux Variation in Ecliptic Pole Direction	3-3
3.5	Orbital Variation in Total Heat Flux	3-3
3.6	Tube Segment Analogue	3-6
3.7	Complete Two Node Analogue	3-6
3.8	Maximum Temperature Variation Along Telescope Tube	3-7
3.9	Thermal Behavior of a 40 Pound Aluminum Telescope Tube (40" Dia. x 80" Long)	3-8
3.10	Instantaneous Temperature Distribution in a Semi-Infinite Fused Silica Slab ( $f = 0.566/\text{Hr.}$ )	3-12
4.1	Single Axis Tracking Sensor Utilizing Diffraction Limited Optics	4-3
4.2	Image Light Energy on One Side of a Knife Edge Boundary	4-4

## LIST OF ILLUSTRATIONS (Continued)

<u>Figure</u>	<u>Title</u>	<u>Page</u>
4.3	Maximum Signal to Noise (S/N) Ratio vs. Stellar Magnitude	4-7
4.4	Minimum RMS Pointing Error ( $E_p$ ) vs. Stellar Magnitude	4-8
4.5	Photomultiplier Cathode Dark Current Equivalent Watts	4-9
4.6	Single Axis Tracking Sensor Utilizing a Single Tube and Optical Chopper	4-10
4.7	S/N vs. Field of View	4-12
4.8	Normalized Signal to Noise vs. Field of View	4-13
4.9	Fundamental Guidance Servo Loop (Single Axis)	4-15
4.10	Servo Utilizing Integration (Single Axis)	4-18
4.11	Bode Plots of Servo Loops With Various Levels of Integration	4-22
4.12	Tracking Error vs. Bandwidth (D = 1 Meter)	4-23
4.13	Tracking Error vs. Bandwidth (D = 3 Meters)	4-23
4.14	Single Axis Sensor Static Transfer Function	4-27
4.15	Phase Plane Plots (Undamped Servo)	4-29
4.16	Field of View vs. Initial Rate and Displacement (Undamped Servo)	4-30
4.17	Phase Plane (With Damping)	4-32

## 1.0 INTRODUCTION

Before defining the design considerations for a 40 inch aperture telescope for the Advanced Princeton Experiment Package, it was first necessary to investigate the factors most likely to compromise the resolution capability of a large aperture telescope for space-borne applications. The general problem areas that were considered included a comparison of the susceptibility of various mirror materials and configurations to elastic strain during test, elastic and plastic strain during launch, and thermal strain and long-term dimensional stability during operation. The results of this portion of the study are documented in Section 2.0.

Section 3.0 includes a detailed investigation of the effects of temporal variation in heat flux on the telescope components. Critical design areas resulting from the thermal changes imposed upon the telescope were determined by defining the temperature distributions and thermal tolerances of the optical components particularly the primary mirror.

A detailed theoretical study was also performed to prove the feasibility of achieving the pointing accuracy requirements as defined by stellar magnitude, aperture diameter and system bandwidth. Design concepts were developed for tracking and acquisition that will provide the desired pointing system accuracy (0.01 arc-seconds).

## 2.0 PRIMARY MIRROR DESIGN CONSIDERATIONS

Until very recently the atmosphere placed severe restrictions on astronomy. Turbulence in the atmosphere caused the seeing ability of large telescopes to vary widely but, even at the best of times, did not permit performance approaching the diffraction limit. Moreover, the constituent gases of the atmosphere did not transmit all of the electro-magnetic spectrum but blanked out large portions including the far ultraviolet spectral region. Now that the upper reaches of the earth's atmosphere, and beyond, have become accessible, large increases in resolution and spectral coverage can be anticipated. But, even for optical systems of moderate size, the resolution limit determined by the wavelength-to-aperture diameter ratio is likely to be seriously compromised by imperfections in the optical system. Generally, the largest single contributor of imperfections is the primary mirror.

Imperfections in a space-borne primary can arise from imperfect simulation of zero "g" during test, plastic strain during launch, and thermo-elastic deformation during operation. To a considerable degree, these sources of error can be minimized with a mirror material and configuration having the appropriate combination of properties. However, before any material is selected on the basis of otherwise desirable physical properties, it is also necessary to consider the long term dimensional stability as well as any anomalous effects brought about by nominal temperature changes. This apparently eliminates a large proportion of mirror material candidates but there remains at least one material besides fused silica which holds some promise for future space-borne optical systems. It also appears possible to combine fused silica and aluminum in a composite structure having the dimensional stability of a fused silica eggcrate and an enhanced conductivity due to the presence of aluminum.

### 2.1 PRESENT STATE-OF-THE-ART

An example of the present state-of-the-art in the manufacture of large mirrors is provided by the 36-inch diameter Stratoscope II mirror, completed about mid-1964. This mirror was ground, polished, and figured in the optical shop in the normal fashion. Testing was done in a horizontal tunnel by autocollimation against a large flat until the mirror appeared error-free under these conditions. Final figuring was carried through seven separate stages beginning with a small pitch lap 6 inches long and 2 inches wide and finally ending with an optician's thumb. After each figuring, the mirror was cleaned, silvered, centered on a special mount and tested in a vertical vacuum tank. During the first five figuring stages, the Foucault test was used to assess the mirror figure. During the last two stages, a method based on the scatterplate interferometer and suggested by Burch was employed. Over 1000 precise measurements were taken to locate the fringe centers on a single photographic plate and this data was fed into a digital computer to derive figure error. The final figure was determined to have an rms deviation from the closest fitting parabola of about  $\lambda/50 \pm 10\%$ . The figure contour predicted by the Burch scatterplate method was qualitatively confirmed by subsequent Foucault tests; however, at this time, no alternate method of testing was available which provided measurement precision comparable with the Burch test.

Since the completion of the Stratoscope II mirror, other large mirrors for space-borne systems have been started. Some difficulties have been experienced with sandwich structures which differ from the solid Stratoscope blank, however, the experience gained on Stratoscope is markedly evident. Measurement techniques are also in the process of being refined; considerable impetus being obtained from the availability of stable laser sources providing high intensity illumination with collimator source apertures of only a few microns diameter. At present, the most difficult task appears to be simulation of the zero "g" environment of space.

## 2.2 MIRROR MATERIALS

A wide variety of materials are possible candidates for mirror blanks. Glasses such as fused silica or pyrex have been used extensively in the past primarily because they take a satisfactory optical polish directly. However, techniques have been developed whereby thin hard films can be deposited on relatively soft crystalline materials, such as aluminum and beryllium, and polished to yield good optical surfaces. An example is the Kanigen process which results in a hard, chemically deposited film of nickel phosphide if the substrate is metallurgically uniform. Nonuniformities result in holes or bubbles which have proven to be particularly troublesome on some aluminum alloy surfaces in the past. Other techniques include vacuum spattering of silicon monoxide and silicon dioxide films of sufficient thickness to form a polishable surface. Film deposition usually results in a slight warping which must be allowed for in the thickness before polishing. Usually, a film thickness of several mills is adequate.

The properties of a variety of possible mirror materials are shown in Table 2-I. A high modulus of elasticity to density ratio is important since it determines the amount of care that must be lavished on the mirror support structure during test and, to a lesser degree, during grinding and polishing. As an example, the Stratoscope mirror was floated on an arrangement of 15 counter-weighted push rods and maintained within  $\pm 0.002$  inch of the test cell center. Assuming a weight imbalance proportional to the mirror volume then it can be shown that the resulting deflection varies as the fourth power of the mirror diameter. While lightweight structures suffer less deformation than solid structures of the same thickness, the strong variation of mirror deformation with size is inescapable. In order to alleviate mirror deformation during testing, insofar as this is possible, and for other reasons relating to dimensional stability and resistance to thermoelastic deformation, large diffraction limited mirrors are more likely to be massive structures than thin shells. Using  $E/\rho$  as a criterion, it would appear that beryllium offers the best possibility for a thin, light mirror structure. Second best, and a long way back, is silicon which is still 50% better than fused silica.

Not included in Table 2-I is yield strength which is nominally 40 Kpsi for beryllium, 23.8 Kpsi for silicon and approximately 10 Kpsi for fused silica. A high yield strength appears to infer an increased ability to withstand launch accelerations without taking a permanent set. However, in a mirror structure, a permanent set of  $10^{-8}$  inches per inch can be deleterious.

TABLE 2-1

PHYSICAL PROPERTIES OF MIRROR MATERIALS \*\*

MATERIAL	DENSITY ( $\rho$ ) gm/cm <sup>3</sup>	MODULUS OF ELASTICITY (E) Newtons/cm <sup>2</sup>	THERMAL CONDUCTIVITY (K) Cal/cm sec °C	SPECIFIC HEAT Cal/gm°C	COEFFICIENT OF EXPANSION ( $\alpha$ )* °C <sup>-1</sup>	E/ $\rho$	1/C $\rho\alpha$	K/C $\rho\alpha$	K/C $\rho$
Fused Silica	2.20	7.0x10 <sup>6</sup>	0.0033	0.188	0.55x10 <sup>-6</sup>	3.18x10 <sup>6</sup>	4400x10 <sup>3</sup>	14.50x10 <sup>3</sup>	0.008
Pyrex-7740	2.35	6.8x10 <sup>6</sup>	0.0027	0.250	3.20x10 <sup>-6</sup>	2.89x10 <sup>6</sup>	530x10 <sup>3</sup>	1.44x10 <sup>3</sup>	0.0046
Aluminum	2.70	6.9x10 <sup>6</sup>	0.5300	0.215	23.90x10 <sup>-6</sup>	2.56x10 <sup>6</sup>	72x10 <sup>3</sup>	38.20x10 <sup>3</sup>	0.92
Beryllium	1.82	28.0x10 <sup>6</sup>	0.3800	0.450	12.40 10 <sup>-6</sup>	15.40x10 <sup>6</sup>	99x10 <sup>3</sup>	37.50x10 <sup>3</sup>	0.465
Invar (36% Ni)	8.00	14.8x10 <sup>6</sup>	0.0260	0.095	1.30x10 <sup>-6</sup>	1.85x10 <sup>6</sup>	1000x10 <sup>3</sup>	26.30x10 <sup>3</sup>	0.034
Silicon	2.33	13.0x10 <sup>6</sup>	0.3900	0.168	4.15x10 <sup>-6</sup>	5.56x10 <sup>6</sup>	610x10 <sup>3</sup>	240.00x10 <sup>3</sup>	1.0

\* At 20°C

\*\* All properties taken from reference (18) except for those of silicon which were taken from reference (15).



To infer an elastic limit of this order, even on a relative basis, from yield strengths seems to be a gross assumption; particularly when the materials being compared are as inherently different as fused silica and beryllium. Resistance to the accelerations produced in the launch environment also depends on the damping ability of the mirror material and the support structure. Fused silica has an exceptionally high Q and requires special precautions if destructive ringing is to be avoided.

Nonuniform temperature distributions create stresses and strains in the mirror structure and, consequently, a loss of optical figure. These can arise from variations in the radiant heat flux absorbed in the primary, or from conductive heat transfer at points where the primary is connected to other parts of the telescope structure. Whether the cause of a nonuniformity is conductive or radiative in nature, the predominant process responsible for the dissipation of the excess heat at an anomaly is almost always conduction. This can be illustrated by considering the change in radiative heat flux due to an incremental change in temperature which is given by

$$\frac{dQ}{dT} = 4\epsilon\sigma T^3 \quad (2-1)$$

where

- dQ = incremental change in heat flux
- dT = incremental change in temperature
- $\epsilon$  = surface emissivity
- $\sigma$  = Stefan-Boltzman constant
- T = absolute temperature

Taking a portion of the front surface of the mirror where the emissivity might be about 0.01 and the ambient 273°K;

$$(\epsilon = 0.01) \quad \frac{dQ}{dT} = 1.1 \times 10^{-6} \text{ Cal/cm}^2 \text{ sec } ^\circ\text{K}$$

Similarly, for a portion of the back surface of the mirror which might be painted black to achieve an emissivity near unity (not necessarily a recommended design philosophy);

$$(\epsilon = 1.0) \quad \frac{dQ}{dT} = 1.1 \times 10^{-4} \text{ Cal/cm}^2 \text{ sec } ^\circ\text{K}$$

Assuming two points on a constant cross-section with an incremental temperature difference between them to be a somewhat analogous situation for conductive heat transfer, then;

$$\frac{dQ}{dT} = \frac{K}{l} \quad (2-2)$$

where

- $K$  = thermal conductivity of the material  
 $l$  = separation between the two points having  
the temperature difference.

The conductive heat path length required to balance heat dissipation due to radiation with that due to conduction can be determined by setting equations (2-1) and (2-2) equal and solving for  $l$ . For fused silica (Table 2-I), this amounts to 3000 cm for the case of a highly reflective front surface and 30 cm for the case of a black back surface. For silicon both numbers are over two orders of magnitude higher.

This type of comparison does not permit classification of mirrors into two categories depending on whether heat conduction or heat radiation plays the dominant role in dissipating heat from anomalous temperature regions. This is at least partially determined by the size and location of the anomaly, etc. However, the comparison does indicate that radiative heat transfer is probably most significant in large, fused silica, egg-crate mirror structures. In this case, radiation serves to couple the front plate to the back plate and the back plate to its immediate surroundings if it is not aluminized. Radiative heat dissipation probably plays a minor role in solid fused silica mirror structures which are aluminized front and back, and also in metal mirror structures, whatever the configuration.

The amount of thermo-elastic distortion accompanying a given temperature distribution is an extremely complex analytical problem for any but the simplest physical configurations and temperature distributions. However, in situations where the temperature distribution is independent of the material conductivity, then the relative amounts of distortion are proportional to the magnitude of the temperature deviation and coefficient of expansion. Assuming the temperature deviation to be inversely proportional to the specific heat (as it can be in a dynamic situation), leads to the use of  $1/C\rho\alpha$  as a mirror material criterion. This is shown for a variety of materials in Table 2-I, but is only applicable to fused silica and Pyrex since it is only with these materials that the amplitude and size of the anomalous temperature regions are likely to be independent of the material conductivity. Where the physical properties of the mirror material determine the temperature distribution then  $K/C\rho\alpha$  appears to be a more suitable criterion. This is shown in Table 2-I along with  $K/C\rho$ . The latter is known as the thermal diffusivity and is inversely proportional to the time constant of the mirror structure. A short time constant (large  $K/C\rho$ ) is generally considered desirable since it minimizes the time required to adjust to a new thermal environment.

Using  $K/C\rho\alpha$  as a basis, silicon appears to be the best mirror material being about 6 times better than runners-up, aluminum and beryllium, and an order of magnitude or so better than fused silica depending on the operating temperature and the relative importance of conduction and radiation in dissipating the heat from anomalous temperature regions. The low

coefficient of expansion of the type of Invar used in the comparison did not compensate sufficiently for the low heat conductivity to provide any obvious advantage. There are special Invar compositions which do have coefficients of expansion which are much smaller than the one chosen as an example<sup>1</sup> but the coefficient is small only over a narrow temperature range which detracts from the usefulness of such materials.

The data in Table 2-I provides a reasonably good comparison if the operating temperature range is close to the temperature range over which the coefficient of expansion was measured. In space-borne systems the operating temperature of mirrors and associated structures is often far below the nominal temperatures inferred in Table 2-I and, as a result, the coefficient of expansion can differ markedly. Fused silica is such an example; the coefficient of expansion falls with temperature and, in fact, crosses zero at temperatures which vary widely depending on the supplier. Figure 2.1 shows the variation of coefficient with temperature for a typical sample (Engelhard Industries, Inc., Hillside, New Jersey). The coefficient of expansion of silicon does not exhibit any marked temperature dependency.

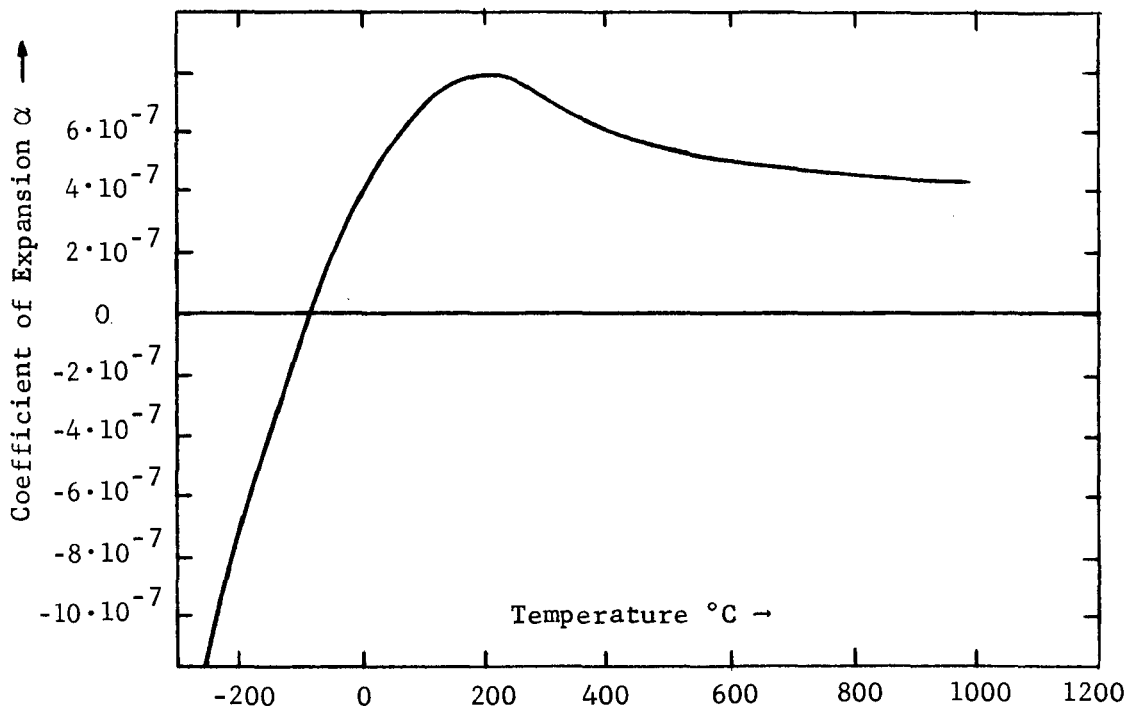


Figure 2.1. Fused Silica Coefficient of Expansion Variation with Temperature

A number of de-vitrified glass materials such as Pyroceram (Corning Glass Works, Corning, New York) and Cer-Vit (Owens-Illinois, Toledo, Ohio) have recently become available. These materials can be tailored to hug the zero coefficient of expansion line over an extended temperature range. Unlike the early types of Pyroceram, the new materials closely resemble true glasses, are polishable, and do not exhibit the severe scattering of earlier materials.

Even more recently, a true glass having an extremely low coefficient of expansion has been developed by Owens-Illinois. The new material is designated as type RZ glass and has a zero expansion coefficient at selected temperatures. Apparently, there are quite a few glass forming systems which only require adroit manipulation to achieve a coefficient of expansion which crosses zero near the intended temperature. Thus, in the future, there are likely to be as many zero expansion glasses available as there are glass manufacturers. Assuming the behavior of the new glasses to be similar to that of fused silica, then the coefficient of expansion will be within  $\pm 0.1 \times 10^{-6}/^{\circ}\text{C}$  over a  $20^{\circ}\text{C}$  temperature range.

In conclusion, it is perhaps worth noting that fused silica tailored to have a coefficient of expansion of  $0.1 \times 10^{-6}/^{\circ}\text{C}$  is still a factor of three below silicon if  $K/C\rho\alpha$  is used as a basis of comparison, and a factor of two below silicon using  $E/\rho$  as a criterion. Furthermore, the thermal diffusivity of silicon is 125 times that of fused silica indicating a proportionally shorter time constant.

### 2.3 DIMENSIONAL STABILITY

Although mirror materials resistant to deformation in deleterious thermal and "g" force environments are desirable, the very possibility of a diffraction-limited telescope design is predicted upon the existence of materials which exhibit sufficient dimensional stability. Present evidence indicates that sufficient stability in this case is not to be taken for granted, but may be difficult to find; particularly in combination with desirable properties such as a high thermal diffusivity and strength-to-weight ratio.

The stability required to achieve diffraction-limited performance in a large mirror can be estimated from the maximum strain corresponding to the just tolerable surface deviation. For a mirror blank which is bent so as to become slightly cylindrical, the maximum strain occurs at the front and back surfaces and is given by

$$\epsilon_{\max} = \frac{4d}{D} \left( \frac{\lambda}{n} \right) \quad (2-3)$$

where

$d$  = mirror blank thickness

$D$  = mirror blank diameter

$\frac{\lambda}{n}$  = peak-to-peak mirror surface tolerance

Taking the 36-inch Stratoscope mirror as an example: the rms figure corresponds to about  $\lambda/50$  at  $5461\text{\AA}$ , which is equivalent to about  $\lambda/20$  on a peak-to-peak basis. Assuming a dimensional instability tolerance equal to the figure error, and taking the mirror thickness as 5.5 inches, then from equation (2-3), the instability tolerance corresponds to a maximum strain of  $2 \times 10^{-8}$ . This is an incredibly small number which illustrates exceptional dimensional stability required by large diffraction-limited mirrors.

### 2.3.1 Experimental Evidence

Generally speaking very little information is available on the dimensional stability of materials subject to low stresses and nominal temperatures. Of the available data, perhaps the most comprehensive is the research done by the M.I.T. Department of Metallurgy.<sup>2,3</sup> This work has included an investigation of dimensional changes occurring in a constant temperature environment as well as changes induced by cyclic temperature changes. The test specimens were rods  $3/8$  inch in diameter and 4 inches long, and included wrought and cast alloys of iron, aluminum, magnesium, copper and nickel which had undergone various heat treatments.

The time stability of the various specimens was investigated for aging temperatures at  $20^{\circ}\text{C}$  and  $70^{\circ}\text{C}$ . Changes in specimen length were determined over the period of a year and were referenced to the length determined approximately 20 minutes after completion of the last step in the heat treatment. During the first 24 hours, dimensional changes were found to occur in nearly all the test specimens. Subsequent changes measured one month and twelve months after heat treatment varied widely from the experiment accuracy limit ( $\pm 3$  microinches per inch) to 45 microinches per inch for one aluminum alloy. All groups of alloys were found to exhibit some instability with deformations of 10 microinches per inch being fairly common. Aluminum and Invar were among the most unstable materials. For Invar, it was concluded that room temperature changes are attributable to lattice changes in the austenite phase and to the relief of residual stresses.<sup>4</sup> Stability was enhanced by heat treatments aimed at stress relief and by reduced carbon content. Several combinations of aluminum alloys and heat treatments were found to be stable. Commercially pure aluminum proved to be too soft for the measurement technique.

The stability of alloys in a changing thermal environment was gauged by measuring changes in the test specimens after 10 temperature cycles between  $20^{\circ}\text{C}$  and  $-70^{\circ}\text{C}$ . A large spread was apparent in the results. Aluminum alloys exhibited a change ranging up to 190 microinches per inch.

Intercomparison of nine standard meter bars by the National Bureau of Standards has also provided some information on material stability.<sup>5</sup> Comparative measurements carried out over the past twenty years to an accuracy of about 0.1 micron have shown that the length of the four platinum-iridium standards of length have remained within the accuracy of measurement; but, the standards composed of other alloys have varied appreciably. Meter 752 (Fix Invar) has shown an approximately linear shrinkage with time amounting to over 7 microns in a twenty-year period, whereas meter 39 (Invar) and meter 153R (42% nickel-steel) have expanded about 4.5 and 1.5 microns respectively. Measurements on meter 39 which extend over a period of nearly half a century indicate that the rate of change has decreased by about a factor of three or four since this standard was first acquired.

More recently, Meyerson et al,<sup>6,7</sup> have examined the stability of gauge blocks using an interferometer. Instabilities in the order of a micro-inch per year were found to be relatively common; however, a number of materials were found which fell within the NBS goal of  $0.2 \times 10^{-6}$  per year.

Experience gained by Meinel<sup>8</sup> in investigations of aluminum mirrors has not been encouraging. All of the large aluminum mirrors tested by Meinel showed a figure degradation at low temperatures and, in one case, the figure loss was permanent, resulting in an edge curled above and below the mean surface by 0.003 inch.

Beryllium has often been touted as an ideal mirror material because of its outstanding strength-to-weight ratio and high thermal diffusivity. Unfortunately, beryllium has one weak point: the crystal lattice is a closely packed hexagonal structure which is anisotropic with respect to the coefficient of expansion. Preparation of beryllium structures using powder metallurgy techniques removes much of the anisotropy; the remainder depends upon the particle size, geometry and fabrication techniques. Jennings et al,<sup>9</sup> using 1.25 inch cubes covered with resistance strain gauges, have determined the anisotropic thermal expansion coefficient produced by a variety of fabrication methods. This ranged from  $0.05 \times 10^{-6}/^{\circ}\text{F}$  for some hotpressed beryllium to  $1.15 \times 10^{-6}/^{\circ}\text{F}$  for heavily worked forged beryllium. Taking the smaller value, which was close to the limit of experimental accuracy, then the maximum temperature excursion that could be tolerated by a 36 inch,  $\lambda/20$  beryllium mirror amounts to only 35°F. Since the average anisotropy in a large mirror blank might reasonably be expected to be larger than in a 1.25 inch cube, the 35°F temperature estimate may be generous. Beryllium can therefore be excluded from serious consideration as a spaceborne mirror material because of its anisotropy and the large temperature excursions normally encountered by such mirrors between the testing and operating environments. The stability of beryllium is a matter of some controversy. Atwood et al<sup>10</sup> have shown that cooling the anisotropic crystalline structure of beryllium from the phase transition temperature leads to  $10^{10}$  times more strain energy than is required to strain a one-meter diameter mirror out of tolerance.

The stability criterion used in judging the M.I.T. test specimens, and the NBS meter bars and gauge blocks was the absolute change in length in one direction. This criterion is not directly applicable to the mirror problem, since a uniform change in all directions would alter the size but not the figure of a mirror. Directional nonuniformity is inferred by the generally accepted theory that stress relief and metallurgical instabilities are chiefly responsible for dimensional changes, since there is no reason to believe that stresses or concentration gradients are symmetrically arranged in all structures. The Stratoscope mirror and the aluminum mirrors tested by Meinel provide data which are directly applicable to the mirror materials problem. Data for the former include tests conducted after the mirror had withstood the rigors of an extended operational period. This showed the figure to be unaltered and indicates that fused silica is an exceptionally stable mirror material. Meinel's experience with aluminum mirrors, while not all-encompassing, is a poor prognosis for the use of this material in future spaceborne telescope mirrors. Even more unlikely is the use of beryllium as a spaceborne mirror material since the measured anisotropy in the best beryllium compositions is sufficient to cause figure loss with a nominal temperature change.

There are a number of mirror materials besides aluminum and beryllium which have superior thermal properties to fused silica and, therefore, deserve serious consideration. However, there are virtually no experimental data which might indicate the stabilities of these materials, and it is therefore necessary to base any judgments that might be made on theory.

### 2.3.2 Energy of Deformation

The spontaneous relaxation (microcreep) of materials is generally attributed to the release of internal energy. Assuming all materials have the same propensity to release internal energy, and that the distribution and the density of the stored energy is about the same, then the stability of mirror structures can be gauged by the energy required to produce a certain deformation.

For a small volume,  $V$ , having a uniform strain,  $\epsilon$ , the elastic energy is given by:

$$E = 1/2 \epsilon^2 YV \quad (2-4)$$

where  $Y$  is the modulus of elasticity.

Assuming a square mirror which is bent so as to become slightly cylindrical, then the average energy per unit volume is given by:

$$\left( \frac{\bar{E}}{V} \right) = \frac{\epsilon_m^2 Y}{6} \quad (2-5)$$

where

$$\begin{aligned} \left( \frac{\bar{E}}{V} \right) &= \text{average energy per unit volume} \\ Y &= \text{modulus of elasticity} \\ \epsilon_m &= \text{maximum strain} \end{aligned}$$

Substituting (2-3) into (2-5)

$$\left( \frac{\bar{E}}{V} \right) = \frac{8 Y d^2}{3D^4} \left( \frac{\lambda}{n} \right)^2 \quad (2-6)$$

where

$$\begin{aligned} D &= \text{width of the mirror} \\ d &= \text{mirror thickness} \\ \left( \frac{\lambda}{n} \right) &= \text{deformation} \end{aligned}$$

Equation (2-6) indicates the minimum average energy density which, if optimally utilized, would produce a cylindrical mirror deformation. In general, the release of energy is not so as to be optimally effective but depends upon the stress distribution within the mirror blank as well as the mechanisms causing release to take place. The energy density predicted by equation (2-6) is, therefore, on the pessimistic side. On a relative basis, equation (2-6) does indicate that a high modulus of elasticity is advantageous and that lightweight structures having a large diameter-to-thickness ratio are most likely to tax material stability.

Applying equation (2-6) to a mirror one meter wide and 10 cm thick, the average energy associated with a  $\lambda/20$  change in the mirror surface is  $1.17 \times 10^{-5}$  ergs/cm<sup>3</sup> based on a modulus of elasticity of  $7.0 \times 10^{11}$  ergs/cm<sup>3</sup> (fused silica). This can be compared with the energy associated with phase changes, generally in the order of about a calorie per gram, or about  $10^8$  erg/cm<sup>3</sup>.

### 2.3.3 Stored Energy and its Distribution

It is difficult to imagine any material which does not contain a relatively large amount of stored energy except perhaps for the rather fictitious case of a perfect single crystal.

If the coefficient of expansion of the impurities differs from that of the host material, then cooling of the mirror blank will result in a stress concentration around each impurity center. This can be estimated by assuming the host material to be infinitely rigid and the impurity to be compressed by an amount depending on the differences in coefficient of expansion and annealing and operating temperatures. The result is:



$$E = \frac{9(\Delta\alpha)^2 (\Delta T)^2 V}{2a} \quad (2-7)$$

where

- E = total strain energy  
 V = volume of impurity  
 $\Delta\alpha$  = difference in linear coefficient of expansion  
 $\Delta T$  = difference between annealing and operating temperatures  
 a = volumetric compressibility

The assumptions are rather crude, but perhaps adequate for establishing orders of magnitude. Taking a value  $5 \times 10^{-6}/^\circ\text{C}$  for  $\alpha$ , a value of  $0.5 \times 10^{-12}$  erg/cm<sup>3</sup> for a, a temperature difference of 200°C, and assuming an impurity concentration of 1 part in 10<sup>4</sup>, then the energy per unit volume is approximately 900 erg/cm<sup>3</sup>. This is 10<sup>8</sup> larger than the optimum energy distribution required to deform a mirror comparable to the Stratoscope II mirror.

If the impurity atoms remain randomly dispersed in the host material, and it is only statistical variations in the impurity concentration which produce any effect, then even a factor of 10<sup>8</sup> in available energy can be shown to be negligibly small. However, a random impurity distribution is generally not achieved. During solidification, impurities tend to be concentrated in the molten state until they precipitate out separately on crystal boundaries in the last portions of the casting to solidify. Since the orientation of crystal boundaries, as well as the location of the last solidifying regions, depend upon the mould geometry; the distribution of impurities is neither uniform nor random.

The conclusion that relaxation of stresses concentrated around impurities can play a dominant role in spontaneous deformation seems inescapable. It is most likely to become apparent in large mirror structures which have a proportionally smaller amount of energy associated with figure loss and which, because of the longer cooling time, tend to achieve a greater concentration of impurities.

#### 2.3.4 Spontaneous Relaxation Mechanisms

Whether or not impurities do play a dominant role in causing spontaneous deformations probably depends on the various relaxation mechanisms available for the release of stored energy. These mechanisms are not well known. Holden<sup>11</sup> in his excellent review on dimensional instability has outlined the various metallurgical changes which could contribute to spontaneous changes. These include phase changes resulting in different allotropic forms, precipitation of a second phase from solid solution, ordering

of interstitial and substitutional atoms, grain boundary migration, and movement of magnetic domain walls. The instability in Invar, which has received considerable attention, has been traced to the precipitation of carbon from solid solution. This indicates that the strong temperature dependence, which normally characterizes processes limited by diffusion in the solid state, cannot always be counted upon to render such processes inoperable at room temperature. The MIT work on stability did find some alloys which remained unaltered within the accuracy of measurement; however, this was at least two orders of magnitude above the stability required by a diffraction-limited mirror having a one-meter aperture size. It is possible that an alloy having an extraordinary degree of chemical equilibrium may be found; however, at the present time, there does not appear to be any alloy which could be justified as a material for large astronomical mirrors.

Crystalline materials are generally rendered susceptible to plastic strain by planes of weakness at grain boundaries or between the sub-microscopic crystal mosaics.<sup>12</sup> The probability of yield occurring depends upon the binding energy between atoms, the lattice structure, the stress distribution, and the type and concentration of impurities. No hard and fast rules exist. On the experimental side, Reichenback et al<sup>13</sup> have measured yield in steel test specimens to  $10^{-7}$  inches per inch. They found that the test specimens did not possess a definite elastic limit, but that plastic strain decreased asymptotically to zero with decreasing stress. They suggest that in steel some dislocations are ready to move even under the influence of very low stresses.

Stress relief in amorphous materials such as glass is believed to be quite different.<sup>14</sup> At high temperatures glass behaves like a viscous liquid and flows to reduce the applied strain. At low temperatures stress relief occurs by the propagation of Griffith cracks which normally originate at the surface. Crack propagation occurs at right angles to the applied stress and appears to be very dependent upon the presence of a suitable gas such as water vapor which can diffuse along the crack face and facilitate the breaking of molecular bonds in regions of concentrated stress by drastically lowering the activation energy.

There are several reasons why an amorphous material might exhibit greater stability than a crystalline material. Impurities which would be segregated during formation of a crystalline structure might remain dissolved in a glass. Inclusions occurring in the middle of an amorphous structure where there are no cracks may cause the adjacent material to approach its theoretical stress limit before yielding. No corresponding situation exists for metals because of the high density of mobile dislocations characteristic of metals.

### 2.3.5 Likely Mirror Materials

The theoretical arguments relating to material stability are largely hypothetical and, in the absence of experimental evidence, do not warrant the exclusion of any material from consideration. However, theory does provide some basis on which promising, but as yet undeveloped, mirror materials can be selected.

The stability of fused silica which is an amorphous material has been well established experimentally. Other glass-forming compounds include the oxides of boron, phosphorous, and germanium to which can be added various amounts of potassium, sodium, magnesium, calcium, and aluminum, and other oxides. The thermal conductivity of all glasses is low and does not vary greatly. The coefficient of expansion does vary markedly with composition being one tenth the value for  $\text{SiO}_2$  glass as for  $\text{B}_2\text{O}_3$  glass. Sodium and potassium additives increase the thermal expansion greatly, and other additives have rather less effect. The coefficient of expansion curve for fused silica, which normally crosses zero at about  $-80^\circ\text{C}$ , can be shifted to higher temperatures by additives such as tungsten.<sup>15</sup> A tailor-made material having a zero coefficient of expansion at the mid-point of an arbitrary operating temperature range appears to be possible, but a uniform composition may be difficult to achieve because of the very high softening temperature of fused silica ( $1650^\circ\text{C}$ ) and the special techniques used in its manufacture. A number of zero expansion materials have recently appeared on the commercial market and are discussed in Paragraph 2.2. Some apparently contain nucleating agents and require a carefully controlled heat treatment, whereas others are true glasses and can be handled by standard glass technology methods; thus, inferring a softening temperature in the  $500^\circ\text{C}$  to  $800^\circ\text{C}$  range. Since significant differences are apparent between the new materials and fused silica, the application of these new materials to large diffraction-limited mirrors requires critical assessment with regard to their uniformity and stability.

If alloys are excluded from consideration on the basis of possible metallurgical instabilities, then in the top of the periodic table, there remains only beryllium, boron, magnesium and aluminum as likely mirror metals. Only aluminum is isotropic<sup>16</sup> and in its pure form it is too soft to be useful.

The two transition elements, carbon and silicon, also deserve consideration. Diamond is the only form of carbon that would be useful for a mirror structure, and is obviously impractical. Silicon has an isotropic diamond cubic structure and has found considerable application in the manufacture of infrared optical components such as IR domes and lenses. It can be ground and polished from cast material using conventional curve generators and polishing laps but requires about 50% more time than fused silica.<sup>17</sup> There is some evidence to indicate that dislocations in silicon are pinned by impurity oxygen atoms and that fracture occurs before motion of the dislocations.<sup>18</sup> Because of its application in the electronics industry silicon technology is well developed and very pure material is available. Silicon is, therefore, recommended for further study as a mirror material.

Other possible mirror materials can be found further down in the periodic table (V, Cr, Mn, Fe) or among the wide variety of inorganic compounds. The merits of each must be considered on an individual basis and with regard to advances in technology. Of all the materials that might eventually find application, silicon appears to be ripest at the present time.

Powder technology, which has done much to enhance the properties of beryllium, might also be applied to isotropic materials as a means of avoiding concentrations of impurities such as normally occur during solidification.

### 2.3.6 The Space Environment

Although operational experience gained as a result of the Stratoscope flights has left fused silica without peers in the realm of dimensional stability, this situation might change in the rigors of outer space. Prolonged exposure to the radiation flux and hard vacuum of outer space may promote chemical changes such as crystallization and diffusion, or stress relaxation of the surface material which is severely deformed during polishing. The magnitude of these effects has not been established and may be inconsequential, but further study appears warranted.

## 2.4 CONFIGURATION

There are a number of requirements which the mirror structure must satisfy. They include rigidity through polishing and testing, survival through launch, and immunity to thermal deformation during operation.

Since spaceborne systems are usually designed with a specific weight limit and aperture size in mind, it is probably most useful to think of the optimum way of distributing the mirror material to achieve the various objectives. The final design ultimately depends on the relative weighting given to each requirement by the designer.

Webbed mirror structures can be made much stiffer than solid structures of the same weight and consequently offer significant advantages during testing. A two-dimensional comparison between representative cross sections out of solid, sandwich and ribbed structures is shown in Figure 2.2. All of the cross sections have an equal area which implies an equal weight if webbing fillets normal to the sections shown are neglected. Comparison of the moments of inertia of the various structures indicates that bending deflections can be reduced by a factor of 5.75 with a sandwich structure and a factor of 4.25 with a ribbed structure. Shear deflections, which are not always insignificant in mirror structures, are relatively independent of the type of cross section.

The maximum stress varies as the deflection and the distance from the neutral axis. Taking the solid section as a basis of comparison, the maximum stress in the sandwich is a factor of 2.87 smaller and the stress in the ribbed section is a factor of 1.7 smaller. The sandwich structure is clearly the most advantageous if launch stresses are to be minimized. A very significant reduction in launching stress can also be obtained by judicious choice of the mounting points and by contouring the mirror structure so that it tapers toward the outer edge. Some idea of the stress reduction can be obtained from consideration of the deflection of a uniformly loaded beam. This varies as the fourth power of the beam length.

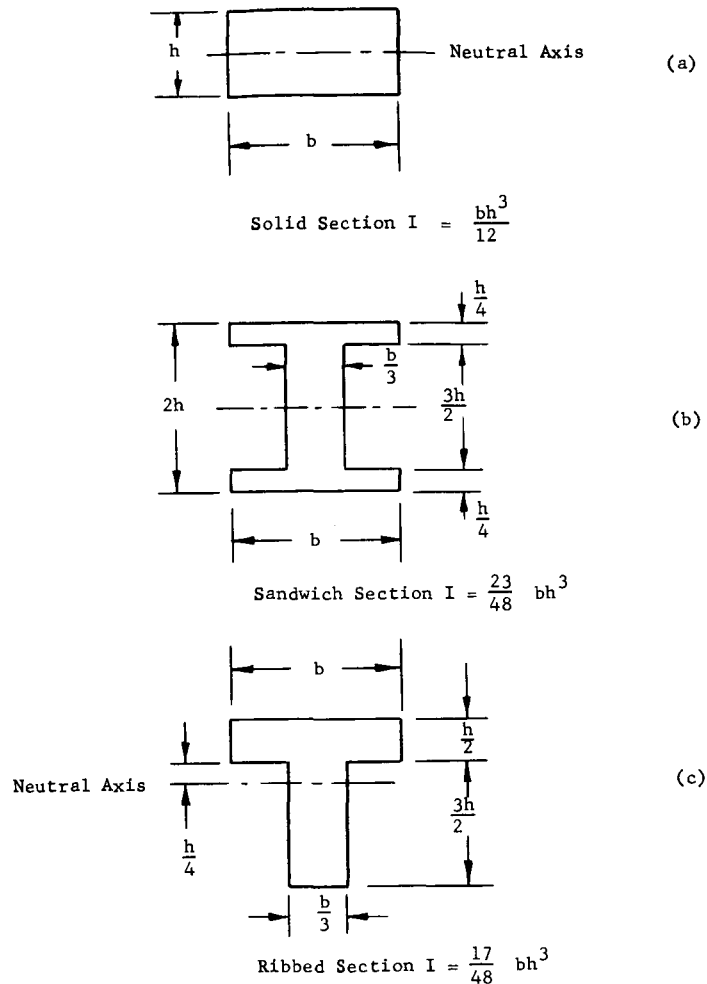


Figure 2.2. Mirror Cross-Sections

The maximum working stress for a mirror material requires critical examination. Usually a conservative working stress is obtained by applying a safety factor to the yield strength which is defined as a stress which will produce 0.2% plastic strain. Since strains on the order of  $10^{-8}$  can noticeably affect optical performance, the merit of a general purpose safety factor is open to question.

The optimum shape to minimize figure loss due to warping caused by a nonuniform temperature environment is a very complex problem. An associated problem, that of determining the change in mirror figure for a particular temperature distribution, has been solved only for a very limited number of cases. Intuitively, it might be expected that the optimum shape depends upon the nature of the temperature nonuniformities which are likely to occur.

In situations where temperature nonuniformities in the primary mirror are determined mainly by radiative heat transfer rather than by conduction, the only method of effectively reducing the thermal distortion is by use of materials with a low coefficient of expansion.

In fused silica the thermal wavelength corresponding to an orbital period of 100 minutes is about 10 inches, so that it is quite possible to achieve temperature distributions across a fused silica mirror which depend mainly on radiative transfer. This situation is reversed for a silicon mirror since a thermal wave of orbital period is about 100 inches long. In the case of a silicon mirror the effect of temperature anomalies, such as might be caused by support structures, depends upon the mirror configuration, since this affects the thermal conductivity between the input point and the rest of the mirror, and also determines the stiffness of the mirror with respect to localized regions of stress. The effect of temperature nonuniformities, which are large compared to the mirror thickness, is probably independent of the mirror stiffness but depends on the thermal conductivity from one side of the mirror to the other and on the coefficient of expansion. In this case, solid and ribbed mirror configurations would have about the same conductivity, but a sandwich structure would be significantly lower because of the relatively high thermal resistance of the webbing separating the front and back plates. On an intuitive basis, temperature nonuniformities near the center of the mirror might be expected to be more degrading than nonuniformities near the outer edges; thus indicating a tapered structure to be advantageous from a thermal distortion point of view as well as from launch stress considerations.

A summary of the conclusions reached on mirror structures is provided in Table 2-II. Before a specific design can be chosen it is necessary

TABLE 2-II  
COMPARISON OF MIRROR CONFIGURATION

Type of Structure	Relative Stiffness	Relative Maximum Strain	Thermo-Elastic Rigidity	General Comments
Solid	1.0	1.0	Good	Simplest to fabricate and analyze.
Sandwich	5.75	0.35	Not as good	Difficult to fabricate with contoured edges.
Ribbed	4.25	0.59	Good	Can be cast.

to determine the compatibility requirements which must be met in order to incorporate the mirror in the optical system design, and to choose a mirror material. These, in turn, determine whether the mirror design should be optimized to minimize deflection during polishing and test, stress during launch, or thermo-elastic warping during operation. Where all of these are of nearly equal importance, the ribbed structure would appear to be a reasonable compromise, although its behavior under transient temperature changes may cause difficulties. An artist's conception of a ribbed mirror such as might be used in the 40-inch design considered in Volume III of this report is shown in Figure 2.3.

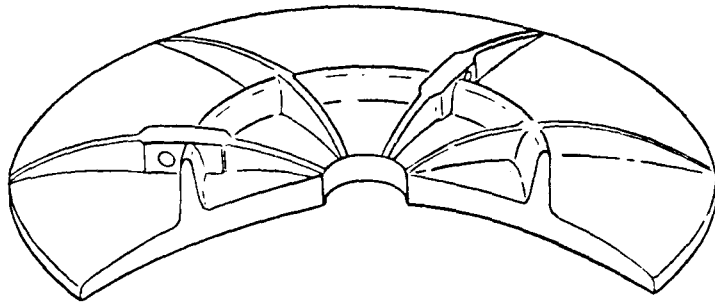


Figure 2.3. Possible Ribbed Mirror Configuration

## 2.5 A COMPOSITE MIRROR STRUCTURE

A composite mirror structure has been suggested which combines the desirable thermal properties of a metal and the dimensional stability and low coefficient of expansion of fused silica. The composite structure could be obtained from a fused silica eggcrate by filling each cell with aluminum wire wool and plating the cell interiors with a thin aluminum coating to insure good thermal contact between the cell walls and the wool fibers. A one percent (by weight) addition of aluminum has been estimated to increase the thermal conductivity of a fused silica eggcrate up to 8 times depending on the mean orientation of the aluminum wool fibers. In a solid piece of fused silica the wavelength of a periodic temperature change having a 90 minute period is about 9 inches. In an eggcrate structure a thermal wave of orbital period is effectively attenuated by the ribbing. As a result, large temperature differentials and appreciable thermo-elastic deformations are possible. In a composite structure, the aluminum wool thermally couples the front and back surfaces so that both the thermal gradients and the resulting deformations are correspondingly reduced.

## 2.6 ACTIVE OPTICAL SYSTEMS

Synthesis of a large aperture mirror from an array of smaller mirrors is being explored by Perkin-Elmer for the National Aeronautics and Space Administration, Langley, under Contract Number NAS1-5198. The primary advantage of a segmented optical system is the greater scope which it provides

to minimize the effect of the many degrading influences to which a large spaceborne optical system is exposed. These include a temperature environment which is spatially and temporally nonuniform, and a zero "g" condition which becomes impossibly difficult to approximate on earth with very large aperture sizes. Other advantages of a segmented optical system include a saving in weight over monolithic structures, a more manageable shock and vibration isolation problem, and a configuration which can be folded during launch and assembled in space to yield an aperture diameter larger than the payload vehicle diameter.

In order to achieve resolution which is characteristic of the total aperture size, it is necessary to ensure that the individual segments are confocal and form parts of a mathematically continuous surface rather than parts of a family of surfaces. A schematic of an actively controlled telescope optical system is shown in Figure 2.4. Each of the mirror segments is positioned with respect to a neighboring mirror by means of ambiguity sensors to form an array equivalent to a single continuous surface. A mirror figure sensor located near the radius of curvature orients each of the segments to achieve a confocal alignment.

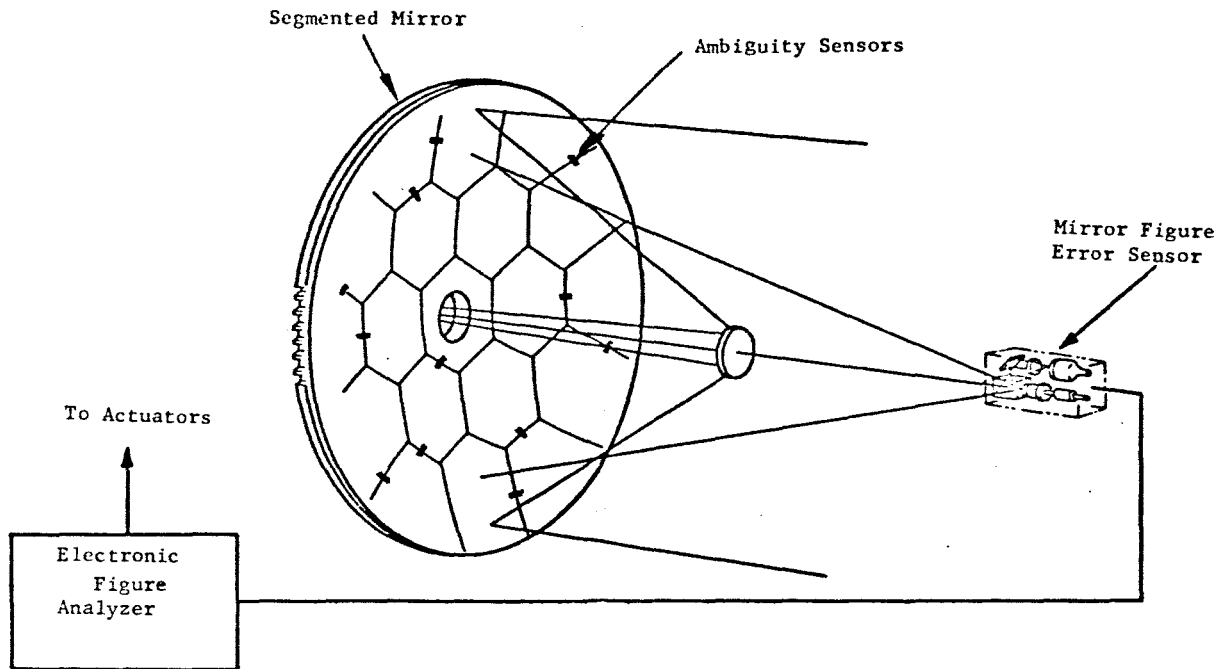


Figure 2.4. Active Optics Telescope Systems



Both the ambiguity sensors and the figure sensor utilize interference phenomena to obtain signals which can be processed to drive micro-actuators fixed to the back of each mirror segment. A wide variety of effects can be utilized in the actuators to obtain motion increments in the order of a microinch at a time. A number of breadboard actuators using magnetostrictive effects have already been built and demonstrated. Control of the integrated figure of a segmented optical system to  $\lambda/50$  rms or better appears to be possible with an active system.

Further work on active optical systems is expected to include a laboratory feasibility demonstration utilizing three actively controlled 40-inch mirrors to synthesize a 120-inch aperture.

## 2.7 COATINGS FOR THE UV SPECTRAL REGION

Below 1600Å the reflectivity of aluminum is strongly affected by the formation of an oxide film which, in itself is absorptive, and which is believed to increase absorption by the aluminum film.<sup>19</sup> The formation of the oxide can be inhibited and the reflectivity of aluminum can be enhanced by coatings of LiF or  $MgF_2$ . Apart from preventing oxide formation, the protective films act as a single layer interference filter and enhance the reflectivity by interference effects. Below 1200Å both  $MgF_2$  and LiF tend to be absorptive, but the highest reflectivity can be obtained with LiF. The present state of the art is indicated in Figure 2.5 which has been taken from a paper by Angel, Hunter and Tousey.<sup>20</sup>

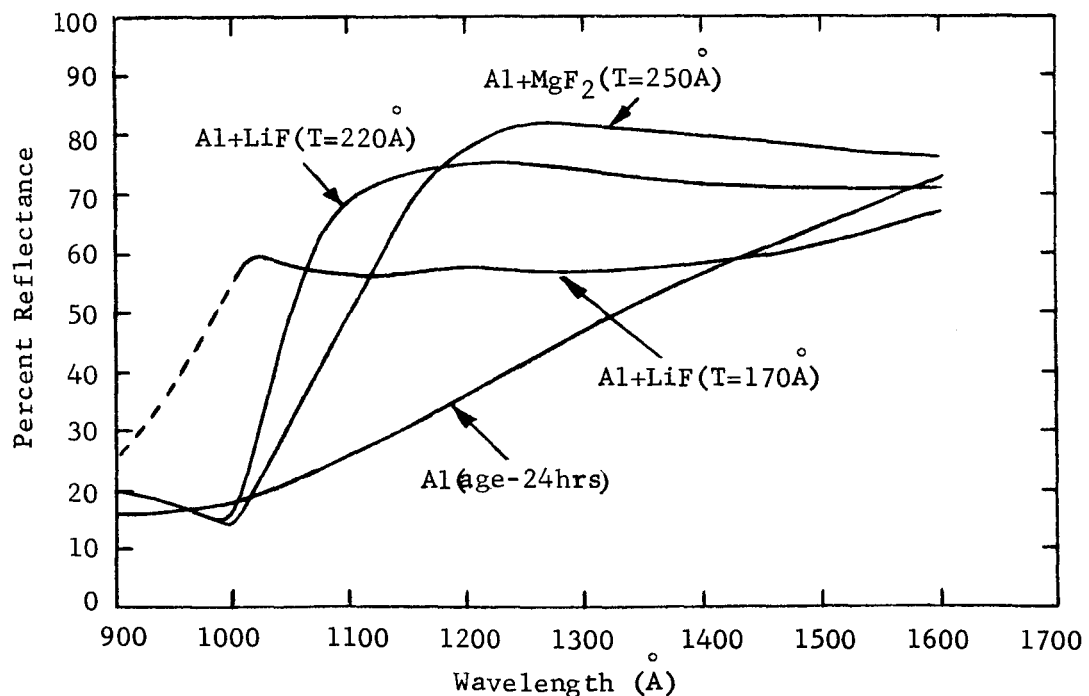


Figure 2.5. Reflectance of Aluminum Based Reflective Coatings

Storage of LiF coatings in air with a humidity below 40 percent results in minimal deterioration, however, the high solubility of LiF renders it sensitive to humidities much above 40 percent. A very thin layer of MgF<sub>2</sub> amounting to only about 15Å superimposed on top of a LiF coating may offer some protection at higher humidities and a negligible reduction in reflectivity due to absorption.

There is apparently some hope of pushing the state-of-the-art of LiF-coated aluminum still further. Angle et al<sup>20</sup> mention that on several occasions reflectivities as high as 76 percent at 1025Å were obtained for reasons unknown. Madden et al<sup>19</sup> have shown that a time delay of only 100 seconds between the deposition of the aluminum and LiF is sufficient to drop the reflectivity at 1025Å from 86 percent to 70 percent and that, even the rate of aluminum deposition produces significant changes. This indicates the possibility of oxygen contamination even on so-called good coatings. Impurities in LiF are known to have an adverse effect on the UV transmission.<sup>21</sup> Close control of the purity of the evaporable material might also lead to significant improvements.

At the present time, there does not appear to be any coatings which can be used to obtain a high reflectivity much below 1000Å with the exception of materials used at angles near or greater than the critical angle. LiF has a strong absorption band centered near 950Å so that even thin pure films of this material are unlikely to provide useful protection to aluminum below 1000Å. Below 825Å aluminum becomes very transparent which limits its usefulness except at high incident angles. The most reflective films for the 600Å to 1000Å region appear to be Pt or Rh films which have a reflectivity of only 10 to 20 percent in this region.<sup>22</sup>

The region from 912Å to 1000Å has not received a great deal of attention. It seems likely that high efficiency, multilayer dielectric films will be developed for this region but these are usually efficient only over a fairly narrow spectral range. Broad band instruments for this region will probably require optical arrangements having shallow incident angles or else contend with coatings having low optical efficiencies.

Very recently, the effect of ultraviolet irradiation and high energy electron (1 Mev) and proton (0.5 Mev) bombardment on MgF<sub>2</sub> overcoated aluminum films was investigated by Cranfield, Hass, and Waylonis.<sup>23</sup> They found that even prolonged exposure to the radiation levels likely to be encountered in space had a negligible effect on the vacuum UV reflectance, although the glass substrates underneath became dark brown. They also found that a very thin oil film, such as might arise from a vacuum system failure during test, had a very deleterious effect on reflectivity; but such films could be removed by rinsing with ether, acetone or Freon TF (Dupont), or by removal of a collodion coating. A combination of rinsing and collodion cleaning proved to be most successful.

The possibility of coating optics in space in order to achieve a pure aluminum film having a much higher reflectivity in the 900Å to 1200Å region than overcoated films is extremely attractive. For a near earth orbit (125 miles to 500 miles) the pressure varies from  $10^{-6}$  to  $10^{-9}$  mm Hg which is similar to pressures achieved with present coating facilities. Oxygen contamination in near earth orbits is, therefore, likely to be as serious a problem as it is in earthbound facilities and no advantage is apparent in this case. For a 20,000 mile synchronous orbit the pressure is below  $10^{-12}$  mm Hg and some advantage may be obtained with a space coating facility provided that outgassing from the satellite did not nullify the effect of a higher orbital altitude. A space coating facility would require a minimum of 5 KW of power for approximately 10 seconds to evaporate the aluminum and a motorized mask assembly to achieve a uniform distribution. In order to prevent a reflective coating being applied to the telescope tube, this structure would probably have to be separated from the primary during the coating process. In conclusion, optical coating in space is unlikely to be attractive until manned missions to synchronous altitude and beyond are contemplated. The advantages to be gained with a spaceborne coating facility, even under the most advantageous conditions, such as with a contaminated or abraded mirror surface, are not readily apparent. They will depend in part on advances in the state-of-the-art with earthbound coating facilities and in part on feasibility experiments aimed at cleaning and coating optical surfaces by future high altitude manned missions.

REFERENCES

- <sup>1</sup>Noble, R.H., et al, Study and Analysis of Lightweight Optical Elements, ASD Technical Report 61-452, Perkin-Elmer Report No. 5857, October 1961.
- <sup>2</sup>Jarosh, J.J., The Dimensional Stability of Metals, August 1950, Instrumentation Laboratory, Massachusetts Institute of Technology.
- <sup>3</sup>Lement, B.S., and B.L. Averbach, Measurement and Control of the Dimensional Behavior of Metals, Instrumentation Laboratory, Massachusetts Institute of Technology.
- <sup>4</sup>Lement, B.S., B.L. Averbach, and Morris Cohen, The Dimensional Behavior of Invar, Trans. Am. Soc. Metals, 43, 1951.
- <sup>5</sup>Page, Benjamin L., Calibration of Meter Line Standards of Length at the National Bureau of Standards, J. of Research of the National Bureau of Standards, Vol. 54, No. 1, January 1955.
- <sup>6</sup>Meyerson, M.R., T.R. Young, and W.R. Ney, Gage Blocks of Superior Stability: Initial Developments in Materials and Measurement, Journal of Research of the National Bureau of Standards, Vol. 64C, No.3, July - September, 1960.
- <sup>7</sup>Meyerson, M.R., and M.C. Soloi, Gage Blocks of Superior Stability III: The Attainment of Ultrastability, Trans. ASM, 57, 164 (1964).
- <sup>8</sup>Meinel, A.B., Report on the Optical Performance of Aluminum Mirrors, Unpublished, August 20, 1962.
- <sup>9</sup>Jennings, C.G., A.G. Gross, L.E. Colteryal, Dimensional Stability and Thermal Expansion Characteristics of Beryllium, presented at the International Symposium on Beryllium Metallurgy and Technology, September, 1964.
- <sup>10</sup>Atwood, J.G., P.H. Lee, J.B. Schroeder, P. Forman, Optical Materials Study, Perkin-Elmer Report No. 8028.
- <sup>11</sup>Holden, F.C., A Review of Dimensional Instability in Metals, Defense Metals Information Center, Batelle Memorial Institute, Memorandum 189.
- <sup>12</sup>Hume-Rotherg and Raynor, The Structure of Metals and Alloys, The Institute of Metals, No. 1, 1956.
- <sup>13</sup>Reichenbach, G.S., D.A. Brown and P.G. Russell, Yield Behavior of Certain Alloy Steels at Low Strain Values.
- <sup>14</sup>Stanworth, Physical Properties of Glass, Oxford at the Clarendon Press, 1950.

- 15 Meinel, A.B., Introduction to the Design of Astronomical Telescopes, Technical Report 1, Optical Sciences, University of Arizona.
- 16 Barrett, Structure of Metals, McGraw-Hill, 1952.
- 17 Ballard, S.S., K.A. McCarthy, W.L. Wolfe, State-of-the-art Report Optical Materials for Infrared Instrumentation - The University of Michigan, Report No. 2389-11-S, January, 1959.
- 18 Read, W.T. Jr., G.L. Pearson, Deformation and Fracture of Silicon - Dislocations and Mechanical Properties of Crystals. John Wiley & Sons,
- 19 Maddin, R.P., L.R. Canfield, and G. Hass, On the Vacuum-Ultraviolet Reflectance of Evaporated Aluminum Before and During Oxidation, J.Opt.Space Soc. Am. 53, 620 (1963).
- 20 Angel, D.W., W.R. Hunter, R. Tousey, Extreme Ultraviolet Reflectance of LiF Coated Aluminum Mirrors. Journal of the Optical Society of America, 913, 51, 1961.
- 21 Kato, Riso, Shin-ichi Nakashima, Haizo Nakamura and Yoichi Uchida, Optical Properties of Irradiated LiF Crystals in the Extreme Ultraviolet Region, J. Phys. Soc. Japan 15 (1960) 2111-2112.
- 22 Hunter, W.R., Reflectance of Materials in the Vacuum Ultraviolet, Symposium on Military Applications of Ultraviolet Radiations, The University of Chicago LAS - TR-199-37, November (1962).
- 23 Canfield, L.R., G. Hass, and J.E. Waylonis, Further Studies on MgF<sub>2</sub> Overcoated Aluminum Mirrors with Highest Reflectance in the Vacuum Ultraviolet. J. of Applied Optics, Vol.5, No.1, January 1966 (45-50).
- 24 Morey, G.W., The Properties of Glass, Reinhold Publishing Corporation, 1938.

### 3.0 THERMAL CONTROL

#### 3.1 THE THERMAL ENVIRONMENT

##### 3.1.1 Open End of the Telescope

The thermal radiation intercepted by the open end of the telescope tube was investigated assuming a 600 nautical mile circular orbit in the ecliptic plane and the three orthogonal pointing directions illustrated in Figure 3.1. The ecliptic plane was chosen primarily to simplify the determination of view factors, and also because a possible inclination is  $8.55^\circ$ ,

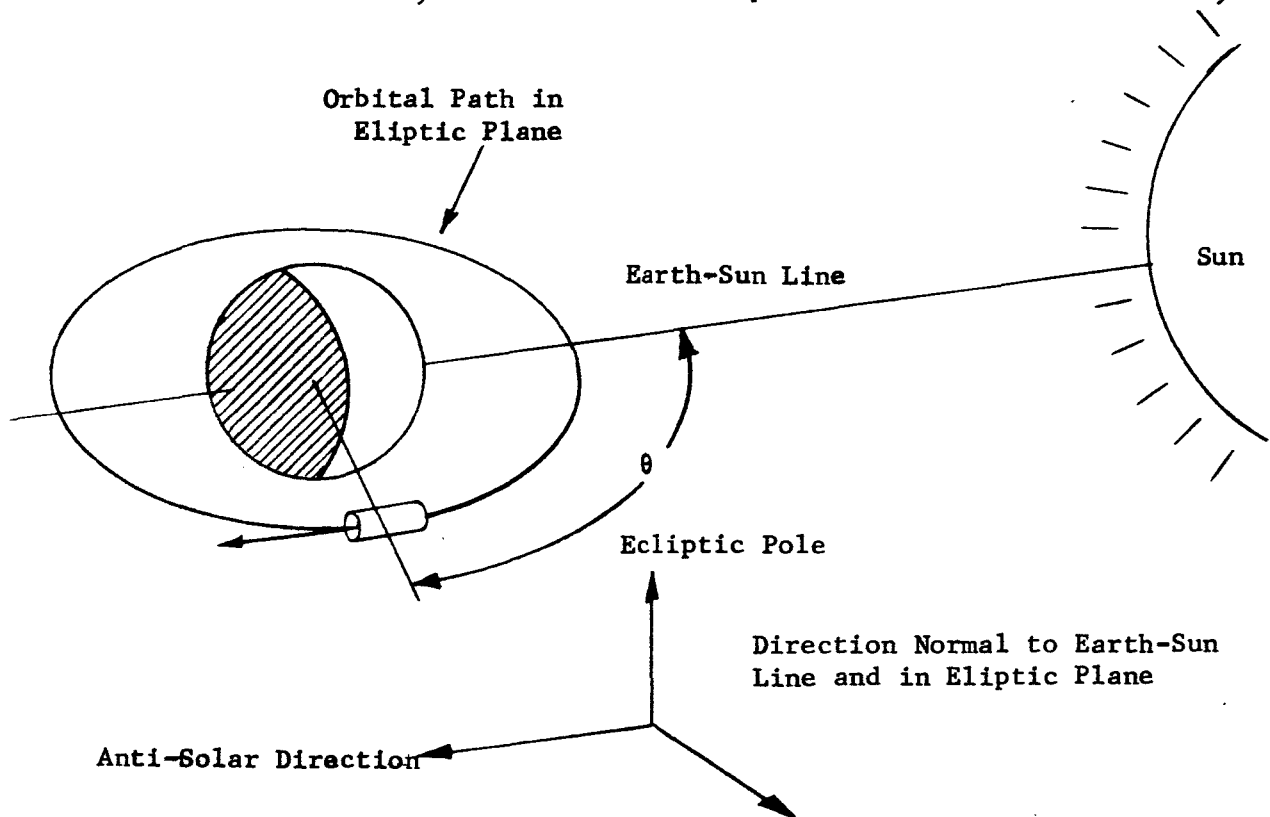


Figure 3.1. Satellite Geometry

making the assumed orbit plane a close approximation. The heat flux components due to earth-reflected sunlight (earth albedo) and infrared emission direct from earth (earth emission) are shown in Figures 3.2 through 3.4 for each of the three pointing directions. The totals are shown in Figure 3.5. The maximum average heat flux occurs when the telescope is pointed in the anti-solar direction and a minimum average heat flux corresponds to a pole star direction. Assuming the open end of the telescope approximates a black-body, and that the telescope is thermally isolated from the remainder of the satellite, then the equilibrium temperatures for the three directions vary from  $-44^\circ\text{C}$  for the anti-sun direction through  $-70^\circ\text{C}$  to  $-84.5^\circ\text{C}$  for the pole star direction.<sup>1</sup>

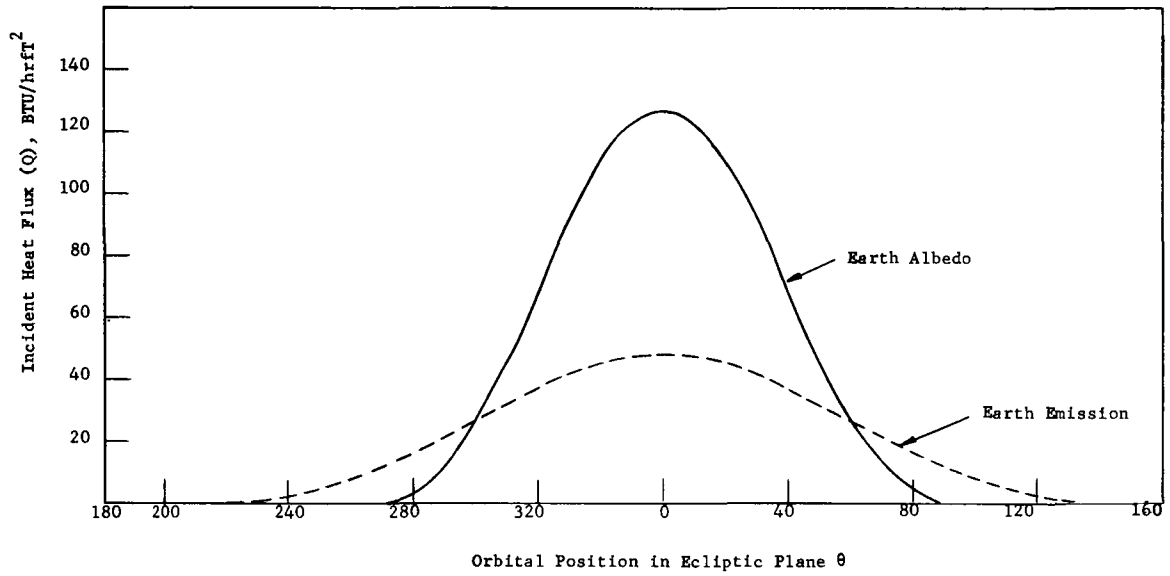


Figure 3.2 Heat Flux Variation In Anti-Solar Direction

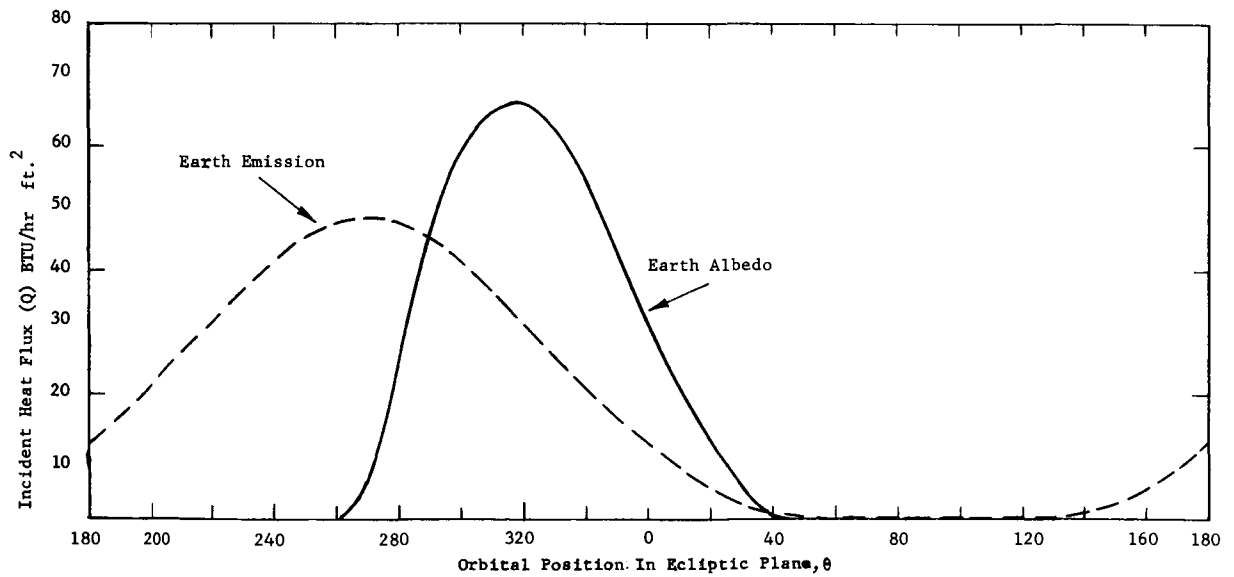


Figure 3.3 Heat Flux Variation in Direction Normal to Earth-Sun Line and in Ecliptic Plane

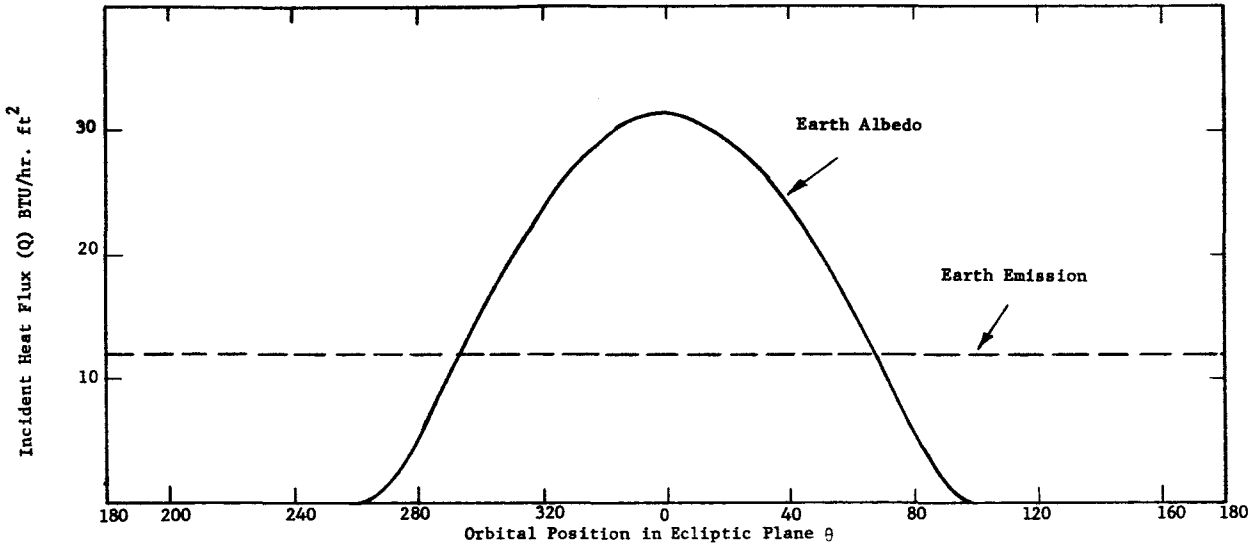


Figure 3.4 Heat Flux Variation in Ecliptic Pole Direction

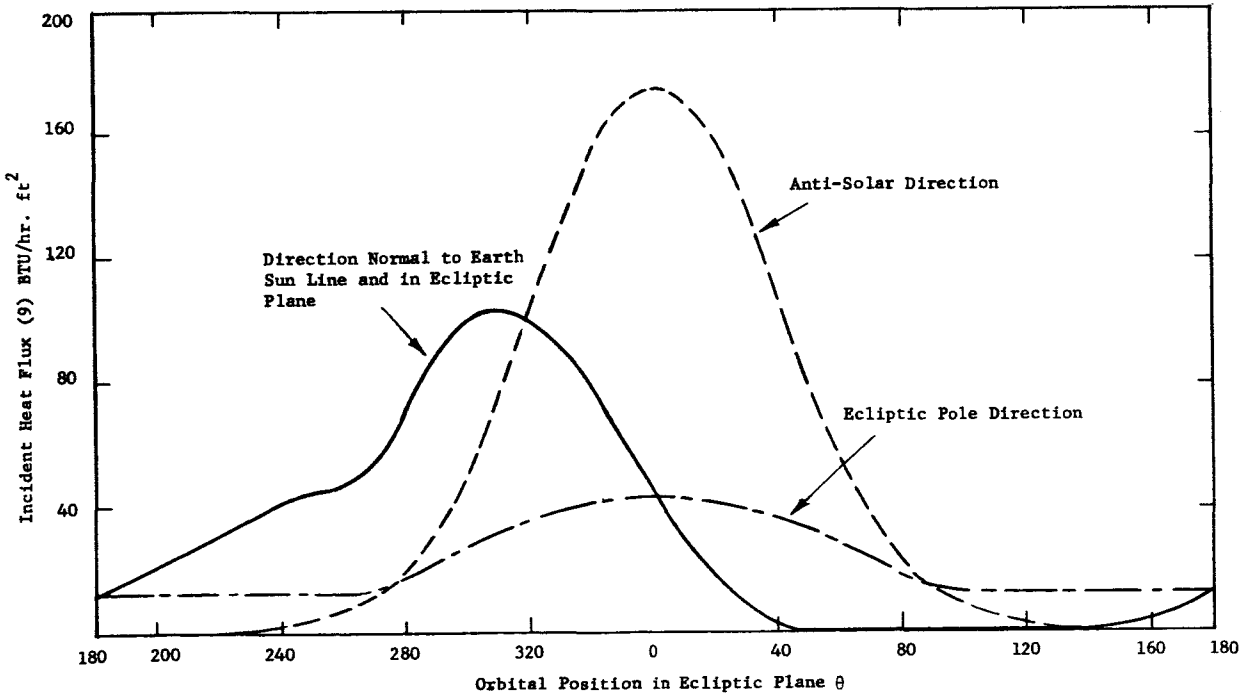


Figure 3.5 Orbital Variation in Total Heat Flux



Changing the orbital altitude to 300 nautical miles increases the total heat flux by about 20 percent for the anti-solar pointing direction and by about 40 percent for the ecliptic pole pointing direction.

3.1.2 The Telescope Tube

The thermal environment seen by the primary and secondary mirrors and their spacing elements depends to a large degree on the thermal properties of the telescope tube. From a thermal point of view, the ideal tube would have an infinite heat capacity and would absorb all incident radiation ( $\epsilon = 1$ ). In this case the tube would appear as a constant heat source to the primary and secondary mirrors, but radiation which reached either mirror without first intercepting the tube wall would remain as a variable heat source.

In practice, the ideal case can be approached by ensuring that the heat capacity of the tube is large in comparison to the variation in thermal flux encountered during one orbit.

The value of  $\epsilon$  for the mirror surface is very low in the infrared ( $\epsilon \approx 0.01$ ) and results in poor radiative coupling between the mirror and tube. This further facilitates the attainment of a nearly ideal telescope tube.

In order to assess more closely the interaction between the telescope tube and the external thermal environment, an analogue simulation was used. The example chosen for simulation was a blackened 40-pound aluminum tube 40 inches in diameter and 80 inches long having a perfectly reflecting mirror at one end. The other end of the tube was assumed to be exposed to a sinusoidal variation in flux equal to the first Fourier component of the worst case example shown in Figure 3.2.

By dividing the tube into a number of segments and assuming the temperature variation to be sufficiently small so that radiative heat loss was a linear function of temperature, an array of differential equations was obtained similar to the following:

$$\begin{aligned}
 A_1 \frac{d}{dt} (T_1) &= B_1 \sin (wt) - C_1 T_1 + D_1 T_2 + E_1 T_3 + F_1 T_4 + \dots \\
 A_2 \frac{d}{dt} (T_2) &= B_2 \sin (wt) - C_2 T_2 + D_2 T_1 + E_2 T_3 + \dots \\
 A_3 \frac{d}{dt} (T_3) &= B_3 \sin (wt) - C_3 T_3 \dots \dots \dots (3-1)
 \end{aligned}$$

where:

$A_n$  is the heat capacity of each segment.

$B_n$  is proportional to the heat absorbed from the open end by each segment.<sup>2</sup>

$C_n$  is proportional to the heat lost by radiation and conduction by each segment.

$D_n, E_n,$  etc., are proportional to the heat gained by radiation and conduction from the other segments.

The electrical analogue for one of the nodes represented by equation (3-1) is shown in Figure 3.6. Taking resistors with no subscript as equal, then the equation relating the input and output voltages is:

$$C_1 \frac{d(V_1)}{dt} = \frac{V_o}{R_o} - \frac{V_1}{R_1} + \frac{V_2}{R_2} + \frac{V_3}{R_3} + \dots + \frac{V_1}{R_1} \quad (3-2)$$

Comparison between equations (3-1) and (3-2) immediately reveals the analogy between the R and C of the electrical components and the constants in the differential equation describing the thermal behavior of the telescope tube. Amplifier number 3 in Figure 3.6 is not essential and can be eliminated by placing  $R_1$  in parallel with  $C_1$ . A complete analogue arrangement for 2 node simulation of the telescope tube is shown in Figure 3.7. The voltages V and V' represent temperatures at the middle of the two tube halves. If only a two node problem is considered then an analytical solution is fairly easy to obtain and analogue simulation is not warranted, however, the analytical complexity is strongly dependent on the number of nodes so that simulation has definite advantages for three or more nodes.

Figure 3.8 shows the maximum temperature variation along the 40-pound aluminum telescope tube predicted by 1, 2, 3, and 4 node solutions. It is apparent that a tube having only a 2:1 length to diameter ratio provides considerable amelioration of the thermal environment seen by the primary mirror.

The relative phase and amplitude of the temperatures obtained in the four node solution is shown in Figure 3.9. When referenced to a sine wave input the phase lag varies from 63.3° for the front end to 131° for the quarter section nearest the mirror.

The variation in heat flow seen by the primary mirror due to the temperature variation in the telescope tube depends upon the view factors between the tube segments and the primary as well as the amplitude and phase of the temperature variation. For the temperature distribution shown in Figure 3.9 the total flux incident on the primary mirror from the tube is given by:

$$Q = 41.7 \sin (\omega t - 112^\circ) \text{ Btu/hr.} \quad (3-3)$$

which amounts to a maximum flux density of 4.8 Btu/hr. ft<sup>2</sup>.

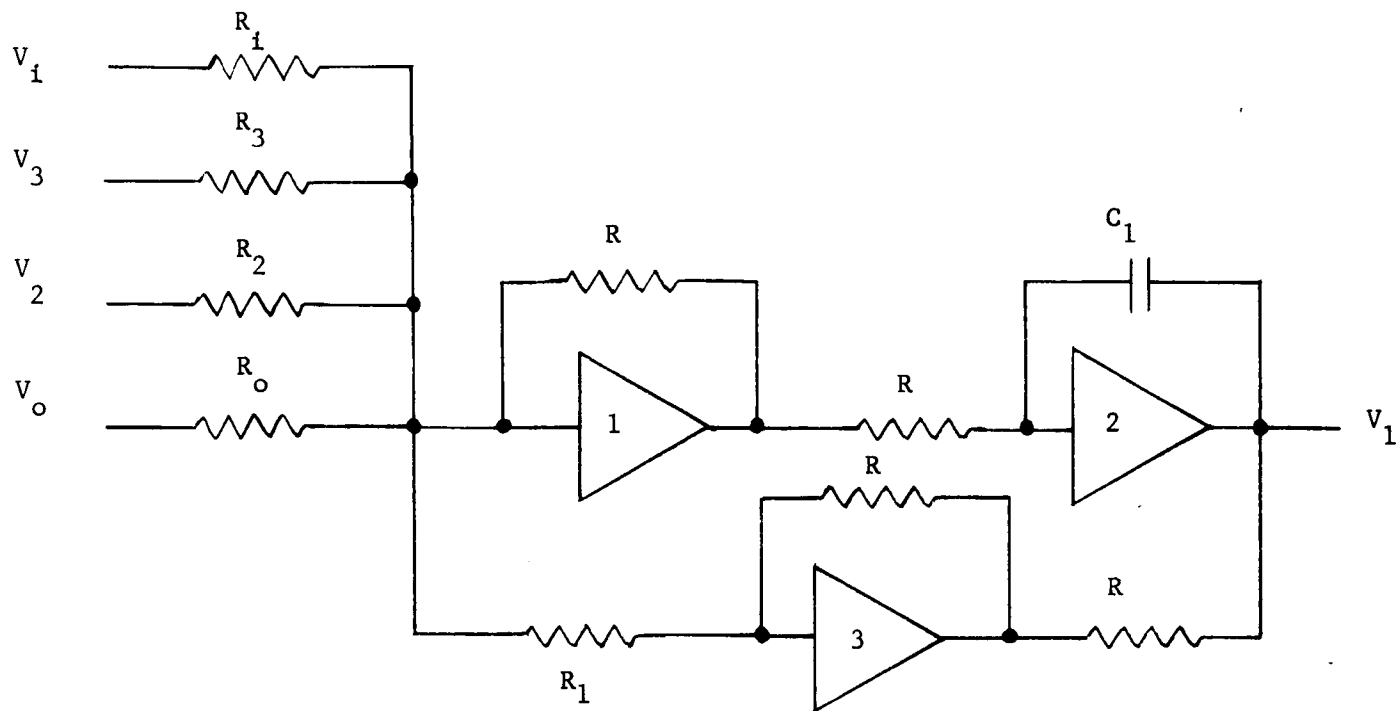


Figure 3.6. Tube Segment Analogue

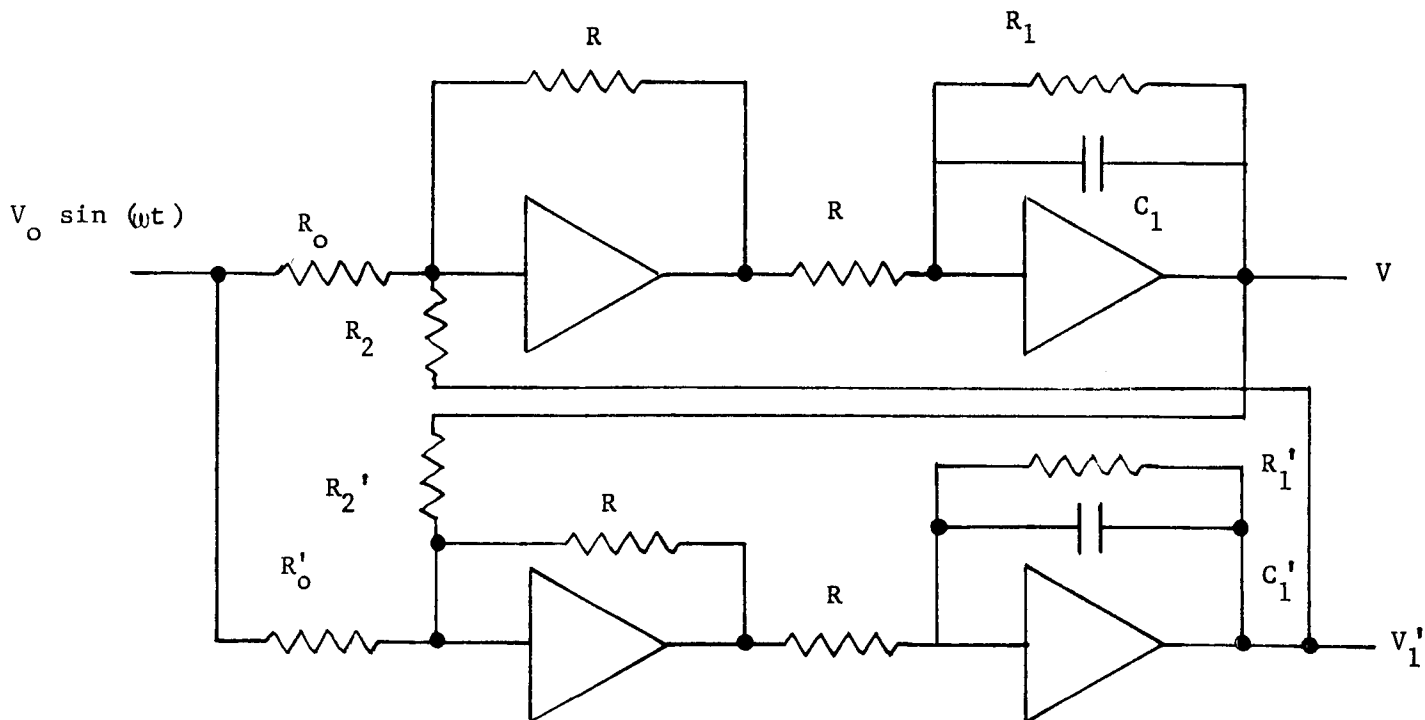


Figure 3.7 Complete Two Node Analogue

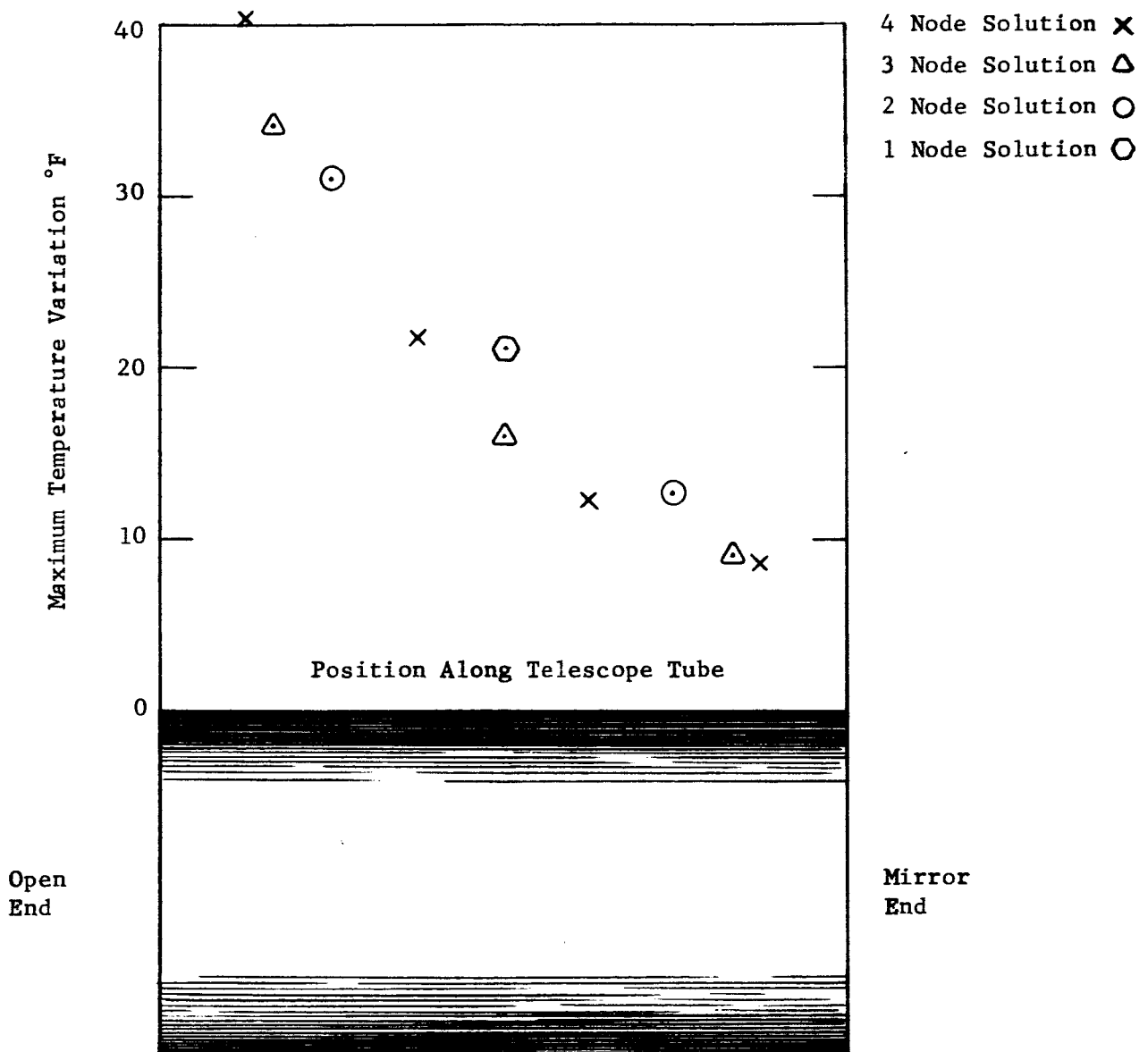


Figure 3.8 Maximum Temperature Variation Along Telescope Tube

A proportion of the flux incident on the open end of the telescope tube reaches the primary mirror directly. For a 2:1 length to diameter ratio about 1/16 or 6.25% of the incident flux reaches the primary directly. In the worst case situation used thus far, this amounts to a maximum of about 4.75 Btu/hr. ft<sup>2</sup> of which about 30% is earth emission and 70% is earth albedo. Assuming the primary to absorb 10% of the incident albedo (primarily visible radiation) and 1.0% of the incident earth and tube emission (far infrared radiation), then the total heat flux absorbed by the primary is made up as shown in Table 3-I.

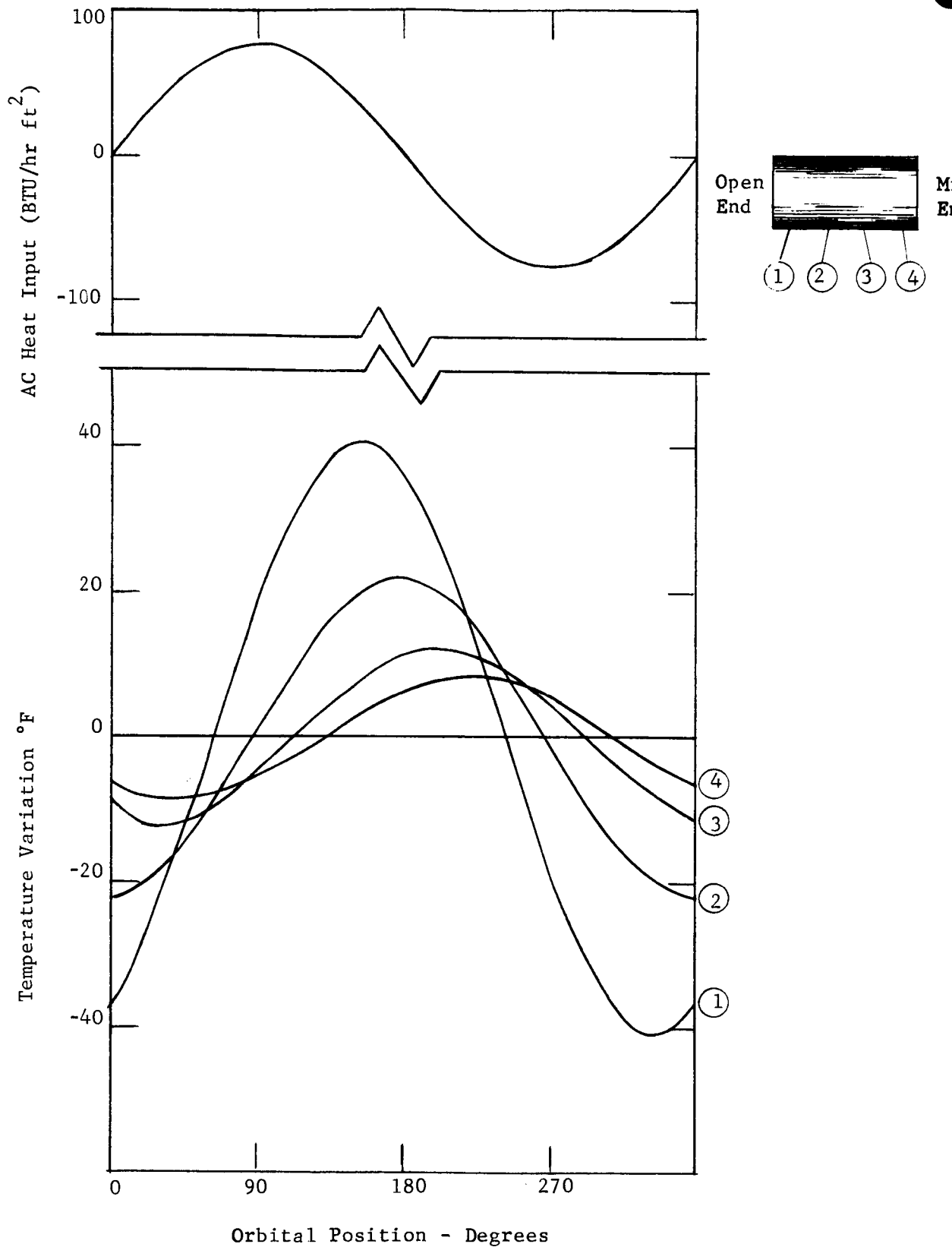


Figure 3.9. Thermal Behavior of a 40 Pound Aluminum Telescope Tube (40" Dia. x 80" Long)

TABLE 3-I

ORBITAL VARIATION IN RADIATION FLUX ABSORBED BY THE PRIMARY

Source	Magnitude (Btu/hr ft <sup>2</sup> )
Earth Albedo	0.33 sin( $\omega t$ )
Earth Emission	0.014 sin( $\omega t$ )
Tube Emission	0.048 sin( $\omega t - 112^\circ$ )
Total	0.326 sin( $\omega t - 8^\circ$ )

It is therefore concluded that an ideal telescope tube which provides a negligible contribution to the primary temperature variation is rather easily obtained in practice; a 40-pound aluminum tube being more than sufficient for a 40-inch  $f/2$  primary.

3.2 CRITICAL COMPONENT TEMPERATURE DISTRIBUTIONS

3.2.1 The Primary Mirror

The possible thermal design alternatives for the primary mirror range from a mirror having a black back surface to one having an aluminized back surface. A black back surface couples the mirror to the instrument package which is expected to have a fairly stable temperature considerably above the equilibrium temperature of the telescope tube. A reflective back surface causes the primary mirror temperature to stabilize approximately half way between the temperatures of the instrument package and the telescope tube. This alternative results in a thermal gradient through the mirror which is approximately half of the resultant gradient when the mirror is thermally tied to the instrument package, but it also results in an equilibrium temperature which fluctuates widely depending on the telescope pointing direction, and an increased susceptibility to the effects of heat conduction through the supports or heat radiation through the mirror edge. It is beyond the scope of this discussion, which deals only with orbital variations in heat flux, to determine which of the two design alternatives is most attractive in terms of overall system performance. In the following analysis a mirror aluminized on both front and back surfaces is assumed.

For a semi-infinite slab in which transients are not present but in which the heat flow has become periodic, the instantaneous surface heat flow rate is given by,

$$q = \Delta T \sqrt{2\pi f K C \rho} \cos(2\pi ft + \pi/4). \quad (\text{Ref. 3}) \quad (3-4)$$

where:

- q = maximum heat flow per unit area
- $\Delta T$  = temperature amplitude (half of the temperature range)
- K = conductivity
- C = specific heat
- $\rho$  = weight per unit volume
- f = frequency of temperature variation
- t = time

Assuming the mirror to be made of solid fused silica and an orbital altitude of 600 nm corresponding to a period of 106 minutes, then:

- f = 0.566/hr
- K = 0.80 Btu/ft hr<sup>°F</sup>
- C = 0.188 Btu/lb<sup>°F</sup>
- $\rho$  = 138 lb/ft<sup>3</sup>

From Table 3-I

$$q = 0.326 \text{ Btu/hr}$$

Substituting in equation (3-4),

$$\Delta T = 0.04^{\circ}\text{F}$$

The steady periodic temperature distribution is given by:

$$\frac{\Delta T'}{\Delta T} = e^{-x \sqrt{\pi f / \alpha}} \cos(2\pi f t - x \sqrt{\pi f / \alpha}) \quad (3-5)$$

where:

- $\Delta T'$  = periodic temperature component at position, x, and time, t.
- x = distance from the front surface
- $\alpha$  = K/C $\rho$

Figure 3.10 shows the temperature distribution indicated by equation (3-5). One thermal wavelength in fused quartz at a period of 106 minutes corresponds to a thickness of about 10 inches. Because of the logarithmic decay however, only about a quarter of a wavelength need be considered as contributing significantly to thermal deformation and the assumption of an infinitely thick slab is a reasonable approximation for mirror thicknesses greater than or equal to a half thermal wavelength.

An alternate type of mirror structure consists of two thin plates separated by a honeycomb structure containing about 20 percent as much material as an equivalent solid spacer. If the front plate is much smaller than a thermal wavelength, then, to a first approximation, the honeycomb can be regarded as a thermal barrier and the front plate temperature can be calculated assuming the total heat input remains in the front plate and changes its temperature accordingly. If  $\Delta T$  is the amplitude of the front plate (half the temperature range) and  $p$  is the thickness:

$$\Delta T C p p = \int_0^{1/4f} q_{\max} \sin(2\pi f t) dt \quad (3-6)$$

Taking  $p$  as 0.5 inches,

$$\Delta T = 0.085^\circ F$$

Thus far the analysis has assumed a worst-case anti-solar pointing direction, a thermally perfect telescope tube, and a geometrical configuration and mirror surface finish such that 0.65 percent of the earth albedo radiation is absorbed in the primary mirror. The orbital temperature variations at the primary mirror surface, which were estimated to be less than  $\pm 0.085^\circ F$  for a honeycomb mirror and less than  $\pm 0.04^\circ F$  for a solid mirror, are believed to be realistic worst-case estimates for a  $f/2$  aluminized primary mirror contained in an optimum satellite design employing passive thermal control.

Further passive amelioration of the thermal environment seen by the primary can be obtained by extending the telescope tube or by using a reflective surface on the primary which absorbs less albedo radiation. Neither alternative appears desirable for the present 40-inch study because of restrictive space and weight limitations and the requirement for an efficient reflector in the UV spectral region.

### 3.2.2 The Secondary Mirror

The orbital variation in thermal flux is not seen by the back of the secondary mirror since it is almost completely shielded by the fairly massive focus adjustment assembly. Of the remaining thermal flux contributions reaching the secondary, the most predominant is albedo reflected from



3-12

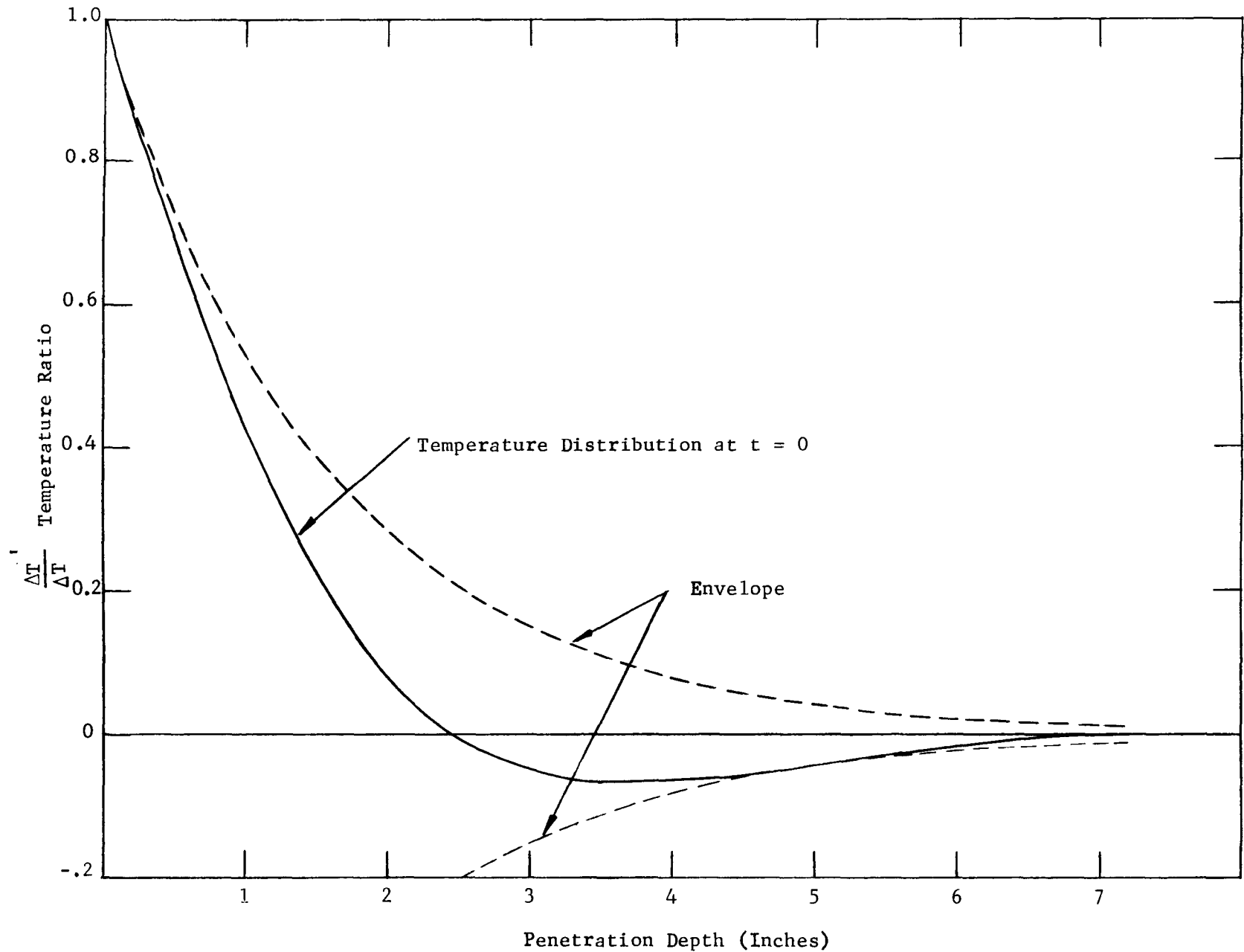


Figure 3.10. Instantaneous Temperature Distribution in a Semi-Infinite

the primary. In a typical Cassegrain arrangement the albedo flux density reaching the secondary is about 60 percent of the flux density at the primary so that a conservative estimate can be obtained by assuming the flux at the secondary to be equal to the flux at the primary.

An estimate of the maximum variation in the secondary mirror temperature can be obtained by assuming the secondary to store the total heat input for a quarter of a period. Assuming a nominal one-inch thickness of fused silica for the secondary, then from equation (3-6):

$$\Delta T = \frac{q_{\max}}{2\pi f C_{\rho p}} \quad (3-7)$$

and

$$\Delta T = 0.042^{\circ}\text{F}$$

An upper limit to the maximum thermal gradient existing through the secondary can be obtained by finding the gradient corresponding to the maximum heat input and assuming it to exist through the entire mirror thickness:

$$q_{\max} = K \left( \frac{dT}{dx} \right)_{\max} \quad (3-8)$$

and

$$\left( \frac{dT}{dx} \right)_{\max} = 0.41^{\circ}\text{F/ft}$$

### 3.2.3 Primary-Secondary Spacing Elements

The members determining the spacing between the primary and secondary mirrors are usually situated along the inside of the telescope tube in order to take advantage of mechanical rigidity offered by the tube structure. Thermal coupling between the spacing elements and the tube can be varied widely, but, depending on the characteristics of the rods, there is probably an optimum degree of thermal coupling which minimizes the need to adjust the focus.

For comparative purposes, the previous analysis, which considered the temperature distribution along a 40-inch diameter by 80-inch long aluminum tube, was extended to include the effects of orbital variations in thermal flux on spacing elements which reflect one extreme of the many possible design philosophies. For this case, the spacing elements were assumed to be one-inch diameter fused silica rods mounted along the side of the telescope tube. The outside surface of the rods was assumed to be aluminized so that the radiative properties of the rod and the front surface of the mirror were identical. Other configurations and surface properties are possible and may be preferable; this analysis is meant to serve only as an illustrative example.

Assuming that the AC component of absorption and emission of infrared radiation is small enough that it can be neglected, then the differential equation for the average rod temperature is as follows:

$$C \frac{dT}{dt} = A_o q_{OA} F_{OR} \epsilon_R \sin(\omega t) \quad (3-9)$$

where

T = mean rod temperature

t = time

C = rod heat capacity

A<sub>o</sub> = area of the open end of the telescope tube

q<sub>OA</sub> = maximum AC component of the albedo flux entering the open end of the tube

F<sub>OR</sub> = view factor from the open tube end to the rod

ε<sub>R</sub> = absorptivity of the rod to albedo radiation

ω = frequency of the AC albedo component in radians/hr

For fused silica,

$$\rho = 0.080 \text{ lbs/in}^3$$

$$C = 0.188 \text{ Btu/lb}^\circ\text{F}$$

Therefore,

$$C = (80) \frac{\pi}{4} (1)^2 (0.080) (0.188) = 0.94 \text{ Btu/}^\circ\text{F}$$

and

$$A_o = \frac{\pi}{4} \frac{(40)^2}{144} = 8.7 \text{ ft}^2$$

$$q_{OA} = 53 \text{ Btu/ft}^2 \text{ hr}$$

$$F_{OR} = 0.00776$$

$$\epsilon_R = 0.1$$

$$\omega = \frac{2\pi(60)}{106} = 3.55 \text{ rad/hr}$$

The solution to equation (3-9) is given by:

$$T = -0.11 \cos(\omega t)^\circ\text{F} + T_{\text{equilibrium}}$$

If necessary, a reduction in this amplitude of temperature variation could be effected by shielding the spacing rods from the open end of the telescope tube.

### 3.3 THERMAL TOLERANCES

#### 3.3.1 Primary Mirror

The primary mirror is the most critical component affecting the thermal design. Temperature changes which alter the radius of curvature require focus sensing and adjustment mechanisms in order to avoid spherical aberration in the image. Nonuniform temperature distributions resulting in mirror figure changes cannot be corrected and must therefore be kept within bounds by careful thermal design.

3.3.1.1 Uniform Temperature Changes - If the spacing elements between the primary and secondary mirrors are fabricated from the same material as the mirrors themselves, then uniform temperature changes tend only to scale the optical system leaving the image quality intact. In general, completely uniform temperature changes cannot be obtained in a satellite environment due to gross differences in the thermal time constants of the various components and their radiation geometry.

Unless a completely automatic system is used, focus adjustment will only be possible during the short time of radio contact obtained once per orbit. A temperature uniformity such that focus adjustment is required, a maximum of once per orbit to accommodate changes in equilibrium temperature brought about by gross changes in telescope orientation, rather than by orbital temperature variations is a worthwhile design objective, whether the adjustment is automated or not. The effect of a uniform temperature change on the primary mirror is given by:

$$\Delta F = \alpha F \Delta T \quad (3-10)$$

where:

$$\begin{aligned} \Delta F &= \text{change in focal length} \\ F &= \text{focal length} \\ \alpha &= \text{coefficient of expansion} \\ \Delta T &= \text{change in temperature} \end{aligned}$$

The allowable change in focus before correction is necessary is somewhat arbitrary but can be represented by:

$$\Delta F \approx \pm 8 \left( \frac{\lambda}{n} \right) \left( \frac{F}{D} \right)^2 \quad (3-11)$$

where:

- $\lambda$  = wavelength  
 $n$  = a number between 4 and 16 depending on the allowable degradation in image quality  
 $D$  = the aperture diameter

Setting equations (3-10) and (3-11) equal:

$$\Delta T = \pm 8 \left( \frac{\lambda}{n} \right) \frac{F}{\alpha D^2} \quad (3-12)$$

For a given f/number (F/D ratio) the allowable temperature change in the primary mirror varies inversely as the diameter. Assuming the thickness of a primary mirror to be proportional to the diameter, then the reduced temperature tolerance of large aperture systems is offset by the larger thermal mass of the primary mirror. The maximum allowable temperature change for a 40-inch fused silica primary mirror may be determined from equation (3-10) assuming:

- $F$  = 80 inches  
 $D$  = 40 inches  
 $\lambda$  =  $0.5\mu$   
 $n$  = 10  
 $\alpha$  =  $0.31 \times 10^{-6}/^{\circ}\text{F}$

which yields:

$$\Delta T = \pm 2.54^{\circ}\text{F}$$

This far exceeds the change in average temperature due to orbital variations in heat flux which is computed in section 3.2.1.

The effect of uniform temperature changes in the primary mirror is therefore concluded to be negligible for a time scale in the order of an orbital period, however, gross changes in telescope orientation resulting in large differences in equilibrium temperature may produce significant long term effects depending on the relative thermal time constants of various components.

3.3.1.2 Linear Temperature Gradients - The distortion of a spherical surface caused by a linear temperature gradient along the optical axis and at right angles to the axis was investigated in Technical Note DAM-001, (App. B, Vol. III). A gradient perpendicular to the optical axis was shown to have a negligible

effect provided the mirror support is near the center. An axial gradient was found to produce a shift in focus given by:

$$\Delta F = 2F^2 \alpha \Delta \left( \frac{dT}{dx} \right) \quad (3-13)$$

where  $\Delta \left( \frac{dT}{dx} \right)$  is the temperature gradient change in degrees per unit length.

Combining equations (3-13) and (3-11), the allowable change in gradient is given by:

$$\Delta \left( \frac{dT}{dx} \right) = \pm \frac{4}{\alpha} \left( \frac{\lambda}{n} \right) \frac{1}{D^2} \quad (3-14)$$

Equation (3-14) indicates that the thermal gradient tolerance becomes tighter as aperture size increases. Unfortunately this relationship is of limited applicability since the temperature distribution in the primary tends to be highly nonlinear as was shown in section 3.2.1. A more general relationship can be obtained from the solution for a thin plate subjected to a temperature distribution which is an arbitrary function of thickness.<sup>4</sup> If the plate is assumed to lie in the x-y plane with the center at z = 0, then the displacement of the centerline in the z direction after the temperature distribution is established is given by:

$$W = \frac{-3M_T(x^2 + y^2)}{4h^3 E} \quad (3-15)$$

where:

$$M_T = \alpha E \int_{-h}^{+h} Tz dz$$

E = modulus of elasticity

$\alpha$  = coefficient of expansion

T = temperature (a function of z)

h = half thickness

Equation (3-15) corresponds to a deformation in the shape of a sphere of radius, r, where,

$$\frac{1}{r} = \frac{-3M_T}{2h^3 E} \quad (3-16)$$

and since the plate was initially flat,

$$d\left(\frac{1}{r}\right) = d\left(\frac{-3M_T}{2h^3E}\right) \quad (3-17)$$

$$\frac{dr}{r^2} = \frac{3}{2h^3E} d(M_T) \quad (3-18)$$

The radius and focal length are related by:

$$F = \frac{r}{2} \quad (3-19)$$

so that

$$\frac{dF}{2F^2} = \frac{dr}{r^2} \quad (3-20)$$

Substituting into (3-18)

$$dF = \frac{3F^2}{h^3E} d(M_T) \quad (3-21)$$

or,

$$\Delta f = \pm \frac{3F^2\alpha}{h^3} \Delta \left( \int_{-h}^{+h} Tz dz \right) \quad (3-22)$$

Equation (3-22) reduces to equation (3-14) for the case of a linear gradient and is similarly only a first approximation to the mirror deformation. Combining equation (3-22) and equation (3-11):

$$D^2 = \left(\frac{\lambda}{n}\right) \frac{8h^3}{3\alpha\Delta \left(\int Tz dz\right)} \quad (3-23)$$

Applying equation (3-23) to the temperature distribution shown in Figure 3.10 and assuming a maximum temperature excursion from  $-0.04^\circ\text{F}$  to  $+0.04^\circ\text{F}$  and a mirror thickness of 5 inches:

$$\Delta \left( \int_{-h}^{+h} Tz dz \right) = 0.075^\circ\text{F in}^2$$

Taking,

$$n = 10$$

$$\lambda = 0.5\mu$$

$$\alpha = 0.31 \times 10^{-6}/^{\circ}\text{F} \text{ (fused silica)}$$

then:

$$D = 57 \text{ inches}$$

The limiting aperture size depends on the mirror thickness used in equation (3-19). However, the calculation based on a 5-inch thick solid mirror is representative of what could be employed in a 40-inch aperture system and indicates achievement of sufficient thermal isolation so that focus adjustment only once per orbit is a possible design objective.

The limiting aperture size for a 5-inch honeycomb mirror can be calculated directly from equation (3-14) by assuming the temperature in the webbing to vary linearly between the two faceplates.

Taking,

$$T' = \frac{(0.085^{\circ}\text{F})}{5 \text{ inches}} = 0.017^{\circ}\text{F}/\text{inch}$$

then:

$$D = 39 \text{ inches}$$

A 40-inch honeycomb mirror, therefore, presents a more serious thermal design problem than a solid mirror unless the thermal conductivity between the two faceplates can be altered drastically.

3.3.1.3 Nonlinear Thermal Gradients - Nonlinear thermal gradients produce stress distributions which are dependent on boundary conditions. Except in a few special cases, an exact solution of the thermo-elastic deformation is not possible in a closed form. The approximate methods which have been developed for handling thermo-elastic problems generally invoke Saint-Venant's principle and thereby neglect the higher order terms describing the loss of optical figure.

For a thin spherical mirror with an arbitrary radial temperature distribution, approximations are readily available in the form of a flat plate with an arbitrary temperature distribution as a function of thickness, or in the form of a complete spherical shell with an arbitrary radial temperature distribution. Neither approximation includes non-spherical deformation terms which appear to exist for the case of a spherical segment.

A satisfactory description of the effects of nonlinear thermal gradients appears to be a very difficult analytical problem. The most



practical means of gaining insight into the problem may be through the use of a few examples solved with reiterative computer techniques or, alternatively, through experimental measurements covering a range of environmental conditions. If honeycomb and similar complex mirror structures are to be considered, then experimental measurements are of the utmost importance and analytical techniques, if they can be applied at all, are useful only as qualitative backup information.

### 3.3.2 Secondary Mirror

The thermal tolerances for the secondary mirror can be determined from equations (3-12) and (3-14) since they hold for situations involving both collimated and uncollimated light beams. Assuming a fused silica secondary having a focal length of 19.8 inches and a diameter of 7.9 inches then the corresponding tolerances are,

$$\begin{aligned}\Delta T &= \pm 16^{\circ}\text{F} \\ \Delta \left( \frac{dT}{dx} \right) &= \pm 0.4^{\circ}\text{F/inch}\end{aligned}$$

Comparing these to the corresponding tolerances for a 40-inch primary, then the temperature tolerance is 6 times and the gradient tolerance 25 times larger for the secondary. As might be expected, the thermal tolerances on the secondary exceed, by a considerable margin of safety, the orbital variations in temperature and temperature gradient which were estimated in section 3.2.2. The allowable change in temperature gradient is the tighter tolerance and this exceeds the maximum predicted gradient by an order of magnitude.

### 3.3.3 Primary-Secondary Spacing Elements

Uncompensated changes in the longitudinal distance between the primary and secondary mirrors results in defocussing analogous to changes in the radius of the primary or secondary mirrors considered previously. The tolerance on the mirror spacing ( $\zeta$ ) is given by the following relationship:

$$\zeta = \pm 8 \left( \frac{\lambda}{n} \right) \frac{(mf_p)^2}{1+m^2} \quad (3-24)$$

where:

- $\lambda$  = wavelength used
- $n$  = number usually between 4 and 16 which characterizes the allowable image degradation
- $m$  = magnification of the secondary
- $f_p$  = f/number of the primary mirror

For a  $f/2$  primary and a secondary having a magnification of 5, a  $\lambda/10$  image criterion leads to the following tolerance at  $0.5\mu$  wavelength:

$$\zeta = \pm 0.606 \times 10^{-4} \text{ inches}$$

Assuming a distance of 65 inches between the primary and secondary mirrors, then this tolerance corresponds to about plus or minus one part in a million. If fused silica is used as the spacing element material then the corresponding temperature range is about  $\pm 3^\circ\text{F}$  or 30 times as large as the orbital variation in spacing rod temperature computed for the example in section 3.2.3.

REFERENCES

- <sup>1</sup>Stevenson and Grafton, Radiation Heat Transfer Analysis for Space Vehicles ASD Technical Report 61-119, Part I.
- <sup>2</sup>Hamilton and Morgan, Radiant Interchange Configuration Factors. NACA Technical Note 2836.
- <sup>3</sup>Schneider, Conduction Heat Transfer, Addison - Wesley, 1955.
- <sup>4</sup>Boley and Weiner, Theory of Thermal Stresses.

#### 4.0 POINTING SERVO

##### 4.1 THEORETICAL CONSIDERATIONS

The initial phases of the telescope pointing system study for the Advanced Princeton Satellite concentrated on four fundamental issues:

- a. The theoretical possibility of pointing the telescope to the extreme accuracies required to remain within the theoretical optical resolution capability using twelfth magnitude guide stars.
- b. If such pointing specifications are theoretically attainable, what are the theoretical limitations?
- c. What design concepts or approaches are feasible for such an extreme accuracy requirement?
- d. What are the implications of the pointing system design concepts in terms of optical design and overall pointing servo performance, i.e., tracking and acquisition?

The results and conclusions of these investigations are presented in this section and provide the groundwork for the telescope pointing system design of Volume III, Section 3.0.

The purpose of the pointing system is to provide pointing control consistent with telescope optical resolution for the Orbiting Astronomical Observatory (OAO) telescope and its associated data-gathering instruments. Pointing control will be achieved using preselected guide stars located in proximity to a stellar source being observed. Optical sensors will angularly determine the location of the stars (i.e., within the sensor field of view) and produce error signals proportional to mispointing which, via the stabilizing electronics and actuators, will hold the telescope pointed at the object of interest. Optimum, long-term pointing accuracy, 0.01 arc-sec (rms), is demanded of the pointing system for a 40-inch aperture telescope as a result of the high optical resolution theoretically possible and the extremely faint (high magnitude) stellar sources being examined. The accuracy requirement is applicable to the telescope vertical (pitch) and horizontal (yaw) axes only. The roll axis accuracies are less ( $\approx 4.0$  arc-sec rms). To achieve pointing control about these three axes a minimum of two guide stars is necessary.

A preliminary decision was made to freely suspend the telescope within the outer spacecraft for the reasons listed below:

- a. The spacecraft guidance system is not capable of pointing the telescope to the accuracies required.

- b. Modifying an existing spacecraft guidance system is not economically feasible and creates severe interface problems.
- c. The vibration and disturbance levels existing in the OAO spacecraft, particularly in manned Apollo configurations for instance, are prohibitive for reasonable guidance system designs (see section 3.4.5, Volume III).

In the freely suspended configuration, the telescope will maintain independent pointing control and the following system analysis was conducted on this basis. In the succeeding discussion a single axis of the pointing system will be considered to consist of three basic blocks:

- a. Guide Star Sensor.
- b. Servo Stabilized Electronics.
- c. Telescope Positioning Devices (i.e., Torquers).

#### 4.2 SIGNAL-TO-NOISE CALCULATIONS

One of the most important phenomena that could prevent the pointing system from achieving specification is the electrical noise characteristic of the optical sensor. Fundamentally, the sensor provides the pointing controls with commands in the form of error signals. False error signals can arise in such a system since there is no method of distinguishing between error signals caused by external disturbances and those caused by internally generated electrical noise. It is, therefore, necessary to determine the signal (mispointing)-to-noise ratio (S/N) that will enable the system to meet pointing specifications. The first important step in this analysis, therefore, involves signal-to-noise calculations based on expected guide star magnitudes and sensor parameters.

To provide a working basis for calculating and analyzing input noise levels, an optical sensor concept must be selected. One common form of a sensor is shown in Figure 4.1, and functions as follows: Starlight entering the optical system converges at the apex of a four-sided prism where a focused image is formed and divided into two parts per axis. Each divided image is collected by a photosensitive element which produces electrical outputs proportional to light intensity. With correct pointing in a given axis, the two photosensors receive equal quantities of light and, if their electrical outputs are differenced, the net output is zero. Mispointing upsets the light division and causes the electrical signal (E) to depart from null.

In order to calculate the sensor noise and/or S/N ratio, a relationship between sensor receiver characteristics, power density at the receiver collector, noise due to background illumination, photon discreteness

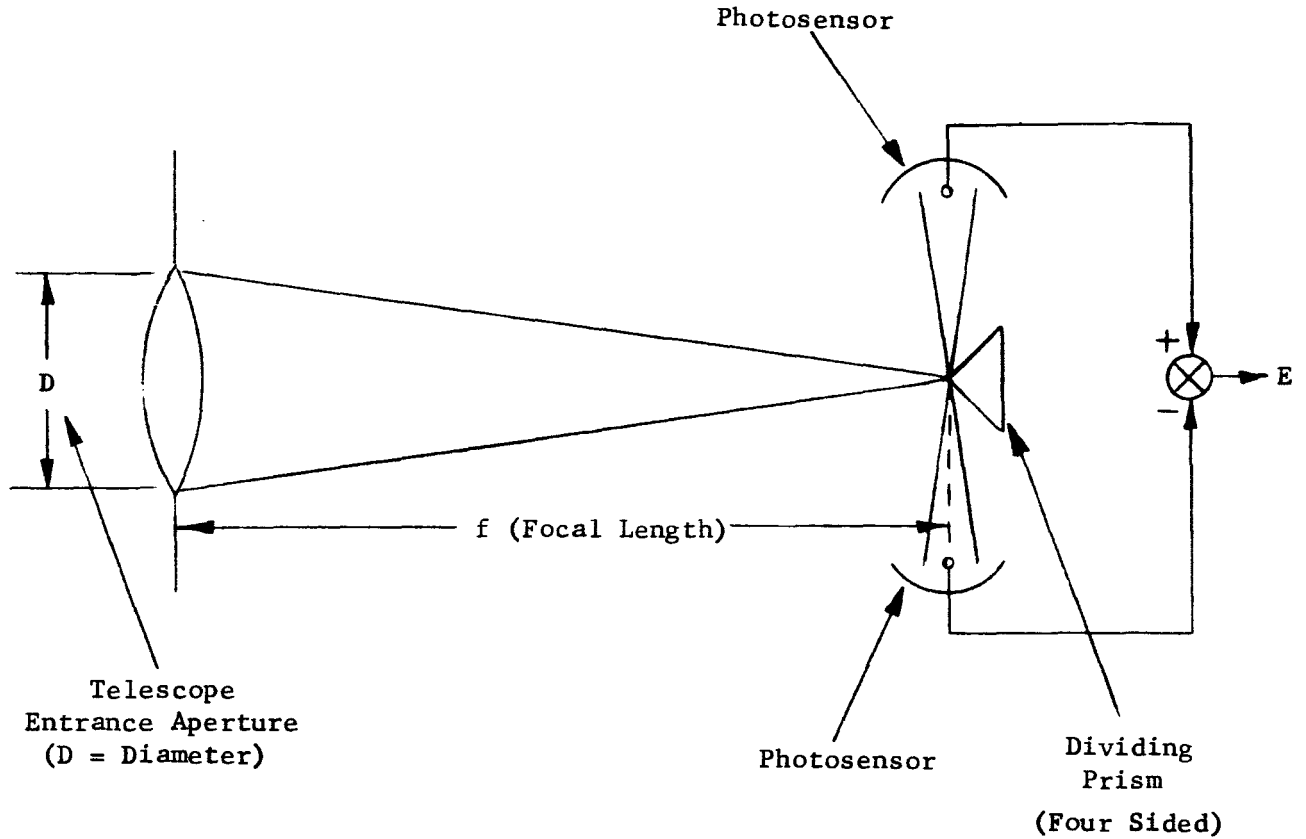


Figure 4.1. Single Axis Tracking Sensor Utilizing Diffraction Limited Optics

or shot noise, detector noise contributions, and servo response bandwidth must be developed.

The analytical relationship between the output signal and the angular pointing error for this type of sensor is determined from the Airy diffraction pattern<sup>1</sup> of the star image formed at the dividing prism. From the diffraction pattern, the image energy transfer curve is derived as a function of the pointing error which can be measured in terms of a fraction of the Airy disk diameter, (see Figure 4.2). Using a straight line approximation to the energy transfer curve, it is evident that the energy transfer at null position is equivalent to the total energy transferred for an angular motion of  $1.22 \lambda/D$  ( $\lambda$  = wavelength,  $D$  = aperture diameter, both in meters). Such an angular motion results in the first bright ring of the diffraction pattern being moved to the apex of the image-dividing prism. Then, since the output of the photosensors are differenced,

$$E_{\text{total}} = 2S \tag{4-1}$$

where  $S$  is signal in terms of angular pointing error relative to the diffraction pattern, and  $E$  is the electrical signal in the photosensor.

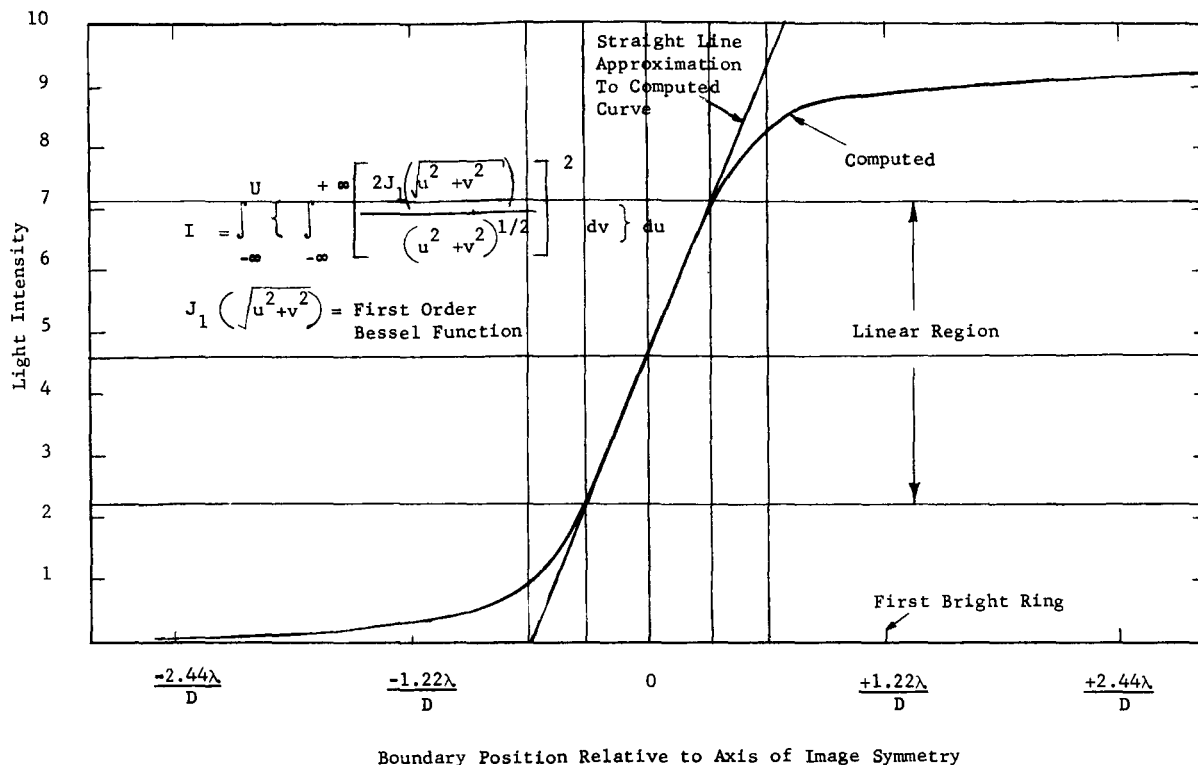


Figure 4.2. Image Light Energy on One Side of a Knife Edge Boundary

Assuming prior knowledge of the S/N ratio in a particular response bandwidth, an rms noise of N in this same bandwidth will, therefore, cause the system to have an rms pointing error ( $E_p$ ) described by

$$E_p = 1.22 \lambda/D \left( \frac{N}{2S} \right) \tag{4-2}$$

or

$$E_p = 0.61 \lambda/D \left( \frac{S}{N} \right)^{-1}$$

for pointing errors close to null.

This expression, which agrees with independent results,<sup>2</sup> is correct even when fairly large central obscurations are present, provided, in all cases, that the S/N ratio is reasonably large (viz.  $S/N \leq 10$ ). As the S/N ratio is lowered, the expression becomes optimistic (due to greater departures of the straight line approximation from the energy transfer curve) and more accurate results can be obtained with other than simple slope approximations.

The S/N ratio is derived statistically from analysis and can be calculated from a knowledge of the optical transmission and photocathode quantum efficiencies, background illumination, photon discreteness, star

irradiance and bandpass frequencies. The final expression for this ratio can then be substituted into equation (4-2) which would complete the relationship necessary to determine the magnitude of the mispointing caused by noise.

A zero magnitude star produces an irradiance ( $I_m$ ) of  $3.8 \times 10^{-12}$  watts/cm<sup>2</sup>/micron at 0.55 micron (or equivalently  $2.6 \times 10^{-10}$  lumens/cm<sup>2</sup> at 0.1 micron). Taking an effective spectral energy range of 0.1 micron (conservative estimate of phototube spectral response in visible. This could in certain cases, be extended to values as large as 0.25 micron) the photon arrival rate of the system can be expressed as

$$P_S = \eta_o I_m \epsilon_q A \tag{4-3}$$

where

$P_S$  = Arrival rate of signal photons at the photon detectors (photons/sec)

$\eta_o$  = System optical transmission efficiency

$I_m$  = Star irradiance for a specific photomultiplier spectral range (watts/meter<sup>2</sup>)

$\epsilon_q$  = Photon quantum energy at a specific wavelength (photons/sec/watt),  $1/hf$

$A$  = Entrance aperture area for the optical system (meter<sup>2</sup>),  $\frac{\pi}{4} D^2$

Substituting values,

$$P_S = \eta_o \frac{3.8 \times 10^{-9}}{(2.51)^{mv}} \left( 2.76 \times 10^{18} \right) \left( \frac{\pi}{4} D^2 \right) \text{photons/sec} \tag{4-4}$$

where,

$mv$  = Guide star visual magnitude.

The signal-to-noise ratio is expressible as

$$\frac{S}{N} = \frac{P_S \eta_Q \Delta t}{\left[ \left( P_S \eta_Q + \epsilon_n \right) \Delta t \right]^{1/2}} \tag{4-5}$$

$\epsilon_n$  = Equivalent photomultiplier quantum energy (rms pulses contributed by dark current, background illumination, and cosmic ray variations) (photons/sec).

$\Delta t$  = Bandwidth period (sec) or sampling interval which equals  $\frac{1}{2 f_{eq}}$  where  $f_{eq}$  (cps) is the equivalent system bandwidth.



$\eta_Q$  = Photocathode quantum efficiency

Calculating,

$$\frac{S}{N} = \frac{\left[ \frac{1.05}{2.51^{mv}} (10^{10}) \left( \frac{\pi}{4} D^2 \right) \eta_o \eta_Q \Delta t \right]}{\left[ \frac{1.05}{2.51^{mv}} (10^{10}) \left( \frac{\pi}{4} D^2 \right) \eta_o \eta_Q \Delta t + \epsilon_n \Delta t \right]}^{1/2} \quad (4-6)$$

If the background illumination, dark current, and other noise sources are neglected, i.e.,  $\epsilon_n = 0$ , the relationship for the theoretical maximum S/N ratio is obtained.

$$\left. \frac{S}{N} \right|_{\epsilon_n = 0} = \left[ \left( \frac{1.05}{2.51^{mv}} \right) (10^{10}) \left( \frac{\pi}{4} D^2 \right) \eta_o \eta_Q \Delta t \right]^{1/2} \quad (4-7)$$

This expression is plotted in Figure 4.3 in terms of S/N versus mv (star magnitude). A comparison between the ground evaluation results of Stratoscope II and that predicted by this equation indicates agreement within a factor of 3 with measured errors being higher than predicted.

If the maximum S/N ratio is substituted into equation (4-2), the final rms pointing error relationship is obtained. In this case,  $\epsilon_n = 0$  and  $E_p$  is considered the minimum pointing error that can be obtained.

$$E_p \text{ (min)} = \left( 0.756 \times 10^{-6} \right) \left( \frac{1}{D^2} \right) \left[ \left( 2.51 \right)^{mv} \frac{1}{\eta_o \eta_Q \Delta t} \right]^{1/2} \text{ arc-sec(rms)} \quad (4-8)$$

This expression is plotted logarithmically against star magnitude in Figure 4.4. The  $E_p$  (min) relationship clearly indicates the effect of aperture diameter on pointing accuracy. It is obviously more difficult to obtain a given pointing accuracy with a 1-meter aperture diameter than to obtain the same accuracy with a 3-meter aperture diameter for the same stellar magnitude and servo bandwidth.

If the dark current and other noise-contributing sources inherent in  $\epsilon_n$  are included, the S/N will be substantially reduced, resulting in an increased rms pointing error. This is particularly true if, for instance, dark current variations due to thermal emission produce photocathode currents not much smaller than those due to signal. However, the amount of  $E_p$  increase due to all the  $\epsilon_n$  factors can be minimized by using reduced temperatures for the photosensors, signal processing techniques, minimal field of view, and restricted servo bandpass. Dark current, for example, due to thermal emission appears as a photocathode output current level having a slow drift rate.

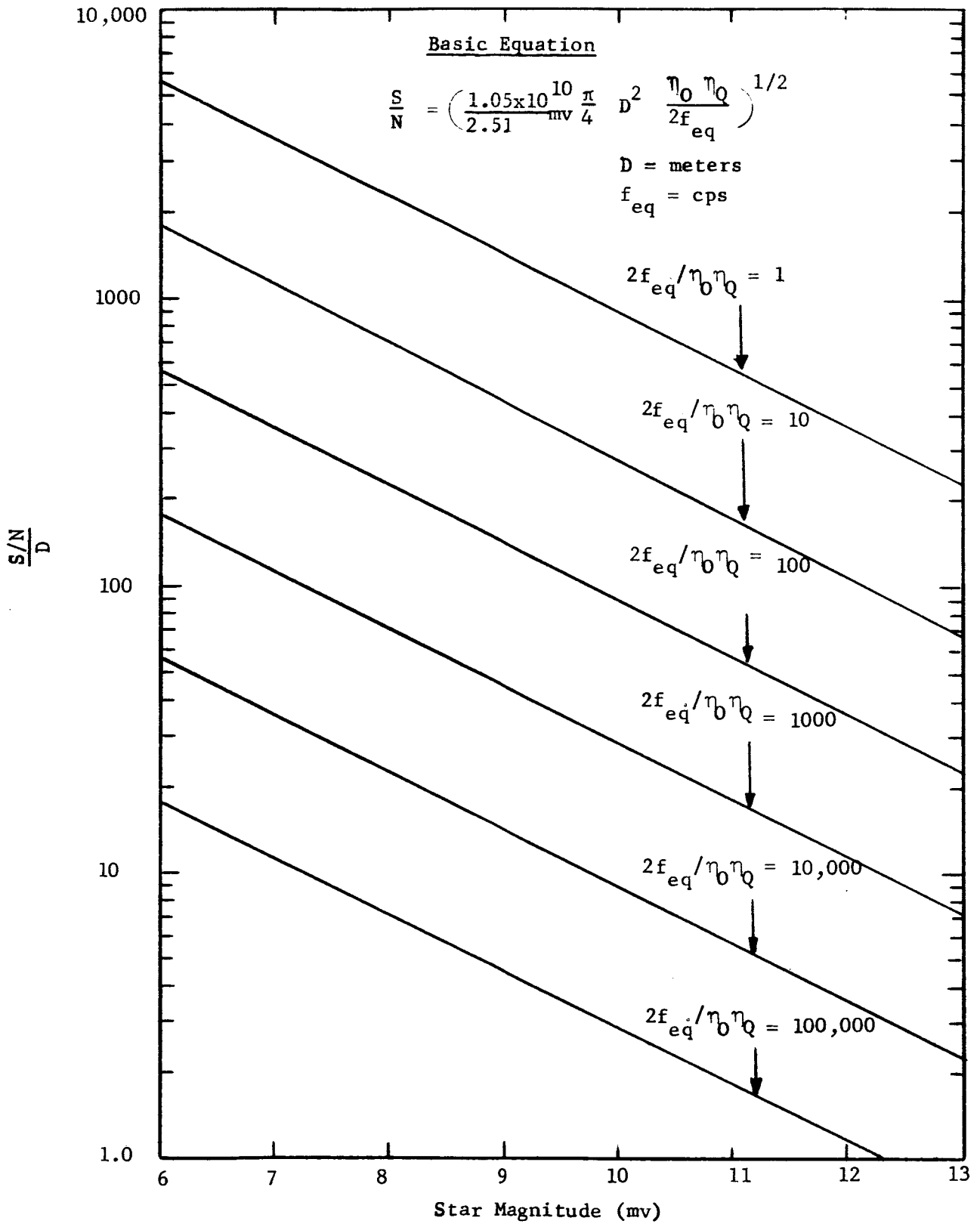


Figure 4.3. Maximum Signal to Noise (S/N) Ratio vs. Stellar Magnitude

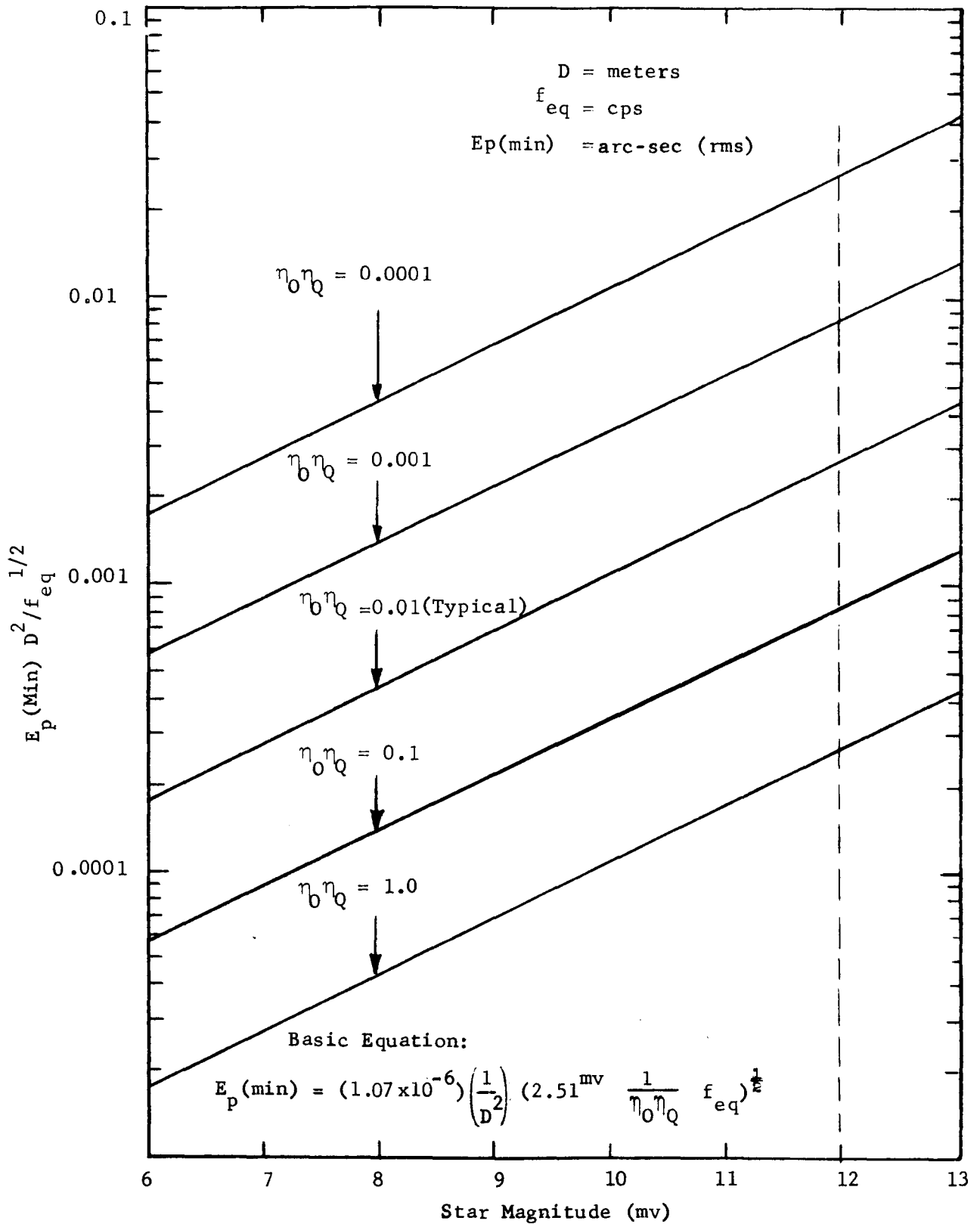


Figure 4.4. Minimum RMS Pointing Error ( $E_p$ ) vs. Stellar Magnitude

Cooling the photocathode markedly reduces these current levels. Figure 4.5 contains a plot of equivalent light intensity versus temperature of dark current, indicating the average performance measured on nine RCA type 7265

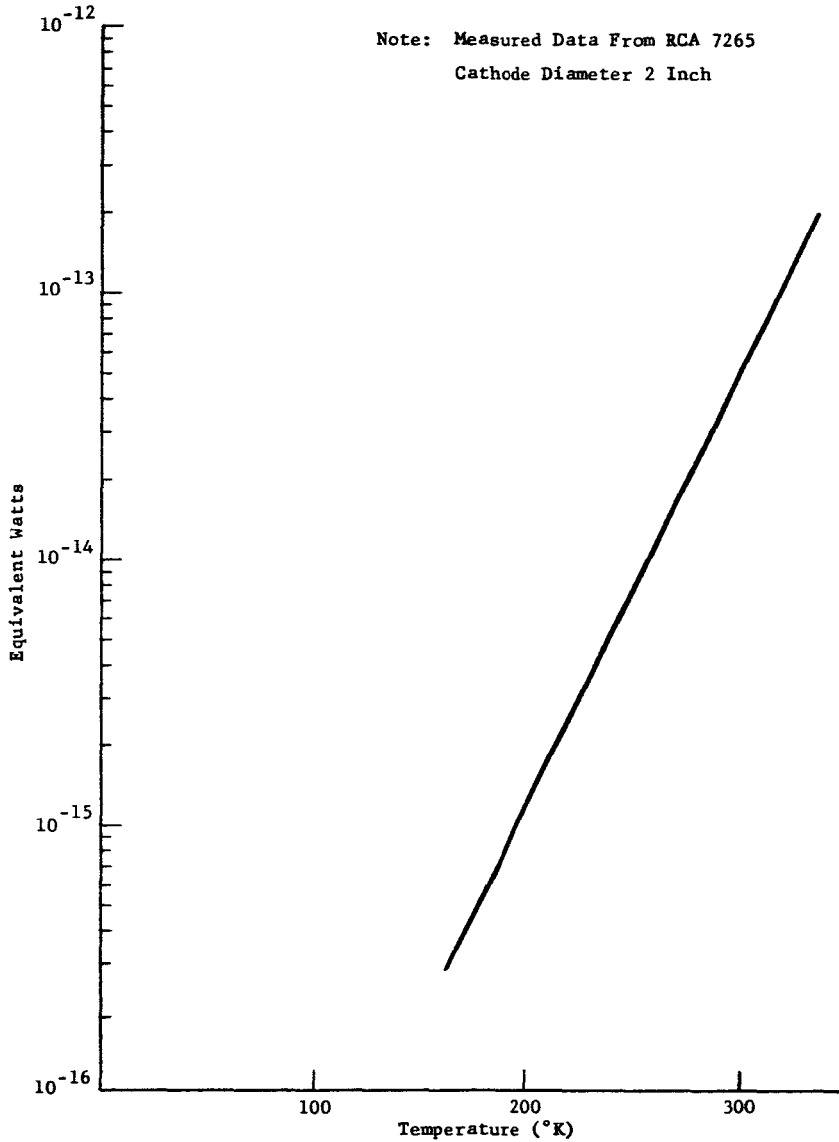


Figure 4.5. Photomultiplier Cathode Dark Current Equivalent Watts

S-20 multipliers. It is seen that the dark current equivalent input at 300°K (27°C) is approximately  $5 \times 10^{-14}$  watts at 0.55 micron which is about the same order as the expected signal from an eleventh magnitude star. For example:

$$\frac{3.8 \times 10^{-9}}{2.51^{11}} D^2 \frac{\pi}{4} \eta_o = 4.0 \times 10^{-14} \text{ watts} \quad (4-9)$$

for  $\eta_o = 0.33$

$D = 1 \text{ meter}$

and a spectral bandwidth of 0.1 microns.

Cooling to 200°K (-73°C), if practical, can reduce the dark current by a factor of nearly 40:1, which would bring it to the light level irradiance of a fifteenth magnitude guide star. Another technique for eliminating the DC component of thermal dark current is optical or electrical chopping of the light signal. The photocathode output current can be made to appear in a coded AC form and with proper electrical processing techniques, photocathode DC or very low frequency variations can be rejected. Quite similarly and worth noting at this point, photocathode spectral sensitivity and gain changes would produce electrical imbalances resulting in pointing errors for a two-tube per axis type of sensor.

Optical chopping has another significant advantage. One tube per axis can be eliminated which, in turn, eliminates the effects of tube imbalance. The single tube concept is accomplished by directing each divided image to a common optical chopper and phototube combination as shown in Figure 4.6. Several signal chopping techniques are feasible and are covered in the telescope design study (Section 3.0, Vol. III) whereby 100 percent of starlight is utilized

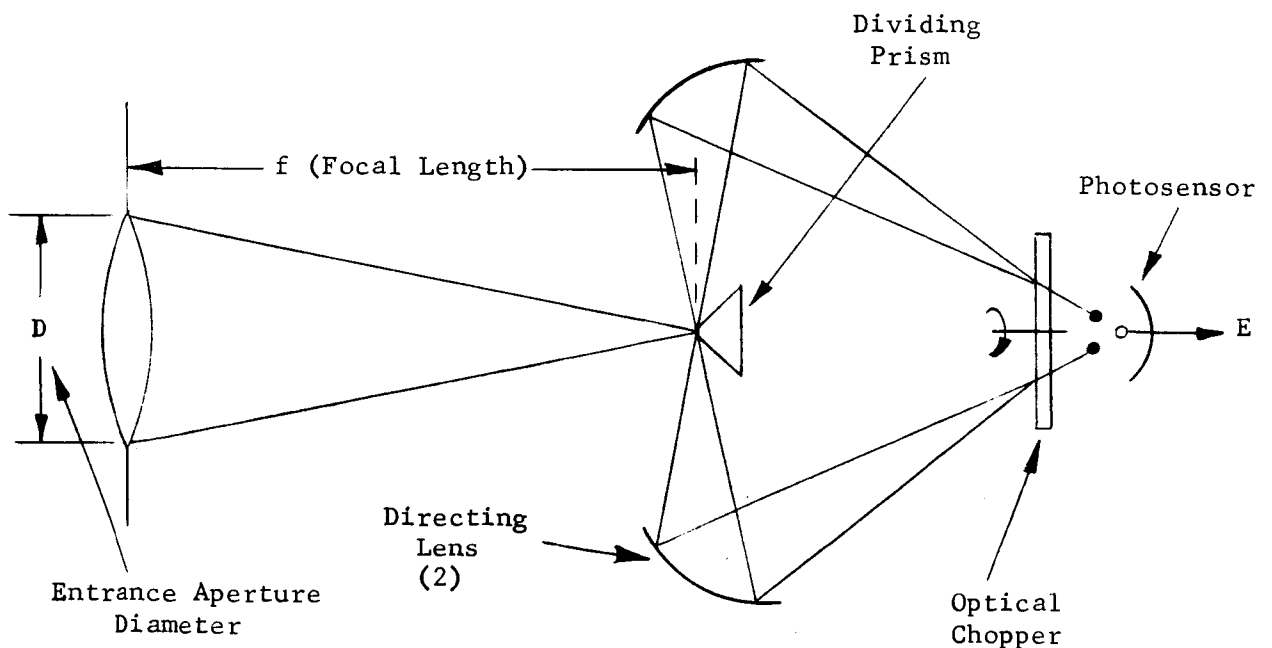


Figure 4.6. Single Axis Tracking Sensor Utilizing a Single Tube and Optical Chopper

to maintain maximum signal to noise-in-signal ratio. By proper phase synchronization in the sensor electronics, the intensity of each divided star image is differenced to accomplish the same purpose, i.e., pointing error proportional to intensity variations.

It is necessary to determine the values of two remaining parameters before final S/N ratios can be established, namely, bandpass frequencies and background illumination. Each of these parameters is considered below.

Background illumination from surrounding stellar sources, scattered light from earth albedo, etc., contributes to noise and is directly dependent on the optical field of view of the sensor. Reducing the field of view will proportionally reduce background noise but will also impose severe performance requirements on the pointing system. This is particularly true in the case of acquisition requirements. Trade-offs are, therefore, necessary to arrive at an optimal field of view. If two fields of view are used with the large diameter field utilized primarily for acquisition, trade-off problems are greatly reduced.

The two-field-of-view approach for the sensors is incorporated in the optical system design and the diameters were initially selected at 1 arc-min (fine) and 3 arc-min (coarse). These diameters were based on S/N and system acquisition requirements which are established in Sections 4.3 and 4.4.

Reducing the fine field of view below 1 arc-minute results in small signal-to-noise improvements (neglecting earth-reflected light). If preliminary estimates of dark current and background noise are used, plots of S/N versus field of view can be obtained in Figures 4.7 and 4.8 which verify this fact. Figure 4.7 is a plot of S/N versus field of view (normalized to bandwidth and for various apertures and optical efficiencies). Figure 4.8 is a plot of the ratio of S/N with and without background and indicates clearly the diminishing returns obtained for fields of view less than 1 arc-minute.

The background noise levels (cosmic ray noise considered negligible by design) were established as being equivalent to an eleventh magnitude star per 16 arc-min<sup>2</sup> for selected stellar experimental sources.<sup>3</sup> This value does not include the earth reflected light during the daylight portions of the orbit. If included, the background noise level using values based on the OAO-C telescope as an example will increase to approximately the equivalent of a fifth magnitude star per 36 arc-min<sup>2</sup>. These calculations of earth-scattered light were based on isotropic scattering and an initial 90 percent absorption within the telescope.<sup>4</sup> The effect of field of view with such values of earth-reflected background noise included is also shown in Figures 4.7 and 4.8. Expected values of earth reflected light for the advanced OAO experiment telescope will be higher.

The system bandwidth enters the S/N calculations as previously indicated by the relationship in equation (4-6) and Figure 4.3. As the bandwidth becomes smaller, i.e.,  $\Delta t$  increases, the S/N increases as indicated by equation (4-6). Basically, any factor in  $e_n$  appearing as statistical noise is also filtered and minimized identically as photon shot noise is minimized.

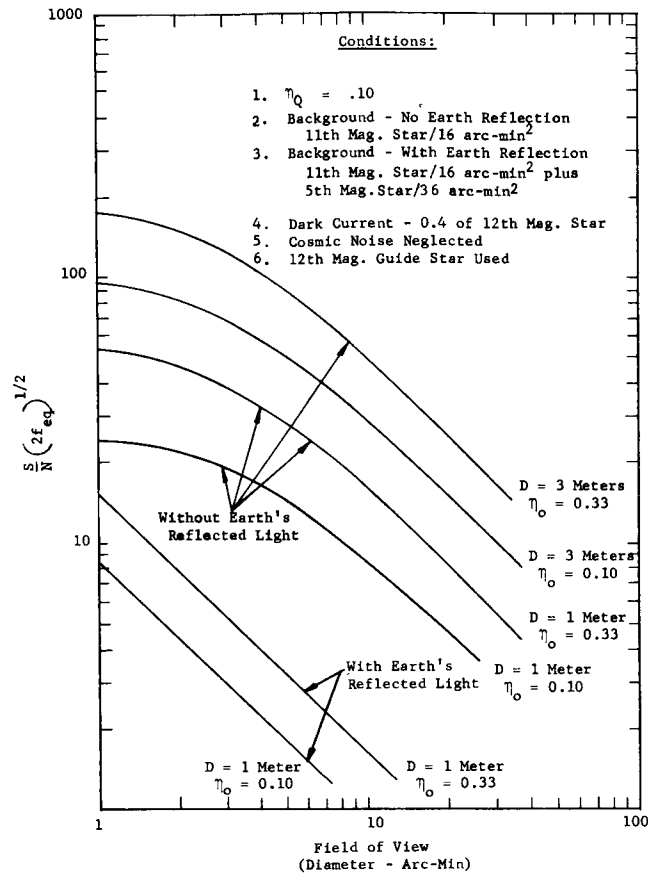


Figure 4.7. S/N vs. Field of View

The bandwidth, however, cannot be reduced to zero since some system response is required to point the telescope and minimize torque disturbances. Once again, a trade-off in system response between noise and disturbing torques exists and is developed in the following section.

#### 4.3 SYSTEM RESPONSE

The approach used to determine the minimum bandwidth in the final tracking mode is based mainly on external torque disturbances. It ignores, for the moment, acquisition requirements. Although acquisition can and does influence system response (see section 4.4), it is only a transient system condition.

The external torque disturbances result from several sources, particularly gravity gradients, aerodynamics and magnetic fields. Conservatively estimated, the peak external torque applied to the telescope is in the order of 20,000 dyne-cm (0.0015 lb-ft). This torque is considered sinusoidal with a 1/2 orbital frequency (2,700 second period).

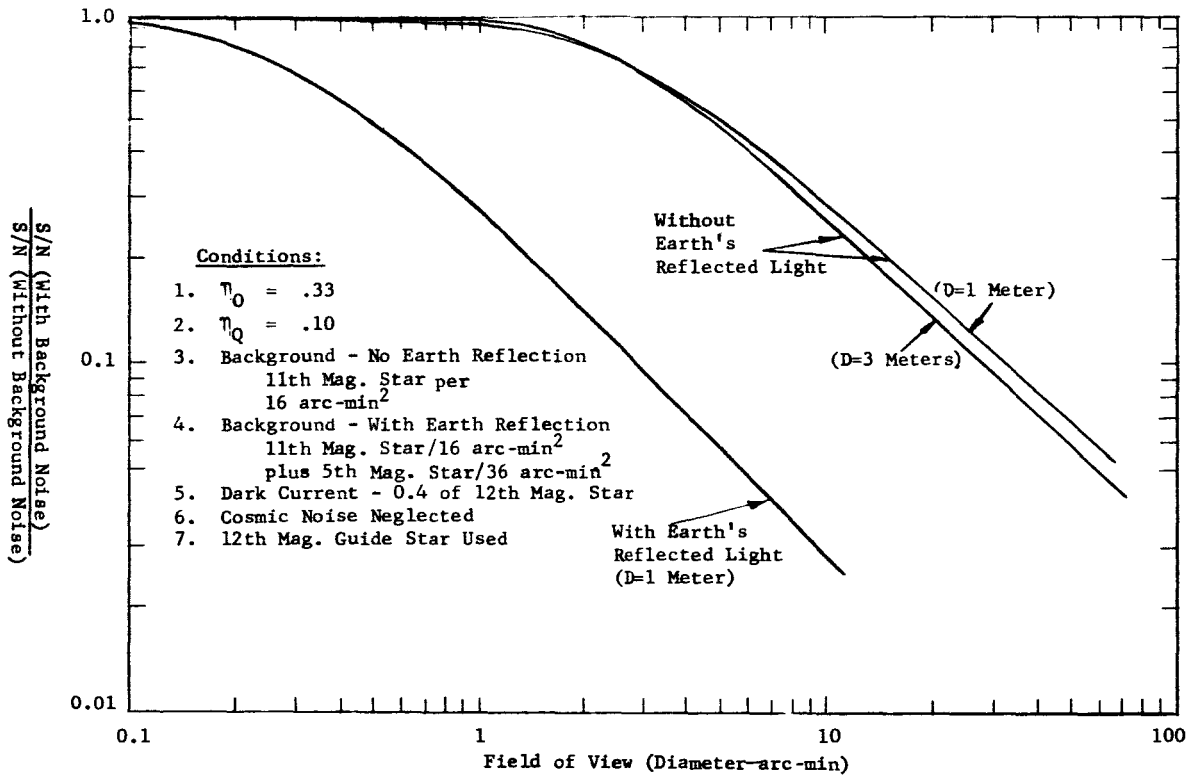


Figure 4.8. Normalized Signal to Noise vs. Field of View

If a 20,000 dyne-cm (or 0.0015 lb-ft) torque was applied to the telescope without the aid of a pointing system, pointing errors of  $2.3 \times 10^5$  to  $5.7 \times 10^5$  arc-sec (peak) would occur based on estimated telescope inertias of 100-250 slug-ft.<sup>2</sup>. These errors are calculated as follows:

$$\tau_d = J \frac{d^2\theta_e}{dt^2} = 20,000 \sin \omega t \tag{4-10}$$

or

$$\theta_e = \frac{1}{J} \iint 20,000 \sin \omega dt dt \tag{4-11}$$

where

- $\tau_d$  = Torque Disturbance (lb-ft)
- $J$  = Telescope Inertia (slug-ft<sup>2</sup>)
- $\omega$  = Orbiting Frequency (rad/sec)
- $\theta_e$  = Pointing Error (arc-sec)



Integrating and calculating, for  $J = 100 \text{ slug-ft}^2$ ,

$$\theta_e = \frac{(.0015)(2700.)^2}{(100)(2\pi)^2} (2.06 \times 10^5) = 5.7 \times 10^5 \text{ arc-sec (peak)}$$

and for  $J = 250 \text{ slug-ft}^2$

$$\theta_e = 2.3 \times 10^5 \text{ arc-sec (peak)}$$

The need for a pointing control is obvious if 0.01 arc-sec or less is to be obtained.

The effect of the external disturbance can be reduced by simply opposing it with an active correcting torque.

$$\tau_d - \tau_c = \tau_e \quad (4-12)$$

where

$\tau_c$  = Corrective torque (lb-ft)

$\tau_e$  = Error torque (lb-ft)

Since  $\tau_e = J\ddot{\theta}_e$ , for  $J = 100 \text{ slug-ft}$  and  $\theta_e = 0.01 \text{ arc-sec (rms)}$  which varies at a period of 2700 seconds,

$$\begin{aligned} \tau_e &= (100) \left( \frac{2\pi}{2,700} \right)^2 \left( \frac{.01}{.707} \right) \left( \frac{1}{2.06} \times 10^{-5} \right) \\ &= 3.72 \times 10^{-11} \text{ lb-ft (peak)} \end{aligned}$$

would, therefore, be the maximum allowable torque error.

A fundamental single axis servo system such as that shown in Figure 4.9 can be conceived which will function to produce correcting torques. An optical sensor detects the pointing error ( $\theta_e$ ) and produces an output signal which is processed and sent to a DC torquer. A correcting torque ( $\tau_c$ ) is produced by the torquer (magnetic "pusher") reacting against the spacecraft.

The servo loop must meet two basic requirements. It must (1) produce correcting torques equal in magnitude to disturbing torques and, therefore, loop gain is important, and (2) the correcting torque must be produced at a rate equal to the rate of  $\tau_d$  ( $20,000 \sin \omega t$ ) so system response is also important.

In terms of response, the servo must have a bandwidth capability equal to or greater than the 1/2700 cps torque disturbing period. The performance capability, i.e., bandwidth and loop gain, of this single axis

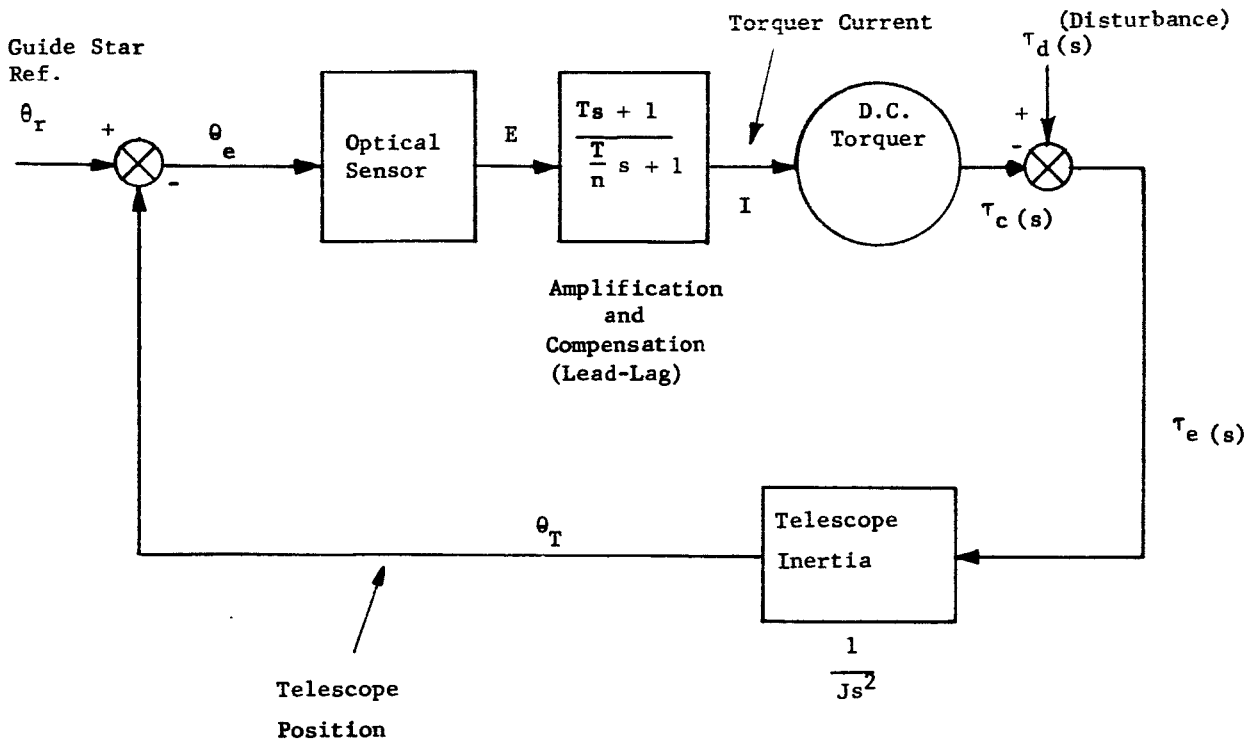


Figure 4.9. Fundamental Guidance Servo Loop (Single Axis)

servo is determined from its closed loop and error transfer functions which are respectively

$$\tau_c(s) = \frac{(T s + 1) \tau_d(s)}{\frac{J}{K} s^2 + T s + 1} \tag{4-13}$$

$$\tau_e(s) = J s^2 \theta_e(s) = \frac{\frac{J}{K} s^2 \tau_d(s)}{\frac{J}{K} s^2 + T s + 1} \tag{4-14}$$

Where T and T/n are the stabilizing network time constants and, in this case,  $n \rightarrow \infty$ . The notation, s, is the Laplace operator.

Now,  $\frac{K}{J} = \omega_c^2$  defines the open loop gain and/or crossover frequency  $\omega_c$ . The frequency  $\omega_c$  is also a reasonable approximation for the servo loop bandpass (-3db point),  $\omega_{bw}$ .

If we initially assume  $\frac{K}{J} \gg \left(\frac{2\pi}{2700}\right)^2$ , then from equation (4-14),  $s = j\omega = j\frac{2\pi}{2700}$ , and  $T = 1.4 \left(\frac{J}{K}\right)^{1/2}$  (damping factor  $\delta = 0.7$  was arbitrarily selected),

$$\tau_e (s) \cong \frac{J}{K} s^2 \tau_d (s) \tag{4-16}$$

Or, in terms of time,

$$\tau_e (t) = \frac{J}{K} \frac{d^2 \tau_d (t)}{dt^2} \tag{4-17}$$

At this point, an open loop gain (or crossover frequency) can be established using the maximum allowable value obtained for  $\tau_e$ ,

$$\begin{aligned} \omega_c^2 &= \left(\frac{2\pi}{2700}\right)^2 (1.5 \times 10^{-3}) / 3.72 \times 10^{-11} \\ \omega_c^2 &= 2.2 \times 10^2 \text{ sec}^{-2} \end{aligned}$$

The assumption is also valid since,

$$\frac{K}{J} = 220 \gg \left(\frac{2\pi}{2700}\right)^2$$

System bandwidth is, therefore, at least equal to

$$\omega_{bw} \cong \omega_c = \left(\frac{K}{J}\right)^{1/2} = (220)^{1/2} = 15 \text{ rad/sec}$$

Certainly, the system bandwidth, forced to be high by the loop gain, is more than adequate compared to the disturbing frequency. The corrective torque ( $\tau_c$ ) does dynamically cancel the disturbing torque ( $\tau_d$ ).

This type of servo would theoretically be adequate for coping with torque disturbances but becomes inadequate if sensor noise is now considered.

Referring once again to the relationship in equation (4-2) ( $E_p = 0.61 \lambda/D \left(\frac{S}{N}\right)^{-1}$ ), the pointing error ( $E_p$ ) for this guidance servo is determined by the S/N ratio. Signal to noise, determined by equation (4-6), at this point can be calculated since  $\Delta t$  (or  $1/2 f_{eq}$ ) is known.

The sensor noise is random and assumed to be white, i.e., power spectral density is constant. The bandwidth,  $f_{eq}$ , is defined as the "equivalent noise bandwidth"<sup>5</sup> for the servo. It is unlike the bandwidth normally

defined in linear network theory and is analytically defined, after normalization, by

$$2 f_{eq} = \frac{1}{2\pi j} \int_{-j\infty}^{+j\infty} G(s) G(-s) ds \quad \text{cps} \quad (4-18)$$

where

$$G(s) = \frac{Ts + 1}{\frac{J}{K} s^2 + Ts + 1} \quad \text{and} \quad (4-19)$$

$G(-s)$  is the conjugate of  $G(s)$ .

Integrating this complex integral using the theory of residues<sup>6</sup>, produces the following result:

$$f_{eq} = \frac{1}{2} \frac{T^2 \frac{K}{J} + 1}{2T} \quad \text{cps} \quad (4-20)$$

Using the values derived for the torque disturbance requirements, i.e.,

$$T = 1.4 \left( \frac{J}{K} \right)^{1/2} \quad \text{and} \quad \frac{K}{J} = 220,$$

results in

$$f_{eq} = 7.86 \quad \text{cps} \quad (4-21)$$

Substituting  $f_{eq}$  into the S/N relationship, using  $\epsilon_n = (0.4)$  twelfth magnitude star plus (1/16) eleventh magnitude star noise inputs, a field of view of 1 arc-min,  $D = 1$  meter,  $\eta_0 = 0.10$  with a twelfth magnitude star, results in

$$S/N \cong 5.8 \quad (4-22)$$

Finally, the telescope rms pointing error due to noise can be calculated.

$$E_p \cong \frac{0.61\lambda}{D} \left( \frac{S}{N} \right)^{-1} = 0.012 \text{ arc-sec (rms)} \quad (4-23)$$

The error due to noise is excessive if 0.01 arc-sec (rms) is the total design goal. By decreasing  $f_{eq}$  an improvement could be made. Decreasing  $f_{eq}$  is valid, but not within the limits of this type of servo without sacrificing pointing errors due to torque disturbances.

It is, therefore, necessary to devise an alternative approach which will relieve some of the noise and torque disturbance trade-off limitations. One such approach, very effective and reasonably simple, involves a modification to the stabilizing electronics. By utilizing integrators between the optical error sensor and the torquers, sufficient open loop gain at the disturbance frequencies can be obtained without resorting to higher bandwidths which increase noise. This system can feature either single or double integration with proportional amplification for stabilization.

Such a servo loop is shown in Figure 4.10 and, in this case, uses double integration.

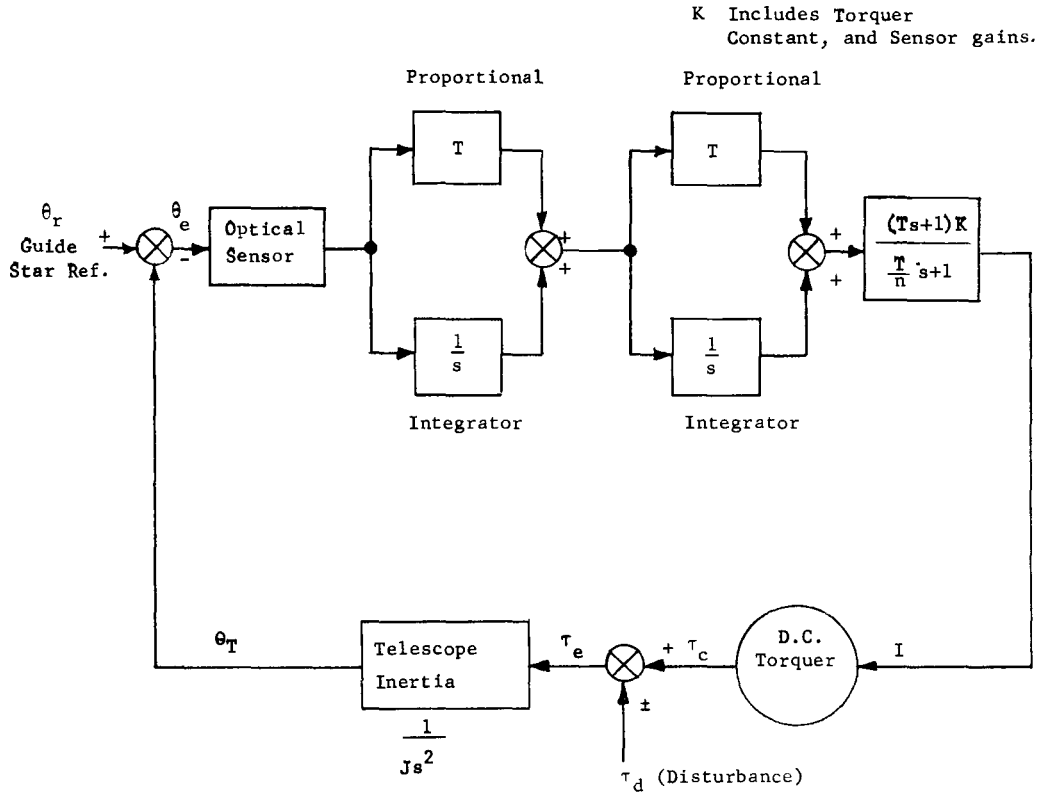


Figure 4.10. Servo Utilizing Integration (Single Axis)

The low bandwidth but high loop gain advantages of the double integration system can readily be seen by examining the servo error transfer function and the equivalent white noise bandwidth. Using feedback relationships, we obtain,

$$\tau_e(s) = \frac{\left(\frac{T}{n}s + 1\right) s^4 \tau_d(s)}{\left(\frac{T}{n}s + 1\right) s^4 + \frac{K}{J} (Ts + 1)^3} \tag{4-24}$$

where, in this case

$$\frac{K}{J} = \omega_c^4 \text{ (which defines Open Loop Gain Crossover frequency)} \tag{4-25}$$

If  $n \rightarrow \infty$  or  $\frac{T}{n}$  is small compared to the disturbing frequency, and  $T$  also represents a frequency much higher than  $\omega = \frac{2\pi}{2700}$  rad/sec, then terms

containing these parameters can be neglected. Secondly, if  $\frac{J}{K} \omega^4$  is much less than unity, (a valid assumption at  $\omega = \frac{2\pi}{2700}$  rad/sec), then

$$\tau_e(s) \cong \frac{J}{K} s^4 \tau_d(s) \tag{4-26}$$

or in terms of time

$$\tau_e(t) = \frac{J}{K} \frac{d^4 \tau_d(t)}{dt^4} \tag{4-27}$$

For  $J = 100$  slug-ft.<sup>2</sup> and  $\tau_e(t) = 3.72 \times 10^{-11}$  lb.ft. (peak) at  $\theta_e = (0.01) (\sqrt{2})$  arc-sec (peak), for example,

$$\omega_c^4 = \left( \frac{2\pi}{2700} \right)^4 (1.5 \times 10^{-3}) \left( \frac{1}{3.72 \times 10^{-11}} \right) \tag{4-28}$$

$$\omega_c^4 = 0.0012 \text{ sec}^{-4}$$

An open loop gain of  $0.0012 \text{ sec}^{-4}$  will, however, only reduce the torque disturbance errors to 0.014 arc-sec (peak). If noise error is included, the 0.01 arc-sec (rms) pointing error will be exceeded. Therefore, if the open loop gain is arbitrarily increased to  $\omega_c^4 = 0.012 \text{ sec}^{-4}$ , the errors due to torque will be reduced to 0.001 arc-sec (rms).

The servo closed loop bandwidth ( $\omega_{bw}$ ) using double integration is, to a reasonable approximation,

$$\omega_{bw} \cong \left( \omega_c^4 \right)^{1/4} \text{ rad/sec} \tag{4-29}$$

Substituting,

$$\omega_{bw} \cong (0.012)^{1/4} = 0.33 \text{ rad/sec}$$

Compared to the disturbing frequency,  $\frac{2\pi}{2700}$  rad/sec, the system response at  $\omega_{bw} = 0.33$  rad/sec is more than adequate.

Note, that unlike the expression (4-17),  $\tau_e(t)$  of (4-27) is proportional to the fourth derivative of  $\tau_d(t)$  rather than the second derivative. Since  $\omega = \frac{2\pi}{2700}$ , the higher powers of  $\omega$  obtained by higher order differentiation effectively reduce the torque errors  $\tau_e(t)$ , a definite advantage is obtained using additional integration.

$$\text{i.e., } \tau_d = 20,000 \sin \omega t \quad \text{dyne-cm} \tag{4-30}$$

$$\tau_e(t) = 20,000 \omega^4 \quad \text{dyne-cm (peak)}$$

Noise error is computed for this system by, again, using the  $f_{eq}$  relationship of (4-18). The closed loop transfer function for a double integration servo loop is, neglecting  $T/n$ ,

$$G(s) = \frac{(Ts + 1)^3}{\frac{J}{K} s^4 + (Ts + 1)^3} \quad (4-31)$$

Substituting this expression into (4-18) and integrating obtains,

$$f_{eq} = \frac{1}{4} \frac{8T^8 + 15T^4 \frac{J}{K} - 3 \left( \frac{J}{K} \right)^2}{\frac{J}{K} \left( 8T^5 - 9T \frac{J}{K} \right)} \quad (4-32)$$

Selecting a stabilizing lead frequency breakpoint of 0.238 rad/sec ( $T = 4.2$  sec), which is typical, and  $\frac{K}{J} = 0.012 \text{ sec}^{-4}$ , then

$$f_{eq} = 0.467 \text{ cps} \quad (4-33)$$

Comparing this value with the one obtained without integration (7.86 cps), it is evident that a large reduction in  $f_{eq}$  has been obtained.

Using  $f_{eq} = 0.47$  cps, the signal to noise ratio for the same conditions specified for (4-22) is,

$$\frac{S}{N} = 24 \quad (4-34)$$

The telescope pointing error due to noise becomes

$$E_p = 0.0029^* \text{ arc-sec (rms)} \quad (4-35)$$

An rms pointing error is now obtainable which is well within the 0.01 arc-sec (rms) selected for both torque and noise. Theoretically, for all

\* Calculated for an optical efficiency of  $\eta_o = 0.10$ . For an efficiency of  $\eta_o = 0.33$ , this error would decrease to 0.0013 arc-second (rms).

the conditions specified, guidance system pointing specifications are, therefore, feasible.

The noise conditions specified in calculating the S/N ratios of (4-22) and (4-34) did not include earth scattered light background during the "daylight" portion of the orbit. Including this additional noise factor, assuming the earth-reflected sunlight enters the telescope without the protection of baffling, results in a definite limitation.

Again using  $e_n$  (earth scattered albedo) equivalent to a fifth magnitude star per 36 arc-min plus an 11th magnitude star, dark current equal to (0.4) 12th magnitude star,  $\eta_0 = 0.10$ , a one arc-min field of view,  $D = 1$  meter,  $f_{eq} = 0.467$  cps, and a twelfth magnitude guide star,

$$S/N \cong 8.6 \quad (4-36)$$

and,

$$E_p \cong 0.008 \text{ arc-sec (rms)} \quad (4-37)$$

Under these conditions, the telescope would be marginally operational for a 0.01 arc-sec (rms) design goal.

If protection is used, such as baffles on the wall of the telescope tube or shrouds extending outward from the entrance aperture, the requirements for these types of devices are still quite severe.

Assuming a 33% decrease in signal to noise can be tolerated (considering  $S/N = 24$  and identical conditions) for a servo loop employing double integration, and an objective of pointing to 0.01 arc-sec (rms) accuracy, the pointing error and S/N would be,

$$E_p = 0.0043 \text{ arc-sec (rms)}$$

and

$$S/N = 16$$

Referring to equation (4-6) using  $S/N = 16$ , the earth-scattered light would have to be equivalent to a seventh magnitude star/36 arc-min<sup>2</sup> at the entrance aperture. This implies the shroud or baffle system must still absorb nearly 85% of the earth reflected sunlight for these values of background illumination which are based on isotropic scattering and 90% initial absorption within the telescope.

Up to this point, only specific examples or conditions of noise, disturbing torques, fields of view, and servo loop dynamics were used. This analysis can be generalized to permit selection of the optimum trade-off of servo loop design versus performance. Servo loops can contain several levels of integration and each level of integration will produce a certain equivalent bandwidth, system response and torque error reduction capability. Three specific servo loops are shown in Figure 4.11 (Bode plots), for example, with zero, one, and two levels of integration. In each of these cases, an identical error



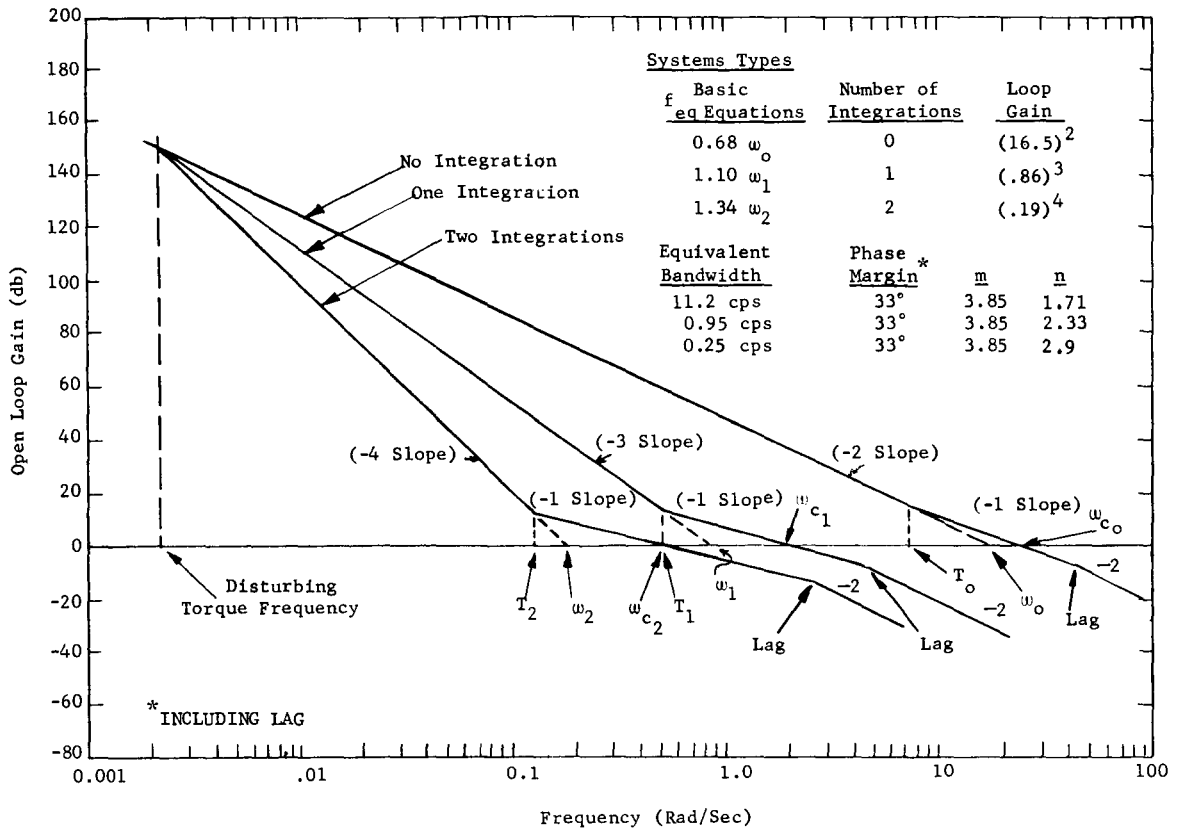


Figure 4.11. Bode Plots of Servo Loops with Various Levels of Integration

will be produced for a 20,000 dyne-cm (2700 sec period) disturbing torque but each will have various equivalent bandwidths. If the system stability is maintained constant for each type of servo loop, (i.e., phase margin does not change), then the equivalent bandwidth can be varied by varying the loop gain  $(\frac{K}{J})$ . This will produce a range of conditions, for each loop in terms of output pointing error due to noise and various disturbing torques. These conditions can be conveniently illustrated using two axes logarithmic plots such as shown in Figure 4.12 (aperture = 1 meter) and Figure 4.13 (aperture = 3 meters) which consist of separate graphs of error due to torque and error due to noise versus equivalent bandwidths. The optimum servo loop trade-offs are then evident and can be selected. Figures 4.12 and 4.13 also demonstrate the effect of sensor field of view on pointing error due to noise. Twelfth magnitude guide stars and the noise conditions listed below were assumed in plotting these graphs.

1. Dark Current - 0.4 Twelfth magnitude star (two phototubes)
2. Background - Eleventh magnitude star/16 arc-min<sup>2</sup>

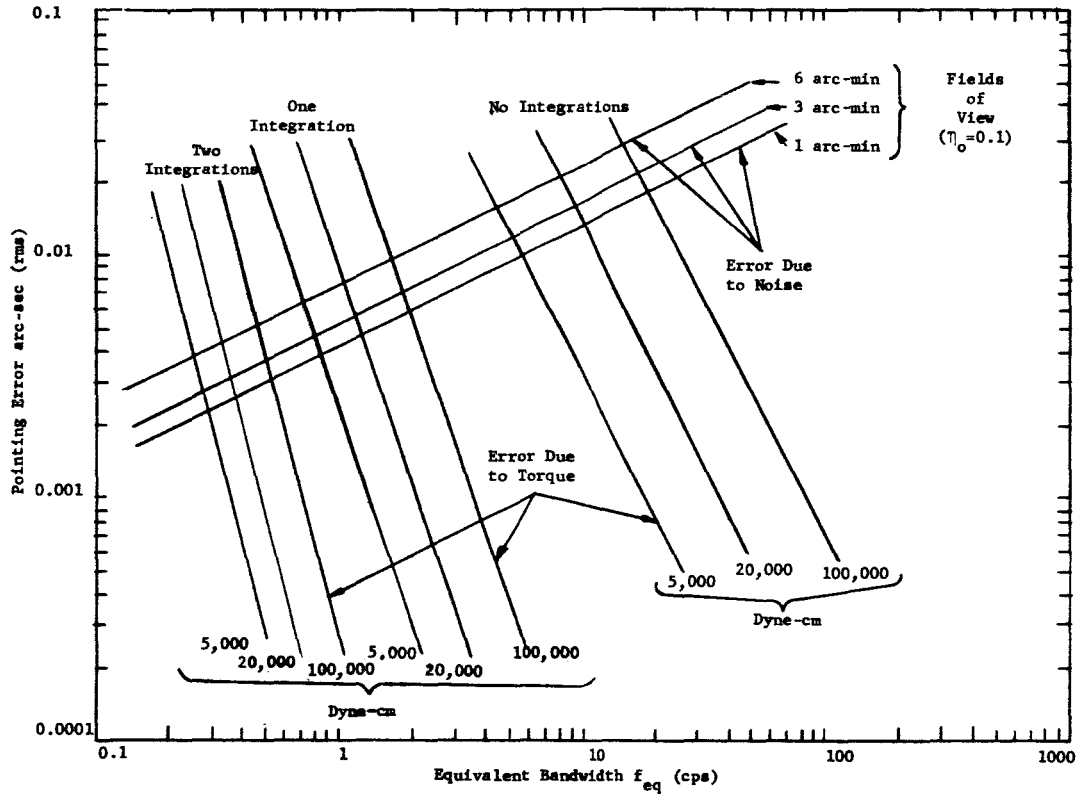


Figure 4.12. Tracking Error vs. Bandwidth (D = 1 Meter)

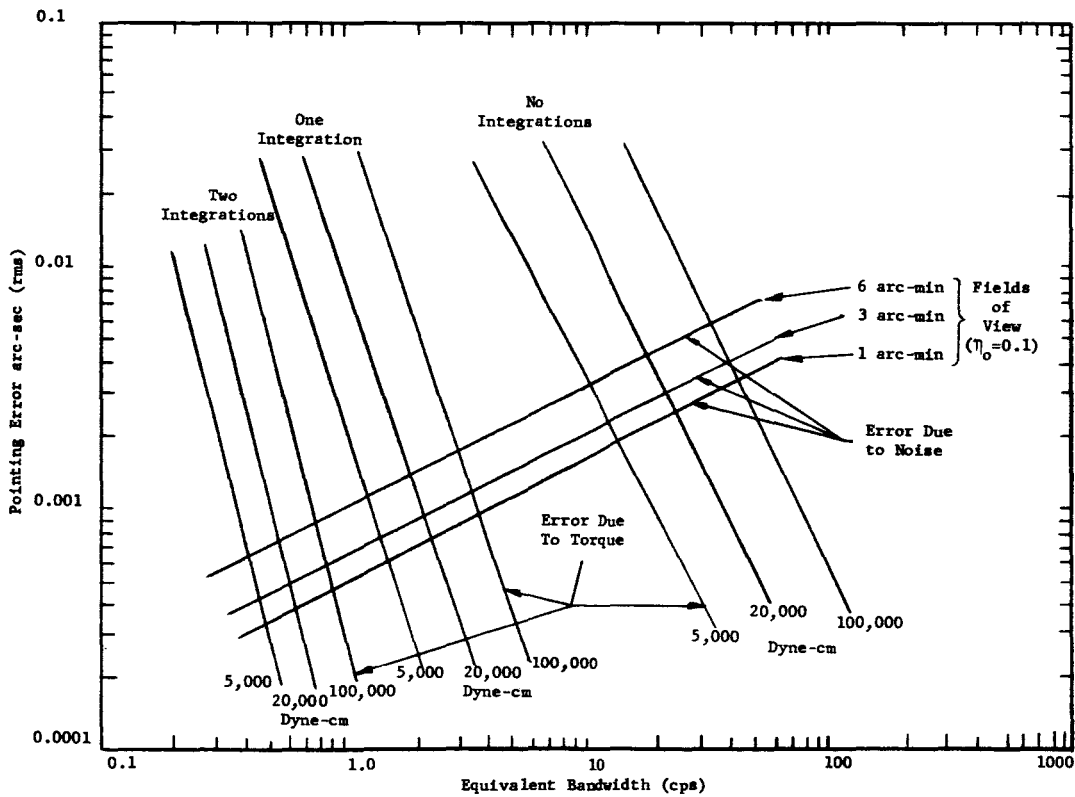


Figure 4.13. Tracking Error vs. Bandwidth (D = 3 Meters)

- 3. Cosmic Noise - Assumed negligible by design
- 4. Optical Efficiency -  $\eta_o = 0.10$

Calculations for Error Versus Bandwidth

The mathematics applicable to the graphs of Figures 4.12 and 4.13 are summarized as follows:

For no integrations (second order system), the open loop transfer function is given by H(s) (neglecting the lag of the stabilizing network)

$$H(s) = \frac{\left( T_o s + 1 \right) \frac{K_o}{J}}{s^2} \tag{4-38}$$

where,

$T_o$  = Lead network time constant (sec) - no integrations

$\frac{K_o}{J}$  = Open loop gain for second order system ( $\text{sec}^{-2}$ ) or crossover frequency squared ( $\omega_o^2$ )

The equivalent bandwidth is defined, for this second order closed loop, by

$$f_{eq} = \frac{\left( T_o^2 + \frac{J}{K_o} \right) \frac{K_o}{J}}{4 T_o} \text{ (cps)} \tag{4-39}$$

If phase margin is to be maintained constant while  $K_o/J$  is varied, this requires the product of the open loop crossover frequency ( $\omega_{co}$ ) and the lead network frequency breakpoint ( $1/T_o$ ) to be held constant.

$$T_o \omega_{co} = m \text{ (Constant)} \tag{4-40}$$

This, in turn, establishes the relationship between  $K_o/J$  (or  $\omega_o^2$ ) and  $\omega_{co}$ .

For large m,

$$\omega_{co} \cong n \left( \frac{K_o}{J} \right)^{1/2} \tag{4-41}$$

where n is a constant.

Substituting equations (4-40) and (4-41) into equation (4-39), results in

$$f_{eq_o} = \left( \frac{K_o}{J} \right)^{1/2} \frac{\left( \frac{m}{n} \right)^2 + 1}{\left( 4 \frac{m}{n} \right)} \text{ (cps)} \tag{4-42}$$

The pointing error due to torque (for 2700 second periods) is obtained from equation (4-17),

$$\theta_{eo}(t) = \frac{20,000 \sin \frac{2\pi}{2700} t}{(J) \left( \frac{K_o}{J} \right)} \quad (4-43)$$

The pointing error due to noise is defined by equation (4-2) where equation (4-6) is used for S/N and equation (4-42) is used for  $(f_{eq_o})$ .

The ratio  $\frac{m}{n}$  is selected (see Figure 4.11) to be

$$\frac{m}{n} = 2.27 \quad (4-44)$$

Similarly, the graphs of one and two integrations can be obtained. Referring to the definitions of Figure 4.11, the equivalent bandwidth for one integration is,

$$f_{eq_1} = \frac{1}{2} \left( \frac{K_1}{J} \right)^{1/3} \left( \frac{2 \left( \frac{m}{n} \right)^5 + 3 \left( \frac{m}{n} \right)^2}{4 \left( \frac{m}{n} \right)^3 - 2} \right) \quad (4-45)$$

Where m and n in this case are defined as

$$T_1 \omega_{c_1} = m \quad (4-46)$$

$$\omega_{c_1} = n \left( \frac{K_1}{J} \right)^{1/3} \quad (4-47)$$

Defining,  $\frac{K_1}{J} =$  Open loop gain for one integration ( $\text{sec}^{-3}$ )

$T_1 =$  Lead network time constant (sec) for one integration

$\omega_{c_1} =$  Open loop crossover frequency (rad/sec) for one integration

Also, for two integrations,

$$f_{eq_2} = \frac{1}{4} \left( \frac{K_2}{J} \right)^{1/4} \frac{8 \left( \frac{m}{n} \right)^8 + 15 \left( \frac{m}{n} \right)^4 - 3}{\left[ 8 \left( \frac{m}{n} \right)^5 - 9 \left( \frac{m}{n} \right) \right]} \quad (4-48)$$

Where m and n are defined by,

$$T_2 \omega_{c_2} = m \quad (4-49)$$

$$\omega_{c2} \cong n \left( \frac{K_2}{J} \right)^{1/4} \quad (4-50)$$

Defining again,

$\frac{K_2}{J}$  = Open loop gain for two integrations ( $\text{sec}^{-4}$ ) or crossover frequency,  $\omega_2^4$ .

$T_2$  = Lead network time constant (sec) for two integrations.

$\omega_{c2}$  = Open loop crossover frequency (rad/sec) for two integrations.

In all cases,  $m = 3.85$  where  $n$  is given in Figure 4.11. The error due to noise is repeatably determined by equations (4-2) and (4-6). The one and two integration torque errors are defined respectively by

$$\theta_{e1}(t) = \frac{\left( 20,000 \cos \frac{2\pi}{2700} t \right) \left( \frac{2\pi}{2700} \right)}{(J) \left( \frac{K_1}{J} \right)} \quad (4-51)$$

$$\theta_{e2}(t) = \frac{\left( 20,000 \sin \frac{2\pi}{2700} t \right) \left( \frac{2\pi}{2700} \right)^2}{J \left( \frac{K_2}{J} \right)} \quad (4-52)$$

#### 4.4 ACQUISITION CONSIDERATIONS

Torque disturbances and initial conditions of pointing displacement and velocity create the inherent difficulties in acquiring a guide star. The pointing system must adequately respond to null out these conditions and place the telescope free of transients, into the final tracking mode. Based on spacecraft guidance system capabilities, initial conditions in the order of a few arc-min/sec and arc-minutes can possibly exist in the vertical and horizontal directions once the telescope has been released. Roll initial conditions are on the order of a few degrees. These conditions, combined with disturbing torques (noise and the multiple integrations used in the loop electronics), eventually demand various levels of electronic switching and gain changing techniques to acquire the guide stars.

The problems of acquisition due to torque and initial conditions of pointing error rate and displacement can be adequately demonstrated by considering single axis control in phase space, i.e., error rate versus position, for a second order system. The effect of adding the integrations and noise becomes somewhat unwieldy using this type of technique and only the trends or effects of these two items will be analyzed. (In section 3.3.4 an analog computer study is described which evaluated noise effects by simulation and also served to develop the electronic switching techniques.)

The following discussion will, once again, begin by centering around a simplified guidance servo loop identical to the one shown in Figure 4.9 using the same loop gain ( $\frac{K}{J} = 220 \text{ sec}^{-2}$ ). Only the sensor nonlinearities will be considered. The torquer saturation limits will initially be selected to lie outside the normal torque operating range.

The guide star sensors (two fields of view are considered here, fine and coarse) have extremely small linear areas of operation about null and for the most part, the servo operates in the nonlinear areas of the sensors during acquisition. The sensor static transfer function, voltage output versus angular error input, is shown in Figure 4.14.

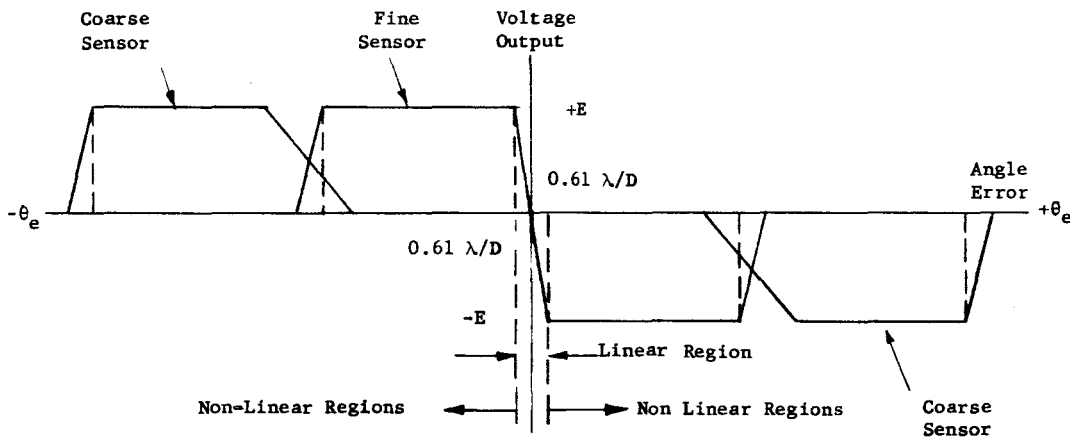


Figure 4.14. Single Axis Sensor Static Transfer Function

The linear area is basically determined by the radius of the first dark ring of the diffraction pattern ( $0.61\lambda/D$ ) for the fine sensor. Outside this area, the transfer function exhibits a constant or flat characteristic on out to the edge of the field. If the displacement error exceeds the fine sensor field of view, the coarse sensor becomes active and, apart from overlapping of fields, also exhibits a zero rate transfer characteristic on out to its field limits.

Consider a system with no electrical damping ( $T=0$ , Figure 4.9) which cycles at the limits of displacement where the servo loop can be described by second order differential equations in both the linear and nonlinear regions.

$$\theta_R(t) = \frac{J}{K} \frac{d^2 \theta_T(t)}{dt^2} + \theta_T(t) \quad (\text{Linear}) \quad (4-53)$$

where,

$$\theta_T(t) = \text{Telescope Angular Position}$$

$$\theta_R(t) = \text{Guide Star Reference (Line of Sight)}$$

J = Telescope Inertia

K = Sensor to Torquer Output Gain (Sensor Sensitivity normalized to unity)

Also,

$$E = \frac{J}{K} \frac{d^2 \theta_T}{dt^2} \quad (\text{Nonlinear}) \quad (4-54)$$

for,

$$-0.61\lambda/D \geq \theta_R - \theta_T \geq + 0.61\lambda/D$$

where,

E = Sensor saturation signal at 0.61λ/D

Rearranging and time scaling ( $\tau = \left(\frac{K}{J}\right)^{1/2} t$ ), equations (4-53) and (4-54) become,

$$\frac{\theta_T}{\theta_R - \theta_T} = \frac{1}{d\dot{\theta}_T/d\theta_T} \quad (\text{function of } \tau) \quad (4-55)$$

and

$$\dot{\theta}_T \frac{d\dot{\theta}_T}{d\theta_T} = E \quad (\text{function of } \tau) \quad (4-56)$$

If equation (4-56) is integrated with respect to  $\theta_T$ , we obtain

$$\int \dot{\theta}_T d\dot{\theta}_T = E \int d\theta_T \quad (4-57)$$

$$\dot{\theta}_T^2 = 2E\theta_T + C \quad (\text{Constant}) \quad (4-58)$$

The constant (C) can be evaluated at the initial conditions of rate and displacement resulting in a phase plane equation of the form,

$$\dot{\theta}_T^2 - \dot{\theta}_T^2(0) = 2E \left( \theta_T - \theta_T(0) \right) \quad (4-59)$$

where,

$$\theta_T(0) = \text{Initial displacement}$$

$$\dot{\theta}_T(0) = \text{Initial rate}$$

Assuming  $\dot{\theta}_T(0) = 0$  and  $\theta_T(0) = 1 \text{ arc-min.} \left(\frac{K}{J}\right)^{1/2} = 15 \text{ rad/sec}$ , and  $E = 0.1 \text{ arc-sec}$ , the equation (4-59) can be plotted as shown in Figure 4.15 plot A. The phase plane trajectory will somewhat resemble a circle which indicates conditional stability. The servo will, in fact, oscillate at a period given by;

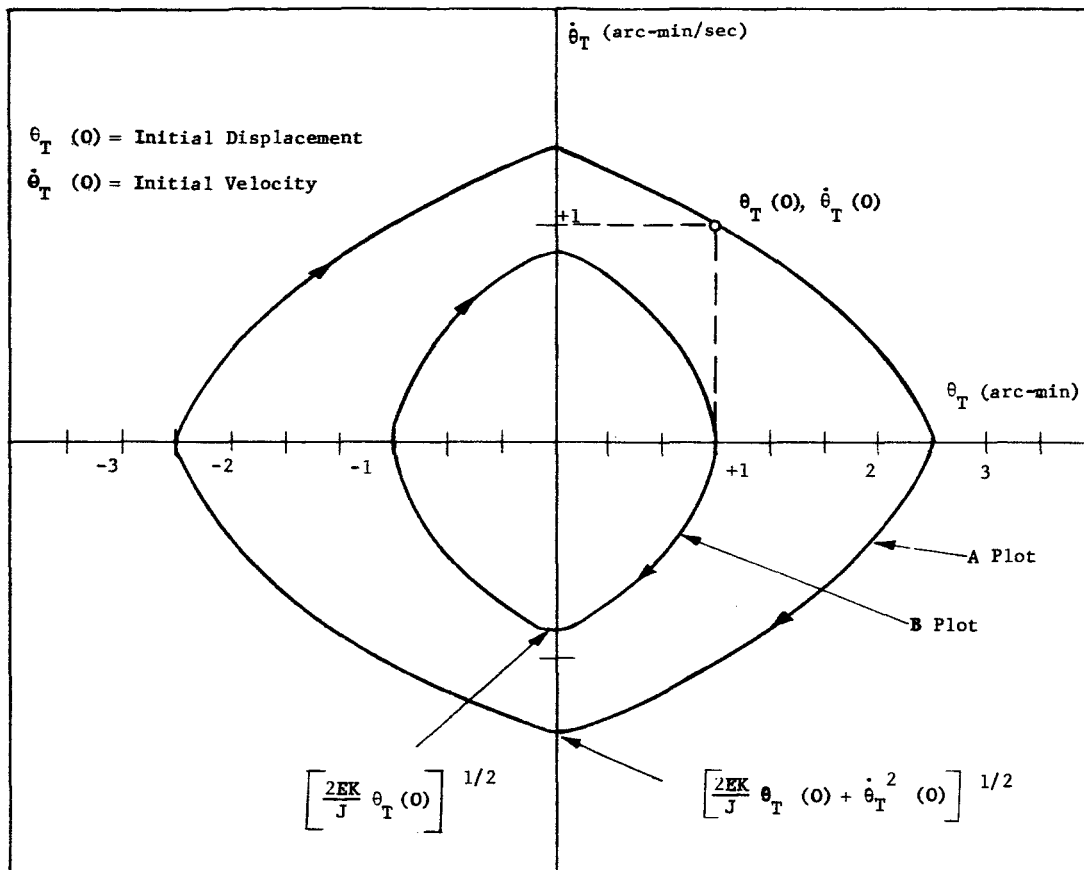


Figure 4.15. Phase Plane Plots (Undamped Servo)

Period of Oscillation =  $4 \left[ \frac{2J}{EK} \theta_T(0) \right]^{1/2} = 9 \text{ seconds} \quad (4-60)$   
 between the limits of  $+\theta_T(0)$  and  $-\theta_T(0)$ .

This servo loop is representative of a "Bang-Bang" controller since the linear region of the sensor is extremely narrow. This is not necessarily a disadvantage for a second order system. Optimum time control, i.e., the minimum time required to reach a certain settling point, is usually best achieved using "Bang-Bang" devices.

If an initial velocity of 1 arc-min/sec exists in addition to the 1 arc-min displacement, the phase plane trajectory will have a large radius as shown in Figure 4.15 Plot B. Based on these two initial conditions alone, the sensor fields of view must be at least 4.6 arc-min. If the K/J gain constant is lowered, the peak velocities will be less, but the lower limit of amplitude will still be determined by the initial conditions of displacement regardless of loop gain (K/J).



If small torque disturbances ( $\tau_d$ ) are added, the effect is negligible. For a loop gain of  $K/J = 220 \text{ sec}^{-2}$  and a 0.0015 lb-ft disturbing torque, for example, the equivalent error (at 1/2 orbiting frequency) is only an additional 0.01 arc-sec and, since the torque saturation is high, i.e.,  $\tau_{\text{sat}} \gg \tau_d$ , small disturbing torques will add only slightly to displacements.

In general, for a second order servo with a sensor that for all practical purposes, exhibits "Bang-Bang" (extremely narrow linear region) characteristics, field-of-view radius can be obtained as a function of initial rate and displacements. Figure 4.16 contains plots of initial displacements

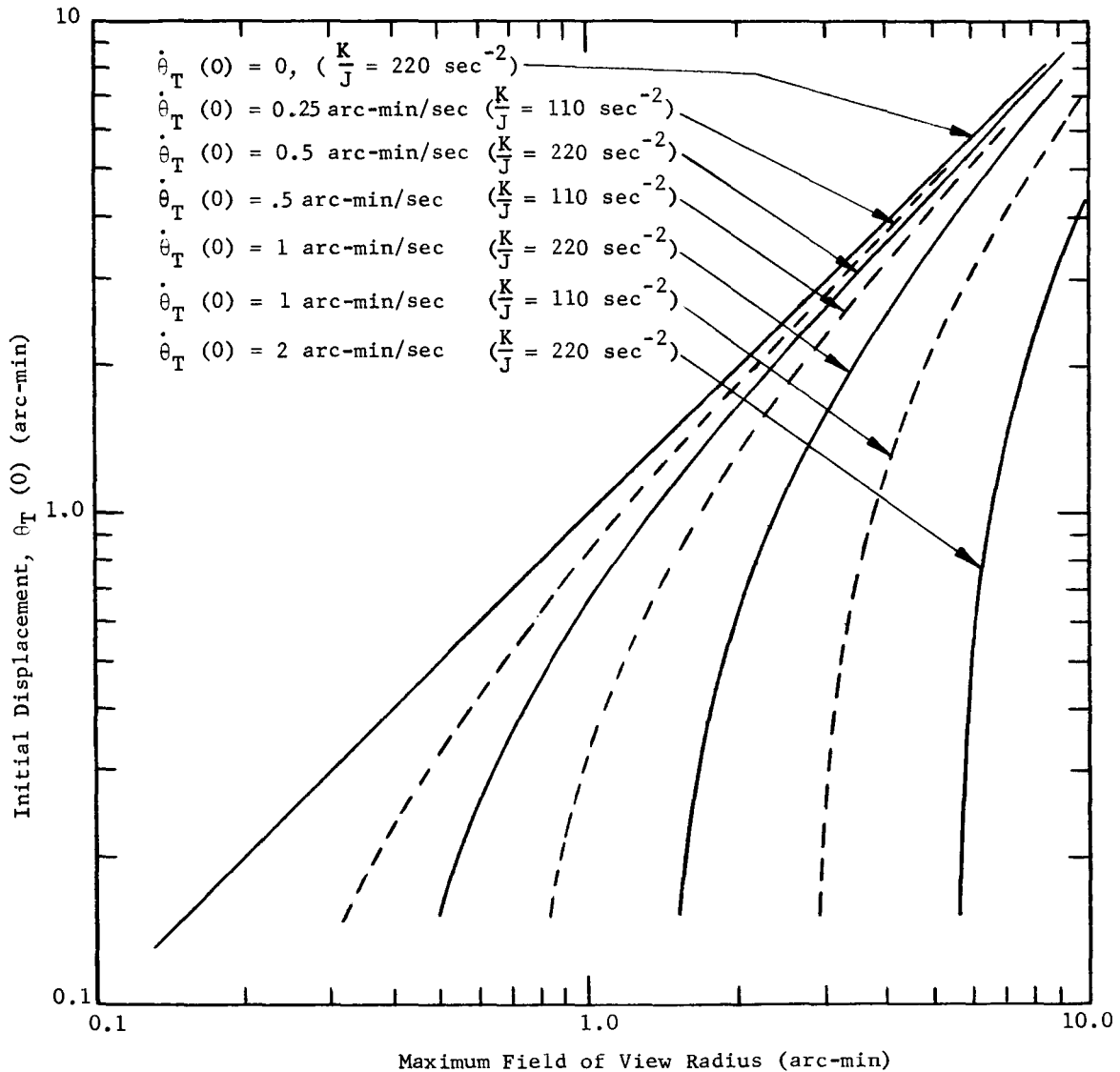


Figure 4.16. Field of View vs. Initial Rate and Displacement (Undamped Servo)

versus field-of-view for various conditions of initial rates. Once again, the servo was assumed to have zero electrical damping so the plots of Figure 4.16 represent maximum field-of-view conditions. The effect of reducing the loop gain (K/J) by 1/2 is also shown, plotted using dotted lines.

The oscillations can be effectively damped by adding electrical error rate networks between the optical sensor and torques of the form,

$$\frac{Ts+1}{\frac{T}{n}s+1}$$

As shown below, these networks provide anticipatory velocity correction impulses to the torquers whenever the sensor signal reverses.

As noted above, the linear region can be neglected, so the phase plane equations for error rate damping are derived for the nonlinear sensor region only.

In terms of the Laplace operator, the error rate equation is defined by

$$\frac{EK}{J} \left( \frac{Ts+1}{\frac{T}{n}s+1} \right) s^2 = \theta_T(s) \tag{4-62}$$

If n is assumed very large, the  $\frac{T}{n}$  term can be neglected without misrepresenting the basic dynamics,

$$\frac{EK}{J} \left( \frac{Ts+1}{s} \right) = \theta_T(s) \tag{4-63}$$

In terms of time, therefore,

$$\frac{TK}{J} \frac{dE}{dt} + \frac{EK}{J} = \frac{d^2\theta_T(t)}{dt^2} \tag{4-64}$$

Integrating equation (4-64) with respect to time, we obtain

$$\frac{TK}{J} E + \frac{EK}{J} t = \dot{\theta}_T + C \text{ (Constant)} \tag{4-65}$$

The constant (C) is evaluated for initial velocity conditions. At t = 0,  $\theta_T = \dot{\theta}_T(0)$ , E = 0, and equation (4-65) becomes,

$$\frac{TK}{J} E - \dot{\theta}_T(0) + \frac{EK}{J} t = \dot{\theta}_T(0) \tag{4-66}$$

The effect of the lead (T) of the error rate network is therefore, to simply modify the initial velocity condition as a function of E or at displacement error reversals. As stated, a velocity impulse correction occurs.

Therefore, defining

$$\dot{\theta}'_T(0) = \frac{TK}{J} E - \dot{\theta}_T(0) \tag{4-67}$$

From this point, equation (4-59) (general form of phase plane equation) can be applied using  $\dot{\theta}'_T(0)$  as the revised initial velocity conditions,

$$\dot{\theta}_T^2 - \dot{\theta}_T^{\prime 2}(0) = 2E \left( \theta_T - \theta_T(0) \right) \tag{4-68}$$

Selecting a  $\theta_T(0) = 1$  arc-min and  $T = 0.46$  sec, which in this case represents greater than critical damping in the linear region for  $K/J = 220 \text{ sec}^{-2}$ , the servo would "spiral" in towards the linear region as shown in Figure 4.17. As  $T$  is increased, the system will recover with fewer overshoots in shorter times. In the theoretical limit, the system would recover as indicated by the dotted lines. Total recovery time would be

$$\text{Theoretical limit for recovery time} = \frac{J}{EKT} \theta_T(0) \tag{4-69}$$

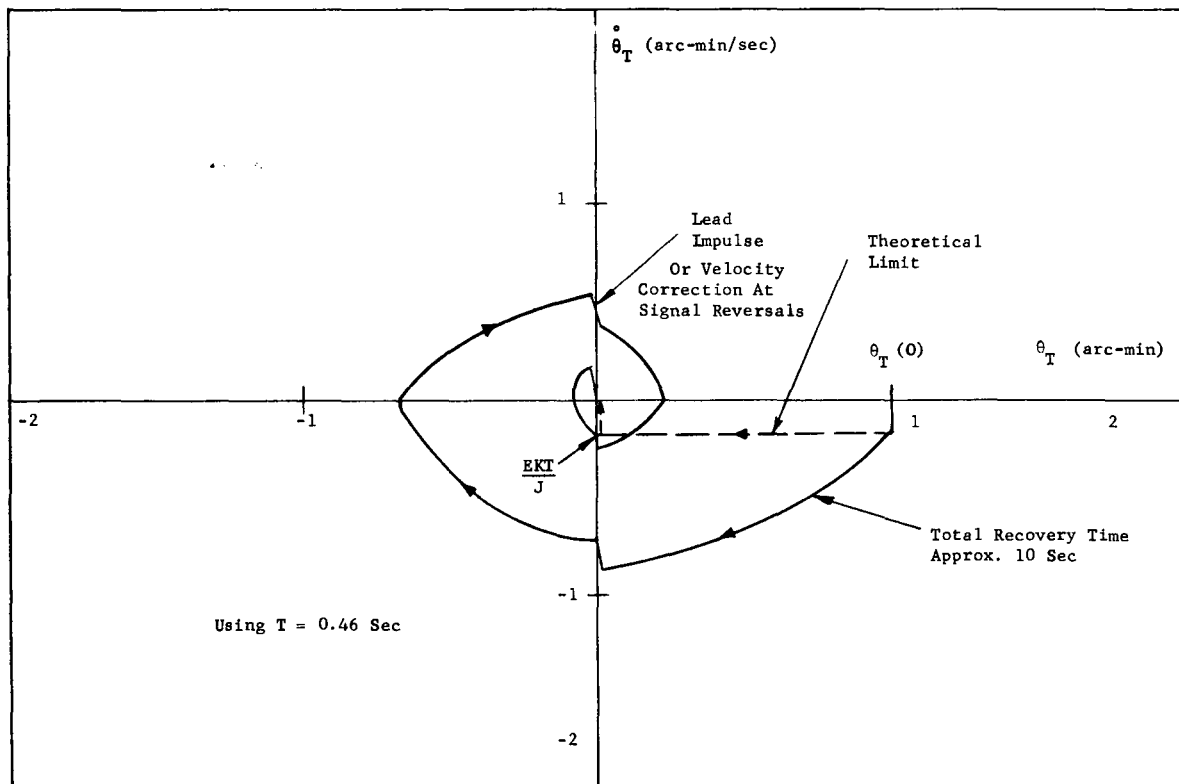


Figure 4.17. Phase Plane (With Damping)

Consequently, a second order system with approximate "Bang-Bang" characteristics can certainly be made to acquire without much difficulty. However, as discussed in section 4.3, electronic integrators are required once the servo settles into the linear region. If the integrators are added during nonlinear acquisition, they will have the effect of cancelling the error rate networks and the system will be oscillatory. The addition of the integrators must, therefore, be accomplished after the system has settled into the linear sensor regions. This imposes an additional requirement on the nonlinear servo design of reducing rates to small values before settling into the linear regions to allow the low gain multiple integration loop to stabilize.

A certain amount of electronic switching becomes necessary to assure acquisition since the system must operate in different modes for linear and nonlinear sensor regions due to the integrators. The switching design details are described in section 3.3.4 of Volume III for a 40-inch aperture telescope.

The preceding analysis is only valid if, as stated, the torquer saturation limits lie outside the normal range of operation. To assure these limits are reasonable, the following calculations are made.

In the second order system without electrical error rate networks, the torque saturation limits are small and can be determined by,

$$T_{sat} = (0.61\lambda/D) K \text{ (for } D = 1 \text{ meter)} \tag{4-70}$$

$$T_{sat} = (5 \times 10^{-7}) (2.20 \times 10^4) = 0.011 \text{ lb-ft.}$$

If the error rate networks are included, the impulse height of the network output basically determines the saturation level,

$$\begin{aligned} \lim_{t \rightarrow 0} T_{sat} &= \lim_{s \rightarrow \infty} s (0.61\lambda/D) (K) \left( \frac{Ts+1}{T/n s+1} \right) \left( \frac{1}{s} \right) \tag{4-71} \\ &= 0.61\lambda/D K n \end{aligned}$$

For  $n = 10,$

$$T_{sat} = (5 \times 10^{-7}) (2.20 \times 10^4) (10) = 0.11 \text{ lb-ft.}$$

Minimum torque saturation levels of  $\pm 0.2$  lb-ft. would be adequate and reasonable for a 1-meter aperture telescope and larger.

The remaining consideration is noise and its effect on acquisition. For large fields of view, the background illumination increases and the signal to noise decreases. When the system is operating in a coarse sensor area (large field of view), it is a second order servo and has an equivalent noise bandwidth identical to the one given in equation (4-20). Using a loop gain of  $220 \text{ sec}^{-2}$ , a 6 arc-min field of view,  $\eta_0 = 0.1$ , 12th magnitude guide star, and  $D = 1\text{-meter}$ ,

$$f_{eq} = 7.86 \text{ cps}$$

Using identical noise conditions, i.e.,

Dark current = (0.4) 12th magnitude star

Background = 11th magnitude star/16 arc-min<sup>2</sup>

The signal-to-noise ratio is,

$$S/N \cong 3.33$$

and the rms error is,

$$E_p = 0.020 \text{ arc-sec (rms)}$$

The rms pointing error due to noise is not excessive for acquisition in the coarse sensor region. Basically, all that is required are DC directional signals to command the servo or telescope to seek the fine sensor field. Once within the fine sensor region, the noise level drops to values within specifications. The only adverse effect the coarse sensor noise may have is to impart slightly erroneous initial velocity and displacement conditions as the telescope drops into the fine sensor field of view, and extend the acquisition time.

#### 4.5 SUMMARY AND CONCLUSIONS

The first problem to which this section of the study was devoted is concerned with the theoretical possibility of pointing a spaceborne telescope at a star with sufficient accuracy to realize diffraction-limited optical performance when the guide stars are no brighter than the twelfth magnitude. Figure 4.4 shows clearly that for a 1-meter aperture telescope and readily achievable optical efficiencies and photosensor quantum efficiencies, pointing inaccuracies that are only a small fraction of the diffraction image size are theoretically possible, provided that the equivalent servo bandwidth can be kept small enough.

The second problem studied involved the theoretical and practical limitations on high-accuracy pointing performance. The effects of external disturbances, such as background light, scattered light, dark current, and externally-applied torques were considered. From this study, the fundamental servo loop parameters were determined.

When the servo loop performance requirements based on external disturbances (i.e., servo loop gain) were coupled with pointing accuracy dependence upon servo bandwidth, it became obvious that either a compromise must be reached, or that an ingenious electronic system would have to be designed that would give low equivalent bandwidth but high resistance to external disturbances. The latter approach was taken and proved feasible. By using a double integration scheme in parallel with the direct signal loop, the equivalent bandwidth can be lowered by more than an order of magnitude. The results show that 0.01 arc-second (rms) pointing accuracy can indeed be achieved (even with some reserve margin) for the entire spectrum of disturbances, whether externally or internally generated.

As the study progressed, a fairly-well defined design concept emerged and is well-substantiated by the analysis. The final portion of the study is devoted to the problem of acquisition, or settling down to fine pointing after the servo is turned on with initial large pointing errors and error rates. From this analysis, the coarse guidance portion of the servo evolved. The complete pointing servo concept is that of "nested" sensor, with the outer (coarse) servo passing control to the inner (fine) servo when the pointing errors are reduced to sufficiently small values.

A preliminary design study of the mechanization of the pointing servo concepts developed in this volume is contained in Volume III of this study.

REFERENCES

- <sup>1</sup>Born and Wolf, Airy Diffraction Patterns - Principles of Optics (2nd Edition), Pergamon Press, 1964.
- <sup>2</sup>Falconi, Oscar, Maximum Sensitivities of Optical Distortion and Twist Measuring Instrument, JOSA, November 1954, pp. 1315-1320.
- <sup>3</sup>Princeton University Satellite Design Review Meeting, May 5, 1965.
- <sup>4</sup>Spitzer, Dr., L. Memo: Princeton University Observatory, February 3, 1966.
- <sup>5</sup>Prince, Theory of Servo Mechanisms, Chapter 7.
- <sup>6</sup>Wylie, C.R., Jr., Advanced Engineering Mathematics, Chapter 14, (Second Edition).

N66 34371

Report No. 8346(III)

 PERKIN-ELMER

VOLUME III



## TABLE OF CONTENTS

<u>Section</u>	<u>Title</u>	<u>Page</u>
1.0	GENERAL DESCRIPTION OF THE 40-INCH SYSTEM	1-1
2.0	OPTICAL DESIGN OF A 40-INCH SYSTEM	2-1
	2.1 Primary Optics	2-1
	2.2 Image Movers	2-4
	2.3 Image System	2-12
	2.4 Instrument Package	2-19
	2.5 Infinite Exit Pupil Telescope	2-22
3.0	POINTING SYSTEM DESIGN FOR A FORTY-INCH SYSTEM	3-1
	3.1 Introduction	3-1
	3.2 Specifications and Design Philosophy	3-1
	3.3 Overall System Description	3-4
	3.4 Servo System Analysis	3-23
	3.5 Optical Sensor and Processing Electronics	3-70
	3.6 Gyro and Linear Sensors	3-80
	3.7 Pointing Servo Electronics	3-89
	3.8 Pointing System Redundancy	3-99
	3.9 Electronics Instrumentation and Telemetry	3-100
	3.10 Recommendations for Further Investi- gations	3-102
4.0	SPECTROGRAPH DESIGN	4-1
	4.1 General Properties of an Echelle Spectrograph	4-1
	4.2 Four-Element Spectrograph	4-6
	4.3 Two-Element Design	4-6
	4.4 Recommendations	4-9
5.0	SPECIAL COMPONENTS	5-1
	5.1 Focus and Coma Sensing Correcting Mechanism	5-1
	5.2 Auxiliary Tracking System	5-7

## TABLE OF CONTENTS (Continued)

<u>Section</u>	<u>Title</u>	<u>Page</u>
6.0	RECOMMENDATIONS	6-1
	6.1 Pointing and Suspension System	6-1
	6.2 Optics	6-2
	6.3 Spectrograph	6-3
	6.4 Thermal Analysis	6-3
	6.5 Astronaut Participation	6-4
	6.6 The 120-Inch Telescope	6-4
Appendix A	GUIDE STAR ORIENTATION AS RELATED TO THE TELESCOPE COORDINATES	A-i
Appendix B	TECHNICAL NOTES	B-i
	D.A.M., G.C.-004	B-1
	D.A.M.-003	B-9
	J.J.G.-002	B-17
	D.A.M.-001	B-29
	R.V.S.-010	B-37
	D.A.M.-005	B-47

## LIST OF ILLUSTRATIONS

<u>Figure</u>	<u>Title</u>	<u>Page</u>
1.1	QAO Vehicle	1-1
1.2	Instrument Package (Side View)	1-3
1.3	Instrument Package	1-4
1.4	Mirror Support Structure	1-5
2.1	Cassegrain Telescope and Corrector	2-1
2.2	Telescope Field Corrector Details	2-2
2.3	Image Mover Assembly	2-6
2.4	Image Mover in Skewed Position	2-7
2.5	Image Mover Lens Elements	2-8
2.6	On-Axis Image Mover Performance	2-10
2.7	Coarse Pointing System	2-11
2.8	Fine Pointing System	2-13
2.9	Wide Field Microscope Objective ( $f/3.7$ , $0.2\mu - 0.6\mu$ )	2-14
2.10	UV Ball Lens Performance	2-15
2.11	UV Lens Materials	2-17
2.12	Imaging System	2-18
2.13	Flip Mirror	2-19
2.14	Spectrograph System	2-21
2.15	Instrument Package Optical Layout	2-22
2.16	Telescope With Entrance Pupil at Infinity	2-23

## LIST OF ILLUSTRATIONS (Continued)

<u>Figure</u>	<u>Title</u>	<u>Page</u>
3.1	Apollo - OAO System	3-5
3.2	Image Mover Principle (Single Guide Star)	3-7
3.3	Guide Star Optical Sensor Principle (Single Axis-Schematic)	3-10
3.4	Telescope Pointing System - Coordinates	3-11
3.5	Telescope Torquer Arrangement	3-12
3.6	System Block Diagram	3-15
3.7	Fine Sensor Signal Logic	3-19
3.8	Fine Sensor Signal Logic With Gyro	3-21
3.9	Fine-Coarse Sensor Transfer Functions (Single Axis)	3-28
3.10	Electronic Gain Change	3-30
3.11	Single Axis (Vertical or Horizontal) Analytical Block Diagram	3-32
3.12	Bode Diagram-Vertical and Horizontal Axes	3-34
3.13	Error Versus Torque Disturbances (Final Track- ing Mode - Vertical and Horizontal Axes)	3-35
3.14	Pointing Error vs. Star Magnitudes (Vertical and Horizontal Axes)	3-37
3.15	Equivalent Roll Errors as Related to Sensor Vertical Image Motions	3-41
3.16	Roll Pointing Error Requirements vs. Guide Star Locations	3-43
3.17	Roll Axis Analytical Block Diagram	3-45
3.18	Bode Diagram Roll Axis (Final Track Mode)	3-46

## LIST OF ILLUSTRATIONS (Continued)

<u>Figure</u>	<u>Title</u>	<u>Page</u>
3.19	Roll Axis Pointing Errors vs. Disturbance Torques	3-47
3.20	Analog Computer Single Axis Simulation	3-51
3.21	Telescope Acquisition	3-54
3.22	System Checks	3-55
3.23	Centering System Block Diagram (Single Axis, Typical)	3-58
3.24	Centering Forces (Single Axis)	3-59
3.25	Bode Diagram Centering and Auxiliary Rotation Systems (Single Axis)	3-62
3.26	Centering System Coupling (Single Axis- Typical), Block Diagram	3-64
3.27	Centering System Coupling (Single Axis- Typical) Analytical Diagram	3-65
3.28	Centering System Coupling Errors Due to Torquer Unbalances	3-66
3.29	Centering System Coupling Errors Due to Torque Unbalance	3-67
3.30	Auxiliary Rotational (Single Axis) Block Diagram	3-68
3.31	Optical Sensor Mechanization	3-72
3.32	Image Location on Reticle Face	3-73
3.33	Sensor Electronics (Two Axis)	3-75
3.34	Typical Output Wave Forms	3-76
3.35	Torques Acting on Gyro Gimbal	3-82
3.36	Gyro "Spring" Loop	3-83

## LIST OF ILLUSTRATIONS (Continued)

<u>Figure</u>	<u>Title</u>	<u>Page</u>
3.37	Rate Gyro Loop Error Curves	3-85
3.38	Single Capacitive Type Sensor (Typical Arrangement)	3-87
3.39	Data Handling Equipment	3-91
3.40	Chain Link Transformer Principle	3-92
3.41	Power Controller	3-95
3.42	Power Drain Profile	3-98
4.1	Echelle Spectrograph Format	4-5
4.2	Four-Element Spectrograph	4-7
4.3	Two-Element Spectrograph Design	4-8
5.1	Coma Detector	

## 1.0 GENERAL DESCRIPTION OF THE 40-INCH SYSTEM

The Princeton Advanced Satellite is a second generation experiment package tailored to fit in the same outer vehicle used for the Orbiting Astronomical Observatory (OAO) series of satellites. The design goal is a telescope having the largest possible diameter compatible with the OAO vehicle which can be used for high-resolution spectrophotometry as well as diffraction-limited imagery. The primary data transducers are envisaged to be two SEC vidicons arranged in a redundant configuration so that failure of one does not preclude imagery or spectrography with the other.

Figure 1.1 shows a cut-away view of the annular OAO vehicle and the cylindrical experiment package. The outer vehicle is an octagonally shaped aluminum structure 118 inches long and 80 inches across flats which is segmented into a number of compartments containing all the equipment necessary to service the experiment. This includes star trackers, solar trackers, rate gyros, and magnetometers to sense attitude and motion; as well as gas jets, coarse and fine inertia wheels, and magnetic coils for stabilization and orientation. Also included are a multichannel communication system, equipment associated with power conversion and storage and data processing and storage

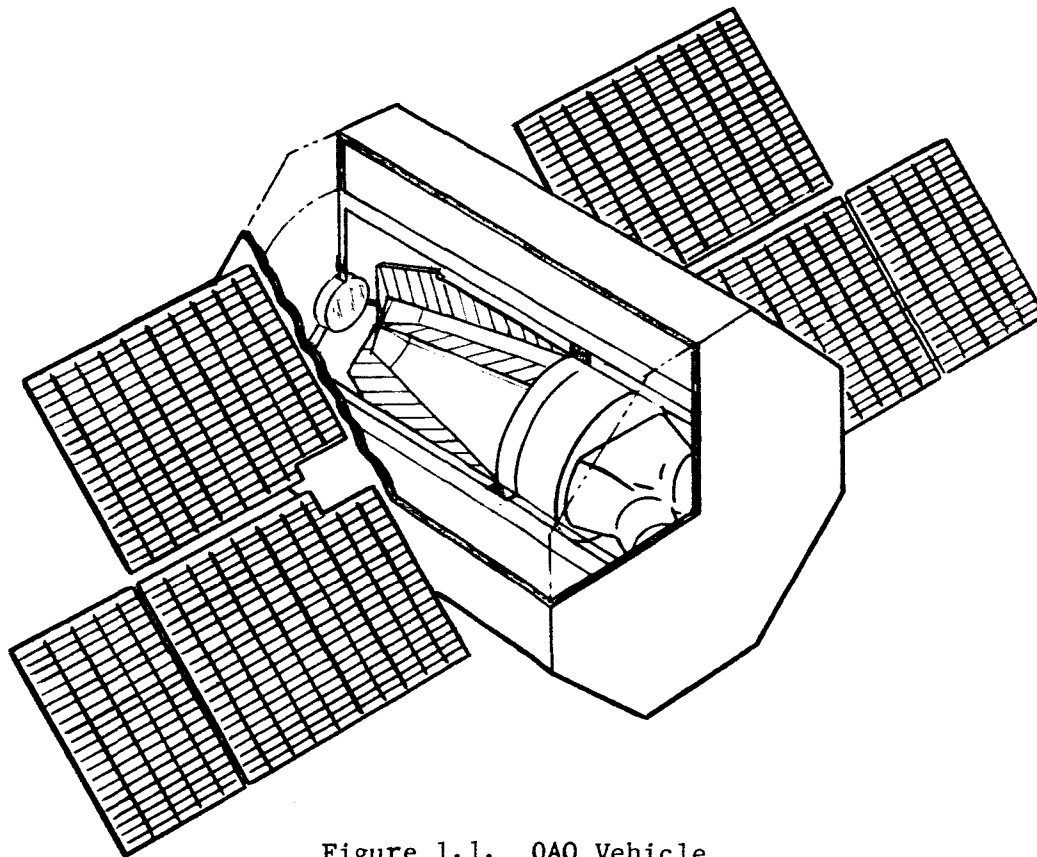


Figure 1.1. OAO Vehicle

equipment. A sun shade attached to the front end of the OAO vehicle prevents direct viewing of the sun by the experiment.

The experiment package is contained in the concentric cylindrical hole extending the length of the outer vehicle. The hole is nominally 48 inches in diameter, but contains several trusses and four (4) large mounting brackets situated about two-thirds of the way back from the open end. In order to obtain an aperture of maximum size, the experiment package has been designed with a stepped diameter so that the small end containing the instrument section can be slid past the mounting brackets and the large end containing the telescope can protrude beyond the brackets taking full advantage of the available space. This is illustrated in Figures 1.2 and 1.3.

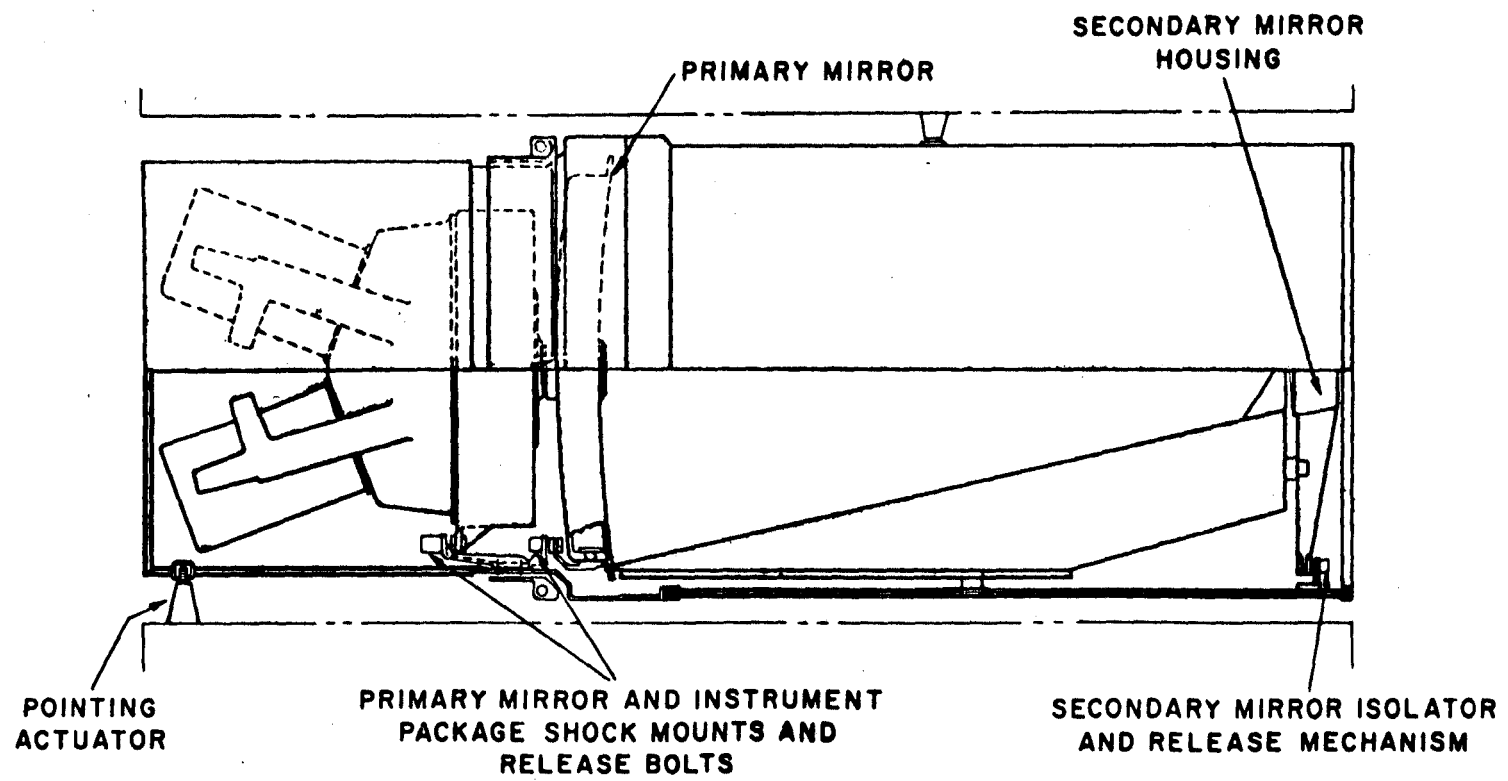
During launch, the experiment package is separated into three sections, the instrument package, the primary mirror, and the secondary mirror support system. Each is independently clamped and mounted to an adapter ring which is permanently fixed to the four (4) mounting lugs. During the transition from launch to orbital configuration, the rigid mechanical coupling between the experiment package and the outer vehicle is severed via quick release mechanisms mounted on the adapter ring, and the three (3) sections of the experiment package are pulled together to form a single rigid structure which floats inside the central cylinder of the spacecraft during operation of the telescope.

A floating experiment package is a major innovation whose principal advantage is immunity of the telescope to perturbations arising in the outer spacecraft and its pointing system. Some electromechanical coupling between the inner and outer vehicles is required to prevent gross separation or collision. However, with a reasonable separation between the vehicles this coupling can be made extremely weak and the degree of isolation correspondingly high. Signals and power must be transferred between the two vehicles but this can be accomplished without compromising the isolation of the experiment package.

The absence of a rigid connection also permits the experiment package to use the outer spacecraft as a convenient momentum wheel against which it can torque to nullify magnetic field and gravity gradient moments. The angular momentum which accumulates in the outer vehicle can be dumped via magnetic coils momentum wheels, or gas jets without regard to the experiment status thereby permitting independent and concurrent operation of the outer vehicle and telescope pointing systems.

A caging mechanism allows the spacecraft and experiment package to be coupled so that the pointing system on the outer spacecraft can be used to slew the telescope to within a few minutes of arc of the required pointing direction. After release of the experiment package by the caging mechanism and subsequent actuation of the telescope pointing system, pointing accuracy of a hundredth of an arc-second is achieved. If the coarse orientation provided by the outer spacecraft is not sufficient to place guide star images in the field of the telescope pointing system, then the telescope field can be moved in a scanning pattern until the presence of images in the telescope guidance field is detected.





1-3

Figure 1.2. Instrument Package (Side View)

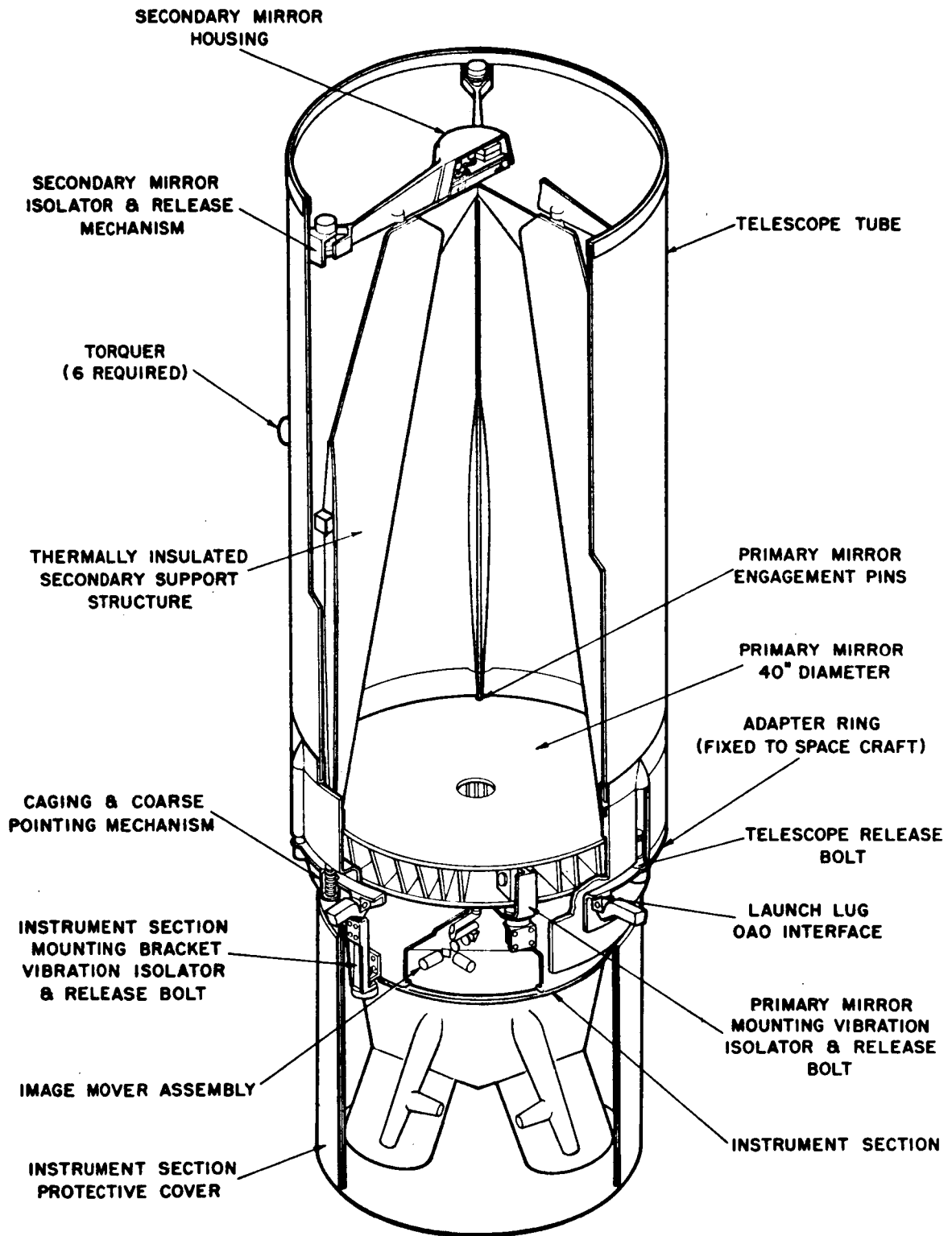


Figure 1.3 Instrument Package

The orientation of the telescope is controlled by means of six (6) small magnetic "pushers" arranged diametrically about the center of mass of the experiment package so as to produce torques in each of three orthogonal planes. Torque disturbances arising from coupling between the magnetic pushers and the Earth's magnetic field are minimized by a pusher design which resembles a conventional speaker magnet.

Apart from controlling the three degrees of angular freedom, the magnetic pushers are also useful for controlling the spatial position of the telescope with respect to the boundaries of the cylinder in which it floats. This possibility is explored in section 3.3.5.2, Volume III and an alternate possibility that of employing a passive system is discussed in Appendix B (DAM-GC-004), Volume III.

The blackened aluminum tube, which encloses the Cassegrain telescope portion of the experiment package, provides a convenient support for the secondary support structure in the launch configuration. It also aids in keeping the thermo-elastic deformations of the primary mirror within bounds set by diffraction-limited performance criteria, without resorting to active control systems. An end view of the experiment package from in front of the secondary mirror is shown in Figure 1.4. In this concept, a thin web spider connects the three support legs to form a rigid structure resembling a tripod.

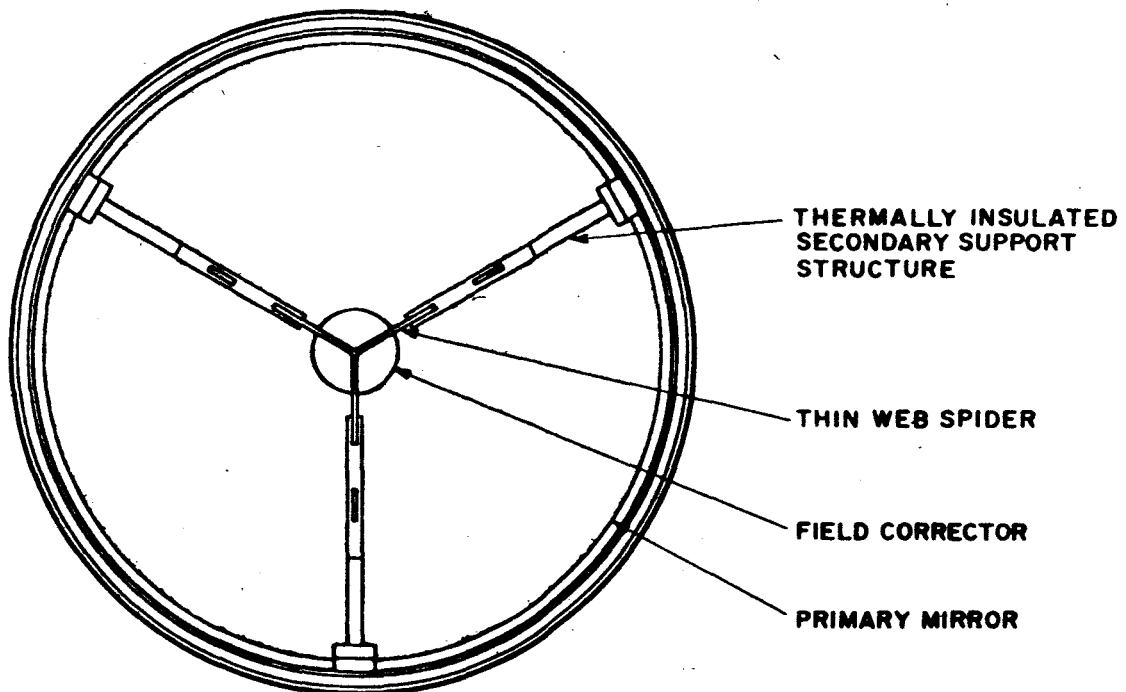


Figure 1.4. Mirror Support Structure

The telescope is a 40-inch aperture Cassegrain design with a fast  $f/2$  primary and a relatively strong secondary, resulting in a very compact design with an  $f/10$  image plane about 10 inches behind the primary. A three-element refractive corrector situated about three inches above the  $f/10$  focal plane extends the useful field to 30 minutes of arc diameter in the visible region. Color and high order aberration terms prevent further extension of this field. A conical hole through the center of the corrector elements allows rays in the small aberration-free zone near the axis to pass unimpeded, thus permitting access to the far UV portion of the spectrum.

A small diagonal flip mirror situated in the  $f/10$  image plane separates the spectrograph and imagery portions of the optical system. The image field is reflected from the mirror into a microscope, but images intended for spectrographic examination are aligned so that they pass through a small slit in the diagonal mirror and on to the first spectrograph element. Both the small diagonal mirror and the first spectrograph element are made so that they can be rotated about the optical axis to switch between two redundant vidicon and fine pointing systems.

Two microscope objectives on either side of the diagonal flip mirror provide a 20 times magnified portion of the on-axis image field at one or the other vidicon depending on the orientation of the flip mirror. This magnification power was selected in order to insure that the telescope optics, rather than the vidicon, limit the resolution of the system. The rectangular vidicon surface subtends a field of about 15 by 20 seconds of arc, a small portion of which contains one side of the spectrograph entrance slit. The microscope objective contains fused silica and LiF elements which form a system that is color corrected from 0.2 to 0.6 microns. An appreciable change in power over this spectral region makes it necessary to adjust the focus between the 0.2-0.4 micron region and the 0.4-0.6 micron region.

The echelle spectrograph was initially expected to operate in the 1100Å to 3000Å spectral region with vidicon-limited resolution of 10,000. Later, when the possibility of a manned mission was considered, the desired spectral range was increased to include the 800Å to 1100Å spectral region and a higher resolution capability was suggested in order to take advantage of the increased potentialities of photographic film. A two-element and a four-element spectrograph have been proposed for further study. If the resolution of the two-element system proves adequate, then it is to be preferred since high losses due to absorption and scattering occur with each reflection in the spectral region near 1100Å.

A telescope pointing stability of the order of 0.01 second of arc is required in order to avoid appreciable smearing of the 0.1 second of arc diffraction-limited images. Apart from signal-to-noise effects, pointing errors greatly exceeding this limit can arise from slight changes in the orientation of optical surfaces due to temperature variations. For this reason, the present design utilizes the same optical elements for the pointing and imagery optical systems, except for a pair of image moving devices located between the  $f/10$  focal plane and the last telescope field-correcting element. The image movers displace two

small fields of view about three minutes of arc in diameter from a variable position in the corrected telescope field to a fixed position close to the on-axis image field. When set to coincide with the position of two bright guide stars in the telescope field, the image movers cause a one minute of arc diameter field about each image to be reflected from the same diagonal mirror and through the same microscope objective as the on-axis image field. The guide stars are imaged either side of the vidicon in the  $f/200$  image plane on the apex of a pair of shallow prisms. These divide each image into four quadrants, which are then compared to derive guidance signals. In the  $f/200$  image plane, the one minute of arc diameter fine guidance field corresponds to about 2 1/2 inches. Space limitations prevent a further increase of the guidance field in the  $f/200$  plane. However, an extension of the guidance field out to three minutes of arc diameter is achieved by a coarse pointing system situated near the  $f/10$  focal plane.

The electronics associated with guidance signal processing forms a major part of this report and is described in section 3.5 of this volume. The tracking system has been designed to operate well within a 0.01 second of arc rms error tolerance using 12th (visual) magnitude guide stars in the presence of appreciable background radiation and low frequency gravity gradient and magnetic torque disturbances. Nonlinear amplification and the signal processing possibilities inherent in a pointing system having separate coarse and fine pointing fields have been utilized to achieve a system which satisfies the somewhat contradictory requirements posed by acquisition and tracking.

A number of special components have been included in the design study. Some of these components, such as the focus and alignment sensing and correcting mechanisms, are essential accessories for a large orbital telescope. Other components are required as a result of the design philosophy which separated the telescope and outer vehicle. One example is the chain link power transformer which permits power to be transferred without any physical contact and without producing any forces between the telescope and outer vehicle. The magnetic pushers are another example. Pointing error signals cause opposing pushers to exert a torque on the telescope, whereas centering errors, occurring between the telescope and outer vehicle, cause paired pushers to act in the same direction.

To date, design effort has been aimed primarily at establishing feasibility. No detailed analysis has been done on the size and shape of various structural members best suited to withstand the launch accelerations. Recommendations for continued design effort are contained in Section 6.0 of this volume.

The extent to which associating the experiment with a manned Apollo mission can extend the data acquisition capability and increase the probability of a successful mission is explored in Volume IV of this study. A manned mission allows the use of photographic film which can provide an increase in the total amount of data in a form which is directly useful, and can also extend spectrophotometric coverage down to 800Å. In connection with the manned portion of the study a full-scale mockup of the experiment package has been constructed.

As the design continues, this mockup will be kept current and used to establish design choices which enhance the repairability and accessibility of the experiment package.

## 2.0 OPTICAL DESIGN OF A 40" SYSTEM

The salient features of the optical design which has resulted from this study are:

- 1) Diffraction-limited imagery in the visible spectrum.
- 2) Spectrographic coverage to  $1000\text{\AA}$  using common telescope optics concurrent (if desired) with imaging of the object being observed.
- 3) Pointing control utilizing most of the same optical elements.
- 4) Complete redundancy of read-out equipment and optics beyond the  $f/10$  image plane.
- 5) All of these features are realized with an extreme economy of space, permitting use of the existing OAO vehicle.

Using Stratoscope II as an example, since it is roughly comparable in aperture size though more limited in experiment objectives, the present design offers about a 60% reduction in space. This reduction is made possible by a very compact Cassegrain telescope which fits in front of the mounting lugs in the OAO spacecraft and allows the instrument package to be placed behind where it cannot vignette the field of view.

### 2.1 PRIMARY OPTICS

The primary and secondary mirrors in the present system are figured to produce a paraboloid-hyperboloid combination which is free of spherical aberration. However, the effects of coma limits the useful field to about 5 minutes of arc diameter. It is possible to eliminate coma as well as spherical aberration by aspherizing the primary and secondary mirror surfaces to form a Ritchey-Chretien type of system. In this case, field curvature and astigmatism, which are not influenced by high order aspheric terms, limit the useful field to about 10 minutes of arc diameter.

The primary optical system is shown in Figure 2.1. A fast,  $f/2$

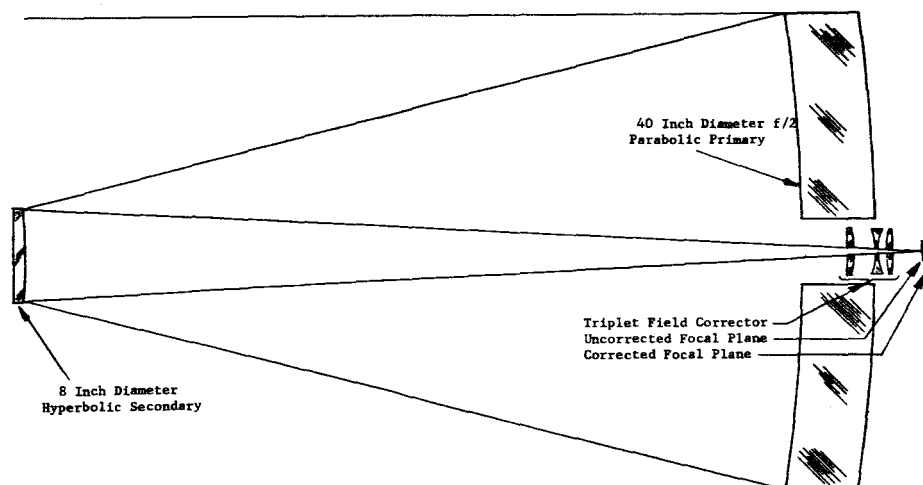


Figure 2.1. Cassegrain Telescope and Corrector

primary, and a secondary with 5X magnification form an f/10 optical system with a focal plane about 10 inches behind the primary and the secondary about 65 inches in front.

The telescope field which can be viewed by the vidicon or utilized by the spectrograph is substantially less than one minute of arc diameter. However, a large field at least 30 minutes of arc in diameter is required by the pointing system to achieve a reasonably good probability of having two stars of sufficient intensity in the field to stabilize the telescope pointing direction. This is achieved by using a three-element refractive field corrector which corrects the aberrations present in the outer field of the telescope, but which allows on-axis field rays to pass unimpeded through a conical hole in the center of the corrector elements. The corrector design was based on a paraboloid-hyperboloid telescope since it is as easy to balance the comatic aberration contributions of the telescope with those of the corrector as it is to design a coma-free corrector. The larger uncorrected field provided by a Ritchey-Chretien design cannot be advantageously utilized and poses a more difficult task during test.

The position of the corrector elements with respect to the primary mirror and the uncorrected and corrected focal planes is shown in Figure 2.2. The numbers which are attached to each optical surface refer to Table 2-I

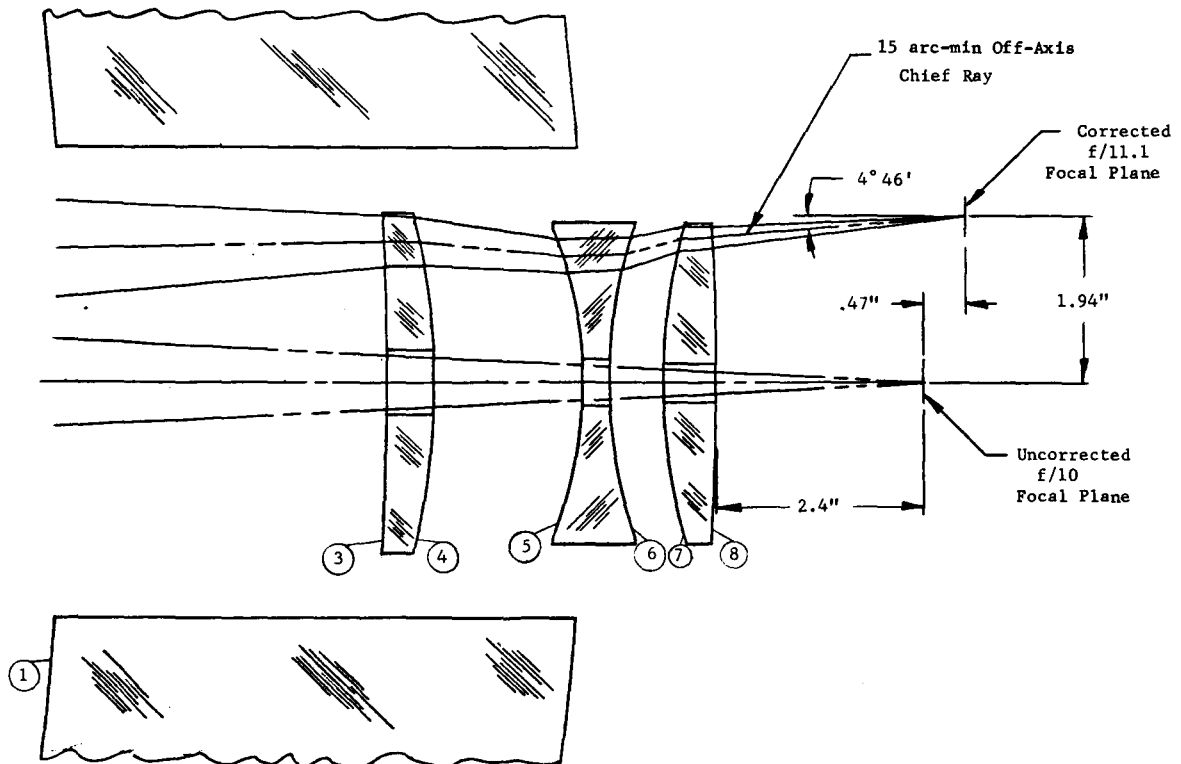


Figure 2.2. Telescope Field Corrector Details



TABLE 2-I

PRINCETON ADVANCED SATELLITE OPTICAL DESIGN		
SURFACE	RADIUS (mm)	SEPARATION (mm)
1 Primary*	-4099.38	-1665.55
2 Secondary**	-960.79	1759.45
3	-2229.71	15.18
4	-206.23	43.18
5	-122.99	7.59
6	146.50	15.82
7	173.10	15.18
8	-1167.93	72.71
F. L. = 11298 mm      f/11.12		
* parabolic surface ** hyperbolic surface aspheric coefficient -1.2535  All elements SK-16 $n_C$ - 1.61728 $n_F$ - 1.62757 $n_h$ - 1.63776		

in which the radii of curvature and separation distances of the optical surfaces comprising the telescope are included. The corrector elements have a slight net negative power which shifts the corrected focal plane behind the uncorrected focal plane by about 0.47 inches. A chief ray which strikes the center of the primary at a 15 minute of arc off-axis angle intersects the f/10 focal plane 1.94 inches off-axis at an angle of  $4^{\circ}46'$  with respect to the optical axis. The 19-fold increase in the angle made by a chief ray between entering the optical system and being brought to a focus is a serious disadvantage in other portions of the optical system but cannot be avoided with the present design. An alternate design having the exit pupil at infinity and a corrected field significantly larger than the present 30 minutes of arc diameter limit is described in section 2.5.

### 2.1.1 Pointing Systems

Diffraction-limited resolution of very faint stellar sources requires that the optical systems associated with pointing and imaging remain very accurately boresighted over long periods of time. For a 40-inch aperture system, the boresight tolerance amounts to about 0.01 seconds of arc or one part in 20 million. This seems impractical even with a massive telescope

structure; however, the problem can be reduced simply by using the same telescope for both imaging and pointing. There are a number of possible methods for achieving this. One of the first to be considered involved positioning a pair of image dividers in the  $f/10$  focal plane so that the apex of each corresponds to guide star image positions. Telescope pointing errors result in unequal image division which is sensed by phototubes and subsequently corrected by the pointing system.

Another scheme involved relaying the two halves of the  $f/10$  pointing field through separate optical systems containing collimated light paths. Guide star images in each of the two field halves were positioned on fixed image dividers by means of gimballed mirrors situated in the collimated light path.

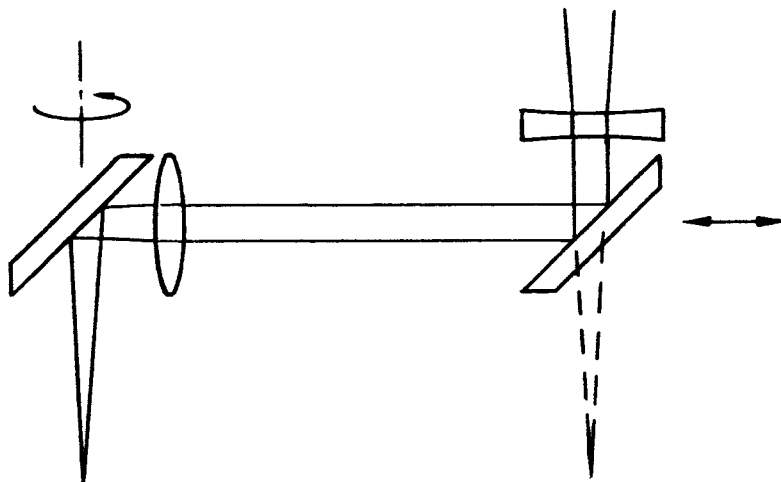
Both schemes permit the imaging and pointing systems to share the same telescope but not the same microscope objective. As a result, the optical alignment of the two systems remains dependent upon the long term stability of the orientation and position of the optical elements in the microscope system. For the microscope objective the allowable motion corresponds to about one part in 2 million which is still far from an ideal solution.

Space limitations do not permit the pointing systems to share the same microscope directly. In the  $f/200$  image plane the  $0.5^\circ$  telescope field utilized by the pointing system corresponds to a circle about 70 inches in diameter. This obviously would not fit into the experiment package. However, it is possible to use the microscope for both imaging and pointing indirectly by causing the guide star images to occupy fixed positions in the  $f/10$  plane corresponding to image dividers in the  $f/200$  image plane. This is achieved by means of a pair of image moving devices located in the small space between the last telescope field correcting element and the  $f/10$  focal plane. The fixed positions for the guide star images are located close to the optical axis to minimize the microscope field of view and also to permit rigid coupling of the guide star image dividers to the vidicons; thus inhibiting any tendency for relative motion which would be deleterious to imaging. With this arrangement small changes in the orientation or position of elements in the telescope or the microscope system produce equal errors in the imaging and pointing systems which are indistinguishable from telescope pointing errors and are, therefore, compensated by changes in the telescope orientation. The image movers are not common to both optical systems and, therefore, require particular attention to ensure that they do not introduce telescope pointing errors. As will be seen presently, however, the image mover design is (to first order) insensitive to translational displacements of the entire assembly and only rotational displacements are important.

## 2.2 IMAGE MOVERS

The image mover principle was first conceived by Dr. M. Schwarzschild of Princeton University. In its original form the image mover device consisted of a very simple system of lenses and mirrors which could be arranged to shift

a guide star image from an arbitrary position to a fixed position. The optical arrangement required to achieve this is illustrated below.

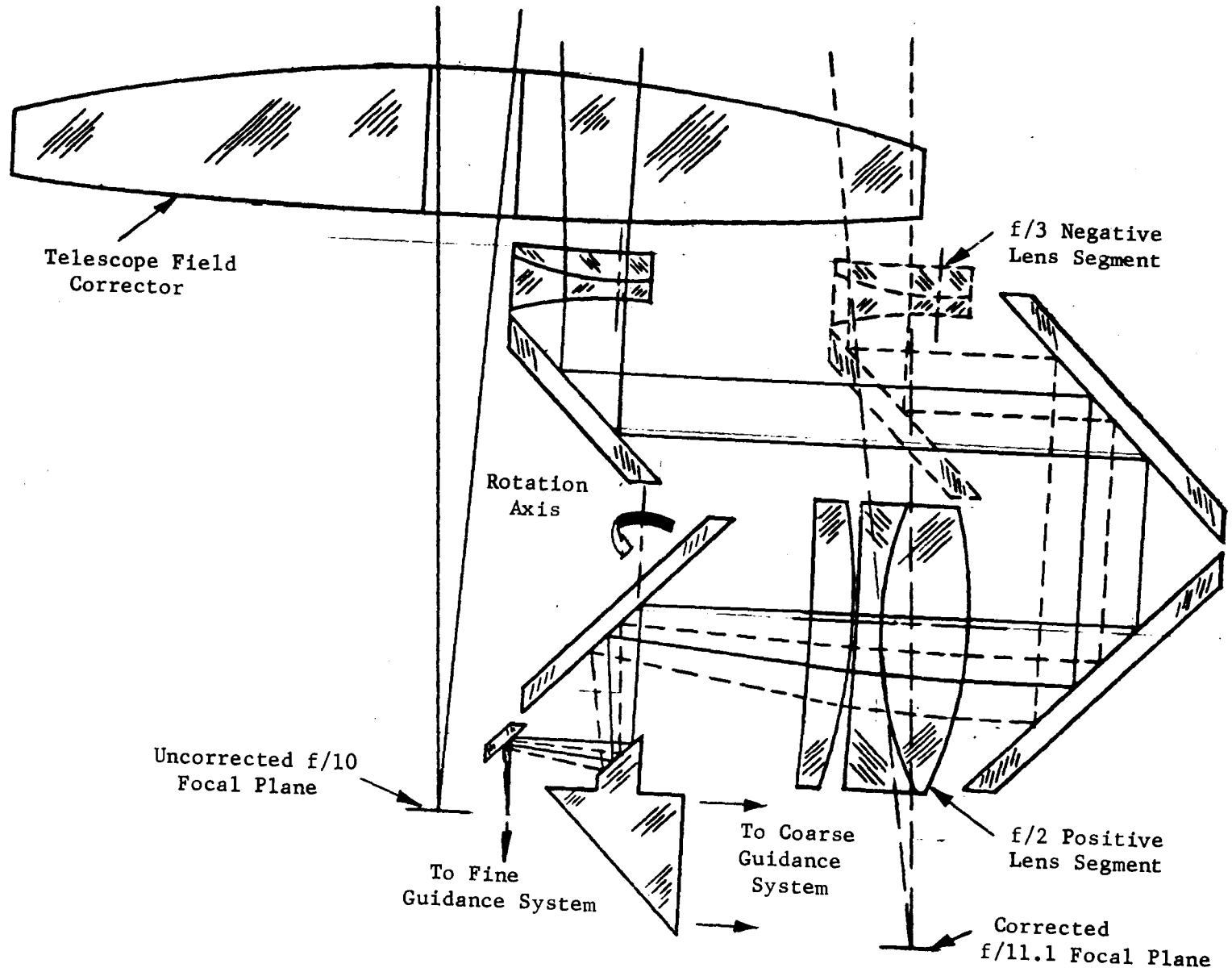


A converging bundle of light from a guide star is intercepted before coming to a focus by a negative lens which renders the rays parallel. A small diagonal mirror turns the collimated beam through a right angle which intersects a positive lens. This refocuses the bundle so that after reflection from a second diagonal mirror the guide star image lies in the same focal plane as before. The image mover can be adjusted to shift guide star images from arbitrary positions by moving the negative lens and diagonal mirror horizontally toward or away from the positive lens and by rotating the entire image mover assembly about an axis through the positive lens diagonal.

An image mover which affords a number of advantages to the pointing system at the cost of additional optical surfaces is shown in Figure 2.3. This design also utilizes a collimated light path between positive and negative lens elements but the increased number of mirror surfaces provides coverage over a greater proportion of the telescope field and a larger acquisition zone around the nominal position of the guide star image.

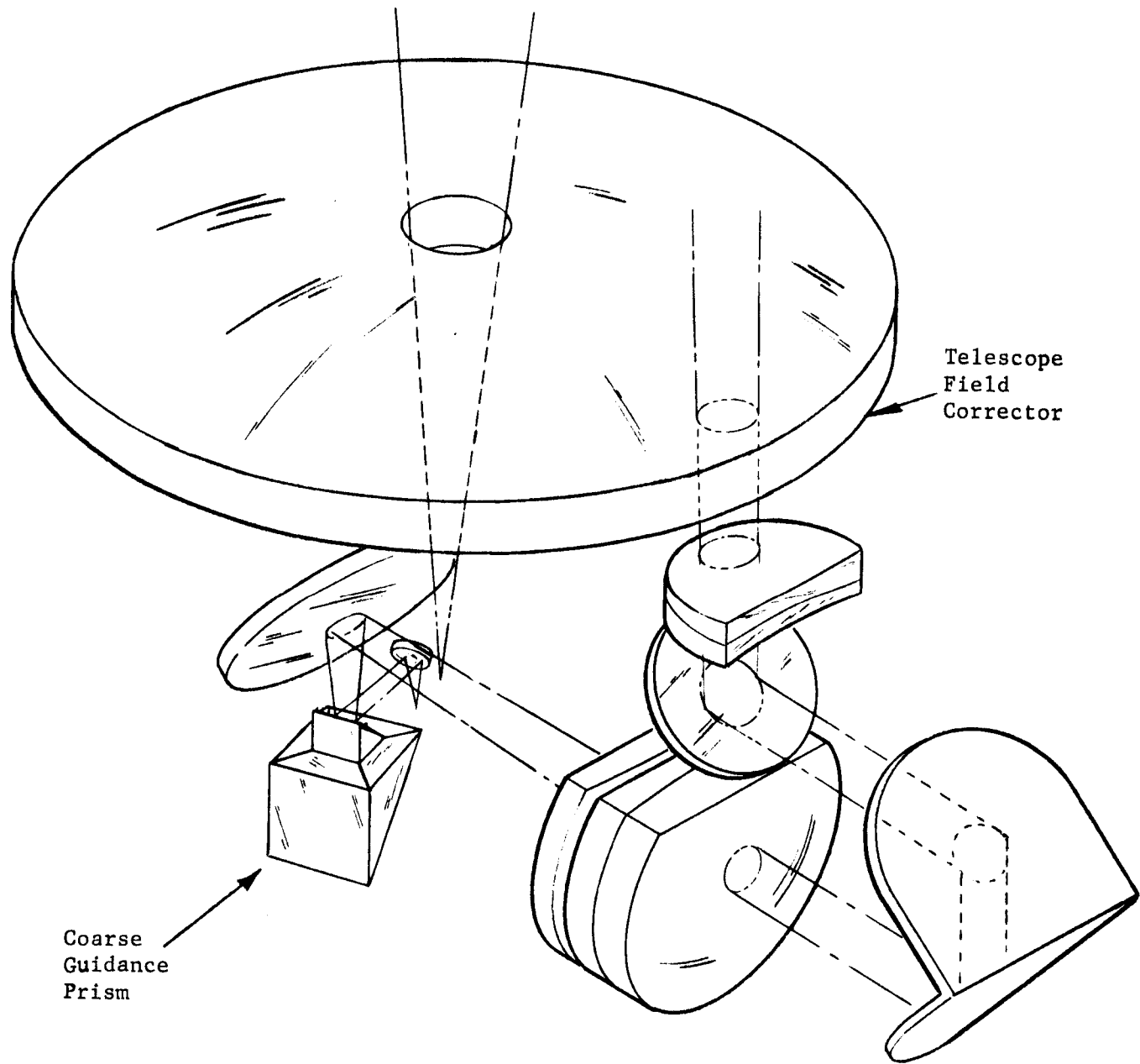
The portion of the telescope field to be relayed by the image mover is determined by the position of the negative doublet and diagonal combination, which can vary between the two extremes shown in bold and phantom in Figure 2.3, and by the angular orientation of the image mover assembly which pivots about an axis through the mirror diagonal behind the positive triplet. The image mover orientation for a skew position in the telescope field is shown in Figure 2.4. The coarse pointing prism and the small mirror immediately above the  $f/10$  focal plane do not rotate with the rest of the assembly but remain fixed.

The size of the portion of the telescope field which is relayed by the image mover to the pointing system is important since it affects the maximum



2-6

Figure 2.3 Image Mover Assembly



2-7

Figure 2.4 Image Mover in Skewed Position

angular position and velocity errors which can be handled by the telescope pointing system. In the design shown in Figure 2.3 the image field capability of the image mover is not sharply defined but can be roughly gauged by the amount of vignetting which occurs for various angles off of the nominal position. This amounts to about 50% for image positions lying in a 3 minute of arc diameter circle about the nominal position.

Another advantage of this image mover design is that it divides the 3 minute of arc diameter field seen by the pointing system into separate inner and outer zones, thus affording greater scope to the pointing logic system. The split occurs at the coarse pointing prism. The central portion of the image field is extracted by a small diagonal mirror on the top of the prism so that after reflection from another small diagonal mirror it falls on the uncorrected  $f/10$  focal plane close to the axial image field. The outer portion of the image mover field passes into the prism and is internally reflected in a direction away from the optical axis and into a coarse pointing system.

In order to establish feasibility a preliminary optical design was attempted. The results are shown in Figure 2.5. The number attached to each optical surface refers to Table 2-II, which lists the radius, separation and

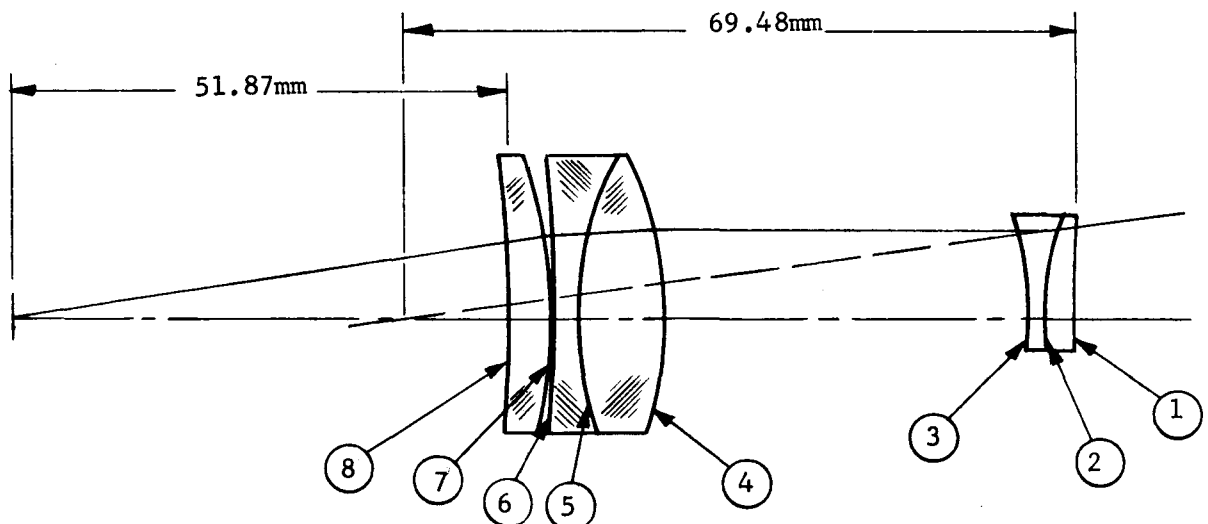


Figure 2.5. Image Mover Lens Elements

glass type for each surface. Since the rotation axis of the image mover coincides with the optical axis of all the lens elements as well as the apex of the pointing divider when the optical system is unfolded, it was only necessary to correct both lens groups for spherical aberration and color.

Several criteria were used in the optical design. The thickness and spacing of the lens elements was chosen so that an  $f/3$  negative lens and an  $f/1.7$  positive lens were physically possible, since these values are required in order to achieve a 3 minute of arc diameter acquisition field. The image mover system,

TABLE 2-II

## IMAGE MOVER LENS ELEMENTS

SURFACE	RADIUS (mm)	SEPARATION (mm)	MATERIAL
1*	-164.55	3.00	SF-8
2	-31.68	2.00	BAK-1
3	39.96	variable	-
4	42.38	9.00	BAK-1
5	35.09	2.50	SF-8
6	418.65	.10	-
7	59.77	4.50	SK-4
8**	298.85	-	-

\* BFL from surface 1 69.48 mm

\*\* BFL from surface 8 51.87 mm

which includes both the positive and negative lens groups, was optimized with respect to an  $f/3.75$  aperture since this is roughly equivalent to the aperture used when the image mover is positioned so as to relay a guide star image lying in the outermost part of the telescope field. This is illustrated in Figure 2.3 and arises from the divergence of the chief rays in the outer part of the telescope field. Finally, the criteria used in judging the performance of the optimized optical system was the same as that for an  $f/10$  image beam since this is approximately the  $f$ /number of beams entering and leaving the image mover system.

The optical performance of the image mover system is illustrated in Figure 2.6 which shows the geometrical image size versus aperture for 3 colors. The abscissa ( $TA'$ ) is the height above or below the optical axis at which geometrically-traced rays intersect the focal plane. The Rayleigh limit or  $\lambda/4$  wavefront deformation tolerance for chromatic aberrations corresponds to a  $TA'$  limit of  $\pm 5$  microns which is well outside of the image mover system performance for apertures smaller than the  $f/3.75$  design limit.

As might be expected, a small rotation of the image mover about the telescope axis or a small shift in the position of the negative doublet with respect to the positive triplet can produce a relatively large pointing error. It is, therefore, essential that the mechanism which positions the image mover elements be designed so that such motions can be minimized during the operation of the telescope. This can probably be achieved most easily by a mechanical design which locks the elements with respect to each other and the instrument

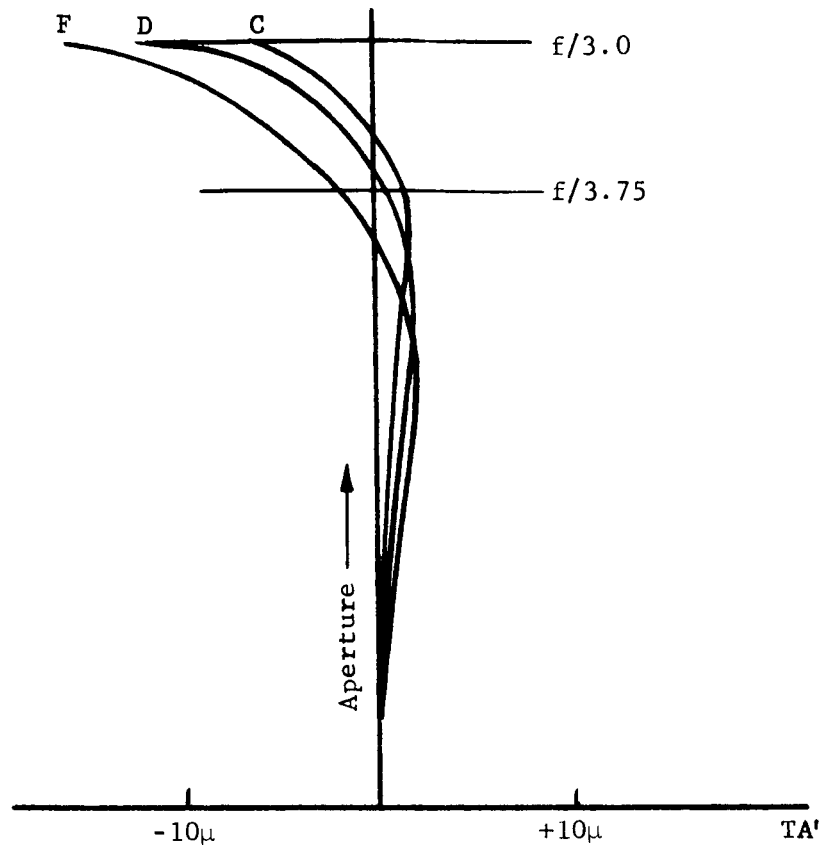


Figure 2.6. On-Axis Image Mover Performance

package frame once they have been positioned correctly. Small translational displacements of the entire image mover system have a negligible effect on the position of the guide star images if the  $f$ /number of the incoming and outgoing image beams are equal. In this case, the image mover system is analogous to a window in a collimated light path; it introduces an amount of parallax depending on the angular orientation, but translational motions have no effect since the optical power is unity. This advantage is utilized in the present design with the exception that the field correcting elements are assumed part of the image moving system thus yielding equal  $f$ /numbers for the uncorrected on-axis image beam and the guide star beams emerging from the image movers.

The optical design of the image mover elements has been sufficient to demonstrate feasibility, but there remains considerable scope for further improvements. The optical efficiency of the image mover system can probably be enhanced by reducing the number of air-glass interfaces and by employing internally reflecting prisms rather than mirror surfaces. A reduction in the total number of lens components may also be possible. In the present design, the negative doublet and positive triplet were individually corrected for spherical aberration and color. The additional design latitude obtained by requiring only that the system be well corrected may be sufficient to reduce



the number of elements. Additional work is also required on the mechanical aspects of the image mover design and on the effect of long term temperature changes on system performance.

### 2.2.1 Coarse Pointing System

A schematic of the optical train employed in the coarse pointing system is shown in Figure 2.7. Guide star images which fall outside of the fine pointing field of view, determined by the small diagonal mirror on the top of the coarse pointing prism, are intercepted by the coarse pointing prism. The top of this prism is bevelled to form a 4-quadrant image divider with a missing center. The image divider causes an image of the telescope entrance pupil

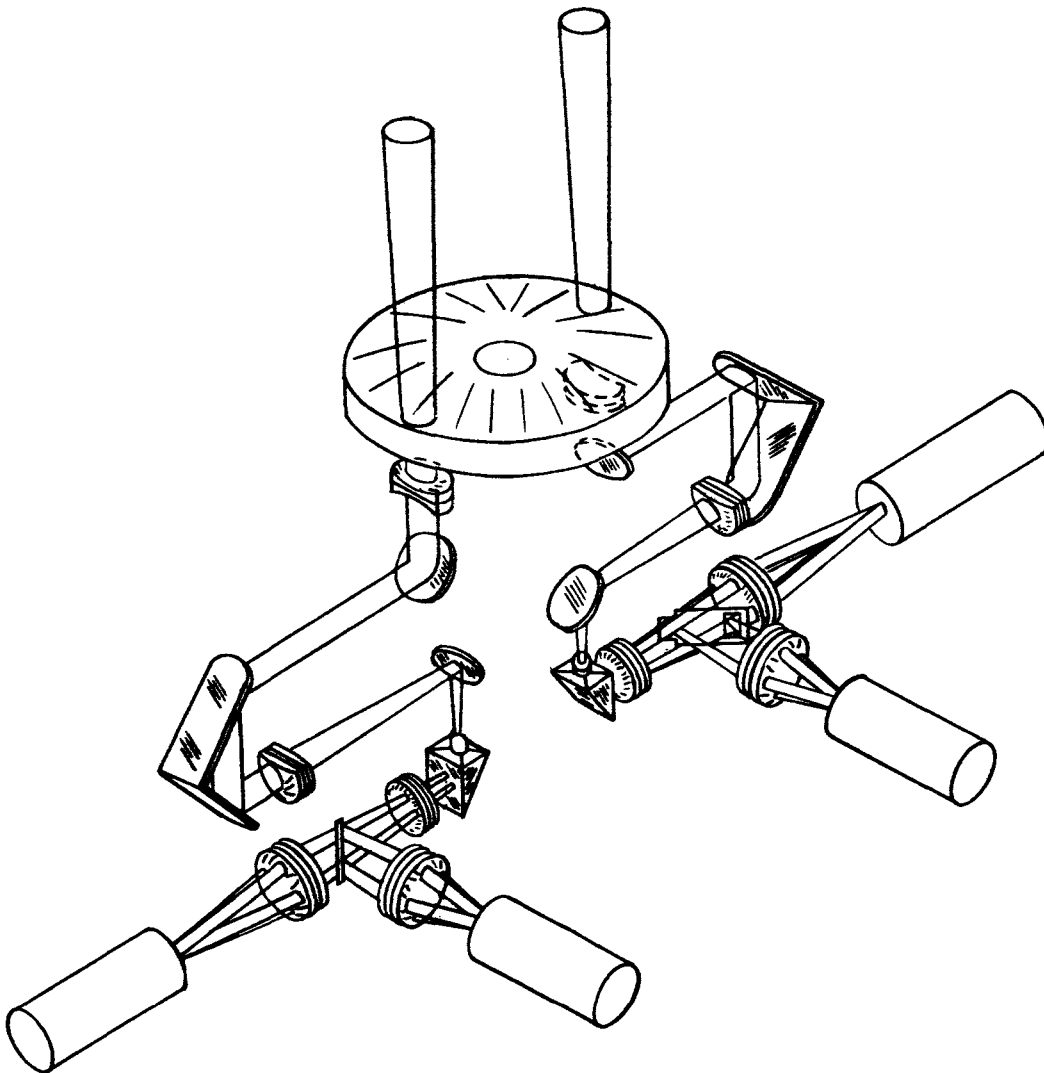


Figure 2.7. Coarse Pointing System

formed by a condenser next to the prism, to occupy one of 4 positions depending on the quadrant intersected by the image beam. Each position is optically encoded in a distinct fashion by a reticle which diagonally intersects the mean position of the entrance pupil image plane. Light passing through the reticle is collected at one phototube and light reflected from the reticle is collected at another to form a push-pull signal processing arrangement. Not only does this permit better use of the incoming photon beam than encoding schemes which discard half of the incoming photons, but it also permits continued operation (at a reduced signal-to-noise ratio) if one of the phototubes were to fail.

### 2.2.2 Fine Pointing System

The fine pointing system is shown in schematic form in Figure 2.8. In this case, the guide star image beams are intercepted by the small diagonal mirrors on the coarse pointing prisms and after another reflection are focused along side of the on-axis image beam. A small diagonal mirror located just under the last mirrors in the image movers pivots about the optical axis to direct the fine pointing beams through the microscope objective.

After emerging from the microscope objective the two guide star image beams gradually diverge from the on-axis image beam and after two reflections are focused on a pair of image dividers situated in the  $f/200$  image field on either side of both vidicons. The image dividers are canted with respect to the vidicon and shifted forward slightly to compensate for field curvature in the  $f/200$  image plane. Past the image dividers, the optical paths in the coarse and fine pointing systems are similar.

## 2.3 IMAGE SYSTEM

The primary purpose of the image system is to relay the small on-axis telescope image field to an  $f/200$  image plane at the photosensitive surface of each vidicon. A magnification of 20 is required to match the vidicon resolution of the diffraction-limited resolution of the telescope. For this purpose, a narrow field microscope having an  $f/10$  entrance aperture and a spectral range extending from 1100A to 6000A would be ideal.

A second function which is required of the image system is to relay the two guide star image fields located on either side of the telescope axis to corresponding positions in the  $f/200$  image plane. For this purpose, a wide field,  $f/3.7$  microscope having a spectral range from 4000A to 6000A would be adequate, assuming a field lens could be incorporated into the system. The  $f/3.7$  aperture requirement applies to the image mover as well as the microscope objective and results from the close proximity of telescope exit pupil when viewed through the field corrector.

Taken individually either requirement is achievable. The spectral range of the on-axis image system can be achieved with a reflective microscope system consisting of two spherical elements arranged concentrically and as part of a low  $f$ /number system so that the  $f/10$  image beam passes off-axis without suffering any obscuration. The wide field and low  $f$ /number required for

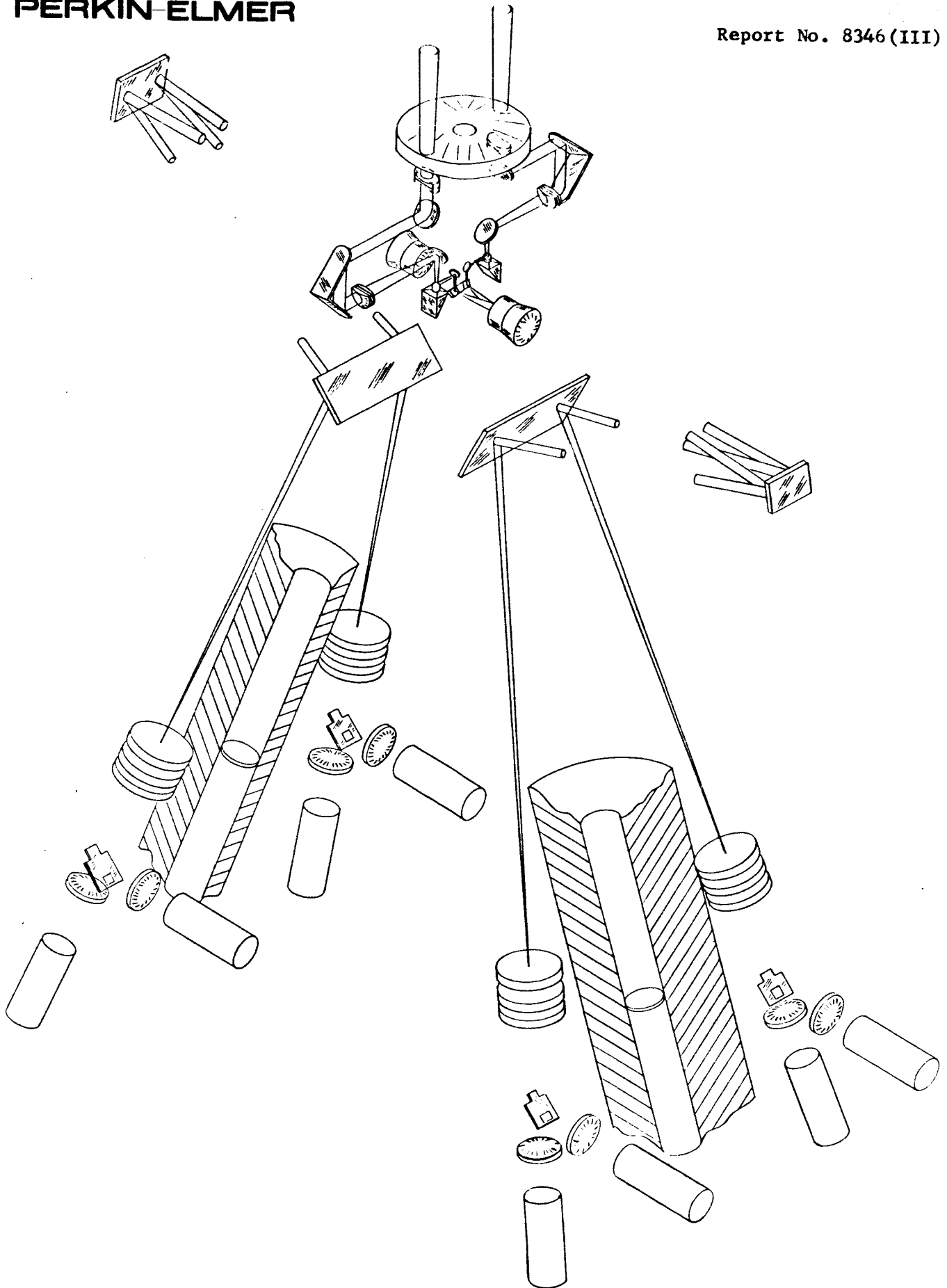


Figure 2.8 Fine Pointing System

relaying the pointing field is more difficult. It cannot be achieved with an off-axis reflective system but it is possible with a refractive system.

The best compromise for both requirements appears to be a ball lens type of refractive system illustrated in Figure 2.9. The unique feature of this type of design is that the radii of curvature for all elements have a common center. This imposes rather severe limitations on the number of parameters which can be varied during optimization; however, only spherical aberration and longitudinal color need be corrected in order to achieve a wide field objective with concentric focal plane. This is because there is no single axis, and therefore, no off-axis image beam, in a rotational symmetric system.

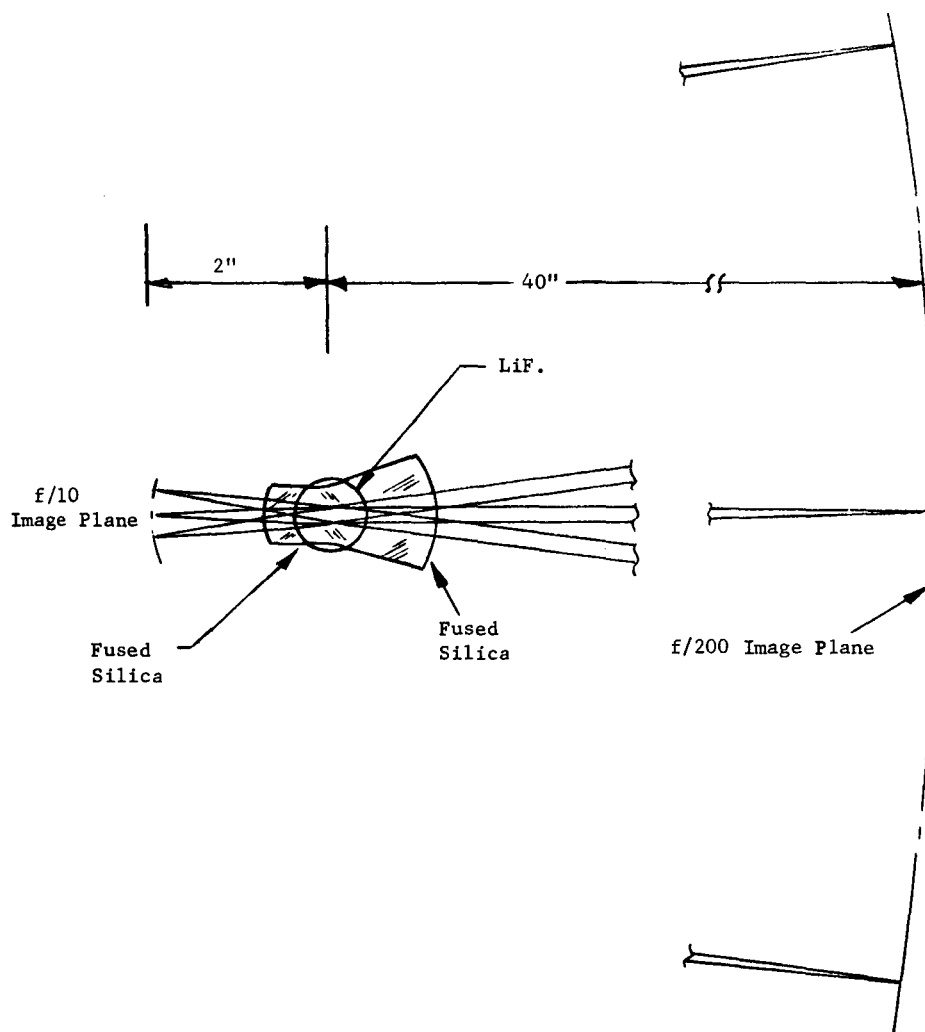


Figure 2.9. Wide Field Microscope Objective ( $f/3.7$ ,  $0.2\mu - 0.6\mu$ )

The radii shown in Figure 2.9 are the result of a preliminary optical design aimed at establishing the feasibility of an optical system composed of lithium fluoride and fused silica elements. The performance of such a system is illustrated in Figure 2.10. Again, the parameter TA' is the height above or below the optical axis which is intersected by rays geometrically traced through the optical system to the focal plane. For rays passing through the optical system TA' is zero but varies with height in the presence of spherical aberration, and with wavelength in the presence of longitudinal color. Both aberrations are evident in Figure 2.10.

The  $\lambda/4$  peak-to-peak wavefront deformation tolerance transverse chromatic aberrations is given by:

$$TA'_{CR} = \pm \lambda f$$

where

$\lambda$  = mean wavelength

f = f/number of image beam.

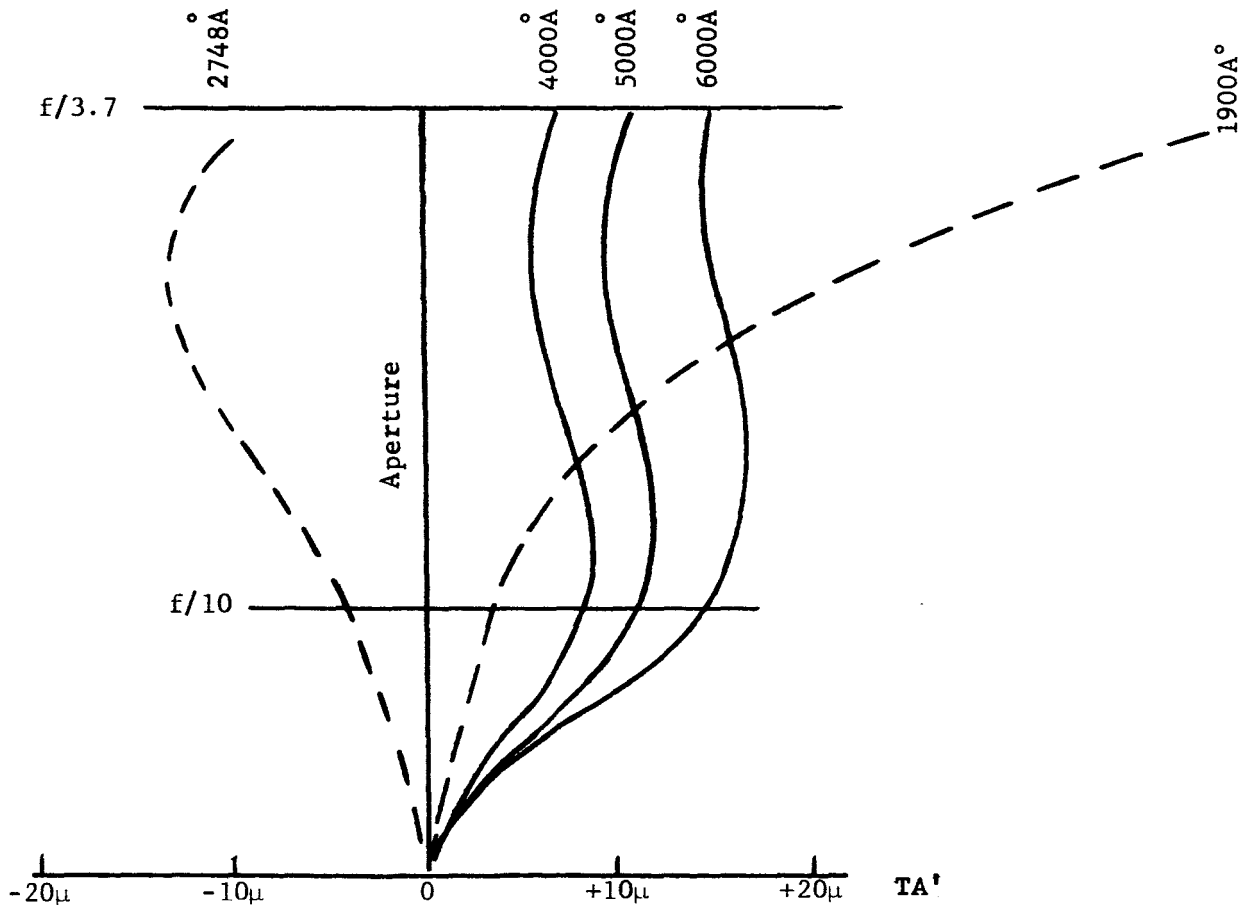


Figure 2.10. UV Ball Lens Performance

This corresponds to  $\pm 3$  microns in the 2000Å to 4000Å region and  $\pm 5$  microns in the 4000Å to 6000Å region. The aberrations in the on-axis image field, which are indicated by the f/10 line on Figure 2.10 exceed these tolerances by a factor of 2. A final design having chromatic aberrations within  $\lambda/4$  Rayleigh tolerance is a recommended design goal. Even so, a factor of 2 greater than the  $\lambda/4$  limit does not indicate a catastrophic degradation in image quality, but rather a well defined image surrounded by a halo of scattered light. Many designers would consider a chromatic tolerance equal to double the Rayleigh limit satisfactory because it does not appreciably affect the image size but results in a loss of light at the image center which is added to the diffraction rings. (The design of Figure 2.16 reaches the  $\lambda/4$  goal.)

The three elements in the microscope objective permit color correction at two wavelengths which, in turn, yields a minimum focal length. In the present design, the minimum focal length occurs at 2748Å and the corrected regions occur near 2400Å and 3400Å. If narrow bandpass filters are used in front of the vidicon then the aberrations can be reduced to negligible values by giving the filters sufficient power to achieve the optimum focus for each pass band. The reduction in the geometrical image size which is achievable by a focal shift may be estimated by rotating each of the curves on Figure 2.10 about the origin until the positive and negative deviations balance. Up to the f/10 aperture size, all of the curves are nearly linear; thus indicating very low residual aberrations once the effects of longitudinal color have been eliminated by narrow bandpass filters and compensating focal shifts.

The region above f/10 applies only to the guide star image beams. These subtend an f/10 cone angle, however, the position of the cone in the objective entrance aperture is a function of the guide star position in the telescope field. As a result, the total aperture required by the guide star image beams is equal to f/3.7. The criterion used in judging the seriousness of the aberrations is determined by the cone angle and this remains the same as before. Only the 4000Å to 6000Å spectral region need be considered with respect to the guide star image beams since this is where the bulk of the detectable guide star energy lies and where the telescope field corrector and image mover lens elements have been corrected.

The total chromatic aberration in the 4000Å to 6000Å region can be reduced to double the Rayleigh criterion over the entire f/3.7 aperture by a focal shift of 120 microns in the f/10 focal plane or about 2 inches in the f/200 focal plane. The resultant image quality is probably more than adequate for pointing since the transfer function associated with moving the image across an edge is only slightly affected.

The preliminary design of the microscope objective was sufficient to indicate feasibility but falls somewhat short of a quarter wave design goal (i.e., quarter wave peak-to-peak). Small improvements in the present design might be anticipated from a more judicious choice of the wavelength at which the minimum focal length occurs. Considerably more correction might be gained by allowing spaces between the fused silica and lithium fluoride elements. A

third possibility is the use of barium fluoride as a component material for one or both of the fused silica elements.

A comparison of the refractive properties of  $BaF_2$ ,  $LiF$ , and fused silica is shown in Figure 2.11. Toward 2000A the index of fused silica breaks sharply upward indicating a high dispersion in this region. By making one or both of the negative elements in the objective  $BaF_2$  it may be possible to match more closely the dispersion of the positive  $LiF$  element, thereby reducing the amount of color in the objective.

A schematic showing the path traced by the on-axis image beam through the image system is shown in Figure 2.12. Almost identical paths are traced by the guide star image beams which are shown in the fine pointing system on Figure 2.8.

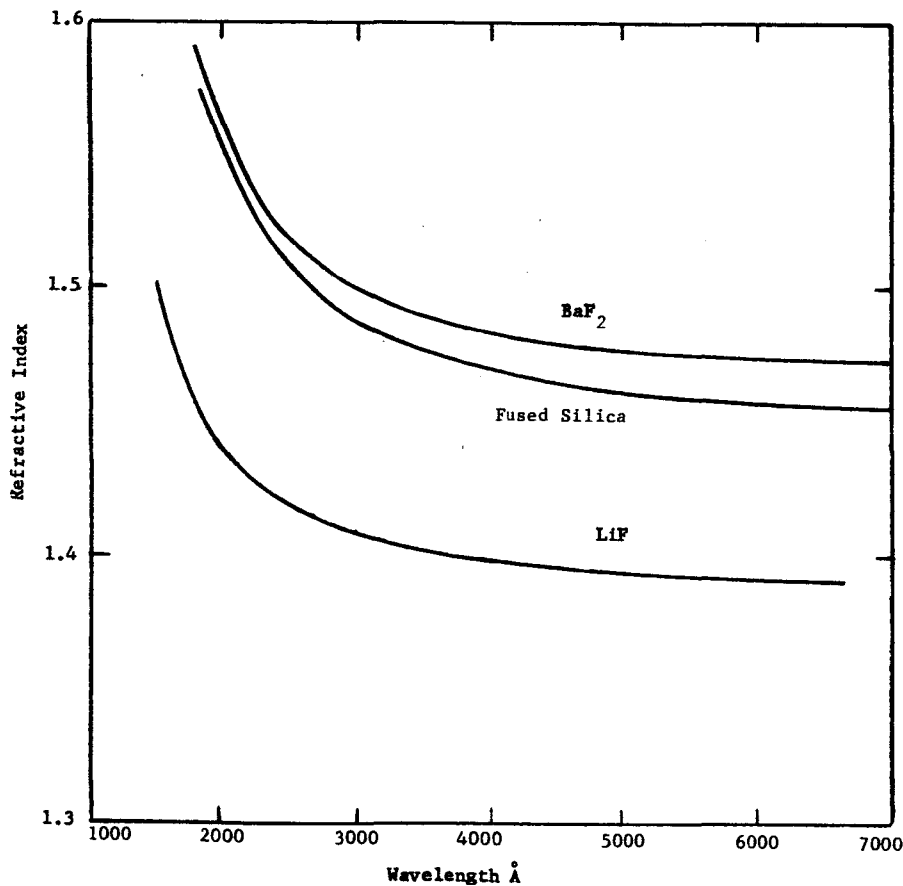


Figure 2.11. UV Lens Materials

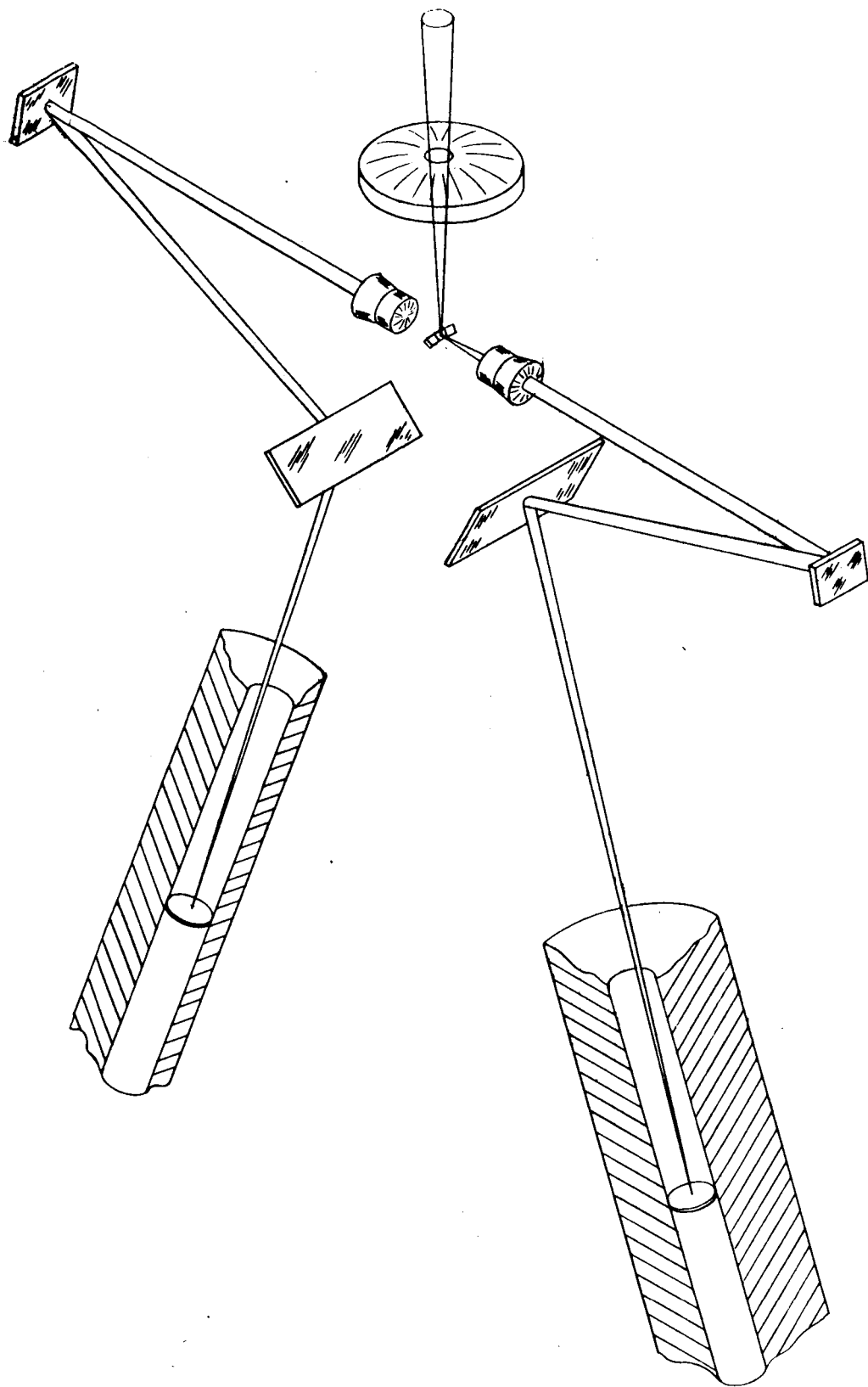


Figure 2.12 Imaging System



A key role is played by the small diagonal flip mirror near the  $f/10$  image plane. The mirror pivots about the optical axis so as to direct the imaging and pointing beams to optical systems associated with either the right or left vidicons. The spectrograph slit, which is contained in the flip mirror where it cuts the  $f/10$  focal plane, gets turned end for end as the mirror pivots from the left to the right optical systems but remains in focus. The wing sections on the ends of the flip mirror are slightly tilted with respect to the central section. These act as a field lens for the pointing beams directing them towards the center of the microscope objective and compensating for the curved field of the microscope. An enlarged view of the region around the flip mirror is shown in Figure 2.13.

2.4 INSTRUMENT PACKAGE

The only portion of the optics which has not been described thus far is the spectrograph. A thorough description of the merits of various

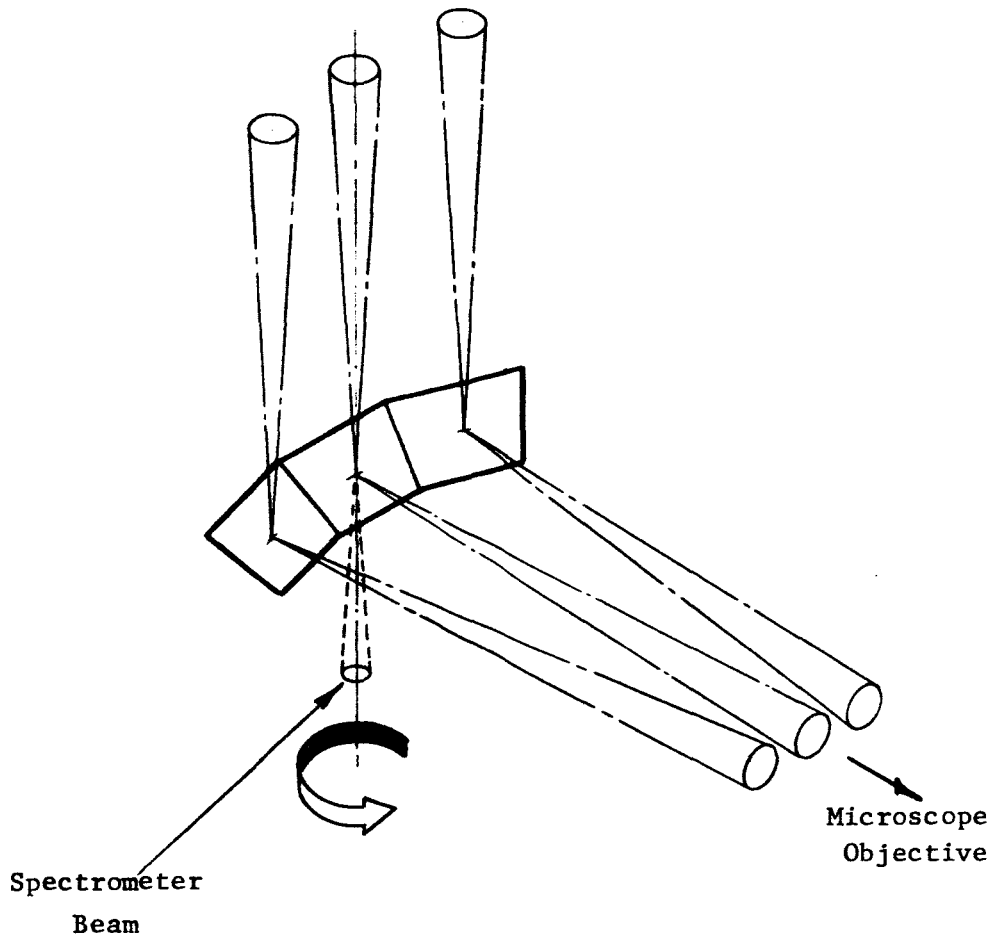


Figure 2.13. Flip Mirror

spectrograph arrangements is included in Section 4.0. However, a definite configuration has not been established even on a preliminary design basis.

For the sake of completeness a schematic of one of the possible spectrograph configurations is indicated in Figure 2.14. In this configuration, a low dispersion spherical grating and a high dispersion echelle grating produce a folded spectrum on the sensitive surface of the vidicon. Since the spectrograph exit beam is approximately  $f/20$  and has a rather shallow depth of focus, it is necessary to ensure that the focal plane of the spectrograph is accurately aligned with the vidicon sensitive surface. This causes the  $f/200$  focal plane of the on-axis image field to be canted slightly with respect to the sensitive surface, however, this is not serious since the depth of focus at  $f/200$  is in the order of an inch.

The spectrograph format is switched from one vidicon to the other in much the same way as the image field is changed. The first spectrograph element is pivoted so that it can be rotated about the optical axis to direct the predispersed energy to one of two similar echelle gratings arranged on the axis of each vidicon.

A cut-away view showing the location of the larger optical components in the instrument package is shown in Figure 2.15.

The entire optical system represents various stages in optical design. The telescope and corrector design have probably received most attention and there does not appear to be much scope for additional improvement within the present design constraints. The image mover and microscope objective have received sufficient optical design effort to indicate feasibility but considerable additional effort will be required to achieve optimum designs. The optics associated with the image dividers in both coarse and fine pointing systems have received only cursory attention excluding even a first order ray trace. In this portion of the system, optical aberrations are of no consequence but it is essential to keep the optical efficiency as high as possible by keeping the number of optical surfaces low, and by making the apex of the fine pointing divider as sharp as possible. When the final optimization of the optical design is performed it will be necessary to allocate figure tolerances to each optical element in order to ensure that diffraction-limited performance is not seriously compromised.

Probably, the major disadvantage of the present design is the  $1000\text{\AA}$  to  $2000\text{\AA}$  spectral region not passed by the microscope objective. Two ways of overcoming this limitation have been found. Both permit an off-axis reflective microscope to be employed but involve a sacrifice in reliability. One means is offered by a telescope design having the exit pupil at infinity which is described in section 2.5. This requires a deployable secondary mirror. A second possibility is an image mover which contains a pivoted glass cube in the collimated light path. Rotation of the cube shifts the collimated light bundle up or down so as to coincide with the center of the positive lens system. This is an additional moving element in a critical portion of the system and was, therefore, not proposed.

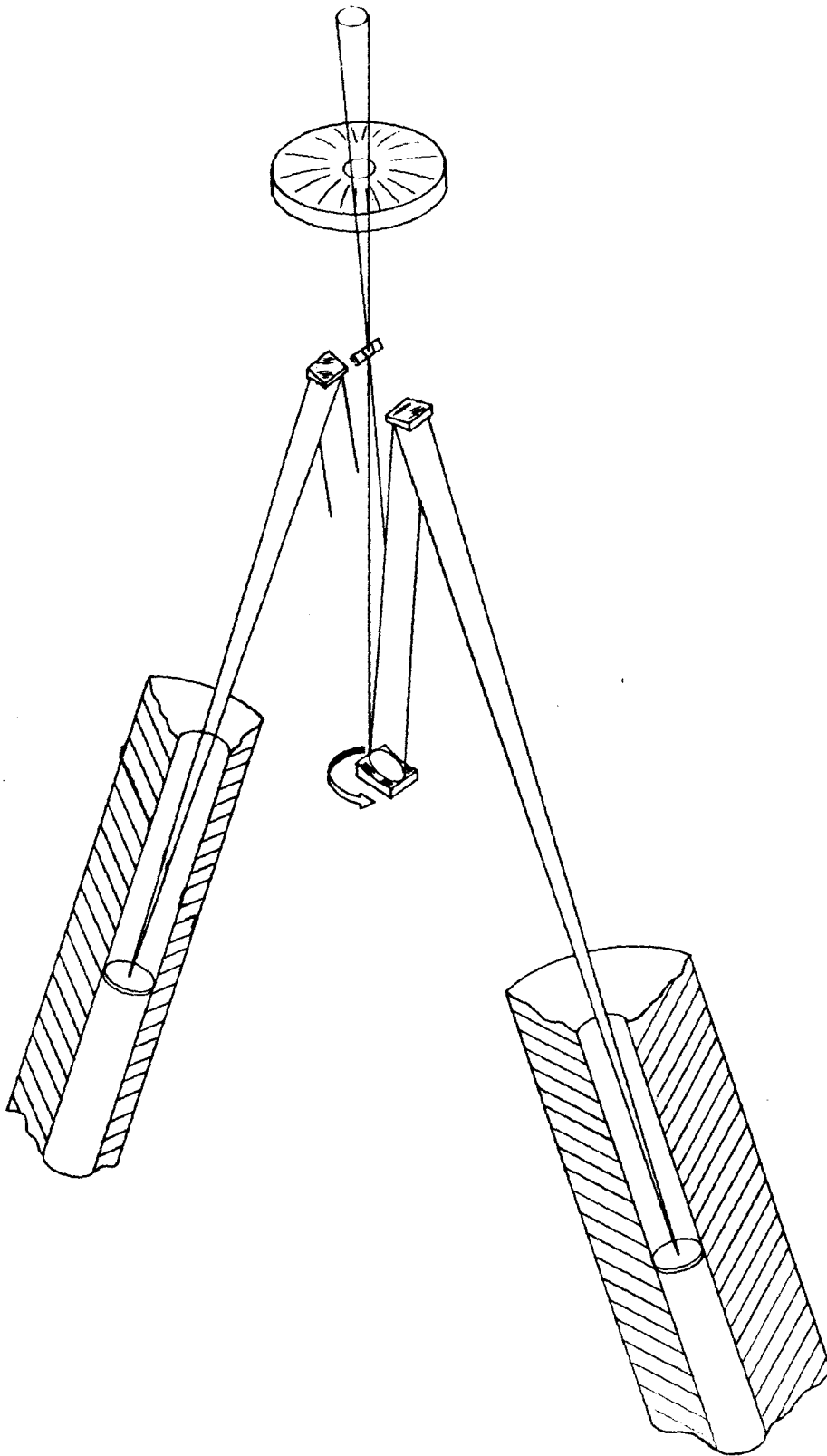


Figure 2.14 Spectrograph System

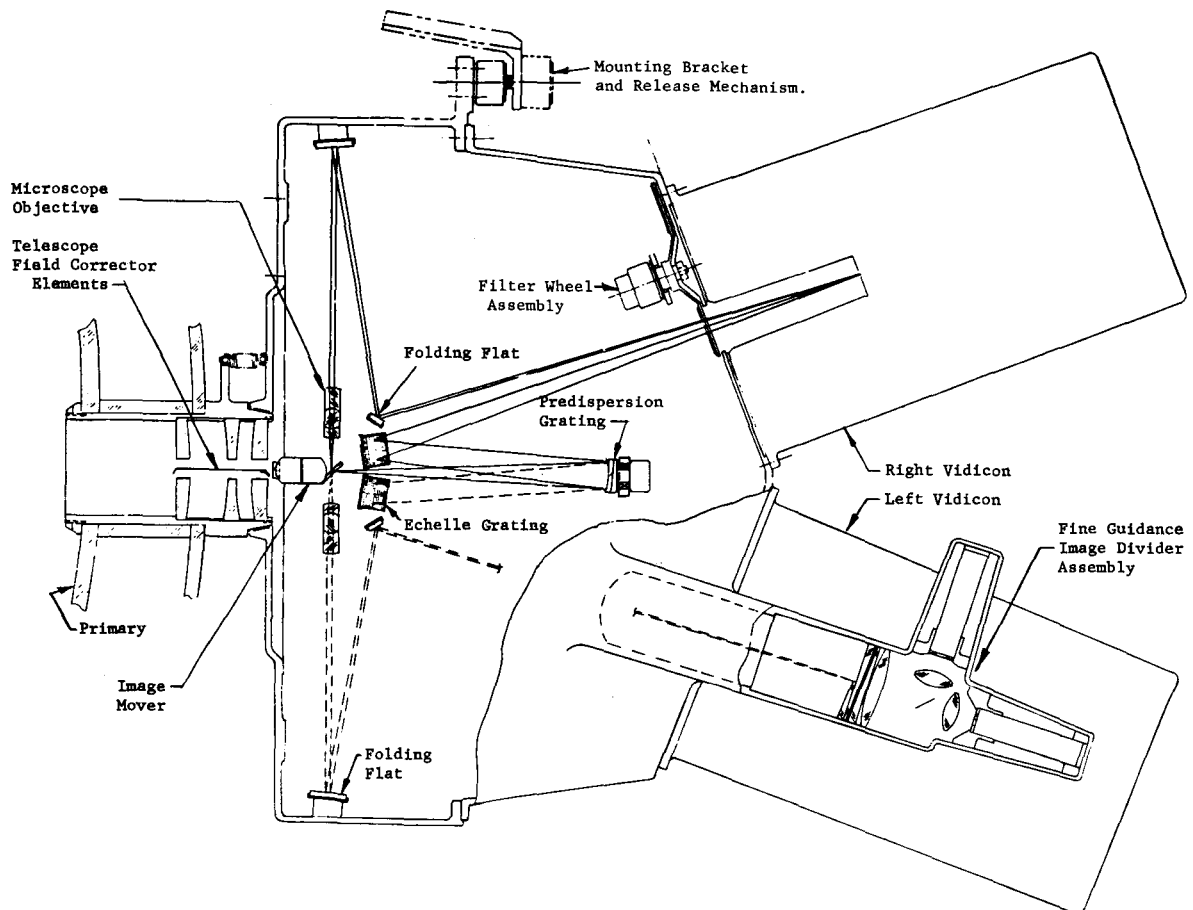


Figure 2.15. Instrument Package Optical Layout

In conclusion, it appears that an optical system has been found which combines the diffraction-limited imagery capability of Stratoscope II with the far ultraviolet, high-resolution spectrophotometric capability of OAO-C in a single OAO experiment package.

## 2.5 INFINITE EXIT PUPIL TELESCOPE

In the present telescope design, the exit pupil occurs close to the focal plane resulting in a large divergence angle between chief rays on opposite extremes of the telescope field. This, in turn, increases the size of the image mover lens elements and also the size of the microscope objective. The increase corresponds approximately to a change from an  $f/10$  to an  $f/3.7$  system.

A telescope design having an exit pupil at infinity would place far less stringent requirements on the image mover and microscope systems, thus providing considerable scope for improved performance, relaxed tolerances and perhaps a reduction in the total number of optical surfaces. Such a design does not appear to be possible under the present design constraints, but it becomes possible if the separation between the primary and secondary mirrors is allowed to increase beyond the present 65-inch limit. Such a system is shown in Figure 2.16. The primary-secondary spacing is about double

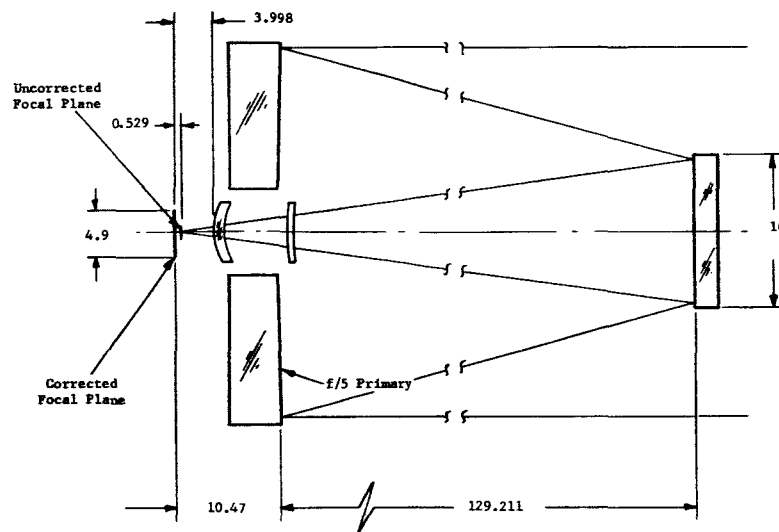


Figure 2.16. Telescope with Entrance Pupil at Infinity

the present design limit and the curvatures on the primary and secondary mirrors are considerably reduced.

Apart from the advantages which accrue to the rest of the optical system, the infinite exit pupil telescope also offers a larger and better corrected field ( $0.7^\circ$  diameter compared to  $0.5^\circ$  diameter for the present system) and reduced alignment tolerances between the primary and secondary mirrors. The design does not appear to be compatible with the present design philosophy predicted on a remote operation capability. However, if a change in philosophy is indicated as a result of the manned experiment portion of this study, then the OAO interface problems caused by a protruding telescope might be considered in relation to the increased capabilities provided by such a design.

### 3.0 POINTING SYSTEM DESIGN FOR A FORTY-INCH SYSTEM

#### 3.1 INTRODUCTION

This portion of the study is devoted to arriving at a single feasible electronics design approach for a 40-inch aperture telescope which is to be contained and supported by an OAO spacecraft. It includes overall system considerations in addition to examining theoretical and practical design aspects. Such subjects as ground commands, telemetry, electrical power, suspension systems, caging systems, sensors design redundancy, operational sequences and other areas pertinent to an orbiting forty-inch telescope have been pursued.

The study is organized in the following manner. The first part (3.2) discusses the major system specifications, study results, and some basic concepts. The second part (3.3) includes a generalized overall description of the total satellite system including a discussion of a typical operational sequence involving some of the expected ground control and OAO spacecraft functions; concepts for the telescope pointing system in context with the operational procedures; complete description of the telescope pointing\* system; and a study is made of the details of telescope acquisition logic and switching functions.

The final portions of this section (3.4 and on) are mostly devoted to detailed analyses and design considerations.

#### 3.2 SPECIFICATIONS AND DESIGN PHILOSOPHY

The pointing system was designed to a very basic set of specifications which are given in Table 3-I. The most critical specification, and the main system design goal, is the 0.01 arc-sec (rms) pointing accuracy requirement. As stated in Volume II, Section 4.0, this specification originates from the telescope spectroscopic and image recording instruments. As discussed in the above-cited section, the ability to track to 0.01 arc-sec (rms) depends largely on the guide star magnitudes used. The range of magnitudes selected (9-12th visual magnitude) was based on the probable availability of guide stars in a 30 arc-min field of view surrounding the stellar source intended for viewing.<sup>1</sup>

The initial conditions of displacement and rate used for acquisition were obtained from the limits of performance of the OAO spacecraft guidance system.<sup>2</sup> The remaining specifications are estimates based on the optical design (2.0), package-size, and typical photomultiplier characteristics.

The results of the study indicate a system design capable of 0.01 arc-sec (rms) pointing accuracy is feasible under the expected disturbing

---

\*In this section as in other sections of the study, the words "pointing" and "guidance" are used interchangeably and with the same meaning.

TABLE 3-1

SPECIFICATIONS FOR GUIDANCE SYSTEM

Telescope Initial Position Errors (Vertical and Horizontal Axes)	$\psi, \phi$	$\pm 1$ arc-min ( $\pm 4$ arc-min search mode)
Telescope Initial Rate Error (Vertical and Horizontal Axes)	$\psi, \phi$	$\pm 1.0$ arc-min/sec
Telescope Initial Position Error (Roll)	$\theta$	$\pm 2$ degrees
Guide Star Visual Magnitude	$M_V$	9th to 12th
Telescope Aperture	D	1 meter
Telescope Optical Efficiency	$\eta_o$	10%
Line of Sight Pointing Error (Vertical Axis)	$E_p(\phi)$	$\leq 0.01$ arc-sec (rms)
Line of Sight Pointing Error (Horizontal Axis)	$E_p(\psi)$	$\leq 0.01$ arc-sec (rms)
Line of Sight Pointing Error (Roll Axis)	$E_p(\theta)$	$\leq 4.0$ arc-sec (rms) at 15 arc-min field of view
Environmental Temperature	T	- 30°C
Telescope Inertia	J	100-200 slug-ft <sup>2</sup>
Telescope Mass	M	30 slugs
Torque Capability (Vertical and Horizontal)	$\tau_{sat.}$	1.0 lb-ft (each axis)
Force Capability (Magnetic Actuator)	$F_{sat.}$	0.3 lb (each axis)
Telescope Torque Disturbance	$T_d$	Sinusoidal torque -20,000 dyne-cm at a 45 min. period
Power Allocation	P	30 watts (avg.), 60 watts (peak)
Photomultiplier Spectral Response	$\mu$	0.1-0.25 microns
Telescope Acquisition Time	t	$\leq 2$ minutes
Photosensor Quantum Efficiency	$\eta_q$	10%
Background Illumination (Without Earth Reflected Light)	$E_n$	One 11th magnitude star/16 arc-min <sup>2</sup>
Clearance Requirements (Maximum)	X, Y, Z	$\leq \pm 0.50$ inch

9. A centering servo system is used to maintain clearance between the telescope and OAO spacecraft and will utilize the same magnetic pushers as are used in telescope pointing.
10. An auxiliary three-axis servo system, referenced to the spacecraft rotational axes, is incorporated. It serves as a vernier caging mechanism and in addition to other functions, will be used in scanning in the event the OAO spacecraft guidance is not sufficiently accurate to place the guide stars images on the optical sensors.
11. The telescope pointing system will be physically isolated from the OAO spacecraft. The pointing system will not depend upon the spacecraft for anything but power, initial pointing, and torque reactions.

The final mode of telescope tracking will rely on the two optical fine sensors to obtain the long term 0.01 arc-sec (rms) pointing accuracy. A roll gyro will, therefore, serve as a back-up device and be used for final tracking only in the case of failure or the absence of a second guide star. However, since it is available, it will be used in roll as a prime means of facilitating acquisition. A back-up roll acquisition system utilizing the optical sensors will be incorporated (with some sacrifice in roll acquisition performance) if the gyro should fail.

### 3.3 OVERALL SYSTEM DESCRIPTION

#### 3.3.1 Basic Satellite System

The space scientific observatory is scheduled to conduct experiments for a minimum of one year. It will be orbiting the earth once every 101 minutes at approximately 300 nautical miles. The most probable overall satellite configuration is shown in Figure 3.1 and consists of three nearly independent subsystems. Briefly, they are the manned Apollo (CSM) spacecraft, the OAO experimental spacecraft and the 40-inch aperture telescope instrument package.

The Apollo space capsule will only be stationed with the OAO spacecraft-OAO telescope combination during part of the experimental program (30 days). The manned interval is presently assumed to occur during the first 30-day period following launch but could occur up to six months subsequent to launch. This phase will depend to a large extent on the operating condition of the OAO spacecraft and telescope once it is in space. A complete study of the manned mission requirements is included in Volume IV of this report.



torques and using 12th magnitude guide stars. The verifications of these results are contained in subsequent sections. However, to enhance an earlier understanding of the design philosophy used, some very basic system concepts are listed below.

1. Linear magnetic "Pushers" will be used to provide telescope torque control in each axis. Located at a fixed radius with respect to the telescope mass center, controlling torques will be developed by reacting against the outer OAO spacecraft. The telescope will be freely suspended, using the OAO spacecraft as an inertial torquing reference.
2. Two linear X-Y image movers will serve to locate the two guide stars within the 30 arc-min field of view of the telescope and will place the star images within the field of view of the optical sensors.
3. Two identical optical sensors are used to fulfill two interchangeable functions. The functions are (a) to develop error signals relative to the line of sight to one of the two guide stars, and (b) to sense the rotational motions of the telescope with respect to the second guide star. Each sensor will have concentric fine (1 arc-minute) and coarse (3 arc-minutes) fields of view.
4. The optical sensors will incorporate the proven four-sided image dividing prism concept discussed in Volume II, Section 4.2 and optical chopping techniques.
5. Single and double integration will be incorporated in the rotational axis ( $\psi$ ,  $\theta$ ,  $\phi$ ) servo loops as discussed in Volume II, Section 4.3.
6. Nonlinear error detecting and electronic switching will be used to equip the pointing system with reasonable acquisition capabilities.
7. Displacement gyros will be incorporated to sense telescope roll ( $\theta$ ) motions during acquisition and in the event a second guide star is not available.
8. An auxiliary rotation ( $\theta$ ) tracker looking at right angles to the line of sight will be used as a back-up roll axis device.

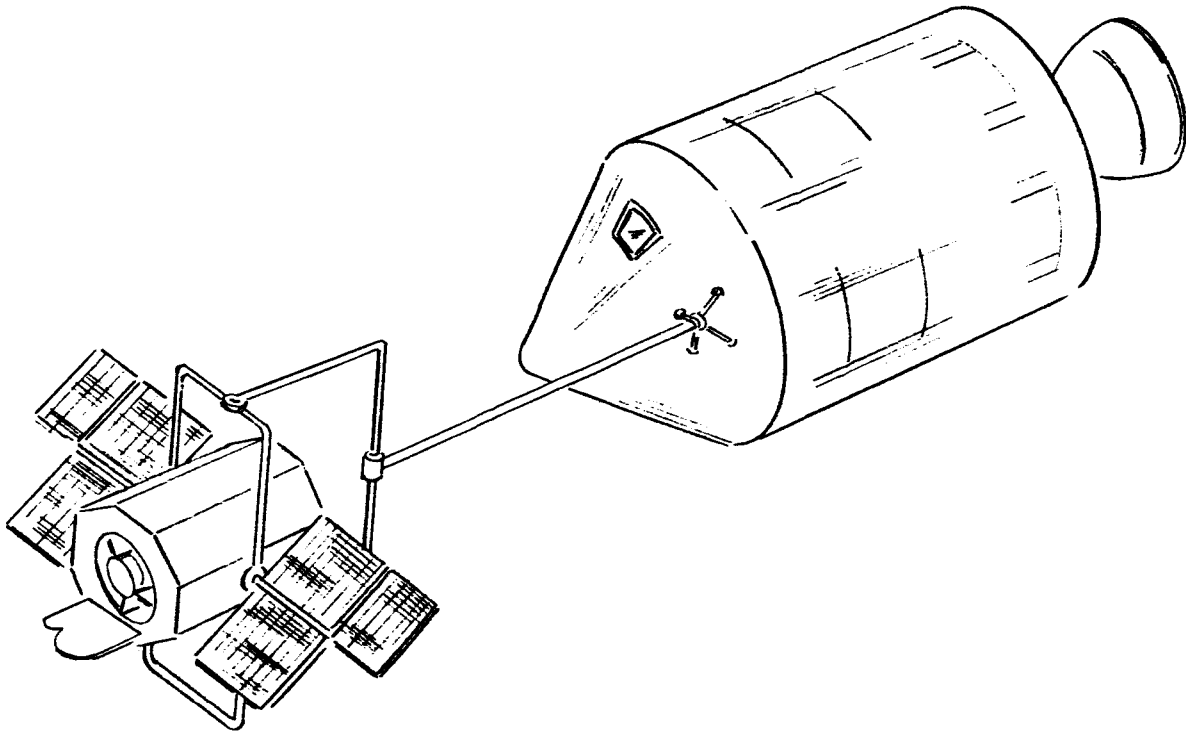


Figure 3.1. Apollo - OAO System

The OAO spacecraft will be attached to the Apollo by means of a flexible suspension system, essentially a boom. During this experiment phase, commands to the OAO spacecraft and telescope will originate both from the ground and the Apollo station. Upon completion of the manned experiment phase, the Apollo will detach itself from the OAO spacecraft and return to earth. Ground stations will then become the sole means for directing and evaluating scientific experiments.

The 40-inch aperture optical system and its associated spectrometer and S.E.C. vidicon will be contained within the OAO spacecraft. The telescope will be caged or rigidly attached to the OAO spacecraft when experiments are not being conducted. During experiments when precision pointing is required, the telescope will uncage and become freely suspended functioning entirely with its own pointing system.

### 3.3.2 Operational Procedures

A typical experiment would proceed as follows:

According to a predetermined experiment plan, a stellar source will be selected for scientific viewing. In proximity of the source of

interest, two stars are also selected which will appear within the field of view of the telescope when it is pointed at the experiment source. These two stars (called "guide" stars) will be used as references for the telescope pointing system. When the source and stars are to be observed, supporting standby power (including gyro power) and telemetry systems in the OAO spacecraft and telescope will be remotely activated. Subsequently, several pre-operational commands occur while the telescope is still caged. The first pre-operational directives either from the ground or the Apollo capsule will be the fine sensor and guide star selection commands. Since two independent fine sensors exist for reliability purposes, either can be used with the selection based on relative quality or performance. Either guide star can also serve as the telescope rotational reference or alternatively, the horizontal (azimuth) or vertical (elevation) references. This selection may be based on the location of the stars with respect to the telescope center of rotation and their relative magnitudes. Following guide star and sensor selections, commands to coarsely erect the rate integrating gyro to the proper position are then given. The gyro serves as a rotational displacement inertial reference. It will function as an acquisition aid but is also capable of being used as a fine guidance rotational sensor for relatively short exposures in the absence of a second guide star. If the latter condition exists, command signals to the telescope are necessary to route the gyro outputs to the roll servo loop for fine tracking.

The remaining pre-operational command will be a positioning signal fed to the "Image Movers" located in the telescope optical system. The image movers serve to locate the images of the two guide stars in the telescope optics and direct these images to the optical pointing sensors. A better understanding of this and succeeding functions can be obtained by a brief discussion of the telescope pointing concepts.

First, the position of the guide stars with respect to the stellar source must be known accurately enough for the guide stars to be picked up by the image mover lenses. Furthermore, since the guide stars can have a variety of locations with respect to the stellar data sources, the pointing optical system must also have the capability of precise adjustments. Achieving this versatility is complex both optically and mechanically. The details of the optical-mechanical system are given in Volume III, Section 2.2. This concept is demonstrated in Figure 3.2 in a very simplified schematic but nonetheless, representative of the image mover principle. As shown in this figure, the sensor optics are moved to the predicted location of the guide star and locked in this position. Any small angular deviations by the telescope about this new position with respect to the guide star are then sensed and corrected by the pointing controls. Since the detector and optical pointing sensors are fixed to the same structure, the angular deviations about the detector line of sight are also corrected.

Referring once again to the system operational sequence, the image mover position commands are followed by commands which cause the OAO spacecraft guidance system to acquire a star with its star trackers. Once the OAO

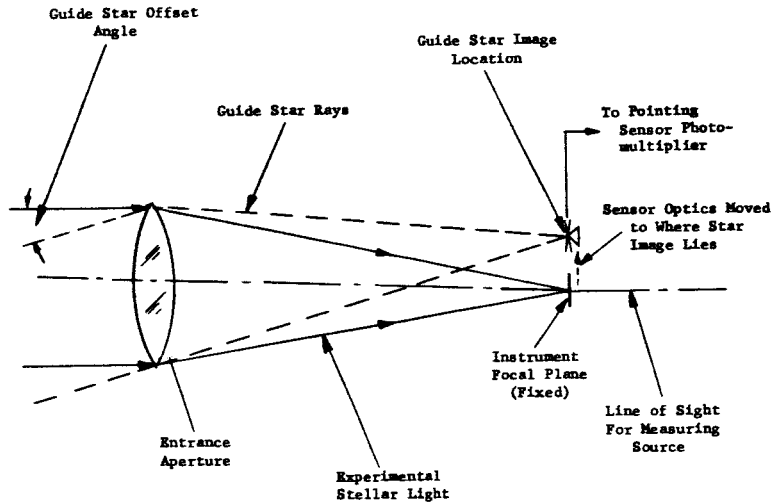


Figure 3.2. Image Mover Principle  
(Single Guide Star)

spacecraft has stabilized to its pointing accuracies  $\pm 1.0$  arc-minutes maximum in pitch and yaw and  $\pm 2.0$  degrees in roll) the telescope pointing system will be activated and the telescope will be uncaged. Confronted with various initial conditions of rate and displacement as well as external disturbing torques, the telescope will proceed to acquire the two guide stars in the following manner:

The telescope pointing system will initially transfer into a centering and auxiliary rotational servo system which obtains its reference from the OAO spacecraft by using linear capacitive type sensors. The telescope will temporarily assume the same pointing angles as the OAO spacecraft in the suspended mode and will simultaneously maintain clearance with respect to the spacecraft. During this time the roll gyro will also be erected to its final reference position. As the auxiliary rotational system stabilizes, the fine and coarse pointing sensors are monitored for star presence signals. If these signals exist, the telescope will switch from the auxiliary rotational servo loop and acquire the two guide stars aided by the gyro and sensor signals. If star presence signals are not available in one or both of the sensors (due perhaps to excessive mispointing by the OAO spacecraft) commands to do a spiral scan starting at the center, will be fed to the auxiliary roll servo loop. The scanning signals are merely "offset" voltages fed into the auxiliary roll servo loop at the capacitive sensor summing

points and can be programmed automatically or manually. The telescope will follow these scan commands and if necessary, point to angular offsets of up to  $\pm 0.5$  degrees in all directions (with respect to the OAO spacecraft) until the guide stars are located.

Following the guide star acquisition phase or, more explicitly, when the telescope has stabilized to acceptable pointing accuracies, the final command is to start detector operation. This then completes the basic sequence of operation (with one exception).

Following final telescope acquisition or just prior to recording data, a servo optimization sequence may or may not occur, depending on the final tracking performance. Subject to further investigation, a self-adapting servo loop gain control is envisioned which will optimize pointing errors due to noise and torque disturbances for the particular guide stars being used.

The experimental procedure discussed here is summarized in Table 3-II with generalized times for each event. The pointing requirements for each phase are also listed. The several independent sequences which allow the telescope itself to acquire and track, once it has been uncaged, are discussed in the following section in context with a more detailed telescope pointing system description.

### 3.3.3 Detailed Telescope Pointing System Description

3.3.3.1 Basic Pointing System Functions - The three telescope axes about which the system is torqued to maintain control in space will be referred to as the vertical ( $\phi$ ), horizontal ( $\psi$ ), and rotational ( $\theta$ ) axes. Two optical sensors, one for each guide star, and six linear magnetic torquers (pushers), two for each axis, a displacement gyro, and six linear displacement sensors comprise the main pointing system components. Each of the optical sensors have two fields of view, wide (3 arc-min) and narrow (1 arc-min). In the final tracking mode, the optical sensors, as discussed in section 4.2, Volume II, detect the small angular deviations of the telescope about the guide stars in all three axes and develop electrical output signals proportional to these errors. (The roll axis sensor actually derives roll motions from the right angle components of the vertical and horizontal motions created by the rotational disturbances.) These electrical signals are then processed through stabilization electronics and fed to the telescope torquers which, by reacting against the OAO spacecraft, repositions the telescope to correct for the errors. The gyro will serve as the roll reference in the absence of a second guide star and continually as a roll acquisition aid. The linear sensors provide the signals which keep the telescope centered with respect to the OAO spacecraft.

To provide a wider acquisition range (see Volume II, 4.4), a wide field of view is required in addition to the fine or narrow field of view. The method by which the two fields of view are implemented with two sensors is analogous to a 3 arc-minute reflecting mirror with a 1 arc-minute hole as shown in Figure 3.3. For angular errors greater than  $1/2$  arc-minute, the

TABLE 3-II

EXPERIMENT PROCEDURE

COMMANDS	SYSTEM	REQUIREMENTS	TIMES	COMMENTS
Activate Power, Gyro Run-Up, Etc.	O.A.O. Spacecraft Telescope	Power On, Pointing Systems In Standby	Several Minutes	Ref. O.A.O. Spacecraft Handbook
Fine Sensor Selection	Telescope	Fine Sensors Activated	Seconds	Plus Coarse Sensors Activated
Guide Star Selection	Telescope	Sensor Signals Are Routed To The Proper Servo Loops	Seconds	
Position Roll Displ. Gyro	Telescope	Gyro Activated And Coarsely Referenced	Minutes	Position Dependent On Spacecraft Perturbations At This Point
Gyro vs Fine Sensor Selection	Telescope	Roll Servo Loop Gyro Signal Routing Complete	Seconds	Optional: Used Only When The Second Guide Star Is Absent
Image Mover Positioning	Telescope	Image Movers Must Be Positioned To arc-seconds	Minutes	Both Left And Right Image Movers
O.A.O. Guidance System Activated	O.A.O. Spacecraft	Pointing Of $\pm 1.0$ arc-min (Vert. and Horiz.) And $\pm 2$ degrees (Roll)	Minutes	Brighter Guide Stars Used
Uncage	Telescope	Aligned To O.A.O. To $\pm 1/2$ arc-min (All Axes) And $\pm 0.10$ Inches or Less (All Axes)	Minutes	Telescope In Auxiliary Rotation And Centering Servo Modes
Final Gyro Positioning	Telescope	Erected To $\pm 1$ arc-min (Roll)	Minutes	Telescope In Auxiliary Rotation And Centering Servo Modes
Scan To Locate Guide Stars	Telescope	Star Presence Signals In Optical Sensors	Minutes	Optional: Dependent On O.A.O. Spacecraft Pointing Performance
Final Acquisition	Telescope	Point To $\pm 0.01$ arc-sec (rms) And $\pm 4$ arc-sec (Roll) rms	Minutes	
Servo Optimization	Telescope	Point To $\pm 0.01$ arc-sec (rms) And $\pm 4$ arc-sec (Roll) rms	Minutes	Optional: Dependent On Tracking Performance
Data Record	Telescope Instruments	Spectrometer And UV Vidicon Activated	Seconds - To Activate Up To Hours - To Record	

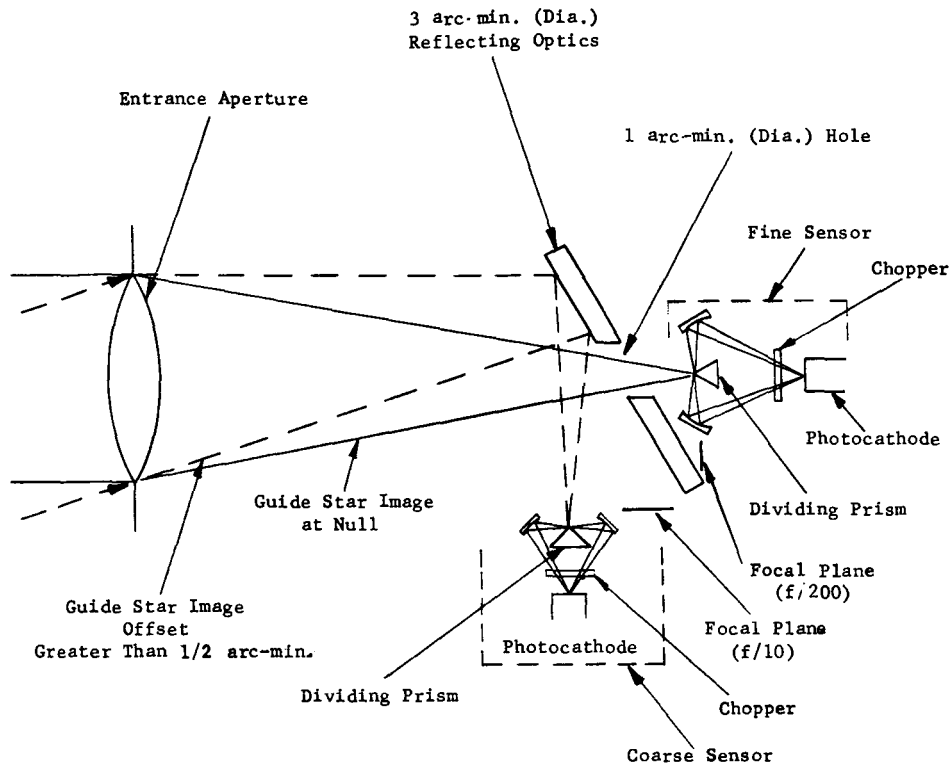
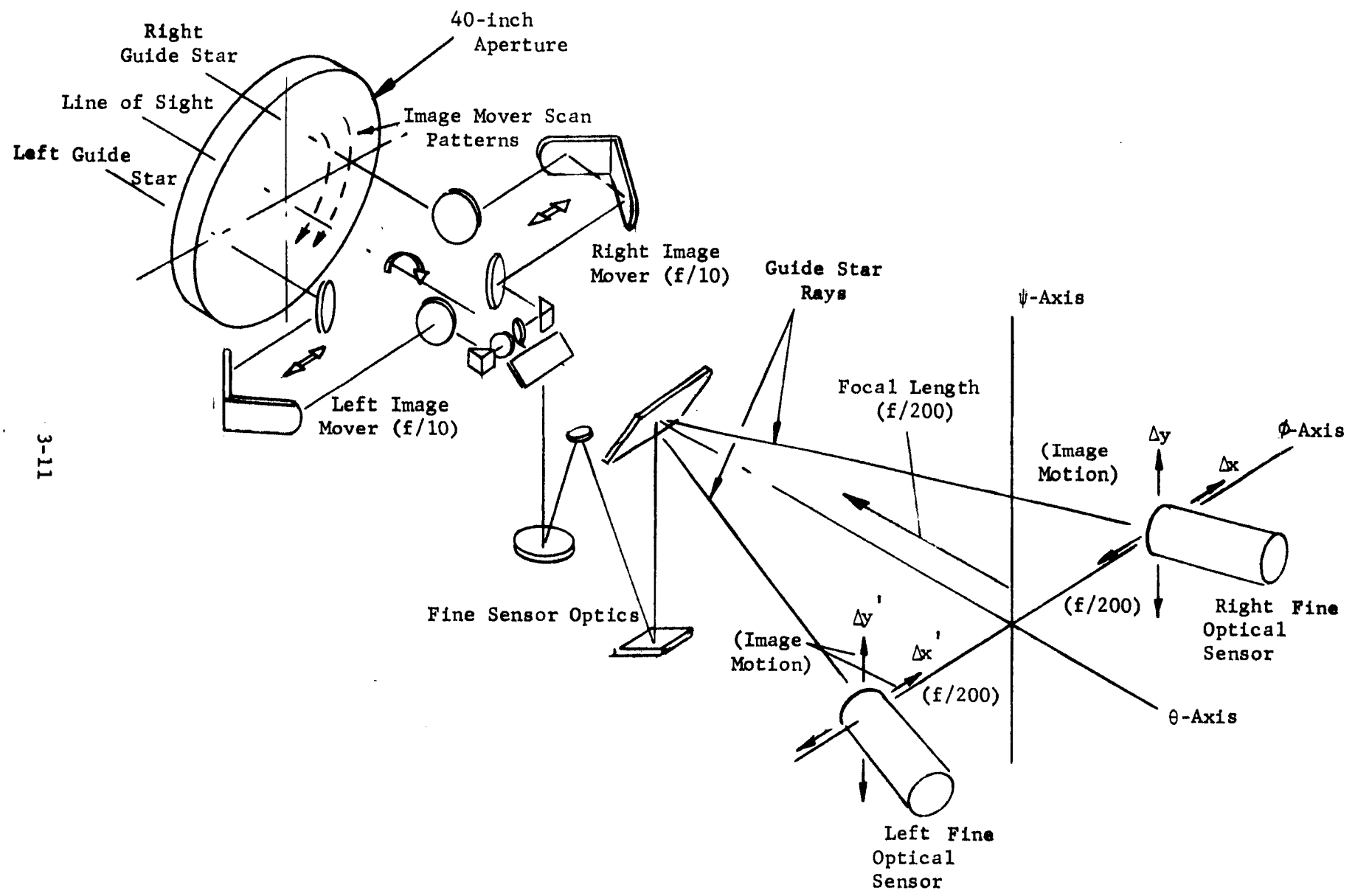


Figure 3.3. Guide Star Optical Sensor Principle  
(Single Axis-Schematic)

guide star light entering the main telescope aperture is reflected by a mirror to the coarse sensor dividing prism. For errors less than  $\pm 1/2$  arc-minutes, the guide star light passes through the coarse reflecting optics and images to the fine sensor dividing prism. (Section 2.2 of this volume includes the design details for the two field of view sensors.)

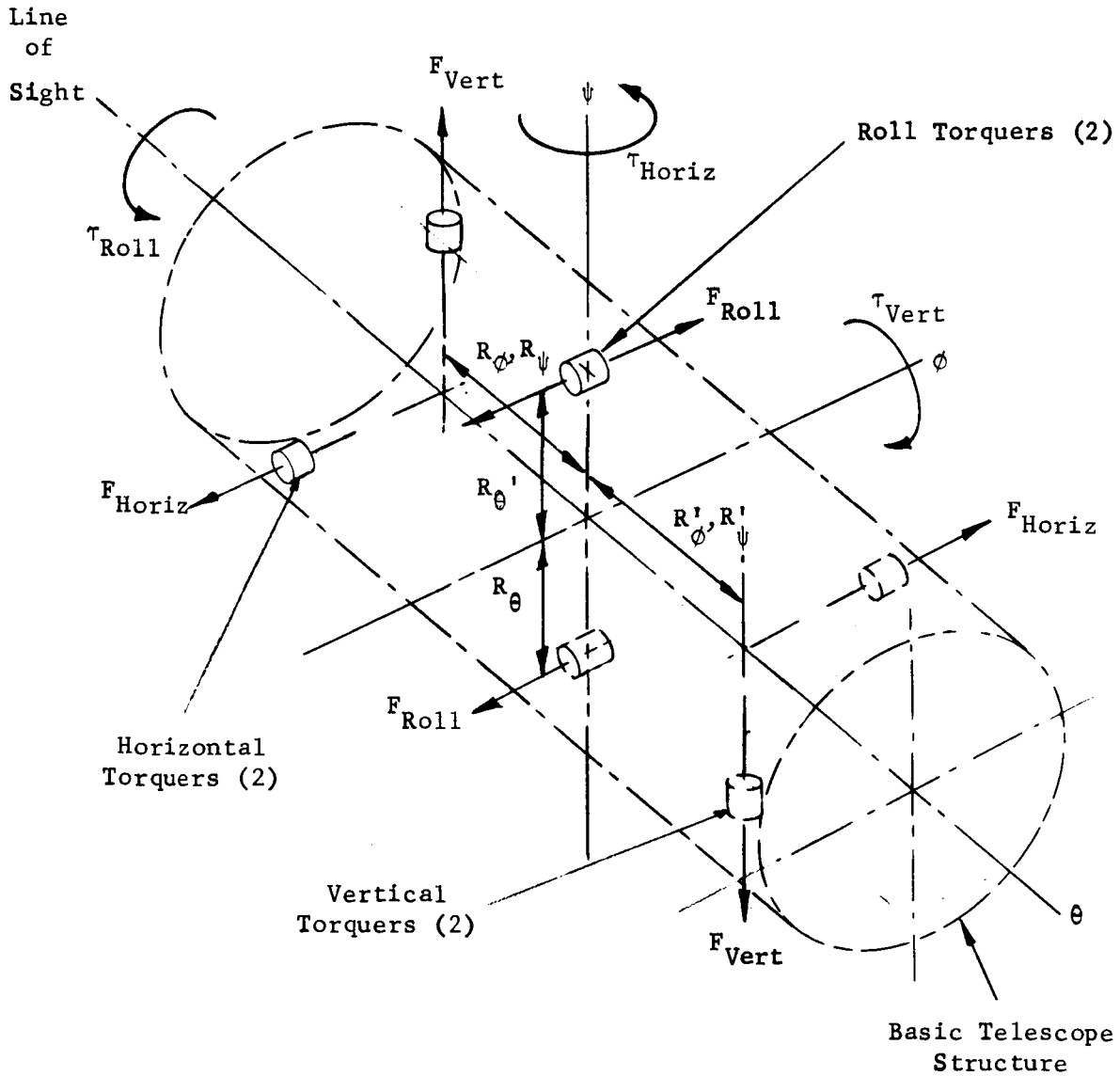
The complete system, sensors, torquers (pointing actuators) gyro and image movers, is schematically shown in Figures 3.4 and 3.5. A physical layout of the telescope showing the location of torquers, sensors, etc., has also been provided in section 1.0, Figures 1.2 and 1.3. Figure 3.4 illustrates in a schematic form the basic coordinate system and a relative orientation of the image movers and fine sensors. Figure 3.5 provides a general layout of the magnetic torquers using the same coordinates. The basic X-Y-Z space coordinate system illustrated is taken with respect to the experiment stellar source. The Z (or roll) axis extends in theory through the experiment source and represents the optical axis or line of sight. The X (vertical) and Y (horizontal) axes are the orthogonal axes of the rectangular coordinate system and intersect the Z axis at the center of gravity of the



3-11

Figure 3.4. Telescope Pointing System - Coordinates





$R' = R = \text{Moment Arms}$

$$\tau_{\text{Roll}} = 2R_{\theta} F_{\text{Roll}}$$

$$\tau_{\text{Vert}} = 2R_{\phi} F_{\text{Vert}}$$

$$\tau_{\text{Horiz}} = 2R_{\psi} F_{\text{Horiz}}$$

Figure 3.5. Telescope Torquer Arrangement

telescope. The telescope system torques and controls about this coordinate system. To illustrate, for instance, an angular offset  $\phi_e$  with respect to the guide star line of sight will basically result in an image motion  $\Delta y$  and  $\Delta y'$  at the fine optical sensor focal plane. This image motion will generate a proportional sensor electrical output signal which is processed and fed to the vertical or  $\phi$  axis torquers. The two vertical torquers (see Figure 3.5) will then produce a balanced couple about the  $\phi$  axis to correct for the angular deviation. The correction of angular displacement errors are similarly accomplished in the other two axes with slight exception taken in roll in terms of sensor output signal routing. Rotational motions will actually develop components of vertical and horizontal signals in both sensors, the magnitude of which is dependent on the orientation of the guide stars with respect to the telescope center of rotation. To prevent these components from disturbing the  $\phi$ - $\psi$  axis servos, a certain amount of signal logic is necessary at the output of the two sensors to derive the correct signals for each of the three axes in the linear (sensor) ranges. (Appendix A derives the geometric relationships between sensors and image movers and from these relationships, develops the signal logic.)

Either guide star can also be used for the vertical-horizontal reference or alternately, either guide star can be used for the rotational reference. The servo system design includes switching functions (see Figure 3.6) which achieves this flexibility. The reasons for incorporating this flexibility is to (1) basically assure that the brightest star is used for the  $\psi$ - $\phi$  reference since the greatest tracking accuracy is required in these axes, and (2) if possible, the roll guide star will be the one located farthest from the program star.

In the absence of a second guide star, the gyro is used as the roll axis reference, but its output must also be fed to the sensor signal logic circuits to again eliminate the roll axis components in the  $\psi$ - $\phi$  axes.

Apart from the main or final tracking mode servo system, the telescope contains, in addition, a centering and an auxiliary rotational servo system. The former (centering) servo system maintains linear clearance between the OAO spacecraft and the telescope in the suspended mode. The latter system maintains rotational (three-axis) clearance with respect to the OAO spacecraft, i.e., assumes the same pointing angles as the spacecraft in the suspended mode. The auxiliary rotational mode is an intermediate tracking system which is used to transfer the telescope from the caged mode into the final guide star tracking mode. It serves as a scanning system to coarsely locate guide stars and allows the gyros to erect accurately. The same magnetic torquers are used with linear displacement sensors for both servos.

Both the centering and auxiliary servo systems are described in more detail in section 3.4.5.

3.3.3.2 System Block Diagram and Brief Description - The components of the telescope pointing system are shown in an overall system block diagram given in Figure 3.6. Included in this block diagram are all the intermediate electronic blocks through which the optical sensor signals, gyro signals and the linear displacement signals are processed before reaching the torquers. The basic telescope switching functions are also shown and explained in more detail in the following section. Not discussed up to this point, but also introduced in Figure 3.6, are the redundant fine pointing sensors. If a sensor fails, its guide star image can be directed to an alternate sensor which functions identically to restore operation. The transfer of the guide star image from one sensor to another is accomplished in the  $f/10$  focal plane by a "flip" mirror (or beamsplitter). The flip mirror is located optically as shown in Figure 2.8 (or 2.13) of Volume III and is simply a reflecting mirror that directs the guide star rays to one fine sensor or the other.

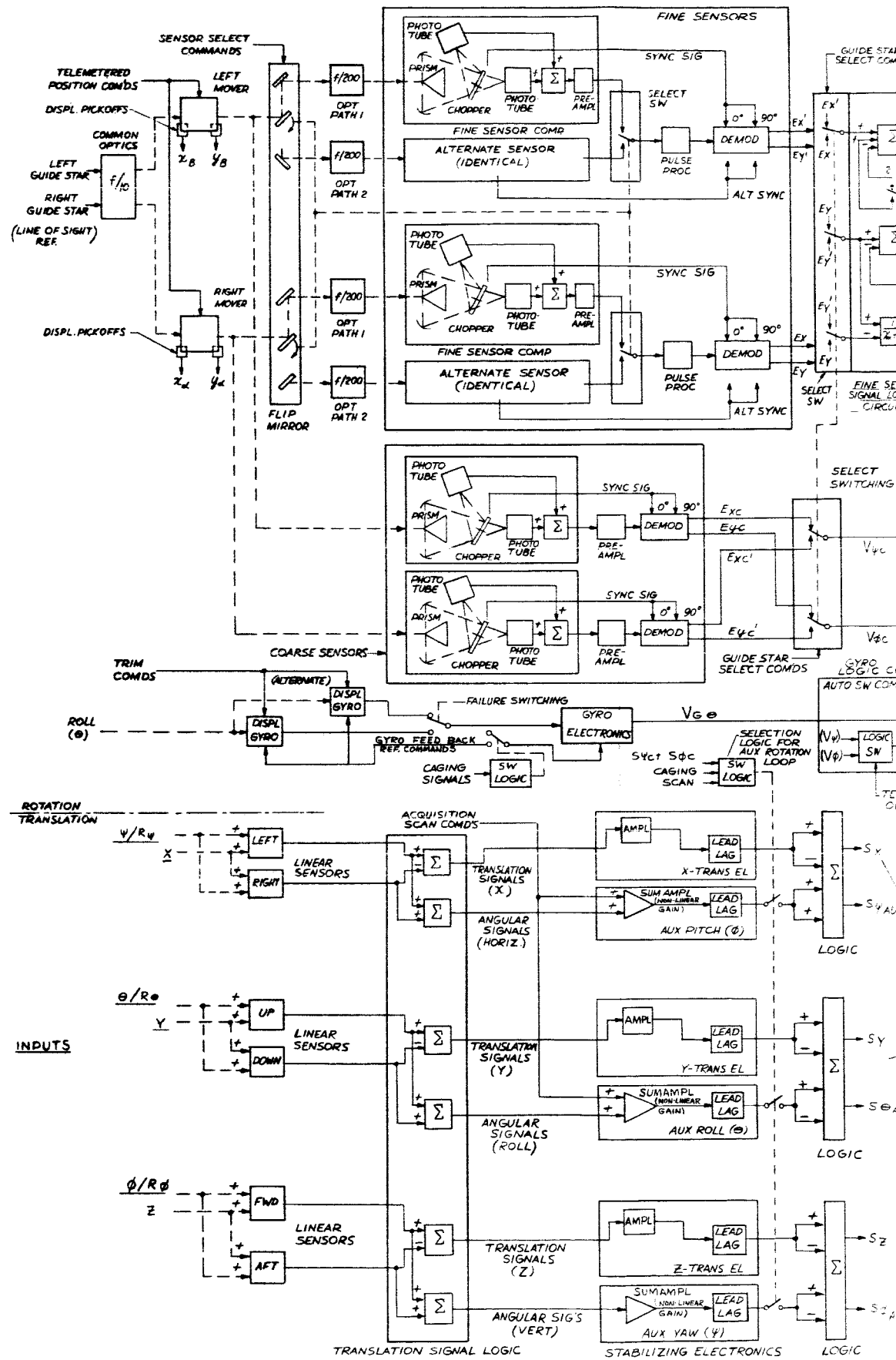
The fine optical sensor error output voltages are denoted by  $E_x$ ,  $E_y$ ,  $E_x'$ , and  $E_y'$ . These voltages are fed to the fine sensor signal logic circuit. The correct horizontal, vertical and roll signal voltages (denoted by  $V_\phi$ ,  $V_\psi$ , and  $V_\theta$ ) are derived in the logic circuits and fed to the stabilizing electronics, the torquer DC amplifiers and finally the torquers themselves. The coarse voltage outputs denoted by  $V_{\psi_c}$  and  $V_{\phi_c}$  are fed directly to the stabilizing electronics which then feed the torquers in the vertical and horizontal directions. The coarse sensor output voltages do not require signal processing since they are only used for acquisition and quite importantly, they are not used for roll axis references (see Section 3.4.3). The gyro output voltage (denoted by  $V_{G\theta}$ ) is routed during acquisition as shown, through the roll stabilizing electronics.

The linear displacement sensor (two per axis) signals are added and subtracted to obtain displacement and rotation. Each of these servo loops has separate stabilizing electronics and signal logic circuits as shown.

Optical chopper techniques are incorporated in the fine and coarse sensors to derive output voltages proportional to angular inputs prior to sensor signal demodulation which then recaptures the signal in DC voltage form. Pulse processing techniques are applied to the modulated signals to minimize the effect of cosmic ray noise. The theory applicable to the chopping techniques is explained in section 3.5.

The stabilizing servo electronics are not identical for the coarse and fine sensors. The fine sensor servo loop employs the double integration techniques described in Volume II, 4.3 which are necessary to achieve high loop gain at disturbing torque frequencies and at the same time maintain low bandpass frequencies to filter noise. The coarse sensors only utilize lead (impulse) networks since their primary function is acquisition.

Repeated references will be made to the system block diagram during the course of the ensuing description and analysis to aid in the further understanding of all the detailed functions of the pointing system.



3-15-1

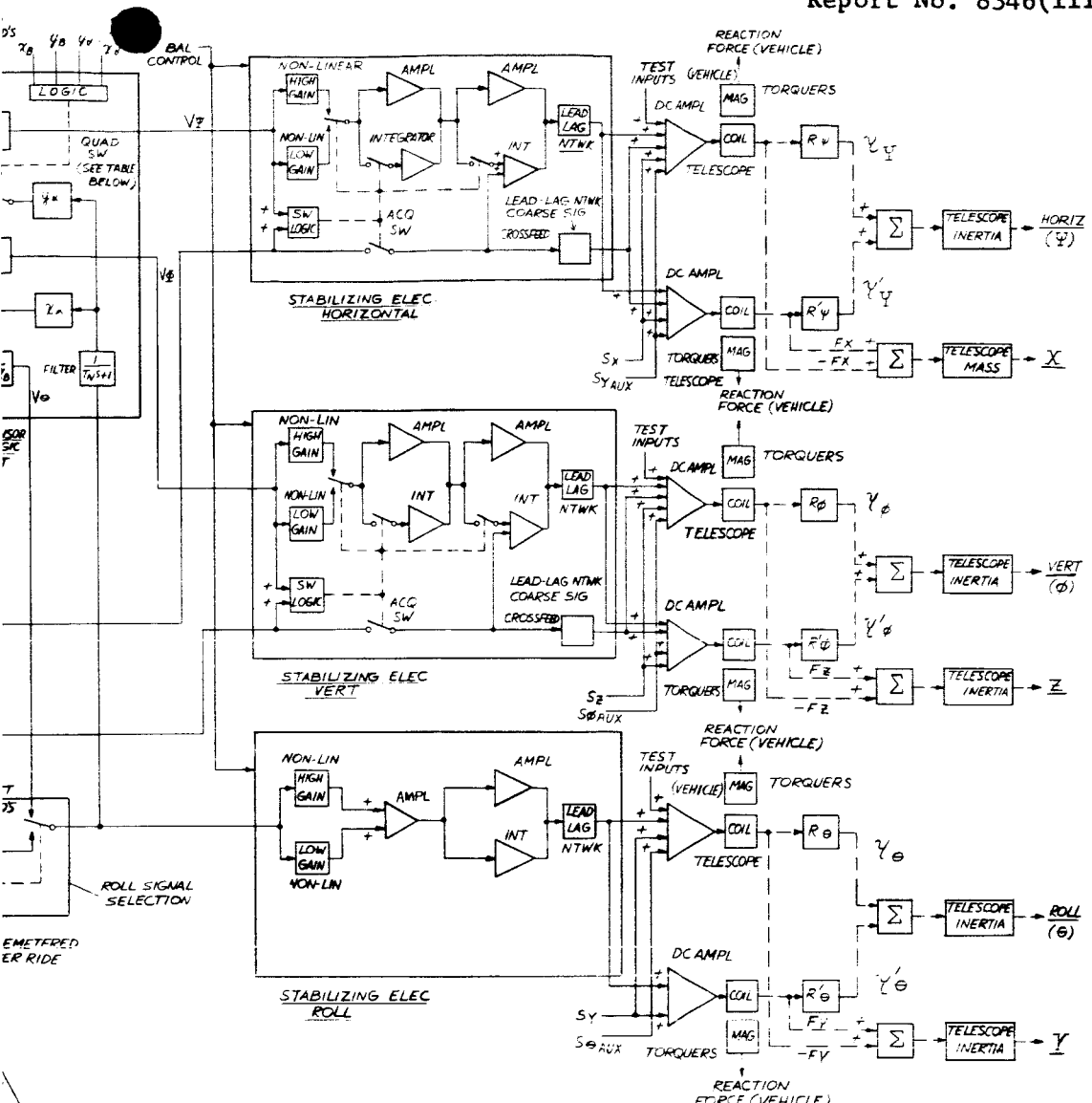
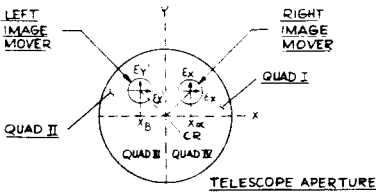
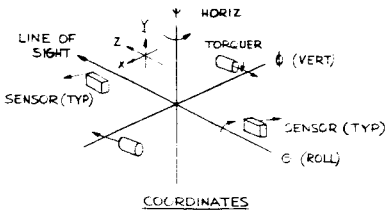


TABLE SWITCHING FUNCTIONS

QUADS I, II SW. POS. 1  
 I, III  
 QUADS II, IV SW. POS. 2  
 III, IV



— ELECT SIGNALS  
 - - - MECH SIGNALS  
 OPT SIGNALS  
 SWITCHING



GUIDANCE SYSTEM  
 (PRINCETON ADV. SATELLITE STUDY)

Figure 3.6. System Block Diagram



3.3.3.3 Telescope Switching Functions and Acquisition Logic - The entire telescope switching logic sequence is summarized in Table 3-III and, to a certain extent, is a review of some of the main experiment procedures. The following discussion, however, is expanded to include more explanation and technical detail of each switching function, particularly in the areas of telescope acquisition and fine sensor signal logic.

The discussion of this section will adhere to the order of events specified in Table 3-III.

The selection of the fine sensor requires a command to a mechanized flip mirror (or a beamsplitter) which directs the guide star rays into one of two optical fine sensors (see Figure 3.6). The same processing electronics (with exception of photomultiplier biasing networks and preamplifiers) will be used for each fine sensor. In order to make each fine sensor a self-contained unit, the electrical frequency synchronization signals from the choppers to the sensor output demodulators are also independent.

One source of information which determines the need for changing fine sensors is the vidicon monitor which will examine the image of the stellar source. If excessive angular motion is detected due to perhaps the poor quality of the fine sensor output signals, the alternate sensor will be activated. Other information sources would be sensor failure monitors (light indicators) and oscilloscope displays of the sensor outputs during manned operation.

Selecting the proper guide stars for the roll or vertical and horizontal axes involves routing the fine and coarse sensor output signals through the correct signal processing logic and on to the proper stabilization networks and torquers. If the left guide star (corresponding to the left image mover) is used as the roll axis reference, for example, its line of sight commands or optical signals are channeled through the fine sensor and eventually on to the roll stabilization electronics and torquers.

The sensor output signal switching actually takes place in the fine sensor logic circuits and at the coarse sensor outputs. The coarse sensor signal selection is illustrated in the system block diagram (Figure 3.6). The fine sensor output signal switching is slightly more complicated and is separately shown in Figure 3.7. The signal flow logic of Figure 3.7 is derived and more fully explained in Appendix A. These figures are only shown here to illustrate the switching functions. In its complete form, the fine sensor signal logic network consists of not only signal routing logic to derive the correct vertical, horizontal and roll signals, but also quadrant switching. Depending on the quadrant location of the image movers, the phasing of the roll axis signal cross-feeds to the horizontal channel will change and must be corrected.

The gyro signals are continually used as roll axis references during acquisition until the guide star images lie within the linear range

TABLE 3-III

ROTATIONAL SWITCHING FUNCTIONS

FUNCTION	DETERMINED BY	COMMAND SOURCE	PURPOSE	SWITCHING AREAS	COMMENTS
Fine Sensor Selection	Vidicon Image Display	Telemetry (Ground Or Apollo)	Sensor Failure Or Quality Degradation	Flip Mirror, Fine Sensor Outputs And Sensor Demod. Sync. Signals	
Selection Of Guide Stars For The Roll, Horizontal, Or Vertical Axes	Star Magnitudes And Star Location With Respect To L.O.S. (Left Or Right)	Telemetry (Ground Or Apollo)	Obtain Best S/N In Vert. And Horiz. Axes	Fine Sensor Signal Logic. Coarse Sensor Output Signals	Assuming Two Guide Stars Are Available
Gyro Versus Fine Sensor Selection	Star Availability	Telemetry (Sig. Select) Or Automatic (Acq.)	Roll Axis Reference And Acquisition Aid	Gyro Logic Circuit	
Acquisition Logic, (Coarse Sensor Activation)	Sensor Errors (Coarse)	Automatic (Switching Logic Circuits In Stab. Electronics)	Acquisition For Errors > 1 Min. Crossfeed To Null Torques	Coarse Sensor Output In Stab. Electronics	Inherently, The Coarse Sensor Is Activated By The Image Location
Acquisition Logic, (Fine Sensor Gain)	Sensor Errors (Fine And Coarse)	Automatic (Switching Logic Circuits In Stab. Electronics)	Acquisition For Errors < 1 Min.	Stab. Electronics	Fine Sensor Activated By Image Location
Acquisition Logic, (Fine Sensor Integrators)	Sensor Errors (Fine And Coarse)	Automatic (Switching Logic Circuits In Stab. Electronics)	Acquisition For Errors > 0.1 Sec.	Stab. Electronics	

Position (1) - Right Image mover is vertical-horizontal reference  
 (2) - Left image mover is vertical horizontal reference

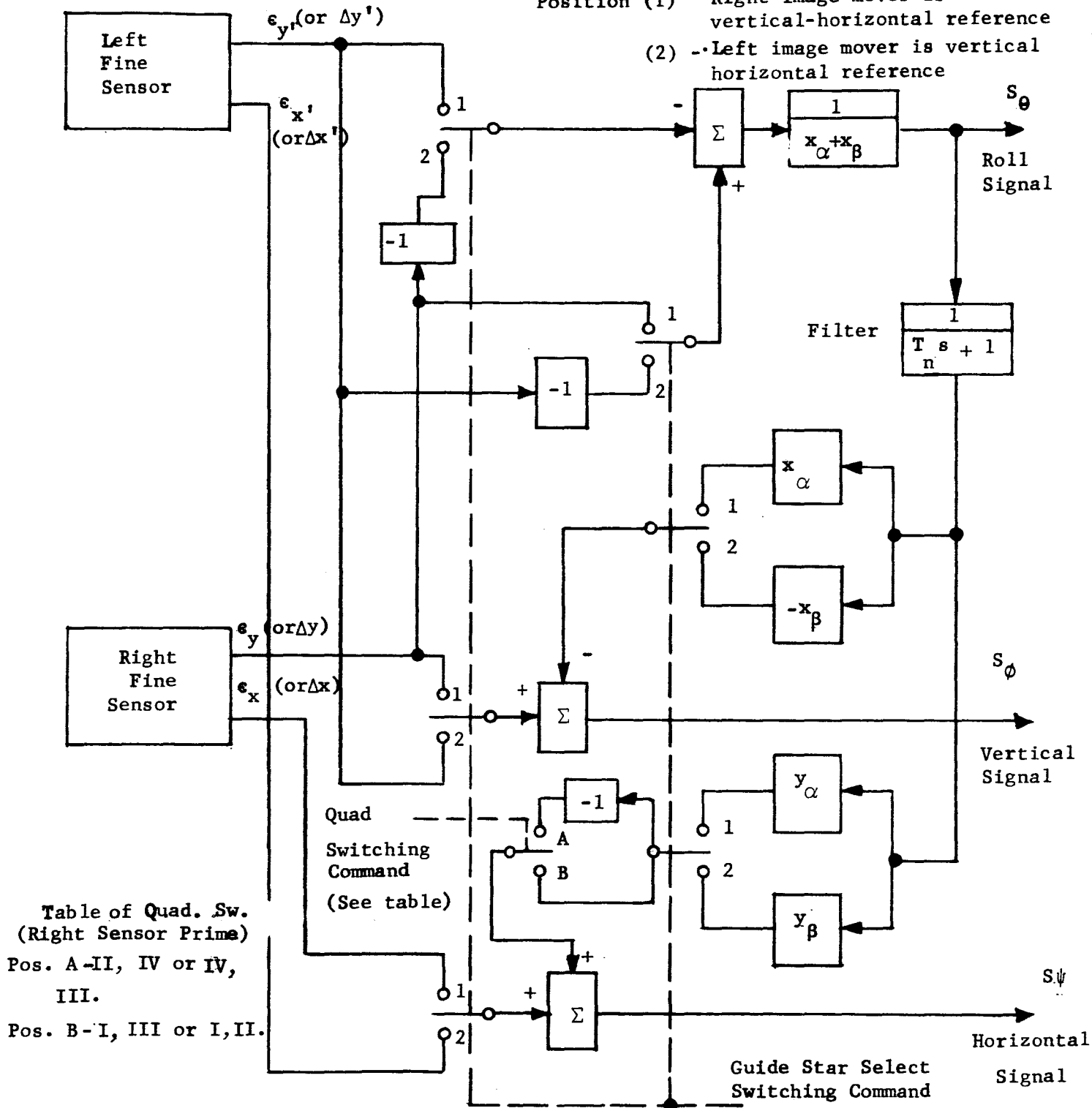


Figure 3.7. Fine Sensor Signal Logic



of the fine optical sensors. Once the image lies within this linear range, the fine sensor signals are automatically switched in to replace the gyro signals (assuming two guide stars are available). If a second guide star is unavailable, the gyro is permanently used as the rotational reference and this requires its signals to be switched into the fine sensor signal' logic circuits for the duration of the experiment. Again, the purpose of the logic circuits is to eliminate the roll axis components in the vertical-horizontal fine sensors (identical to the roll axis cross-feeds when both fine sensors are active). Precisely where the gyro signals are routed in this case is shown in Figure 3.8 using the right fine sensor as an example. An override command to the gyro logic circuit (see Figure 3.6) will activate the permanent use of the gyro signals for a roll reference.

The only switching necessary between the fine and coarse sensors is the automatic removal of the coarse sensor signals to the stabilizing electronics when the fine sensor is active (see Figure 3.6 - Stabilizing Electronic Blocks). This switching function exists to prevent background noise or other coarse sensor errors from creating unnecessary pointing errors in the final tracking mode.

This completes the review of preliminary switching functions prior to telescope final acquisition. Before proceeding further, a detailed description of the telescope acquisition logic is necessary to understand the remaining telescope switching functions.

The final telescope acquisition mode operates from initial conditions of 1 arc-min (peak), 1/2 arc-min/second (peak), and disturbing torques equal to 0.0015 lb-ft (peak), as specified in Table 3-1 for the vertical and horizontal axes. Several gain changes and switching functions must be performed in the servo loop to overcome these conditions and bring the telescope to a stabilized 0.01 arc-sec (rms) tracking accuracy. Initially, for a 1 arc-min error, the coarse sensor is active. With its stabilizing electronics (lead-lag plus amplification), it drives the telescope to bring the displacement error within the 1 arc-min fine sensor field of view. When the star image falls into the 1 arc-min field of view, the fine sensor will seek to stabilize and point the telescope to 0.01 arc-sec (rms) accuracy. If the conditions of rates and torques are low at the moment the guide star image activates the fine sensor, the telescope will stabilize. If the conditions are excessive or beyond the fine sensor servo loop capabilities, the guide star image will pass through the fine sensor field and back into the coarse sensor field of view. However, during the transient from coarse-fine-coarse sensor, the pointing error will have been partially reduced. The first overshoot into the coarse sensor will, therefore be less than the initial displacement angles. A certain period of cycling will occur between the fine and coarse sensor until the initial conditions and disturbing torque errors are sufficiently reduced to allow the fine sensor loop to capture and stabilize the telescope.

The external disturbing torques, if not properly handled, can substantially increase the telescope acquisition cycling time. The fine sensor servo loop, to reiterate, contains two stages of electrical integration.

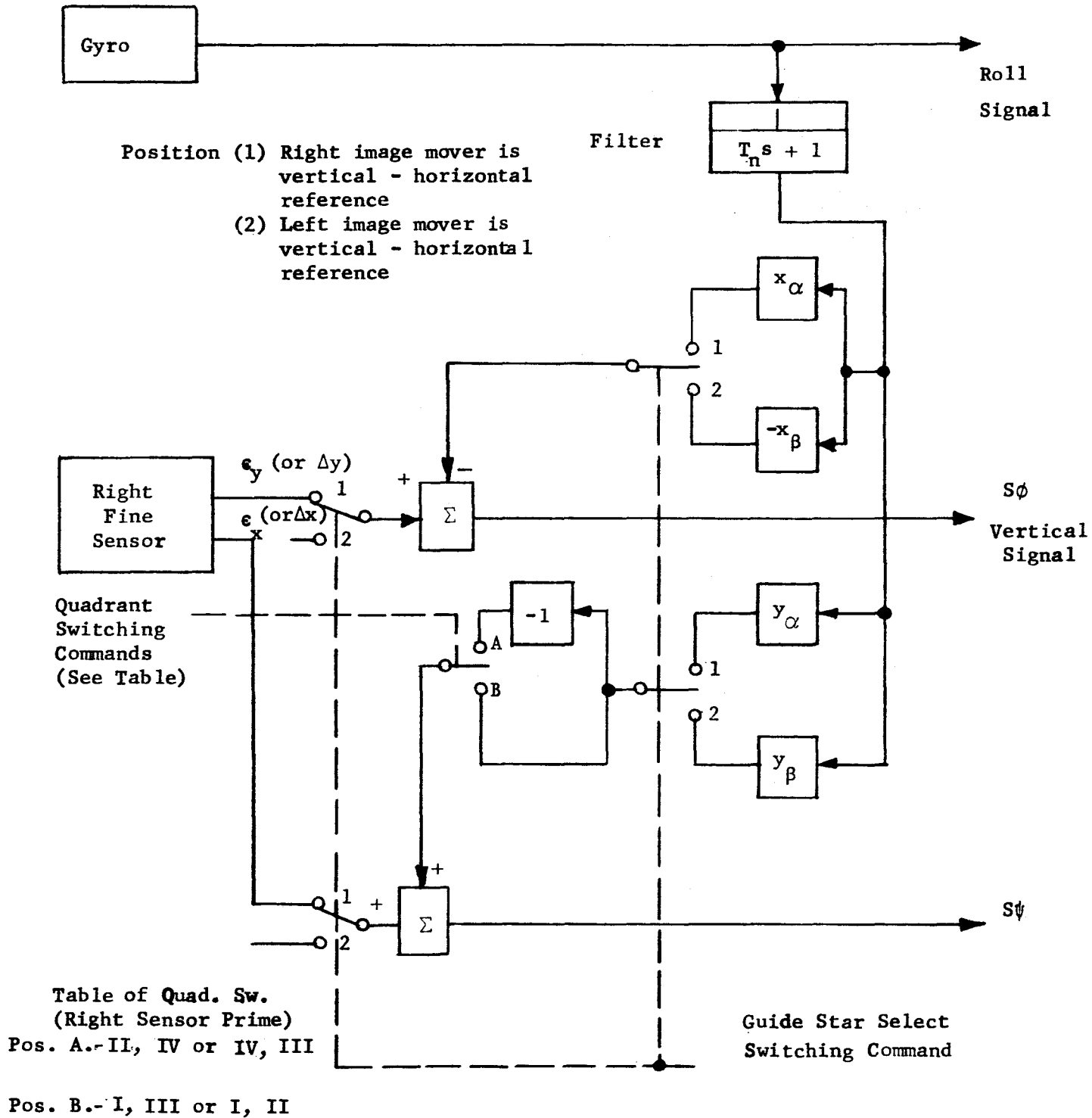


Figure 3.8. Fine Sensor Signal Logic with Gyro

One of the functions of the last stage integrator feeding the DC torquers is to offset external disturbing torques. Due to the low gain or low response of the fine sensor servo loop in the linear range ( $\pm 0.07$  arc-sec), this integrator will not respond quickly enough during transients through the 1 arc-min field to null the level of disturbing torque. The guide star image will be continually rejected from the linear sensor range until the error is integrated. To remedy this situation, an electrical crossfeed is used (see Figure 3.6) whereby the coarse sensor feeds the last stage integrator to set it prior to the star image settling into the fine sensor field. The crossfeed is a very effective method (see Computer Simulation 3.4.4) for coping with torque disturbances and does not interfere with the pointing performance in the fine sensor tracking loop modes.

Acquisition recovery periods can also be unreasonably lengthy if corrective measures are not employed to compensate for the low gain of the fine sensor outside the linear region. Once the fine sensor output voltage saturates at  $\pm 0.14$  arc-sec, the DC torquers will fail to build up opposing output torques proportional to errors greater than  $\pm 0.14$  arc-sec. This situation is improved by gain switching in the fine sensor servo region. As the fine sensor angular error increases, the loop gain is proportionally increased until saturation and at this point, an additional gain step is employed. During this time, the opposing torques delivered to counter the external disturbances are proportionally increased resulting in much better recovery times.

The lack of a larger fine sensor linear range is detrimental in one other respect. The two electrical integrators will continue to be driven into high unwanted voltage levels whenever the fine sensor remains in saturation. This tends to cancel the advantages of any lead networks. The problem is overcome by removing the fine sensor inputs to these integrators whenever the sensor saturates, thereby preventing the occurrence of false integrator levels. The integrator switching is done in synchronization with the servo loop step gain switching whenever the angular error exceeds  $\pm 0.07$  arc-sec. The integrator and gain switching circuits as shown in Figure 3.6, operate from the coarse sensor outputs to prevent drop-out when the fine sensor is inactive at errors greater than 1 arc-min. It is desirable to keep the integrators inactive even in the coarse sensor mode to prevent fine sensor residue noise unnecessarily disturbing their output levels.

Listed below are typical acquisition cycling times. The times are divided or allotted to each phase of the telescope acquisition.

Initial conditions:

Displacement = 1.0 arc-min  
Velocity = 1.0 arc-min/sec

Initial recovery time

From coarse sensor field - 10-20 seconds

Integrator charging time

60 - 80 seconds

Fine sensor servo loop recovery time

10 - 20 seconds

Total time

80 - 120 seconds

### 3.4 SERVO SYSTEM ANALYSIS

#### 3.4.1 Introduction and Summary of Results

A specific six degree of freedom (three axis rotation and three axis centering) telescope pointing system design was analyzed and is discussed in this section. The major performance results, error budget, and stability criteria for the design are summarized in Table 3-IV. An analog computer simulation was undertaken in addition to the analysis, and although primarily directed at the acquisition problem, it also verified linear calculations of noise response and stability.

The first part of the servo analysis concerns itself with only the telescope in rotation. Two of the axes, vertical and horizontal, are identical; therefore, only a single axis is analyzed in this case. The roll axis is analyzed independently, including the effects of using a roll sensing displacement gyro. Brief derivations and discussions for each analytical relationship are given, throughout which a particular component is described. In some of these component areas, important assumptions were made and require noting. Finally, the latter part of the analysis pursues translation of the telescope with respect to the OAO spacecraft since maintaining clearance between the two is important.

#### 3.4.2 Servo Analysis - Vertical and Horizontal Axes

3.4.2.1 Sensor Transfer Functions - The fine sensor has a linear output voltage to angular error input transfer function in each of the two axes. The linear range extends to  $0.61\lambda/D$  (0.069 arc-sec for  $\lambda = 0.55\mu$ ,  $D = 1$  meter) for each polarity as explained in Volume II, 4.4. Beyond the  $0.61\lambda/D$  limits the output sensor voltage remains quite flat as the angle increases, out to approximately 0.5 arc-min (1/2 diameter field-of-view). For angles greater than 1/2 arc-min, the coarse sensor becomes active. The coarse sensor transfer function is generally flat from approximately 0.5 arc-min to 1.5 arc-min. At 1.5 arc-min, the coarse sensor output signal begins to decrease to zero as the angle continues to increase.

The transition from fine to coarse sensor is not sharp by the nature of the optical system. The fine sensor output begins to decrease slightly before the 0.5 arc-min point at which time the coarse sensor signal begins to build. The process continues gradually as graphically represented in Figure 3.9.

TABLE 3-IV  
GUIDANCE SYSTEM PARAMETERS  
 (ROTATIONAL AXES)

EQUIPMENT

AXIS	SENSORS	RANGE	NO. OF INTEGRATORS	TORQUE CAPABILITY	TELESCOPE MASS INERTIA
Vertical	Fine Optical	1 min (F.O.V.)	2	± 1.0 lb-ft (R = 3-1/3 ft)	100-200 slug-ft <sup>2</sup>
Vertical	Coarse Optical	3 min (F.O.V.)			
Horizontal	Fine Optical	1 min (F.O.V.)	2	± 1.0 lb-ft (R = 3-1/3 ft)	100-200 slug-ft <sup>2</sup>
Horizontal	Coarse Optical	3 min (F.O.V.)			
Roll	Fine Optical	13.4 deg. (F.O.V.)	1	± .5 lb-ft (R = 1.67 ft)	100-200 slug-ft <sup>2</sup>
Roll	Gyro		1		

STABILIZATION

AXIS	PHASE MARGIN	LOOP GAIN	EQUIV. BANDWIDTH	ACQUISITION
Vertical	26°	0.011 sec <sup>-4</sup>	0.45 cps	120 seconds $\phi_{Ic} = 1 \text{ min/sec}$ $\phi_{Ic} = 1 \text{ min}$
Horizontal	26°	0.011 sec <sup>-4</sup>	0.45 cps	120 seconds $\psi_{Ic} = 1 \text{ min/sec}$ $\psi_{Ic} = 1 \text{ min}$
Roll	40°	.0056 sec <sup>-3</sup>	0.18 cps	45 seconds
Roll	40°	.0056 sec <sup>-3</sup>	0.18 cps	45 seconds

DISTURBANCES

DISTURBANCE INPUTS	UNCAGING IMPULSES
20,000 dyne-cm (2700 sec. period)	NA
20,000 dyne-cm (2700 sec. period)	NA
20,000 dyne-cm (2700 sec period)	NA

3-24

TABLE 3-IV (Continued)  
 GUIDANCE SYSTEM PARAMETERS  
 (ROTATIONAL AXES) (Continued)

ERROR BUDGET

AXIS	MAGNITUDE STAR	NOISE ERRORS	DISTURBANCE ERRORS	COUPLING ERRORS	FIELD OF VIEW
Vertical	12th	0.003 arc-sec (rms)	.001 sec (rms)	Centering - .0007 arc-sec (rms) Roll-.002 arc-sec (rms)	1 min (F.O.V.)
Horizontal	12th	0.003 arc-sec (rms)	.001 sec (rms)	Centering - .0007 arc-sec (rms) Roll-.002 arc-sec (rms)	1 min (F.O.V.)
Roll	12th	*1.50 arc-sec (rms)	0.9 sec (rms)	Centering - 0.1 arc-sec (rms) Vertical-0.2 arc-sec (rms)	1 min (F.O.V.) (Equivalent)
Roll (Gyro)	NA	**1.62 arc-sec (peak)	0.9 sec (rms)	Centering - 0.1 arc-sec (rms)	NA

\* Referenced to telescope 7.5 arc-min field, minimum error, 8 arc-sec (rms)

\*\* Gyro Drift for 10 min. at 0.0027 arc-sec/sec (time)

TABLE 3-IV (Continued)  
GUIDANCE SYSTEM PARAMETERS  
 (CENTERING AXES)

EQUIPMENT

AXIS	SENSORS	LINEAR RANGE	NO. OF INTEGRATORS	DUAL TORQUERS	TELESCOPE MASS & INERTIA
Centering (Z)	Fwd-Aft Linear	± 1/2 inch	0	± 0.3 pounds	32 slugs
Centering (X)	Left-Right Linear	± 1/2 inch	0	± 0.3 pounds	32 slugs
Centering (Y)	Up-Down Linear	± 1/2 inch	0	± 0.3 pounds	32 slugs

STABILIZATION

ERROR BUDGET

DISTURBANCES

AXIS	PHASE MARGIN	LOOP GAIN	ACQUISITION	DISTURBANCE ERROR	DISTURBANCE INPUTS (OAO)	UNCAGING IMPULSES
Centering (Z)	42°	0.023 sec <sup>-2</sup>	30 Seconds Due to Uncaging Impulses	0.002 inch (peak)	± 0.1 in. at .02 rad/sec	0.5 lbs for 0.5 sec
Centering (X)	42°	0.023 sec <sup>-2</sup>	30 Seconds Due to Uncaging Impulses	0.002 inch (peak)	± 0.1 in. at .02 rad/sec	0.5 lbs for 0.5 sec
Centering (Y)	42°	0.023 sec <sup>-2</sup>	30 Seconds Due to Uncaging Impulses	0.002 inch (peak)	± 0.1 in. at .02 rad/sec	0.5 lbs for 0.5 sec

TABLE 3-IV (Continued)

GUIDANCE SYSTEM PARAMETERS  
(AUXILIARY AXES)

EQUIPMENT

AXIS	SENSORS	RANGE	NO. OF INTEGRATORS	DUAL TORQUERS	TELESCOPE MASS & INERTIA
Aux. Rotation Pitch ( $\phi/R_\phi$ )	Fwd-Aft Linear	$\pm .6^\circ$	0	$\pm 1.0$ lb-ft ( R = 3.33 ft)	100-200 slug-ft <sup>2</sup>
Aux. Rotation Yaw ( $\psi/R_\psi$ )	Left-Right Linear	$\pm .6^\circ$	0	$\pm 1.0$ lb-ft ( R = 3.33 ft)	100-200 slug-ft <sup>2</sup>
Aux. Rotation Roll ( $\theta/R_\theta$ )	Up-Down Linear	$\pm .6^\circ$	0	$\pm 0.5$ lb-ft ( R = 1.67 ft)	100-200 slug-ft <sup>2</sup>

STABILIZATION

AXIS	PHASE MARGIN	LOOP GAIN	ACQUISITION
Aux. Rotation Pitch ( $\phi/R_\phi$ )	45°	0.008 sec <sup>-2</sup> (Low Gain)	30 Seconds Due to Uncaging Impulses Using High Gain Mode
Aux. Rotation Yaw ( $\psi/R_\psi$ )	45°	0.008 sec <sup>-2</sup> (Low Gain)	30 Seconds Due to Uncaging Impulses Using High Gain Mode
Aux. Rotation Roll ( $\theta/R_\theta$ )	45°	0.008 sec <sup>-2</sup> (Low Gain)	30 Seconds Due to Uncaging Impulses Using High Gain Mode

ERROR BUDGET

DISTURBANCE ERRORS
0.5 arc-min (rms)
0.5 arc-min (rms)
0.1 degrees (rms)

DISTURBANCES

DISTURBANCE INPUTS (OAO)	UNCAGING IMPULSES
Spacecraft Perturbations	0.5 lb-ft for 0.5 sec
Spacecraft Perturbations	0.5 lb-ft for 0.5 sec
Spacecraft Perturbations	0.5 lb-ft for 0.5 sec



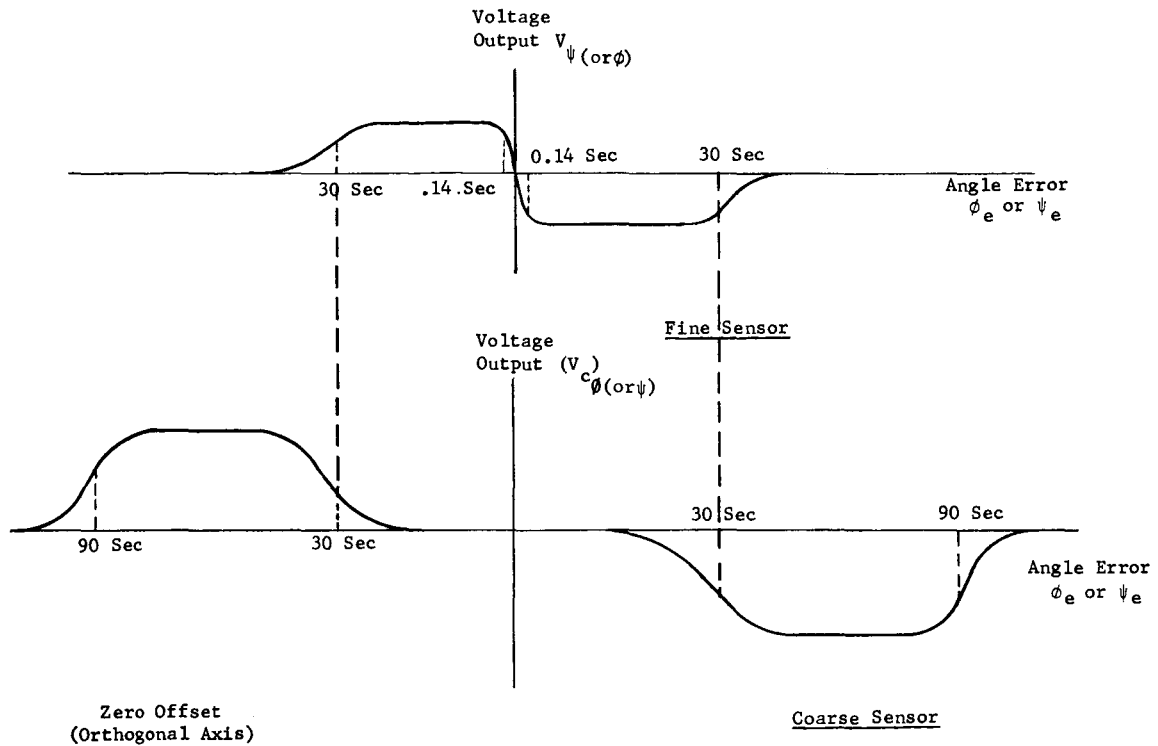


Figure 3.9. Fine-Coarse Sensor Transfer Functions (Single Axis)

The information bandpass, i.e., modulation frequencies of both the fine and coarse sensors are several magnitudes higher than the servo loop bandpass frequencies. Consequently, the transfer function of the optical sensor (single axis) in the linear region is for all practical purposes equal to a constant times a first order filter. The filter represents the main frequency breakpoint in the sensor output electronics. In terms of Laplace,

$$\frac{V_{\psi(\text{or } \phi)}(s)}{\psi_e(s) \text{ (or } \phi_e(s))} = \frac{K_f}{T_f s + 1} \quad \frac{\text{Volts}}{\text{Radian}} \quad (3-1)$$

$$\text{for } 0 \leq \psi_e \text{ (or } \phi_e) \leq 0.61\lambda/D$$

where,

$K_f$  = sensor sensitivity (volts/radian)

$T_f$  = filter time constant (sec)

$V_{\phi}(s), V_{\psi}(s)$  = fine sensor output voltages

$\psi_e(s), \phi_e(s)$  = pointing error (radians) in the horizontal and vertical axes respectively.

For linear stability and performance analysis, equation (3-1) is valid. This equation, as well as all the remaining relationships, has taken into consideration the fine sensor signal processing logic circuits. The voltage  $V_\psi(s)$  for instance, is at the output of the logic circuits.

For errors greater than  $0.61\lambda/D$ , the sensor transfer functions are assumed constant (assuming a straight line approximation).

$$V_{\psi(\text{or } \phi)}(s) = \frac{K_f(1.22\lambda/D)}{T_f s+1} \quad (3-2)$$

The coarse sensor transfer functions are also represented by a constant ( $K_c$ ). A filter is placed at the output to reduce noise resulting in

$$V_{c\phi(\text{or } \psi)}(s) = \frac{(1.22\lambda/D) (217)K_c}{T_c s+1} \quad (3-3)$$

where

$(1.22\lambda/D) (217) = 30$  arc-sec (field of view radius)

$V_{c\phi}(s), V_{c\psi}(s)$  = coarse sensor output voltages

$K_c$  = sensor sensitivity (volts/radian)

$T_c$  = filter time constant (sec)

3.4.2.2 Stabilizing Network Relationships - In the final tracking mode or for the linear operating range of the fine sensor, the stabilizing electronics take the form described by equation (3-4) below,

$$\frac{V_t(s)}{V_{\psi(\text{or } \phi)}(s)} = \frac{(T_1 s+1)^3 K_e}{s^2 (T_2 s+1)} \quad \psi_e(\text{or } \phi_e) \leq 0.61\lambda/D \quad (3-4)$$

where,

$V_t(s)$  = torquer amplifier input voltage

$K_e$  = electronic loop gain (variable)

$T_1$  &  $T_2$  = network time constants (seconds)

The electronic loop gain  $K_e$  is variable as a function of  $\psi_e(s)$  or  $\phi_e(s)$  as shown in Figure 3.10. As explained in paragraph 3.3.2.3, the purpose of the variable gain is to aid acquisition.

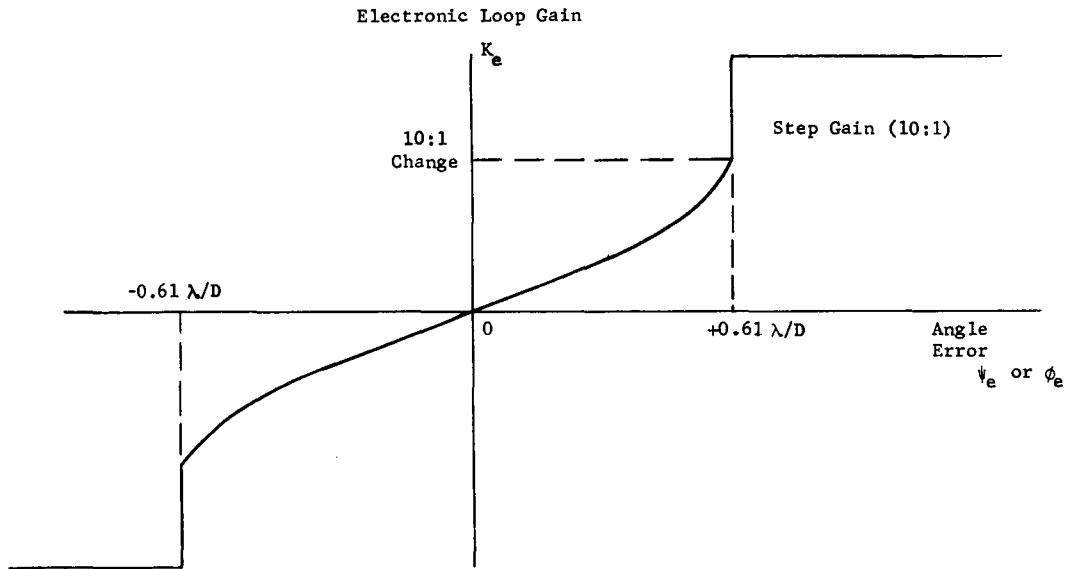


Figure 3.10. Electronic Gain Change

At the point where the angle error exceeds  $0.61\lambda/D$  and the loop gain is stepped higher, the two integrators are removed. The relationship of equation (3-4) becomes modified as described by equation (3-5).

$$\frac{V_t(s)}{V_{\psi(\text{or } \phi)}(s)} = \frac{(T_1)^2 (T_1+1) K_e}{(T_2s+1)} \quad (3-5)$$

for

$$\psi_e(\text{or } \phi_e) \geq 0.61\lambda/D$$

During the acquisition modes or during the time the coarse sensor is active, the fine sensor signal falls to zero, and the relationships (3-3), (3-4) and (3-5) apply.

The coarse sensor compensating electronics only require a "lead-lag" stabilizing network. However, the crossfeed to the last stage integrator must be added to complete the relationship. Normally,

$$\frac{V_{tc}(s)}{V_{c\psi(\text{or } \phi)}(s)} = \frac{T_3s+1}{T_4s+1} K_{ec} \quad (3-6)$$

for

$$0.5 \text{ arc-min} \cong \psi_e \text{ (or } \phi_e) \cong 1.5 \text{ arc-min}$$

with crossfeed,

$$\frac{V_{tc}(s) + V'_{tc}(s)}{V_{c\psi \text{ (or } \phi)}(s)} = \left( \frac{T_1 s+1}{T_2 s+1} \right) \left( \frac{K_{cf}}{s} \right) + \left( \frac{T_3 s+1}{T_4 s+1} \right) (K_{ec}) \quad (3-7)$$

for

$$0.5 \text{ arc-min} \cong \psi_e \text{ (or } \phi_e) \cong 1.5 \text{ arc-min}$$

where,

$$V'_{tc}(s) = \text{voltage in torquer amplifier due to coarse sensor crossfeed signal}$$

For all practical considerations,  $V_{c\psi \text{ (or } \phi)}(s)$  is constant when equation (3-7) is active. Nonlinear analysis is required in this region.

3.4.2.3 Magnetic Torquers and Telescope Relationships - Since the telescope is freely suspended, torquers applied to it see an ideal inertial source, i.e., no friction. Using the vertical axis for example,

$$\tau_d = \tau_d - \tau_c = Js^2 \phi_t \quad (3-8)$$

where,

- $\tau_d$  = disturbance torques (lb-ft)
- $\tau_c$  = corrective torques (lb-ft)
- $J$  = telescope inertia (slug-ft<sup>2</sup>)
- $\phi_t$  = telescope displacement (radians)

The corrective torque ( $\tau_c$ ) is generated by the magnetic torquers. The torquers in combination with the DC power amplifiers are represented by a linear constant for angle errors ( $\phi_e$ ).

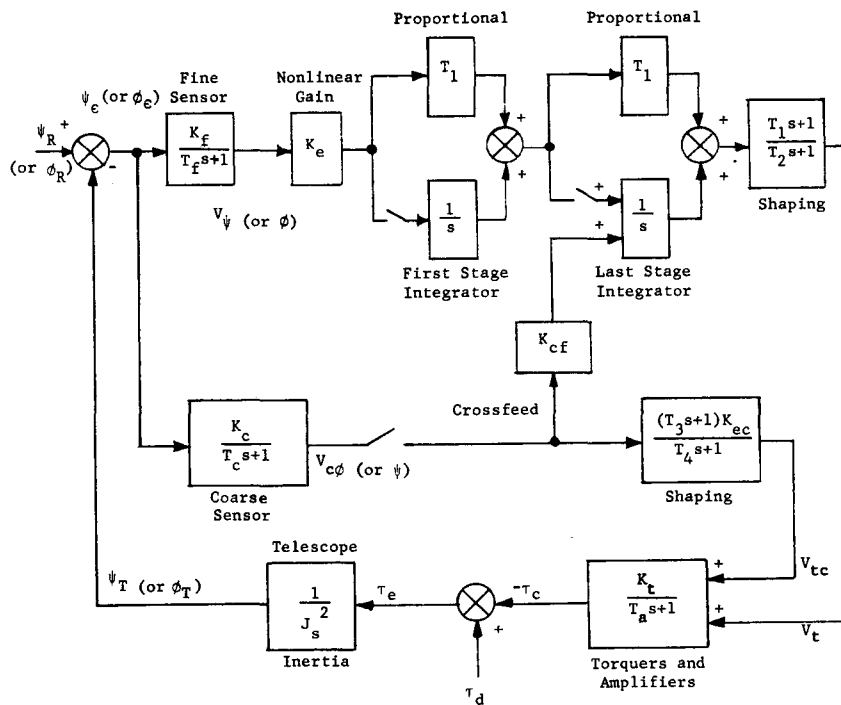
$$\tau_c(s) = \frac{K_t (V_t(s) + V_{tc}(s))}{T_a s+1} \quad (3-9)$$

where,

- $K_t$  = torque per volt constant (includes D.C. amplifier gain)
- $T_a$  = torquer time constant (seconds)

Equation (3-9) involves three assumptions. First, EMF feedback is neglected. Secondly, a variable gap between the brushless torquer field coil and magnet is assumed to have a negligible effect, i.e.,  $K_t$  remains constant. Finally, the D.C. amplifiers have high frequency response; and, for that matter,  $T_a$  is also very small.

3.4.2.4 Complete Single Axis Representation and Analysis - At this point, single axis open loop transfer functions can be obtained for analysis by simply multiplying and substituting into equations (3-1) to (3-9). All the relationships summarized so far and combined below are shown in block diagram form in Figure 3.11.



$\psi_R$  (or  $\phi_R$ ) = Guide Star Angular Ref.  
 $\psi_T$  (or  $\phi_T$ ) = Telescope Angular Displ.

Figure 3.11. Single Axis (Vertical or Horizontal) Analytical Block Diagram

$$\frac{\tau_c(s)}{\tau_e(s)} = \frac{(T_1s+1)^3 K_f K_e K_t}{J_s^4 (T_f s+1)(T_2s+1)(T_a s+1)} \quad (3-10)$$

for

$$0 \leq \psi_e \text{ (or } \phi_e) \leq 0.61\lambda/D$$

This transfer function (3-10) represents the linear fine sensor servo loop (fine tracking).

$$\tau_c(s) = \frac{(T_1)^2 (T_1s+1) K_e K_t K_f (1.22\lambda/D)}{J_s^2 (T_2s+1)(T_a s+1)(T_f s+1)} \quad (3-11)$$

for

$$0.5 \text{ arc-min} \leq \psi_e \text{ (or } \phi_e) \leq 0.61\lambda/D$$

where,

$V_{\psi \text{ (or } \phi)}$  is constant. Equations (3-11) represents the fine sensor loop during saturation.

$$\tau_d(s) = \frac{1}{J_s^2} \left[ \left( \frac{T_1s+1}{T_2s+1} \right) \left( \frac{K_{cf}}{s} \right) + \left( \frac{T_3s+1}{T_4s+1} \right) \left( K_{ec} \right) \right] \left[ \left( \frac{K_t}{T_a s+1} \right) \left( \frac{(1.22\lambda/D) (217) K_c}{T_c s+1} \right) \right] \quad (3-12)$$

for

$$0.5 \text{ arc-min} \leq \psi_e \text{ (or } \phi_e) \leq 1.5 \text{ arc-min}$$

The voltage  $V_{c\phi_e \text{ (or } \psi_e)}$ , is constant. Equation (3-12) describes the coarse sensor servo loop, single axis.

The single axis performance and stability is determined in the linear fine sensor region (or final tracking mode) using equation (3-10) as shown in Figure 3.12 using Bode amplitude versus frequency plots. Three additional Bode plots have been shown to provide insight into the type of dynamics the saturated region of the fine sensor and the coarse sensor (equations (3-11) and (3-12)) would have if they were linear. They are, of course, not actually definable on Bode diagrams in the strict sense. The phase margins and gains for the linear servo loop (fine sensor tracking) have been listed in Table 3-IV, as well as other parameters such as telescope inertias. Inertias of 100-200 slug-ft<sup>2</sup> are generally considered.

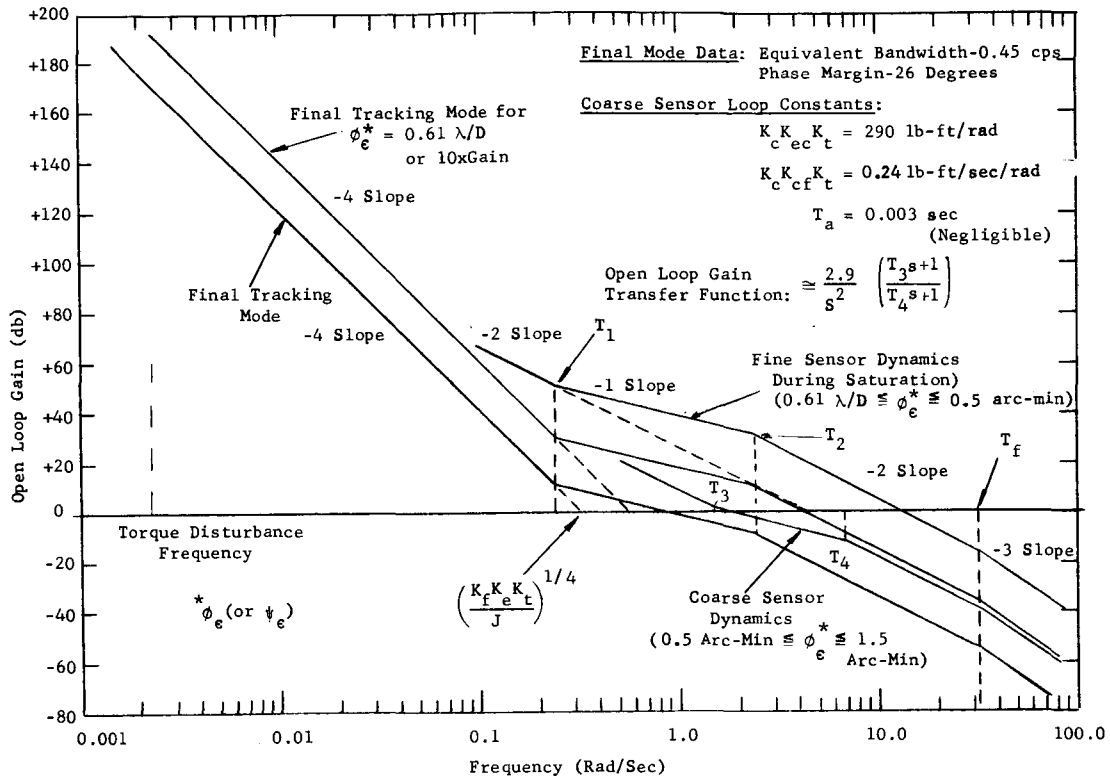


Figure 3.12. Bode Diagram-Vertical And Horizontal Axes

Regardless of the inertia values however, the loop gain will be selected to compensate as required. Where inertia values are required for specific calculations of error versus disturbing torques, the worst case value (100 slug-ft<sup>2</sup>) of inertia was used.

The open loop gain in the final track mode has been selected on the basis of the torque versus noise optimizing plots in Volume II for a 1 arc-min field-of-view sensor and a 20,000 dyne-cm torque disturbance. With this gain, a 20,000 dyne-cm torque will produce displacement errors of 0.001 arc-sec (rms) at periods of 2700 seconds. If the period varies or the disturbing torque amplitude varies for this fixed loop gain, the pointing errors will vary. Graphical plots of disturbing torque versus frequency are given in Figure 3.13 for the system open loop gain of Figure 3.12 ( $K/J = 0.011 \text{ sec}^{-4}$ ) in the final track modes assuming a minimum value of  $K_e$  (see Figure 3.10).

The remaining performance specifications for the design represented by the Bode of Figure 3.12 are the errors due to noise. For the fine sensor, using a 12th magnitude guide star, 1 arc-min field of view, optical

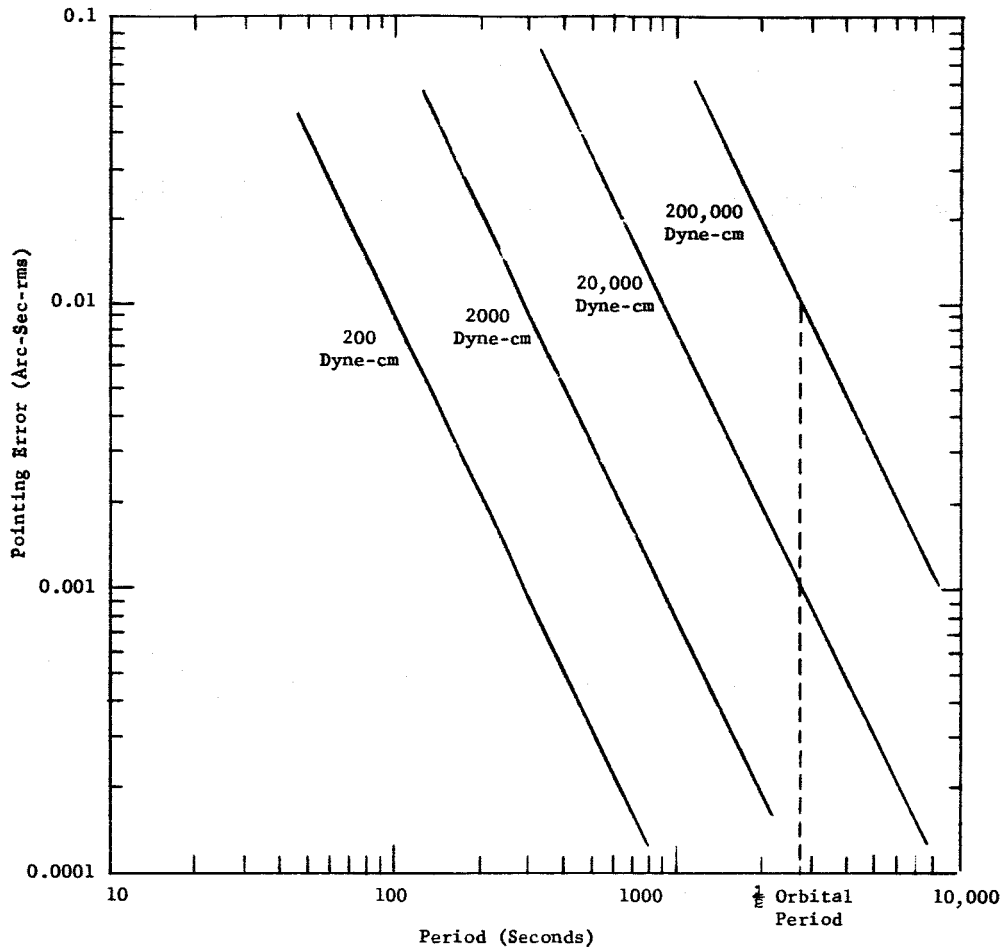


Figure 3.13. Error Versus Torque Disturbances  
(Final Tracking Mode - Vertical  
and Horizontal Axes)

efficiency of  $\eta_o = 0.10$ , dark current equals (0.4) 12th magnitude star, and background equivalent to an 11th magnitude star/16 arc-min<sup>2</sup>, the signal-to-noise is

$$S/N = 24 \tag{3-13}$$

This ratio was based on an equivalent bandwidth of  $f_{eq} = 0.45$  cps which was obtained from the parameters of the fine sensor servo loop using the minimum value of  $K_e$  (variable gain).



Substituting into the equation  $E_p = 0.61\lambda/D (S/N)^{-1}$ , the pointing error becomes,

$$E_p(\phi \text{ or } \psi) = 0.003 \text{ arc-sec (rms)} \quad (3-14)$$

If a brighter star is selected for guidance such as an 11th magnitude star, the performance is considerably improved for the same conditions. According to calculations,

$$S/N = 48 \quad (3-15)$$

and

$$E_p(\phi \text{ or } \psi) = 0.0014 \text{ arc-sec (rms)} \quad (3-16)$$

For a range of guide stars from the 9th to 13th magnitude, the system tracking errors due to noise can be determined as shown in Figure 3.14 using the same servo loop gain and phase margin (signal-to-noise plots are also included). The sensitivity increase from the phototubes due to brighter stars is adjusted automatically in the sensor electronics (see Section 3.5) to maintain the same sensor voltage output to angular error input gain.

Considering the larger (3 arc-min) field-of-view in the coarse sensor, the signal-to-noise (S/N) is less for this sensor for the same background conditions. Using an equivalent bandwidth frequency of 0.852 cps derived from the transfer function (3-12) the signal-to-noise ratio for the coarse sensor is

$$S/N = 14.4 \quad (3-17)$$

This ratio was based on an equivalent bandwidth taken for a linear approximation to the coarse sensor transfer function (see Figure 3.9).

The pointing error for this sensor due to noise is,

$$E_p(\phi \text{ or } \psi) = 0.005 \text{ arc-sec (rms)} \quad (3-18)$$

Although the pointing errors ( $E_p$ ) in the coarse sensor region are higher, they are not detrimental, since the coarse sensor mode is primarily one of acquisition. This conclusion was verified during the analog computer simulation using predicted noise inputs (see Section 3.4.4).

In regard to acquisition, the general transfer functions (3-10), (3-11), and (3-12) are applicable, particularly the relationships (3-11) and (3-12) where the system becomes nonlinear. Each of the relationships

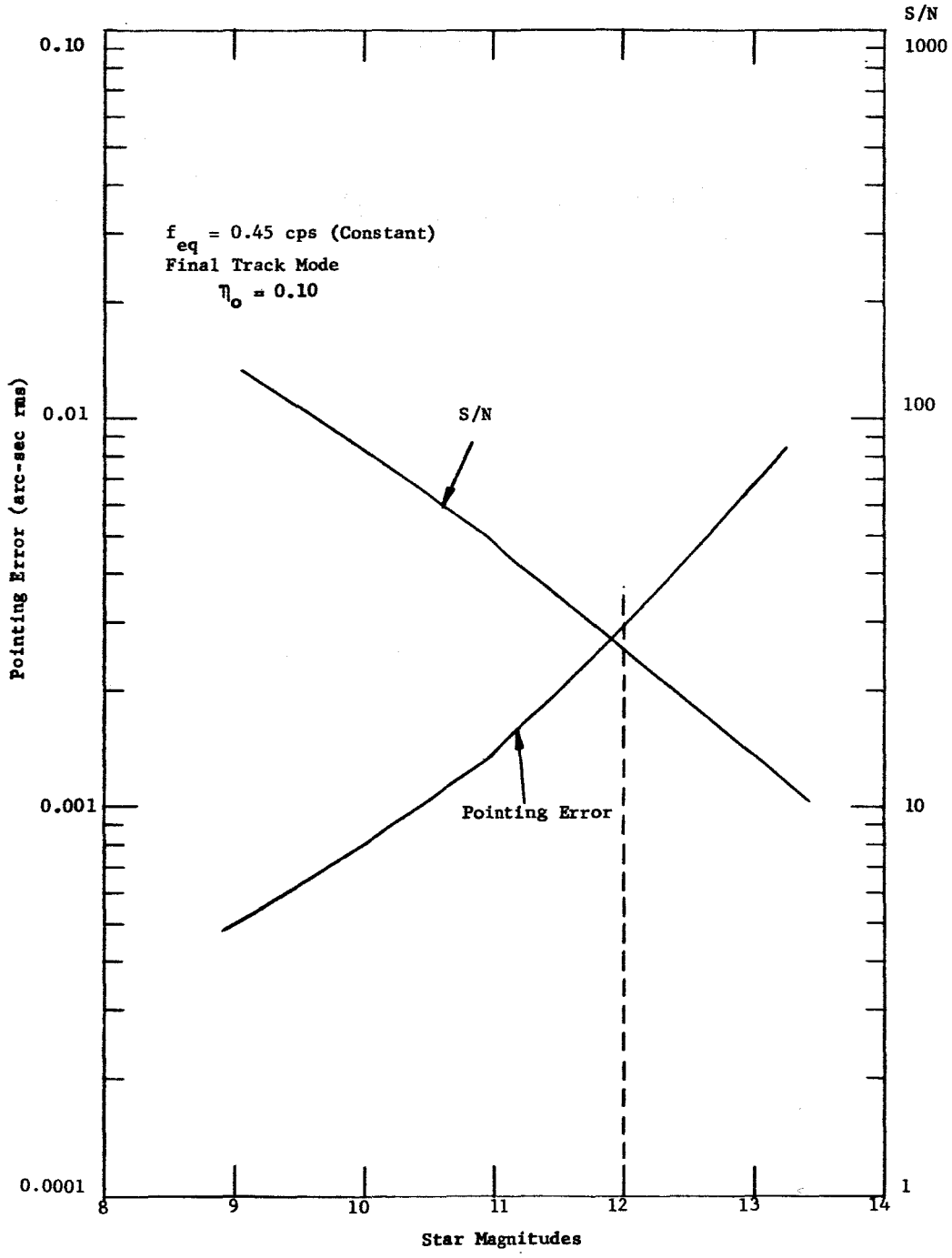


Figure 3.14 Pointing Error vs. Star Magnitudes (Vertical and Horizontal Axes)

is higher than second order differential equations, and if the acquisition switching, noise conditions and exact sensor nonlinearities are considered simultaneously, analytical techniques become unwieldy. Acquisition was therefore studied using the analog computer. The values (gains, time constants, etc.) used during acquisition can be obtained from Figure 3.12 for equations (3-10), (3-11), and (3-12).

Throughout the preceding analysis (and also the computer simulation) the torquer saturation was selected at  $\pm 0.30$  lb-ft for the vertical and horizontal axes although originally specified at  $\pm 1.0$  lb-ft. The gains and error rate network time constant ratios selected did result in torque output saturation. For instance, during the time the coarse sensor is initially active or for impulse type of inputs, the theoretical saturation limit is 1.0 lb-ft. However, as proved during the computer study, the system is still able to acquire for these worst case conditions.

3.4.2.5 Other Sources of Pointing Errors - There are at least two other sources of pointing error in the horizontal and vertical axes. They are,

1. Centering system coupling errors
2. Roll axis coupling errors

Each source is an internally generated type of disturbance resulting mainly from hardware or design imperfections. The errors from each of these sources are summarized in Table 3-IV.

The centering errors are a result of sensitivity (force output to electrical signal input) unbalances in the dual amplifier and torquer combinations since the same torquers are used to position the telescope in both translation and rotation. These errors are in the order of 0.0007 arc-sec (peak) or less for suspension systems with natural frequencies of 0.02 rad/sec, 0.05 inch amplitudes and 10 percent torquer unbalances. (Section 3.4.5 includes a complete analysis of the centering system.)

The previous analysis assumes telescope roll errors in the vertical-horizontal sensor have been totally eliminated by the crossfeeds in the fine sensor logic circuits. For practical reasons, this will never quite be the case. Noise from the roll signal crossfeeds, although heavily filtered, will still create additional horizontal and vertical errors and crossfeed scaling accuracy will never be perfect.

In determining the crossfeed roll errors due to noise, the left and right guide stars sensors are assumed to have identical characteristics and bandwidths for the same magnitude guide stars. The crossfeed filter ( $T_n$ ) breakpoint is selected to lie well below the horizontal and vertical equivalent bandpass frequencies but sufficiently high to allow the low frequency roll cross-coupling components to be eliminated in the final tracking mode. The noise errors from roll axis crossfeeds are in the order of 0.002 arc-sec (rms).

The crossfeed static scaling inaccuracies will not be greater than 5 percent. For guide star positions that create the largest components of roll motions in the vertical and horizontal axis, these inaccuracies result in errors of 0.0004 arc-sec (rms) or less.

### 3.4.3 Servo Analysis - Roll Axis

3.4.3.1 General Considerations - The telescope roll axis differs from the horizontal and vertical axes in four major respects

1. A coarse sensor is not required.
2. Only a single integration is employed. Crossfeeds and gain changes are eliminated in the stabilization electronics.
3. An alternate sensor, a gyro, is used interchangeably with the fine optical sensor which eliminates most of the acquisition switching from the roll stabilization electronics.
4. Rotational pointing accuracy requirements are less.

The allowable roll pointing errors, subdivided by cause, are 1.0 arc-sec (rms) due to torque disturbances and 2.0 arc-sec (rms) due to noise. These form the minimum (or worst case) design goals in this axis. Errors of 4 arc-sec (rms) at the telescope field limits (15 arc-min) are the allowable angular deviation. These errors are derived on the basis of the guide star locations (or image mover locations) with respect to the telescope center of rotation. Due to the small rotational moment arm (as opposed to the telescope focal length in the vertical and horizontal axes), the roll pointing requirements are considerably less. For the same reason, a coarse sensor is not required in roll since the minimum fine sensor field of view (1 arc-min in the vertical and horizontal axes) is equivalent to 6.7 degrees minimum in roll.

3.4.3.2 Analytical Relationships - The individual component transfer functions for the telescope roll axis vary somewhat from those derived for the vertical and horizontal axes (see Sections 3.4.2.1, 3.4.2.2, and 3.4.2.3). Coarse sensor transfer functions are absent, which simplifies the equations and, in addition, the roll coordinate geometry alters the transfer functions.

The rotational commands in the final track mode are derived by subtracting the two optical sensor vertical outputs. (Alternately, the horizontal components could be subtracted for certain portions of quadrants I and III or II and IV to yield roll angles (see Appendix A).) When the guide stars are located in quadrants I and II, for example, the roll angular error is determined by

$$\theta_e = \frac{\epsilon_{y_R} + \epsilon'_{y_R}}{R_\alpha \cos\alpha + R_\beta \cos\beta} \quad (3-19)$$

where

- $\theta_e$  = roll pointing error (radians)
- $\epsilon'_{y_R}, \epsilon_{y_R}$  = optical sensor image motion (left and right, respectively) due to telescope roll motions (inches)
- $R_\alpha, R_\beta$  = image mover radial distance (inches) from telescope center of rotation
- $\alpha, \beta$  = image mover angular position (degrees) with respect to telescope coordinates.

Normally, the sensor image motion due to vertical and horizontal motions is determined by the telescope optical focal length. For example, in the vertical axis,

$$\phi_e = \frac{\epsilon_y}{L_f} \quad (3-20)$$

where,

- $\phi_e$  = vertical pointing error (radians)
- $\epsilon_y$  = right optical sensor image motion due to vertical axis motion (inches)
- $L_f$  = telescope focal length (inches) in this case, to the f/200 focal point

The roll moment arms ( $R_\alpha$  and  $R_\beta$ ) are much less than the focal length (8000 inches at f/200) and, therefore, for the equivalent vertical sensor image motion ( $\epsilon_{y_R}$  or  $\epsilon'_{y_R}$ ) about the guide stars, the allowable roll errors are much larger. Referring to Figure 3.15 and letting  $\alpha = \beta = 0$  and  $R_\alpha = R_\beta = 10$  inches (or equivalently, a guide star location of 7-1/2 arc-minutes in the telescope f/10 field), a 0.01 arc-sec vertical (or horizontal) pointing error produces an equivalent 8.0 arc-sec roll error which is calculated as follows,

$$\epsilon_y = (40)(200)(0.01) \left( \frac{1}{2.06 \times 10^5} \right) = 0.00039 \text{ inch} \quad (3-21)$$

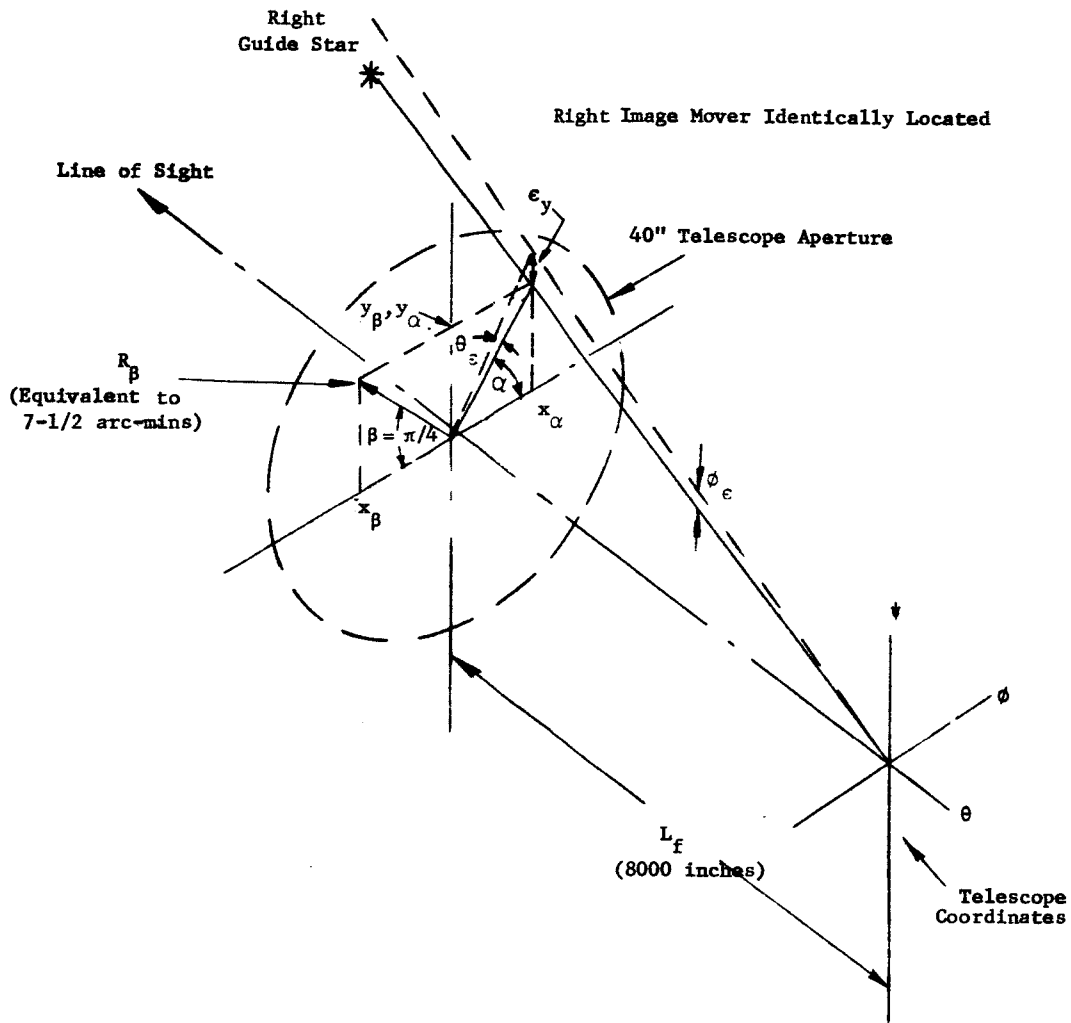


Figure 3.15. Equivalent Roll Errors as Related to Sensor Vertical Image Motions

If,

$$\epsilon_y = \epsilon_{y_R} = \epsilon'_{y_R} \tag{3-22}$$

then,

$$\theta_e = \frac{2\epsilon_y}{\cos\alpha R_\alpha + \cos\beta R_\beta} = \frac{\epsilon_y}{R_\alpha(\text{or } R_\beta)\cos\alpha(\text{or } \beta)} \tag{3-23}$$

$$\theta_e = \frac{0.00039}{10} (2.06 \times 10^5) = 8.0 \text{ arc-sec}$$

At the telescope field of view extremes (15 arc-minutes and  $\alpha = \beta = 0$ ), this would reduce to 4 arc-sec for 0.01 arc-sec equivalent vertical ( $\phi$ ) motions which determines the roll axis pointing specification. Figure 3.16 plots roll pointing requirements as a function of guide star (or image mover) locations.

The fine sensor transfer function as related to roll remains identical in characteristic (see Figure 3.9) but again, due to the geometry, changes scale. Equation (3-1) can be modified for roll obtaining,

$$\frac{V_{\theta}(s)}{\theta_e(s)} = \frac{K_f}{T_f s+1} \left[ \frac{R_{\alpha} \cos \alpha}{L_f} + \frac{R_{\beta} \cos \beta}{L_f} \right] \left( \frac{\text{volts}}{\text{radians}} \right) \quad (3-24)$$

Equation (3-24) is valid for roll errors of less than

$$(0.61\lambda/D) \left( \frac{R_{\alpha} \cos \alpha}{L_f} \right)^{-1} \text{ and } (0.61\lambda/D) \left( \frac{R_{\beta} \cos \beta}{L_f} \right)^{-1}.$$

Roll errors exceeding these values drive the fine sensors into saturation and at this point, the roll displacement gyro provides signals to the stabilization electronics. The gyro transfer function is

$$\frac{V_g(s)}{\theta_e(s)} = \frac{K_g}{T_g s+1} \left( \frac{\text{volts}}{\text{radians}} \right) \quad (3-25)$$

where,

$$V_e(s) = \text{sensor}(s) \text{ roll output voltage (volts)}$$

$$V_g(s) = \text{gyro output voltage (volts)}$$

$$K_g = \text{gyro sensitivity (volts/rad)}$$

$$T_g = \text{gyro time constant (sec)}$$

$$\theta_e(s) = \text{roll pointing error (rad)}$$

The roll stabilizing networks are identical to equation (3-4) with the exception of one less integral plus proportional network. Since a loss of gain is experienced in the optical sensors as related to roll (see equation (3-24)), the servo loop gain and bandwidth would be considerably reduced. To compensate, the roll axis (only) incorporates a single integration which increases the bandwidth for the same loop gain at torque disturbing frequencies. Therefore, the stabilizing networks are described by,

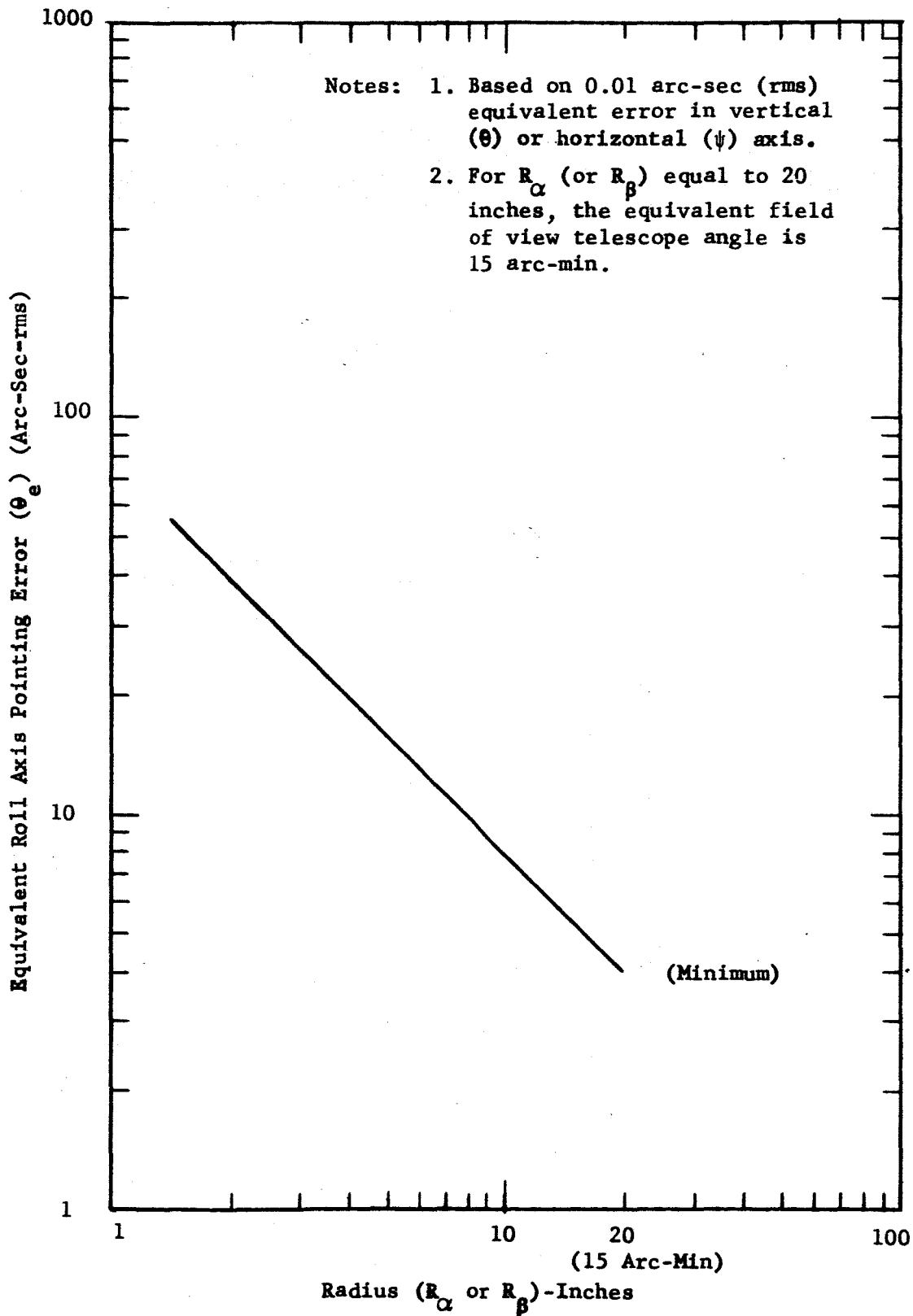


Figure 3.16. Roll Pointing Error Requirements vs. Guide Star Locations



$$\frac{V_t(s)}{V_\theta(s)} = \frac{(T_1 s + 1)^2 K_e}{s(T_2 s + 1)} \quad (3-26)$$

or equally, for the gyro

$$\frac{V_t(s)}{V_g(s)} = \frac{(T_1 s + 1)^2 K_e}{s(T_2 s + 1)} \quad (3-27)$$

In this case,  $K_e$  is linear. The values of  $T_1$ ,  $T_2$ , and  $K_e$  will differ from the roll axis. The magnetic torquer and telescope relationship for roll are identical to those summarized in paragraph 3.4.2.3.

3.4.3.3 Complete Roll Axis Representation and Analysis - Combining the equations of the previous section results in the following overall roll transfer functions using the fine optical sensors and gyro respectively,

$$\frac{\tau_c(s)}{\tau_e(s)} = \frac{(T_1 s + 1)^2 K'_f K_e K_t}{J s^3 (T_f s + 1)(T_2 s + 1)(T_a s + 1)} \quad (3-28)$$

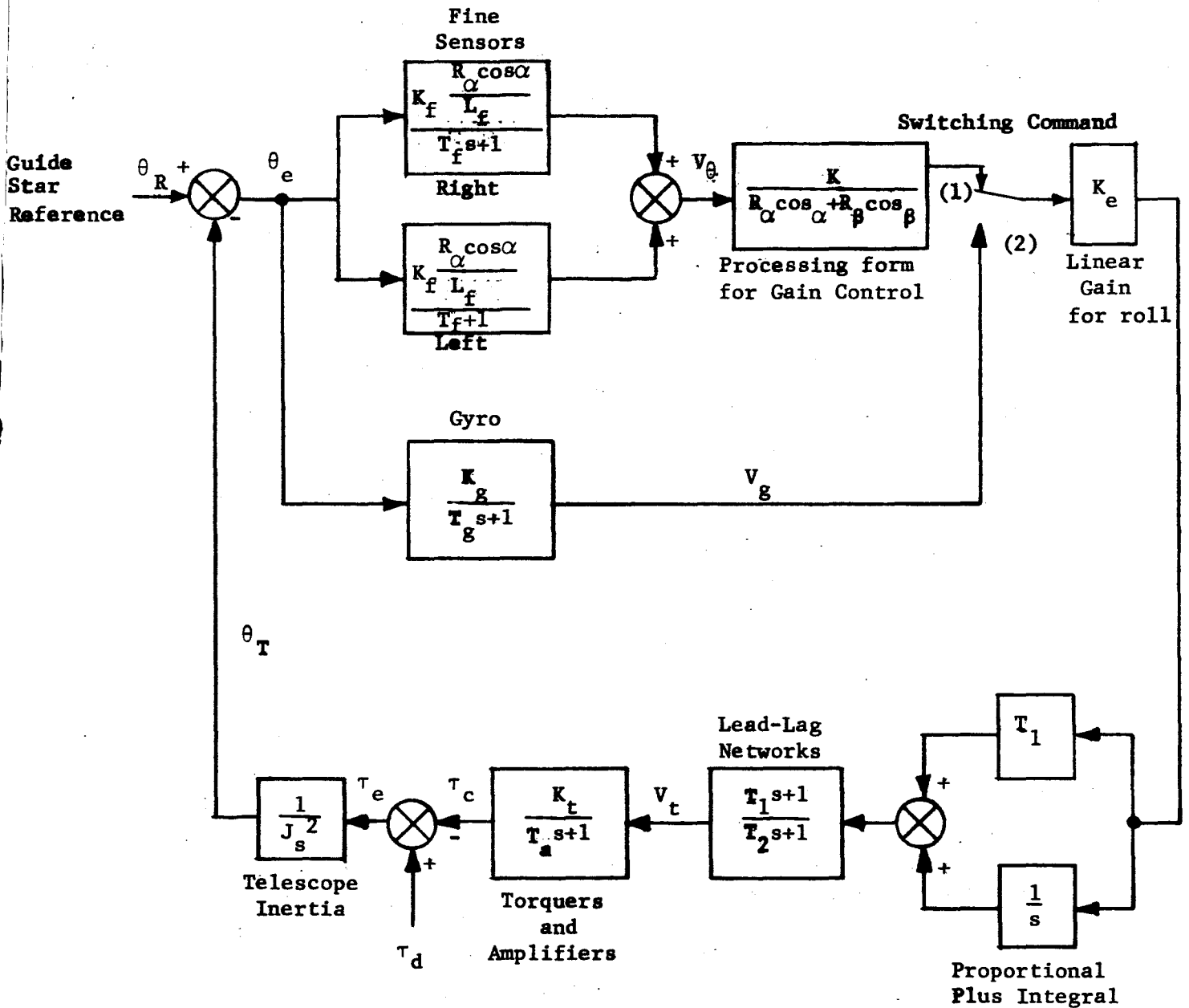
$$\frac{\tau_c(s)}{\tau_e(s)} = \frac{(T_1 s + 1)^2 K_g K_e K_t}{J s^3 (T_g s + 1)(T_2 s + 1)(T_a s + 1)} \quad (3-29)$$

The analytical block diagram representing these transfer functions is given in Figure 3.17 and includes one exception. A function representing the reciprocal of  $R_\alpha \cos \alpha + R_\beta \cos \beta$  is inserted in the servo loop to compensate for the change in gain for different guide star locations. Therefore, the term  $K'_f$  is the modified sensor gain resulting from the geometric conversions in roll and remains constant.

The roll axis performance and stability can be determined using Bode diagrams as shown in Figure 3.18. Less complex than the vertical and horizontal axes, the system can be represented by a single plot that only differs by the sensor and gyro time constants ( $T_f$  or  $T_g$ ). Table 3-IV summarizes the roll axis performance.

For the open loop gain selected ( $0.0056 \text{ sec}^{-3}$ ), a 20,000 dyne-cm torque at a 2700 second period would produce a 0.90 arc-sec (rms) error. Graphical plots of torque levels at various frequencies can also be generated for the roll axis as shown in Figure 3.19. An inertia of  $100 \text{ slug-ft}^2$  was used.

Switch Position (1)  $0 \leq \theta_e \leq 0.61 \frac{\lambda}{D} \left( \frac{R_\beta \cos \beta}{L_f} \right)^{-1}$       (2)  $\theta_e \geq 0.61 \frac{\lambda}{D} \left( \frac{R_\beta \cos \beta}{L_f} \right)^{-1}$   
 [or  $0.61 \frac{\lambda}{D} \left( \frac{R_\alpha \cos \alpha}{L_f} \right)^{-1}$ ]      [or  $0.61 \frac{\lambda}{D} \left( \frac{R_\alpha \cos \alpha}{L_f} \right)^{-1}$ ]



$\theta_R$  = Guide Star Angular Ref.  
 $\theta_T$  = Telescope Angular Displ.

Figure 3.17. Roll Axis Analytical Block Diagram

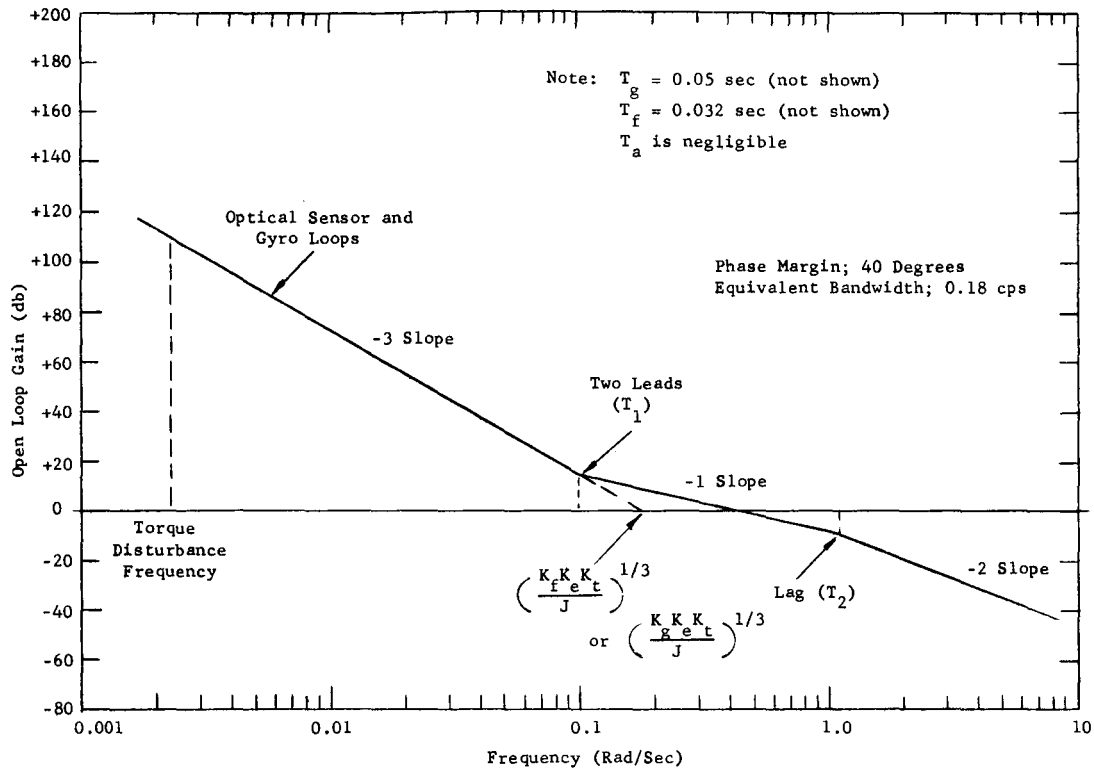


Figure 3.18. Bode Diagram Roll Axis (Final Track Mode)

The roll pointing error due to noise involves a slightly more complicated calculation compared to the vertical and horizontal axes since the noise into the roll servo loop is a function of both the left and right guide star sensors.

Assuming the sensors are identical, the roll pointing error due to noise becomes expressible as

$$E_p(\text{roll}) = \left[ E_p^2(\text{right sensor}) + E_p^2(\text{left sensor}) \right]^{1/2} \tag{3-30}$$

or

$$E_p(\theta) = \left[ E_{pR}^2(\theta) + E_{pL}^2(\theta) \right]^{1/2} \text{ rms} \tag{3-31}$$

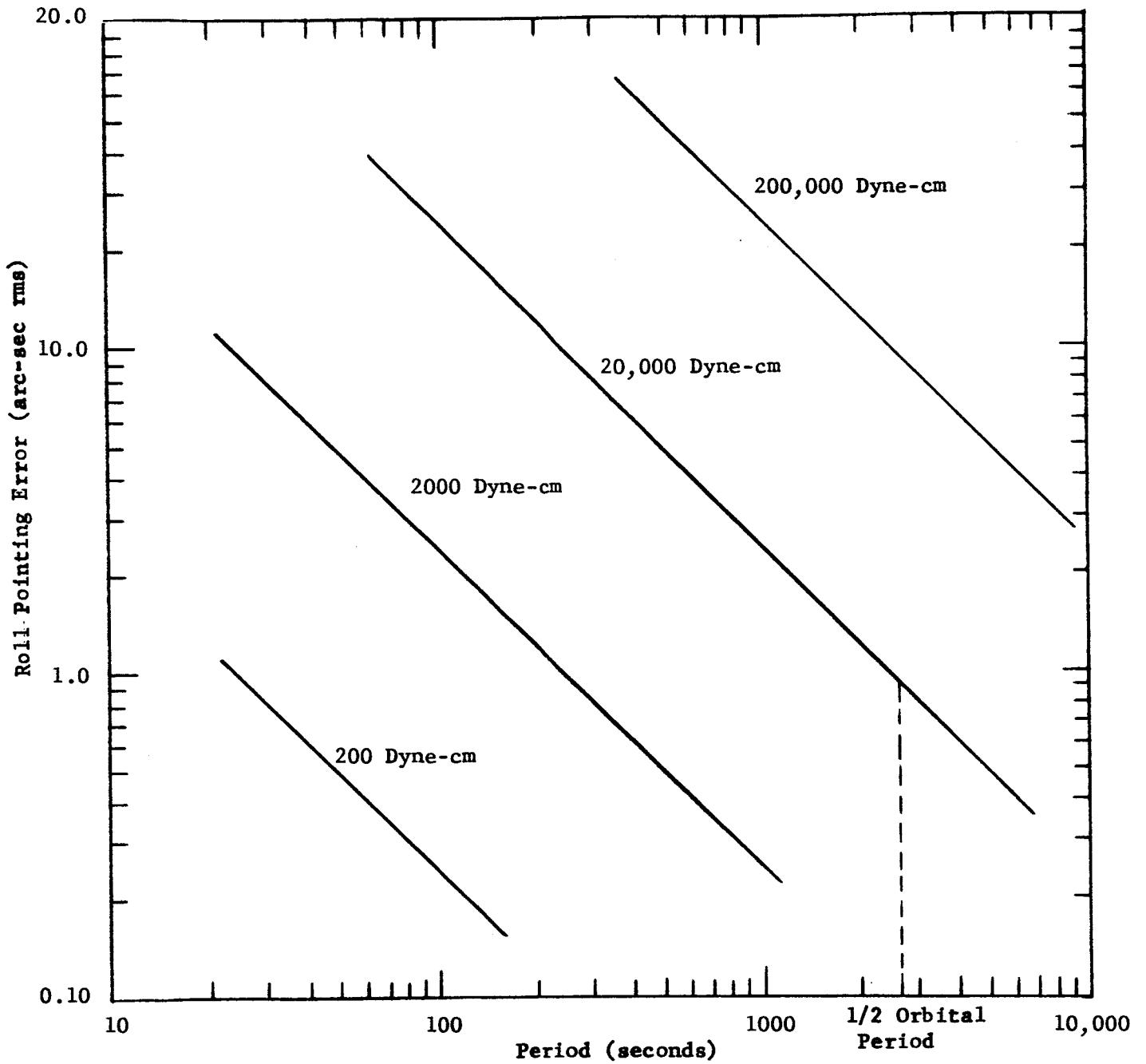


Figure 3.19. Roll Axis Pointing Errors vs. Disturbance Torques

The expressions  $E_{pR}(\theta)$  and  $E_{pL}(\theta)$  are the basic sensor  $0.61\lambda/D$   $(S/N)^{-1}$  pointing error relationships modified by the geometry associated with the roll axis,

$$E_{P_R}(\theta) = 0.61\lambda/D \frac{(L_f)}{(R_\alpha \cos\alpha)} (S/N)^{-1} \text{ rms} \quad (3-32)$$

$$E_{P_L}(\theta) = 0.61\lambda/D \frac{(L_f)}{(R_\beta \cos\beta)} (S/N)^{-1} \text{ rms} \quad (3-33)$$

therefore,

$$E_p(\theta) = 0.61\lambda/D (S/N)^{-1} \left[ \left( \frac{L_f}{R_\beta \cos\beta} \right)^2 + \left( \frac{L_f}{R_\alpha \cos\alpha} \right)^2 \right]^{1/2} \text{ rms} \quad (3-34)$$

The S/N ratio remains unchanged for various guide star locations since the loop gain is held constant.

If mean values of  $R_\beta$ ,  $R_\alpha$ ,  $\beta$ , and  $\alpha$  are used such as

$$R_\beta = R_\alpha = 10 \text{ inches (equivalent to 7-1/2 arc-min field angle)}$$

$$\alpha = \beta = 0$$

Then, calculating for the given conditions stated below,

$$E_p(\theta) = 1.50 \text{ arc-sec (rms)}$$

for

$$S/N = 55$$

In this case at a 10 inch equivalent radius, the tolerable pointing error is 8 arc-sec (rms) (see Figure 3.16) which is equivalent to 0.01 arc-sec (rms) in the vertical and horizontal axes.

This S/N ratio and pointing error ( $E_p(\theta)$ ) was calculated using the values obtained from the Bode plot of Figure 3.18 which results in an equivalent bandwidth of

$$f_{eq} = 0.18 \text{ cps}$$

The background noise and dark current used were equivalent to an 11th magnitude star per 16 arc-min<sup>2</sup> and (0.4) 12th magnitude star respectively. The field of view of the sensor is 1 arc-min (as related to the vertical or horizontal axes). The optical efficiency was selected at 0.1.

Brighter guide stars would similarly decrease pointing errors due to noise as discussed in paragraph 3.4.2.4. The ratio of performance increase in roll would be typical of the results obtained in Figure 3.14.

The remaining sources of pointing errors are the centering system, gyro referencing inaccuracies, and the vertical axis coupling errors.

For the same torque sensitivity unbalances (10%) and centering disturbances (0.02 rad/sec natural frequencies) used in the vertical and horizontal axes, errors due to the centering system coupling are in the order of 0.10 arc-sec or less for roll as derived in Section 3.4.5.

Vertical axis coupling errors, based on 5 percent (total) calibration inaccuracies in the fine sensor logic networks, (inaccuracies in the ability to subtract out the vertical axis components) would be in the order of 0.20 arc-sec in the final tracking mode.

The roll gyro will be referenced in inertial space while the telescope is in the auxiliary rotational modes. Due to the roll motions of the spacecraft ( $\pm 2$  degrees in the OAO stabilization fine pointing mode), certain inaccuracies or offsets in the gyro roll reference angle will result. The nulling or referencing gyro system in conjunction with the roll auxiliary servo will in probability, average out most of the OAO spacecraft perturbations but only within limits. Based on the dynamics of the spacecraft disturbances and the gyro referencing system performance, reference offset errors were estimated to be much less than  $\pm 1$  arc-min (peak) with residue rates of 0.0013 arc-sec/sec. A 1 arc-min roll error would only result in static horizontal and vertical offsets in the order of  $\pm 0.667$  arc-sec (peak) which can be trimmed out by electrical offset commands based on S.E.C. vidicon information or the auxiliary tracker signal.

Acquisition in roll requires a minimum of switching since the servos continually see a linear sensor signal. Recovery times for initial conditions of rate, displacement and torque are simply a function of the linear closed loop dynamics of the roll servo. Referring to equations (3-28) and (3-29), letting,

$$K_g = K'_f \quad (3-35)$$

the closed loop transfer function is,

$$\frac{\tau_c(s)}{\tau_d(s)} = \frac{(T_1 s + 1)^2}{\frac{J}{K_g K_e K_t} s^3 + (T_1 s + 1)^2} \quad (3-36)$$

Where,  $T_g$ ,  $T_2$ , and  $T_a$  are neglected for this analysis.

Substituting values (see Figure 3.18), and factoring, equation (3-36) becomes, for a step torque ( $\tau_d$ ),

$$\tau_c(s) = \frac{(10s+1)^2 \tau_d(s)}{s(15s+1)(13.3s^2+5.77s+1)} \quad (3-37)$$

where,

$$\frac{J}{K_g K_e K_t} = 200 \text{ sec}^{-3}$$

and

$$T_1 = 10 \text{ sec}$$

equation (3-37) has the solution (where a and b are constants),

$$\tau_c(s) = \tau_d \left[ 1 - ae^{-t/15} + be^{-t/4.6} \sin(0.17t - \psi) \right] \quad (3-38)$$

The frequency of oscillation is 0.17 rad/sec (1.1 cps) which to a good approximation (5%) will diminish in

$$(4.6) (3) \cong 14.0 \text{ seconds}$$

The main recovery time however, is determined by the 15 second time constant of the first exponential term: total recovery time is therefore approximately

$$15 (3) = 45 \text{ seconds.}$$

Similar recovery times result for initial conditions of rate and displacements.

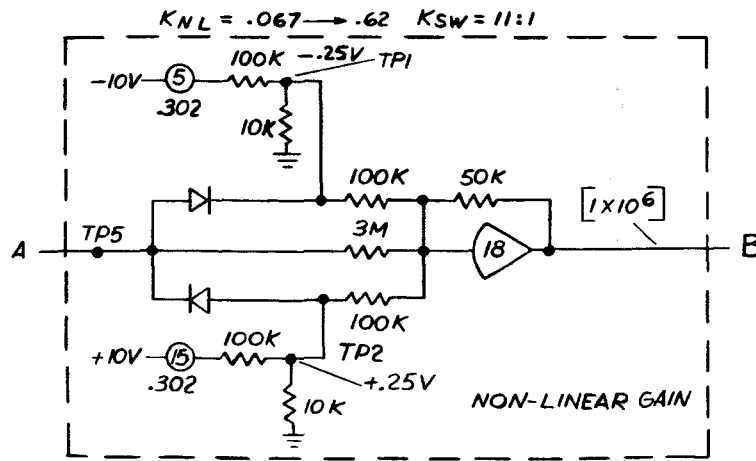
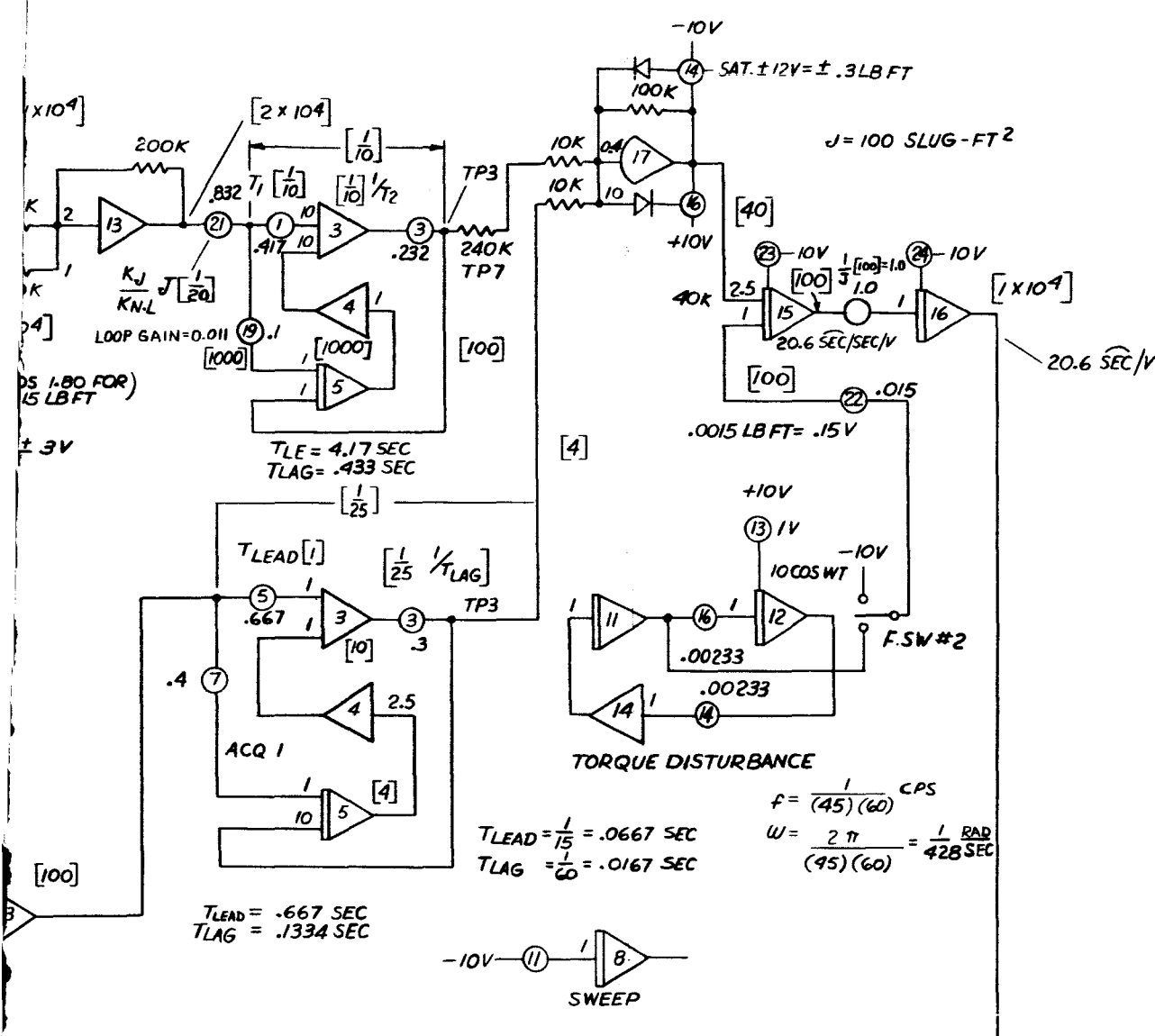
#### 3.4.4 Analog Computer Simulation

A single axis of the telescope pointing system was simulated on an analog computer (see Figure 3.20). The simulation was done for the translational guide star using twelfth magnitude guide star noise levels and included the following nonlinearities:

1. Fine sensor transfer function characteristics (see Figure 3.9).
2. Coarse sensor transfer function characteristics (see Figure 3.9).







- LEGEND**
- SUMMER
  - INTEGRATOR
  - POTENTIOMETER
  - DIODE
  - RESISTOR
  - $[ ]$  — SCALING FACTORS

Figure 3.20. Analog Computer Single Axis Simulation

3. White noise inputs to both fine and coarse sensors using worst case S/N ratios for each.
4. Magnetic torquer saturation.
5. Complete single axis acquisition switching, gain changes and crossfeeds.
6. Simulated external torque disturbances and predicted initial rate and displacement conditions.

The purpose of the simulation was to further verify and develop the acquisition scheme first presented in Section 3.3.3.3 (Vertical and Horizontal Axes). The simulation simultaneously included the multiple conditions of external torques, initial conditions and noise. In addition, the simulation verified several of the final tracking results of Table 3-IV.

White noise was simulated using a random function noise generator with filtering to produce an equivalent noise bandwidth of 52 cps. Since the pointing system bandpass frequencies are less than 1 cps in any mode, the 52 cps noise cut-off frequency remained a good approximation for white noise.

The results of the simulation are listed in Table 3-IV and several representative time-based plots are presented in Figures 3.21 and 3.22 to illustrate the dynamics of the pointing system as it proceeds through its acquisition cycles.

Figure 3.21 gives the plots of the telescope position and sensor outputs during acquisition. The plots of this figure were not taken simultaneously and should not be compared on the same time basis. Due to random noise, each acquisition sequence will cycle somewhat differently. The jagged traces are due to the white noise simulated inputs.

Figure 3.22 illustrates verification plots of the system pointing errors in the final tracking mode. The initial transient in the telescope position is due to the recovery time required to stabilize to the rate of the externally applied torque. In this case, disturbing torques of 0.0015 lb-ft were used at periods of 140 seconds, which are much higher than the orbiting 2700 second periods. Interestingly, the error would normally be 0.14 arc-sec for this type of disturbance but with the nonlinear gain ( $K_e$ ), the error is only 0.03 arc-sec.

Noise was not included in obtaining the plots of Figure 3.22.

Conditions for all plots:

- 1) Full Noise, S/N = 1.8:1 (Coarse Sensor)  
S/N = 4:1 (Fine Sensor)
- 2)  $\phi_{IC}, \dot{\phi}_{IC} = +1 \text{ arc min}, +1 \text{ arc-min/sec}$
- 3) Constant Torque - .0015 Lb-Ft (p)

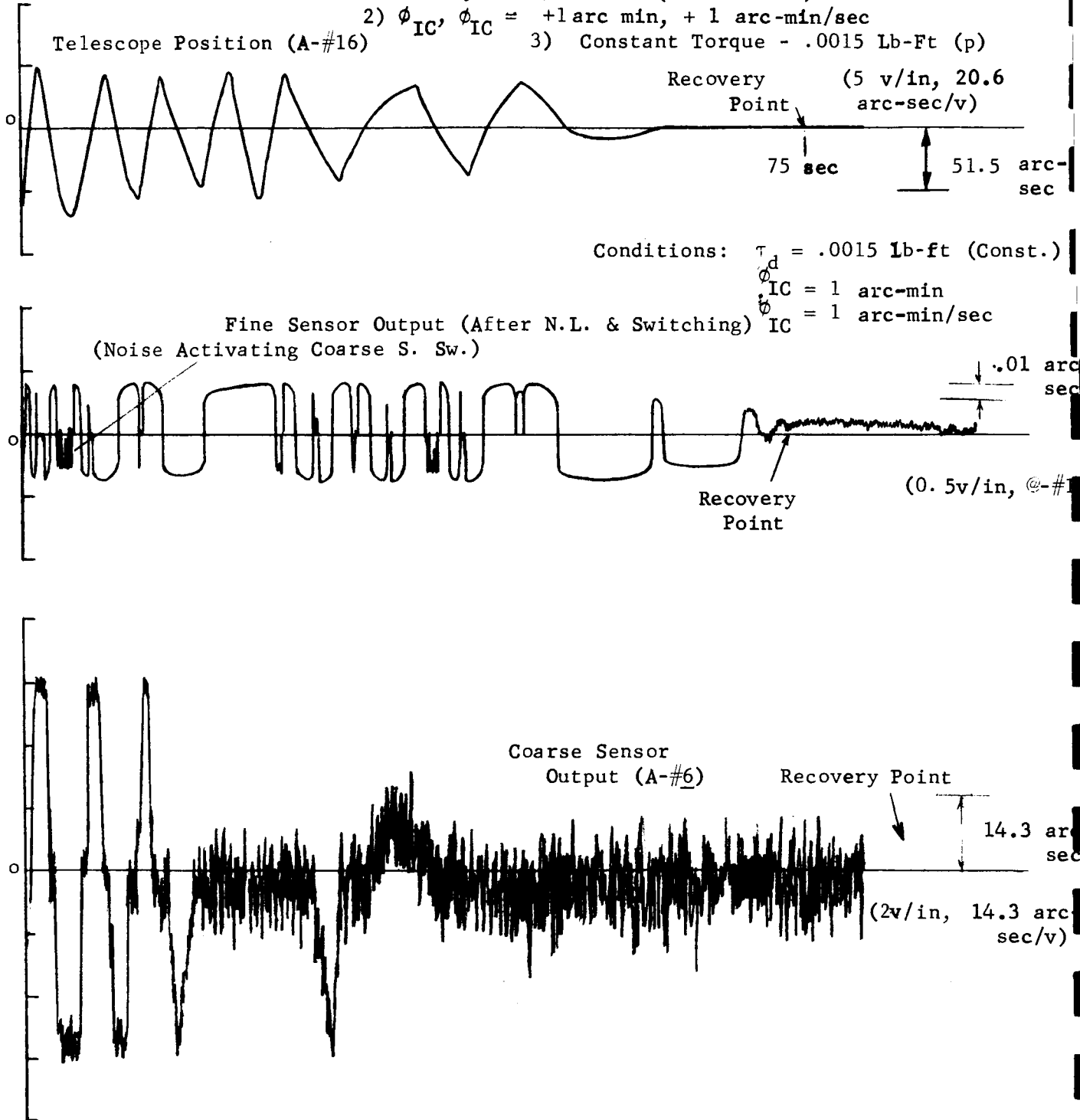


Figure 3.21 Telescope Acquisition

3-55

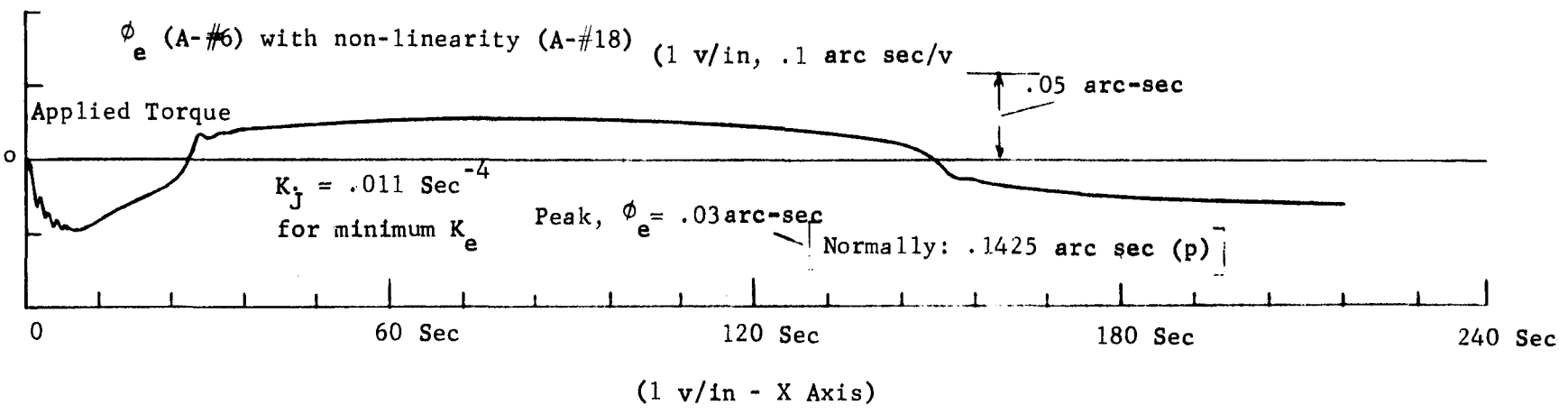
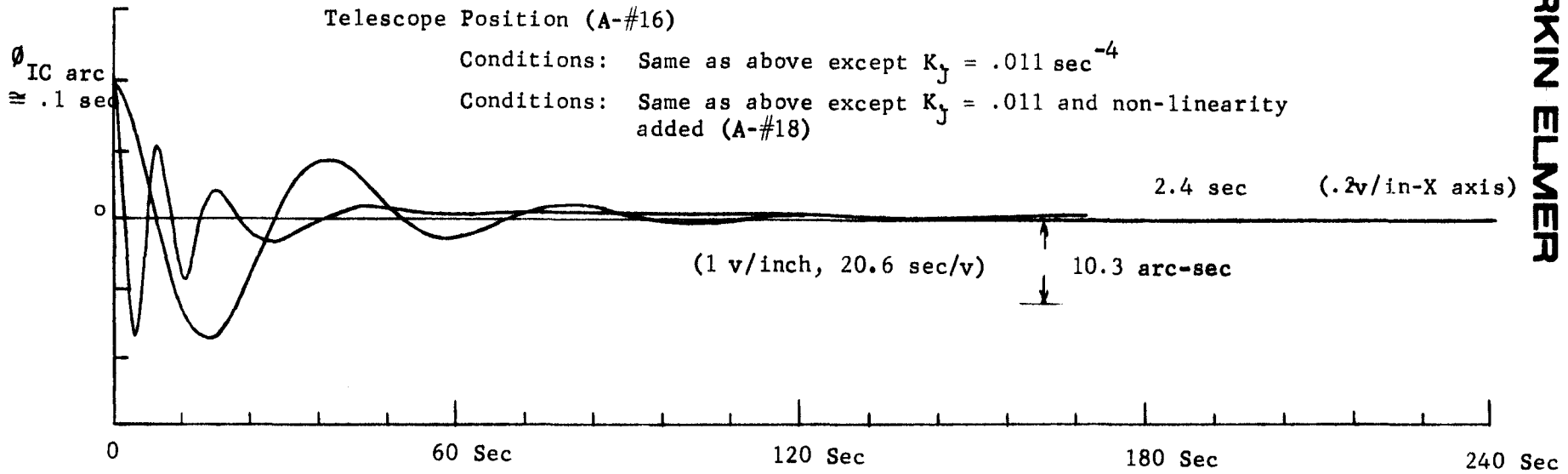


Figure 3.22 System Checks

### 3.4.5 Servo Analysis - Centering and Auxiliary Rotation

3.4.5.1 General Considerations - Preliminary calculations based on estimated linear disturbing forces indicate the relative linear motion or translation between the OAO spacecraft and telescope can be significant over short periods. To avoid unnecessary repetitive telescope caging sequences during experiment periods, a certain amount of translational control must be applied to maintain clearances between the OAO spacecraft and the telescope. The translation or centering control mechanism is the main topic described and analyzed in this section.

Two fundamental design approaches exist:

1. The telescope can be allowed to translate freely and the OAO spacecraft maintains the proper clearances with respect to the telescope with its control system.
2. The telescope via its own translating control system, maintains clearances with respect to the OAO spacecraft.

The first approach has merit in that the telescope is not subjected to the possibility of having pointing errors created by imperfections in the translation control system. However, controlling the spacecraft with respect to the telescope implies the entire system must be allowed to drift within its orbit. More importantly, since the manned Apollo spacecraft is required to maintain position with respect to the OAO spacecraft to avoid excessive "wind-ups" in the coil spring (or equivalent) suspension system, unnecessary and distracting maneuvering requirements are placed on the Apollo spacecraft.

Incorporating a translation system in the OAO spacecraft could also require a sizeable modification to the spacecraft which violates the design philosophy set forth for the telescope.

The second approach avoids the complicated interface problems with the spacecraft. The telescope translation control mechanism is relatively simple since the magnetic torquers used to achieve rotational stability can also be used for translation, consequently, the second approach appears to be the most feasible.

With a small amount of additional implementation, the telescope centering controls can also be utilized as an auxiliary three-axis rotational control which uses the OAO spacecraft as its reference. This affords several additional advantages. It can provide a scanning facility to locate the guide stars in the case of mispointing by the OAO spacecraft. Larger uncaging impulses can also be tolerated if the auxiliary rotational servos are used as an intermediate acquisition mode thereby unburdening the system design

requirements for the mechanical caging mechanism. The auxiliary system also provides a better means of erecting the gyro to its correct position.

**3.4.5.2 Centering System Description** - The telescope translational control mechanism takes the form of an active servo system. It must maintain clearances of  $\pm 1/2$  inch (maximum) in three directions for any disturbance condition in both acquisition and telescope tracking modes. Errors greater than  $\pm 1/2$  inch will cage the telescope.

Translational disturbances arise from several sources such as uncaging impulses, telescope torquer unbalances, and most importantly, Apollo-OAO spacecraft suspension system translations. Each of these disturbances vary in magnitude, frequency, and form. For the ensuing analysis, each type of disturbance was handled independently and the resulting servo errors are presented separately.

The results of this portion of the study are also summarized in Table 3-IV. In general, translation errors can be held to less than  $\pm 0.1$  inch without difficulty which is well within the  $\pm 0.5$  inch required.

The single axis translation servo system is shown in Figure 3.23 in block diagram form. A single axis servo loop consists of a linear displacement sensor which senses the relative displacement between the OAO spacecraft and telescope. Output signals from the sensor are processed by stabilizing networks and eventually feed the magnetic torquers to produce translation corrections. All three servo loops are identical in form. Translation servo errors may vary in each axis due to the type and direction of disturbances but a single maximum value of disturbance was selected and used for all three axes.

The physical orientation of the displacement sensors are shown in Figure 3.24. These sensors, requiring a special design, are discussed in detail in section 3.6.2. Two sensors are used per axis which provide both centering and auxiliary rotation signals.

**3.4.5.3 Centering System Servo Analysis** - Translation of the floating telescope can be simply obtained by unbalancing the linear magnetic torquers in any axis. Referring to the sketch in Figure 3.24, if a force offset command ( $\Delta F$ ) is properly phased and fed to the two torquers, the telescope will begin to translate in the  $\Delta x$  direction.

$$\Sigma F_x = (F_x + \Delta F_x) - (F'_x - \Delta F'_x) = M \frac{dx}{dt}^2 \quad (3-39)$$

and

$$\Delta F_x + \Delta F'_x = M \frac{d^2x}{dt^2} \quad (3-40)$$

for

$$F_x = F'_x$$

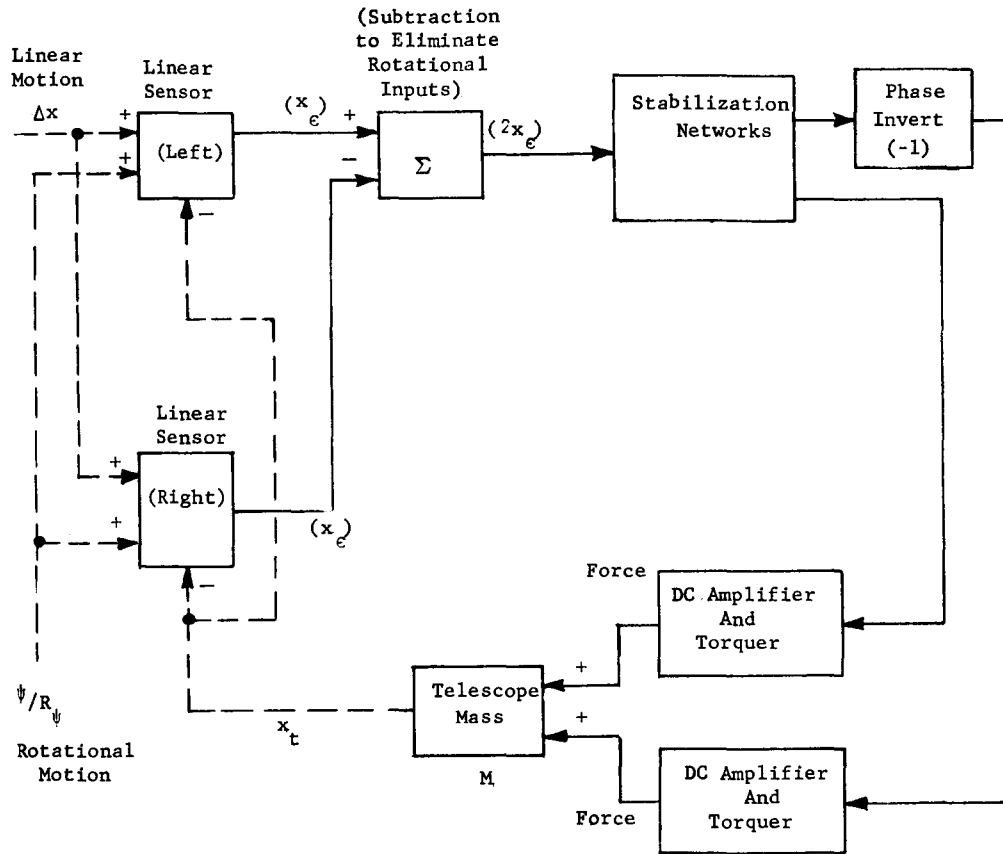


Figure 3.23. Centering System Block Diagram (Single Axis, Typical)

where,  $M$  is the mass of the telescope and  $F_x$ ,  $F'_x$  represent typical forces applied to correct rotational disturbances.

Furthermore, since

$$\sum \tau_\psi = R_\psi (F_x + \Delta F_x) + R'_\psi (F'_x - \Delta F'_x) = J \frac{d^2 \psi}{dt^2} \tag{3-41}$$

then

$$\tau_\psi = 2R_\psi (F_x + F'_x) \text{ for } R_\psi = R'_\psi,$$

and the centering force commands ( $\Delta F$ ) will not upset the rotational servos for the conditions specified. However, achieving ideal balanced conditions, i.e.,  $R_\psi = R'_\psi$  and  $F_x = F'_x$ , is not completely possible for practical reasons and the rotational ( $\psi$ ,  $\phi$ , and  $\theta$  motions) and centering servos will couple

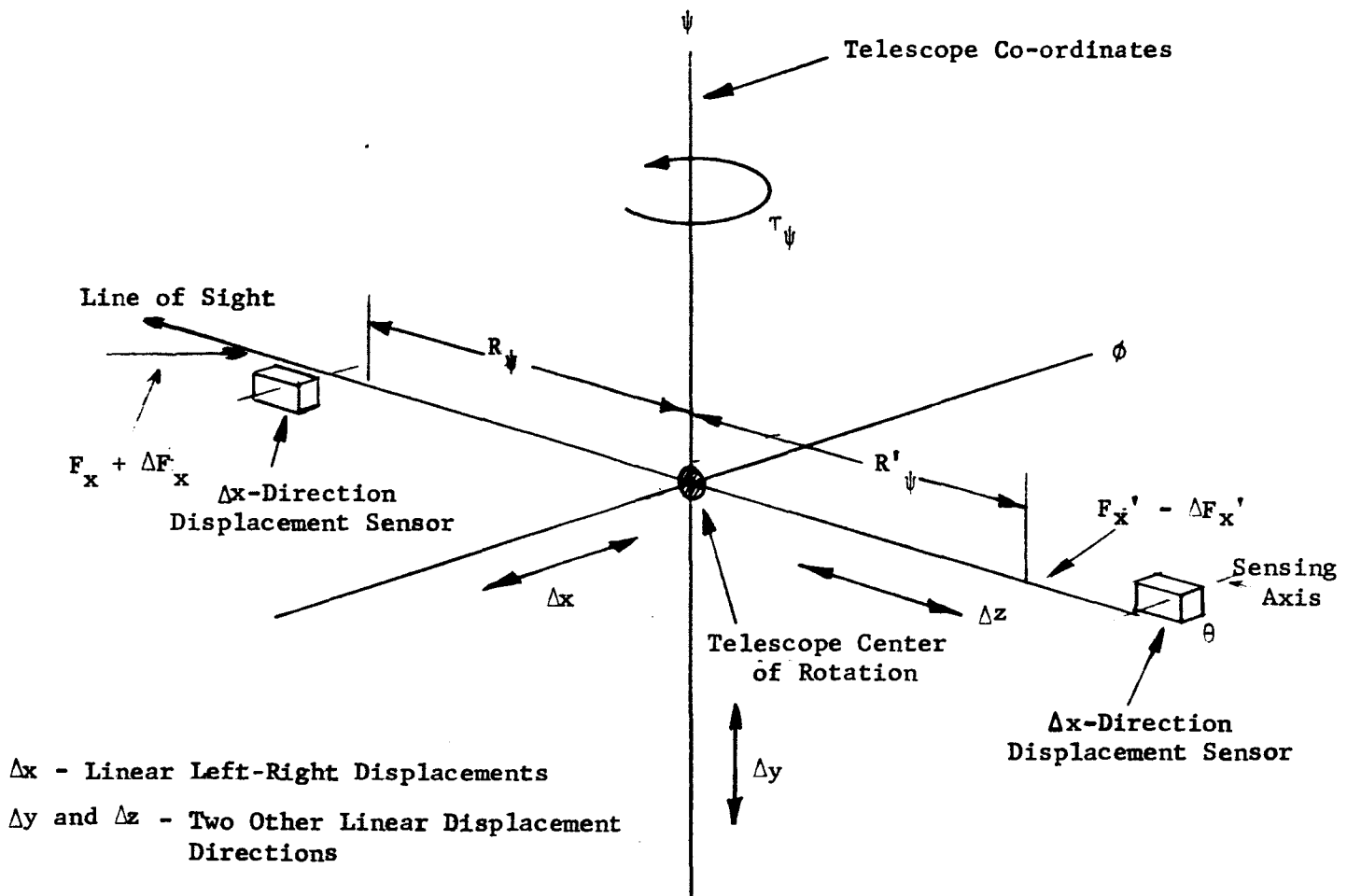


Figure 3.24. Centering Forces (Single Axis)

into each other. The main source of coupling will probably be due to the mismatch in the transfer sensitivity characteristics of the torquer and D.C. amplifier combinations in each axis. This coupling, particularly from linear motion into rotation, must be minimized to avoid degradation in pointing performance. Single axis torque cross coupling therefore becomes one of the key factors for determining the translation servo system design response.

Briefly summarizing, the factors that go into selecting the centering system design are:

1. OAO spacecraft translation dynamics
2. Centering system coupling into the pointing (guide star) axes
3. External disturbances, i.e., caging impulses and suspension system translations.



The centering servo system does not employ the integration techniques used in the rotational servo loops to achieve narrow bandwidths since sensor noise can be made negligibly small in this case. These servos (three-axis) are therefore basically second order systems containing only error rate networks to achieve a reasonable degree of stability. The servo analysis of single centering axis is summarized by the following transfer functions.

The capacitive type sensors, for all practical considerations, can be represented by a sensitivity constant,

$$\frac{V_s}{x_e} = K_{ca} \quad (3-42)$$

where,

- $K_{ca}$  = sensitivity (volts/inch)
- $V_s$  = sensor output voltage (volts)
- $x_e$  = centering displacement error (inch).  
(This error is the result of the subtraction of two sensors per axis and is actually equal to  $2x_e$ , where  $x_e$  is the relative displacement between the spacecraft and telescope.)

The rate networks are described by

$$\frac{V_{ts}}{V_s} = \frac{T_1 s + 1}{T_2 s + 1} K_b \quad (3-43)$$

where,

- $V_{ts}$  = total input voltage to torquer amplifiers (volts)
- $T_1$  = lead time constant (seconds)
- $T_2$  = lag time constant (seconds)
- $K_b$  = gain factor

The torquers, D.C. amplifier and telescope dynamics are represented by the following relationships for linear motion,

$$F_d - F_c = F_e = M \frac{d^2 x_t}{dt^2} \quad (3-44)$$

$$F_c = \frac{V_{ts} K_{ts}}{T_a s + 1} \quad (3-45)$$

$$x_d - x_t = x_e \quad (3-46)$$

where,

$F_d$  = force disturbance (lbs)

$F_c$  = force correction - sum of  $F_x + F'_x$  (lbs)

$F_e$  = error force (lbs)

$M$  = telescope mass (slugs)

$K_{ts}$  = torquer - amplifier sensitivity (  $\frac{\text{lbs}}{\text{volts}}$  )

$T_a$  = torquer - amplifier time constant (sec)

$x_d$  = displacement disturbance (inch)

$x_t$  = telescope displacement (inch)

These transfer functions can be combined to yield the centering servo open loop transfer function in terms of displacements,

$$\frac{x_d}{x_e} = \frac{(T_1 s + 1) K_{ca} K_b K_{ts}}{s^2 M (T_2 s + 1) (T_a s + 1)} \quad (3-47)$$

The transfer function (3-47) can be represented on a Bode diagram of amplitude versus frequency as shown in Figure 3.25. From Figure 3.25 the cross-over frequency was selected at 0.21 rad/sec with an open loop gain of  $0.023 \text{ sec}^{-2}$ . Using displacement disturbances of  $\pm 0.1$  inch at sinusoidal frequencies of 0.02 rad/sec a displacement servo lag error of less than 0.002 inch (peak) would occur which can be determined from the following error transfer function.

$$x_e \approx \frac{d^2 x_d / dt^2}{K_a K_b K_t} M \quad (3-48)$$

Equation (3-48) is valid for frequencies up to approximately 0.08 rad/sec.

If an uncaging force impulse of 0.5 lb is applied for a period of 0.5 second, initial velocities of 0.10 inch/sec and initial displacements of 0.025 inch would be imparted to the telescope if the centering servos are

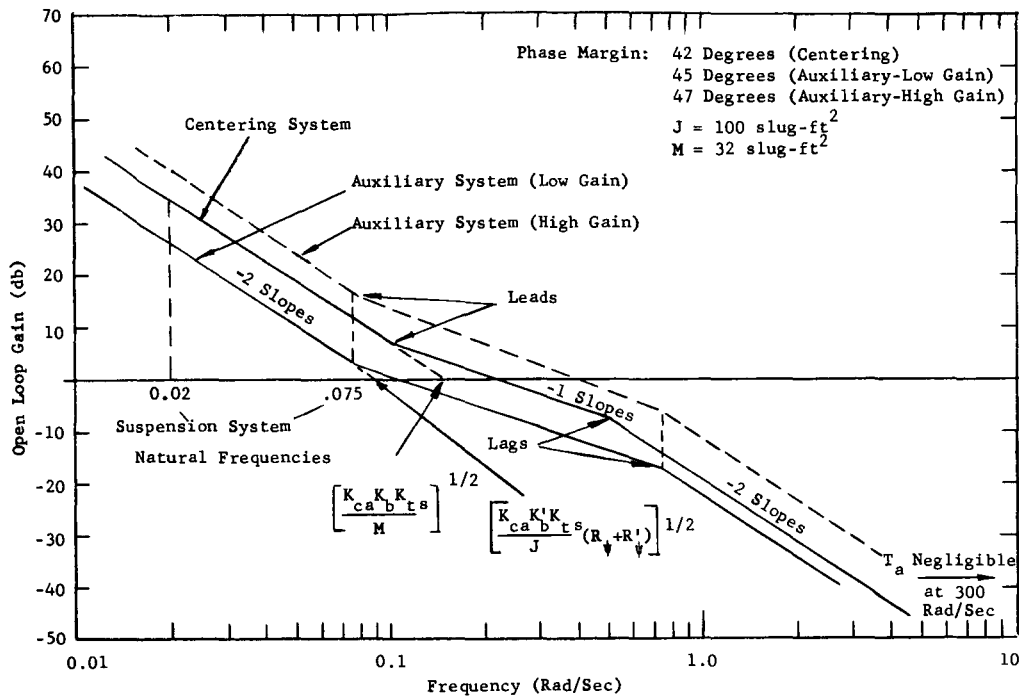


Figure 3.25. Bode Diagram Centering and Auxiliary Rotation Systems (Single Axis)

inactive at this time. (In reality the servos will be active at the time of uncaging. The transients of this nature are worst case examples.) The time to recover from these uncaging transients is approximately 30 seconds with peak overshoots in the order of 0.33 inch. The system would therefore not again cage due to uncaging transients. The design requirements for the caging mechanism are not severe in terms of the centering system performance. Similar results can be expected of the auxiliary rotational servo loops as pointed out later in this discussion.

Perhaps the most important consideration of the centering system design are the errors it couples into the rotational axes ( $\psi$ ,  $\phi$ , and  $\theta$ ) due to torquer sensitivity unbalances. (Sensitivity unbalances in the linear displacement sensors will not create conditions whereby errors due to disturbances such as uncaging or spacecraft suspension system disturbances cause pointing errors. Rotational angular motions coupled through the sensors will, however, disturb the centering system to a degree, but such pointing errors are extremely small in the final tracking mode.) For centering commands, torquer sensitivity unbalances on each axis cause force output unbalances which will torque the telescope during translation. (Conversely, pointing signals can cause translational forces for this condition.)

This type of coupling is best understood by considering the two Figures 3.26 and 3.27. Figure 3.26 shows the rotational and centering signals (single axis) being fed to the torquer — D.C. amplifier combinations represented by  $K_{ts}$  and  $K'_{ts}$ . In this case

$$K_{ts} \neq K'_{ts} \quad (3-49)$$

or

$$K_{ts} = e_b K'_{ts} \quad (e_b = \text{constant}) \quad (3-50)$$

and the vertical axis is used as an example.

From the block diagram of Figure 3.26 the analytical diagram of Figure 3.27 can be derived. Two coupling paths (No. 1 and No. 2) can exist between the centering and rotational axes but path No. 2 is neglected for the following reasons.

1. Rotational disturbances ( $\psi_d$  or torque,  $\tau_d$ ) coupling into the centering system (path No. 2) create negligible centering errors in final track.
2. The centering system, by reacting to correct rotational cross-coupling disturbances, will recouple into the rotational loop by path No. 1. However, this second order coupling becomes reduced by  $(K'_{ts} - K_{ts})^2$  and is negligible.
3. Similarly, for centering disturbances ( $x_d$  or  $F_{xd}$ ) path No. 2 is a secondary coupling error and is also reduced by  $(K'_{ts} - K_{ts})^2$ .

Therefore, considering only centering into rotational axis coupling (path No. 1), plots of pointing errors versus percentage torquer unbalance ( $e_b$ ) and centering disturbances ( $x_d$ ) can be obtained which evaluate the coupling effects. One such plot is shown in Figure 3.28 derived for the following conditions;

1. The largest centering disturbances will be due to the OAO spacecraft and specifically, those due to the suspension system (see Volume IV, Section 3.2.2.3).
2. The system or servos are in the final track modes.
3. The vertical and horizontal axes are only considered in this case.

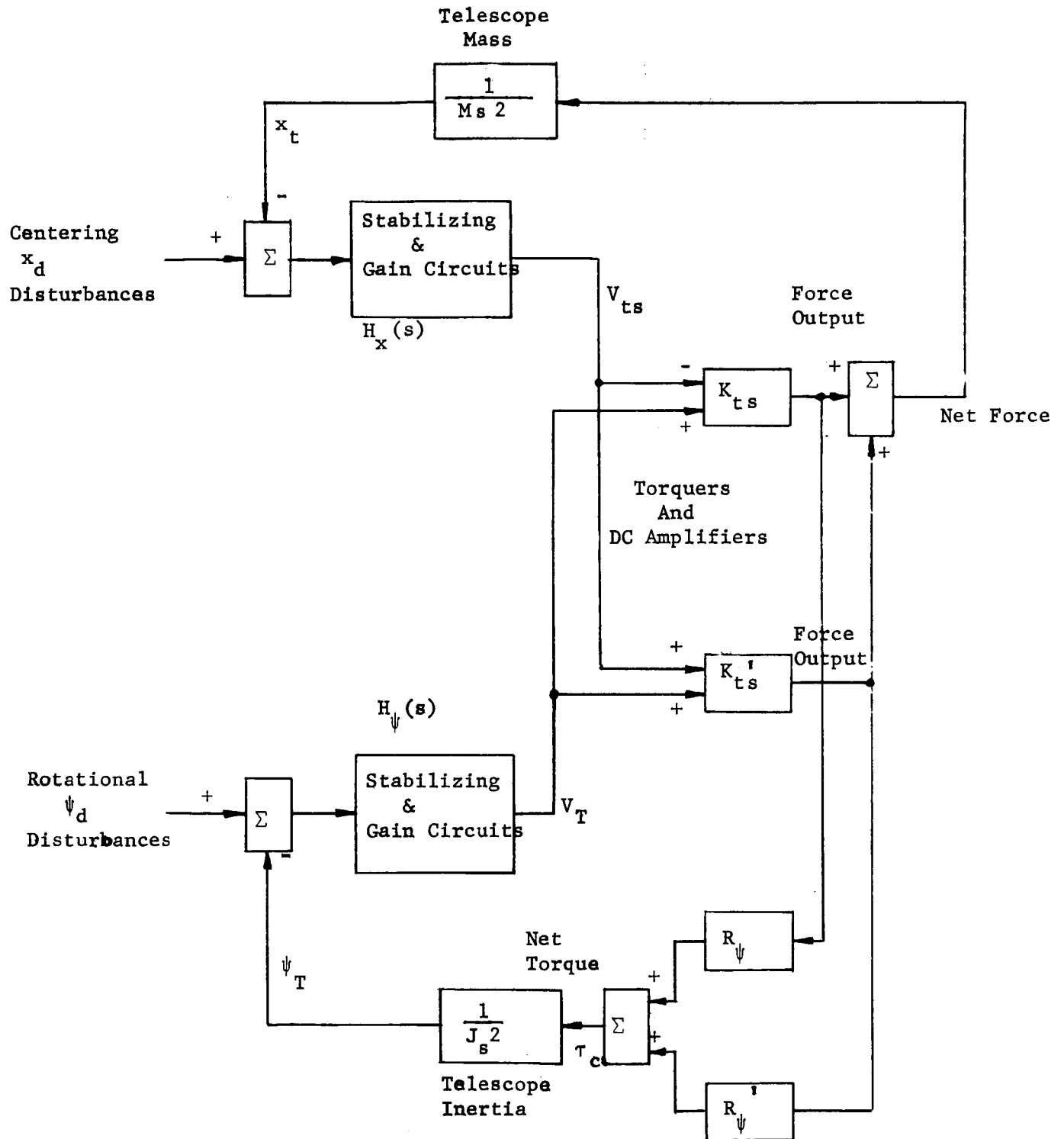


Figure 3.26. Centering System Coupling (Single Axis-Typical), Block Diagram

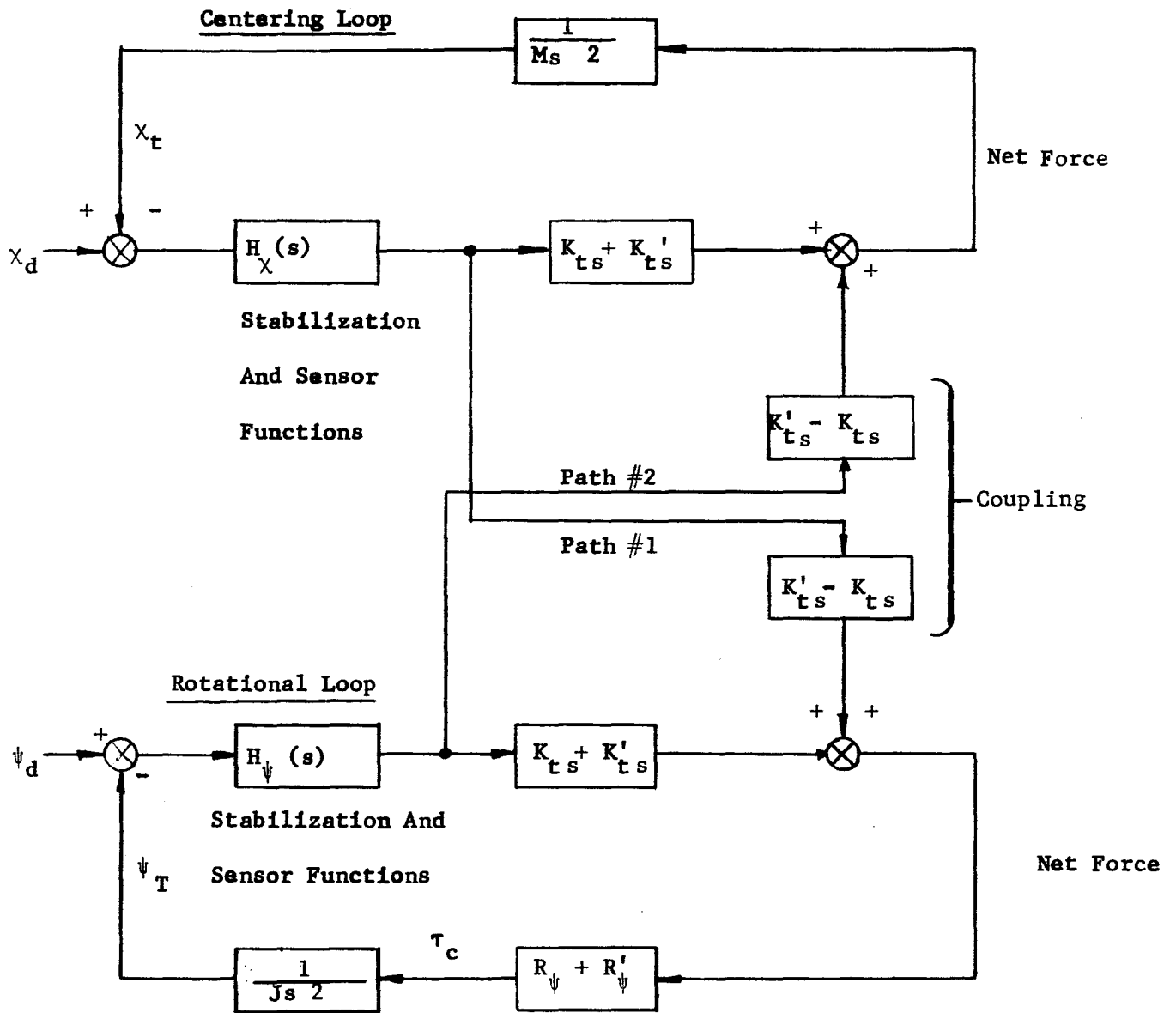


Figure 3.27. Centering System Coupling (Single Axis-Typical) Analytical Diagram

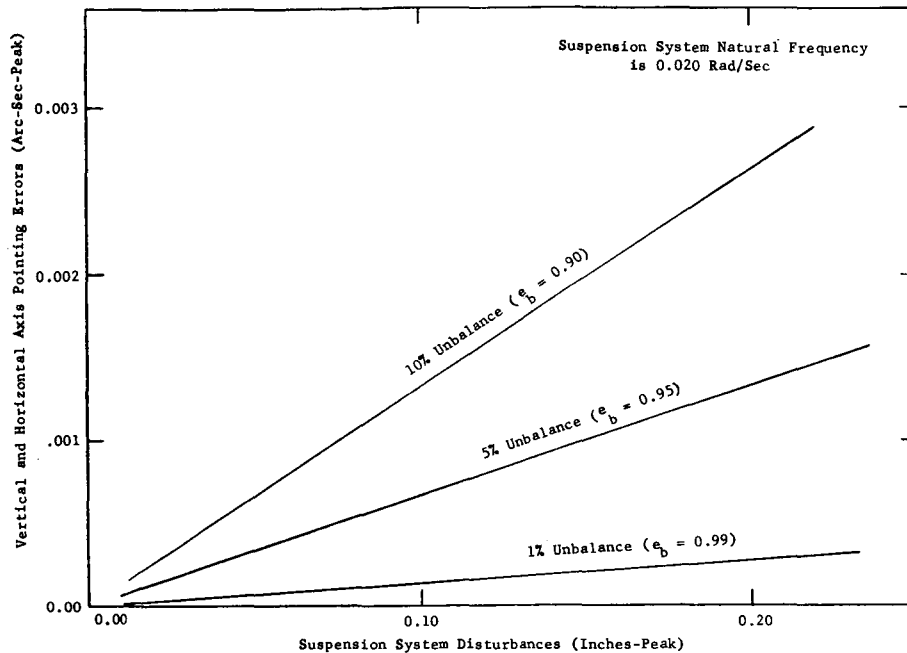


Figure 3.28. Centering System Coupling Errors Due to Torquer Unbalances

4. A moment arm ( $R$ ,  $R'$ , etc.) of 3-1/3 feet and an inertia of 100 slug-ft<sup>2</sup> was used.

Figure 3.29 has the same conditions except for the spacecraft disturbances. A natural coil spring frequency of 0.075 rad/sec was used as opposed to 0.02 rad/sec at various peak displacements.

In regard to the roll axis, coupling from the centering system is negligible for torque unbalances of 10 percent and a suspension system with 0.020 rad/sec natural frequency. One reason, of course, is due to the smaller moment arm in roll, 1.67 feet (radius). The second reason is the geometric advantage inherent in roll as explained in sections 3.4.3 (Roll Servo Analysis). For instance, at a suspension system natural frequency of 0.020 rad/sec and  $\pm 0.10$  inch displacement, a 10 percent torquer sensitivity unbalance using the final roll tracking mode, the pointing error would be (for 100 slug-ft<sup>2</sup> inertia), 0.0725 arc-sec (peak). Compared to the 4 arc-sec (rms) pointing error required (worst case), this is a negligible effect. Higher natural (0.075 rad/sec) suspension system frequencies are more severe but not as intolerable as those shown in Figure 3.29 for

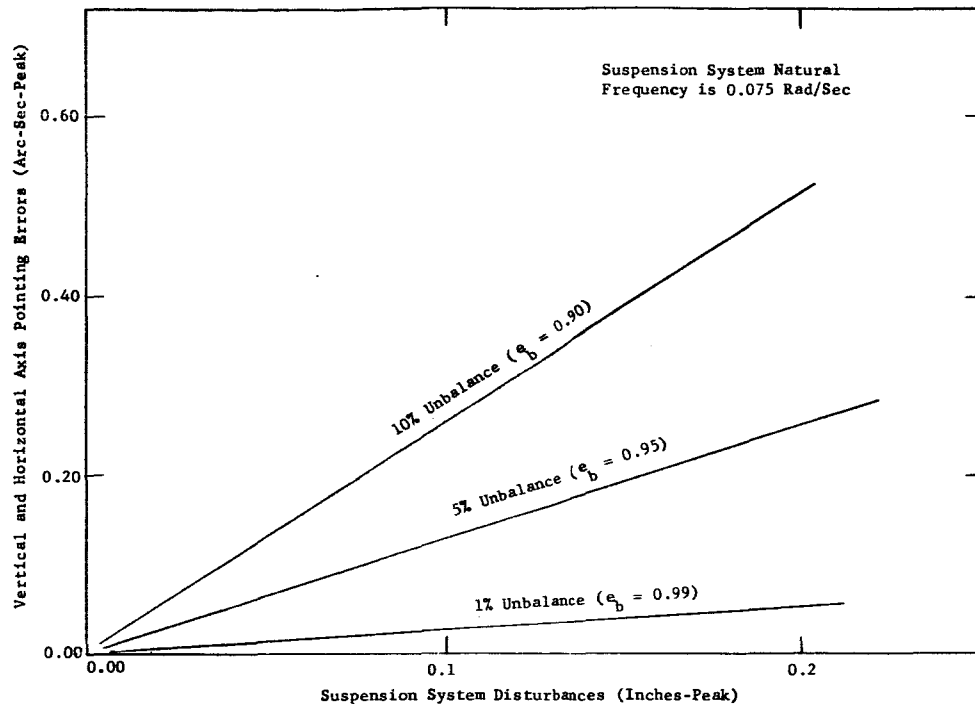


Figure 3.29. Centering System Coupling Errors Due to Torque Unbalance

the vertical and horizontal axes. At a peak displacement of  $\pm 0.10$  inch and 10 percent torquer unbalance, roll pointing errors are in the order of 3.5 arc-sec (peak) which is still within the 4 arc-sec (rms) required for guide star locations.

**3.4.5.4 Auxiliary Rotational Loop Description** - The auxiliary rotational servo loops are nearly identical to the centering servo loops. The inputs to the torquer and amplifier combinations are phased to produce telescope rotation rather than translation. The linear sensor outputs are added rather than subtracted to obtain rotational signals (with respect to the OAO spacecraft) free of centering signals. A block diagram is shown in Figure 3.30 for a single axis auxiliary rotational servo.

The pointing specifications selected for the auxiliary servos are  $\pm 0.5$  arc-min in all three axes. These angular errors are specified with respect to the OAO spacecraft. If the displacement sensors are located at a 55-inch radius (typical), they must sense displacements of at least 0.008 inch.

**3.4.5.5 Auxiliary Rotational Servo Analysis** - The servo dynamics in this control mode are nearly identical to the centering system in terms of transfer functions. The closed loop servo is basically a second order system



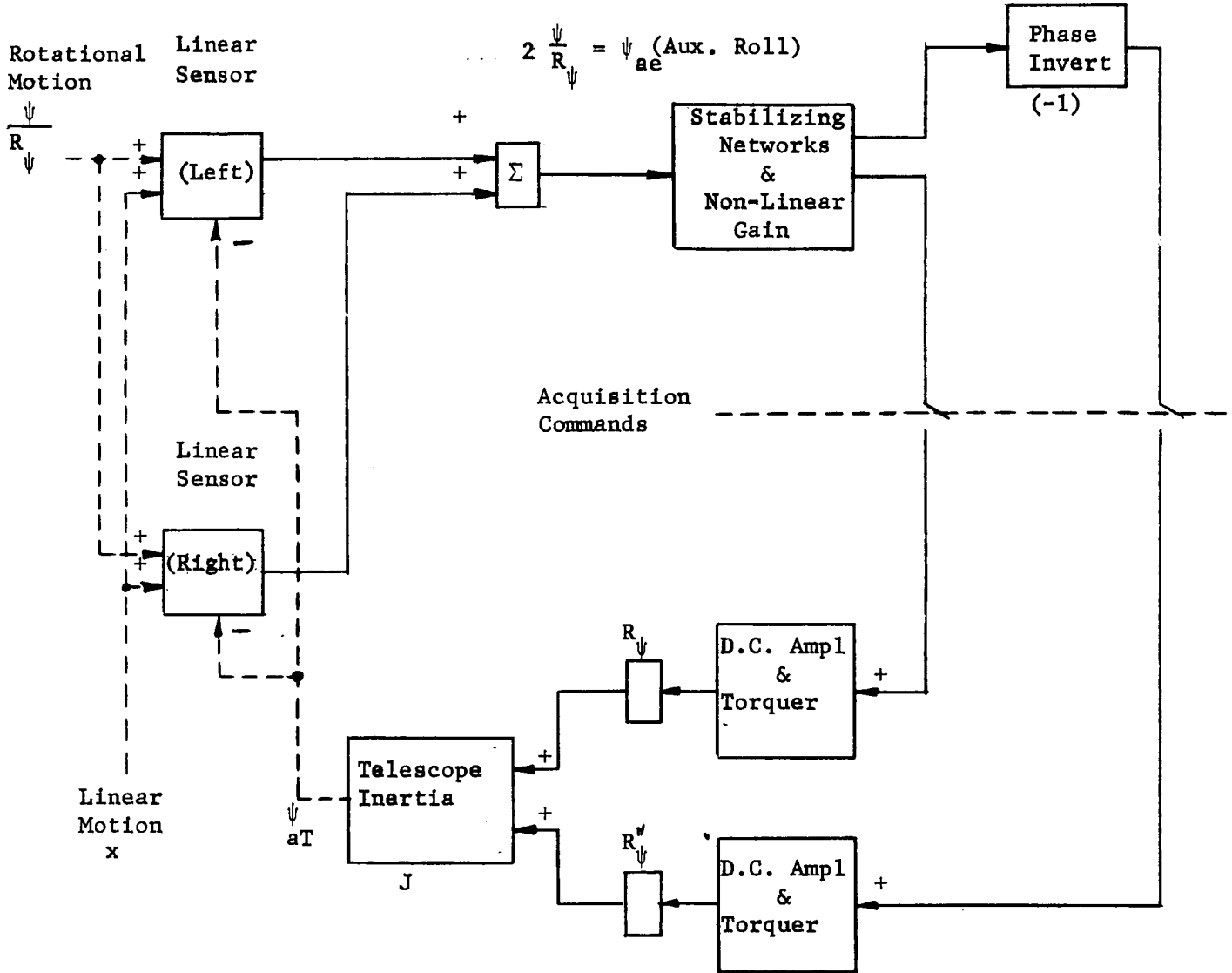


Figure 3.30. Auxiliary Rotational (Single Axis) Block Diagram

consisting of error rate networks to achieve stability. The equation for the displacement sensor, error rate networks, and torquer-amplifiers are identical to those given in Section 3.4.5.3. The only exception is the nonlinear gain ( $K'_b$ ) explained later. The telescope inertia relationships can be substituted for the mass relationships of Section 3.4.5.3 and by substitution, the final open loop transfer function can be obtained for a single axis, in this case, the horizontal axis.

$$\frac{\psi_d}{\psi_{ae}} = \frac{(T_1 s + 1) K_{ca} K'_b K_{ts} (R_\psi + R'_\psi)}{J_s^2 (T_a s + 1) (T_a s + 1)} \quad (3-51)$$

where,

- $\psi_d$  = angular displacement disturbance (rad)
- $\psi_{ae}$  = angular relative error between spacecraft and telescope (rad)
- $K_{ca}$  = sensor sensitivity (volt/inch)
- $K'_b$  = adjusted loop gain for the auxiliary servo loop (nonlinear)
- $K_{ts}$  = torquer sensitivity (lbs/volt)
- $J$  = telescope inertia (slug-ft<sup>2</sup>)
- $T_1, T_2$  = error rate network time constants (sec)
- $R_\psi, R'_\psi$  = moment arms for torquers (ft)
- $T_a$  = torquer-amplifier lag (sec)

The vertical and roll auxiliary axes are identical.

Equation (3-51) has been plotted in Figure 3.25 with actual values. The loop gain was selected at 0.008 sec<sup>-2</sup> (low) and 0.04 sec<sup>-2</sup> (high) with a phase margin of 45 degrees in the low gain mode. The low gain mode will reduce the high frequency OAO spacecraft perturbations sufficiently to allow the gyro to erect with the minimum amount of error. The high gain mode is used mainly to quickly reduce the effects of uncaging impulses. The nonlinear gain ( $K'_b$ ) will be simply a 5:1 linear variation with angular displacement error. With this type of performance, the auxiliary loops can be easily used for "Vernier Caging" or positioning (scanning) applications at reasonable cycling rates. Uncaging impulses similar to those used for the centering system can also be tolerated (see Table IV).

### 3.5 OPTICAL SENSOR AND PROCESSING ELECTRONICS

#### 3.5.1 Requirements

Several optical sensor design features are desirable if minimum telescope pointing errors are to be realized and hardware reliability is to be maximized. An optimum sensor mechanization in this regard would be one which offers all of the following advantages.

1. Utilizes the photon beam signal at all times to maintain maximum signal to noise (S/N) ratios for a given bandwidth.
2. Uses photomultipliers with high quantum efficiency, wide wavelength response, and low dark current with gain high enough to avoid noise contribution from subsequent electronics.
3. Uses the minimum number of photomultipliers.
4. Has the ability to continue functioning, at perhaps reduced performance level, in the event of a photomultiplier failure (assuming, of course, more than one tube performs the same function).
5. Employs techniques to maintain low ambient temperature around the phototubes to minimize dark current changes.
6. Is mechanized to avoid pointing errors due to changes in photomultiplier gain and dark current.
7. Utilizes biasing and preamplifier electrical designs requiring minimum power.
8. Includes techniques (such as pressurization) to avoid high voltage breakdown between closely spaced electrodes in space environments.
9. Incorporates electrical pulse processing techniques to minimize cosmic radiation noise contributions.
10. Designed to be capable of long-term operation in a hard vacuum.
11. Employs techniques to optimize the signal-to-noise ratio for a wide variety of light intensity sources.

Several of these advantages are attained immediately by use of frequency or phase-coded optical chopping, or light modulation (see Volume II, 4.2). Specifically, item six is a direct advantage of optical chopping techniques. Items three, four and seven result because fewer phototubes can be used for sensing. The remaining requirements involve the details of hardware design which are discussed in context in the following section of a specific optical sensor design.

### 3.5.2 General Description

In this discussion, signal-to-noise (S/N) considerations for the sensor itself will not be pursued to any extent since it is a subject which has been quite thoroughly investigated in Volume II, Section 4.0 and the previous portions of this section. Signal-to-noise is mostly a matter of photometric calculations in conjunction with a photocathode which, in this case as well as previous cases, is considered to be of the S-20 response variety. A second consideration, in this respect, would be noise contribution from the sensor electronics. However, these noise sources are generally small by comparison since the S-20 type photomultipliers have relatively high sensitivity, i.e., 0.043 amp/watt at 0.5m wavelength.

The RCA 7265 phototube studied has an S-20 response characteristic. General specifications for the RCA 7265 14-stage tube are:

Spectral Response - S-20	- Typical 10% quantum efficiency with a spectral response of 0.1 micron (conservative, can extend to 0.25 micron at a 0.55 micron wavelength).
Maximum Response	- 4200 ±500 angstroms
Window Area (Head on)	- 2.2 sq. in.
Maximum Voltage Rating	- 3000 vdc between cathode and anode
Current Amplification	- $9.35 \times 10^6$ median
Equivalent Anode Dark Current (measured at a 2870° tungsten color temperature and using filters)	- $2 \times 10^{-10}$ lumens (median)

Among the numerous specific sensor mechanisms considered, the approach that satisfied the majority of requirements is the one shown in Figure 3.31 which incorporates the below listed salient features.

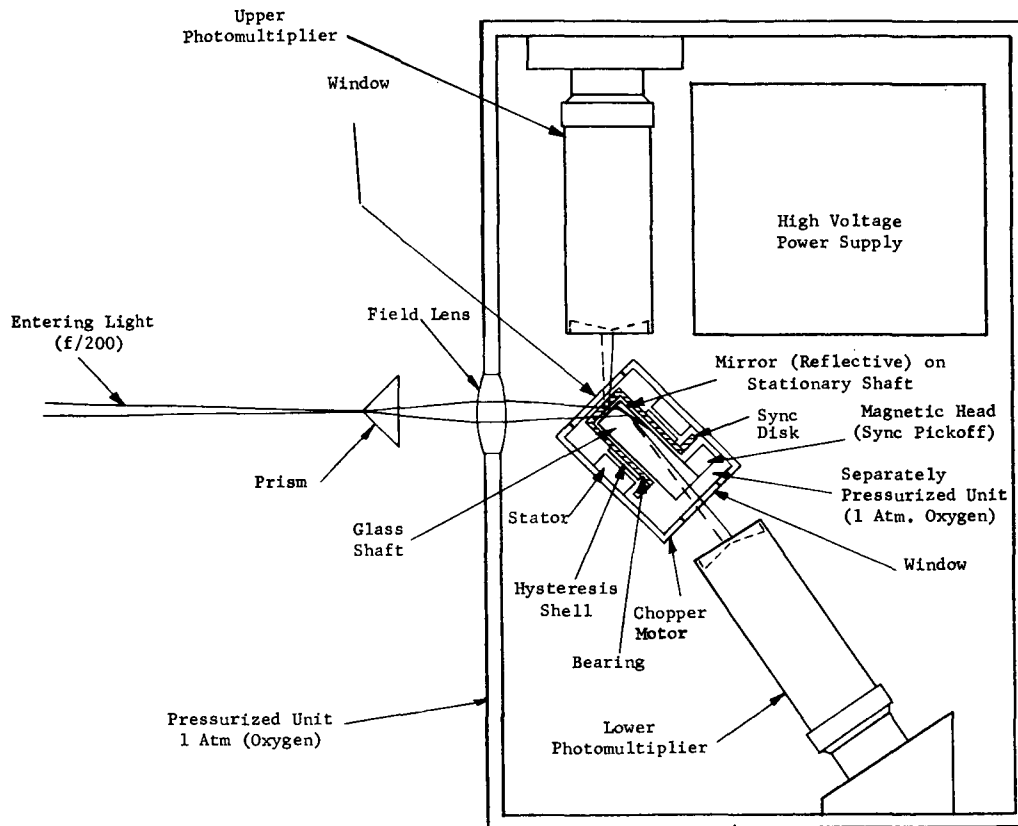


Figure 3.31. Optical Sensor Mechanization

1. An image dividing prism with a positive field lens which serves to keep the guide star images relatively fixed in space for angular telescope motions of up to  $\pm 30$  arc-seconds.
2. An optical chopper that utilizes a circular spinning reticle and an air-bearing hysteresis motor.
3. Two photomultipliers (type S-20) with high sensitivity characteristics are utilized to collect one hundred percent of the optical signal (guide star light).
4. A pressurized chamber which contains the photomultipliers, optical chopper and a high voltage power supply.

This sensor scheme operates in the following manner:

Guide star light entering the 40 inch telescope aperture is eventually focussed at the apex of the prism in the f/200 focal plane to form a single image. The prism divides the images into four equal parts for zero angular pointing errors, spacing them symmetrically and separating them adequately. For angular offsets, the image intensities become proportionately unbalanced and permit determination of angular displacement errors. These images are then directed through a field lens which fixes their position in space, or more specifically, on the face of the spinning reticle for all pointing errors. Normally, in the f/200 optical focal plane, image motion is 1 inch for 25.7 arc-seconds of angular error. This would result in large reticle size since image motion can occur over the full sensor field of view, which is at least 1 arc-minute. The field lens effectively reduces this image motion to negligible values. The divided images (0.03 inch in diameter) are shown in Figure 3-32 as they appear on the reticle face, with typical dimensions for the f/200 focal plane. The reticle itself

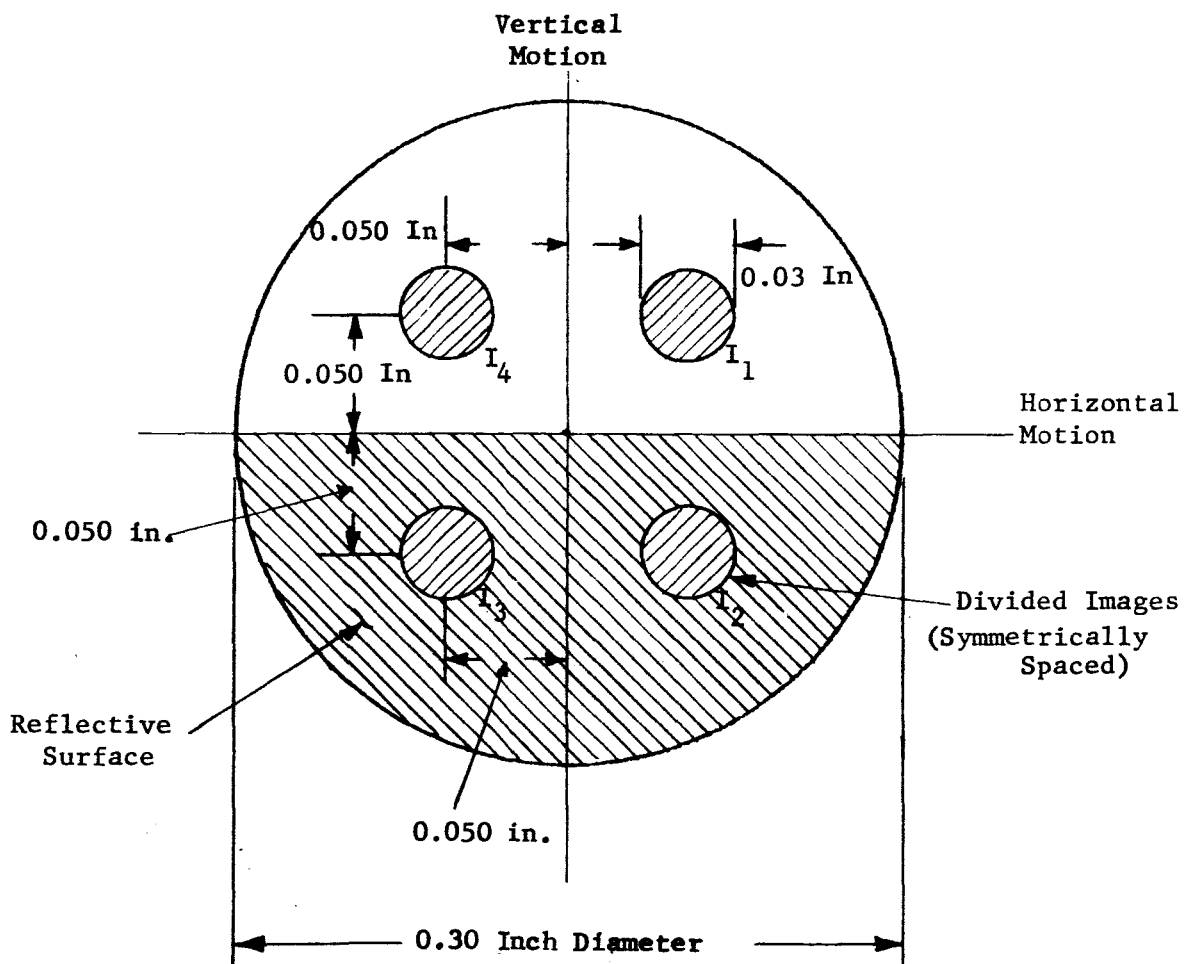


Figure 3.32. Image Location on Reticle Face

is located at a distance of approximately six inches behind the prism. It is circular and equally divided into a reflecting surface and a transparent surface.

Two photomultipliers are used to collect one hundred percent of the star light. Considering the images of Figure 3.32 denoted by intensities  $I_1$ ,  $I_2$ , and  $I_4$  for instance, images  $I_2$  and  $I_3$  would be reflected into the "upper" phototube of Figure 3.31, while images  $I_1$  and  $I_4$  would pass through the reticle and glass motor shaft to the "lower" phototube. One of the phototubes could fail and the sensor would continue to operate; however, a 2:1 reduction in signal would result.

The optical chopping principle is best described by waveforms at the preamplifier outputs. The reticle spins at an angular rate of 2400 rpm, chopping the images to produce 40 cps square wave photomultiplier outputs. The phototube outputs are then A.C. coupled to a wideband preamplifier which eliminates the D.C. component as well as amplifies the electrical signals (see Figure 3.33 for the electrical schematic). The result is the preamplifier output waveforms shown in Figure 3.34, where the amplitude of each waveform is proportional to the image intensity. The angular error phasing, amplitude and axis information is then obtained from these waveforms by (1) summing the two preamplifier output signals (reflected and transmitted), (2) feeding these signals through a pair of pulse processing networks,\* and (3) feeding the pulse processing circuit outputs to two synchronous demodulators which have been excited by the horizontal and vertical synchronization frequencies (also shown as waveforms in Figure 3.34. The synchronization frequencies are obtained from a magnetic head which accurately (3-5 degrees) determines the angular position of the spinning reticle to detect the instant the images are chopped. One frequency is phased 90 degrees with respect to the other to obtain the proper axis information. The output of the demodulators are summed and subtracted as follows to yield D.C. voltages proportional to telescope angular error in each axis and both angular directions.

$$\text{Horizontal Demodulator Output: } V_{I_3} - V_{I_1} \quad (3-52)$$

$$\text{Vertical Demodulator Output: } V_{I_4} - V_{I_2} \quad (3-53)$$

Subtracting the horizontal and vertical demodulator outputs results in,

$$V_{\phi} = (V_{I_3} + V_{I_2}) - (V_{I_1} + V_{I_4}) \quad (3-54)$$

---

\*Subject to further investigation.

3-75

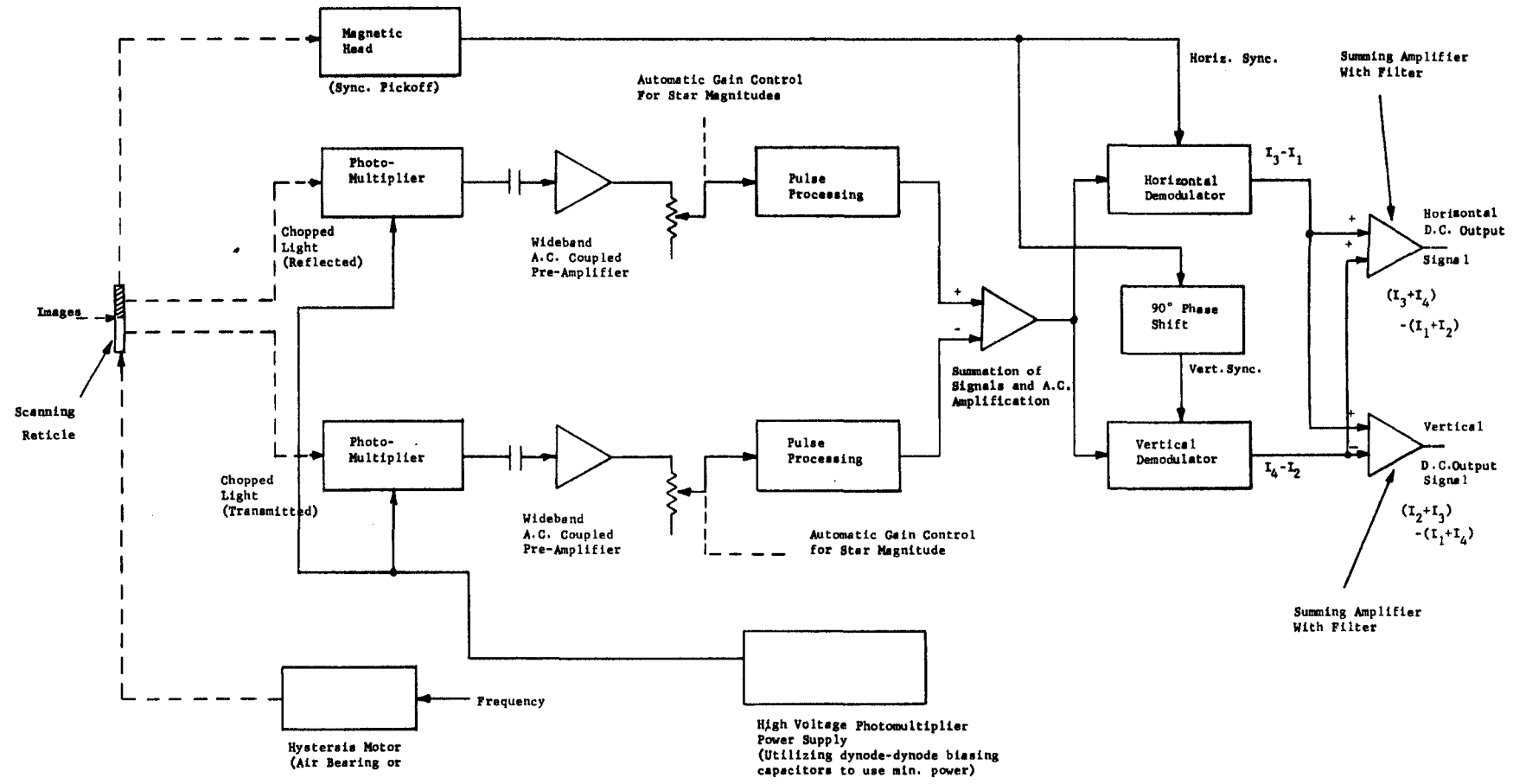


Figure 3.33. Sensor Electronics (Two Axis)



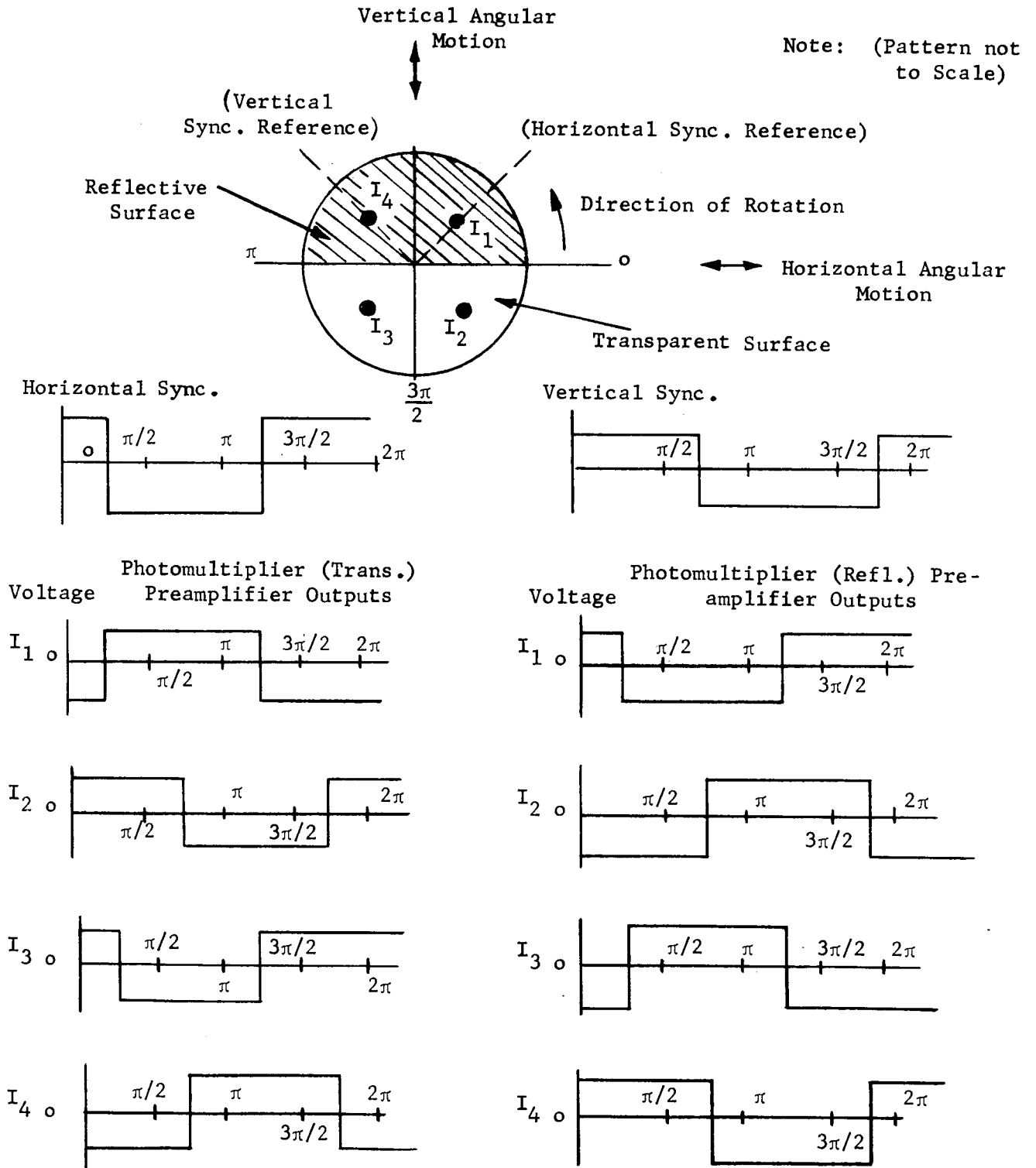


Figure 3.34. Typical Output Wave Forms

Adding the horizontal and vertical demodulator outputs signals in,

$$V_{\psi} = (V_{I_4} + V_{I_3}) - (V_{I_1} + V_{I_2}) \quad (3-55)$$

where,

$V_{I_1}, V_{I_2}, V_{I_3}, V_{I_4}$  = the individual voltage components proportional to each image intensity (I).

$V_{\phi}$  = the voltage output proportional to vertical angular error.

$V_{\psi}$  = the voltage output proportional to horizontal angular error.

Equations (3-54) and (3-55) are valid for both the linear and nonlinear sensor regions (see Figure 3.9).

One other major feature that is incorporated in the sensor electronics is an automatic gain control. Essentially a variable potentiometer, the sensor gain is adjusted or controlled as a function of photomultiplier output current. In the case of brighter stars, the photomultiplier output current will be higher and thus a gain reduction is necessary to maintain the same volts to angular displacement sensitivity at the sensor output.

Further design details are given in the following section but, at this point, some of the advantages of the system can be enumerated.

The optical chopping technique reduces the required number of photomultipliers to one although a second is used (reflective) to achieve full advantage of the optical signal (or star light). Secondly, slow varying D.C. components of dark current due to temperature changes are effectively eliminated by A.C. coupling the photomultipliers to preamplifiers which is only possible if the phototube outputs are modulated or of A.C. form. Finally, excessive photomultiplier sensitivity changes are taken into consideration automatically with the automatic gain changing control.

The optical chopper or spinning reticle design was selected on the basis of functional simplicity. Other techniques such as vibrating reeds encounter difficulties. Achieving large motions or displacements (see Figure 3.32) at high frequencies required is a problem for a reed or a tuning fork. Secondly, if phase synchronization (or phase modulation) techniques are to be used such as discussed above, to recapture the information in the forms of a D.C. voltage output, at least two sets of reeds are required per sensor.

Frequency modulation techniques can be employed which reduce the amount of vibrating reeds to one set, but with this technique, higher harmonics can create severe axis cross-coupling errors. A rotary chopper avoids most of these problems.

The one major drawback of a rotary chopper is the requirement for a bearing which, in space, can be a source of failure. This reliability problem is nearly eliminated, however, with air bearing motors as discussed in the following sections.

### 3.5.3 Detailed Design Considerations

3.5.3.1 Reticle Misalignment Errors - Reticle misalignments will contribute to steady-state offset pointing errors. This source of pointing error is not simply a result of the image displacement at the  $f/200$  focal length (25.7 arc-seconds per inch) but rather a function of the image intensity balance characteristics of the sensor. An evaluation of this source indicates that the tolerance required is not particularly difficult to meet. A reticle misalignment of 0.02 inch would only create an angular offset error of 0.017 arc-second. This error is D.C. in nature and simply means the object would appear slightly offset in the detector formats which for comparison will have at least a 20 x 20 arc-second format.

3.5.3.2 Synchronization and Cross-Coupling Errors - Unlike the reticle misalignments, synchronization errors will not create steady-state offset pointing errors but instead result in a loss of sensitivity and cross coupling. Synchronization errors result from the inability to perfectly determine the reticle position in time due to alignment imperfections. Fortunately, the requirements are not severe. The experience obtained from presently operating star trackers (Perkin-Elmer instruments) using similar types of optical choppers indicate synchronization errors can be held to 3-5 degrees. The loss in signal level due to this type of error for a single axis is 3.3 - 5.5% at  $\pm 1.22\lambda/D$  ( $\pm 0.140$  arc-second) angular displacements. In terms of servo pointing errors, this is a negligible offset. At errors of 0.001 arc-second for instance, the error would increase by only  $5.5 \times 10^{-4}$  arc-seconds. Axis coupling is also quite negligible. For a horizontal synchronization error of 5 degrees, cross coupling into the vertical axis would only amount to 0.0077 arc-second for a maximum horizontal signal of 0.14 arc-second.

Another source of cross coupling in the sensor electronics could occur from cross feed inaccuracies from the demodulator outputs to the summing amplifier inputs. However, with accurate calibrations and temperature compensated circuit designs, coupling errors of this nature can be made negligible, i.e., 2 percent or less.

3.5.3.3 Chopper Implementation - The most critical area of implementation will be the optical chopper mechanism. As stated, reliability is a problem with rotating devices and is the reason for utilizing an air bearing. Air bearings have extremely long operational lives, on the order of years, if proper pressurization is maintained and they are not subjected to severe vibration or shock. In space, the zero "g" environment, of course, aids their reliability. During launch, in the case of high "g" forces, they will be stationary and protected since the chopper motors will be inoperative during this time.

The hysteresis motor assembly has been shown in Figure 3.31. It consists of the air bearing, a hollow cylinder to which the reticle is mounted and suspended on the pressure of a gas (such as oxygen). Other gases can be used such as helium but are more difficult to contain. Oxygen does not have high conductivity in terms of heat transfer, but this does not appear to be a problem at this time. Inside the air bearing is a fixed transparent (glass) shaft which contains a reflecting mirror that directs the entering light through the motor. A pancake configuration of the shaft could avoid this latter complexity but a general requirement of these motors is to maintain a length of shaft to diameter ratio of 3. A hysteresis shell is also mounted on the bearing directly opposite, or concentric with, the stator. The air bearing-reticle-hysteresis shell combination is, therefore, freely suspended by oxygen pressure. To the rear of the air bearing, a "sync" disk is mounted which, in conjunction with a magnetic head mounted adjacent to the sync disk and fixed to the motor frame, serves to provide the synchronization signals for the sensor demodulators. The air bearing and motor assembly is pressurized to approximately one atmosphere. A sealed frame surrounds the motor assembly with a front and rear window to allow the guide star images to enter and exit. Minimum pressurization levels are in the order of 1/2 atmosphere. The one atmosphere pressurization level allows a considerable leak rate margin. Similar pressurization techniques used in OAO - C (such as in the chopper assemblies) indicate leak rates are in the order of  $5-6 \times 10^{-7}$  cc/sec for helium have been achieved. At this rate, it would take several years to lose 7.5 psi or 1/2 atmosphere. Oxygen leak rates are comparable if not lower. In addition, for other reasons explained later, the motor will be located inside a larger container which is also pressurized to an identical value. Theoretically, therefore, assuming no temperature gradient exists, zero leak rate will occur from the motor to the inside of the larger container as long as the outer container is leak free.

The motor is a hysteresis device which can provide a constant rpm to high accuracies commensurate with the excitation accuracy. The motor speed was selected at 2400 rpm (40 cps) for the following reasons. To conserve power, a low spin rate is desirable, but due to practical considerations, air bearing motors are rarely operated lower than 1700-1800 rpm. A slightly higher rpm such as 2400 rpm, provides a margin of safety, but will remain below a frequency of 60 cps. For testing purposes, chopping at frequencies other than 60 cps is desirable to avoid interferences. Finally, frequencies of 40 cps are more than adequate in terms of information sampling rates. The servo loop bandpass frequencies are usually no higher than 1/3 cps and, in general, sampling frequencies of twenty times this value are sufficient.

3.5.3.4 High Voltage Considerations - High D.C. voltages in the order of 2000-2400 VDC are going to be required to bias the photomultipliers. One of the most troublesome problems with high voltages is the susceptibility to flashover between adjacent photomultiplier electrodes and chronic arcing in slight atmospheres. In a report submitted by Edmonds & Rahn (Electronic Equipment Engineering, October, 1959, it is shown that arcing can occur,

for instance, at potentials (between electrodes) of less than 150 VDC for electrode spacing of 0.30 inch and low relative air densities of 1.5 mm. If the air density is increased to 1 atmosphere (760 mm), flashover would not occur until 9000 VDC. For the photomultiplier considered here (RCA 7265) electrode spacing of 0.2 to 0.3 inches is typical with potentials between electrodes of no greater than 200 VDC. In space, atmosphere is, of course, normally non-existent but could possibly be created by sources such as the OAO gas jets used for stabilization. Pressurizing the high voltages sources, therefore, provides a safety feature in space and even during launch for varying air densities. For these reasons, as well as the pressurization requirements of the hysteresis air bearing motor, it is desirable to encapsulate the photomultipliers as well as the high voltage power supply in a pressurized chamber. Such a chamber is shown in Figure 3.31 with a sealed window to allow the guide star images to enter. Leakage from the chamber can be made low and is not a problem since (1) the hysteresis motor is separately pressured and (2) the 9000 VDC flashover potential obtained at 1 atmosphere could be reduced to 500 VDC (0.03 atmospheres or less) which is still a reasonable margin of safety.

### 3.6 GYRO AND LINEAR SENSORS

#### 3.6.1 Gyro and Electronics

The gyroscope will be used as a roll reference for the telescope pointing system in the absence of a second guide star and will also act as an aid during acquisition. The gyro to be used is the single degree of freedom floated rate integrating type similar to the Honeywell Type GG159 gas bearing gyro. The theory of the gyro is well known and will not be given here.<sup>3,4</sup>

The equation describing the relative angle between the case and the floated gimbal is

$$\theta_{gc} = \frac{\frac{H}{C} \dot{\theta}_1}{s \left( \frac{J}{C} s + 1 \right)} - \frac{\frac{K_t I_{tg}}{C}}{s \left( \frac{J}{C} s + 1 \right)} - \frac{\frac{J}{C} \ddot{\theta}_o}{s \left( \frac{J}{C} s + 1 \right)} \quad (3-56)$$

where

$\theta_{gc}$  = relative angle between the case and the floated gimbal (radians).

H = angular momentum of the gyro wheel (dyne-cm-secs).

C = viscous damping coefficient of the gyro fluid (dyne-cm-secs).

J = polar moment of inertia of the output axis of the gyro (dyne-cm-sec<sup>2</sup>).

$$\begin{aligned} \dot{\theta}_i &= \text{angular rate of the gyro case about the input} \\ &\quad \text{axis with respect to space (sec}^{-1}\text{)} \\ \ddot{\theta}_o &= \text{angular acceleration of the gyro case about} \\ &\quad \text{the output axis with respect to space (sec}^{-2}\text{)} \\ K_t &= \text{gyro torque generator scale factor } \left( \frac{\text{dyne-cm}}{\text{amp}} \right) \\ i_{tg} &= \text{current in the torque generator (amps)} \end{aligned}$$

The equation results in the equivalent block diagram of Figure 3.35, where the torques acting about the gyro output axis are shown. (From the equation, it can be seen that, in the steady state where  $i_{tg} = 0$ ,

$$\theta_{gc} \approx \left( \frac{H}{C} \right) \left( \frac{\dot{\theta}_I}{s} \right)$$

which is the reason these gyros are called rate integrating gyros.

The block diagram shows a block called "spurious torques." In normal applications these torques consist of gravity sensitive torques and non-gravity sensitive torques. Gravity sensitive torques, for obvious reasons, will be neglected here.

The non-gravity sensitive torques are attributable to two sources:

1) Magnetic reluctance torques due to asymmetry in the magnetic paths around the signal generator and torque generator. These torques are effectively spring gradient type and are a function of the relative angle between the gimbal and case. Careful manufacturing techniques match the null of these gradient torques with the null of the signal generator.

2) Flex lead torques caused by the electrical leads which are brought from the case to the gimbal.

Both of these torques are made as close to zero as is possible by the gyro manufacturer and normally create trimable drift rates less than  $0.1^\circ/\text{hour}$ . These torques also have a stochastic characteristic. This random characteristic is usually found by measuring the "random deviation in drift rate for a stabilized gyro with the output axis of the gyro vertical." Since the output axis is vertical the g sensitive drifts are zero (with the exception of the density gradient drift). For gas bearing type gyros, these random drift rates are typically less than  $0.003^\circ/\text{hour}$ .

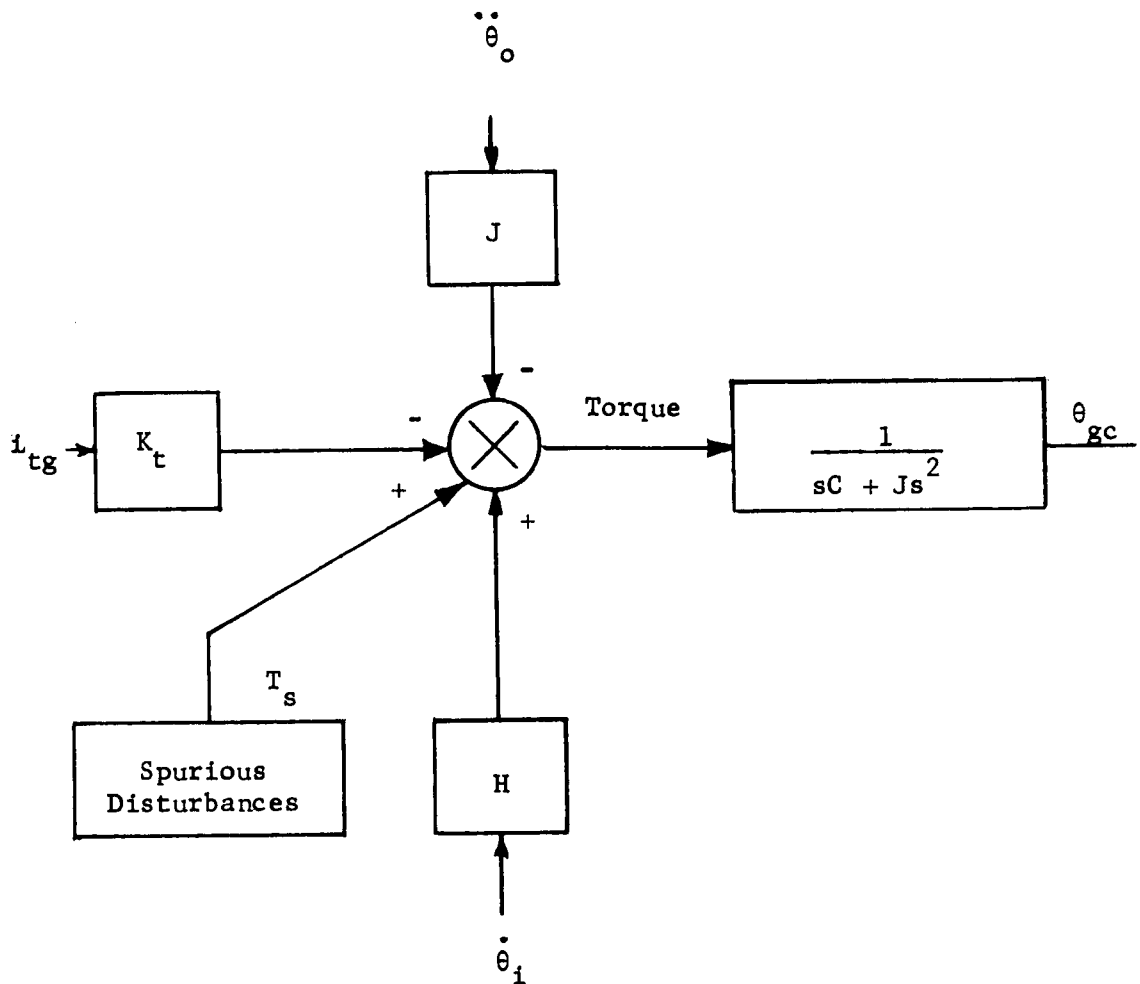


Figure 3.35. Torques Acting on Gyro Gimbal

The term  $\ddot{\theta}_o \frac{J}{s \left( \frac{J}{C} s + 1 \right)}$  is a torque coupled into the gimbal by angular accelerations about the output axis. In our configuration,  $\ddot{\theta}_o$  would represent pitching and/or yawing accelerations of the telescope which are negligible.

To use the gyro as a stable positional reference, it is necessary that the spurious torque terms be balanced. To achieve this, the gyro is first put into a "spring mode." A block diagram of this is shown in Figure 3.36.

This scheme trims out residual drift by placing switch S1 in its down position until the rate of the telescope is essentially zero with respect to inertial space. The voltage output of the operational amplifier

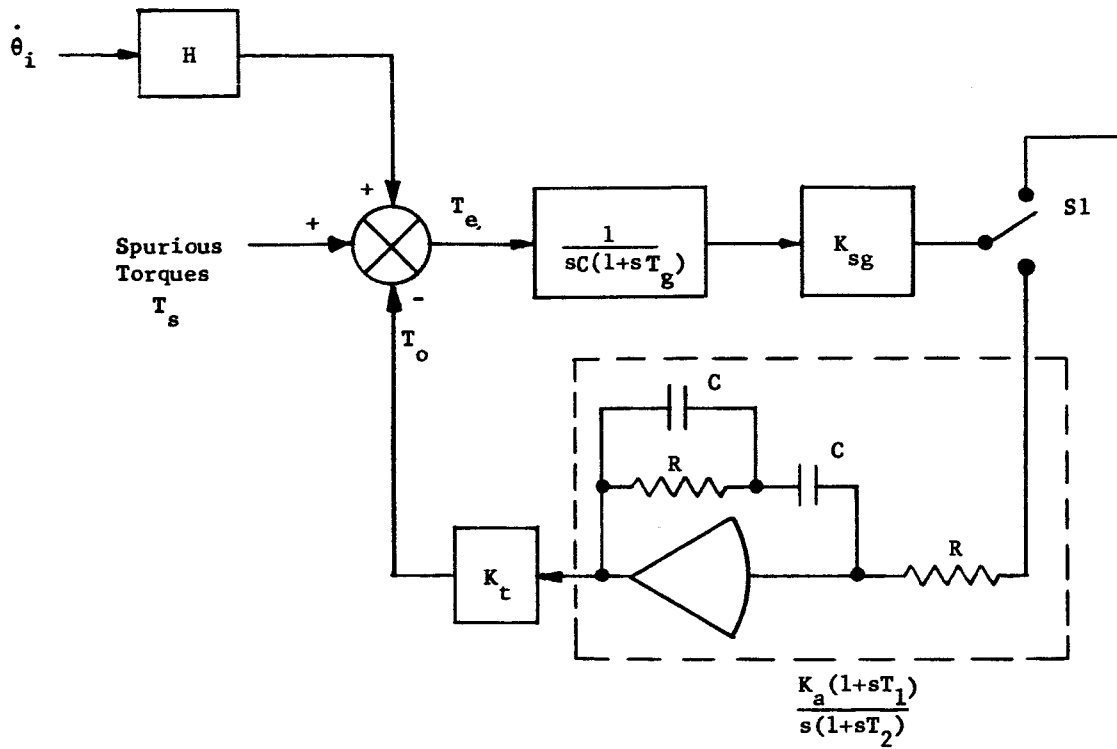


Figure 3.36. Gyro "Spring" Loop

is then the voltage required to generate a torque equal and opposite to the spurious torques. This voltage is held at the input to the torque generator when switch S1 is placed in its "up" position, and the gyro output will thereafter be equal to the telescope motion, plus the integral of the random part of the spurious torques.

An analysis of this servo loop is given by:

$$\frac{T_o}{T_e} = \frac{\frac{1}{C}}{s(1+sT_g)} K_{sg} K_a \frac{1}{s} \frac{1+sT_1}{1+sT_2} K_T \quad (3-57)$$

where

$T_o$  = torque generated by the signal generator (dyne-cm)

$T_d$  = torque due to spacecraft motion ( $\dot{\theta}_1 H$ ) and the spurious torques  $T_s$  (dyne-cm)

$T_e = T_d - T_o$

$K_{sg}$  = signal generator scale factor  $\left( \frac{\text{volts}}{\text{rad}} \right)$

$K_a$  = amplifier gain (amp/sec/v)



- $K_t$  = torque generator scale factor  $\left( \frac{\text{dyne-cm}}{\text{amp}} \right)$
- $T_g$  = gyro time constant =  $\left( \frac{J}{C} \right)$  (sec)
- $T_1$  = an amplifier time constant (sec)
- $T_2$  = an amplifier time constant (sec)

Choosing

$$K_t \frac{K_a K_{sg}}{C} = 0.013 \text{ sec}^{-2}$$

$$T_1 = \frac{1}{0.064} = 15.6 \text{ (sec)}$$

$$T_2 = \frac{1}{0.64} = 1.56 \text{ (sec)}$$

Since  $T_g$  is normally less than 0.01 seconds, we shall neglect the term containing  $T_g$ , and with the constants shown;

$$\frac{T_o}{T_e} = \frac{0.013}{s^2} \frac{\left[ 1 + \frac{s}{0.064} \right]}{1 + \left[ \frac{s}{0.64} \right]}$$

$$T_o = \frac{\left( 1 + \frac{s}{0.064} \right) \left( T_s + \dot{\theta}_i H \right)}{\left( 1 + \frac{s}{0.12} \right) \left( 1 + \frac{s}{0.26 + j0.03} \right) \left( 1 + \frac{s}{0.26 - j0.03} \right)}$$

Since the complex poles have a small imaginary part we may consider the system critically damped at  $s = 0.26$ .

$$\frac{T_o}{T_d} = \frac{\left( 1 + \frac{s}{0.064} \right) \left( T_s + \dot{\theta}_i H \right)}{\left( 1 + \frac{s}{0.12} \right) \left( 1 + \frac{s}{0.26} \right)^2}$$

$$\theta_{gc} = \left( \frac{T_s}{C} + \frac{\dot{\theta}_i H}{C} \right) \frac{1}{s} \frac{\left( 1 + \frac{s}{0.064} \right)}{\left( 1 + \frac{s}{0.12} \right) \left( 1 + \frac{s}{0.26} \right)^2}$$

These two functions are shown in Figure 3.37. The spurious torque has a zero frequency component that will result in an offset error. There will, however, be an input to the torque generator to compensate for the spacecraft and telescope rates. If we place S1 in its "up" position while

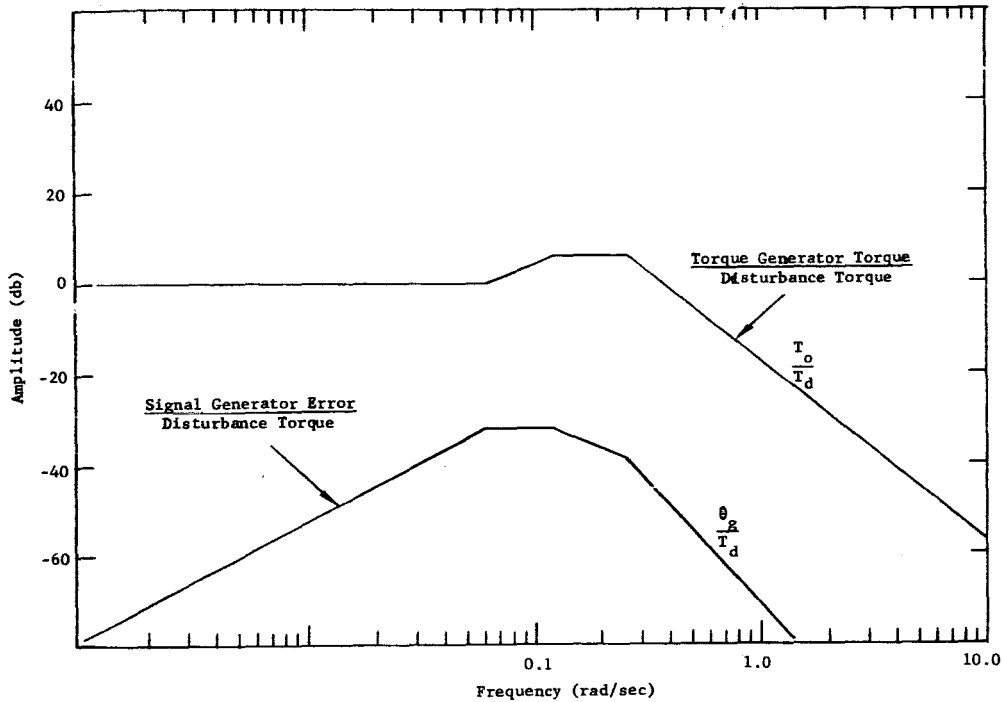


Figure 3.37. Rate Gyro Loop Error Curves

this input is present, a rate error will result and the gimbal of the gyro will move with respect to inertial space at this rate. The error will be a function of the maximum rates of spacecraft and their frequency (see Figure 3.37). While exact data is not available, the order of magnitude of these rates are 18 arc-sec/sec at approximately 3 rad/sec (0.5 cps). If the telescope were rigidly attached to the spacecraft during this time, the response of the gyro servo is down 36 db and an equivalent rate of 0.28 arc-sec/sec would result, which is higher than the desired rate. Therefore, the final computation of the spurious torques must take place while the telescope is in its auxiliary roll mode. Referring to Figure 3.25, it is seen that the auxiliary roll mode (low gain) will reduce the telescope motion by a factor of -47 db. Adding to this the -36 db of the gyro loop gives

-38 db for a total error rate of  $0.0013 \frac{\text{Sec}}{\text{Sec}}$  to give a root sum square error of  $0.003 \frac{\text{Sec}}{\text{Sec}}$ .

Larger rates from the spacecraft, or rates occurring at a lower frequency, could be accommodated by lowering the natural frequency of the "spring" loop. However, this would also increase the time required for the computation.

### 3.6.2 Linear Sensors

Centering of the telescope with respect to OAO will be accomplished through the use of the linear sensors. These sensors will develop a voltage proportional to the distance between its nominal and actual locations with respect to the OAO spacecraft.

The method used to sense the linear motion depends upon the change in capacitance between sets of plates mounted on the telescope and corresponding sets of plates mounted to the OAO (see Figure 3.38). The capacitance of the plate mounted on the OAO and the plate mounted to the telescope is defined by (for vacuum),

$$C = \frac{0.225A}{d} \quad (3-58)$$

where

C = capacitance in pf

A = plate area in square inches

d = distance between plates in inches

Viewed as a one port network, we have two capacitors in series. The voltage drop "V" across capacitor "C" is given by

$$V = \frac{I}{2\pi fC} \quad (3-59)$$

where

I = capacitor current

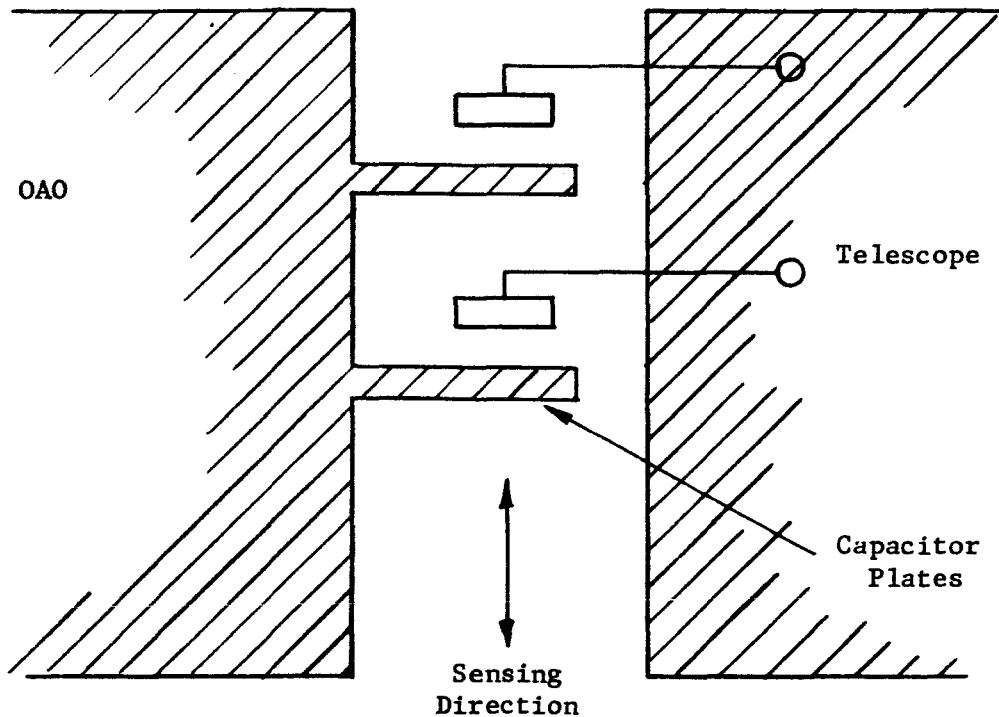
f = the excitation frequency

Calling the capacitance seen by one plate  $C_1$ , and the capacitance seen by the other  $C_2$ , then the total capacity, "C", is given by

$$\frac{1}{C} = \frac{1}{C_1} + \frac{1}{C_2}$$

Initially both sets of plates have a separation  $d_o$  and areas A

$$\frac{1}{C_o} = \frac{d_o}{0.225A} = \frac{d_o}{0.225A}$$



Equivalent Circuit

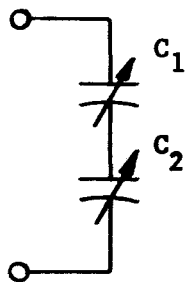


Figure 3.38 . Single Capacitive Type Sensor  
(Typical Arrangement)

If there is a relative motion between the telescope and OAO of  $\Delta d$  inches, then

$$\frac{1}{C} = \frac{2(d_o + \Delta d)}{0.225A} = \frac{1}{C_o} \left( 1 + \frac{\Delta d}{d_o} \right) \quad (3-60)$$

The output voltage will be  $V = \frac{K}{C_o} \left( 1 + \frac{\Delta d}{d_o} \right)$  where  $K$  is  $\frac{I}{2\pi f}$ .

Subtracting from this expression the constant term  $\frac{K}{C_o}$  gives an output voltage which is a straight line function of the linear motion of the telescope with respect to OAO.

The actual transducer used will be similar to the Decker Type T42. This transducer is designed for two differential capacitors. However, in our configuration, one capacitor will be fixed while the other capacitor will be the "two capacitors in series" arrangement. This will give a signal output of 5 volts per inch with a noise level of less than 3 millivolts (equivalent to  $0.6 \times 10^{-3}$  inches).

For an initial gap of 0.6" and a plate of 3" x 3" each, the value of  $C_o$  is approximately 2pf. If the gap goes to 1.1", the value of  $C$  will go to 1.1pf while decreasing the value of the gap to 0.1" increases  $C$  to 12pf, which corresponds to  $\pm 0.5$ " of motion. Since the linear range of operation for this type of transducer is 1.0pf - 50pf, this size plate appears reasonable.

Since a voltage exists between these two sets of plates, there will be an electrostatic force tending to pull the plates together.

This force is given by

$$F = \frac{1}{2} \epsilon_o \mathcal{E}^2 A \quad (3-61)$$

where

$F$  = force in newtons

$\epsilon_o$  = permeability of free space in  $\frac{\text{Coulomb}^2}{\text{newton meter}^2}$   
( $8.85 \times 10^{-12}$ )

$\mathcal{E}$  = field intensity between the plates in volts/meter

$A$  = area in meter<sup>2</sup>.

Using the worst case where the plates are 0.1 inch apart and with a working voltage of 15 volts per set of plates, the force will be 0.01 dyne per plate, of 0.02 dyne per sensor. This force should not present a problem.

### 3.7 POINTING SERVO ELECTRONICS

#### 3.7.1 Introduction

The majority of the pointing system electronics have been discussed in text throughout this section. The system block diagram of 3.6 illustrates the servo electronics for instance, which for the most part consists of operational amplifiers. Envisioned are integrated amplifier circuits or amplifiers of the miniaturized transistor package variety. The switching shown in the system block diagram will be mostly solid state.

The optical sensor electronics, gyro electronics, and linear sensor electronics have all been considered in Sections 3.5 and 3.6. The two areas which have not been considered, but are included here, are the telemetry and power systems.

#### 3.7.2 Telemetry

The present scope of the mission is to have the OAO and experiment monitored and controlled by the Apollo spacecraft for thirty days of the mission. At the end of thirty days, the Apollo vehicle will return to earth and the telescope will be monitored and controlled by ground stations.

The ground stations will be in contact with the OAO for less than eight minutes of the orbit. During this time, the data from the last orbit will be read out from data storage, and an experiment routine will be programmed for the next orbit.

A typical orbit will last 101 minutes. An experiment may take place for an entire orbit. This means that for up to 95 minutes of the experiment, there will be no direct contact between the experiment and the ground station. Information about the experiment must be stored during this time.

This information may be divided into two classifications:

1. Pointing and Experiment Control Data
2. Vidicon Data

Storage of the vidicon data takes place inside the vidicon. The vidicon has one hundred minutes storage capability with a readout time of one minute and will not be treated here.<sup>5</sup> Storage of information about the telescope guidance and control will take place in the Data Storage section of the OAO Primary Processor and Data Storage (PPDS) Subsystem.

The PPDS has a total capacity of 102,400 bits of information in a redundant mode. The data storage receives information from the Spacecraft Data Handling Equipment (SDHE) and the Experiment Data Handling Equipment (EDHE).<sup>5</sup>

We may assume that most of the memory is available for the experiment; i.e., that the experiment will store two bits of data for every one bit stored by the SDHE. The EDHE may, therefore, transmit 67,000 bits of data to the PPDS data storage.

There are approximately 100 signal voltages which may be monitored and as many power supplies. Assume for the moment that each of these signals is encoded into 8 bits, (one part in  $2^7$  plus polarity) and each line is sampled once per second, we would be transmitting 1600 bits/sec to the PPDS. The PPDS would be filled with data in 40 seconds. This would not be acceptable and it is, therefore, necessary to divide the data to be stored into two categories:

1. Overall status data which gives an indication that telescope pointing system is functioning properly.
2. Fine data about individual components and servo loops.

The data handling philosophy will be to look at group one in the normal operation, with provision to look and store any desired constituent element of group two when the data from group one indicates a malfunction in part of the pointing system.

In addition to this, the overall status data may be divided into data which should be continuously monitored (rms error, for instance) and data which do not require continuous monitoring.

A block diagram of the data handling equipment is shown in Figure 3.39. All the information wires will be fed into a multiplexer which will be driven by a programmable ring counter. The output of the multiplexer will be sent to OAO through the RF window. Inside the OAO, the data will be encoded and stored by the PPDS.

The multiplexer will be driven by the ring counter which will have a previously programmed subroutine system. Such a routine for instance might be, sample and store channels 1-20 ten times, sample and store channels 21-100 once and then repeat.

The available storage of the OAO constrains the system to sample at approximately one (eight bit) voltage per second for a hundred minute experiment. Such a rate may be too slow if it is desired to view some of the fine data signals and wasteful if the experiment time is less than 100 minutes. The system will, therefore, be provided with several clock rates

3-91

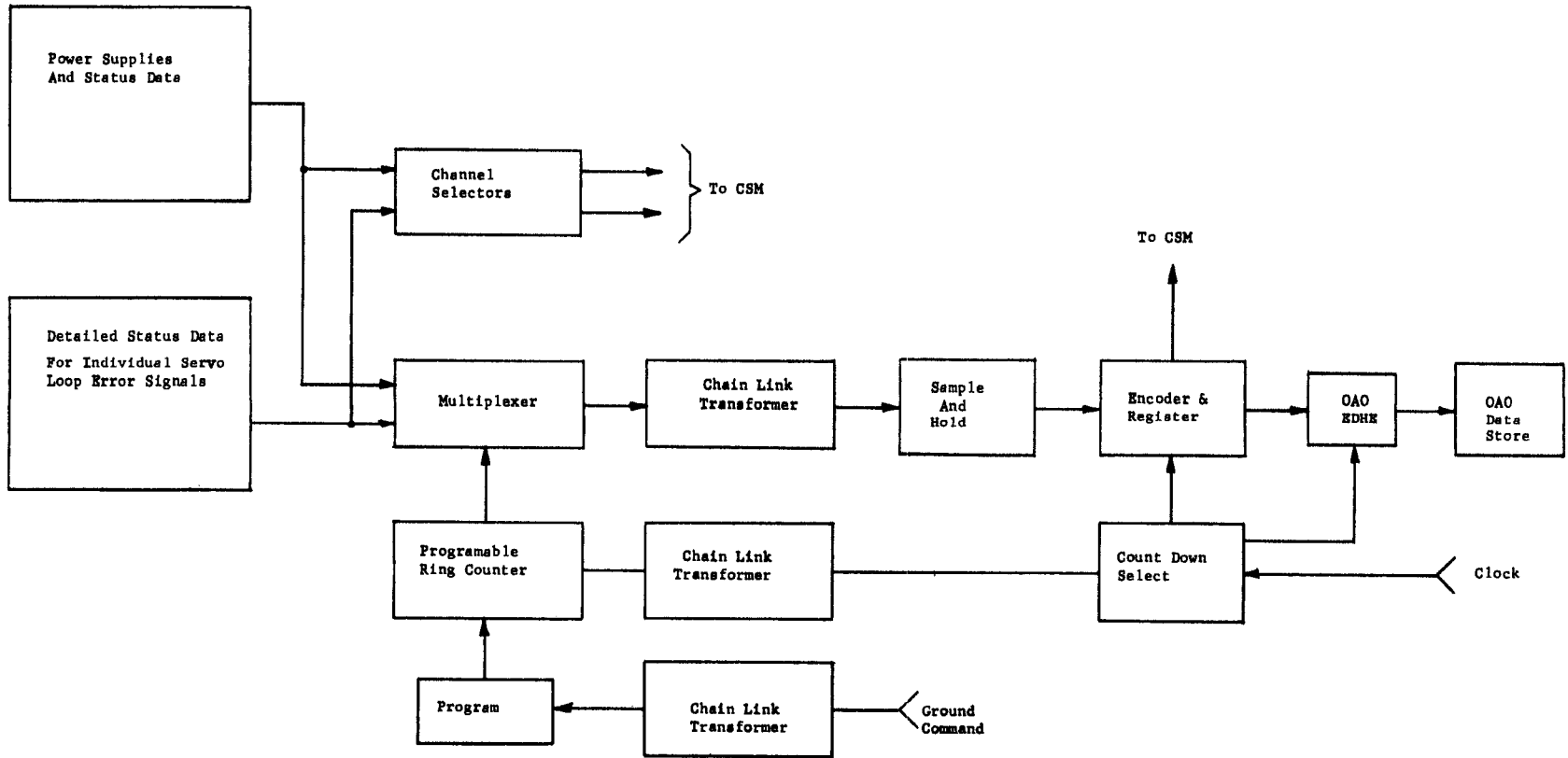


Figure 3.39. Data Handling Equipment



which will be integral multiples of each other and may be pre-programmed. In this way, data may be sampled at 1, 1.5, 2, 3, 4 or 10 samples/second.

This scheme still is too slow for the type of data which should be sent to the astronauts. The data to be sent to the astronauts will, therefore, be fed directly by low-power RF transmitters. Channel selection capability will be provided so that the astronauts may view, on a continuous basis, any of the channels which are being fed to the multiplexer. Another transmitter will be provided so that the astronaut may observe the output of the encoder. The exact number of continuous time signals which may be simultaneously monitored by the astronauts will depend upon the volume and power constraints of the system.

### 3.7.3 The Chain Link Transformer

The chain link transformer will be used to bring power from the spacecraft to the telescope without making physical contact between the spacecraft and the telescope. As its name implies, the transformer looks like a set of chain links, one link corresponding to the primary and the second link corresponding to the secondary.

The primary is a tightly wound toroidal solenoid. The secondary consists of several turns of wire threaded through the toroid. A sketch of this arrangement is shown in Figure 3.40.

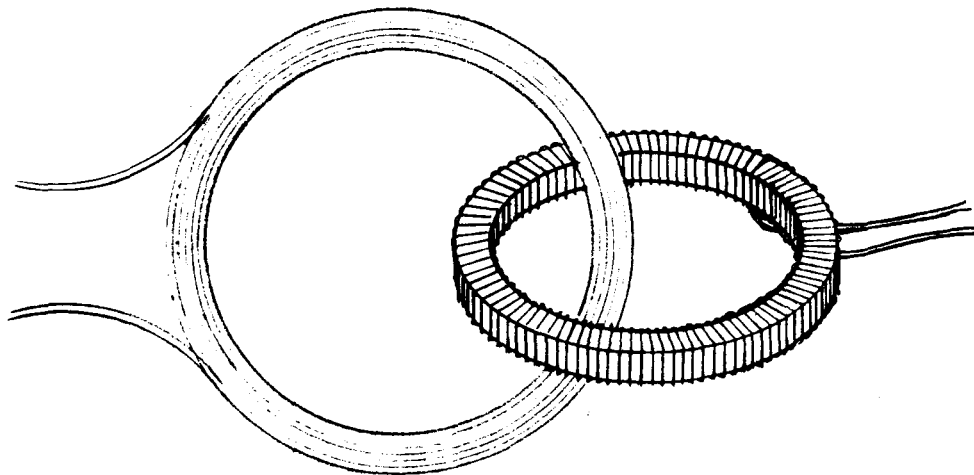


Figure 3.40. Chain Link Transformer Principle

Assuming that motor action exists between the primary and the secondary, from the law of conservation of energy

$$dW_{pe} = dW_f + dW_m + dW_{se} \quad (3-62)$$

where,

- $dW_{pe}$  = the differential electrical energy input to the primary
- $dW_f$  = the increase in energy stored in the magnetic field
- $dW_m$  = the differential mechanical output energy
- $dW_{se}$  = the electrical power output into the secondary load.

The term  $dW_m$  represents the energy converted into mechanical work. Defining the output mechanical work as a force "F" moved through a distance "ds".

$$dW_m = Fds = dW_{pe} - dW_{se} \tag{3-63}$$

$$F = \frac{dW_{pe}}{ds} - \frac{dW_f}{ds} - \frac{dW_{se}}{ds}$$

Similarly, defining the output differential mechanical energy as a torque, T moved through angle  $d\theta$

$$dW_m = Td\theta = dW_{pe} - dW_{se} \tag{3-64}$$

$$T = \frac{dW_{pe}}{d\theta} - \frac{dW_f}{d\theta} - \frac{dW_{se}}{d\theta}$$

We shall now show that the chain link arrangement theoretically makes a transformer where translational or angular motion of the secondary will not affect the coupling between the input electrical source, the magnetic field or the secondary load, yielding zero force (F) and zero torque (T). This permits transmission of considerable power without coercive forces disturbing the pointing of the telescope.

Consider the toroid aligned in a three-dimensional, right-handed cylindrical coordinate system with the axis of the toroid coincident with the "Z" axis. From the symmetry of the problem all the flux in the primary is directed in the same direction or " $\phi$ " (where  $\phi = \tan^{-1} \frac{y}{x}$ ) and the flux density is constant for constant  $\rho$  and  $z$  (where  $\rho = \sqrt{x^2 + y^2}$ ).

Calling the magnetic field intensity " $\vec{H}$ " and an incremental distance " $\vec{ds}$ ", then from physical reasoning  $\int \vec{H} \cdot \vec{ds}$ , along a path of constant  $\rho$  and  $z$ , is zero for any path that does not go inside the toroid, since that path would enclose no net current. Hence, the primary magnetic field exists only for those values of  $\rho$  and  $z$  which are inside the toroid.

If a winding is threaded through the toroid, there will be a voltage induced into that winding equal to the time rate of change of flux through any arbitrary surface having the winding as its perimeter. From this, it can be seen that, for any arbitrary orientation of the secondary, a surface integral of the flux through the secondary is always unchanged. The total magnetomotive force due to current in secondary is similarly independent of the way that the secondary winding encircles the primary.

Hence, the magnetic field and the coupling between primary and secondary are independent of position of the secondary with respect to the primary and, therefore, no motor action results.

This analysis is based upon the assumption that the primary flux is purely circular about the  $z$ -axis. This requires a uniform winding and homogeneous core materials. That such an arrangement can be physically realized was verified in an experiment performed by Perkin-Elmer in May of 1965.<sup>6</sup> In this experiment, the primary was fixed and the secondary was suspended on a six-foot simple pendulum with a natural period of 2.7 seconds and a spring gradient of 0.07 oz/in.

With the system at rest, and power initially off, a time exposure photograph was made for 8 seconds, during which time power was applied. An examination of the photograph indicated no discernable motion. Assuming that an excursion of 0.02" peak-to-peak could just be detected, such a peak-to-peak motion, if it existed, would have been caused by  $7 \times 10^{-4}$  ounces of force. The saturated force output of the torque motors, for comparison, is 4.8 ounces which is 6750 times this amount.

The toroidal primary of the transformer used in this experiment had an outer diameter of 2.0", an inner diameter of 1.6" and was 0.3" thick. Winding this primary in a center-tapped configuration with the center tap connected to +28VDC, and an output frequency of 800 cps - the DC resistance of the winding at room temperature would be 0.05 ohm per side. At 30 watts output, the rms current in the entire primary would be 0.75 amp, giving a winding dissipation of 0.056 watt. At a 60 watt peak drain, the power loss would be 0.225 watt. Since this configuration allows  $\pm 0.08$ " of motion in an initial volume approximately 3" x 2" x 2", it satisfies the design requirements.

#### 3.7.4 Power Budget

The allowable power load that the experiment package may impose on the OAO spacecraft is 30 watts average and 60 watts peak. This load will

be placed upon the DC line only. Any AC power that the experiment requires will be generated by supplies within the experiment package.

To assure that power drains do not exceed this level, the power requirements of all components and the requirement for their operation during a particular mode have been carefully examined. Equipment not required during a particular mode of operation will be turned off during that mode so that other equipment may be turned on.

A block diagram of the power controller is shown in Figure 3.41.

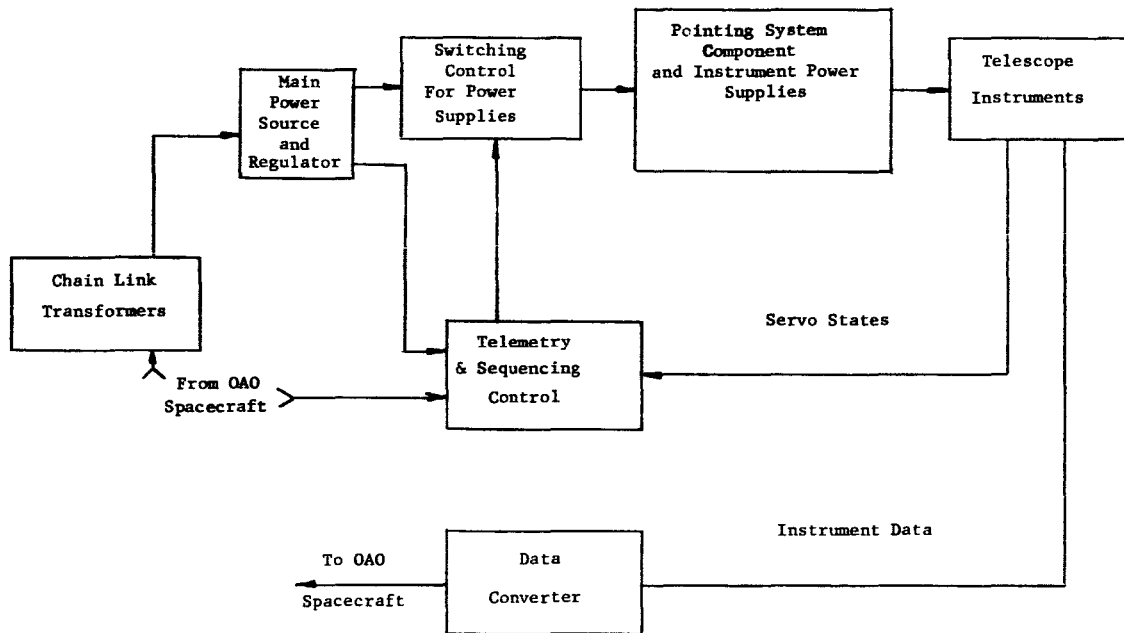


Figure 3.41. Power Controller

The power drain for the individual control components, (including their individual power supplies) is shown in Table 3-V. . The sequencing of the power is shown in Table 3-VI. , and is indicated graphically in Figure 3.42 as a function of time. The power controller operates on the basis of an interlock scheme depending upon the state of the telescope pointing subsystems. The controller, for instance, will be inhibited from going to state four (Table 3-XIII) until the gyro has reached its operating temperature.

Note that the heat required by the floated gyro is supplied in part by the heat losses of the spin motor. Turning on the spin motor supply, therefore, reduces the heater power required. The total power at the end of state 4 is increased by the power drain of the gyro control electronics.

TABLE 3-V

<u>Component</u>	<u>Used In</u>	<u>Peak Power</u>	<u>Average Power</u>
Photomultiplier Tube Pair	Fine Sensor Coarse Sensor	1.0	1.0
Preamp/Summer	Fine Sensor Coarse Sensor	0.8	0.8
Chopper	Fine Sensor Coarse Summer	0.5	0.5
Pulse Processor	Fine Sensor	0.1	0.1
Demodulator	Fine Sensor Coarse Sensor	.015 .015	.015 .015
Operational Amplifier	Summers and Integrators	.150	.150
Gyro Wheel	Acquisition and Absence of 2nd Star	14	5
Gyro Heater		20	6 Wheel Off 1 Wheel On
Gyro Control Electronics		0.5	0.5
Mirror Movers	Guide Star Selection	1	0
Telemetry and Control Pkg	All Modes	2.5	2.5
UV Vidicon	Instrument	7.0	7.0
Vidicon Telemetry	Instrument	0.5	0.5
Spectrometer Mirror Mover	Frame Indexing	1.0	0
Guide Star Mirror Mover	Initial Programming	1.0	0
Cage/Uncage Mechanism	Caging/Uncaging	10.0	0
Roll Torquers and Amplifiers	Acquisition and Final Track	4	0.5
Horizontal Torquers and Amplifiers	Acquisition and Final Track	1	0.12
Vertical Torquer and Amplifiers	Acquisition and Final Track	1	0.12

TABLE 3-VI

POWER DRAIN OF TELESCOPE SYSTEM  
DURING SEQUENCING

STATE	OPERATIONS	DEVICES TURNED ON	TOTAL PEAK COMPONENT POWER WATTS	TOTAL COMPONENT POWER AT END OF STATE WATTS	PEAK SUM POWER INCLUDING SUPPLY LOSSES	SUM FINAL POWER INCLUDING MAIN SUPPLY LOSSES
1	Power On	Telemetry and Sequency	2.5	2.5	2.75	2.75
2	Position Image Movers and Flip Mirror	Image Mover Drive and Flip Mirror Drive	4.5	2.5	4.9	2.75
3	Heat Gyro	Gyro Heater Amplifier	23.0	8.5	25.2	9.35
4	Gyro	Gyro Wheel Gyro Electronics	22.5	9.0	24.8	9.9
5	Coarse	Coarse Photomultiplier, Choppers, Preamps and Demods	13.6	13.6	15.0	15.0
6	Fine	Fine Photomultipliers, Choppers, Preamps Processor, and Demod	18.5	18.5	20.4	20.4
7	Linear Sensors	6 Linear Sensors	21.8	21.8	24.0	24.0
8	Uncage	Uncage Mechanism	31.8	21.8	35.0	24.0
9	Servo Scan, Acquisition and Optimization	Operational Amplifiers, Torquer Amplifiers, Sensor Logic	30.2	24.4	33.2	26.8
10	Turn Off*		19.30	19.30	21.2	21.2
11	UV Vidicon	UV Vidicon	26.8	26.8	29.5	29.5
12	Vidicon Format Index	Spectrometer Mirror Indexer	27.8	26.8	30.6	29.5

\* Devices Turned Off: Coarse Photomultipliers, Choppers, Preamps and Demodulator, Auxiliary Roll Electronics

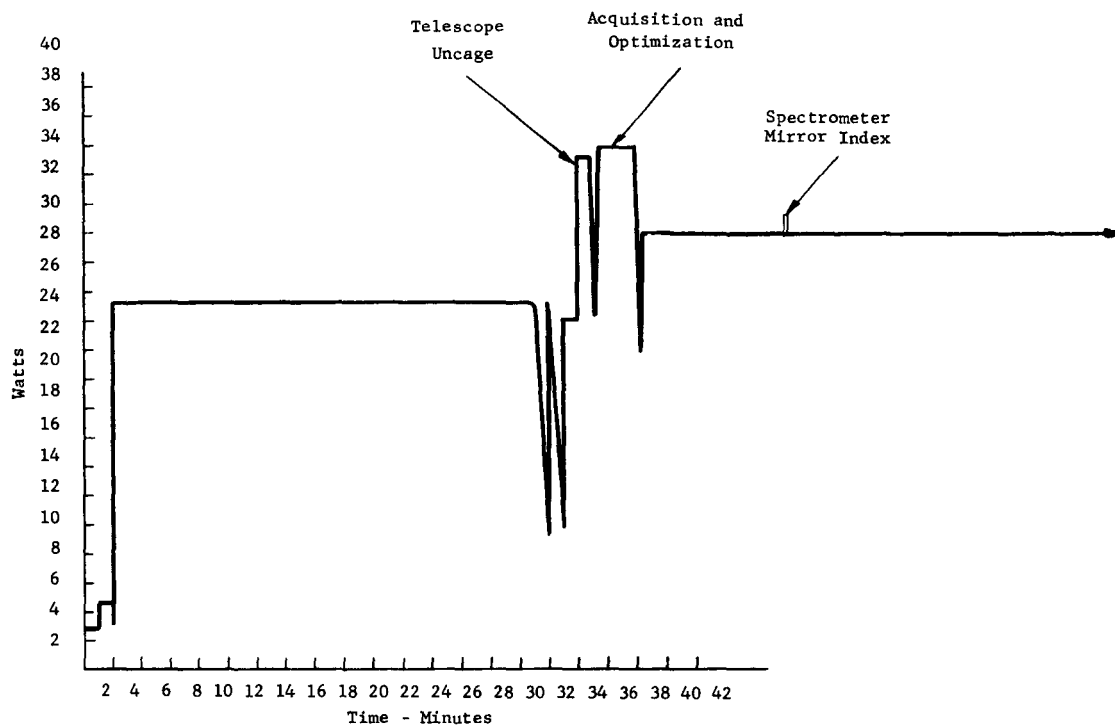


Figure 3.42. Power Drain Profile

Table 3-VI has an additional set of columns, taking into account the power supply losses of the main power converter and the chain link transformer. Adding these losses yields the last two columns of Table 3-XIII.

In the event that the vidicon or auxiliary tracker indicates improper pointing, the system will be commanded back to state 9 and retrimmed. If the error indicated by the vidicon is small, the gyro and/or the fine sensor will be biased to reduce errors.

Table 3-VI shows that the final power drain of telescope and the vidicon comes close to the maximum allowed by the OAO spacecraft. To assure that some margin exists, the possibility of removing power from the gyroscope has been considered. While this is not advisable because of the long warmup time of the gyro, turning off the gyro provides a factor of safety of 6.5 watts of component power. In the absence of a second guide star (where it would be impossible to turn off the gyro), the second guide star fine sensor electronics could be turned off providing 2.4 watts of reserve.

### 3.8 POINTING SYSTEM REDUNDANCY

Without question, reliability is one of the major pointing system design considerations. The OAO spacecraft and 40-inch telescope system must remain operative for a period of at least one year which places stringent, long-term operational requirements on the system and its associated components. Although each system component will be designed to be as reliable as possible, certain components are very critical and, in these cases, redundant components will be incorporated.

#### 3.8.1 System Philosophy

Redundancy is an inherent aspect of the telescope pointing system design. Without considering, for instance, the redundant fine optical sensors, a fine sensor (or image mover) could fail completely without stopping the experiment. There are several reasons for this. The existing roll displacement gyro, normally used as a substitute in the absence of a second guide star, could partially replace the function of the failed sensor permitting at least short exposures. Since the fine optical sensors are used interchangeably for vertical-horizontal and roll axis error references, the remaining operating sensor would provide the vertical-horizontal axis pointing reference. Secondly, a side-looking auxiliary sensor is available which can also be used for a roll axis reference. Finally, in the event of a catastrophic failure where the gyro(s), auxiliary side-looking roll sensor, and one of the fine sensors have all failed, the roll axis of the auxiliary rotational servo system could be used. This servo loop receives its references from the OAO spacecraft. If loosely slaved to the spacecraft in the suspended mode to reduce the roll pointing errors ( $\pm 2$  degrees) to acceptable errors ( $\pm 4$  arc-seconds), the experiment could still be conducted without complete degradation in performance.

The gyro is used interchangeably with the fine optical sensor (roll reference) in the final tracking mode in the absence of a second guide star. It also serves as a reference or aid for roll axis acquisition. However, a gyro failure will by no means render the pointing system inoperative in acquisition. By lowering the gain of the roll axis servo loop with respect to the vertical-horizontal axis servos, and by-passing the fine sensor signal logic, the telescope has the facility to acquire both guide stars with the fine and coarse optical sensors alone. Here a scanning mode to find the guide stars may be required with a modification to permit roll scanning alone. In addition, the side-looking auxiliary sensor is available as a roll reference.

#### 3.8.2 Component Redundancy

Numerous subsystems and components will have redundant backups. The critical component areas are listed below:

1. Power - Dual chain link power transformers will be incorporated since, without question, a failure in the main telescope power link cannot be tolerated.



Critical power areas such as the high voltage supplies for the photomultipliers will be redundant. Fail-safe switching will be used to transfer from a failed supply to its backup. Due to the critical power load situation, operating redundant power supplies simultaneously does not seem possible.

2. Fine Optical Sensors - Two completely independent fine optical sensors are available. Each sensor also contains dual photomultipliers, which can back each other up.
3. Gyros - A redundant roll displacement gyro has been incorporated.
4. Magnetic Torquers and Amplifiers - An extremely critical failure area, the torquers and amplifier combinations will all be redundant as units. If one combination should fail, fail-safe switching will replace a complete amplifier-torquer combination with an identically calibrated unit.
5. Linear Displacement Sensors - The proposed type of linear sensor is a capacitive type and mechanical failures are nearly impossible. However, each sensor will contain a redundant set of electronics.
6. Servo Electronics - Operational amplifiers and solid-state switching circuits will be designed to have progressively degraded performance rather than catastrophic failure in the event of failures.

### 3.9 ELECTRONICS INSTRUMENTATION AND TELEMETRY

#### 3.9.1 Description

This section is devoted to defining the instrumentation and telemetry that will be required in the telescope electronics system. The instrumentation will perform two basic functions:

1. Command Monitor - Directly related to input command functions, command monitoring instrumentation will determine whether certain telescope commands have been properly executed. Examples of this would be pre-operational sequences such as caging and uncaging, or image mover positioning.
2. Status Monitor - Synonymous with failure monitoring, status monitoring instrumentation will examine crucial signals to determine if the equipment is operating properly. This would include system power voltages, telemetry and data handling, and might include tracking performance.

The list of functions presented subsequently does not imply that each of these functions must be monitored continuously. Certain equipment such as power supplies can be monitored periodically.

### 3.9.2 Instrumentation

The list of instrumentation given here specifies components. The type of instrumentation will be denoted by CM (command monitor) and SM (status monitor).

1. Fine and Coarse Optical Sensor Instrumentation - Visual display of outputs (SM) - This will provide a means of determining tracking accuracies in the final servo modes and whether the correct fine sensor has been selected. Total sensor failure will also be evident.

Optical Chopper Monitor (SM) - Required for failure detection.

2. Displacement Gyro - Visual display of outputs (SM) - This will determine the servo performance and drift when tracking on two guide stars.

Gyro wheel speed and heater monitors (SM) - Required for failure detection.

3. Centering Sensors - Sensor output meters (SM) - Provides a means of determining if the telescope is properly centered in both translation and rotation with respect to the OAO spacecraft. The failure of any sensor will also be detected.

4. Image Movers - Position Readout (CM) - Provides image mover position information with high accuracy to determine if these devices have been correctly located.

Drive System Monitor (SM) - Required for failure detection and location of failures in the image mover drives.

5. Torquers and DC Amplifiers - Output current monitors (SM) - Mainly required for failure detection in the DC amplifiers.

6. Caging Solenoids - Current monitor (SM) - Required for the detection of failure and erroneous re-cycling.

7. Stabilization Components (All Axes) - Operational amplifier output monitors (SM) - Required for the detection of failure in the servo stabilization electronics.

Acquisition switching network monitors (SM) - Provides a means of detecting switching failures as well as determining erroneous acquisition recycling.

Fine sensor processing logic circuit monitors (SM) - Required for failure detection in either signal flow, sensor selection or guide star location gain adjustment circuits.

8. Power Supplies - Power meters (SM) - Required for the detection of either excessive overload or failures.

9. Telemetry and Data Handling - Telemetry and data handling monitors (SM- CM) - Required for real-time data status and failure detection.

Conversion Electronic Monitors (CM) - Provides a means of monitoring D/A or A/D converters, multiplexers, transmitters, or receivers for failure detection.

### 3.10 RECOMMENDATIONS FOR FURTHER INVESTIGATIONS

The majority of the areas listed below and recommended as areas requiring further study, pertains to detailed investigation of subsystems in the electronics. The one exception, and perhaps the most important recommendation for advanced study, is the investigation of the complete telescope pointing system using computer (Analog or Digital) simulation techniques, and including the dynamics of the OAO spacecraft.

1. Computer Simulation - A multiple axis simulation is recommended, which would simultaneously take into consideration the three-pointing axes (vertical, horizontal, and roll), the three-centering axes, the auxiliary vernier caging three-axis system and the outer OAO spacecraft guidance system (in simplified form) to study the inter-relations of each. System cross-coupling studies in the present system have been quite cursory.

2. Acquisition - The acquisition implementation is also recommended for further study to devise means of eliminating the electronic switching.

3. Mechanical Resonance and Rigid Body Cross-Coupling - The study did not consider the effects of telescope mechanical resonances on performance which can be detrimental. In addition, coupling due to the axial misalignment between the torquing and principle axis requires investigations.

4. Power Optimization - Means of reducing power requirements to afford a reasonable safety margin require additional study.

5. Packaging - The use of integrated circuits to reduce space requirements for the telescope pointing system electronics and components including telemetry should be investigated.

6. Image Mover Controls and Pickoffs - A detailed design study is required in this area.

7. Caging Mechanisms and Controls - Again, a complete detailed design study is required.

8. Pulse Processing Techniques and Optical Sensor Chopping Techniques - Based on recent discoveries of the nature of cosmic radiation, present sensor pulse processing techniques are not applicable. An investigation to develop

new techniques to reduce sensor cosmic noise is recommended. Several alternate optical chopping techniques are also available and should be more fully studied.

9. Telemetry - Further study to develop the telemetry design and perhaps more importantly, the development of simplified concepts in the telescope data handling system is recommended.

Additional areas recommended for further study, but not major considerations are,

a. Disturbance Torque Analysis - Once the telescope inertia, weight distribution, aerodynamic shape (from telescope tube extensions), current flow and other areas have been better determined, a re-analysis of telescope torque disturbances should be conducted. At this time, the 20,000 dyne-cm torque used in the study (in all three axes) is thought to be considerably higher than the system will actually experience. Therefore, pointing errors due to torque may be lower, which will also indirectly allow a further reduction in error due to noise. Torques from axis to axis will also vary.

b. Failure Analysis - An investigation to devise a means of detecting failures and automatically employing redundant systems without unduly burdening the telemetry and data storage capabilities of the system is recommended.

c. Adaptable Servo Controls - The possibility of utilizing self-adapting servo systems is a possible area of advanced study. The intent would be to develop a pointing system which will automatically provide the telescope with the minimum pointing errors for all conditions.

REFERENCES

- <sup>1</sup>Princeton University.
- <sup>2</sup>"OAO Spacecraft Handbook," Grumman Aircraft Engineering Corporation, (September, 1961).
- <sup>3</sup>Inertia Guidance Primer, Honeywell.
- <sup>4</sup>Technical Information for the Engineer, Kearfott Division, General Precision, Inc.
- <sup>5</sup>Final Report "Study of the Design Problems of Integrating Television Tube for Astronomical Research," Westinghouse Electric Tube Division (December, 1964).
- <sup>6</sup>Memorandum, (May 18, 1965), Larkin Scott.

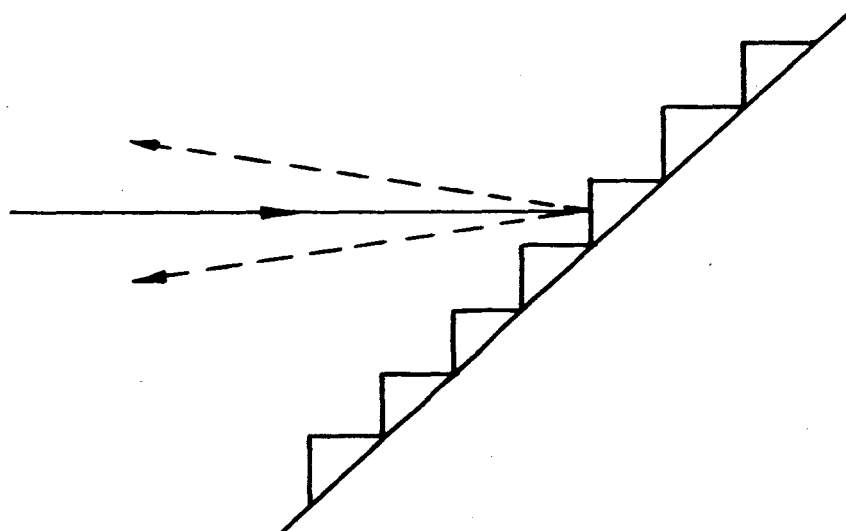
#### 4.0 SPECTROGRAPH DESIGN

The use of vidicons as the primary data transducers not only allows the possibility of imaging but also promises a large increase in the rate of acquisition of spectrophotometric data from weak stellar sources. In order to take full advantage of this large data capacity, it is necessary to fold the spectrum so that it covers as much of the sensitive surface of the vidicon as is feasible. Such an arrangement is provided by an echelle spectrograph.

Initially it was expected that the spectrograph would be used to cover the 1100Å to 3000Å spectral region and that a resolution of 10,000 would be adequate. Later, when the possibility of a manned mission was considered, the desired spectral range was increased to include the 800Å to 1100Å spectral region and an even higher resolution capability was suggested in order to take advantage of the increased potentialities of photographic film.

#### 4.1 GENERAL PROPERTIES OF AN ECHELLE SPECTROGRAPH

Echelle gratings differ from more conventional gratings by having deep grooves, relatively widely spaced, as shown below



When used at high angles of incidence the echelle grating provides high dispersion at high orders of diffraction. In the usual echelle spectrograph arrangement, a low dispersion predisperser and an echelle grating are arranged so that their dispersion directions are crossed. The high orders produced by the echelle are separated by the predisperser creating a folded spectrum resembling the lines of type on a printed page. Each line corresponds to a different order at the echelle grating.

The folded spectrum provides a substantial increase in the amount of spectral data that can be integrated with the SEC vidicon and readout in a single step. However, it is necessary to insure that each spectral resolution element covers a number of vidicon resolution elements so that a minimum of spurious detail is introduced by irregularities intrinsic to the vidicon. When the spectral source is diffuse, averaging is effected over the length of the entrance slit which is effectively 0.7 mm long and contains a narrow section 0.025 mm across at one end, and a wide section 0.1 mm across at the other. Point sources do not fill the spectrograph entrance slit and averaging of individual wavelengths does not occur unless the spectrum is smeared normal to the high dispersion direction. Smearing could be introduced by bending a spectrometer element into a cylindrical shape so as to produce an astigmatic image, by rocking one of the spectrometer elements, or by dithering the whole optical package.

The 0.7 mm effective length of the entrance slit sets the minimum line spacing on the spectrograph format at about 1.0 mm in order that some room be left to separate adjacent spectra. A compromise between the requirements for resolution and spectral coverage was made by setting the dispersion at 1000Å equal to 1.0Å/mm. This dispersion and a resolution of 10,000 correspond to about 10 resolution elements per mm which appears to be well within the capability of the vidicon assuming an image tube transfer function of 50 percent at a frequency of 10 lines per mm. In order to ensure that the vidicon is the resolution limiting component, the design goal for the transfer function describing the performance of the spectrograph optics, was set at above 50 percent at 20 lines per mm.

The properties of an echelle spectrograph are briefly outlined in App. B (DAM-003) Vol. III. In the note it was assumed that both the high and low dispersion elements were plane gratings operating on a collimated beam. With this arrangement, the diffraction order at the echelle grating can be determined from the grating equation and is given by:

$$n = \frac{\lambda}{\Delta x \frac{d\lambda}{dx}} \quad (4-1)$$

where

$n$  = order number

$\lambda$  = wavelength

$\Delta x$  = format width

$\frac{d\lambda}{dx}$  = dispersion

Since a dispersion of 1.0°/mm at 1000Å has been indicated as providing a reasonable compromise between resolution and spectral coverage, selection of a value for either the diffraction order or the corresponding format width is sufficient to determine the remaining parameter. When information becomes available on the efficiencies of various echelle gratings in the far

UV spectral region, then an optimum value of  $n$  may become apparent and this will determine the corresponding format width. In the absence of any experimental results, it is informative to select arbitrary values such as 40 for  $n$  and a corresponding value of 25 mm for  $\Delta x$ . As will be seen subsequently, it is not particularly advantageous for the spectrograph format width to bear any direct relationship to the 20 mm by 15 mm vidicon format size. Since the order times the wavelength is approximately equal over the echelle format, the 3000Å limit corresponds to about the 17th order. By considering the distribution of diffracted energy, as well as the dispersion relations defined by the grating equation, it is possible to determine a relationship between the grating spacing and the focal length seen by the image plane. This is:

$$\frac{1}{m} = n \left[ \frac{\lambda^2}{4} + F^2 \left( \frac{d\lambda}{dx} \right)^2 \right]^{1/2} \quad (4-2)$$

where

$m$  = number of lines per unit length on the grating

$n$  = diffraction order defined by (4-1)

$\lambda$  = wavelength

$\frac{d\lambda}{dx}$  = dispersion in the image plane

$F$  = focal length

The optical layout of the instrument section does not permit much variation in  $F$  so that it cannot really be a variable, but must be approximately equal to 400 mm. Substituting this value of  $F$  and the previously determined values of  $\lambda$ ,  $\left( \frac{d\lambda}{dx} \right)$  and  $n$  into equation (4-2) yields a value of 390 lines/mm for  $m$ . This line spacing is not available from present ruling engines so that a grating with either 400 lines/mm or 384/mm would have to be used in practice.

An equation similar to (4-2) can be derived for the predispersion grating. For this case  $n$  equals 1 and  $\left( \frac{d\lambda}{dx} \right)$  refers to the change in wavelength in going from line to line on the format (25Å/mm). Substituting these values into (4-2) results in a grating having 1000 lines/mm. The nearest grating that can be produced commercially is 960 lines/mm, or on the other side, 1152 lines/mm.

The angle at which each grating is used, assuming equal incidence and diffraction angles, is given by:



$$\tan\theta = \frac{\lambda}{2F \frac{d\lambda}{dx}} \quad (4-3)$$

where  $\theta$  is the angle between the grating normal and the angles of incidence or diffraction.

Using the previously determined values for  $F$ ,  $\lambda$ , and  $\frac{d\lambda}{dx}$ , the angle for the echelle grating is approximately 51 degrees and that for the predisperser is 3 degrees. Since the predisperser is used so that the angles of incidence and diffraction are of opposite sign, the 3 degree angle computed for the predisperser indicates the angle between the reflected (zero order) beam and the diffracted beam. An angular separation of only 3 degrees between the zero order and diffracted beams, indicates a rather severe condition which cannot be avoided as long as a 25 to 1 dispersion ratio between the echelle and predispersion gratings is required. Not only is the separation of the zero order and diffracted beams likely to be difficult, but a groove geometry (blaze angle) which minimizes scattering, while at the same time providing high efficiency, may be difficult to achieve.

The format produced by an echelle spectrograph having the dispersion and line separation dictated by system requirements is shown in Figure 4.1. Lines corresponding to longer wavelengths and lower diffraction orders become longer and the space between them increases rapidly. The format is much too large to be placed on a 20 x 15 mm vidicon face. A number of steps will be required to record the entire 1000Å to 3000Å spectral region. However, all the steps need not be read out individually. Since the space between lines increases with wavelength, steps in the longer wavelength end of the spectrum could be interleaved on the target of the vidicon and readout simultaneously.

The deterioration of the compact format at long wavelengths is a direct outcome of the grating properties and can not be avoided if only two gratings are used to cover the 1000Å to 3000Å spectral region. By changing to a different predisperser grating longward of 1600Å, it would be possible to compress the total size of the spectrum format somewhat. Similarly, if a refractive predisperser could be used instead of a grating, then a much more optimum line spacing would be possible. However, a thick LiF prism, in addition to the thin LiF window on the vidicon, would reduce spectral coverage near the LiF cutoff at 1050Å where it is most desired.

Although the vidicon window is a definite liability in regard to spectral coverage, it does provide an incidental advantage by filtering out the very short wavelengths which could otherwise be superimposed on the desired spectrum at higher orders. In the 2000Å to 3000Å portion of the spectrum, interference from the 1000Å to 1500Å region is possible due to second order diffraction at the predisperser. This can be avoided only by inserting a short wavelength cut-off filter into the optical path when the 2000Å to 3000Å region is being examined. Fused silica is a possible filter material since it has a cutoff near 1800Å.

PERKIN-ELMER

Order  
Number

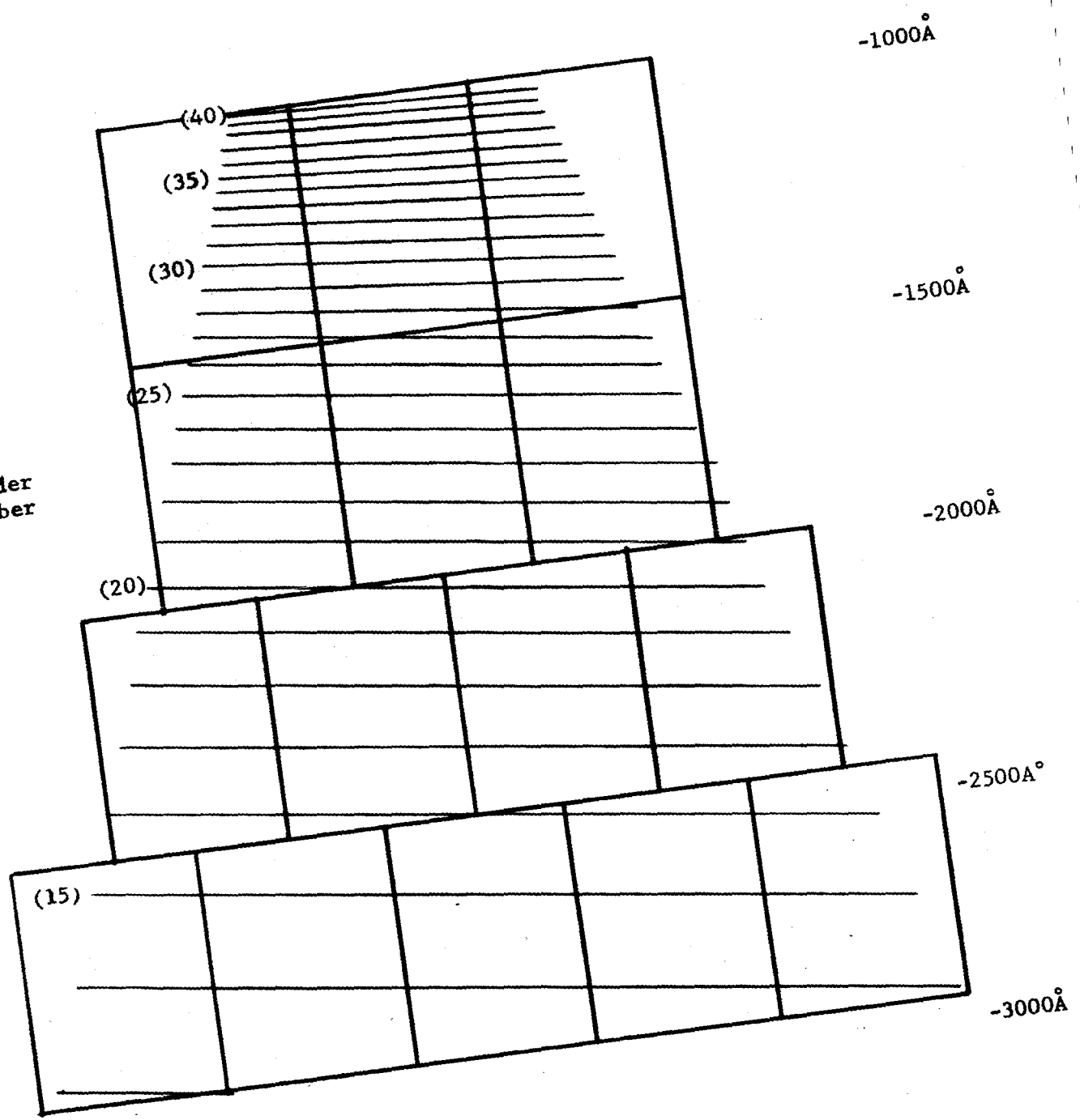


Figure 4.1. Echelle Spectrograph Format

#### 4.2 FOUR ELEMENT SPECTROGRAPH

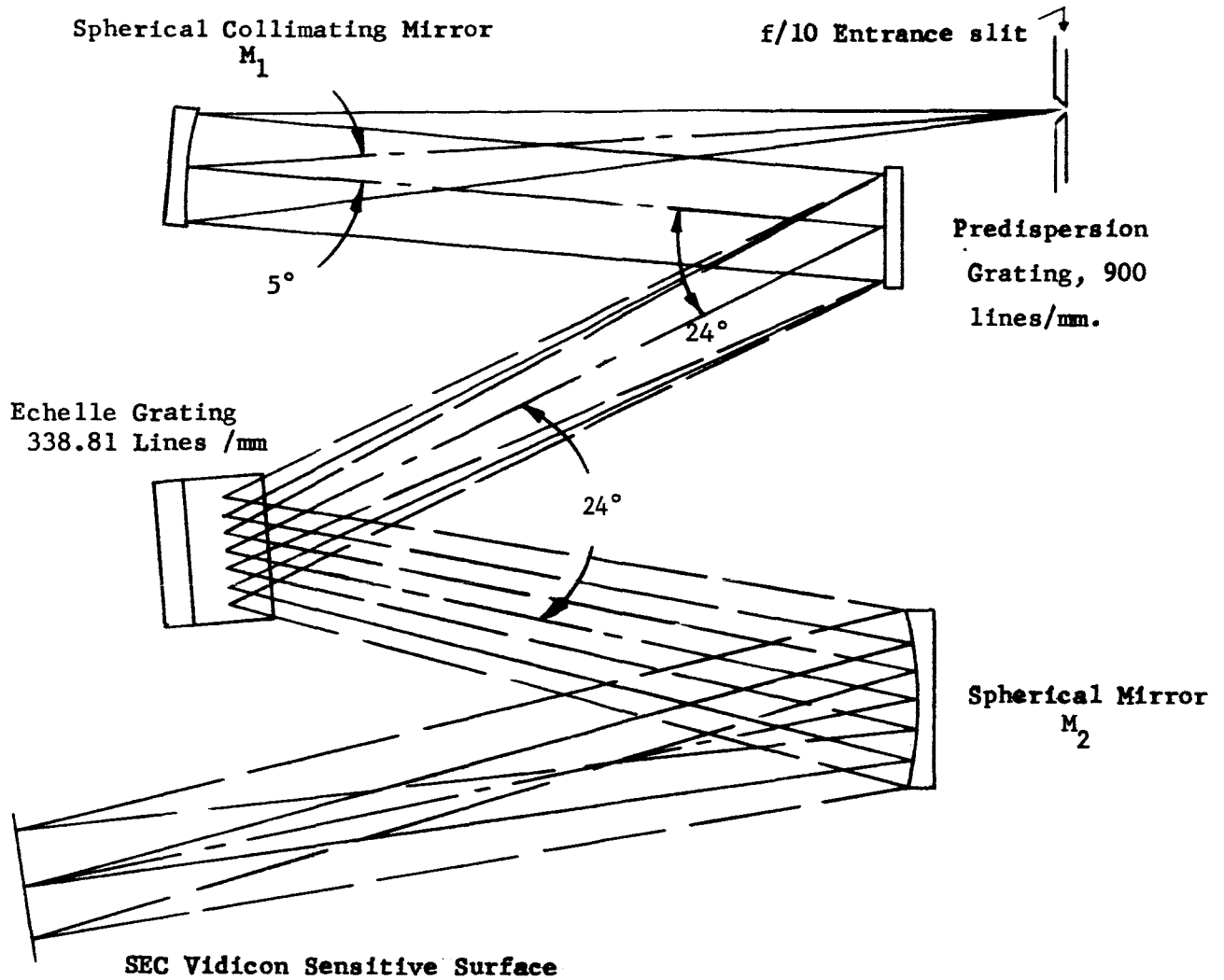
Figure 4.2 shows one of the early spectrograph designs that was considered. Mirror  $M_1$  directs a collimated beam toward the predispersion grating which is ruled normal to the plan view. After being diffracted by the predisperser, the radiation strikes the echelle grating at a steep angle and is diffracted in the front view plane. Mirror  $M_2$  receives the energy diffracted by the echelle and focuses it onto the sensitive surface of the vidicon.

The optical characteristics of the four-element spectrograph were examined on the computer. Preliminary results based on a few extreme field positions indicated that the incident angles at mirrors  $M_1$  and  $M_2$  could be arranged so that coma was minimal over the field. Astigmatism and other aberrations were found to be much larger than could ordinarily be tolerated by an image system required to have a 50 percent transfer function at 20 lines/mm. At this point, the possibility of a two-element spectrograph became apparent and further exploration of the four-element design was curtailed, although the potentialities were by no means completely explored. Should the characteristics of the two-element design prove not as attractive as anticipated, then the four-element design should be reconsidered with a view toward utilizing the sagittal or tangential planes to obtain a minimum image size in the high dispersion direction. Further scope in the four-element design is provided by the possibility of aspheric surfaces which can be placed on the gratings as well as on the mirrors.

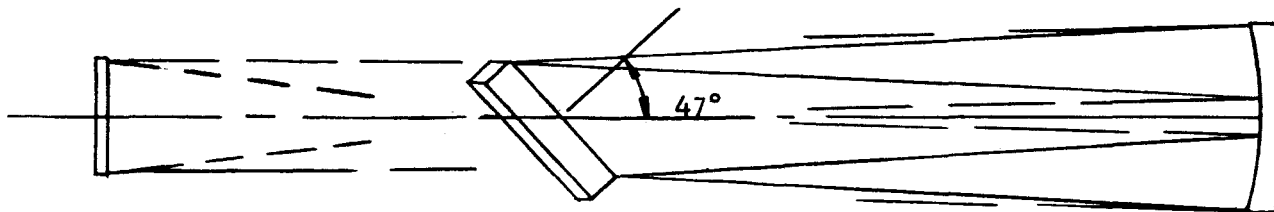
#### 4.3 TWO-ELEMENT DESIGN

A two-element spectrograph design is shown in Figure 4.3. The entrance slit, which is about 100 mm away from a spherical predispersion grating, is reimaged at a distance of 600 mm. Before coming to a focus, the predispersed energy is intercepted by a flat echelle grating which folds the optical path so that the image falls behind the first grating. Some of the astigmatism arising from the first grating is cancelled by the second grating even though it is flat, since it operates on a convergent beam. The two plan views shown in Figure 4.3 illustrate the changes in the predisperser orientation which are required to cover the spectrum. Changes are also required in the echelle orientation and these are not shown. The optical aberrations of a two-element spectrograph system have not been explored. A number of arrangements appear possible including the combination spherical and plane grating system shown in Figure 4.2.

Both the two and four-element spectrograph arrangements are compatible with the general arrangement envisaged for the instrument package. Various three-element spectrograph designs were briefly considered but all appeared to be either very difficult to incorporate into the overall optical layout, or very unpromising optical arrangements which would not yield sufficient resolution. The primary advantage of the two-element design is that it reduces to a bare minimum the number of reflections encountered by the



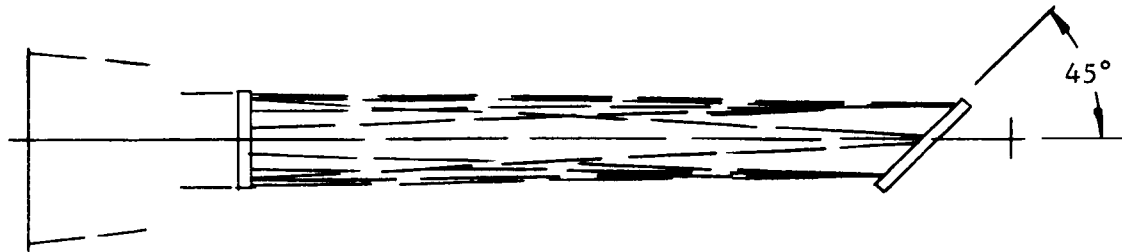
Plan View



Front View

Figure 4.2 Four-Element Spectrograph

PERKIN-ELMER



Front View

Spherical Predispersion  
Grating 720 Lines/MM

Entrance Aperture f/10

Sec Vidicon  
Face



Plan View-Short Wavelength



Plan View-Long Wavelength

Figure 4.3 Two-Element Spectrograph Design

incoming radiation. In the far UV region of the spectrum, the efficiency of reflective coatings deteriorates rapidly towards shorter wavelengths. At 1200Å, elimination of two surfaces is about equivalent to an increase in efficiency of 50 percent. A substantially larger increase might be anticipated closer to 1000Å.

#### 4.4 RECOMMENDATIONS

1. The two-element spectrometer design appears most promising from an efficiency point of view. It is, therefore, recommended that the resolution capabilities of this instrument be explored. The first step might possibly include a literature search and an elementary paper and pencil investigation of some of the simpler forms of the two-element system. The more promising designs brought to light in this part of the study might then be verified and, if necessary, optimized with the aid of a computer. Should the two-element design fail to come up to expectations, then the four-element design, or other alternatives, might be investigated.

Computer analysis of grating systems is not as straightforward as could be hoped, since gratings lie beyond the scope of the usual ray tracing programs. One possibility is a special purpose ray tracing program known as SPRYT. This is capable of handling aspheric, tilted and decentered diffraction grating surfaces and is available from the University of Rochester. A second possibility is creation of an in-house program sufficient for analysis of the two-element spectrograph, but not as general as the SPRYT program.

2. In conjunction with the analytical study of the properties of the two-element system, it is recommended that an analogous visual wavelength model of the spectrograph system be constructed. Scaling would be done by altering the grating spacing as well as the physical size of the components so that aberrations predicted in the analytical study could be directly verified in or near the visible part of the spectrum. The effect of changes in the spectrograph design which might be suggested by unforeseen practical difficulties, or by changes elsewhere in the system, could be more easily explored with a model once a preliminary design was available. The model would also be useful in discovering unsuspected weaknesses in both the mechanical and optical aspects of the spectrograph design. These might include unwanted reflections, built-in alignment errors, etc.
3. The most difficult problem is anticipated to be that of developing gratings of the type required by the echelle spectrograph which are efficient in the far UV. Grating efficiency measurements in the far UV are generally fraught with difficulties. These include large proportions of scattered radiation due to almost imperceptible amounts of dust, polarization effects, ghosts, anomalies, and the

mundane testing problems associated with high energy, intermittent sources and hard vacuums. Both the predisperser and the echelle grating required by the spectrograph require extreme groove geometries; the former being a very shallow groove face and the latter a very steep groove face. Furthermore, the  $1000\text{\AA}$  to  $3000\text{\AA}$  spectral range which must be covered by the predisperser in a single order is about twice the normal range covered by gratings. This will undoubtedly result in some loss of efficiency which will have to be suitably apportioned to various parts of the spectrum. Since the instrument package layout requires that some of the spectrograph elements be redundant, it may be possible to arrange for differing regions of maximum sensitivity depending on the vidicon used. It is, therefore, recommended that a considerable effort be devoted to grating development. This would include the assembly of a facility for making unambiguous grating efficiency measurements, insofar as this is possible, and the trial ruling and testing of a number of gratings.

## 5.0 SPECIAL COMPONENTS

### 5.1 FOCUS AND COMA SENSING CORRECTING MECHANISM

In a well-corrected optical system, lateral alignment errors will cause coma and astigmatism in the image, while errors in the axial placement of the optical elements will cause spherical aberration in the image. Alignment and axial positioning of the optical elements can be improved by utilizing information obtained from two types of measurements: a direct measurement of the centering, tipping, and axial displacement of the various elements, and secondly dissection and analysis of the image itself. These two types of measurement are not necessarily mutually exclusive, and it appears that one type (direct measurement of displacement and angles) might be most useful for correcting gross alignment errors, while the second might be useful for the final "trimming-in" of alignment and focus.

In every astronomical instrument, the first type of measurement is made, usually by hand and during the erection of the instrument, while the second has been used (to the best of our knowledge) in only one instrument, the Project Stratoscope II telescope. In this instrument, a slit and a photocell is used to detect coma in the manner described in Tech Memo RVS-101 (App. B, Vol.III). The output of the photodetector (an RCA 7265 photomultiplier) is telemetered to the ground, where a chart recorder reproduces the signal which is, in effect, the intensity profile of the image. (see Figures 1 and 2 of RVS-101 for a close approximation of the tracings). By using multiple slits arranged in sets such that each succeeding group is orthogonal to the last, it is possible to detect the amount of coma and the direction of the comatic flare. With this information, the operators can correct the alignment of the primary and secondary mirror foci during the flight by moving the secondary mirror in a plane perpendicular to the optical axis through ground control of the motors built into the secondary mirror mount.

In addition to alignment corrections during the Stratoscope flights, the coma detection device is used in focusing the instrument. The measurement consists of determining the width of the peak at the 50 percent intensity points (see Figure 1, RVS-101). Best focus corresponds to a minimum for this value. The focus adjustment is made by ground command of a motor which moves the secondary mirror parallel to the optical axis.

In a general way, the measurement of the image profile is more desirable than direct measurement of optical element tilt and lateral displacement, because the image profile measurement gives a direct measurement of the "output," so to speak, of the telescope, while image quality is merely inferred from measurements of the displacement and tilt of the optical element. Also, adjustments to produce the optimum image profile may partially compensate for other unknown changes (for example, tilt of the optical axis due to a lateral temperature gradient) while inferences made from measurement of element tilt and displacement may not take such changes into account.



For this reason, it seems desirable to incorporate a coma detector similar in principle to that used in Stratoscope II.

It is certain that measurements of the positions of the various optical elements of the satellite telescope will be made during construction of the instrument. The question is whether the telescope should be designed so that these adjustments can also be made in flight, and if so, whether the adjustments should be automatized, ground-controllable, or controlled by the astronaut. The question can be answered by determining the likelihood of the assembly alignment being preserved through launch and orbit well enough for the coma detector to function.

A second question concerns the form the mechanization of the coma detection and correction scheme should take. Since there is a chance that parts of the mechanization may be common to the two measurements, this question will be deferred until the first is determined.

#### 5.1.1 Requirements

As shown in Technical Note DAM-005 (App. B, Vol. III), the axial tolerance for positioning the secondary mirror relative to the primary mirror (for an  $f/2$  primary and a secondary with a magnification of five) is  $\pm 1.54$  microns, assuming a  $\lambda/10$  wavefront deformation criterion and  $\lambda = 0.5$  micron. (This axial tolerance is one fifth as large as the tolerance for Stratoscope II, and is quite severe, and would be even more stringent if a  $\lambda/16$  criterion were used as in Stratoscope II.)

The lateral alignment tolerance for the primary and secondary foci is also determined in the above-referenced Technical Note. For the same conditions, this works out to be 26.6 microns, which is also about five times as severe as the Stratoscope II requirement.

To summarize the two important requirements:

Axial Tolerance:  $\pm 1.54$  microns

Lateral Tolerance:  $\pm 26.6$  microns

#### 5.1.2 Expected Disturbances

The primary known disturbance to alignment will be caused by the change in the thermal environment. If the change were completely isothermal and the primary-secondary separators of the same material as the mirrors, there would be no lateral misalignment, and the focal length of the mirrors would change an amount that would compensate for the change in spacing. However, this state of affairs is unlikely to exist. The secondary will generally be at a different temperature than the primary, and the separators will be at temperatures different than that of either mirror.

5.1.3 Axial Displacement

The limits on the equilibrium temperature differentials which may be permitted in the secondary or separator rods may be computed as follows:

$$\text{Separator rod length} = 165 \text{ cm}$$

$$\begin{aligned} \text{Primary mirror focal length} - \text{separator rod length} \\ = 200 - 165 = 35 \text{ cm} \end{aligned}$$

Assume one rod is warmer than balance of system. Then the secondary would tip relative to the primary and the axial displacement of secondary vertex =  $\delta_{ax} = \frac{1}{2} l (\alpha \Delta t)$  where  $l$  is length of rod,  $\alpha$  is temperature coefficient of expansion ( $0.55 \times 10^{-6}$ ) and  $\Delta t$  is the temperature differential.

$$\text{Let } \delta_{ax} = 1.54 \times 10^{-4} \text{ cm} = \frac{1}{2} 165 (0.55 \times 10^{-6} \Delta t)$$

$$\Delta t = \frac{1.54 \times 10^{-4}}{0.55 \times 10^{-6} \times 82.5} = 3.4^{\circ}\text{C}$$

Assume rods at uniform temperature, but the secondary at a different temperature, then allowable  $\Delta t = 8^{\circ}\text{C}$ .

Thus between  $3^{\circ}\text{C}$  and  $8^{\circ}\text{C}$  steady-state temperature differentials may be allowed before the axial misalignment just equals the tolerance. Exactly what the equilibrium temperatures will be is unknown, but small differences such as these seem quite likely and an initial alignment touch-up is almost a necessity. In addition to the steady temperature-induced axial misalignments, we must examine the temperature variations which would occur in a single orbit revolution. Section 3.1, entitled "The Thermal Environment" demonstrates the relationship between the expected thermal disturbances and the focus tolerances. If, through some combination of circumstances, the orbital thermal disturbances should all happen to cause changes in focal length or displacements which add, then the worst predicted case would be a defocusing shift of 0.15 micron, or an order of magnitude less than the tolerance above. This focal shift may be computed as follows:

$$\begin{aligned} \text{Total cyclic temperature variations equal,} \\ (0.11^{\circ}\text{F} + 0.045^{\circ}\text{F} + 0.085^{\circ}\text{F}) 5/9 = 0.132^{\circ}\text{C} \end{aligned}$$

where  $0.11^{\circ}\text{F}$ ,  $0.045^{\circ}\text{F}$ , and  $0.085^{\circ}\text{F}$  are the cyclic variations in temperature for the spacer rods, secondary mirror, and primary mirror, respectively, as computed in sections 3.2.1, 3.2.2, and 3.2.3.

Assuming worst case,

$$\begin{aligned}\delta_{ax} &= 2 \times 10^2 \times 0.55 \times 10^{-6} \times 0.132 \\ &= 0.145 \times 10^{-4} \text{ cm or } 0.145 \text{ micron}\end{aligned}$$

Thus, if the temperature variations computed in section 3.1 are indeed realized, there seems to be no need for a device to sense and correct the primary-secondary mirror spacing during a single orbit.

There are, however, many possibilities for unpredictable thermal distortions. For example, there may be a temperature gradient across one of the spacing rods tending to make it bow as in a bimetallic element. This effect may be minimized by proper attachment of the spacing rods to the outer structure of the telescope. Indeed, practically any distortion which may be foreseen can be at least partially compensated or corrected for in the construction of the telescope. But it is those distortions which cannot be predicted that can be most damaging.

#### 5.1.4 Lateral Displacement

As was seen in the previous section, while it is necessary to touch up axial alignment when temperature equilibrium is reached, there seems to be little or no need to measure the axial displacements continuously during each revolution, since the cyclic disturbances from thermal causes seem to be sufficiently small. Furthermore, if there was a uniform lateral temperature variation in the rods, causing the secondary mirror to tip, then the lateral motion of the secondary mirror back focal conjugate relative to the optical axis of the primary would be amplified by the ratio of the distance to the focus and the spacer rod separation:

$$\delta_{lat} \approx \delta_{ax} \frac{f_s}{l_s}$$

where  $f_s$  is the distance to the back focal conjugate of the secondary and  $l_s$  is the lateral separation of the spacer rods at the secondary (which is 10 cm).

$$\delta_{lat} = \text{the lateral displacement of secondary focal conjugate}$$

$$\delta_{lat} = \frac{35}{10} \delta_{ax}$$

Thus, for the maximum allowable axial displacement, the lateral displacement would be only  $3.5 \times 1.54 = 5.4$  microns, well within the lateral tolerance. Thus, when the maximum axial displacement takes place, this effect gives a negligible lateral displacement.

The only other effect which might cause lateral misalignment may be deflections caused by gravity during the set-up procedure which would then disappear once the telescope is in orbit; however, a good, rigid structural design and careful measurements of relative positions of the primary and secondary foci during assembly while rolling the structure about its longitudinal axis, should assure that the deflections are sufficiently small before launch to avoid any difficulty in orbit.

The answer to the first question raised above is, therefore, no, it is not necessary to mechanize the direct measurement of the tilt and alignment of the optical elements and it is highly likely that a coma detector such as was used in Stratoscope II would be well within its range of operation for thermal variations in orbit.

In such a complex instrument as the one described herein, it does not seem warranted to depend upon passive alignment of the optics alone, even though computations do not show a strong case against it. It is, therefore, recommended that the instrument be equipped at least with an automatic focus correction system.

#### 5.1.5 Design Considerations for Coma Detector

In order to make the coma detector work, it is necessary to find and cause a star of sufficient brightness to fall into its aperture. To accomplish this, it is proposed that a tilt-table flat mirror be provided near the aperture of the SEC vidicon. A single, bright "alignment star" would be pointed to and located on the vidicon, and then the image movers programmed to move in such a direction that the alignment star would be reflected from the flat mirror. The image of the star would then fall on a gridwork of slits placed at a focal plane as shown in Figure 5.1. The gridwork of slits would be in a thin plate, and the image of the star would be caused to move cyclically, first in a direction perpendicular to half the slits and then, after a slow scan, in a direction at right angles to this. A photomultiplier tube behind the plate containing the slits would sense the variation of energy passing through the slits.

After suitable signal processing, the time varying signal representing the image profile would be time multiplexed into perhaps twenty elements. Each of these twenty elements, representing the intensity at a particular location in the image, would be stored and digitized in a memory unit. Then an arithmetic processor would pick out the maximum from among the twenty elements. From a prior knowledge of the image diameter, the two equidistant elements corresponding in the first bright ring or "skirts" of the image profile would be selected and compared with each other. The difference between these two values is a measure of coma. This information can be obtained in real-time by the ground station or by the Apollo spacecraft at any time during the manned portion of the mission. This information would be used to initiate a command to the lateral drive motors on the secondary mirror. The process would then be repeated on the orthogonal axis. Then, the

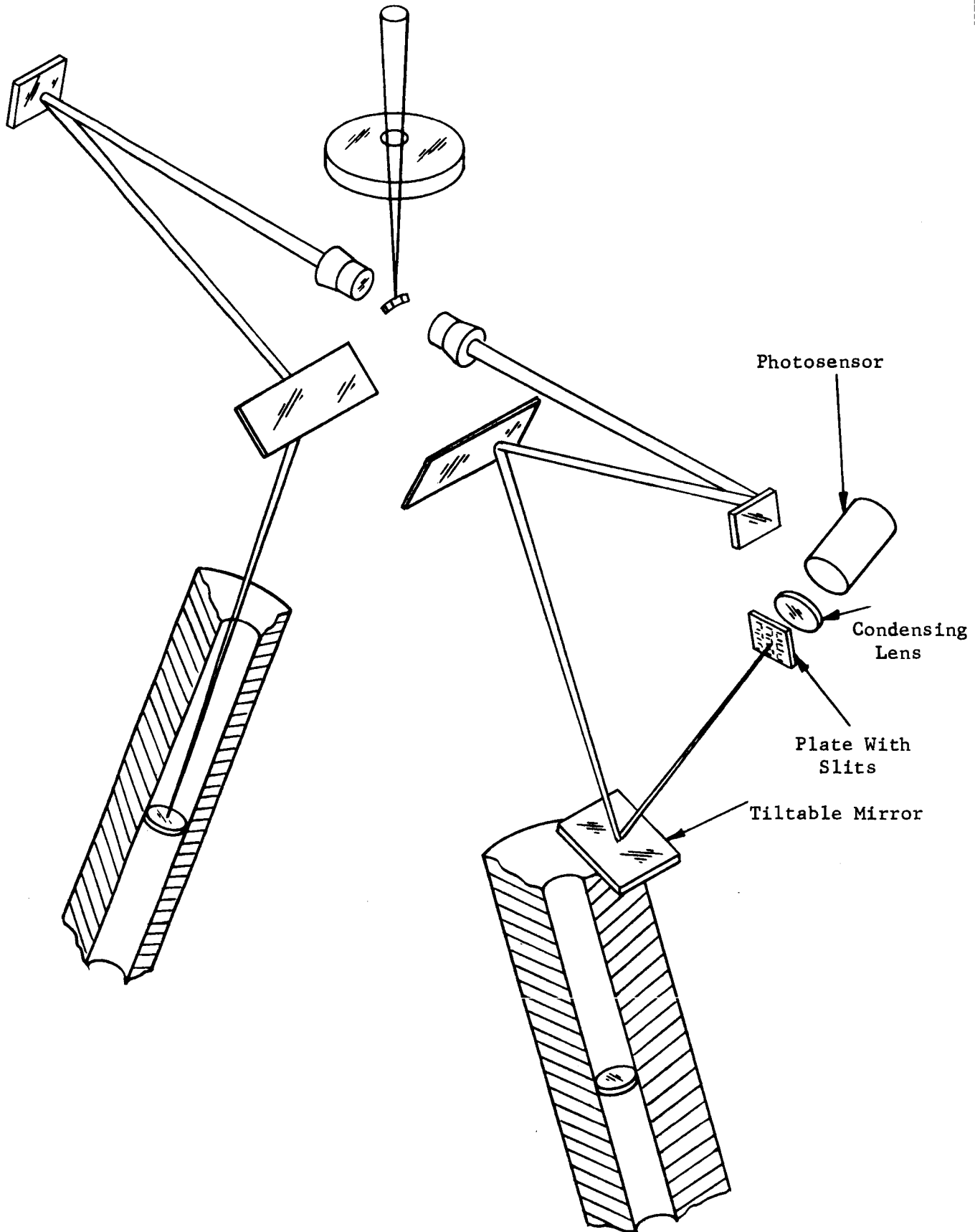


Figure 5.1 Coma Detector

first axis would be sampled again, and the process repeated until the coma signal on both axes is simultaneously zero.

#### 5.1.6 Focus Adjustment

The touching-up of focus could be performed in a similar manner except that the number of elements between the storage registers containing intensities one-half that of the central peak would be counted to determine the image spread. Ambiguity is presented by the fact that there is no information contained in the profile of the image when it is out of focus as to which direction to go in order to get to better focus.

A possible way of determining the proper direction in which to focus would be to move the secondary mirror cyclically and compare the phase of the mirror motion with the phase of the signal produced by the coma detector. The position of the mirror when the signal is maximum relative to the position of the mirror when it is minimum determines the direction in which to go. A direction switch is then set and the mirror moved in small steps until the computation of focus indicates that the image is focused sufficiently well. At this point, the focussing operation would stop and coma detection and alignment would commence. At the end of this process, the telescope would be pointed at the object of interest and observations would resume.

An alternate method for obtaining the intensity profile of the image is to select that TV scan line which passes through the center of the image. This video signal could be reproduced on board and sent to the time multiplexer and arithmetic processor unit described previously. Because of possible interface problems this technique is not preferred. It is doubtful that coma detection would be possible using the vidicon due to poorer resolution capabilities, but focus might be accomplished in this manner. The question might be raised that if the vidicon cannot detect coma, why be concerned with it? It is suspected that coma due to misalignment may reduce the intensity at the center of the image, although further study is required to settle this question.

A preliminary calculation of the required magnitude for the alignment star indicates that for a signal-to-noise ratio of 10, an optical efficiency of 10 percent, but with no filtering for monochromaticity, a 7.6 magnitude star can be used. With a star this dim, the alignment measurement will require in the order of forty seconds of time.

## 5.2 AUXILIARY TRACKING SYSTEM

In order to have a backup in case that one of the critical image shifters not only gets stuck, but for some reason, becomes totally inoperative, an auxiliary guidance subsystem is recommended to be mounted on the optical package. Roll axis stabilization to 2.5 arc-seconds rms is required for the worst case condition with respect to the translation guide star position within the guidance field.

Based on taking 10 minute recordings when using the back-up system and allowing a maximum drift of 2.5 arc-seconds during the recording, a maximum drift rate for the auxiliary subsystem of 1/240 arc-sec/second is allowable.

A single axis startracker mounted to the optical package structure at the forward end is arranged such that it causes a minimum amount of primary mirror obscuration and can sense motion around the roll axis. The startracker will be on a sliding mount allowing it to pop out beyond the forward end of the spacecraft so that it can look at 90 degrees to the optical axis when the sunshade is opened.

A 2-inch aperture, f/10 optical system with a 37 arc-minute diameter field of view is visualized. Such a system, which employs a single photomultiplier will be able to track on a 4.5 magnitude or brighter star with the required minimum pointing error of 2.5 arc-seconds rms.

In view of relatively large boresight errors expected due to gross thermal effects as well as the sliding mount arrangement for the startracker, the acquisition mode using this auxiliary subsystem for roll guidance requires an in-orbit boresight calibration before use. With the optical package in the caged position, the spacecraft can be pointed so that a sufficiently bright star falls within the auxiliary startracker's field of view. By commanding the spacecraft around the roll axis via the spacecraft startrackers to null out the auxiliary startracker subsystem error signal, the boresight offset between the optical axis of the optical package and the spacecraft startrackers axis can be held to within  $\pm 2$  arc-minutes  $\times \sin(15 \text{ arc-minutes}) = \pm 0.48$  arc-second.

After completion of the boresight calibration, the measured offset will be put into the program of the spacecraft startrackers for the roll star position settings before the optical package is uncaged to lock onto its guide stars.

The probable maximum recording star offset is in the order of  $\pm 2.5$  percent of the larger dimension from the center of the program star field of view, a quite acceptable condition, leaving enough margin for additional boresight misalignments.

Thermal drifts affecting the relative position between the optical package and the startracker subsystem are considered small within a ten minute period of time, since the expected time constants of drift are much larger than the recording period. This has to be verified during the design phase of the APEP.

## 6.0 RECOMMENDATIONS

The results of the Princeton Advanced Satellite Study have clearly established the feasibility of a 40-inch high resolution, optical instrument for spectral investigations as well as direct imagery of stars.

However, before a final hardware design is implemented, certain critical areas of the Advanced Princeton Experiment Package (APEP) should be more thoroughly investigated so that the system concept can be advanced from a general feasible approach to that of optimization. Areas falling into this category are:

- Pointing and Suspension System
- Optics
- Spectrograph
- Thermal Analysis
- Adaptation to Astronaut Participation

### 6.1 POINTING AND SUSPENSION SYSTEM

In order to carry the pointing system study from a single axis simulation to a 3 axis analog computer simulation, the actual servo electronics design should be carried out to the point that critical circuit components can be specified, especially nonlinear elements and switching devices. Also the sensor design should be carried out to the degree that the chopping method is more fully analyzed (type of rotating reticle, etc.) and the detailed characteristics of the sensor output have been verified.

In parallel with the basic effort for a 3-axis computer simulation, a magnetic torquer breadboard should be designed and evaluated, especially from the point of view of obtaining a torquer with two windings within one assembly, so that it can torque around two perpendicular axes.

The suspension system for maintaining lateral positions of the telescope with respect to the spacecraft have been conceived and analyzed, but several design areas remain to be investigated. An analog computer simulation should follow for verification.

While the redundancy requirement in the pointing has been recognized throughout this study, little work has been done in this area. Of specific interest is the further investigation of extremely low drift rate space-qualified gyros.

An arrangement for release and assembly of the telescope during the launch phase and its release in orbit should be finalized. This area is very much adaptive to the efficient use of an astronaut as backup to ready the instrument once the spacecraft has attained proper orbit.



Circuit design schemes should be studied with respect to the reduction or elimination of noise due to cosmic radiation.

Integration of the results in these areas will result in an integrated pointing and suspension system design.

## 6.2 OPTICS

Additional study of materials for the primary mirror and various constructions for the blank are recommended. In particular, the element silicon should be studied further; and the desirability of a composite, fused silica-aluminum wool eggcrate mirror blank should be explored via experiment.

In parallel, it is recommended that the telescope optical design be reviewed with emphasis on increasing the field of view without losing good imagery. In particular, the configuration of Figure 2.16 utilizing the deployable secondary mirror is recommended for further study.

The relaying microscope optical design should be optimized and the figure tolerances of the optical elements should be specified as well as performance at various operational temperatures.

In parallel with these two efforts the optical image shifter concept must be verified and a detailed layout design of the mechanism should be made. Since the image shifters are the foundation for locking on to the guide stars, a thorough check can then be carried out to determine the sensitivity of the image shifters to slight motion as a locked-up assembly. If such a check is affirmative the final optical design of all elements will be carried out.

With the optical design completed in the three optical subassemblies, that is, the telescope primary optics, the image shifters, and the relaying microscope, the results of basic ray tracings will be available and an optics compatibility check can be carried out. The apportionment of tolerances to the several optical elements and their alignment will be accomplished after ray tracing.

In order to assure a high degree of confidence in the critical image shifter subassembly, it is then proposed that a breadboard be built and subsequent environmental and optical testing be performed.

A more detailed design of the optics for the auxiliary star tracker and the sensor for automatic monitoring and correction of focus, and real-time coma correction should be investigated, since this area has had only little attention during this study program. The effects of small amounts of coma upon the central intensity peak of the image should be determined.

### 6.3 SPECTROGRAPH

It is proposed that a scaled-up-in-wavelength version of the echelle spectrograph will be breadboarded, while in parallel more analytical exploration of the two element echelle spectrograph takes place. With breadboard results in hand and analytical verification of the system completed, a computer analysis should be carried out. Depending on cost involved either Perkin-Elmer would generate an in-house computer program for this analysis, or use an existing computer program. If this investigation should show that a two-element spectrograph cannot achieve the desired performance, then the four-element design investigated in this study should be optimized and a breadboard constructed as recommended above.

The results of the analysis would permit the final spectrometer layout to cover the 800Å to 3000Å region as a design objective, with the 900Å lower limit as a must for photographic work. The layout would also include the mechanisms for interleaving the spectral lines and spectrograph redundancy switching.

Simultaneously with the above, a program should be underway to develop a method for making efficiency measurements on gratings in the far UV part of the spectrum. The first step in this program is a search for techniques. Equipment required will include a UV monochromator and vacuum tank, a calibrated UV source, and a suitable UV detector. Much of this equipment must be developed, although Perkin-Elmer is in a position to supply some portions already. A number of trial gratings should be ruled and measurements made. A major effort is recommended in this area.

Once the finally selected gratings are procured, efficiency measurements should be verified by an independent source.

The last step would be to take the calibrated elements and set them up as a spectrograph breadboard in a hard vacuum tank to verify the spectrometer design.

### 6.4 THERMAL ANALYSIS

The thermal analysis during this study dealt mainly with the effect of orbital heat flux variations on critical elements of the optical instrument. It did not take into account the conduction problems associated with the specific telescope design and the effect of heat sources in the instrument. This additional effort cannot be undertaken until the layout and packaging of the Advanced Princeton Experiment Package (APEP) have been carried out further. In particular, the problem of the thermal treatment of the back face of the primary mirror requires further study as the heat sources in the instrument package are identified.

It is recommended that this effort be started as soon as possible because there will undoubtedly be interaction between final design and packaging

and the results of the more specific thermal conduction and radiation analyses. It should be extensive enough to determine the thermal effects on pointing servo component function and alignment, spectrometer components, and, of course, the primary and secondary mirrors.

#### 6.5 ASTRONAUT PARTICIPATION

In order that the goal of in-orbit malfunction problem-solving can be achieved, it is recommended that the full-scale mock-up be continually revised and maintained current with detail design thinking as it evolves. In this way, accessibility, spatial clearances, and, later, training can be accomplished.

Additional experimental and study efforts which should be carried out with regard to the use of photographic recording media are: (1) experiments to determine the efficiency of low temperature in reducing reciprocity failures, in Schuman emulsion films in particular, (2) further work on an optimum film shielding configuration, (3) a study of the radiation environment at synchronous altitude, and (4) development of a wet processor for film in a zero-g environment.

#### 6.6 THE 120-INCH TELESCOPE

While considerations as contained in Volume II of this study are applicable to large astronomical space telescopes of apertures ranging from 30 to 120 inch diameters, a specific feasible concept has been established only for the 40-inch Advanced Princeton Experiment Package.

However, it is apparent that a large number of limitations imposed on the APEP by tailoring it to existing OAO hardware would not exist for a 120-inch telescope. An astronomical telescope with a 120-inch aperture would be a logical next step. It is a big step and will require careful planning to achieve sufficient advancement in space technology. Such a telescope would be an "all-reflective" diffraction-limited design, and probably could be placed into synchronous earth-orbit. Thus, an astronomical observatory capable of long life, wide wavelength capability, high real-time communication data rates, and multiple sensors could be accomplished within 5 to 10 years after APEP operates in a low earth orbit.

It is recommended that in parallel with efforts following this study with respect to APEP, a feasibility study be conducted for a specific 120-inch telescope, so that continuity is maintained towards the ultimate goal of a large National Astronomical Space Station. This will assure that the results and experience of the present effort can be utilized without delay and with a high degree of efficiency.

APPENDIX A

GUIDE STAR ORIENTATION AS RELATED TO  
THE TELESCOPE COORDINATES

## APPENDIX A

GUIDE STAR ORIENTATION AS RELATED TO THE TELESCOPE COORDINATES

## A.1 INTRODUCTION

The method by which the guide star fine sensor signals are processed and fed to the magnetic pushers is obtained from the geometric relationships derived in this appendix. Normally, without these signal processing techniques, severe axis coupling would exist in the telescope guidance system.

Referring to Figure A.1, the right sensor coordinates will be defined by  $y$  and  $x$  and the left sensor by  $y'$  and  $x'$ . The axes  $\psi$ ,  $\phi$ , and  $\theta$  (horizontal, vertical, and rotation) are the telescope rotational axes about the center of rotation (center of gravity). The image movers can occupy any of the four quadrants although they are only shown located in quadrants I and II of Figure A.1. Note, however, that the right image mover can only occupy quadrants I and IV while the left image mover only occupies quadrants II and III. The image mover coordinates with respect to the telescope axes denoted by  $R_\alpha$ ,  $R_\beta$ ,  $\alpha$  and  $\beta$ .

The geometry, as initially developed here, basically uses the right sensor to obtain vertical and horizontal axis information. Both sensors are used to obtain roll axis information. The sensor roles can be reversed without changing the geometric concepts although a certain amount of additional phasing logic is required as shown subsequently. The left and right sensors are assumed to be identically calibrated for this development.

Throughout this analysis, the symbols  $\Delta y$  and  $\Delta x$  represent the image motions which generate the sensor outputs denoted by  $\epsilon y$  and  $\epsilon x$  in Section 3.0.

## A.2 GEOMETRY - QUADRANTS I AND II

For the right and left sensors, the following relationships can be derived for vertical, horizontal, and roll motions:

Vertical and Horizontal Motions (Denoted by Subscripts "T")

$$\text{Vertical:} \quad \Delta\phi = \Delta y_T \quad (\text{A-1})$$

$$\Delta\phi = \Delta y'_T \quad (\text{A-2})$$

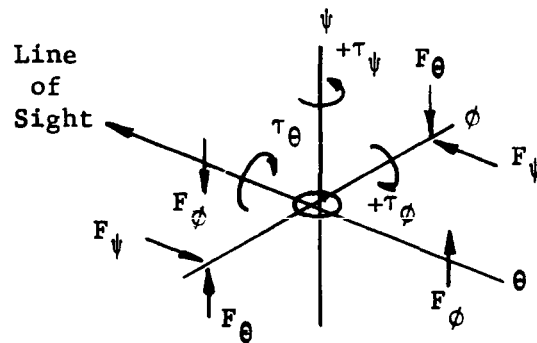
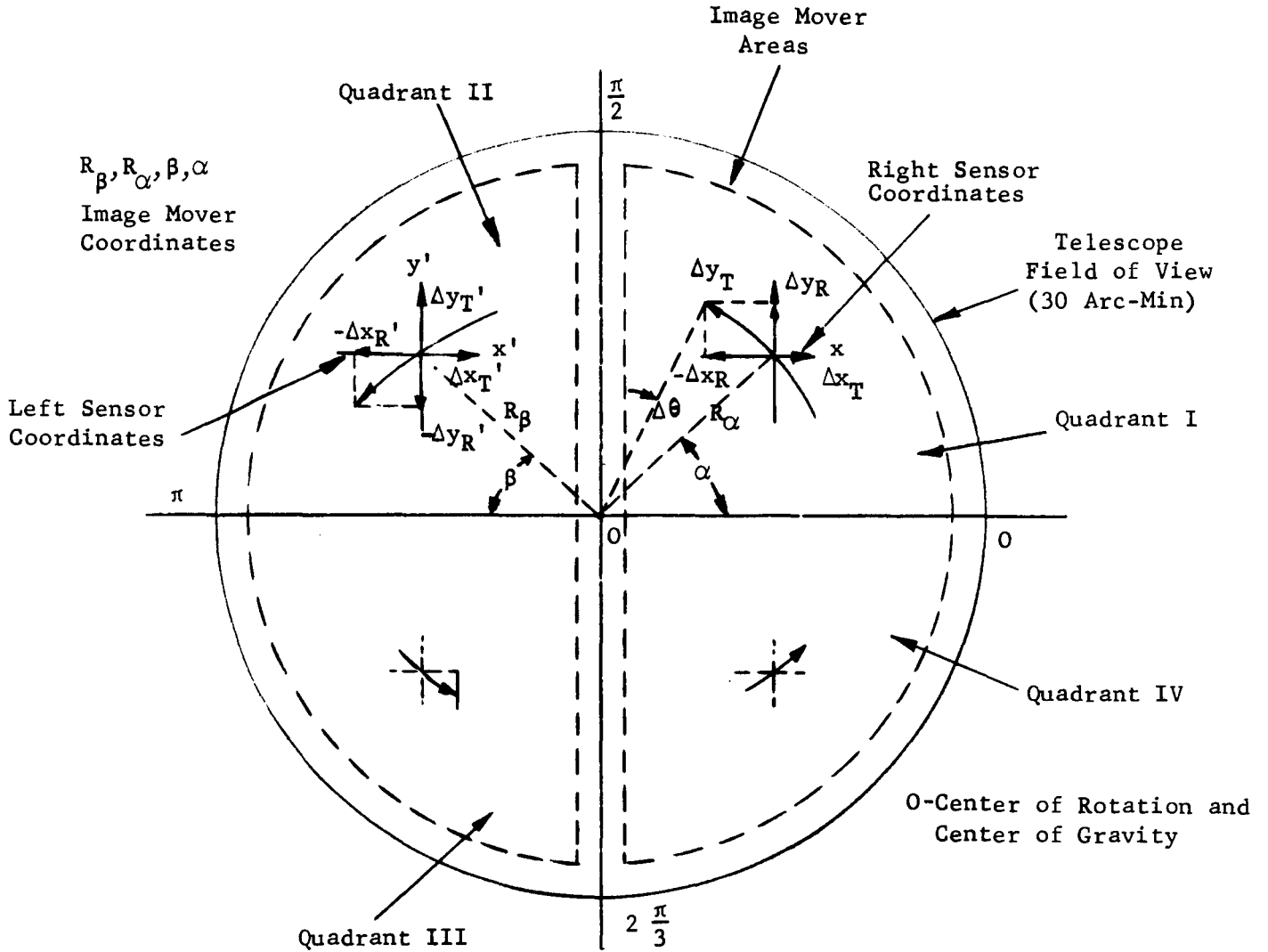


Figure A.1. Telescope Coordinates

which states, for a telescope motion in the vertical direction  $\Delta\phi$ , sensor image motions (or signals)  $\Delta y_T'$  and  $\Delta y_T$  are generated.

$$\text{Horizontal: } \Delta\psi = \Delta x_T \tag{A-3}$$

$$\Delta\psi = \Delta x_T' \tag{A-4}$$

For a telescope motion in the horizontal direction  $\Delta\psi$ , sensor signals  $\Delta x_T$  and  $\Delta x_T'$  are generated.

Rotational Motions (Denoted by Subscripts "R")

$$\Delta y_R = \Delta\theta R_\alpha \cos\alpha \tag{A-5}$$

$$\Delta x_R = -\Delta\theta R_\alpha \sin\alpha \tag{A-6}$$

where

$\Delta\theta =$  telescope rotation about line of sight.

The assumption

$$R_\alpha \sin\Delta\theta \cong R_\alpha \Delta\theta \text{ is also made.}$$

Equations (A-5) and (A-6) state, for a telescope rotation of  $\Delta\theta$ , the vertical ( $\Delta y_R$ ) and horizontal ( $\Delta x_R$ ) right sensor signals are generated.

$$\Delta y_R' = -\Delta\theta R_\beta \cos\beta \tag{A-7}$$

$$\Delta x_R' = -\Delta\theta R_\beta \sin\beta \tag{A-8}$$

where,  $\Delta y_R'$  and  $\Delta x_R'$  are signals generated for the left sensor.

To obtain the rotational torquer signals independent of vertical motions, the right and left sensor  $\Delta y$  components are subtracted.

$$\left( \Delta y_T + \Delta y_R \right) - \left( \Delta y_T' - \Delta y_R' \right) = \Delta y_R + \Delta y_R' \tag{A-9}$$

Using Equations (A-5) and (A-7) and substituting,

$$\Delta y_R + \Delta y_R' = \Delta\theta \left[ R_\alpha \cos\alpha + R_\beta \cos\beta \right]$$

and

$$\Delta\theta = \frac{\Delta y_R + \Delta y_R'}{R_\alpha \cos\alpha + R_\beta \cos\beta} \tag{A-10}$$

The rotational component  $\Delta\theta$  eventually is used to provide commands for the telescope roll servo loops.

The relationship (A-10) has restrictions. Two guide stars cannot be selected to be in a plane defined by the  $\psi$  and  $\theta$  axes ( $\alpha = \beta = \pi/2$ ) or at the center ( $R_\alpha = R_\beta = 0$ ) since the  $\Delta\theta$  function becomes discontinuous at these locations.

To derive the vertical signals (for  $F_\phi$  or  $\tau_\phi$ ) independent of rotational motions, the right sensor  $\Delta y$  signals are used from which the rotational components are subtracted. Normally,

$$\Delta\phi = \Delta y_T + \Delta y_R \quad (\text{A-11})$$

and using Equation (A-5), roll cross-coupling is evident,

$$\Delta\phi = \Delta y_T + \Delta\theta R_\alpha \cos\alpha \quad (\text{A-12})$$

However, if Equation (A-10) is multiplied by  $R_\alpha \cos\alpha$  and the product is subtracted from (A-12), we obtain

$$\Delta\phi = \Delta y_T + \Delta\theta R_\alpha \cos\alpha - \frac{\Delta y_R + \Delta y'_R}{R_\alpha \cos\alpha + R_\beta \cos\beta}$$

Therefore,

$$\Delta\phi = \Delta y_T \quad (\text{A-13})$$

The  $\Delta\phi$  sensor signal of Equation (A-13) is used to provide signals for the vertical servo loops.

Finally, the horizontal torque signals can be obtained independent of rotational motions by using the sensor  $\Delta x$  signals and adding the rotational component. Normally,

$$\Delta\psi = \Delta x_T - \Delta x_R \quad (\text{A-14})$$

and using Equation (A-6), roll cross-coupling is obvious,

$$\Delta\psi = \Delta x_T - \Delta\theta R_\alpha \sin\alpha \quad (\text{A-15})$$

If Equation (A-10) is multiplied by  $R_\alpha \sin\alpha$  and the product is added to (A-15),

$$\Delta\psi = \Delta x_T \quad (\text{A-16})$$

The  $\Delta\psi$  sensor signal is used to command the horizontal servos.



A.3 GEOMETRY - QUADRANTS I AND III

Equations (A-1) through (A-7) remain identical. Equation (A-8) reverses polarity for these quadrants. The roll commands are obtained identically with the result given by (A-10). Similarly, the vertical signals are derived (A-11), (A-12) producing a result identical to (A-13) and for horizontal signals, a result identical to (A-16).

For diagonally opposite quadrants such as I and III, the right and left sensor  $\Delta x$  components could also be subtracted to yield a rotation signal ( $\Delta\theta$ ) independent of translation, i.e.,

$$\Delta\theta = \frac{\Delta x_R + \Delta x'_R}{R_\beta \sin\theta + R_\alpha \sin\beta} \tag{A-17}$$

However, this relationship is discontinuous at  $\alpha = \beta = 0$  and also at  $R_\beta = R_\alpha = 0$ . Similar to the discontinuities of (A-10) at  $\alpha = \beta = \pi/2$ . If desired, although more complex in terms of implementation, both  $\Delta\theta$  relationships (A-10) and (A-17) could be used in diagonally opposite quadrants to avoid on or near axis guide star location restrictions (exception at  $R_\beta = R_\alpha = 0$ ). For example, in quadrant III, use  $\Delta\theta$  (y components) for  $\pi \leq \beta \leq \pi + \pi/4$

$$\text{and } \Delta\theta \text{ (x components) for } \pi + \pi/4 \leq \beta \leq \frac{2\pi}{3} .$$

A.4 GEOMETRY - QUADRANTS II AND IV

Equations (A-1) through (A-5), (A-7), and (A-8) remain identical. Equation (A-6) reverses polarity for these quadrants.

The result in (A-10) is identical for these quadrants for the rotational signal components. Similarly, Equation (A-13) holds for the vertical signals.

Due to the polarity reversal in  $\Delta x_R$ , the derivation for the horizontal signals is slightly altered. The  $\Delta x$  component sensor signals must be added,

$$\Delta\psi = \Delta x_T + \Delta x_R \tag{A-18}$$

Using Equation (A-6)

$$\Delta\psi = \Delta x_T + \Delta\theta R_\alpha \sin\alpha \tag{A-19}$$

Using (A-10) multiplied by  $R_\alpha \sin\alpha$  and subtracting from (A-18) produces

$$\Delta\psi = \Delta x'_T \tag{A-20}$$

The  $\Delta\psi$  is the horizontal signal for quadrants II and IV.

## A.5 GEOMETRY - QUADRANTS III and IV

Although Equations (A-6) and (A-8) reverse polarity, the equations from (A-1) to (A-5) and (A-7) are identical. Therefore, the processing is identical to that obtained in Section A.4 for quadrants II and IV.

## A.6 SIGNAL FLOW DIAGRAM

The processing logic can be summarized by means of a single flow diagram such as that shown in Figure A.2. It includes all four quadrants of operation. The conversion from polar to rectangle coordinates for the image movers has also been included using the following four relationships.

$$x_{\alpha} = R_{\alpha} \cos \alpha \quad (\text{A-21})$$

$$x_{\beta} = R_{\beta} \cos \beta \quad (\text{A-22})$$

$$y_{\alpha} = R_{\alpha} \sin \alpha \quad (\text{A-23})$$

$$y_{\beta} = R_{\beta} \sin \beta \quad (\text{A-24})$$

## A.7 SENSOR REVERSAL SIGNAL FLOW

If the left sensor is used as the horizontal and vertical axes prime reference, the signal processing logic becomes somewhat altered.

Summarizing, Equations (A-1) through (A-8) remain identical and the roll signals are derived in the same manner as defined by Equations (A-9) and (A-10). Eliminating the roll components in the vertical axis, however, requires adding the roll coupling term since by convention (quadrants I and II),

$$\Delta \theta = \Delta y'_T - \Delta y'_R \quad (\text{A-25})$$

Using Equation (A-7),

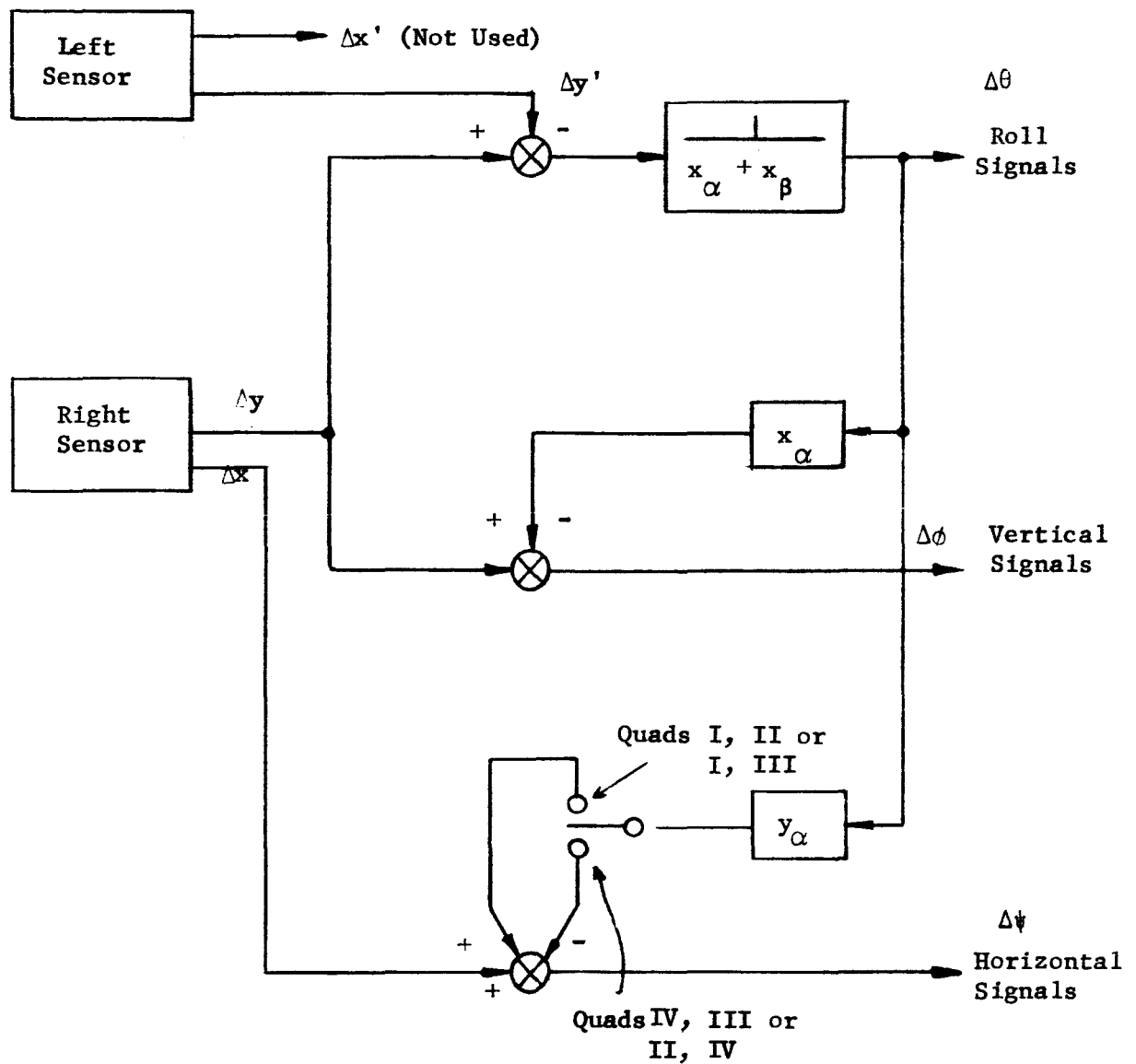
$$\Delta \theta = \Delta y'_T - \Delta \theta R_{\beta} \cos \beta \quad (\text{A-26})$$

Then, by multiplying Equation (A-10) by  $R \cos$  and adding,

$$\Delta \theta = \Delta y'_T \quad (\text{A-27})$$

The derivation of the horizontal components in the I and II quadrants are identical but differ in the I and III quadrants,

$$\Delta \psi = \Delta x'_T - \Delta x'_R \quad (\text{A-28})$$



NOTE:  $\Delta y$ ,  $\Delta x$ ,  $\Delta y'$ ,  $\Delta x'$  represent the sum or subtraction of the  $\Delta y_R$ ,  $\Delta y_T$ ,  $\Delta x_R$ ,  $\Delta x_T$ , (and primed) components.

Figure A.2. Signal Flow Diagram (Right Sensor Prime)

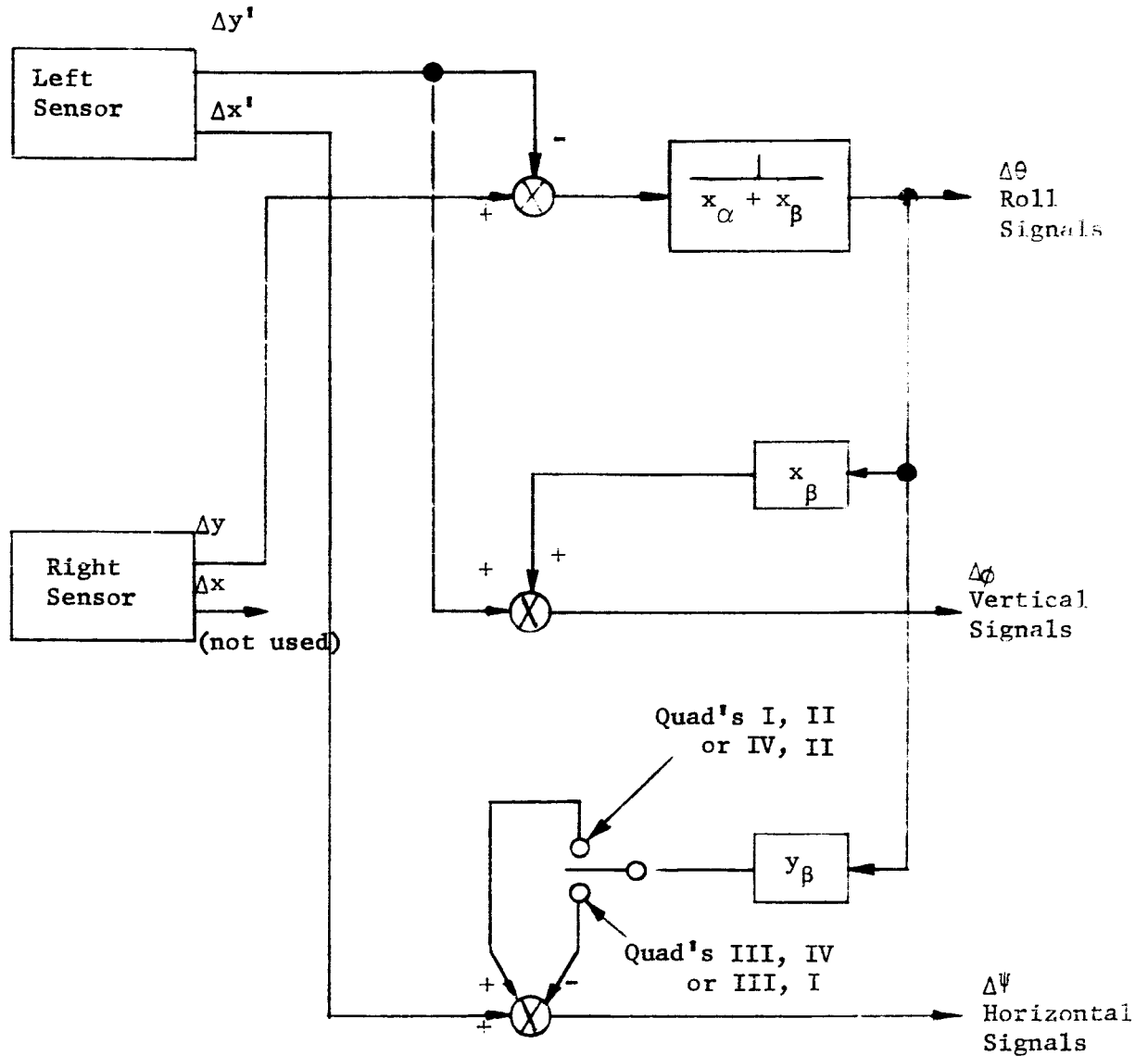
Using Equation (A-8),

$$\Delta\psi = \Delta x'_T - \Delta^{\theta} R_{\beta} \sin\beta \quad (\text{A-29})$$

If Equation (A-10) is multiplied by  $R \sin$  and the product is added to (A-29),

$$\Delta\psi = \Delta x'_T \quad (\text{A-30})$$

Equation (A-30) is valid for quadrants I, III, and III, IV. For quadrants I, II and II, IV, the roll cross-feed polarity must be reversed as shown in Figure A.3.



**Note:**  $\Delta y$ ,  $\Delta x$ ,  $\Delta y'$ ,  $\Delta x'$  represent the sum or subtraction of the  $\Delta y_R$ ,  $\Delta y_T$ ,  $\Delta x_R$ ,  $\Delta x_T$ , (and primed) components

Figure A.3 . Signal Flow Diagram (Left Sensor Prime)

APPENDIX B

TECHNICAL NOTES

D. A. M. , G. C. -004

D. A. M. -003

J. J. G. -002

D. A. M. -001

R. V. S. -101

D. A. M. -005

TECHNICAL NOTE  
D.A.M., G.C.-004

## TELESCOPE RESTRAINT SYSTEM

### General

Two passive restraint systems were considered which would limit the linear displacement between the telescope and the outer spacecraft and at the same time allow sufficient rotational freedom for telescope orientation. The most severe requirement for both systems was the attenuation factor required to isolate the telescope from the spacecraft jitter caused by hunting of its coarse guidance system.

### Elastic and Snubber Systems

The elastic system, shown in Figure 1, consists of spring and damping elements arranged to connect the cg of the telescope to the spacecraft. Ideally this results in providing linear restraint without rotational coupling. The snubber system shown in Figure 2 consists of a ball and socket structure located at the cg of the telescope. A gap between the ball and socket allows complete isolation except during the period of telescope-spacecraft collision.

Both systems have certain disadvantages. In the elastic system the common coupling point is of finite size; therefore the springs act as a radius arm from the cg and thus produce restoring torques which the telescope guidance system has to act against. In the snubber system, an angular impulse is imparted to the telescope during each collision, if the collision forces are not transmitted through the telescope cg.

Both the magnitude of the angular impulse exchanged during collision and the frequency of collision determine the snubber parameters. Damping can also be employed in the snubber system to reduce the impulse magnitude and rate.

Table I contains the spacecraft and telescope parameters used to estimate the limitations of the two restraint systems.

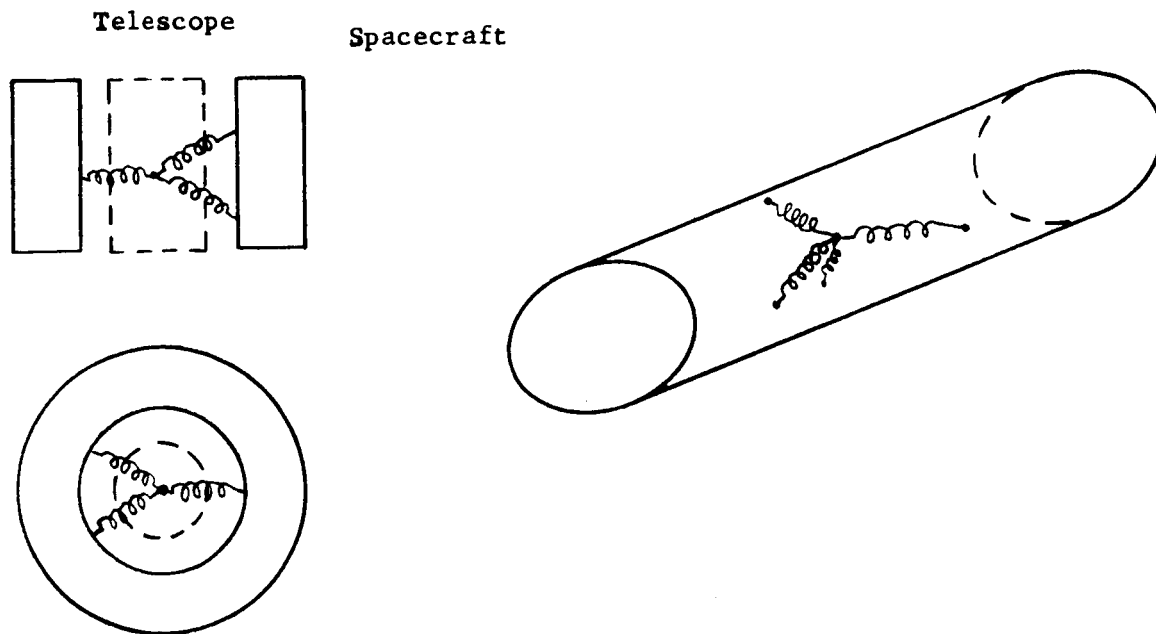


Figure 1. Elastic System

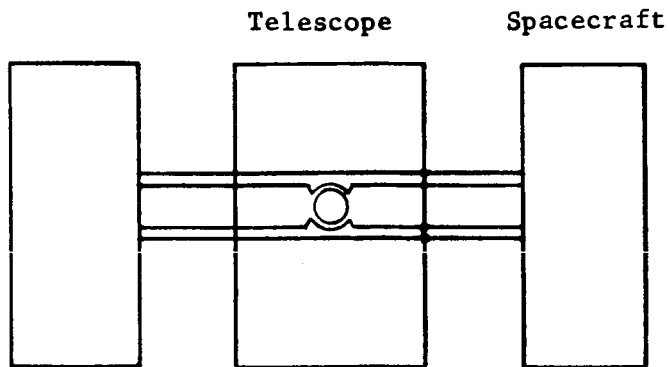


Figure 2. Snubber System



TABLE I

SPACECRAFT-TELESCOPE PARAMETERS

Symbol	Description	Estimated Value
Jsc	Spacecraft moment of inertia	$2.0 \times 10^3$ slug - ft <sup>2</sup>
Jt	Telescope moment of inertia	$2.0 \times 10^2$ slug - ft <sup>2</sup>
Msc	Mass of spacecraft	80 slugs
Mt	Mass of telescope	30 slugs
$\dot{\theta}$	Max. angular rate of spacecraft while tracking	1 min/sec
$\theta$	Max. angular displacement of spacecraft while tracking	2 min

Estimated values for the telescope requirements are summarized in Table II. These estimates are used only for the purpose of comparing the two systems.

TABLE II

TELESCOPE REQUIREMENTS

Symbol	Description	Estimated Value
T Max.	Max. allowable torque applied to telescope	$\pm 100$ dyne-cm
Pa Max.	Max. allowable angular impulse imparted to telescope	$\pm 100$ dyne-cm-sec
L Max.	Max. linear range of telescope displacement	.040 in.

Table III presents the parameter limitations for each system determined from the data of Tables I and II. For the elastic system the max. values for the spring constants  $K_t$  and  $K_c$  were determined from the torque limitation of 100 dyne-cm and maximum angular misalignment between the telescope and vehicle of  $\pm 15$  min. The minimum value of  $K_c$  was determined assuming a 5% imbalance in torquers resulting in a displacement force of 10 dynes, and a max. translational displacement of .040 in.

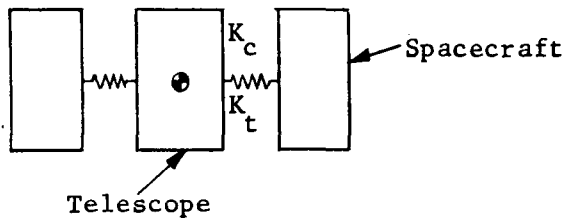
TABLE III

RESTRAINT SYSTEM PARAMETERS

Elastic System

Symbol	Description	Limit of Values	Determination of Limits
$K_t$	Torsional Spring Constant	$0 \leq K_t \leq .218 \frac{\text{ft-lb}}{\text{degree}}$	$K_t$ max-max torque
$K_c$	Rectilinear Spring Constant	$5.5 \times 10^{-4} \leq K_c \leq 1.0$ (lb./in)	$K_c$ max - estimate $K_c$ min - 5% torquer imbalance

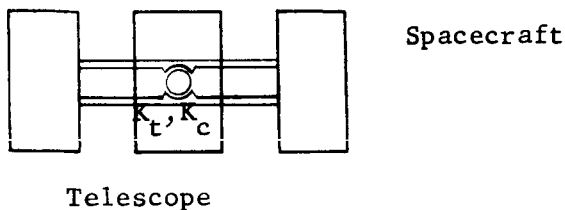
MODEL:

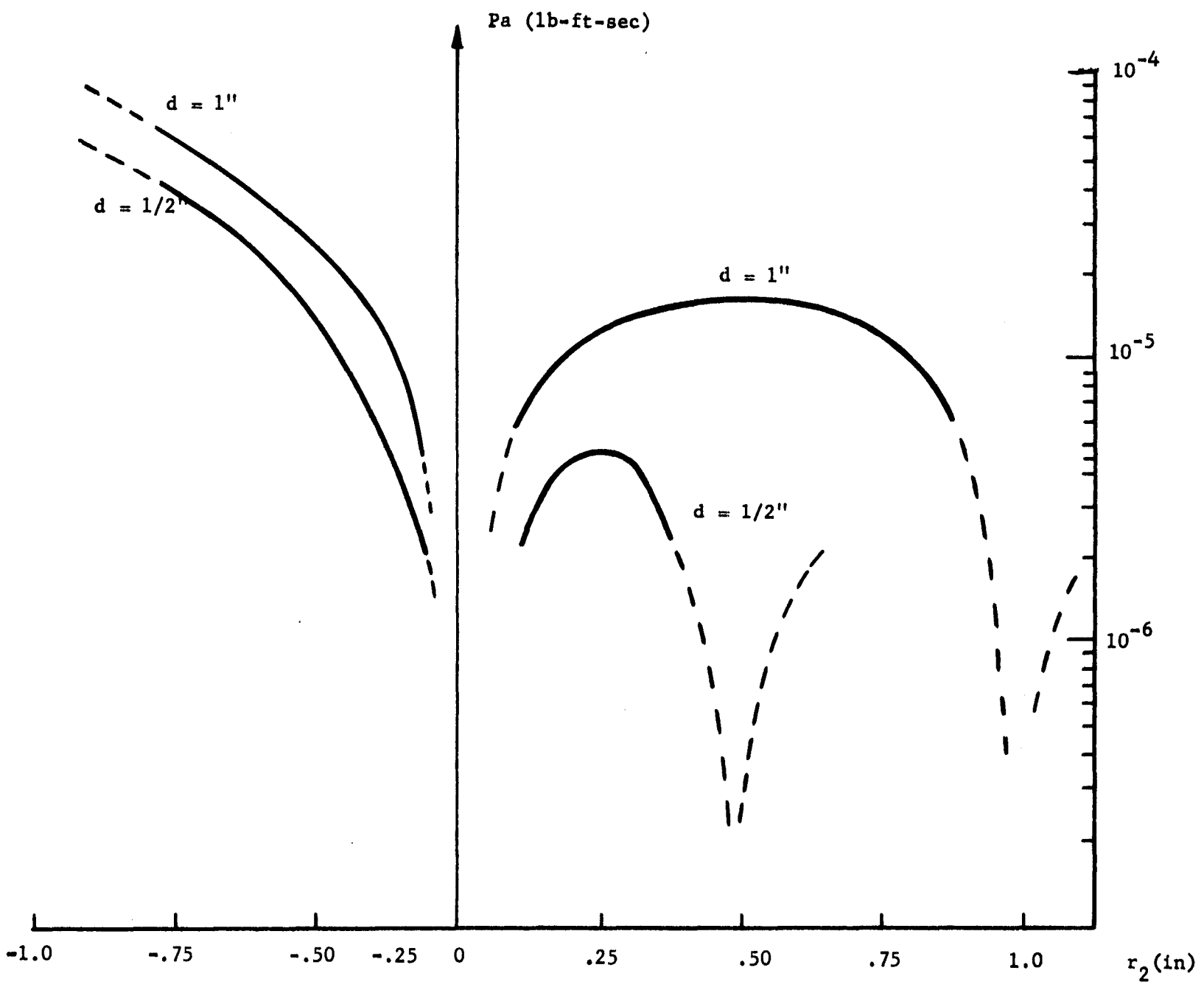


Snubber System

Symbol	Description	Limit of Values	Description of Limits
$K_t$	Torsional Spring Constant	$\frac{K_t}{K_c} \leq 1.7 \times 10^{-4}$ max $\frac{\text{ft}^2}{\text{rad}}$	Based on Max. angular impulse which can be imparted to telescope during collision.
$K_c$	Rectilinear Spring Constant		

MODEL:





B-5

The snubber system was assumed to have uniform properties in all directions so that the time of collision was independent of position and inversely proportional to a system spring constant  $K_c$ . Assuming the cg's of telescope and spacecraft to be coincident, then the angular impulse transferred to the telescope was found to depend upon the ratio of  $K_t$  to  $K_c$  where  $K_t$  was the system torsional spring constant.

Figure 3 shows how far the cg's could be separated and how far the collision point of the snubber system could be displaced from the telescope cg such that the requirement of max, angular impulse was not exceeded. The model used in deriving Figure 3 is shown in Figure 4.

When the cg's of the vehicles are coincident to within 1 inch, the radius of the snubber ball has to be  $r \leq 1/4$  inch. The period between collision, without damping in the snubber system was found to be  $T = 280$  sec for the case where  $d = 3/4$ " and  $r = 1/4$ ".

Thus far either system appears to be satisfactory, however, the effect of a DC force acting on the telescope has not been investigated. Such a force could arise from an imbalanced pair of torquers operating to counteract a DC disturbing torque. Assuming that the torquers have a 5% imbalance, a DC output of 20,000 dyne-cm, and a 100 cm separation between torquers, the net translating force was estimated to be about 10 dynes.

For the elastically restrained system, this force results in a small telescope displacement which is well within the requirement limits.

Figure 5 shows a model which was used to investigate the effect of a small force on the snubber system. When a collision occurs at point (a), no angular momentum is imparted to the telescope since the collision forces act through the telescope's cg. When point (b) is the impact point then an angular impulse is imparted to the telescope which can be estimated assuming an elastic collision (no damping). Assuming,  $r_2 = 1/4$ ", the telescope mass  $M_t = 30$  slugs, and that the telescope is accelerated across a .040 in. gap with a translating force  $F_x = 10$  dynes, the angular impulse on collision is approximately  $1.2 \times 10^3$  dyne-cm-sec. occurring 200 sec after uncaging. This is an unacceptable value. The angular impulse can be reduced to 100 dyne-cm-sec by setting  $r_2 = .060$  in. and the gap equal to .005 in.

This places a severe restriction on the size of the snubber since the radius of the ball must be of the same magnitude as  $r_2$ . Because the telescope has to be attached to the ball in some manner, it appears questionable as to whether the snubber system can be designed with realizable dimensions to satisfy the requirements set on  $r_2$  and the gap size.

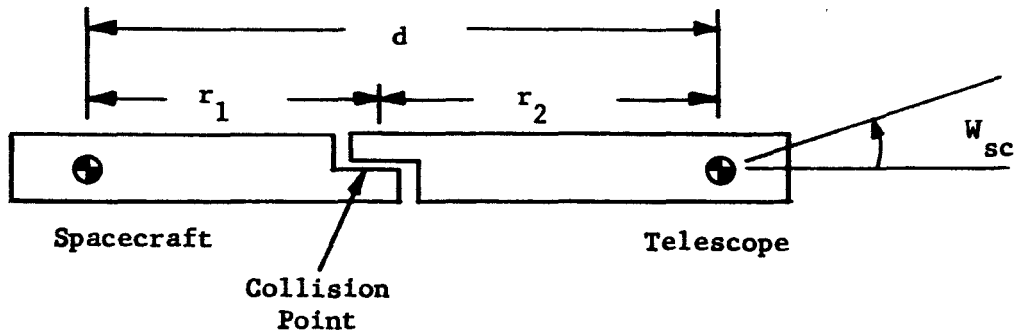


Figure 4. Snubber Model

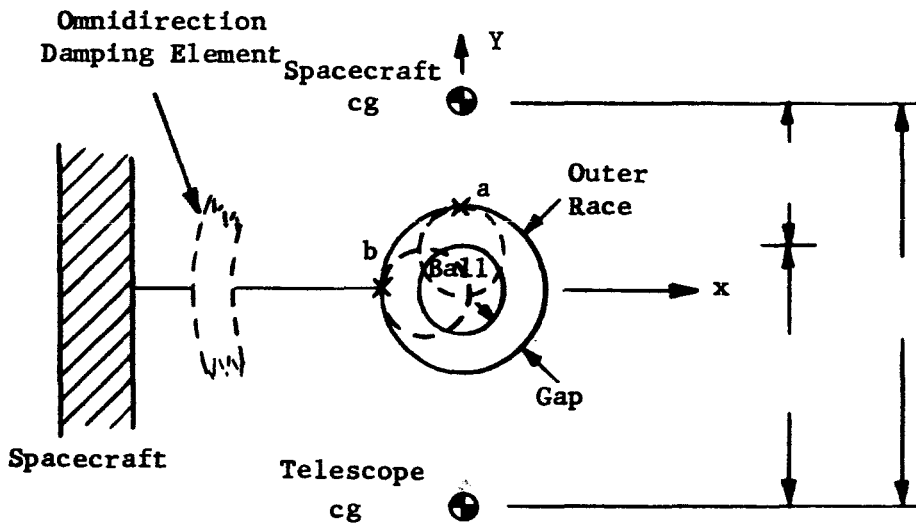


Figure 5. Snubber Model

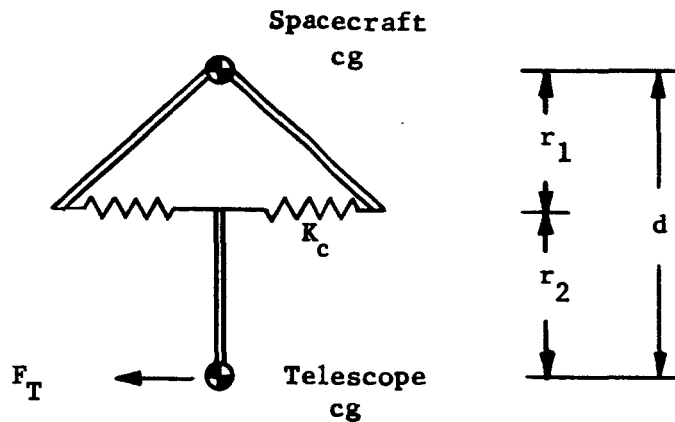


Figure 6. Hybrid Model

Hybrid System

A hybrid system consisting of an elastically suspended snubber appears to offer the most advantages. The main advantage of this hybrid system is that torsional coupling depends on the normal force and the coefficient of friction as compared to direct coupling in the elastic system.

As a result of damping, the telescope ball will eventually be held by the translating force of 10 dynes in continual contact with the outer race. If the spacecraft rotates in the XY plane with its cg as the center of rotation and the telescope is in contact with point (a), coupling to the outer race is provided by the friction between the snubber parts. Assuming  $r_2 = 1/4"$ , the coefficient of friction  $\mu = .1$  and the telescope moment of inertia  $J = 10^2$  slug-ft<sup>2</sup>, then the torque acting on the telescope is .7 dyne-cm. If this torque acts for 1 sec. (estimated time constant for the spacecraft guidance system) an angular displacement of  $10^{-4}$  sec. results. This disturbance can be adequately handled by the telescope guidance system. At point (b) the spacecraft disturbances are transmitted, through the damping element, to the telescope. The problem then is to get enough attenuation so that  $r_2$  can be reasonably large and that the disturbances can be handled by the telescope guidance system. It should be noted that this is analogous to the elastic system design problem.

The model shown in Figure 6 was used to estimate the parameters of the hybrid system. The maximum value of  $K_c$  was found to be proportional to the maximum torque (T) allowed to act on the telescope and inversely proportional to  $r_1 r_2$ . Assuming (T Max) to be 100 dyne-cm and  $r_1$  and  $r_2$  to equal 1.27 cm, realizable values, the maximum value of  $K_c$  was estimated to be .3 lb/in. The limits for  $K_c$  were found to be:  $5.5 \times 10^{-4} \leq K_c \leq .3$  lb/in. The maximum value of  $K_c$  could be increased further by placing more severe restrictions on  $r_1$  and  $r_2$ .

Conclusion

The analysis has shown that a rigid snubber type system is susceptible to forces arising from imbalanced torquers which accelerate the telescope into the snubber sides. In order to limit the torque impulse imparted during the collision to 100 dyne-cm-sec, the telescope must be balanced to within very close limits and the ball and gap size for the rigid snubber system must be very small. Both the elastic system and an elastically suspended snubber system appear to be feasible although both systems have a very small spring constant (0.3 lb/in) for cg imbalances of about 1.27 cm. The elastic system has an additional limitation on the torsional spring constant, whereas the elastically suspended snubber might be more difficult to place in a crowded telescope than an elastic system.

---

D. A. Markle - August 5, 1965

---

G. Carpenter - August 5, 1965

TECHNICAL NOTE  
D.A.M.-003

SPECTROMETER DESIGN NOTES (1)

The general dispersion formula for a plane grating in a collimated beam can be written as:

$$n\lambda = \frac{1}{m} (\sin \theta_i + \sin \theta_d) \quad (1)$$

where

$\lambda$  is the wavelength.

$n$  is the diffraction order.

$m$  is the number of grooves per unit length.

$\theta_i$  is the angle of incidence.

$\theta_d$  is the angle of diffraction.

In general for any value of  $\theta_d$  a number of wavelengths are present corresponding to different orders. Taking an arbitrary value of  $\theta_d$  as a center line then the wavelengths on the center line can be found by a simplified form of equation (1).

$$\lambda_c = \frac{K}{n} \quad (2)$$

If  $\Delta\lambda$  represents the gap in wavelength between two wavelengths falling on the center line and corresponding to successive orders such as  $n$  and  $(n+1)$  then:

$$\Delta\lambda = \frac{K}{n} - \frac{K}{n+1} \quad (3)$$

$$\text{if } n \gg 1 \quad \Delta\lambda \approx \frac{K}{n} \left(1 - \frac{1}{n+1}\right) \quad (4)$$

$$\Delta\lambda \approx \frac{K}{n^2} \quad (5)$$

$$\Delta\lambda \approx \frac{\lambda_c}{n} \quad (6)$$

In order to obtain the wavelengths which do not fall on the center line it is necessary to include an angle  $\Delta\theta$  which corresponds to the wavelength gap  $\Delta\lambda$ . The included angle is easily found by differentiating equation (1) with respect to  $\theta_d$ :

$$nd\lambda = \frac{\cos \theta_d}{m} d\theta \quad (7)$$

and from (6)

$$\Delta\theta = \frac{m\lambda c}{\cos \theta_d} \quad (8)$$

Another requirement which influences spectrometer design is the relative intensity of the diffracted beam. In general, the intensity is a function of wavelength, polarization, blaze angle, etc.; however, the major portion of the diffracted energy is contained in an arc  $\Delta\theta_d$  given by:

$$\Delta\theta_d = \frac{\lambda}{a}$$

where  $a$  is the width the diffracting surface and  $\lambda$  a or  $n$  1.

In the case of a grating  $a = \frac{\cos \theta_i}{m}$

$$\Delta\theta_d = \frac{m\lambda}{\cos \theta_i} \quad (9)$$

Comparison between (8) and (9) shows that the angles of incidence and dispersion should be approximately equal.

If  $\theta_i$  and  $\theta_d$  are not equal then equation (1) can be written as:

$$\frac{\sin \theta \cos \alpha}{m} = \frac{n\lambda}{2}$$

where

$$\theta_i = \theta + \frac{\alpha}{2}$$

and

$$\theta_d = \theta - \frac{\alpha}{2}$$

Since  $\theta_i$  and  $\theta_d$  should be approximately equal from intensity considerations and in fact are usually within about 20 or 30 degrees in most spectrometer designs, then to a close approximation.

$$\frac{\sin \theta}{m} = \frac{n\lambda c}{2} \quad (10)$$



If the collimated energy diffracted from the grating is imaged by a mirror of focal length F on a format of width  $\Delta x$  then,

$$\Delta\theta = \frac{\Delta x}{F} \quad (11)$$

and 
$$\frac{d\lambda}{d\theta} = \frac{Fd\lambda}{dx} \quad (12)$$

Substituting (12) into (7) and (11) into (8);

$$\frac{\cos \theta}{m} = nF \frac{d\lambda}{dx} \quad (13)$$

and 
$$\frac{\cos \theta}{m} = \frac{F\lambda}{\Delta x} \quad (14)$$

Using (13) and (14) to solve for n,

$$n = \frac{\lambda}{\Delta x \frac{d\lambda}{dx}} \quad (15)$$

Substituting (15) into (10),

$$\frac{\sin \theta}{m} = \frac{\lambda^2}{2\Delta x \frac{d\lambda}{dx}} \quad (16)$$

Squaring and adding (16) and (14),

$$\frac{1}{m^2} (\sin^2 \theta + \cos^2 \theta) = \frac{\lambda^2}{dx^2} \left[ \frac{\lambda^2}{4 \left(\frac{d\lambda}{dx}\right)^2} + F^2 \right] \quad (17)$$

$$\frac{1}{m} = \frac{\lambda}{\Delta x} \left[ \frac{\lambda^2}{4 \left(\frac{d\lambda}{dx}\right)^2} + F^2 \right]^{1/2} \quad (18)$$

If it is also assumed that dispersion takes place in the y direction from a grating of  $m'$  lines per unit length and that this grating is used in the first order only then from (18) and (15),

$$\frac{1}{m'} = \left( \frac{\lambda^2}{4} + F^2 \left(\frac{d\lambda}{dy}\right)^2 \right)^{1/2} \quad (19)$$

An example is shown in Figure 1 which illustrates how  $m$  and  $m'$ , the pitch of the gratings used in the  $x$  and  $y$  directions, varies with focal length  $F$ . In the example shown a dispersion of 1A per mm at 1000A was assumed with a 25 mm wide format having a 1 mm space between adjacent lines.

The lower limit of 200 mm for  $F$  was arbitrarily selected as the minimum focal length over which good imaging could be obtained over a 25 mm field. The upper limit for  $F$  is also arbitrary but was set at 1000 mm because of space and weight limitations which increase with  $F$ .

The range of values for  $F$  is further restricted by the limited number of grating pitches which can be prepared by ruling engines. As can be seen from Figure 1, very few combinations of high and low dispersion grating pitches correspond to the same focal length. Some slight compromise is, therefore, required on the initial dispersion requirement either in the  $x$  or  $y$  directions.

The angle at which each grating is used is also a function of the focal length which is obtained from (14) and (16).

$$\tan \theta_x = \frac{\lambda}{\frac{2Fd\lambda}{dx}} \quad (20)$$

$$\tan \theta_y = \frac{\lambda}{\frac{2Fd\lambda}{dy}} \quad (21)$$

The angles  $\theta_x$  and  $\theta_y$  in turn determine the blaze angle for each grating. The focal length  $F$  might also therefore be further restricted by judicious selection of blaze angles based on experience or perhaps limitations in the range of the apparatus used to measure grating efficiency, etc.

Figure 2 illustrates the format obtained using the same parameters as were used in Figure 1. Although a fairly compact format is available at short wavelengths it rapidly deteriorates at long wavelengths. This is a direct outcome of the grating equation and cannot be avoided if only 2 gratings are used to produce a format covering the 1000A to 3000A region.

Figure 3 illustrates one method of covering the whole format with 7 steps. Since the format is slightly larger than the outline covered by the seven steps and no allowance has been made for overlap, some compromise on resolution appears to be necessary. If the format is to be placed on an image tube which is also to be used as a memory device then it is not necessary to read out each time another step is taken. For example, only about 3 or 4 lines are contained in the bottom third of the format so that the 3 steps needed to cover the bottom third can be easily superimposed on the memory section to obtain a format which still leaves lots of room between lines. Similarly the two center sections of the format can be superimposed on the memory leaving a total of 4 readouts to cover the entire spectrum.

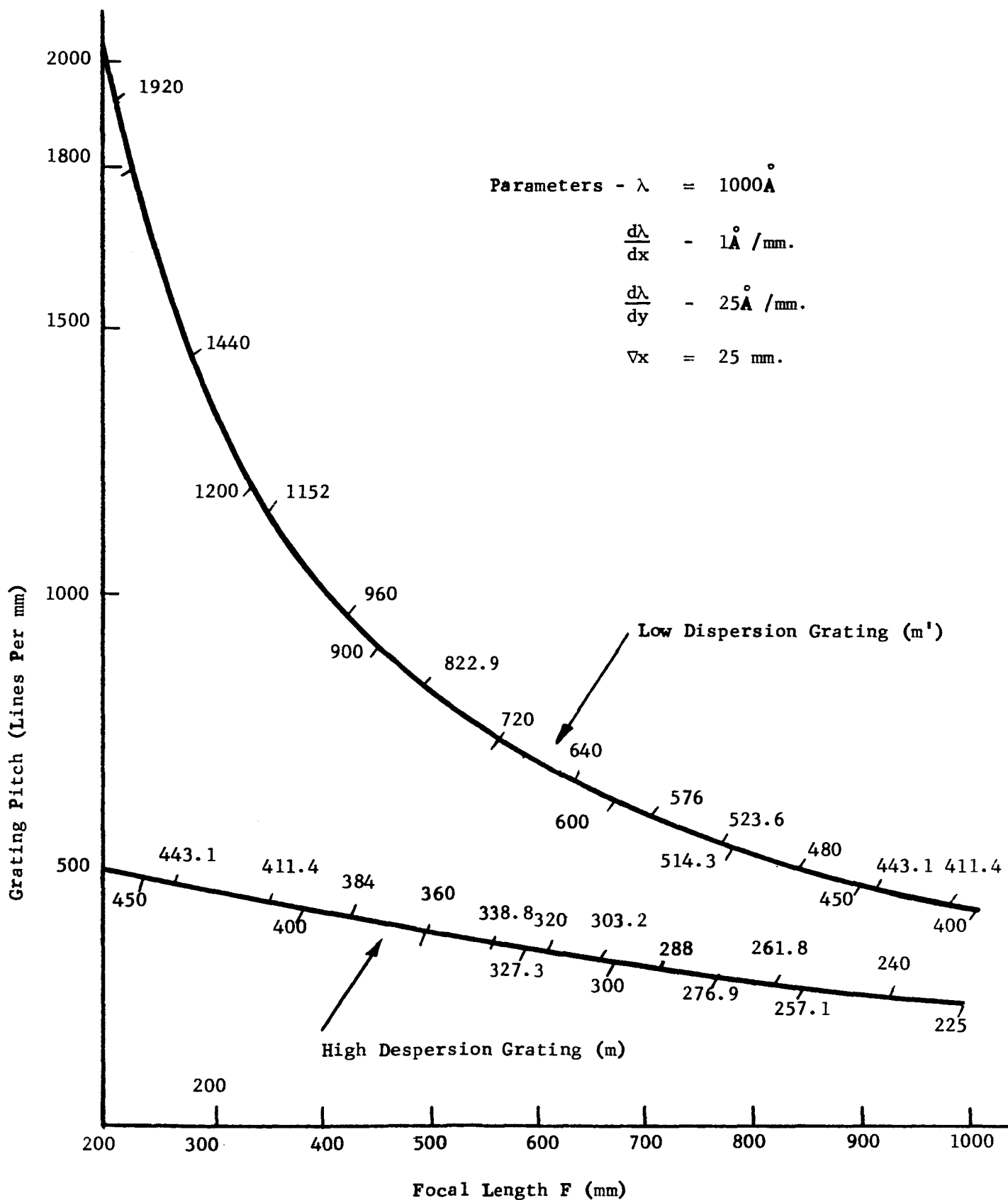


Figure 1. Grating Pitch Versus Focal Length

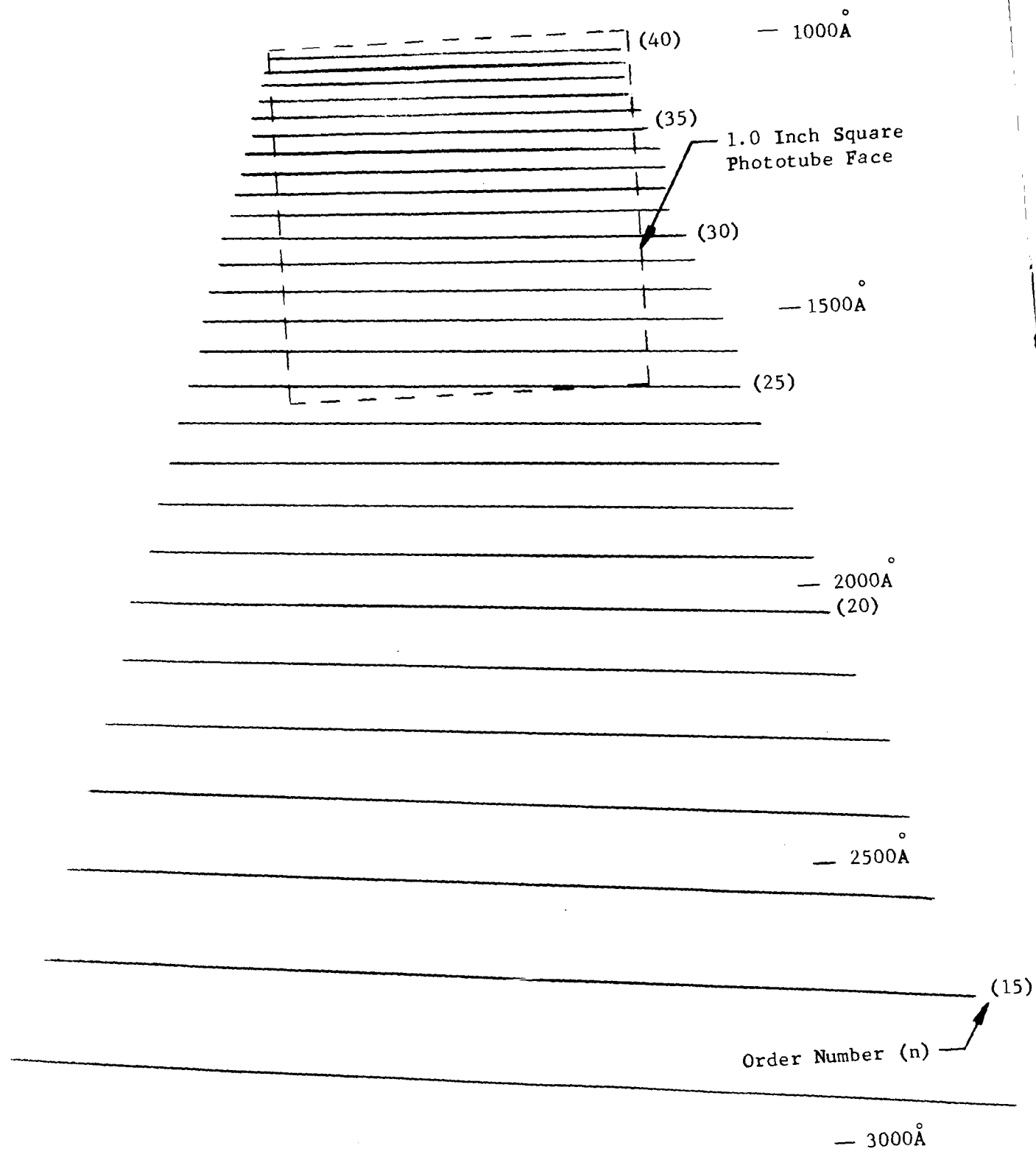


Figure 2  
Spectrometer Format  
Scale 2.5:1.0

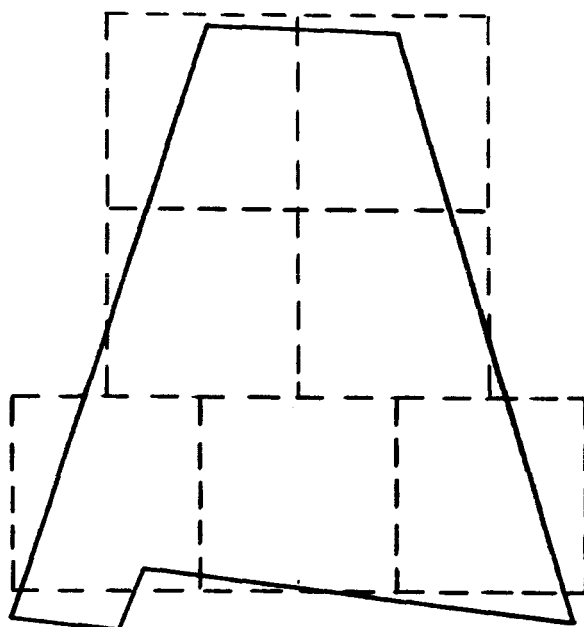


Figure 3  
Folded Spectrometer Format

Another possibility is to change the low dispersion grating after scanning the top third of the spectrum format so that the bottom two thirds is compressed to half the height and can therefore be covered with only 3 steps.

H. Marshall - June 7, 1965

D. A. Markle

TECHNICAL NOTE

J.J.G.-002

**TITLE:** Study of Electro-Magnetic Torquers for Space Telescope Orientation.

1. Abstract

By providing 3 degrees of translational restraint (motion limiting) through mechanical means, a system of electro-magnetic torquers can be employed to provide servo controlled angular orientation about each of the three axes. The volume of permanent magnet material required for a 1 meter aperture telescope of overall length of 2.54 meters is 534 cm<sup>3</sup>. Peak power required to produce 1 foot-pound of torque about the pitch or yaw axes is .58 watts, and for 1 foot pound about the roll axis is 3.72 watts.

2. Introduction

A first-order study has shown that a mechanical motion limiting system can be used to provide 3 axis translational restraint of a space telescope within a spacecraft. Maximum torques transmitted to the telescope can be as low as 100 dyne-cm.

The angular orientation of the telescope can be controlled by electro-magnetic torquers consisting of permanent magnets and an energized force coil. It has been determined that a system of torquers capable of 1 foot pound ( $1.35 \times 10^7$  dyne-cm) will certainly have a large safety margin for torque required in orbital operation. Angular excursions of the telescope have been arbitrarily set at  $\pm 15$  arc-min.

3. System Geometry and Displacement Requirements

A one meter aperture telescope was considered with the dimensions as shown in Figure 3.1.

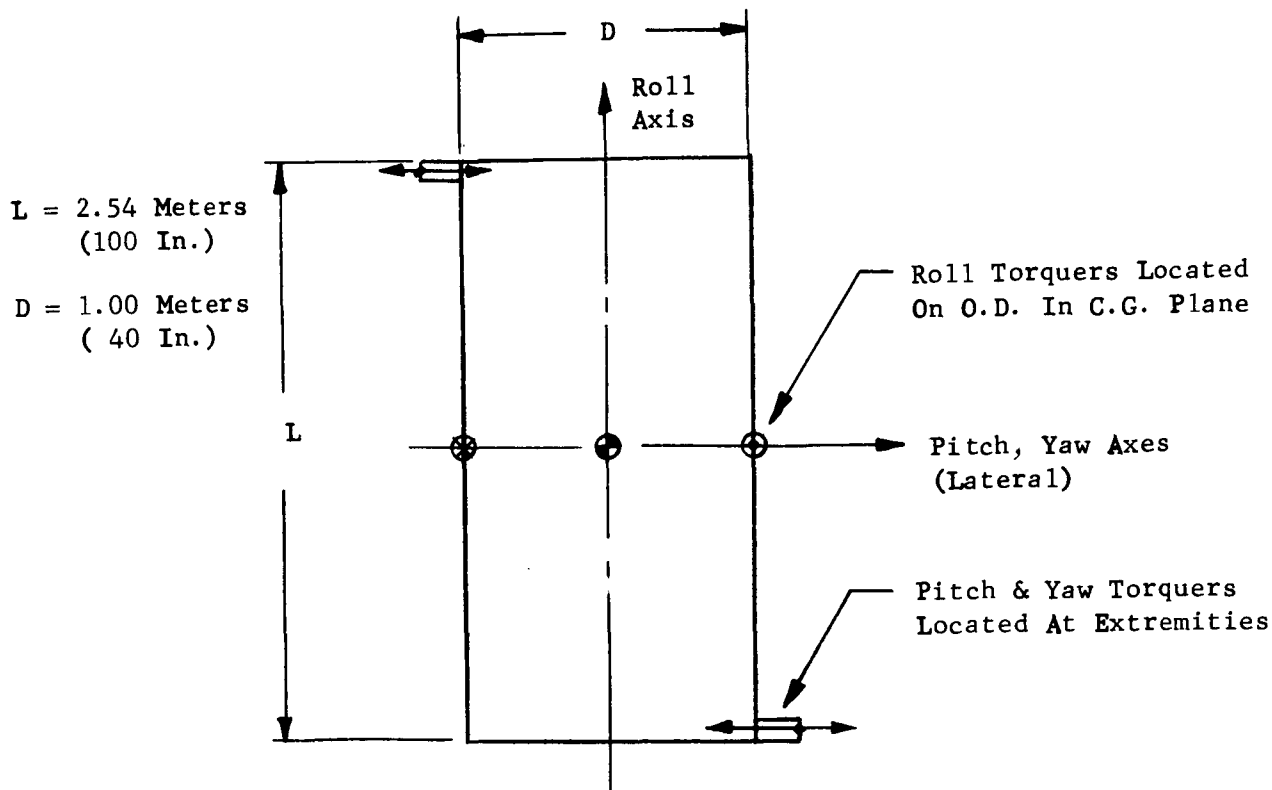


FIGURE 3.1

With the torquers located as shown, the distances from the center of rotation (assumed coincident with the center of gravity) and the displacements which must be accommodated for  $\pm 15$  arc-min angular excursions are given in Table 3.1.

Table 3.1

<u>Axis</u>	<u>Distance from Torquer to Center of Rotation</u>	<u>Motion for <math>\pm 15</math> min. Angular Displacement about c.g.</u>
Roll	$D/2 = 1/2$ meter (20 in)	$\pm .218$ cm ( $\pm .087$ in)
Pitch	$L/2 = 1.27$ meter (50 in)	$\pm .555$ cm ( $\pm .218$ in)
Yaw	$L/2 = 1.27$ meter (50 in)	$\pm .555$ cm ( $\pm .218$ in)

4. Torquer Force Output Requirements

For the required torque of 1.0 foot-pound about each axis, the force output of each torquer may be found as follows:

$$f = \frac{T}{d} \tag{4-1}$$



where  $f$  = individual torquer force output.

$d$  = distance between torquers.

$T$  = output torque about the axis under consideration.

Note - 1 ft-lb. = 1.35 newton-meters

For roll axis orientation,

$$f = \frac{1.35}{1.00} = \underline{1.35} \text{ newton} \quad (4-2)$$

For pitch or yaw axis orientation,

$$f = \frac{1.35}{2.54} = .532 \text{ newton} \quad (4-3)$$

5. Force on a Current-Carrying Conductor in a Magnetic Field

The force experienced by a current carrying conductor residing in a magnetic field is given by<sup>1</sup>:

$$f = (Il) B \sin (Il, B) \quad (5-1)$$

where  $f$  = force in newtons.

$I$  = current in amps.

$l$  = conductor length, meters.

$B$  = flux density, webers/(meter)<sup>2</sup>

$\sin (Il, B)$  = the magnitude of the sine of the smaller angle between the  $Il$  and  $B$  vectors.

For an  $N$ -turn coil in a radially-directed field,

$$f = N^2 \pi r IB \quad (5-2)$$

where  $r$  = coil radius, meters

$$\sin (Il, B) = 1$$

For a coil of 2.54 cm (1.00 inch) radius,

$$f = .16NIB \quad (5-3)$$

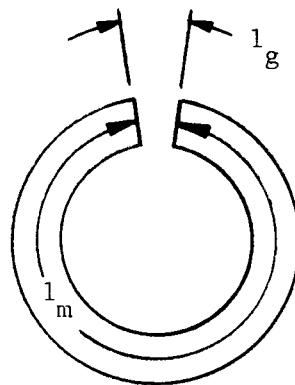
or, for a given force and flux density,

$$NI = 6.25 \frac{f}{B}, \text{ amp-turns} \quad (5-4)$$

6. Permanent magnet Design

The study conducted up to the time of this writing indicates that a permanent magnet design similar to that used in a voice coil will provide a satisfactory hardware approach. It is desired to use any permanent magnet material which will be aboard a spacecraft in a manner which is most efficient from a volume and weight standpoint, as well as one which minimizes the magnetic dipole effect on the spacecraft.

Consider a simple ring magnet, such as the one shown in Figure 6-1 having an air (or free space) gap.



- A = Area of Magnet
- A<sup>m</sup> = Area of Gap
- V<sup>g</sup> = Volume of Magnet
- V<sub>g</sub><sup>m</sup> = Volume of Gap

Figure 6-1

Neglecting all external fields,

$$Hdl = 0 \tag{6-1}$$

Equation 6-1 states that the sum of all the magnetomotive potential drops around a closed path = 0.

$$Hdl = H_m l_m + H_g l_g = 0 \tag{6-2}$$

In the gap,

$$H_g = B_g \quad \underline{\text{in CGS units}} \tag{6-3}$$

And for no flux leakage,

$$B_g A_g = B_m A_m \tag{6-4}$$

Substituting 6-3 into 6-4,

$$H_g A_g = B_m A_m \tag{6-5}$$

Solving 6-2 and 6-5 for H<sub>g</sub>, and multiplying the resulting equations yields:

$$H_g = H_m \frac{l_m}{l_g} \tag{6-6}$$

$$H_g = B_m \frac{A_m}{A_g} \tag{6-7}$$

$$H_g^2 = -B_m H_m \frac{A_m l_m}{A_g l_g} \tag{6-8}$$

Since area x length = volume,

$$H_g^2 = -B_m H_m \frac{V_m}{V_g} \tag{6-9}$$

Equation 6-9 tells us that for a given gap volume, the greatest field strength in the gap will be realized when the product  $B_m H_m$  is maximized. When  $B_m H_m$  is maximized,  $V_m$ , the magnet volume, will be minimized and we will be using the least possible magnetic material to achieve the stated field strength across the required gap.

$B_m H_m$  is called the energy product and is a material property which varies with magnetic induction as shown in Figure 6-2.

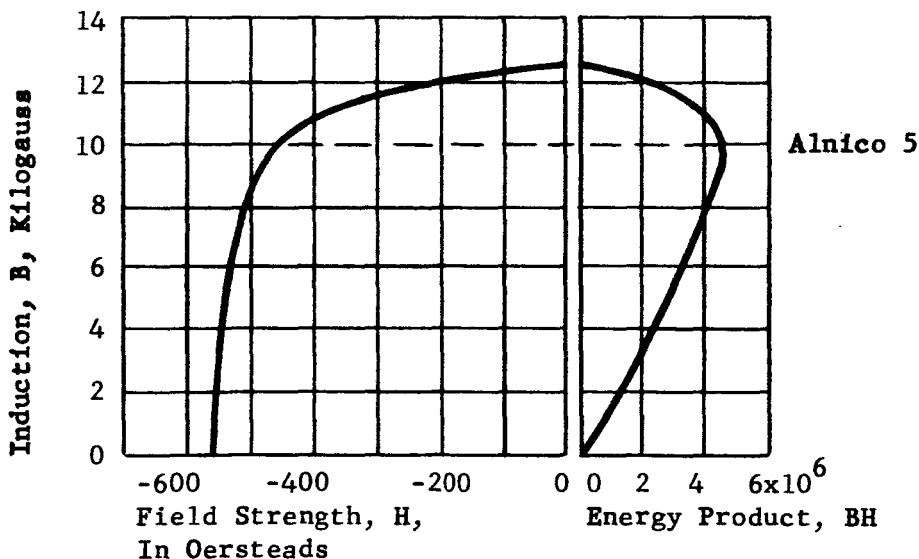


Figure 6-2. Properties Of Alnico 5 - From Bozorth<sup>2</sup>

As can be seen from the curves presented in Figure 6-2, the maximum energy product for Alnico 5 is  $-4.5 \times 10^6$  in CGS units and coincides with an induction of  $10 \times 10^3$  gauss. The design of a permanent magnet made from Alnico 5 with  $B_m H_m = 4.5 \times 10^6$  and  $B_m = 10 \times 10^3$  gauss will be investigated.

The fundamental consideration (aside from material properties) is that of gap size. In Table 3.1, the need for motion clearance of  $\pm .555$  cm is indicated. We must estimate additions to the gap length to accommodate the coil thickness plus clearance needed for motions produced by telescope orientations about all axes. For this investigation we have selected a gap length of,

$$l_g = 1.27 \text{ cm } (.500 \text{ in.})$$

The gap height will be 1.90 cm (.750 in.)

The gap volume is found as follows:

$$\text{the mean gap radius} = 2.54 \text{ cm (see eq. 4-3)}$$

$$\text{the gap I.R} = 2.54 - \frac{1.27}{2} = 1.90 \text{ cm } (.748 \text{ in.})$$

$$\text{the gap O.R} = 2.54 + \frac{1.27}{2} = 3.17 \text{ cm } (1.247 \text{ in.})$$

to account for fringing, we should add  $l_g$  to the gap height giving,

$$h'_g = h_g + l_g = 1.90 + 1.27 = 3.17 \text{ cm,}$$

where  $h'_g$  denotes the height corrected for fringing

$$V_g = \pi (O.R^2 - I.R^2) (h'_g)$$

$$V_g = \pi (3.17^2 - 1.90^2) (3.17)$$

$$= 64 \text{ cm}^3$$

Repeating equation 6-9,

$$H_g^2 = B_m H_m \frac{V_m}{V_g} \tag{6-9}$$

where,

$$(B_m H_m) = -4.5 \times 10^6$$

$$V_g = 64 \text{ cm}^3$$

$$H_g = B_g \text{ in CGS units}$$

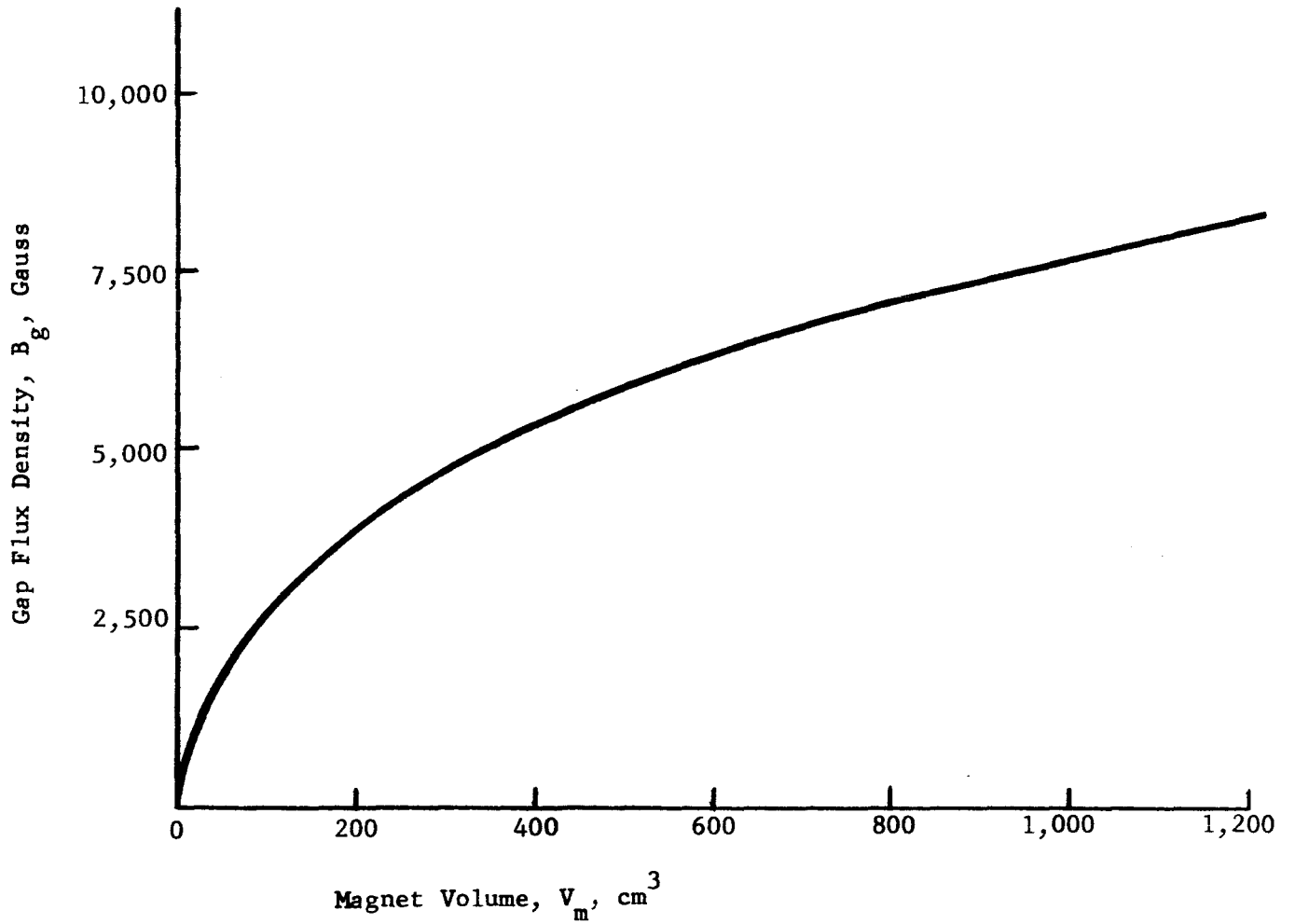


Figure 6-3  
Magnet Volume vs. Flux  
Density In Gap.

These substitutions give,

$$V_m = 14.2 \times 10^{-6} B_g^2 \tag{6-10}$$

Equation 6-10 is plotted in Figure 6-3.

From the curve presented in Figure 6-3 for,

$$B_g = 2500 \text{ gauss,}$$

$$V_m = 89 \text{ cm}^3$$

and we already know:

$$V_g = 64 \text{ cm}^3; A_g = \frac{V_g}{h_g} = 34 \text{ cm}^2$$

$$H_g = 2500 \text{ oersteds}$$

$$B_m = 10,000 \text{ gauss}$$

Figure 6-4 shows the magnet configuration under consideration. Two-cylindrical magnets of equal volume will be arranged in concentric fashion. The volume of each will be:

$$\frac{V_m}{2} = 44.5 \text{ cm}^3$$

The cross-sectional area of each magnet is found from transposing equation 6-4.

$$A_m = \frac{B_g A_g}{B_m} \tag{6-11}$$

$$A_m = \frac{(2500)(34)}{10,000} = 8.5 \text{ cm}^2$$

The length of each magnet will be

$$l_m = \frac{44.5 \text{ cm}^3}{8.5 \text{ cm}^2} = 5.24 \text{ cm (2.06 in.)}$$

For the inner magnet, the O.D. has been set at 3.18 cm; this gives,

$$\text{I.D.} = \sqrt{\text{OD}^2 - \frac{4A_m}{\pi}} = \sqrt{(3.18)^2 - \frac{4}{\pi}(8.5)}$$

$$\text{I.D.} = 1.83 \text{ cm}$$

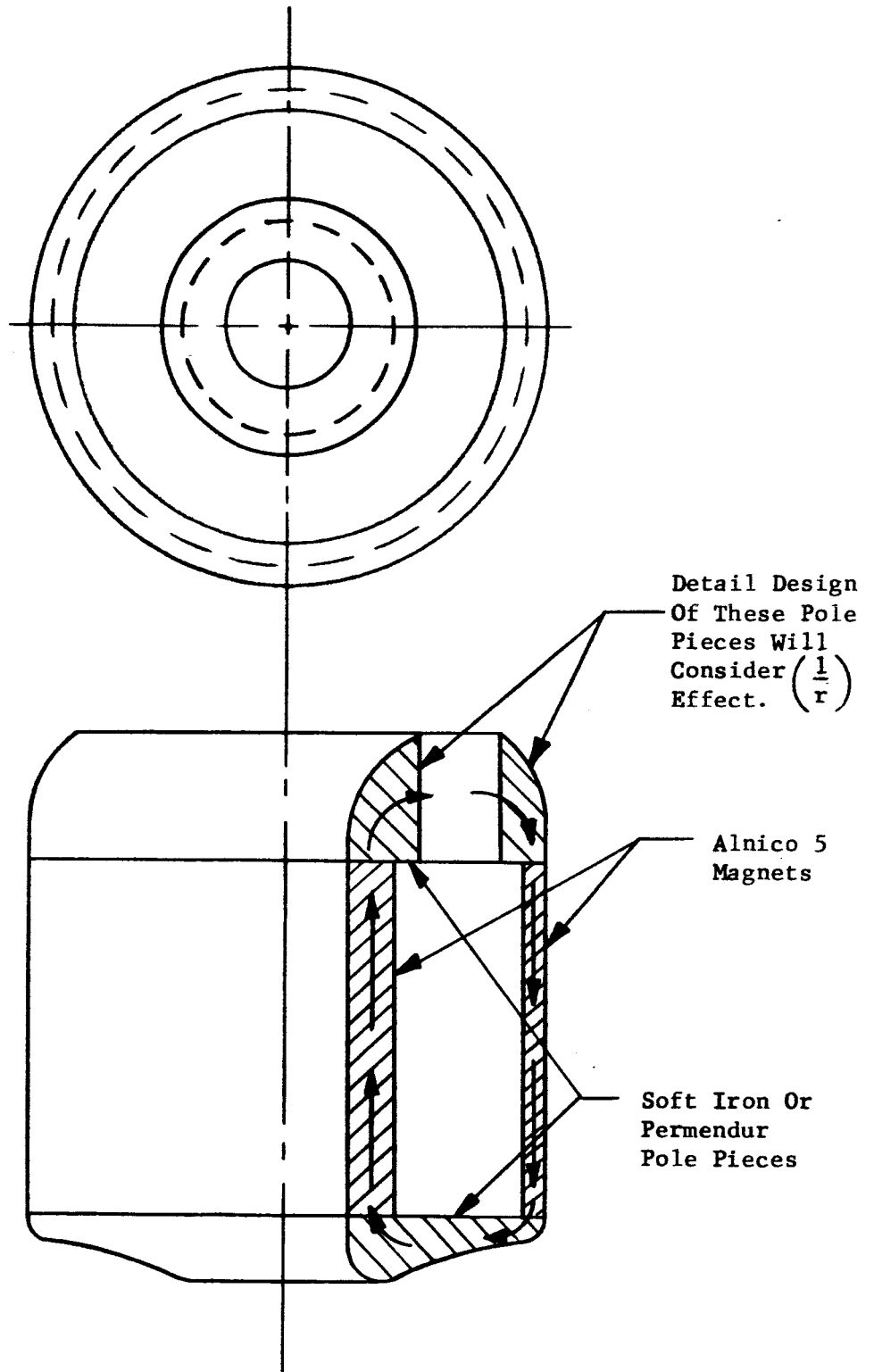


Figure 6-4  
Full Scale Sketch Of  
Permanent Magnet

Similarly, for the outer magnet, the I.D. was set at 7.00 cm, and the O.D. found as 7.60 cm.

The pole-piece design seeks to maintain constant flux density. For a constant pole-piece area of 8.5 cm<sup>2</sup>, the height varies with radius as follows:

$$h = \frac{8.5}{2\pi r} = \frac{1.35}{r} \quad (6-12)$$

This relationship may be observed in the curved shape of the pole-piece seen in cross-section in Figure 6-4. The upper pole pieces are used as a low reluctance path for the magnetic flux prior to the flux traversal of the gap. These pole pieces have face widths equal to h<sub>g</sub> (1.90 cm).

7. Coil Parameters

Repeating equation 5-4,

$$NI = 6.25 \frac{f}{B}$$

where B = 2500x10<sup>-4</sup> weber/meter<sup>2</sup>

Note: 1 gauss = 10<sup>-4</sup> weber/meter<sup>2</sup>

$$NI = 25f \quad (7-1)$$

Equation 7-1 relates the amp-turns required to produce a force f, given in newtons. The torquer force is given by equations 4-1, 4-2 and 4-3.

$$f = \frac{T}{d} \quad (4-1)$$

where T = 1.35 newton-meters.

We can relate NI to output static torque by combining 7-1 and 4-1 as follows:

$$NI d = 25 f d = 25T \quad (7-2)$$

$$\text{or} \quad NI = 25 \frac{T}{d} \quad (7-3)$$

For the roll axis torquers,

$$(NI)_{\text{roll}} = 25 \frac{T}{1.00} = 25T \quad (7-4)$$



For the pitch and yaw axis torquers,

$$(NI)_{\text{pitch, yaw}} = 25 \frac{T}{2.54} = 9.85T \quad (7-5)$$

These relations between amp-turns per actuator for varying torque are given in graphical form in Figure 7-1.

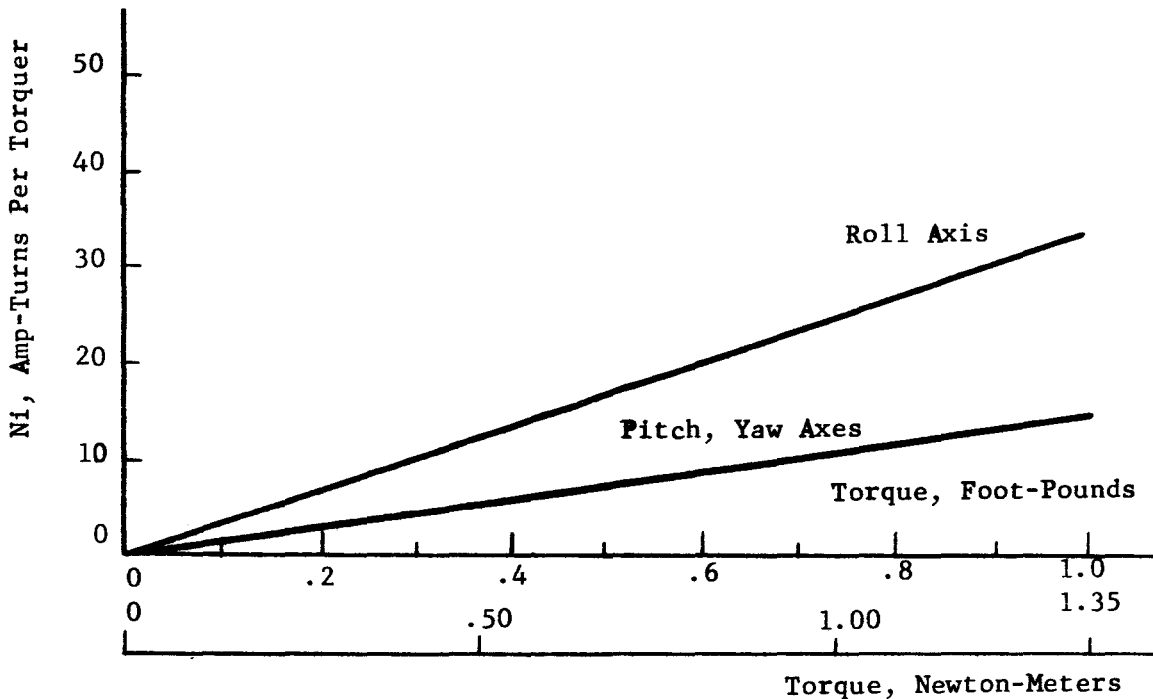


Figure 7-1

The peak power requirements may be estimated as follows:

$$(NI)_{\text{roll max}} = (25) (1.35) = 33.7 \text{ amp-turns per torquer.}$$

$$(NI)_{\text{pitch, yaw max}} = (9.85) (1.35) = 13.3 \text{ amp-turns per torquer.}$$

A 30 turn coil of #30 annealed copper wire would have a total length of:

$$(30) (2\pi) (2.54) = 478 \text{ cm.}$$

For #30 copper wire at 0°C, r = .0031 ohms/cm so the total resistance is,

$$R = (478) (.0031) = 1.48 \text{ ohms}$$

For the roll axis torquers,

$$NI_{\max} = 33.7 \text{ amp-turns per torquer.}$$

$$I_{\max} = 1.12 \text{ amps.}$$

$$V_{\max} = I_{\max} R = (1.12) (1.48) = 1.66 \text{ volts.}$$

$$P_{\max} = V_{\max} I_{\max} = (1.66) (1.12) = 1.86 \text{ watts per roll axis torquer.}$$

For the pitch and yaw axis torquers,

$$NI_{\max} = 13.3 \text{ amp-turns per torquer.}$$

$$I_{\max} = .443 \text{ amps.}$$

$$V_{\max} = I_{\max} R = (.443) (1.48) = .66 \text{ volts.}$$

$$P_{\max} = V_{\max} I_{\max} = (.66) (.443) = .29 \text{ watts per torquer.}$$

## 8. Conclusion

While the design presented in this study has not been subjected to optimization, it does demonstrate the feasibility of electro magnetic positioning. The volume of magnetic material required does not seem to pose a problem at this time. Power requirements are also well below what could be budgeted for the guidance controlled orientation devices.

J. J. Greed - June 1, 1965

## References

1. Corcoran & Reed, Introductory Electrical Engineering, John Wiley & Sons, 1957.
2. Bozorth, R.M. Ferromagnetism, D. Van Nostrand Co., 1951

TECHNICAL NOTE

. D.A.M.-001

**TITLE:** Effect of Temperature Gradients on the Figure of Mirrors

Summary

Two simple cases of temperature gradients across mirrors were investigated. In the case of a linear gradient perpendicular to the optical axis of a mirror supported at the center, the gradient distorts the mirror to a non-spherical shape. In the case of a linear temperature gradient through the thickness of a thin spherical shell, the effect of the gradient is to change the curvature of the shell to a sphere of different radius. Approximations describing the effects of a temperature gradient were obtained by discarding higher order terms where possible and assuming that the mirror thickness and sag were small in comparison to the diameter and focal length.

The results were as follows:

I. A Linear Temperature Gradient Perpendicular to the Optical Axis.

$$\Delta = \frac{(\alpha T')^2 Y^4}{16F}$$

where  $\Delta$  is the change in the mirror surface due to the temperature gradient.

$\alpha$  is the coefficient of expansion.

$T'$  is the temperature gradient in °C/unit length.

$Y$  is the distance from the center of the mirror in the direction of the temperature gradient.

$F$  is the focal length of the mirror.

II. A Linear Temperature Gradient Through the Thickness of A Thin Spherical Shell.

$$\Delta F = -2F^2 \alpha T'$$

where  $\Delta F$  is the change in focal length.

Effect of Temperature Gradients on Mirrors

I. A Linear Gradient Perpendicular to the Optical Axis.

Figure 1 shows a block of homogeneous material before and after a linear temperature gradient has been established in the y direction. If we assume the block to be square with width L before the gradient is applied, then after the gradient the top of the block has a width  $L_T$  given by:

$$L_T = L(1 + \frac{\alpha T' L}{2}) \tag{1}$$

Similarly for the bottom of the block,

$$L_B = L(1 - \frac{\alpha T' L}{2}) \tag{2}$$

Assuming the block bends about a radius of curvature situated on the y axis a distance  $\rho$  below the x-axis then  $L_T$  and  $L_B$  can be determined on the following equations:

$$L_T = (\rho + \frac{L}{2}) \theta \tag{3}$$

$$L_B = (\rho - \frac{L}{2}) \theta \tag{4}$$

$$\text{where } \theta = \frac{L}{\rho}$$

Substituting (3) and (4) into (1) and (2) and solving for  $\rho$  we obtain,

$$\rho = \frac{1}{\alpha T'} \tag{5}$$

For any point (x,y) in the block before the temperature gradient, there is a corresponding point (x', y') after the gradient. The relationship between the two points can be determined from Figure 2 as follows:

$$x' = x(1 + y\alpha T') \tag{6}$$

$$y' = y(1 + \frac{y\alpha T'}{2}) - (y + \frac{y^2\alpha T'}{2} + \rho) (1 - \cos \theta) \tag{7}$$

$$\text{where } \sin \theta = \frac{x'}{y + y^2\alpha T' + \rho} \tag{8}$$

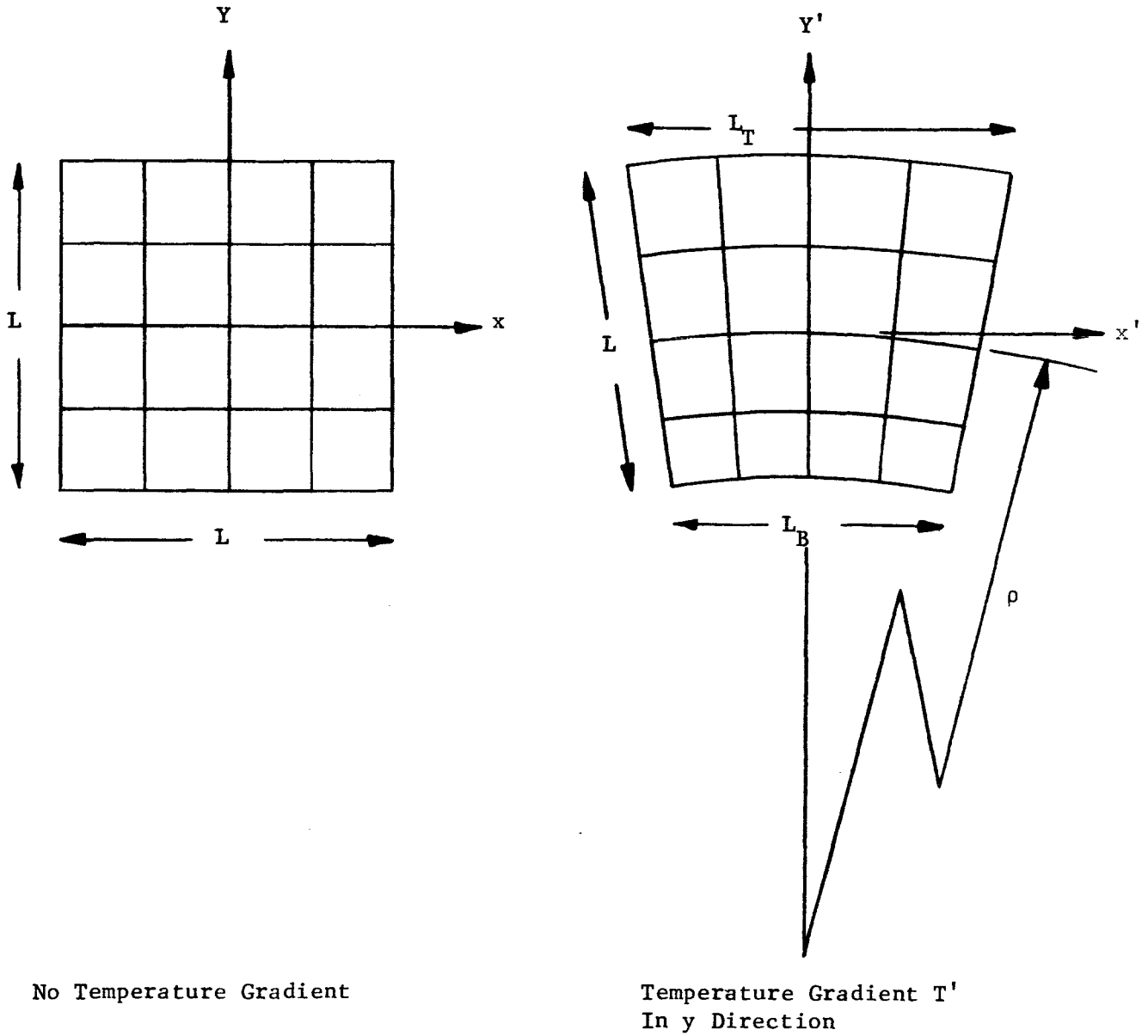


Figure 1  
Effect Of A Linear Temperature Gradient On  
A Homogeneous Material

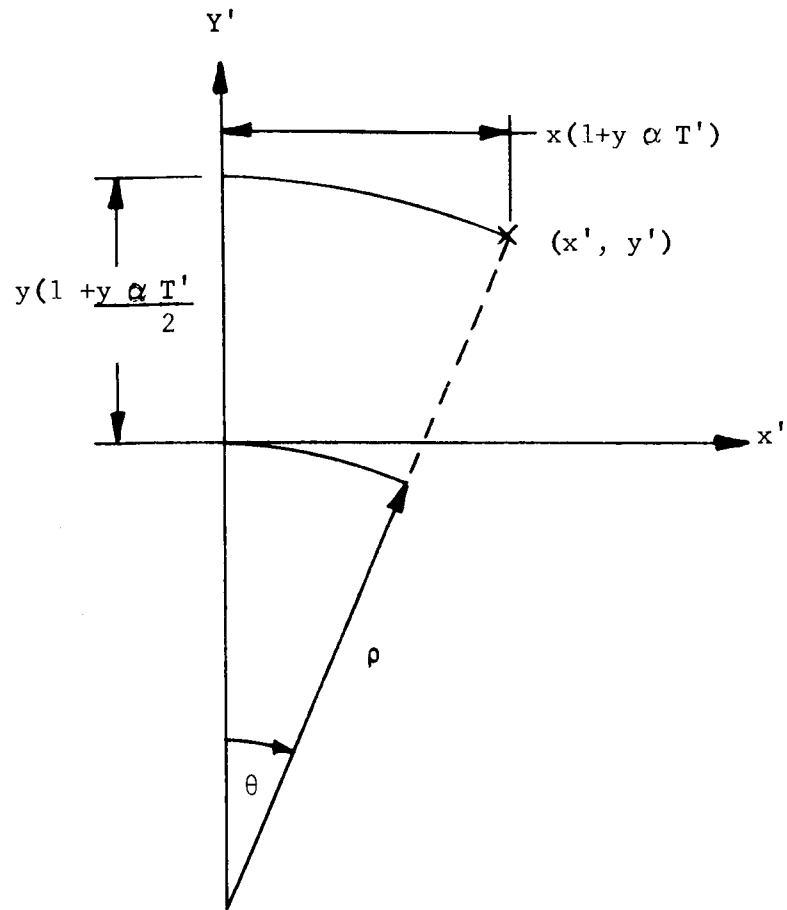


Figure 2  
Relationship Between  $(x,y) + (x',y')$

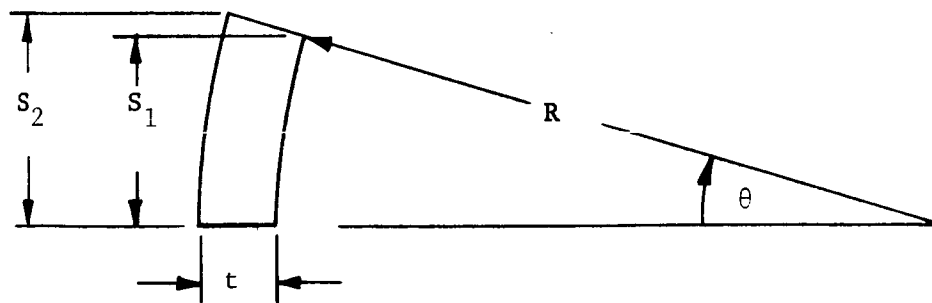


Figure 3  
The Thin Spherical Mirror

Neglecting powers of  $\alpha T'$  higher than the second

$$\theta = \alpha T' x \quad (9)$$

$$1 - \cos \theta = \frac{(\alpha T' x)^2}{2} \quad (10)$$

$$y' = y + \frac{y^2 \alpha T'}{2} - \frac{x^2 \alpha T'}{2} - \frac{x^2 y (\alpha T')^2}{2} \quad (11)$$

Consider a mirror of radius  $R$  with the apex at  $(0,0)$  and the center of curvature at  $x = R$ . Thus,

$$(R-x)^2 + y^2 = R^2 \quad (12)$$

$$x^2 + y^2 - 2Rx = 0 \quad (13)$$

Let  $P$  be the distance between a point on the mirror after the gradient is established and the point  $(R,0)$ . Thus,

$$P = \left[ (R-x')^2 + y'^2 \right]^{1/2} \quad (14)$$

One method of expressing the distortion of the mirror due to the thermal gradient is by means of a quantity  $\Delta$  defined as follows:

$$\Delta = P - R. \quad (15)$$

Substituting (14), (11), and (6) into (15) and making use of (13) to simplify the resulting expression we obtain:

$$\Delta = \left( R^2 + (\alpha T')^2 \left( \frac{x^2}{2} - \frac{y^2}{2} \right)^2 \right)^{1/2} - R \quad (16)$$

If  $y \gg x$  (Diameter  $\gg$  Sag)

$$\Delta \approx \frac{(\alpha T')^2 y^4}{8R} \quad (17)$$

If F is the focal length,

$$F = \frac{R}{2} \tag{18}$$

$$\Delta \approx \frac{(\alpha T')^2 y^4}{16F} \tag{19}$$

Example

Assume a fused quartz mirror 800 mm in diameter and with a 2720 mm focal length has a linear temperature gradient of 10°C across the diameter.

$$\alpha = 5.6 \times 10^{-7} / ^\circ\text{C}$$

$$y_{\text{max}} = 400 \text{ mm}$$

$$T' = 10^\circ\text{C}/800 \text{ mm} = 1.25 \times 10^{-2} \text{ }^\circ\text{C}/\text{mm}$$

$$F = 2720 \text{ mm}$$

$$\Delta_{\text{max}} = \frac{(5.6 \times 10^{-7} \times 1.25 \times 10^{-2})^2 (400)^4}{16 \times 2720} = 2.88 \times 10^{-4} \text{ }^\circ\text{A}$$

II. A Linear Radial Temperature Gradient Across A Thin Spherical Shell.

Consider a small mirror segment as shown in Figure 3. Let  $S_1$  and  $S_2$  be the lengths of fibers along the inner and outer surfaces separated by a distance  $t$ . If we let

$$S_1 = R\theta \tag{20}$$

and  $S_2 = (R+t)\theta \tag{21}$

then  $\frac{S_1}{S_2 - S_1} t = R \tag{22}$

Assume a temperature gradient is established such that the temperature of  $S_1$  does not change but the temperature of  $S_2$  changes by an amount  $T't$  where  $T'$  is the gradient in degrees per unit length. Using primes for the new mirror dimensions and neglecting squared and higher powers of  $\alpha T'$  we get:

$$t' = t \left( 1 + \frac{\alpha t T'}{2} \right) \tag{23}$$



$$S_1' = S_1 = R\theta \quad (24)$$

$$S_2' = \theta(R+t) (1+\alpha t T') \quad (25)$$

From (22),

$$R' = \frac{S_1' t'}{S_2' - S_1'} \quad (26)$$

Substituting (23), (24), and (25) into (26)

$$R' = R \left( 1 - \frac{\alpha t T'}{2} - R\alpha T' \right) \quad (27)$$

If we define

$$\Delta R = R' - R \quad (28)$$

$$\Delta R = -R\alpha T' \left( R + \frac{t}{2} \right) \quad (29)$$

Assuming  $\frac{t}{2} \ll R$

$$\Delta R = R^2 \alpha T' \quad (30)$$

or

$$\Delta F = 2F^2 \alpha T' \quad (31)$$

Example

Assume a fused quartz mirror 152 mm thick and with a focal length of 2720 mm has a linear temperature difference of 1°C from the front to the back:

$$\alpha = 5.6 \times 10^{-7}/^\circ\text{C}$$

$$T' = \frac{1}{152} = 6.58 \times 10^{-3} \text{ }^\circ\text{C/mm}$$

$$F = 2720$$

$$\Delta F = -.0543 \text{ mm}$$

**Page intentionally left blank**

TECHNICAL NOTE

RVS-101

THE DETECTION OF COMA IN THE IMAGE OF A STAR USING A SLIT AND PHOTOCCELL

The apparent profile of a star image scanned by a slit has the same shape as the profile of a line image\* having the same orientation as the slit and scanned by the same slit. If the aberrations affecting the image are small, a relatively strong peak will be observed flanked by a pair of subsidiary peaks (side lobes) the order of one tenth the magnitude of the central peak. The dip between the main lobe and a side lobe does not go to zero (Figure 1).

The presence of coma may be detected by the asymmetry of the side lobes. If the slit is oriented to scan in the direction of the comatic flare, one lobe will be higher than it would be in the absence of coma, and the other lower (Figure 2). The difference in magnitude between the two side lobes can be taken as the "signal" which measures the amount of coma. No other elementary aberration will produce this asymmetry and the presence of other aberrations will not affect its magnitude (at least for small aberrations).

As the slit is rotated, the magnitude of the "signal" varies as the cosine of the angle of rotation (at least for small coma) from the direction of the comatic flare. Therefore, two orthogonal scans are sufficient to determine both the direction and the amount of coma.

What remains to be shown is the manner in which the signal varies with the amount of coma, the sensitivity of the signal, and the effect of the width of the scanning slit on the signal.

These properties can be readily determined by using Steel's method<sup>(1)</sup> for obtaining the transfer function in the presence of small amounts of aberration, multiplying by the transfer function of the slit, and then evaluating the inverse transform.

---

\* The image of an infinitesimally fine line.

First consider the general case. We will use reduced values for both the spatial coordinates and the spatial frequency coordinates in the image plane.

$$\begin{aligned} r &= \frac{\rho}{N\lambda} \\ k &= N\lambda\nu, \end{aligned} \tag{1}$$

where N is the f/no.,  $\lambda$  is the effective wavelength of the light,  $\rho$  is the radial distance from the origin\* in the image plane, and  $\nu$  is the spatial frequency in the image plane. The direction of scan with respect to the direction of the comatic flare will be represented by angle  $\theta$ .

The transfer function is expressed by

$$T(\theta, k) = |T| e^{i\Phi} = |T| \cos\Phi + i |T| \sin\Phi, \tag{2}$$

where both the modulus  $|T|$  and the phase  $\Phi$  of the transfer function are functions of the polar coordinates  $\theta$  and  $k$ .

The line spread function is obtained by the inverse Fourier transform

$$S(\theta, r) = \int_{-\infty}^{\infty} T e^{-i2\pi kr} dk \tag{3}$$

The fraction of the total energy of the star image which passes through the slit is given by

$$E(\theta, r; w) = w \int_{-\infty}^{\infty} T e^{-i2\pi kr} \left[ \frac{\sin\pi wk}{\pi wk} \right] dk \tag{4}$$

where  $w$  is the width of the slit (reduced to the same units as  $r$ ) and the expression in square brackets is the transfer function of the slit. The quantity  $E$  goes to unity as  $w \rightarrow \infty$ .

Because we are interested in the asymmetry of the image, it is advantageous to separate  $S$  into its even and odd parts,

$$S = S_e + S_o, \tag{5}$$

and taking into account the symmetry of the transfer function, we obtain

$$S_e = \int_{-\infty}^{\infty} |T| \cos\Phi \cos(2\pi kr) dk$$

and

$$S_o = \int_{-\infty}^{\infty} |T| \sin\Phi \sin(2\pi kr) dk \tag{6}$$

\* in this case, the position of the maximum of the central peak.

The corresponding energy fractions are

$$E_e = w \int_0^{\infty} |T| \sin \Phi \cos(2\pi kr) \left[ \frac{\sin \pi wk}{\pi wk} \right] dk$$

and

$$E_o = w \int_0^{\infty} |T| \sin \Phi \sin(2\pi kr) \left[ \frac{\sin \pi wk}{\pi wk} \right] dk \tag{7}$$

Our asymmetry "signal" at a distance r from the center of the image is given by

$$s = E_o(\theta, r, w) - E_o(\theta + \pi, r, w) = 2E_o, \tag{8}$$

and our average level at r by

$$\bar{E} = E_e. \tag{9}$$

Assuming that the noise is entirely associated with the light reaching the photocell, and is "white", we have for the noise

$$n = K \sqrt{\bar{E}} \tag{10}$$

and the signal-to-noise ratio is given by

$$s/n = \frac{1}{K} (2E_o / \sqrt{E_e}), \tag{11}$$

which is dependent on w, among other things.

Using Steel's approach, we have for the modulus and the phase of the transfer function (for small coma),

$$|T| = T_o - C^2 (L_1 \cos^2 \theta + L_2 \sin^2 \theta)$$

and

$$\Phi = [C \cos \theta] \Phi_c \tag{12}$$

where  $T_o$  is the aberration-free transfer function, C is the amount of coma in wavelength units,  $L_1$  and  $L_2$  are loss functions (functions of K), and  $\Phi_c$  is the phase function (also a function of K). We have tabulated values of  $T_o$ ,  $L_1$ ,  $L_2$ , and  $\Phi_c$  (and corresponding functions for the elementary aberrations) for annular apertures with aberration ratios running from 0 to 1 in steps of 0.1. For the present problem we will assume an obscuration ratio of 0.3. Figure 3 shows the pertinent functions for this ratio.

It is apparent that  $\phi$  is very small for small coma, say less than  $0.1\lambda$ , and, therefore, we can let

$$\sin \phi = \phi = [C \cos \theta] \phi_c \tag{13}$$

and

$$\cos \phi = 1$$

Then equations (7) become

$$\begin{aligned} E_e &= a - (b \cos^2 \theta + c \sin^2 \theta) C^2 \\ &= a \left[ 1 - \left( \frac{b}{a} \cos^2 \theta + \frac{c}{a} \sin^2 \theta \right) C^2 \right] \end{aligned}$$

and

$$E_o = dC \cos \theta, \tag{14}$$

where

$$\begin{aligned} a &= 2w \int_0^1 T_o \cos(2\pi kr) \left[ \frac{\sin \pi wk}{\pi wk} \right] dk \\ b &= 2w \int_0^1 L_1 \cos(2\pi kr) \left[ \frac{\sin \pi wk}{\pi wk} \right] dk \\ c &= 2w \int_0^1 L_2 \cos(2\pi kr) \left[ \frac{\sin \pi wk}{\pi wk} \right] dk \end{aligned} \tag{15}$$

and

$$d = 2w \int_0^1 T_o \phi_c \sin(2\pi kr) \left[ \frac{\sin \pi wk}{\pi wk} \right] dk.$$

The terms involving the product of  $L_1$  and  $L_2$  with  $\phi_c$  have  $C^3$  as a coefficient, and for small  $C$  can be neglected. In fact, for  $C < 0.1$ ,  $b$  and  $c$  can also be neglected with small error.

Thus, we can find, as a function of slit width,

- (1) The fractional energy of the aberration-free central peak by setting  $r = 0$  and evaluating  $a$ ;
- (2) The fractional energy of the aberration-free side lobe by setting  $r = 1.5$  and evaluating  $a$ ;
- (3) The coma detection factor (which when multiplied by  $C \cos \theta$  gives the asymmetry "signal") by setting  $r = 1.5$  and evaluation  $2d$ ; and
- (4) The signal-to-noise factor by setting  $r = 1.5$ , evaluation  $a$  and  $2d$ , and taking the ratio of  $2d$  to the square root of  $a$ .

The results of these calculations are shown in Figures 4 and 5 and in Table I.

TABLE I

	<u>SLIT WIDTH EFFECTS</u>								
SLIT WIDTH <sup>(1)</sup>	0	.2	.4	.6	.8	1.0	1.2	1.4	1.6
CENTRAL PEAK <sup>(2)</sup>	0	.151	.293	.420	.527	.612	.675	.715	.746
SIDE LOBE <sup>(2)</sup>	0	.018	.033	.046	.057	.067	.076	.088	.102
COMA DETECTION FACTOR <sup>(3)</sup>	0	.087	.168	.236	.288	.326	.349	.358	.363
SIGNAL-TO-NOISE FACTOR <sup>(4)</sup>	0	.329	.460	.549	.600	.629	.633	.605	.568

- (1) Multiply by  $N\lambda$  to get actual slit width.
- (2) Fraction passing through slit of total energy of aberration-free star image. There is no significant change for coma less than  $1/10\lambda$ .
- (3) Multiply by  $C \cos\theta$  ( $C$  = coma in wavelength units,  $\theta$  = orientation angle) to obtain coma detection "signal", i.e., difference between side lobes expressed as fraction of total energy of star image.
- (4) Multiply by  $1/K$  to get signal-to-noise ratio, where  $K$  is the ratio of the observed noise to the square root of the observed signal for the total image ("infinitely" wide slit) or any fraction thereof (e.g., the central peak signal with the operating slit width).

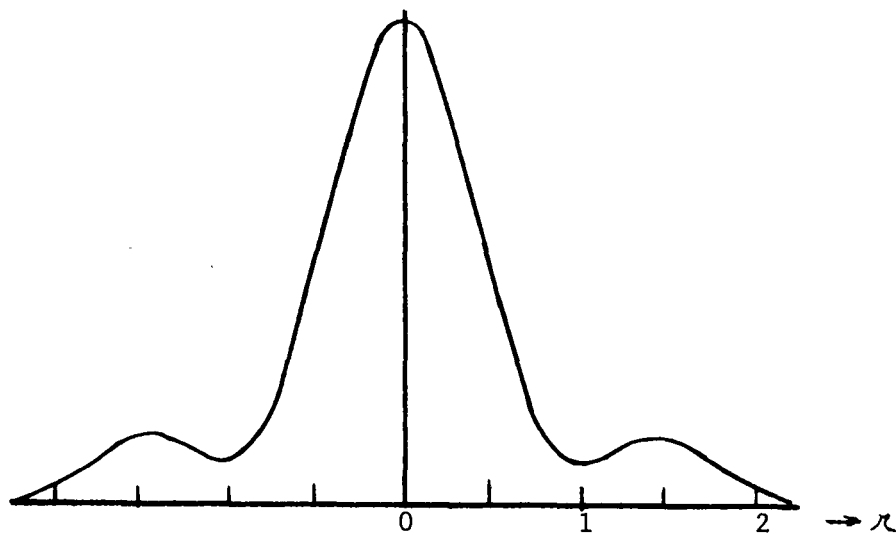


Figure 1. Line Image Profile (Line Spread Function)  
(No Aberration, 33% Obscuration)

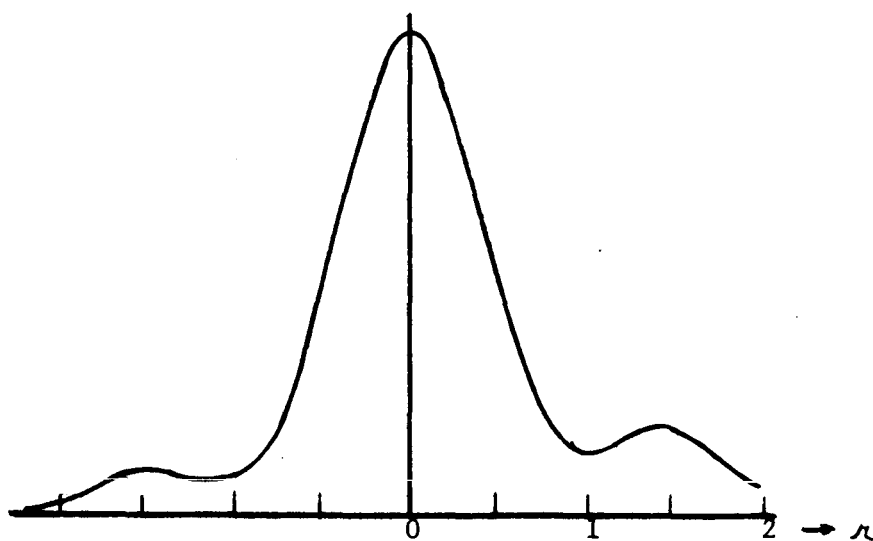


Figure 2. Line Image Profile in Presence of  
Small Amount of Coma  
(33% Obscuration)



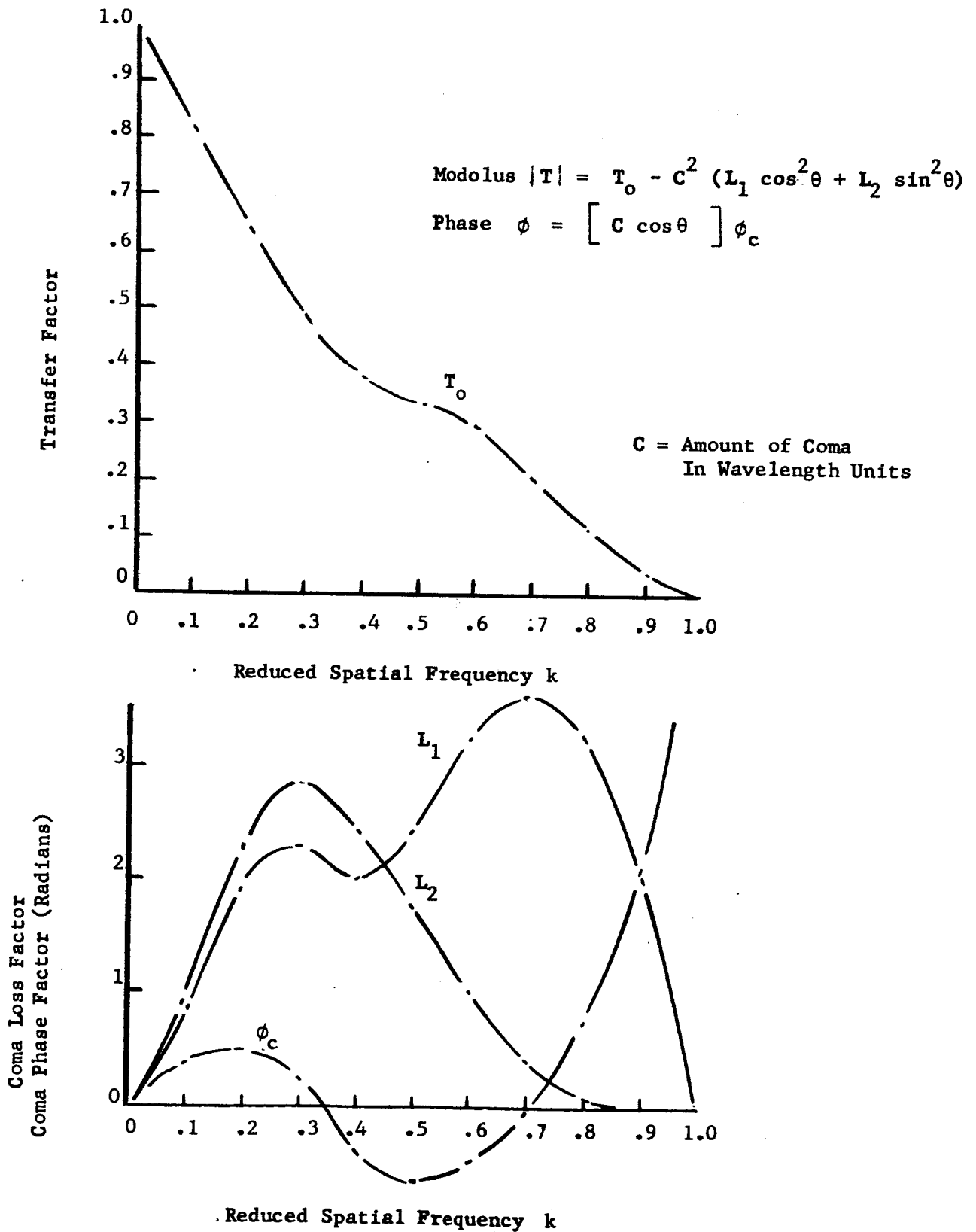


Figure 3. Factors for Calculating Transfer Function in Presence of Small Amount of Coma (Obscuration Ratio = 0.3)

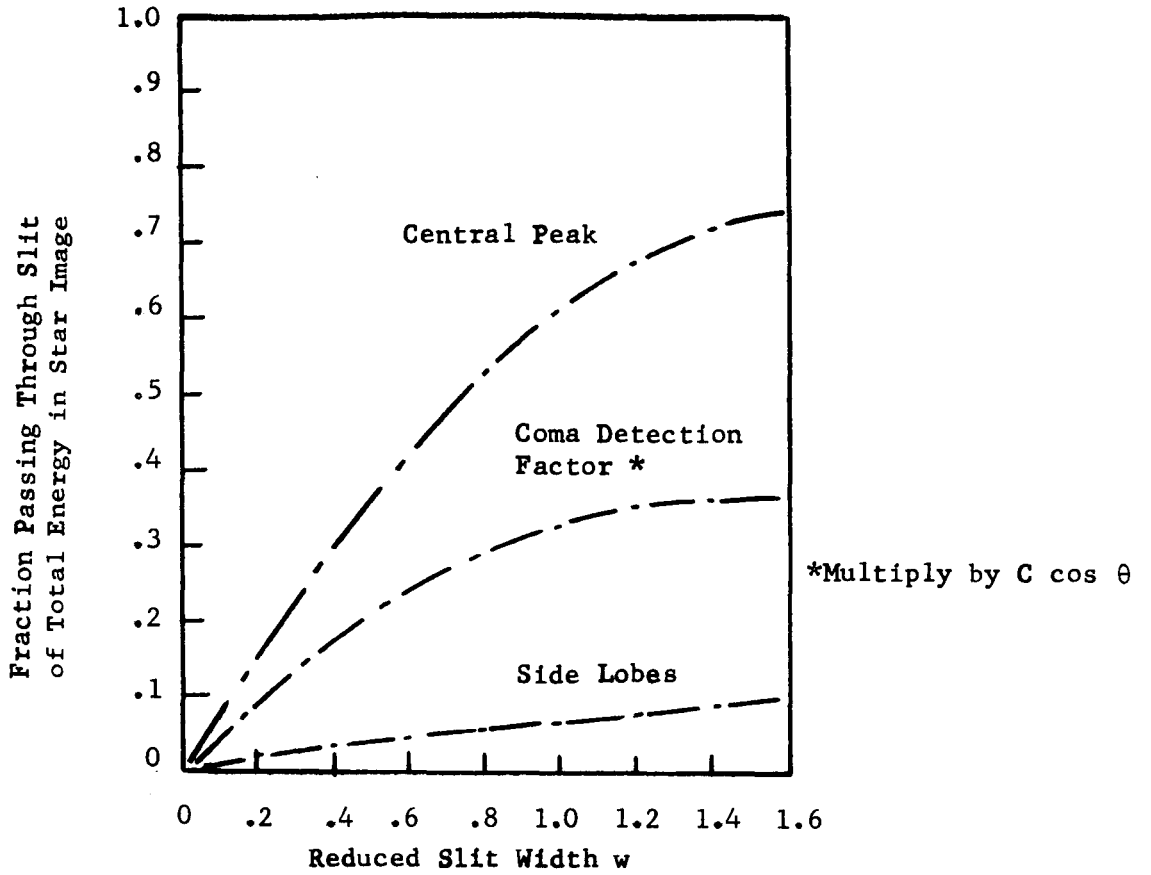


Figure 4. Slit Width Effects

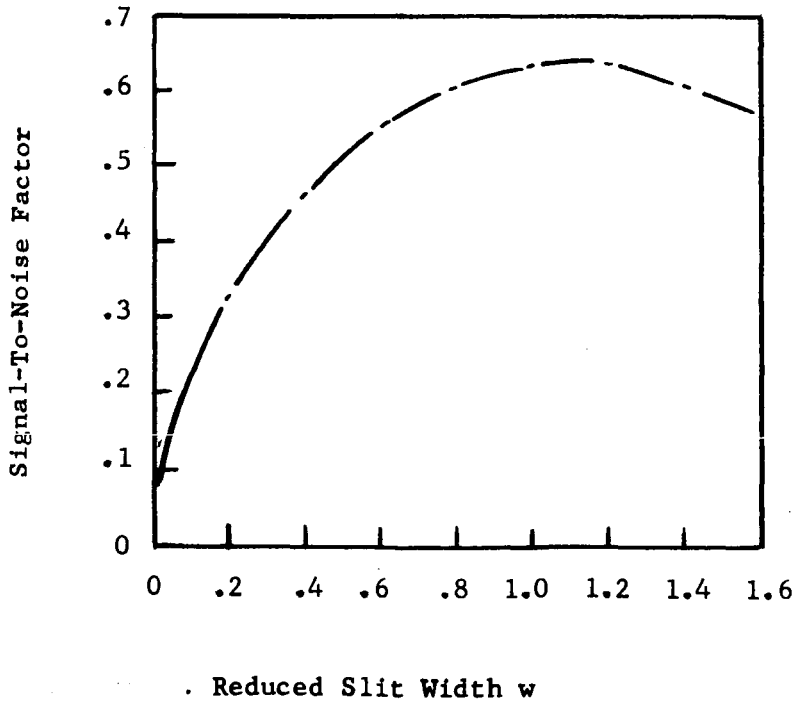


Figure 5. Signal-To-Noise Variation With Slit Width

It can be seen that the optimum slit width from signal-to-noise considerations is about 1.2 or about equal to the radius of the Airy disc. With this slit width, close to 70% of the total light is the image passes through the slit when it is centered on the central peak, and close to 8% of the total light when it is centered on a side lobe. An asymmetry "signal" of 3.5% of the total light (5% of the peak value) corresponds to about  $1/10\lambda$  of coma, and is linearly proportional to it.

---

R. V. Shack

RVS/cgl

Reference

1. Etude des Effets Combines des Aberrations et d'une Obturation Centrale de la Pupille sur le Contraste des Images Optiques, W. H. Steel, Revue d'Optique 32, pp. 162-173 (1953).

**Page intentionally left blank**

TECHNICAL NOTE

D.A.M.-005

OPTICAL TOLERANCES

A. Axial Misalignment Tolerances

One method of setting a tolerance on the position of a focal plane is to assume that the optimum position corresponds to a geometrically perfect focus and that at the tolerance boundaries the wavefront deviation is a fractional part of a wavelength.

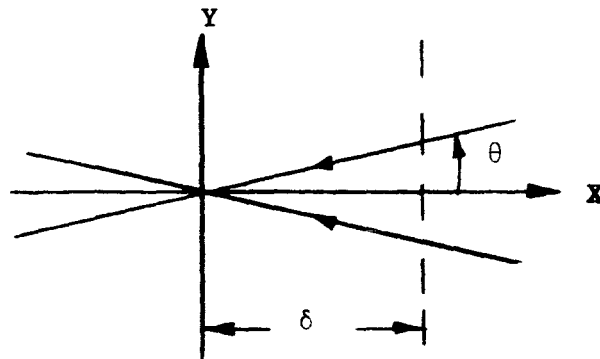


FIGURE 1

Figure 1 illustrates an optical system which has the x axis as the optical axis and the y axis in the point of perfect focus. If  $\theta$  is the angle of a marginal ray with respect to the optical axis, then a shift in focal position corresponds to a change of  $x$  in the path of an axial ray and a change of  $x/\cos \theta$  in the path of a marginal ray. If the maximum allowable shift in focus is  $\delta$ , and this corresponds to a  $\lambda/n$  deviation in path length, then:

$$\frac{\lambda}{n} = \frac{\delta}{\cos \theta} - \delta \tag{1}$$

and to a close approximation:

$$\frac{\lambda}{n} \approx \delta \left( 1 + \frac{\theta^2}{2} - 1 \right) \tag{2}$$

$$\frac{\lambda}{n} \approx \frac{\theta^2}{2} \delta \tag{3}$$

If  $F$  is the focal ratio of the optical system then approximately:

$$2\theta \approx \frac{1}{F} \tag{4}$$

and  $\delta \approx \pm \left(\frac{\lambda}{n}\right) 8F^2 \tag{5}$

The value chosen for  $n$  is somewhat arbitrary. A value of 4, the Rayleigh criterion, corresponds to a 20% loss in intensity at the diffraction pattern center and a value of 16 is about a 1% loss which is generally considered negligible.

The following table gives the values of  $\delta$  for corresponding values of  $F$  and  $n$  assuming a value of  $0.5 \mu$  for  $\lambda$ .

FOCAL POSITION TOLERANCES

<u>F/NO.</u>	$\frac{\lambda}{4}$	$\frac{\lambda}{10}$	$\frac{\lambda}{16}$
10	±.1 mm.	±.04 mm.	±.025 mm.
20	±.4 mm.	±.16 mm.	±.1 mm.
50	±2.5 mm.	±1 mm.	±.625 mm.
100	±10 mm.	±4 mm.	±2.5 mm.
200	±40 mm.	±16 mm.	±10 mm.

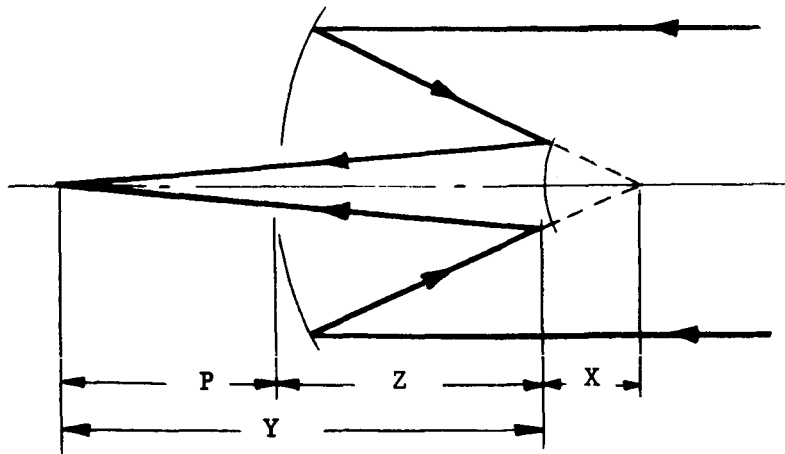


FIGURE 2

The tolerance on the axial position of the secondary in a Cassegrainian telescope can be determined by letting  $x$  and  $y$  represent the distances from the secondary vertex to the conjugate foci. Then:

$$-\frac{1}{y} + \frac{1}{x} = \frac{1}{f} \tag{6}$$

and differentiating,

$$\frac{1}{y} \frac{dy}{dx} - \frac{1}{x^2} = 0 \quad (7)$$

$$\frac{dy}{dx} = \frac{y}{x^2} \quad (8)$$

If  $p$  is the distance from the primary to the focal plane and  $z$  is the distance between the primary and secondary then:

$$p = y - z \quad (9)$$

and,

$$dp = dy - dz \quad (10)$$

also,

$$dx = -dz \quad (11)$$

combining (10) and (11),

$$dp = dy + dx \quad (12)$$

substituting (8) into (12),

$$dp = dx \left( 1 + \frac{y^2}{x^2} \right) \quad (13)$$

If  $\frac{y}{x}$  is the magnification  $m$  then from (11) and (13),

$$dz = \frac{-dp}{(1+m^2)} \quad (14)$$

The maximum allowable value for  $dp$  is given by equation (5). If  $\delta$  represents the tolerance on the secondary position then from (5) and (14):

$$\delta = \pm \frac{\lambda}{n} \frac{8F_c^2}{(1+m^2)} \quad (15)$$

where  $F_c$  is the f ratio of the Cassegrainian system. Using  $F_p$  the focal ratio of the primary instead:

$$F_c = mF_p \quad (16)$$

$$\delta = \pm 8 \frac{\lambda (mF_p)^2}{n(1+m^2)} \quad (17)$$

From (17) it is apparent that in systems with a secondary magnification of 2 or more, the tolerance on the axial position of the secondary varies as  $F_p^2$  so that a fast primary requires very tight control on

the secondary spacing. Assuming the  $\lambda/10$  criterion, a wavelength of  $0.5\mu$  and  $F_p$  and  $m$  equal to 2 and 5 respectively:

$$\left. \begin{aligned} & } = \pm \frac{(0.5\mu)}{10} \frac{8(5)^2(2)^2}{1+5^2} \\ & \circ \pm 1.54\mu \text{ or } \pm .608 \times 10^{-4} \text{ inches} \end{aligned} \right\}$$

B. LATERAL MISALIGNMENT TOLERANCES

If the axes of the primary and secondary mirrors of a Cassegrainian system are not coincident, then an aberration similar to coma results. The geometrical size of the resultant image can be determined by conventional ray tracing techniques (reference 1) or the resultant wave front deformation may be found directly by series expansion of the optical path lengths.

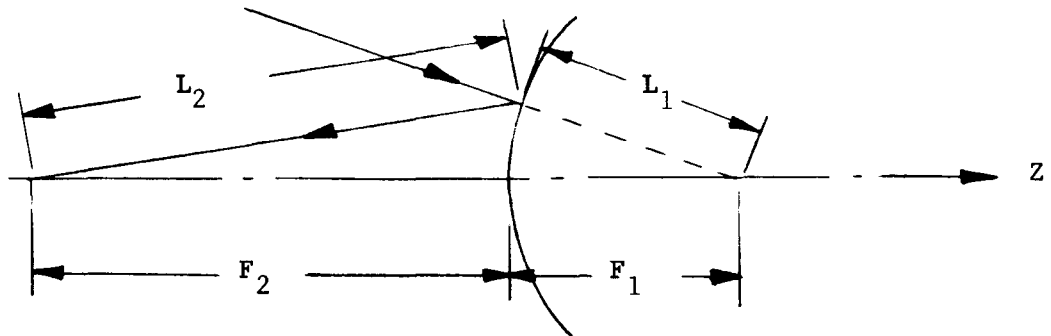


FIGURE 3

Figure 3 shows a hyperbolic secondary mirror having foci a distance  $F_1$  and  $F_2$  from the mirror vertex. One of the properties of a hyperbola is that the path lengths  $l_1$  and  $l_2$  shown in the figure are related by the following equation:

$$l_2 - l_1 = F_2 - F_1 \tag{18}$$

Taking a coordinate system centered at the mirror vertex with the z-axis coincident with the optical axis, then for any point  $x, y, z$  on the mirror surface,

$$l_1 = (F_1 - z)^2 + x^2 + y^2 \tag{19}$$



$$l_2 = \sqrt{(F_2 + z)^2 + x^2 + y^2} \tag{20}$$

Expansion of (19) and (20) into a series yields:

$$l_1 = F_1 \left( 1 - \frac{z}{F_1} + \frac{r^2}{2F_1^2} + \dots \right) \tag{21}$$

$$l_2 = F_2 \left( 1 + \frac{z}{F_2} + \frac{r^2}{2F_2^2} + \dots \right) \tag{22}$$

where,  $r^2 = x^2 + y^2$  (23)

Substituting (21) and (22) into (18):

$$z + \frac{r^2}{2F_2} + z - \frac{r^2}{2F_1} = 0 \tag{24}$$

and,  $z = \frac{r^2}{4} \left( \frac{1}{F_1} - \frac{1}{F_2} \right)$  (25)

Substituting (25) into (21) and (22),

$$l_1 = F_1 + \frac{r^2(F_1 + F_2)}{4F_1F_2} \tag{26}$$

$$l_2 = F_2 + \frac{r^2(F_1 + F_2)}{4F_1F_2} \tag{27}$$

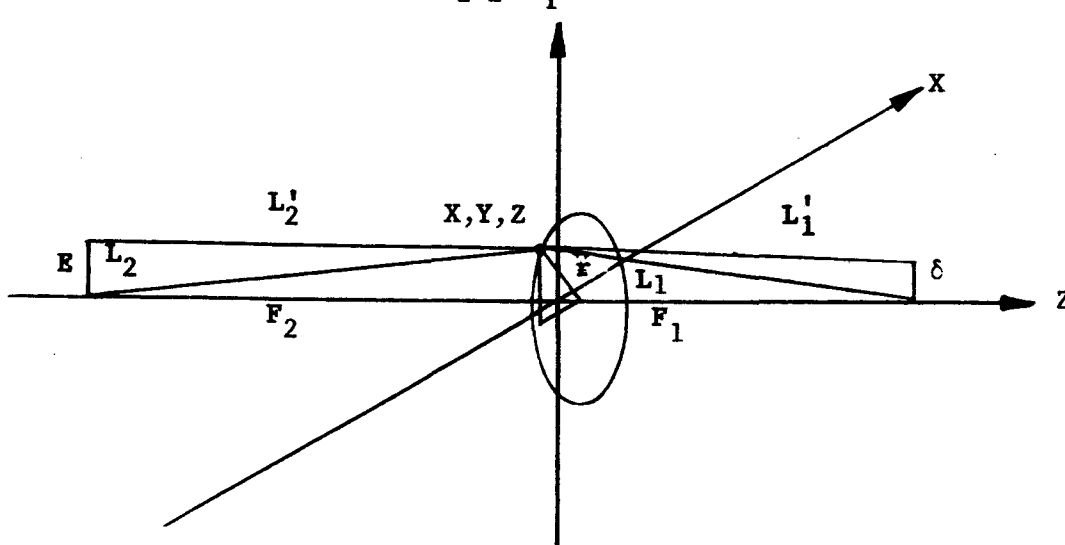


FIGURE 4

Considering points which are vertically above  $F_1$  and  $F_2$  by a small, amount  $\delta$  and  $E$  respectively then the corresponding path lengths  $l_1$  and  $l_2$  shown in Figure 4 are given by:

$$l_1' \approx l_1 - \frac{\delta y}{l_1} \quad (28)$$

$$l_2' \approx l_2 - \frac{E y}{l_2} \quad (29)$$

In Figure 3 the total path length  $\phi$  is given by:

$$\phi = l_2 - l_1 \quad (30)$$

Similarly in Figure 4:

$$\phi = l_2' - l_1' \quad (31)$$

The change in path length is therefore:

$$\Delta\phi = l_2 - l_2' - l_1 + l_1' \quad (32)$$

Substituting (28) and (29) into (32),

$$\Delta\phi = \frac{E y l_1 - \delta y l_2}{l_1 l_2} \quad (33)$$

or approximately,

$$\Delta\phi \approx \frac{E y l_1 - \delta y l_2}{F_1 F_2} \quad (34)$$

Substituting (26) and (27) into (34):

$$\Delta\phi = \frac{y(E F_1 - \delta F_2 + \frac{(E-\delta)(F_1+F_2)(x^2+y^2)}{4 F_1 F_2})}{F_1 F_2} \quad (35)$$

Taking  $x$  as zero and rewriting (35),

$$\Delta\phi = A y + B y^3 \quad (36)$$

A minimum wavefront deviation can be obtained by choosing the constants  $A$  and  $B$  so that the maximum positive and negative values of  $\Delta\phi$  are

equal over the positive range of  $y$  (and similarly for the negative range of  $y$ ). This condition is met if:

$$y_m^2 = \frac{-4A}{3B} \quad (37)$$

where  $\pm y_m$  is the range of  $y$ .

The total range in  $\Delta\phi$  can be determined by substituting (37) into (36) and is given by:

$$\Delta(\Delta\phi) = 2\Delta\phi_{\max} = \frac{By_m^3}{2} \quad (38)$$

Substituting the value for  $B$  defined by (35) and (36) into (38):

$$\Delta(\Delta\phi) = 2\Delta\phi_{\max} = \frac{(E-\delta)(F_1+F_2)y_m^3}{8F_1^2F_2^2} \quad (39)$$

To a first approximation  $E$  is a magnified image of  $\delta$  and is related by:

$$E = \frac{F_2}{F_1} \delta \quad (40)$$

Substituting (40) into (39),

$$\Delta(\Delta\phi) = 2\Delta\phi_{\max} = \delta \frac{(F_2 - 1)(F_1 + F_2)}{F_1} \frac{y_m^3}{8F_1^2F_2^2} \quad (41)$$

The  $F$ /Number of the primary mirror of a Cassegrainian system is related to the back focus of the secondary by:

$$F_p = \frac{F_1}{2y_m} \quad (42)$$

Substituting (42) into (41) and using  $m$ , the secondary magnification for  $F_2/F_1$ :

$$\Delta(\Delta\phi) = \frac{\lambda}{n} = \frac{\delta(m^2-1)}{64m^2 F_p^3} \quad (43)$$

$$\delta = \frac{64 \left(\frac{\lambda}{n}\right) m^2 F_p^3}{(m^2-1)} \quad (44)$$

Example:  $F_p = 2$

$$m = 5$$

$$\lambda = 0.5\mu$$

$$n = 10$$

$$\delta = \frac{64 \times .5 \times 10^{-4} \times 25 \times 8}{2.54 \times 10 \times 24} = 1.05 \times 10^{-3} \text{ inches} = 00105 \text{ inches.}$$

D. A. Markle - January 13, 1966

#### References

1. Military Standardization Handbook 141, Optical Design

N66 34372

PERKIN-ELMER

Report No. 8346(IV)

VOLUME IV

**TABLE OF CONTENTS**

<u>Section</u>	<u>Title</u>	<u>Page</u>
	PREFACE	vi
1.0	INTRODUCTION	1-1
2.0	SUMMARY	2-1
	2.1 Study Objective and Scope	2-1
	2.2 Summary of Technical Studies	2-2
3.0	TECHNICAL STUDIES	3-1
	3.1 General	3-1
	3.2 Mission Definition	3-2
	3.3 Spacecraft Definition	3-63
4.0	RECOMMENDATIONS FOR FUTURE STUDIES	4-1
	4.1 Introduction	4-1
	4.2 Mission Analysis	4-1
	4.3 Systems Analysis	4-2
	4.4 Preliminary Design	4-3
5.0	PHOTOGRAPHIC SYSTEMS IN SPACE ENVIRONMENT	5-1
	5.1 Introduction	5-1
	5.2 Scope of Photosensitive Recording Materials Study	5-1
	5.3 Simplified Nature of Silver Halide Photochemical Reactions	5-1
	5.4 Photographic Emulsion Fogging by Van Allen Belt Radiation	5-3
	5.5 Balancing the Resolution, Exposure, and Spectral Sensitivity Requirements of Photographic Materials	5-4
	5.6 Radiation Environment	5-11
	5.7 Summary and Conclusions	5-18

## TABLE OF CONTENTS (con't)

<u>Appendix</u>	<u>Title</u>	<u>Page</u>
A	Rigid Mount Configuration	A-i
B	Soft Pipe Rack Configuration	B-i
C	Coil Spring Configuration	C-i
D	Crew Schedule	D-i
E	Propulsion Sizing for Orbital Altitude Change	E-i
F	Reproduction of Letter (EX3/L1-66) from National Aeronautics and Space Administration	F-i
G	Reproduction of Letter (66MA4844) from North American Aviation, Inc.	G-i

## LIST OF ILLUSTRATIONS

<u>Figure</u>	<u>Title</u>	<u>Page</u>
3.1	Density vs. Altitude for Three Atmospheric Models	3-5
3.2	OA0 Ballistic Coefficient vs. Angle of Attack	3-7
3.3	OA0 Orbital Decay for Three Atmospheric Models and Four Different Initial Altitudes	3-8
3.4	Initial OA0 Altitude vs. Time to Decay to 200 n.mi. for Three Different Atmospheric Models	3-9
3.5	Initial OA0 Altitude vs. Time to Decay to 200 n.mi. for Maximum Density Atmospheric Models	3-10
3.6	Total Dose Rate Behind Aluminum Shielding for 30° Inclination Circular Orbits	3-11
3.7	Dose Rates Behind Aluminum for 30° Inclination Circular Orbits	3-12
3.8	Intensity Contours for Outer Zone Electrons	3-15
3.9	Total Dose Rate vs. Aluminum Shield Thickness for the 1966 and 1972 Time Period	3-16
3.10	SIB-Apollo Service Module Performance	3-18
3.11	Peak Torques (RSS) vs. Altitude for Various OA0 Configurations	3-22
3.12	Total Average Torques vs. Altitude for Various Configurations	3-23
3.13	Satellite Visibility From Gound Communication Station vs. Orbital Altitude and Minimum Antenna Elevation Angle	3-24
3.14	Communication Time vs. Altitude (Based on Ground Track Through Ground Station)	3-26



## LIST OF ILLUSTRATIONS (Continued)

<u>Figure</u>	<u>Title</u>	<u>Page</u>
3.15a	Normal LEM/CSM Reaction Jet Logic	3-28
3.15b	Modified LEM/CSM Reaction Jet Logic	3-28
3.16a	Stiff and Soft Pipe Rack Suspension	3-29
3.16b	Coil Spring Suspension	3-29
3.16c	Modified Pipe Suspension	3-29
3.17a	End Mount Configuration	3-31
3.17b	Side Mount Configuration	3-31
3.18	Percent Increase in Maximum Torque Disturbances on LEM/CSM Due to Grav. Grad. and Aerodynamic	3-32
3.19	Relative Distance and Acceleration Between OAO Telescope Due to Differential Gravity and Aero Drag	3-33
3.20a	Time Between OAO Fine Inertial Wheel Momentum Dump	3-34
3.20b	Linear Acceleration of Rigid Mounted OAO Due to Man Motion and Jet Impulses	3-34
3.21	Boom Bending Frequency Assuming Steel Tubing	3-37
3.22	Maximum Elastic Stress Limit on Boom Resulting From Man Motion Plus Slewing Maneuver	3-37
3.23	Maximum Translational Acceleration of OAO Due to Man Motion Plus Jet Impulses	3-38
3.24	Trade-off on Maximum Allowable OAO Acceleration ( $2 \times 10^{-4}$ "g") and Boom Stress Limit (70,000 psi)	3-38
3.25	Maximum Translational Velocity of OAO Resulting From Man Motions Plus Limit Cycle in LEM/CSM	3-39

## LIST OF ILLUSTRATIONS (Continued)

<u>Figure</u>	<u>Title</u>	<u>Page</u>
3.26	Maximum Torque Disturbance on OAO Due to Man Motion Plus Reaction Jet Impulses (Offset = 0.10 Inch)	3-40
3.27	Integral Launch Configuration, S1B	3-49
3.28	Configuration A (End Mount)	3-66
3.29	Configuration B (Side Mount)	3-67
3.30	Reliability of OAO Equipment	3-64
3.31	Startracker Reliability	3-75
3.32	Undisturbed Limit Cycle Propellant Requirements at $\pm 5$ Degrees Deadband	3-79
3.33	Undisturbed Limit Cycle Propellant Requirements at $\pm 0.3$ Degree Deadband	3-80
3.34	Disturbed Limit Cycle Attitude Hold Propellant Requirements	3-81
3.35	Control System Block Diagram	3-82
3.36	Control System Detailed Block Diagram	3-83
3.37	Simplified PPDS Block Diagram	3-87
5.1	Log Exposure (meter-candle-seconds)	5-12
5.2	Relative Graininess and Total Fog as a Function of X-Ray Dose	5-13
5.3	Granularity vs. Resolving Power for Various Aerial Films From the "Manual of Physical Properties of Kodak Aerial and Special Sensitized Materials"	5-14
5.4	Shielding Requirements as a Function of Number of Days Exposure	5-17
5.5	Shielding Weight Needed to Shield a Cylindrical Volume (8 inch Diameter by 4 inches) from Doses Exceeding one Rad as a Function of Days Exposure	5-20

PREFACE

During the course of the study for an Advanced Princeton Satellite, it became evident that Apollo Applications Program might be broadened to encompass astronomy. Perkin-Elmer was asked to extend the scope of the study to include questions such as:

1. What roles might a man play in conjunction with an Advanced Orbiting Astronomical Observatory to enhance its operation and experiment objectives?
2. How best to transport the crew to the observatory and how long could they stay (e.g. mission profile definition)?
3. How would the crew best maintain contact with the observatory and work with it?

Since the Grumman Aircraft Engineering Corporation had developed the OAO spacecraft and had already carried out a similar study entitled, "The OAO in Association with a Manned Space Station", the help of this group was solicited by Perkin-Elmer to carry out this aspect of the broadened study, because of their excellent qualifications. The results of the Grumman Study are included in this volume. Also contained in this volume are some data on the Command and Service Modules obtained through Dr. Spitzer from North American Aviation, Inc.\* and the NASA Manned Spacecraft Center at Houston. (See appendices F and G. The drawings attached to the N.A.A. letter could not be reproduced.) Also included are a few of the considerations (from the instrument maker's point of view) of the astronaut's role in regard to the telescope itself, as well as a Perkin-Elmer study of photographic media which might be utilized during a manned mission. The results of the Grumman Study were freely edited by Perkin-Elmer in order to arrive at a practical integrated system concept.

It will be evident, after reading this volume, that the question of whether it is feasible to conduct this experiment using only an Apollo Command and Service module (CSM) and an integral launch with a Saturn IB booster is answerable in two ways, depending upon which source one chooses for Command and Service module weight data and booster capability. Grumman, using published NASA data, concludes that an integral launch using the CSM would be marginal and recommends instead a dual launch with a Lunar Excursion Module (LEM) Laboratory to house the astronauts. Comparison with the North American Aviation and NASA Manned Spacecraft Center data shows the following:

---

\*NOTE: The use of the North American Aviation data in this study was made possible by the very kind permission of Mr. J. A. Moran of North American. Mr. Moran cautions that the data presented there is a rough, tentative estimate.

	<u>Grumman</u>	<u>NAA</u>	<u>MSC</u>
Command Module Basic Weight	10,300	10,800	22,268
Service Module Weight (including Propellants)	13,400	12,000	
Saturn IB Payload	33,800	37,500	31,600
Weight Margin	-2,020	+5,200	+ 117

Obviously, with such large discrepancies in basic data, a firm recommendation cannot be made. While the LEM lab is more commodious, the Command module appears to offer just sufficient space and weight carrying ability to house the necessary instruments for the astronaut's use in orbit. (Development of miniaturized oscilloscopes, TV monitors, etc., is presupposed.)

Therefore, the question of the use of the LEM lab seems to rest solely on the margin in capacity which is to be provided for the astronauts.

If it were economically feasible, the ultimate in reliability would be afforded by an integral launch using the CSM (and a 15 day mission if required by weight considerations) to allow correction of any initial malfunctions, followed by a rendezvous after six months or a year to correct any malfunctions which might have occurred in the interim. Although not a part of the original scope of the study, such a follow-up visit may afford the possibility of replacing thruster fuel, deteriorated components (such as solar panels) thereby permitting additional months of operation. If such a visit were combined with a rendezvous with other OAO satellites, the economics may become more attractive.

## 1.0 INTRODUCTION

The Orbiting Astronomical Observatory (OAO), NASA's largest and most sophisticated satellite will conduct astronomical observations unaffected by the earth's atmosphere. In a study by GAEC, "The OAO in Association with a Manned Space Station," completed in June 1965, the additional capabilities afforded the OAO program by associating it with man and a space station were defined. Included was a preliminary evaluation of the Apollo Applications Program (AAP) space station.

At the request of Dr. L. Spitzer, Jr. of Princeton University and the Perkin-Elmer Corporation, the Grumman Aircraft Engineering Corporation has performed this study, "The OAO with an Advanced Princeton Experiment Package associated with the Apollo Applications Program," under Perkin-Elmer's Purchase Order PECO #11364 S. This report presents the results of GAEC's six month effort and recommendations for future study.

The purpose of APEP is to obtain scientific data in the visible and ultraviolet parts of the spectrum. This data would be collected using a 40-inch, diffraction-limited, Cassegrain telescope with the same detector for both imagery and spectrometry. The experiment package is configured to fit within the central tube of the OAO. About two-thirds of the package is occupied by the Cassegrain telescope. The remaining space contains the instrument section consisting of detector assemblies, support electronics, and fine error sensing assemblies. Perkin-Elmer proposes to magnetically suspend the telescope within the OAO and provide fine tracking ( $\sim 0.01$  arc-seconds) with their fine error sensor and magnetic torquing of the telescope against the OAO. The OAO is required to acquire the guide stars, and point the optical axis to  $\pm 1$  arc minute in pitch and yaw and  $\pm 2$  degrees in roll. Exposure times and thus holding times of 30 minutes and longer are contemplated.

This report is presented in three major sections;

Summary of the results of the study

Details of the technical studies performed

Recommendations for further areas of study

## 2.0 SUMMARY

### 2.1 STUDY OBJECTIVE AND SCOPE

The objective of this study was to identify the design criteria and benefits of associating the OAO carrying an APEP with the AAP. The study was based on the following guidelines:

#### General

- Present OAO performance capabilities
- Present AAP performance requirements
- 1972 launch
- Use of OAO and Apollo ground stations

#### OAO

- Maximum utilization of present OAO systems and technology
- Baseline Spacecraft "C" configuration
- Attitude hold, within  $\pm 1$  arc minute for pitch and yaw,  $\pm 2$  degrees for roll
- Maximum allowable translation of experiment,  $\pm 1/2$  inch with respect to OAO
- 30 day manned operation, and subsequent 330 day unmanned operation

#### AAP

- CSM/LEM Lab, 3 men, 30 day duration
- CSM, 2 men, 30 day duration
- Carry spare equipments and tools for experiment and OAO, and a diagnostic and control system

#### APEP

- Experiment weight 1000 pounds
- Average power 30 watts, peak power 60 watts 10 min. per 101 min. orbital period
- Experiment package mounting identical to present concept. A release mechanism for magnetic suspension is incorporated within experiment package.

Supporting data from the following studies was used in this study:

OAO in Association with a Manned Space Station (Ref. 1)

OAO - Repair in Orbit (Ref. 2)

AAP (Ref. 3)

The major study areas were:

Mission Definition

- Selection of orbital altitude and inclination
- Evaluation of launch vehicle compatibility
- Consideration of mode of operation (gimbal and free)
- Definition of man's role
- Definition of mission profile

Spacecraft Definition

- Determination of typical OAO/APEP/AAP Configuration
- Compatibility with launch environment of Saturn 1B
- Determination of required OAO modifications
- Determination of all-up weight
- Assessment of reliability

## 2.2 SUMMARY OF TECHNICAL STUDIES

The study has resulted in the following conclusions:

### 2.2.1 Mission Definition

**Orbital Altitude:** 300 n mi based on considerations of torque disturbance, orbital decay, radiation environment, and communication time.

**Orbital Inclination:** 32° based on a Cape Kennedy launch and utilization of OAO and Apollo communication ground stations.

**Launch Vehicle Compatibility:** An integral CSM/LEM Lab/OAO placed in a 300 nautical mile orbit must be accomplished with a dual SIB launch of the CSM and the LEM/OAO and a subsequent rendezvous in orbit. This is the present NASA concept for similar flights of the AAP. For a launch into synchronous orbit a single Saturn V must be used.

**Elimination of the LEM Lab from the system** was considered but it appears that a single SIB launch for 30 day, 300 n mi mission may be marginal, based on available SIB capability estimates.

**Mode of Operation:** Under the direction of Dr. Spitzer, the effort concentrated on the gimballed mode of operation. Based on keeping the translation of the floating experiment to less than  $\pm 0.5$  inches with respect to the OAO, in the presence of man motion and limit cycling with the Reaction Control System (RCS), it has been concluded that a 2 axis gimbal with a coil spring isolation system having a natural frequency between 0.02 to 0.075 radians per second

and with 12 to 20 feet distances between the center of mass of the LEM/CSM and the OAO would be satisfactory. This gimbal would provide 15° of rotational freedom in pitch and yaw with the spacecraft providing the roll control.

**Man's Role:** The role of the astronaut for this experiment consists of monitoring, maintaining, and modifying the OAO and the experiment. He will ascertain the reasons for and correct any initial failures that may occur either during deployment or in operation of the experiment. He will retrieve, develop, and examine the exposed film and place new film within the experiment package. At the end of 30 days, he will remove the photographic system and replace it by a uvicon detector assembly and the OAO will be permitted to operate in its unattended mode. From present considerations of the South Atlantic radiation anomaly, and preliminary trajectory analysis, Extra-Vehicular Activity (EVA) is required to insert new film after leaving the anomaly and to remove the exposed film before entering the anomaly.

**Mission Profile:** For this application, many mission launch alternatives are possible. (It has been concluded that a dual launch of the CSM and the OAO/LEM Lab is the recommended approach.)

A launch sequence similar to that described in section 7.1.1.1 of the OAO Space Station Study is anticipated. Following rendezvous and docking, approximately 5 hours after lift off, a crew schedule begins. System status checks, communication and LEM Lab make-ready occur. Following a period allocated for eating, the LEM Lab is checked out and two of the astronauts transfer to the LEM Lab. Details of these and subsequent operations in terms of a crew schedule have been determined. After about 7-1/2 hours, the procedure for EVA will be initiated and two crewmen will leave the LEM Lab to uncage and deploy the OAO. A two hour EVA has been allocated and a possible second day EVA to complete the erection and deployment is available.

The system will be checked out, malfunctions, if any, will be detected and repaired. Since, approximately 4 orbits of every day pass through the South Atlantic anomaly, EVA's will be accomplished to provide an 18 hour photographic experiment time, separated by a 30 hour non-photographic experimentation period to insure that the astronauts and film are not exposed to the anomaly.

During the 18 hour cycle, 9 hours of crew time will be devoted to experiment monitoring with a three man crew or 6 hours for a 2 man crew. During the 30 hour cycle, the comparable times are 18 and 12 hours, respectively. Following the 30 day operation, the photographic detector assembly will be replaced by a uvicon assembly and the OAO will be released for unmanned operation. The film will be returned to earth by the astronauts in the command module.

### 2.2.2 Spacecraft Definition

**Configuration determination:** For an integral OAO/LEM Lab launch, the OAO is stored in the center compartment of a low profile descent stage, made available by the removal of the LEM descent engine. It is supported by a pallet attached to its normal mounting legs, which, in turn, is fastened to the descent



stage by a truss. The launch loads are taken through the descent stage to the Space Launch Adapter (SLA) and then to the SIVB stage.

Two deployment modes have been studied. For the "end" deployment (OAO operating near the descent stage) no additional modifications are required. For the "side" deployment (OAO operating near the front docking port) the rendezvous radar must be relocated, if required. For both modes, a control and diagnostic system, a communication link (OAO/APEP - LEM Lab) and a film developer and analyzer system must be incorporated.

**Launch Environment:** The launch environment imposed by the SIB, as defined in the LEM specifications, is within the design requirements of the present OAO specifications. (Possible resonances/amplifications can only be determined with vibration/shock testing.)

**OAO Modifications:** The OAO modifications identified during this study were for ease of maintenance of the least reliable equipment, APEP compatibility, and gimbal operation. In order to obtain access to equipments the outer skin retention design should be modified for hinged operation using quick release fasteners with captured hardware. Star Tracker Assemblies should be modified to add access covers in existing structure and provide a mounting adapter for out-board installation of bolts into trapped caps. To obtain access to the Primary Process and Data Storage (PPDS), the Solar Array must be removed. This is possible but not recommended since the handling of the Solar Array in the space environment is extremely difficult. Relocation of the system should be considered. The modifications for incorporating the APEP consist of providing an RF Window for communication between the floating experiment and the OAO and providing mounting for the coils of the magnetic torquers. For providing gimbal support structure, the paddle hinges for the Solar Array should be revised to accept spreader bars. No modifications are required for the integral launched mounting.

**All-up Weight Determination:** An all-up weight of 38,602 pounds is required for an integral CSM/LEM Lab/OAO configuration for a 30 day mission. Of this weight, the LEM Lab weighs 8,954 pounds and the OAO with experiment dependent components weighs 4,548 pounds. This analysis indicates that a single SIB cannot launch a CSM/LEM Lab/OAO. Dual launches consisting of a separate CSM and LEM Lab/OAO with two SIB's are recommended as per the present NASA/AAP concept for similar flights.

**Reliability Assessment:** The reliability estimates indicate that there will be an 85% probability of mission success for the first month of operation. At the end of this time, with replacement of failed components the probability of the mission lasting 11 more months is 16.5% as compared to a 14.4% probability for the mission lasting one year with no maintenance. For six months of mission duration, the probability of success is 44.7%. Thus, if the failed components are replaced after a six month interval, the probability of operating successfully for the remaining six months is 44.7%. Similarly, if maintenance occurs every three months, the probability of mission success is 58.4%. It is, therefore, concluded that the optimum operational concept should provide the capability for a visit at the end of six months for refurbishment.

### 3.0 TECHNICAL STUDIES

#### 3.1 GENERAL

The association of an OAO and an AAP vehicle to perform the APEP experiment offers many advantages primarily as a result of the presence of man. During the initial phase of operation he can assist in the deployment of sensitive components, evaluate the effects of launch; and repair accessible initial malfunctioning components. His presence during the operation of the OAO/APEP permits gathering of photographic data, monitoring performance, trimming in of critical adjustments, and the repairing of malfunctioning components. To take advantage of this association, the technical studies were directed to answering these questions:

What should be the orbital altitude and inclination?

What should be the mode of operation (gimbal or free)?

If gimballed, what should the characteristics of the gimbal structure be, and where should it be attached to the AAP.

If launched on an SIB, what is the effect of the launch environment on the OAO/APEP?

What is man's availability to support the OAO/APEP?

What minimal modifications to the OAO are required to associate it with the AAP spacecraft, carry the APEP, and permit limited repairability?

What would be a typical launch configuration of the LEM Lab with the OAO?

What would be a typical launch deployment sequence for LEM Lab/OAO launch?

What effects on the OAO's reliability would be derived from the association of a manned spacecraft?

What would be a typical control and diagnostic system for the OAO/APEP to be carried aboard the AAP spacecraft?

After operation at a lower altitude with the AAP spacecraft, can the OAO be raised to a higher altitude for the remainder of the mission?

The answers to these questions are presented in the Mission Definition and Spacecraft Definition studies in the following sections.

### 3.2 MISSION DEFINITION

The purpose of the Princeton manned astronomical mission is to collect scientific data in the visible and ultraviolet parts of the spectrum. This data would be collected using a 40-inch diameter, diffraction-limited, Cassegrain telescope with various detectors for both imagery and spectrophotometry. For imagery, photographic film would be used only during the time man is available. For unmanned operation, the data would be obtained using vidicon detector assemblies. The experiment package being designed by Perkin-Elmer is configured to fit within the central tube of the OAO. About two-thirds of the package is occupied by the Cassegrain telescope. The remaining space contains the instrument section consisting of detector assemblies, communication system, support electronic and fine error sensing. Perkin-Elmer proposes to magnetically suspend the telescope within the central tube of the OAO and provide fine tracking ( $\sim 0.01$  arc-seconds) with their fine error sensor and magnetic torquing of the telescope against the OAO. The OAO is required to acquire the guide stars and point and hold the optical axis to  $\pm 1$  arc minute in pitch and yaw and  $\pm 2$  degrees in roll. Communication from the OAO to the APEP would be accomplished via an RF link.

To accomplish these objectives, different launch vehicle alternatives were examined. For launching the OAO and AAP spacecrafts integrally, SIB and SV launch vehicles were examined, and are discussed in detail in section 3.2.1.3. For separate launches, the Atlas Agena D and SIB boosters were considered. Based on present booster performance data, current AAP weight estimates (Reference 9) and maximum utilization of present systems technology, it is concluded that a dual launch of the CSM and the OAO/LEM Lab is the recommended approach.

A launch sequence similar to that described in section 7.1.1.1 of the OAO Space Station Study, Reference 1, is anticipated. Following rendezvous and docking, approximately 5 hours after lift off, a crew schedule begins. System status checks, communication and LEM Lab make-ready occur. Following a period allocated for eating, the Lem Lab is checked out and two of the astronauts transfer to the LEM Lab. Details of these and subsequent operations in terms of a crew schedule have been determined. After about 7-1/2 hours, the procedure for EVA will be initiated and two crew men will leave the LEM Lab to uncage and deploy the OAO. A two hour EVA has been allocated and a possible second day EVA to complete the erection and deployment is available.

The system will be checked out, malfunctions, if any, will be detected and repaired. Since approximately 4 orbits of every day pass through the South Atlantic anomaly, EVA's will be accomplished to provide an 18 hour photographic experiment time, separated by a 30 hour non-photographic experimentation period to insure that the astronauts and film are not exposed to the anomaly.

During the 18 hour cycle, 9 hours of crew time will be devoted to experiment monitoring with a three man crew or 6 hours for a 2 man crew. During the 30 hour cycle, the comparable times are 18 and 12 hours, respectively. Following the 30 day operation, the photographic detector assembly will be

replaced by a uvicon assembly and the OAO will be released for unmanned operation. The film will be returned to earth by the astronauts in the command module.

To further define the mission, studies were performed in the following areas:

Orbital Altitude and Inclination

Mode of Operation

Launch Environment

Man's Role

OAO Modifications

### 3.2.1 Orbital Altitude and Inclination

The AAP spacecraft's nominal altitude and inclination is 200 n.mi and 32°, respectively. The operating altitude and inclination of the OAO is approximately 390 n.mi and 32°. When constrained to operate at the altitude of the AAP vehicle, the OAO experiences a higher rate of orbital decay, shorter communication time to ground stations, and higher external disturbance torques. The limiting factors in raising the altitude of the AAP spacecraft to that of the OAO is the launch vehicle payload capability and the charged particle environment, due to the South Atlantic anomaly. The following sections describe the tradeoffs that were performed for the above parameters to determine a mutually satisfactory orbital altitude.

3.2.1.1 Orbital Decay - The orbital path of any spacecraft is perturbed by forces such as atmospheric drag, solar radiation pressure, irregularity of the Earth's shape, attraction of other celestial bodies and charge drag. These perturbing forces result in deflecting the vehicle from a theoretical Keplerian orbit. Calculations to predict the orbital lifetime of the OAO as a function of injection altitude have been made. These calculations are based on a closed form solution to the equations of motion developed in Reference 4. To obtain the closed form solution, the following five principal assumptions are necessary:

- (1) The OAO is in a circular orbit and the orbit remains circular during the decay process.
- (2) The atmospheric density is an exponential function of altitude based on a static model atmosphere.
- (3) The ballistic coefficient,  $W/C_D A$ , is constant.  
(This may be represented by a mean value during one orbital pass.)
- (4) The OAO has zero lift.
- (5) The Earth is spherical.

Results obtained using the closed form solution have compared favorably with the results of a digital computer program that numerically integrates the equations of motion.

The exponential atmospheric density model, in assumption (2), is an approximation to a static atmospheric model, where the static model relates density as a function of altitude only. This contrasts to a dynamic model which defines the density as functions of vehicle position, Sun position, local time, and solar activity (which is a function of time). The dynamic model has been shown to give a more accurate description of the atmospheric density (Reference 5), but complicates the computation of orbital decay. To determine the orbital decay of the OAO while using the simpler static models a mean maximum density, a mean minimum density, and a mean density were defined, Figure 3.1. The mean maximum density is the average density during one day for an active sun, while the mean minimum is the average density, during one day for an inactive sun. The mean density is considered to be the 1962 U. S. Standard Atmosphere (Reference 6).

The equations of Reference 4 were derived assuming a constant scale height between the initial and final altitudes, but for the range of altitudes considered in the study the scale height varies. However, for the atmospheric models used, the density profile can be segmented into constant scale height sections. The decay equations can then be used to compute the decay time through each of the segments, and the decay times can be summed to find the total decay time as a function of altitude. Table 3-I summarizes the values used.

TABLE 3-I  
ATMOSPHERIC SCALE HEIGHT ( $10^{-5}$  FT.  $^{-1}$ )

Altitude (n mi)	Maximum Density	Standard Density	Minimum Density
200	0.451	0.474	0.581
230	0.453	0.431	0.491
254	0.375	0.387	0.444
296	0.365	0.361	0.432
330	0.295	0.340	0.432
362	0.283	0.244	0.432
525			

By using these static models which represent the density extremes of the dynamic model, the variance in orbit life time can be bounded.

Since the vehicle weight,  $W$ , and reference area,  $A$ , are well defined, variations in the ballistic parameter,  $W/C_D A$ , are due to variations in the drag coefficient. These variations are due to changes in vehicles angle of attack and the uncertainty in estimating and measuring the vehicle  $C_D$ .

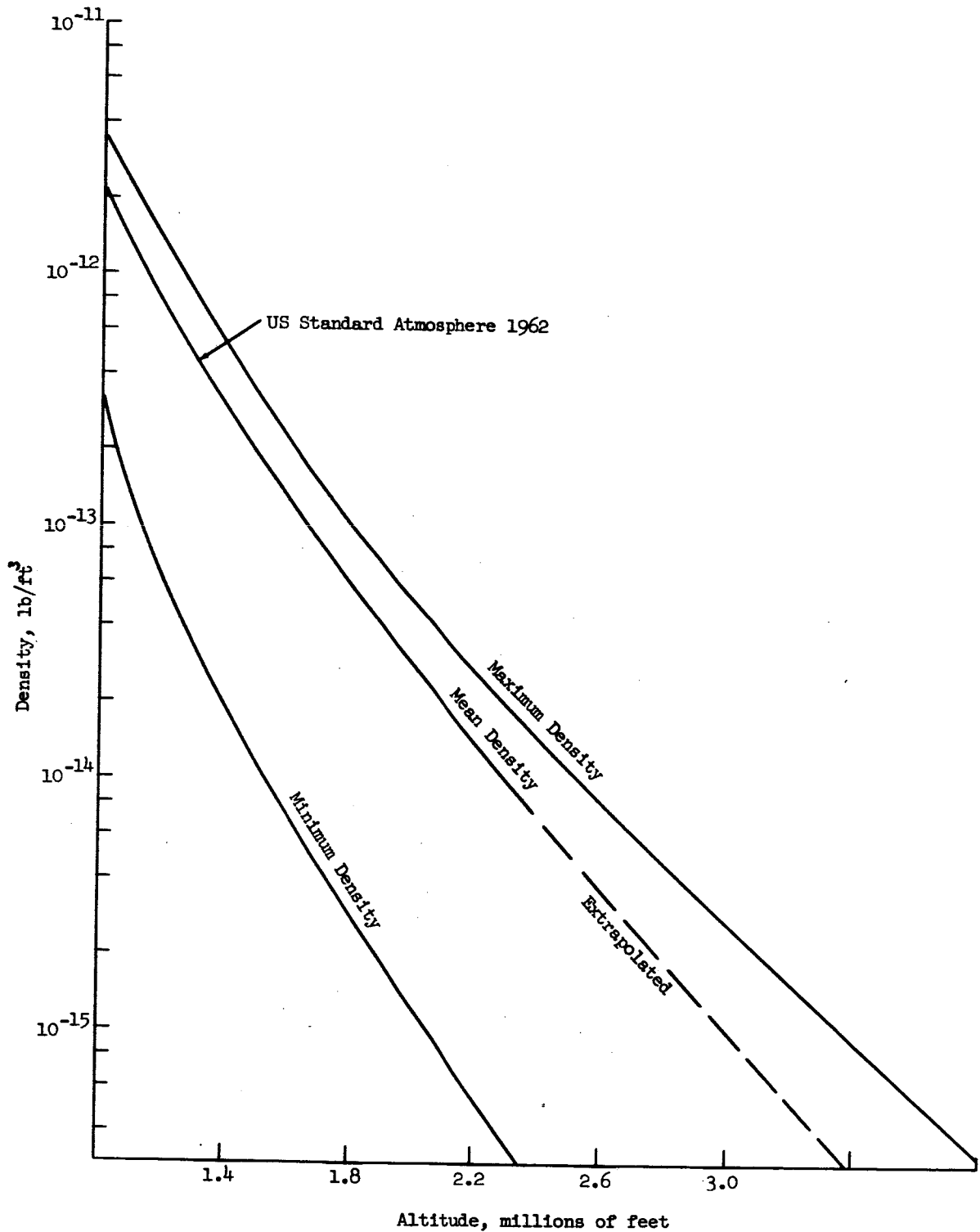


Figure 3.1. Density vs. Altitude for Three Atmospheric Models

Assuming that the OAO holds an inertial attitude (with no vehicle sideslip), the vehicle angle of attack will rotate through  $360^\circ$  for each orbit. Figure 3.2 shows the variation of  $W/C_{DA}$  with angle of attack, and also shows the mean value of  $W/C_{DA}$  evaluated over one orbit.

Altitude decay characteristics were obtained for several initial orbital altitudes, considering the three model atmospheres (represented by segmented scale heights), and various ballistic coefficients. Figure 3.3 shows that the different atmospheric models have a significant effect on orbital life-time. This is dramatically demonstrated in the 250 n. mi case. The actual OAO orbital altitude as a function of time should fall within these minimum and maximum profiles if its  $W/C_{DA}$  is 14-1 lbs/ft<sup>2</sup>. Figure 3.4 shows the time to decay to a 200 n. mi as a function of the initial orbital altitude for each of the atmosphere models. At 200 n. mi, the fine wheels of the OAO become continuously saturated due to the torque disturbances. This will be discussed in more detail in Section 3.2.1.4. To allow one year of useful OAO life, after the AAP vehicle leaves the OAO, a minimum initially established altitude of 274 n. mi is required. Figure 3.5 shows the effect on orbit decay as a result of uncertainty in the ballistic coefficient. Since a lower  $W/C_{DA}$  implies greater drag effects, the lower the ballistic coefficient the faster the orbit decays. The sensitivity of  $W/C_{DA}$  on orbital decay time is 1 to 1. That is, a 1% increase in  $W/C_{DA}$  gives a 1% increase in time to decay to 200 n. mi. This effect is shown in Figure 3.5. If 30% is considered to be an upper bound in the  $W/C_{DA}$  uncertainty, the required initial orbital altitude is approximately 290 n. mi.

3.2.1.2 Radiation Environment - Total Dose Rate Computation: An IBM 7094 computer code was used to calculate the integrated omnidirectional fluxes of particles of a given energy spectrum per day encountered in various orbits. These calculations were performed for a wide variety of circular orbit altitudes at a  $30^\circ$  inclination. The subsequent dose rate calculations behind increasing spherical aluminum shield thicknesses are based on the Freden-White spectrum for the trapped protons and the fission spectrum for the trapped electrons. In each case, it was necessary to assume that the spectrum associated with each particle type remained constant over the regions of interest. It was further assumed that the incident particles have an isotropic distribution. This latter assumption leads to no error in the special case of a spherical shield and is a fairly reasonable good assumption for the integrated fluxes in more general cases. The dose accumulated per day behind various aluminum shield thicknesses for orbital altitudes ranging from 200 to 500 n. mi. and an inclination of  $30^\circ$  is shown in Figures 3.6 and 3.7. The curves in Figure 3.6 include the dose contribution from the primary protons and the primary electrons with their associated bremsstrahlung. The dose estimates for the artificial electrons and their associated secondary radiations (bremsstrahlung) have been adjusted to yield results which should be typical of 1966. Due to the unpredictability of the solar cycle effects on atmospheric density, estimates of the artificial electron fluxes beyond this time are more difficult to determine. However, these fluxes are expected to decay more rapidly during the next period of high solar activity because of increased atmospheric density at higher altitudes and increased geomagnetic activity.

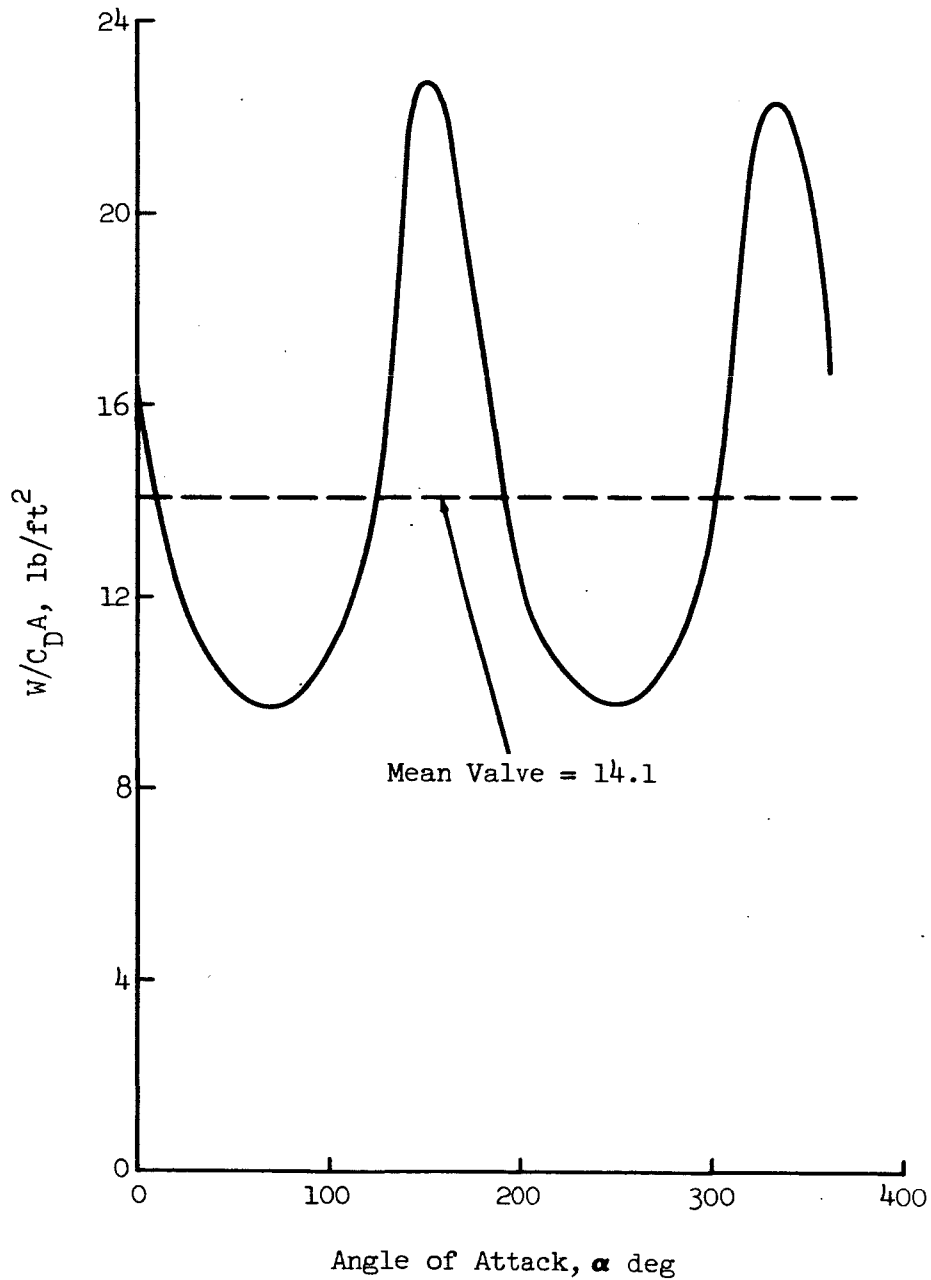
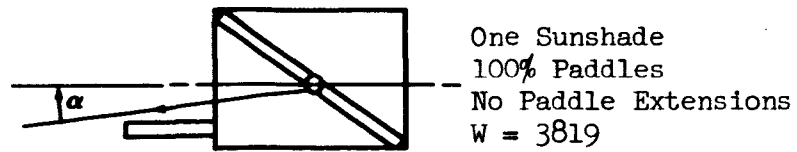


Figure 3.2. OAO Ballistic Coefficient vs. Angle of Attack



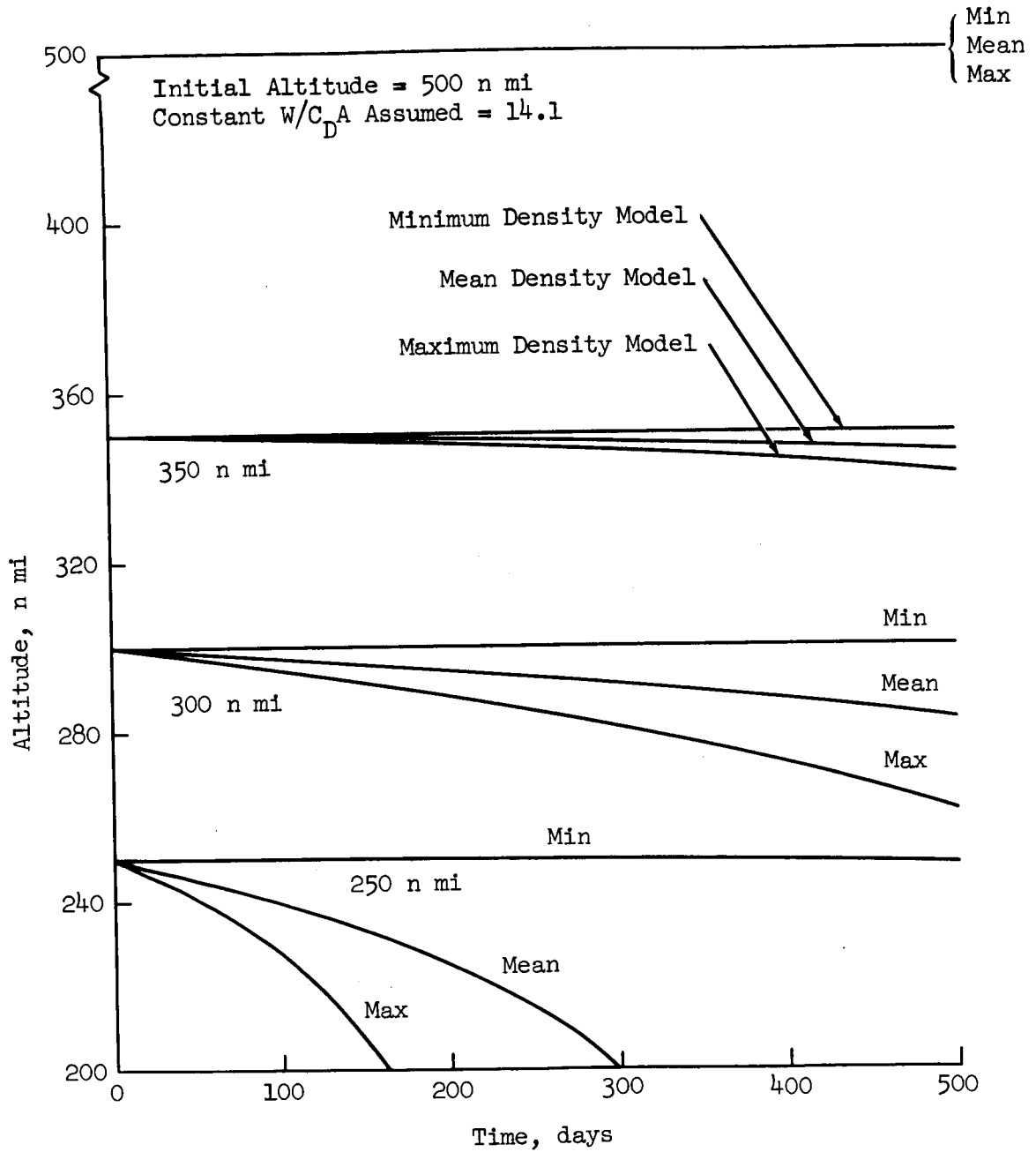


Figure 3.3. OAO Orbital Decay for Three Atmospheric Models and Four Different Initial Altitudes

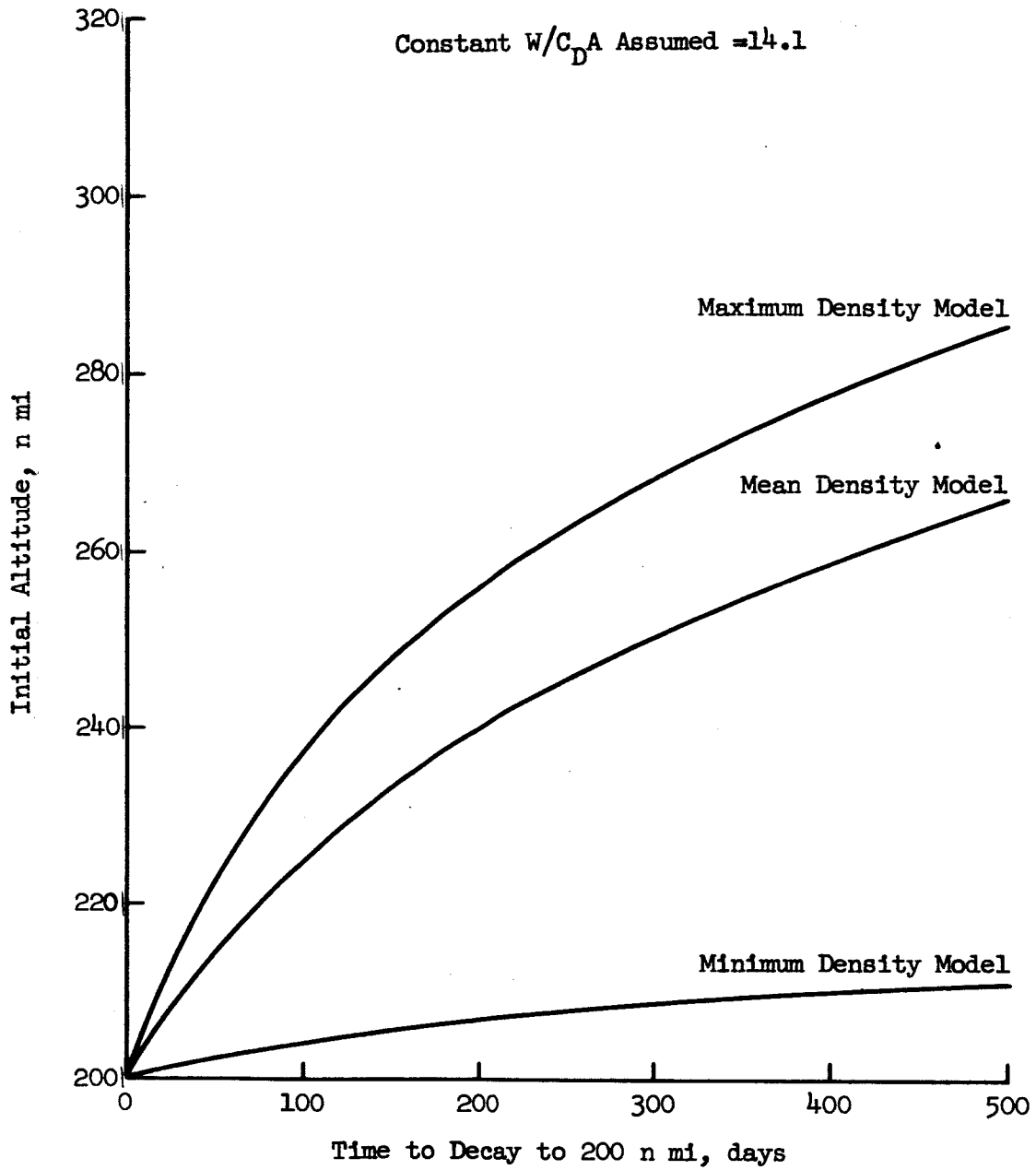


Figure 3.4. Initial OAO Altitude vs. Time to Decay to 200 n. mi. for Three Different Atmospheric Models

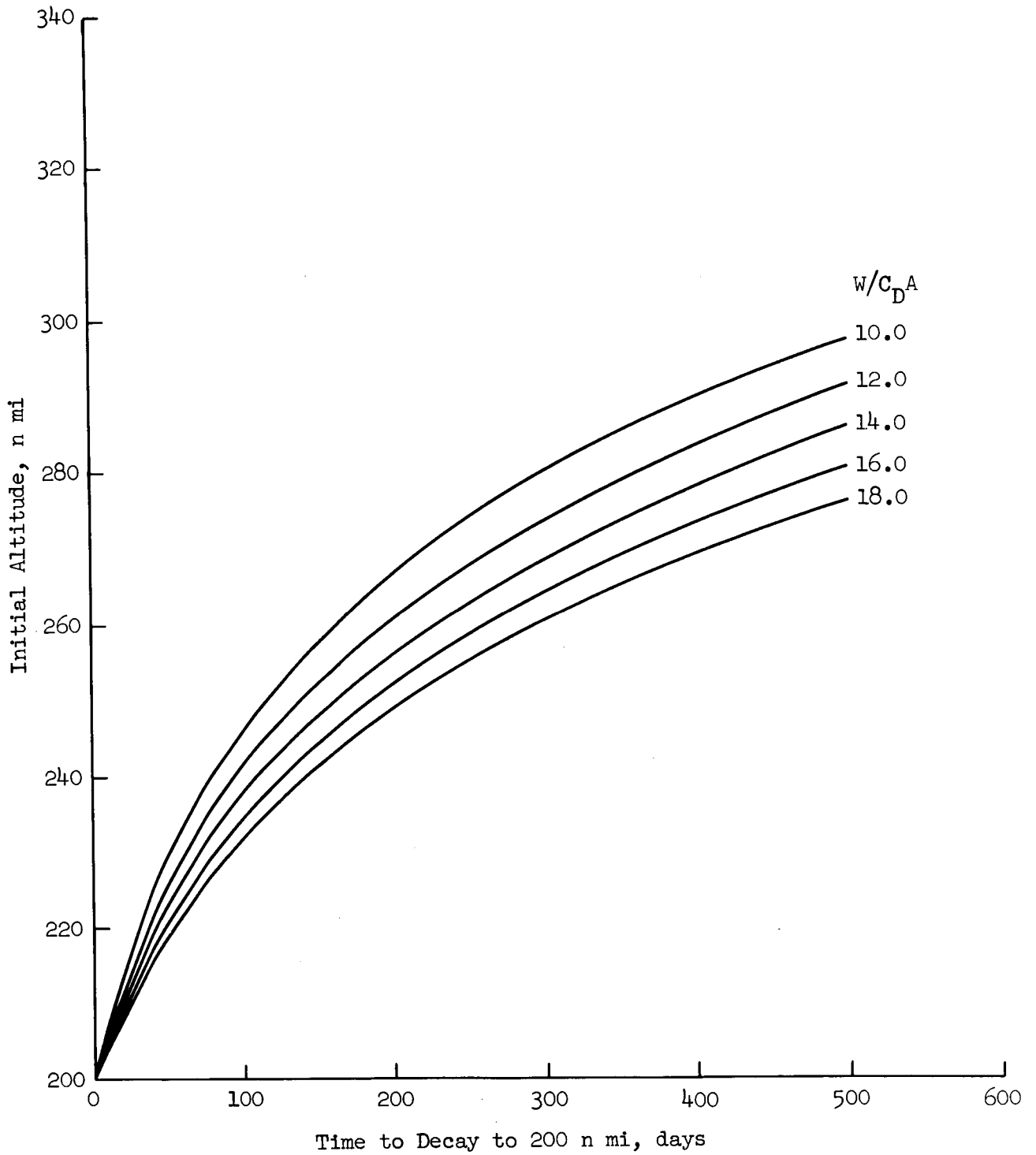


Figure 3.5. Initial OAO Altitude vs. Time to Decay to 200 n. mi. for Maximum Density Atmospheric Model

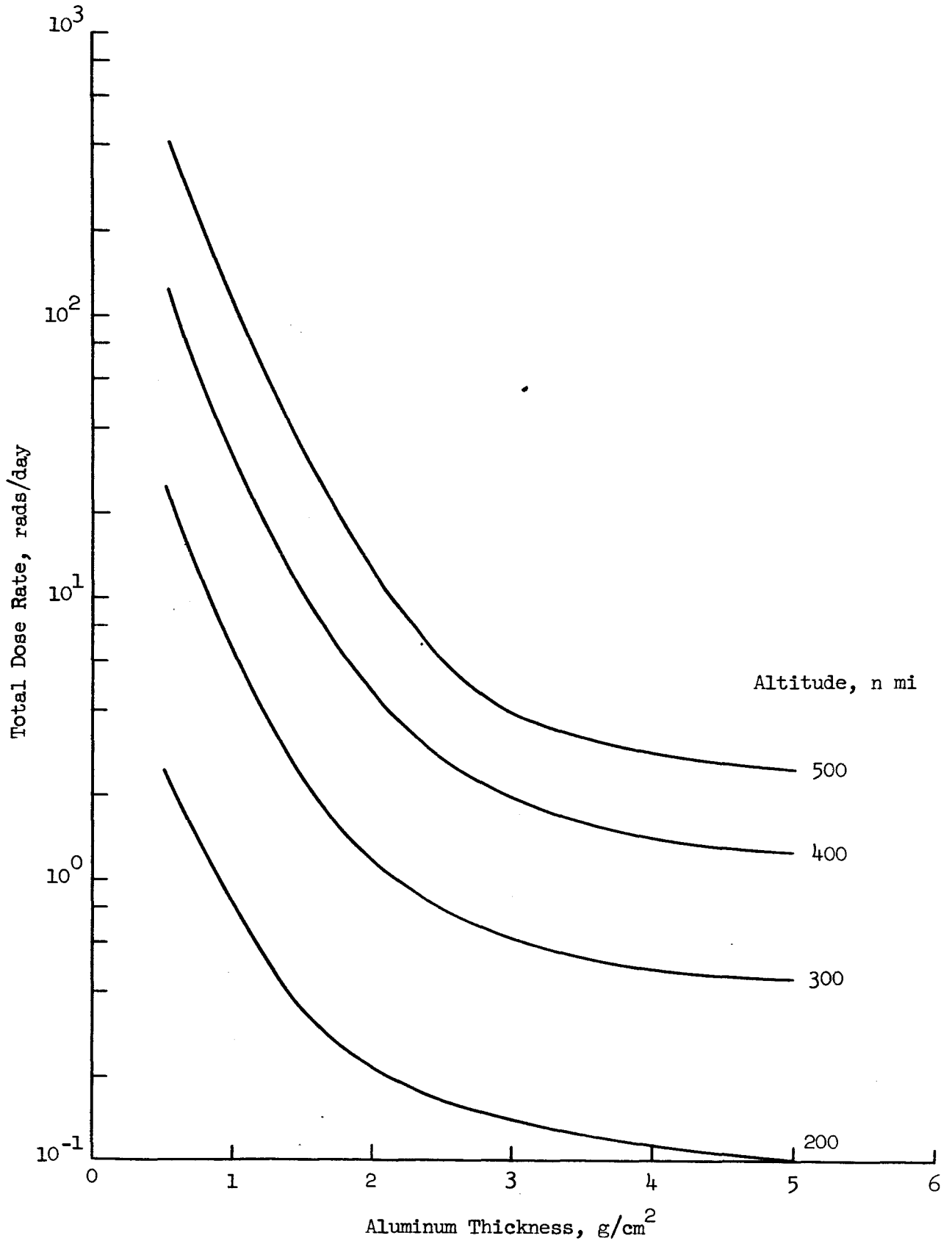


Figure 3.6. Total Dose Rate Behind Aluminum Shielding for 30° Inclination Circular Orbits

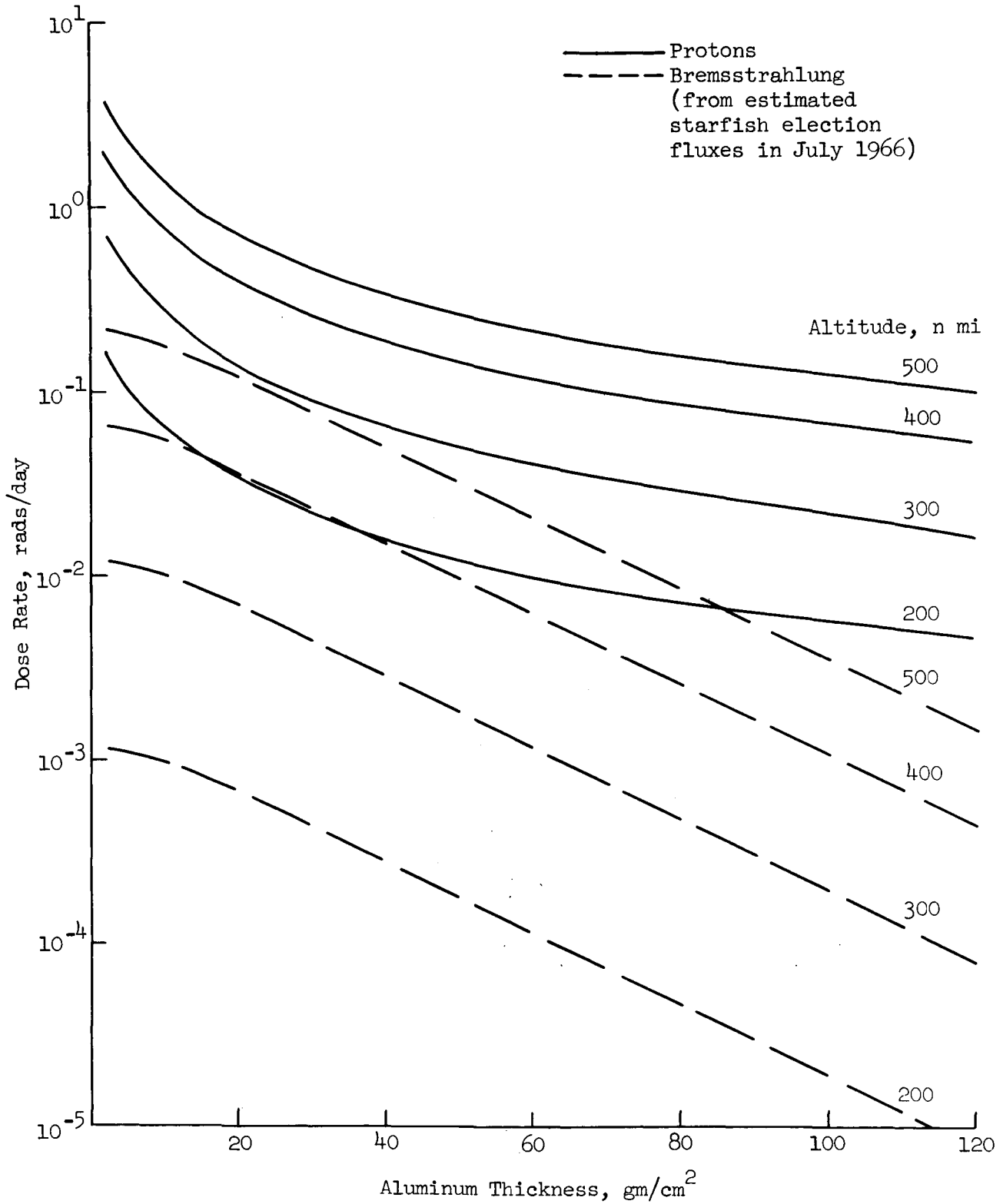


Figure 3.7. Dose Rates Behind Aluminum for 30° Inclination Circular Orbits

The required shielding is sensitive to orbital altitude because of the strong dependence of the trapped particles on altitude. Although not shown in Figure 3.6, the electron dose dominates for the first few  $\text{gm/cm}^2$  of shielding. For the range of altitudes considered, almost all of the dose is accumulated during the short interval of time while the satellite is in the region of the South Atlantic anomaly.

Radiation Protection Criteria: Radiation protection criteria for crew members in earth orbital Apollo missions have been specified by NASA. The nominal limits of exposure (the exposure received in transiting the regions of trapped radiation or other known sources of radiation for which the probability of exposure is 1) are not to exceed the average yearly exposure of Table 3-II.

TABLE 3-II  
AVERAGE YEARLY DOSES FOR INITIAL BODY ORGANS

Critical Organ	Average Yearly Dose (rad)	RBE (rem/rad)
Skin of whole body	233	1.4 (Approx.)
Blood-forming (BFO)	54	1.0
Eyes	27	2

These exposure limits have been set at the same level recommended for occupational exposure in the atomic industry by the International Commission on Radiation Protection and the National Committee for Radiation Protection. Since the average period of exposure of the astronaut to space radiation is estimated at 5 years the permissible average yearly dose shown in Table 3-II is higher than at atomic installations. Furthermore, these levels are considered acceptable in view of the other risks involved in manned space missions.

Vehicle and Suit Shielding: It is difficult to express the shielding effectiveness of both the vehicle and astronaut's space suit because of the non-uniform mass distribution. However, for purposes of estimating the hazard to crew members performing extra-vehicular activity, the suit is assumed to be equivalent to approximately  $0.5 \text{ gm/cm}^2$  of aluminum. The LEM and the CSM are assumed to have an equivalent aluminum shield thickness of 1.0 and  $4.0 \text{ gm/cm}^2$ , respectively. It is further assumed that each astronaut spends approximately 1/3 of the mission time in the LEM. The total accumulated dose at 300 n. mi. for example, for a 30 day mission based on a maximum EVA time of 96 hours is shown in Table 3-III. Only the eyes require any shielding to reduce the dose to a tolerable level. This requirement is effectively solved by personal localized shielding and by scheduling extra vehicular activities away from the anomaly.

TABLE 3-III  
TOTAL ACCUMULATED DOSE (RADS) - 1966

	Skin	BFO	Eyes	Exposure Time (Hrs)
EVA	50.0	0.88	50.0	96
LEM	9.2	1.44	9.2	196
CSM	4.14	2.48	4.14	432
Total	63.3	4.80	63.3	720

Radiation Environment 1972 Prediction: Since the first flights will probably occur around 1972, it is desirable to make some estimates of the radiation environment and compute the total accumulated dose as before. Assuming an exponential decay for the Starfish electrons with a decay time of 18 months, the July 1966 electron fluxes and corresponding doses are multiplied by a factor of  $1.85 \times 10^{-2}$ . Furthermore, 1972 corresponds to a period of high solar activity. At a 30° inclination the trapped proton flux and corresponding dose is reduced by a factor of approximately 3 in going from solar minimum to solar maximum.

Very little data exist on the natural trapped electrons prior to the Starfish explosion. Data obtained since Starfish include natural and artificial electrons and are of limited usefulness for determining the natural electron component. It has been determined that the natural component is an extension of the electron component of the outer belt into the inner belt, i.e., there is no boundary between the inner and outer belts insofar as the natural electron flux is concerned (see Figure 3.8 and Reference 7). The spectrum of the natural electrons as measured by Pizzella, et al. (Reference 8) was found to have a differential energy spectrum of the form:

$$n(E) \approx 10^7 \exp(-E/0.160) \text{ electrons/cm}^2 \text{-sec-ster-Mev}$$

where E is expressed in Mev.

Indications are that the spatial variation of the natural electron flux does not significantly differ from that of the total electron flux as measured by Explorer XV. It, therefore, seems reasonable to assume that the total flux distribution curves can be used for the natural flux distribution when they are normalized to the proper magnitudes.

The total daily dose vs. aluminum shield thickness for an orbital altitude of 300 n. mi. is shown in Figure 3.9. For purposes of comparison the total daily dose for 1966 is shown in the same figure. Assuming the same conditions used to construct Table 3-III, one obtains approximate results for 1972 as shown in Table 3-IV.

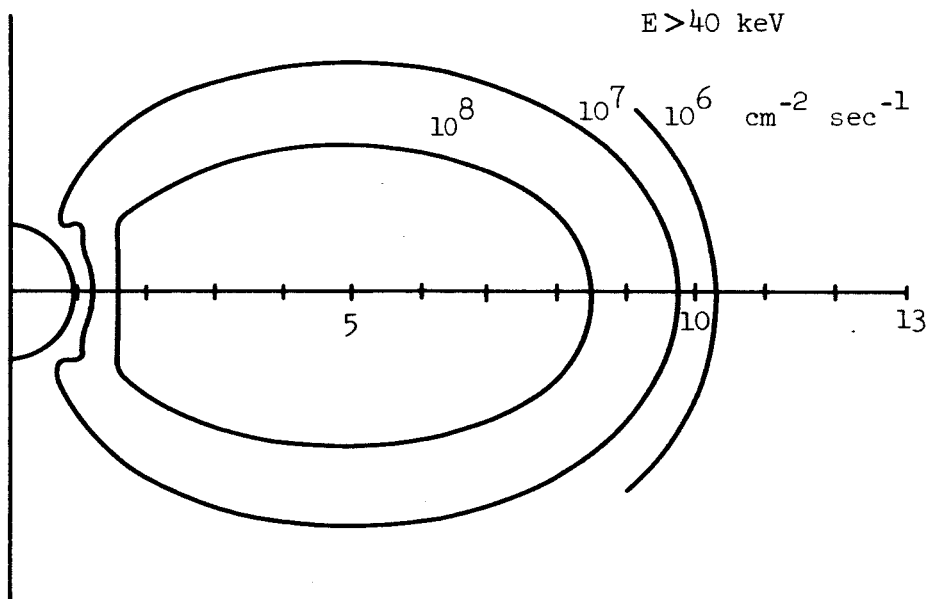
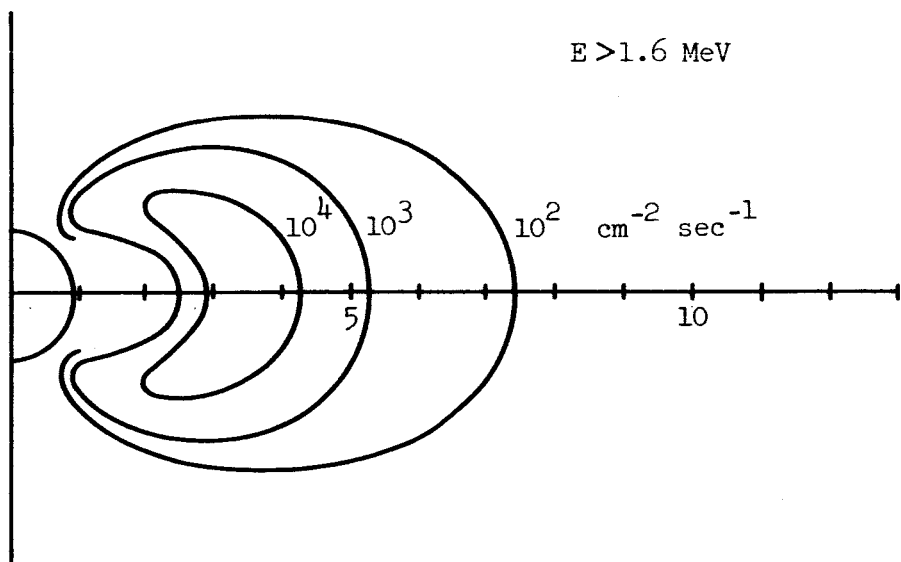


Figure 3.8. Intensity Contours for Outer Zone Electrons



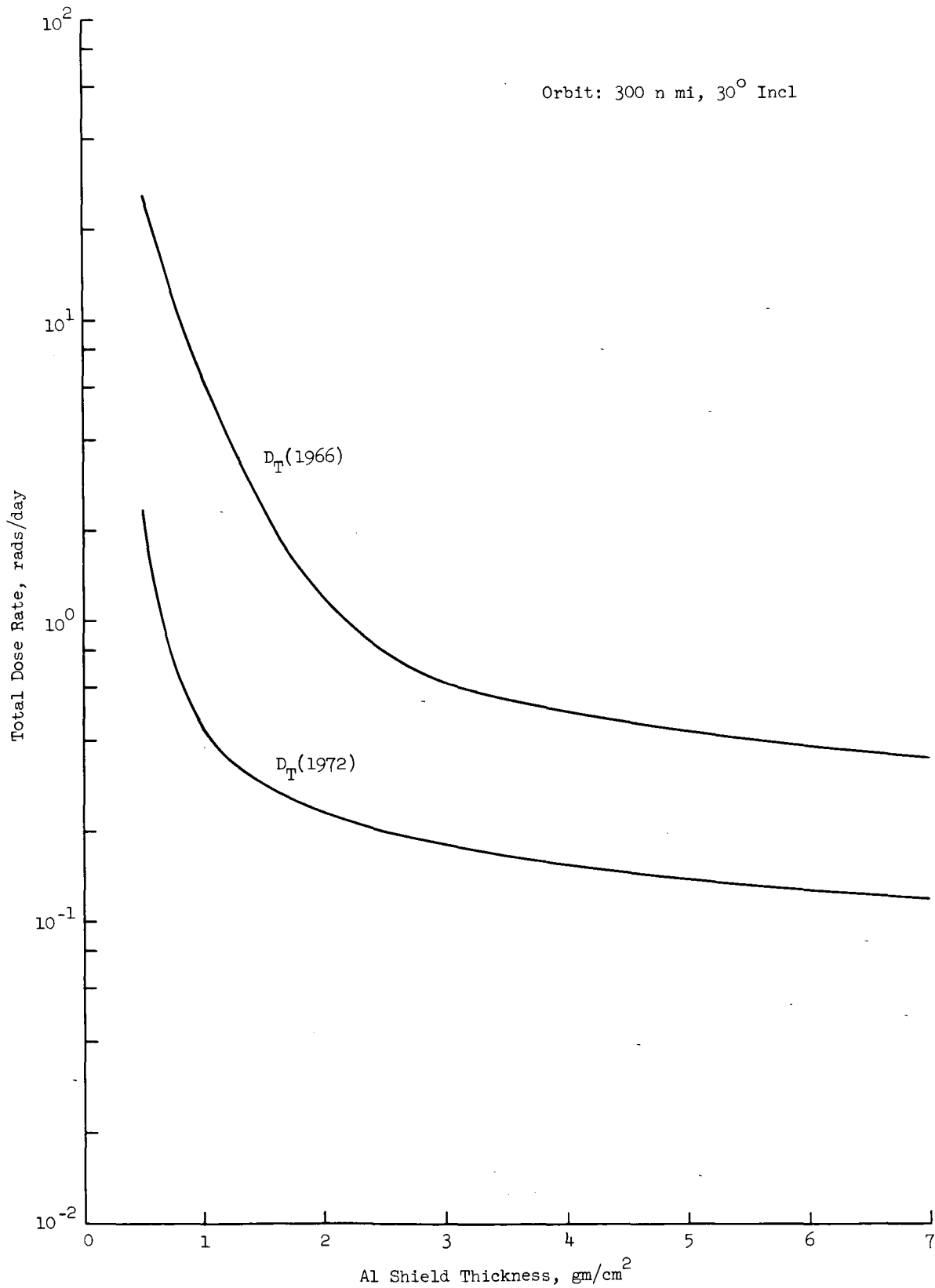


Figure 3.9. Total Dose Rate vs. Aluminum Shield Thickness for the 1966 & 1972 Time Period

TABLE 3-IV

TOTAL ACCUMULATED DOSE (RAD) - 1972

	Skin	BFO	Eyes	Exposure Time (Hrs)
EVA	4.70	0.27	4.70	96
LEM	1.20	0.50	1.20	192
CSM	1.35	0.83	1.35	432
Total	7.25	1.60	7.25	720

3.2.1.3 Launch Vehicle Payload Performance - The object of this portion of the study was to determine if the payload performance of the SIB booster would permit a simple single integral CSM/LEM/OAO/Advanced Princeton Experiment Package launch into a low altitude orbit. Figure 3.10 shows a curve of the payload weight and service module ascent fuel as a function of altitude. The curve assumes a launch into an 80 n. mi. parking orbit where the SIVB structure and adapter are jettisoned. After confirmation and transposition, a Hohmann transfer is made from 80 n. mi. to the desired altitude, using the service module propulsion system. Shown also are the weight estimates for an integral launch as well as a number of launch alternatives. The source of the weight used for the CSM are from the "NASA LEM for AES (AAP) Blue Book" (Reference 9). The weight is for a 45 day mission of 200 n. mi. altitude and 28.5° inclination. Current weight estimates for the 45 day CSM vehicle is approximately 3000 lb greater. Weight estimates for the OAO and LEM are from current Grumman programs. From these estimates, an integral CSM/LEM/OAO launch would not be possible for any altitude. If current weight growth trends continue, an CSM/OAO launch may become marginal for a 30 day mission. Shown in Table 3-V are a number of launch alternatives that were considered. It is recommended that the launch consist of an SIB launch of the CSM and an addition SIB launch of the LEM Lab/OAO.

3.2.1.4 Disturbance Torques - The AAP vehicle nominal altitude of operation is 200 n. mi. whereas the operating altitude of the OAO is 390 n. mi. When operated at the altitude of the space station, the OAO experiences higher external disturbance torques, due mainly, to an increase in air density.

The external disturbance torques on the OAO originate mainly, from the following:

- Solar radiation effects
- Magnetic disturbances
- Gravity gradient effects
- Aerodynamic forces

Hohmann Transfer from 20 Nautical Miles to Higher Altitudes Using Service Module Propulsion 10%  $\Delta$  Contingency -  $I_{SP} = 310$  sec

Curve based on reference S1B Payload Wt = 35,500 lb in 32°, 105 n mi Orbit - SA 206 and Subsequent Vehicles

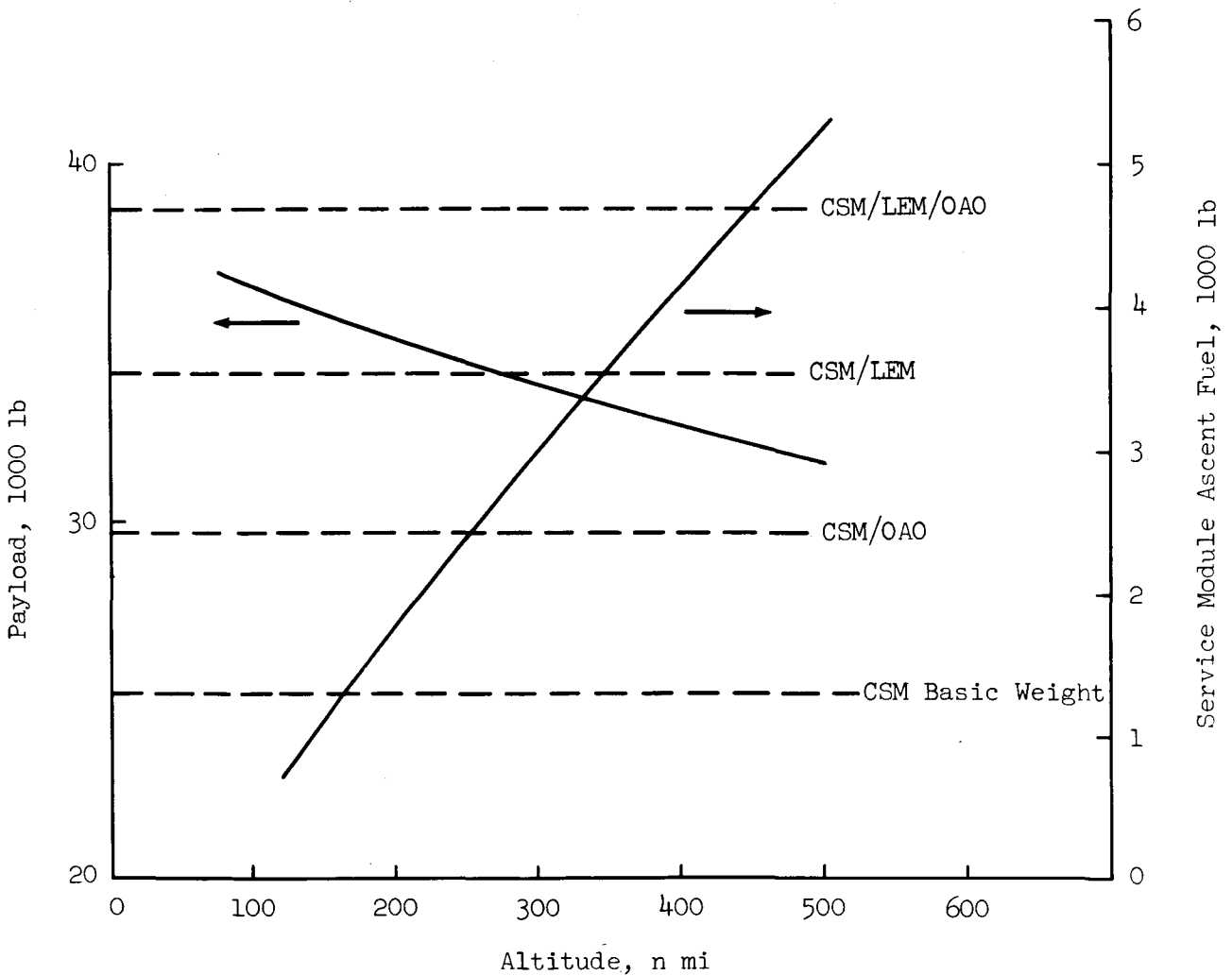


Figure 3-10. S1B-Apollo Service Module Performance

TABLE 3-V

MISSION LAUNCH ALTERNATIVES

Mission Alternatives	Launch Vehicle	Comments
Integral Launch		
- OAO/CSM/LEM Lab	SIB	Cannot achieve 300 n.mi. altitude
	SV	Oversize for payload but could be considered for cynch orbit
- Eliminate LEM Lab	SIB	Volume constraint, 30 day support, no Lab facility
- Eliminate SM	SIB	Used for transposition, docking, Hohman transfer and abort
- Two Man Crew	SIB	Does not result in sufficient weight saving to obtain 300 n. mi. altitude
- 14 day Mission Duration	SIB	
- Gemini/LEM Lab	SIB	Incompatible, major re-design
Dual Launch		
- CSM and OAO/LEM Lab	2 - SIB	Cost of dual launch plus rendezvous and docking
- CSM/LEM Lab and OAO	(2) SIB and Atlas Agena D	Requires rendezvous and docking maneuver

The torque disturbances are summarized in Table 3-VI.

The solar radiation torques are not expected to change significantly with altitude. This torque is caused primarily by an asymmetric sunshade configuration. With improved symmetry it can be minimized. In this study, a value of 250 dyne-cm was used for both peak and average values for all altitudes and configurations.

The magnetic torques estimates are based on present OAO measurements. A peak value of 750 dyne-cm is indicated for the present OAO measurements. An average value of 375 dyne-cm, is estimated for operating at an altitude of between 200-500 statute miles. At synchronous altitude this torque is negligible. The gravity gradient torque, computed on the basis of a 3% unbalance and an inertia of 1450 slug ft<sup>2</sup> is 1150 dyne-cm at 200 nm, and does not change significantly at an altitude of 500 n. mi. A value of one-half the peak, or 575 dyne-cm is again estimated as the most probable average value within the basic 200-500 n. mi. investigated. The effect of altitude manifests itself mainly in the aerodynamic torques experienced by the OAO.

TABLE 3-VI

CONTINUOUS DISTURBANCE TORQUES

Disturbance Torque (Dyne-cm)	Avg.	Peak
Radiation	250	250 RSS
Magnetic	375	750 RSS
Gravity Gradient	575	1150
SUB TOTAL	1200	2150
Aerodynamic		
-200 n. mi.	2,900	14,700
-250 n. mi.	725	3,670
Totals		
-200 n. mi.	4,100	14,750
-250 n. mi.	1,925	3,940
Present OAO (1-1/2 orbits fine wheel saturation pt.)	2100	

- Notes: (1) All torques are continuous and do not include internal transient torques due to man motions, equipment, etc.
- (2) Gravity Gradient torques are for a 3% inertial unbalance.
- (3) Peak torques are Root Sum Squared (RSS) values for one orbit.
- (4) Aerodynamic torques are averaged over 1-1/2 orbits.

For the gimbal-mounted mode of operation, the additional disturbance torques are induced due to internal motions such as that produced by crew movements, RCS firings, and interference effects from the AAP vehicle. The effects of crew movements and limit cycle operation on the control system are discussed in Section 3.2.2.2, Gimbal Mode of Operation.

A detailed torque profile analysis was performed for 200, 250, 300 and 390 n. mi. altitudes. The fine wheel capability is exceeded at 200 n. mi. for the present OAO. Shown in Figures 3.11 and 3.12 is the variation of peak and total average torques, respectively, as a function of altitude (Reference 1).

3.2.1.5 Communication Time - The analysis for this portion of the study, determined the amount of communication time available between the OAO and its three ground station communication stations (Rossman, Quito, and Santiago). Four orbital altitudes and two minimum ground station antenna elevation angles were considered. The orbital inclination of the OAO was fixed at 32 degrees.

If the space vehicle is to communicate with a ground station, it must be within a circular region above the ground station called the "circle of visibility." The radius of the circle of visibility is measured in terms of the angle which it subtends from the center of the Earth. This angle is

$$\theta = \cos^{-1} \left[ \frac{R_E}{R_E + h} \cos \text{RAD} \right] - \text{RAD}$$

where  $R_E$  is the Earth radius,  $h$  is the space vehicle altitude and RAD is the minimum antenna elevation angle of the ground station.

If the ground station is to observe the space vehicle, the latitude of the ground station ( $L$ ) and the inclination of the space vehicle orbit ( $i$ ) must satisfy the relationship.

$$|i| - |L| < \theta$$

This constraint insures that the ground track of the space vehicle orbit will intersect the projection of the circle of visibility on the Earth's surface. This constraint only insures the possibility of visibility, and further restrictions are imposed if visibility is essential frequent intervals. Figure 3.13 shows the radius,  $\theta$ , of the circle of visibility as a function of orbital altitude and antenna elevation angle. This radius increases with increasing orbital altitude and decreases with increasing minimum ground station antenna elevation angle. If more than one ground station is to be available for observation, a decision must be made whether maximum communication time of distribution of communication intervals is the prime consideration. For the OAO, three ground stations are arranged so that the OAO would be visible to at least one of the stations once during each orbit. The visibility analysis for the OAO was made for orbital altitudes of 300, 400, 500, and 600 SM and minimum antenna elevation angles of 0 and 10 degrees.

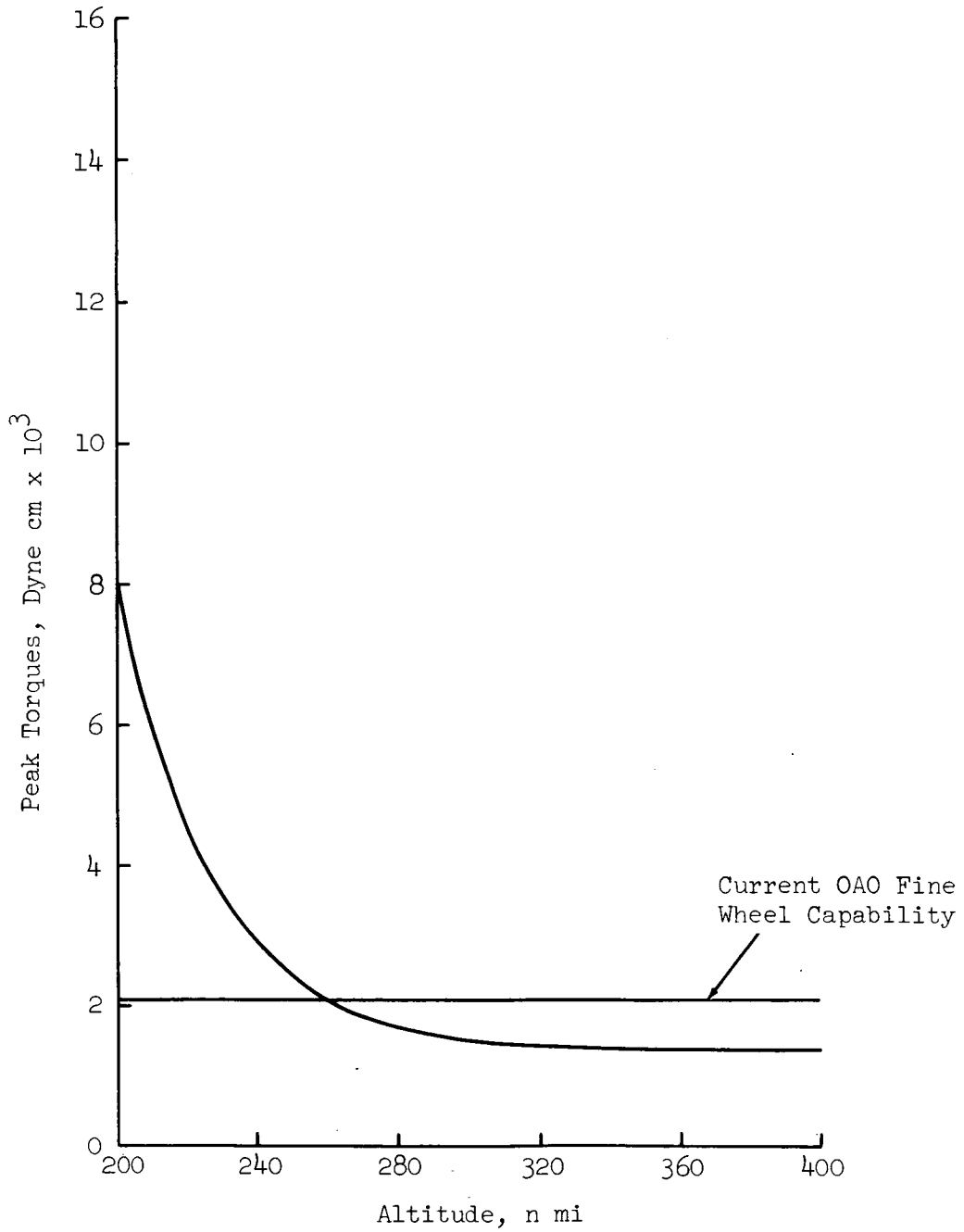


Figure 3.11. Peak Torques (RSS) vs. Altitude for Various OAO Configurations

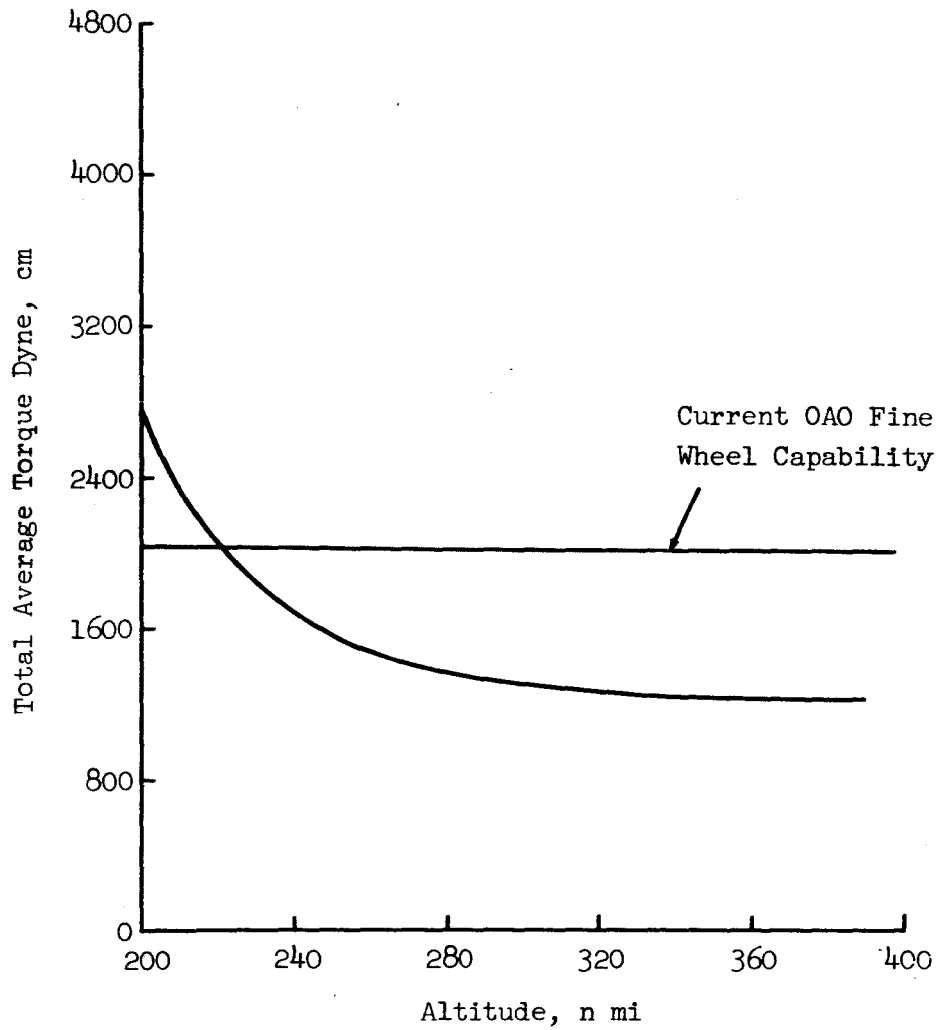


Figure 3.12. Total Average Torques vs. Altitude for Various Configurations



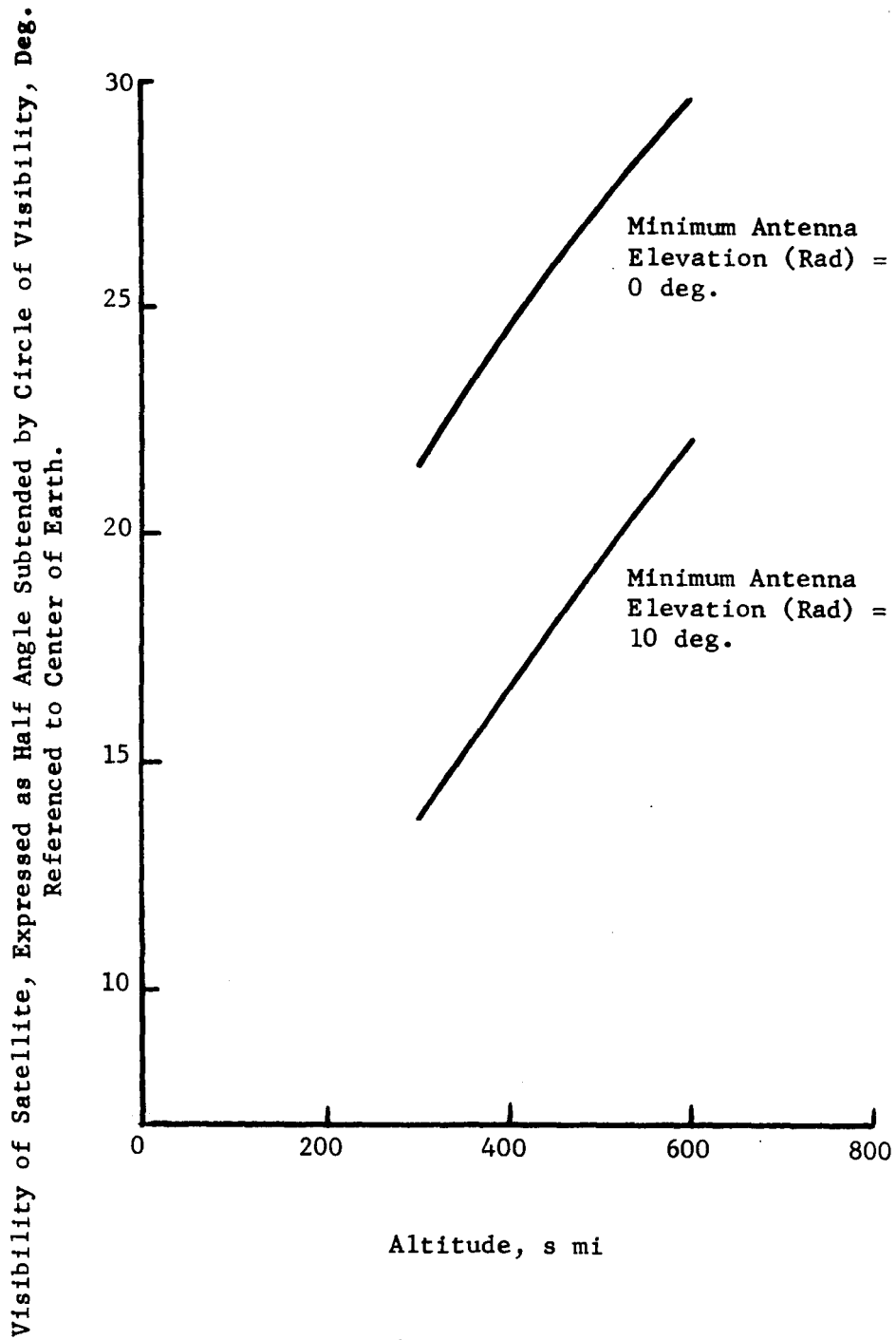


Figure 3.13, Satellite Visibility From Ground Communication Station vs. Orbital Altitude and Minimum Antenna Elevation Angle

Time history trajectories were run to compute the actual communication time for the cases. The initial condition for these trajectories were taken at 32 degrees N. latitude, 76 degrees W. longitude, and heading due East. All of the time histories were run for 2 day intervals. The amount of communication time increases with OAO orbital altitude and decreases with increasing minimum ground station antenna elevation angle, as shown in Figure 3.14. The ground station latitude also affects the communication time, but the above stations are chosen to insure a communication interval once during each orbit.

### 3.2.2 Mode of Operation

The two modes of operation studied were:

- Floating free of the AAP spacecraft
- Gimbal-mounted to the AAP spacecraft.

3.2.2.1 Free Mode - In the free mode of operation the OAO is floating free of the LEM Lab, except for maintenance and experiment modification during the 30 days of manned participation. After the astronaut's return to Earth, the OAO would be operated in the free mode for its remaining life.

During the 30 days of manned participation, rendezvous and docking maneuvers would be required for maintenance and experiment modification (film cassette replacement). The retrieval and docking of the OAO could be accomplished with virtually no change to the present OAO by using a tripod method of docking. The tripod method of docking is described in Section 7.11.1 of Reference 1. The main docking problem is that associated with a major control system malfunction (failed open gas jet and power or command failure) resulting in high random tumbling rates of the OAO. The solution to this malfunction is to wait until low tumbling rates have been achieved. In addition, to protect the critical optical components, docking accelerations of less than 0.25 g are required. Final automatic docking may impart high accelerations. It is, therefore, recommended that the final docking maneuver be accomplished with an EVA.

For communication between the LEM Lab and the OAO, a separation of 20 n. mi., or less, permits the use of the OAO communication system unmodified, with a nominal modification to the LEM Lab (addition of a cavity-backed spiral antenna) and nominal required power. To maintain a maximum separation distance of 20 n. mi., a catch-up maneuver is required, once every 2 days at 250 n. mi. altitude, or approximately once every 6 days at 300 n. mi. This catch-up maneuver results in a fuel expenditure of less than one lb. per maneuver, perhaps less than the fuel necessary to maintain CSM orientation for pointing.

The free mode of operation represents a concept requiring the least modification to the OAO and to the AAP (particularly if separate launches are considered, i.e., OAO by an Atlas-Agena D and CSM/LEM by a Saturn IB). In addition, there are minimum demands on the LEM Lab in terms of attitude maintenance and induced torque disturbances.

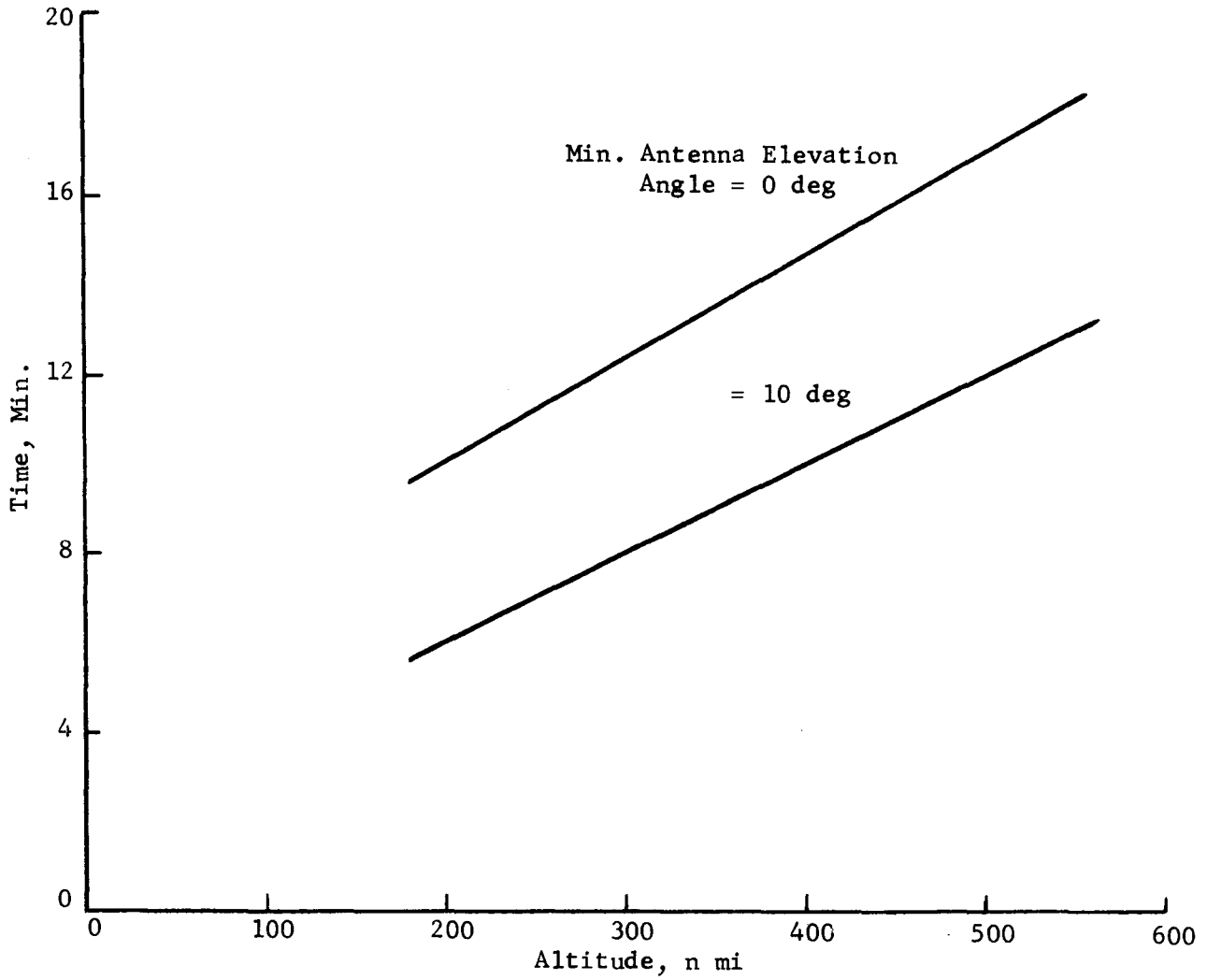


Figure 3.14. Communication Time vs. Altitude (Based on Ground Track Through Ground Station)

3.2.2.2 Gimbal-Mounted Mode of Operation - For the gimbal-mounted mode of operation, the OAO is mounted in a set of gimbals attached to the space station (AAP vehicle) by a suspension system that is either hard (high spring constant) or soft (low spring constant). Gimbaling the OAO to the AAP vehicle restrains the translational motion of the OAO. The prime advantage of this mode is the resulting accessibility to the OAO, and the fact that no rendezvous and docking is required once initial operation is begun. Gimbaling, however, does not eliminate the translational motions that the station imposes on the OAO, nor does it completely eliminate the disturbance torque that results on the OAO, due to these translational accelerations. The induced torque disturbances due to center of mass offset and the translational motion are direct functions of the distances between the center of mass of the CSM/LEM Lab and OAO and the stiffness of this structure. Mounting the gimballed OAO on a soft suspension system, rather than a hard one, reduces the disturbances of the space station transmitted to the OAO.

For hard mounting, a sufficient amount of previous analysis has been performed (References 1 and 10) to conclude that 0.10 arc-seconds pointing accuracy can be achieved, if values in excess of 0.10 arc-seconds can be tolerated for periods of time less than 1.5 seconds. This assumes that the Princeton OAO fine error sensor is used with the existing OAO inertia wheel control, and that the gimbal offset (distance between gimbal mount and OAO center of mass) does not exceed 0.10 inches. These excesses will occur whenever significant man motions take place within the LEM/CSM vehicle, as for example, a man walking in the LEM/CSM vehicle at a moderate to fast pace. In any case, errors greater than one arc-second should rarely be experienced with a hard mounted, gimballed, OAO. It was further concluded from these studies that the above-stated pointing errors could be improved by an order of magnitude, if the sampling rates for the fine error sensor are increased by a factor of five, from the present value, and a decrease in noise levels of approximately 1/100 is realized.

Hard mounting the gimbal will not, however, eliminate the translational motions of the OAO. Figure 3.15a. shows the amount of translational motions that can be expected on the OAO, depending on its mounting location relative to the LEM/CSM center of mass and the limit cycle amplitude of the LEM/CSM. It is seen that a  $\pm 0.20$  degree limit cycle amplitude and a 12.5 foot location from the center of mass will easily exceed the allowable 0.50 inch translational motion. A number of different suspension systems and modifications to the LEM/CSM reaction jet control system were, therefore, investigated which could limit the translational motions of the OAO. The following suspension systems for the gimballed OAO and modifications to the LEM/CSM reaction jet control system were investigated:

- Stiff pipe rack suspension } (Figure 3.16a)
- Soft pipe rack suspension } (Figure 3.16b)
- Coil spring suspension (Figure 3.16b)
- Modified pipe rack suspension (Figure 3.16c)

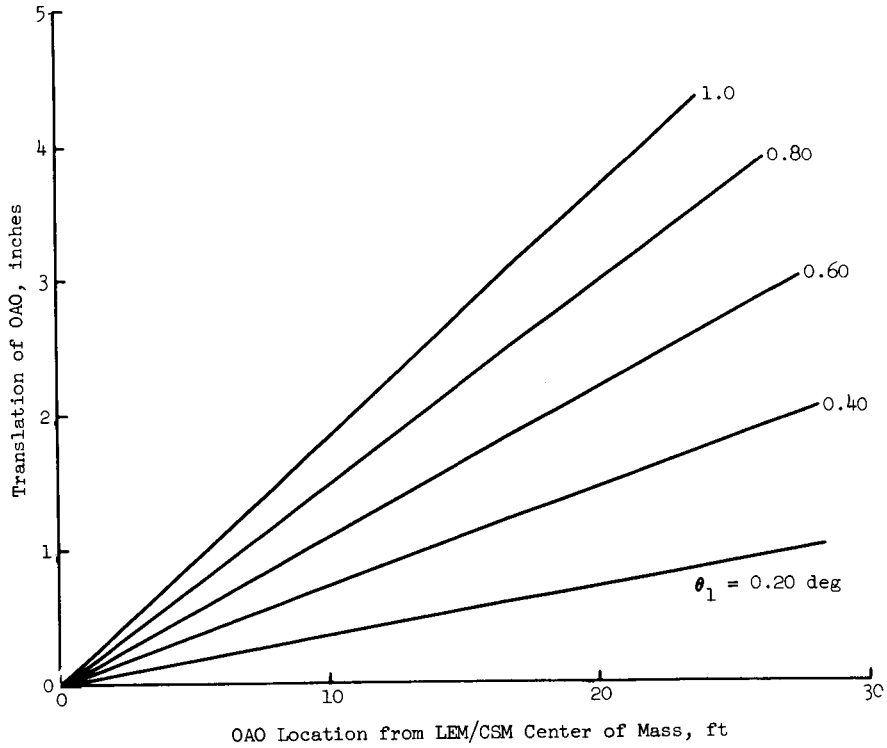


Figure 3.15a. Normal LEM/CSM Reaction Jet Logic

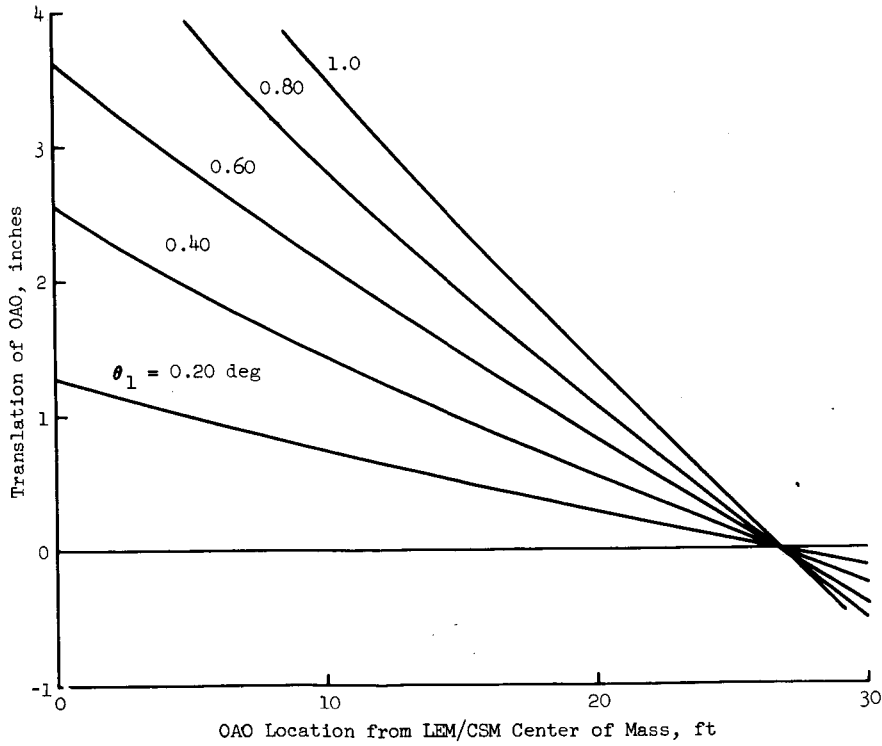


Figure 3.15b. Modified LEM/CSM Reaction Jet Logic

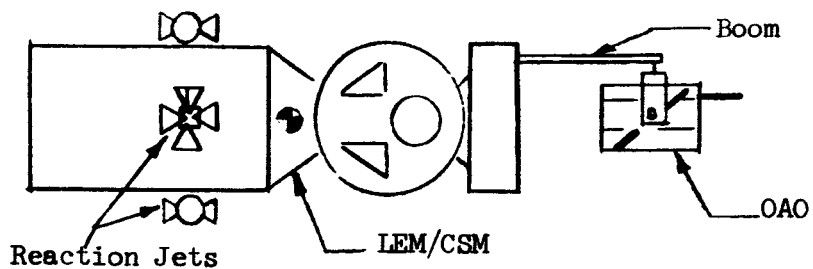


Figure 3.16a. Stiff and Soft Pipe Rack Suspension

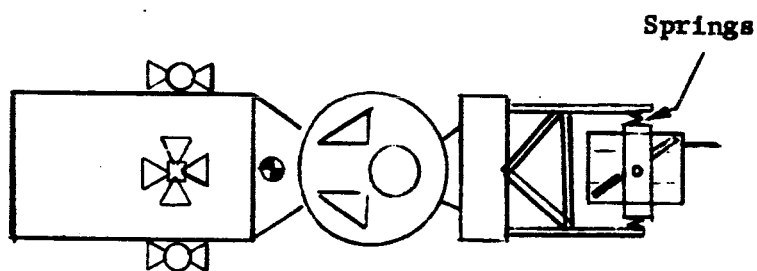


Figure 3.16b. Coil Spring Suspension

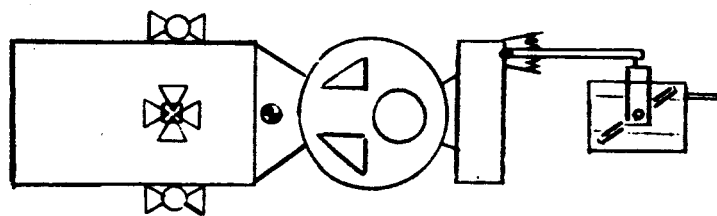


Figure 3.16c. Modified Pipe Suspension

Modify reaction jet firing logic on CSM vehicle

Use proportional thrusters in place of reaction jet pulsing

In addition to the above, two different mounting locations for the gimbaled OAO were considered. (Figures 3.17a and 3.17b).

Before proceeding into a discussion of the performance of the various suspension systems, there are general considerations which influence the desirability of a particular system. These are the torque disturbance on the LEM/CSM vehicle, the differential forces on the telescope, and the inertial unbalance between the OAO and the experiment.

General: Figure 3.18 shows the increase in peak gravity torque and aerodynamic torque disturbances experienced by the LEM/CSM vehicle as a function of the distance the OAO is mounted from the LEM/CSM center of mass. These results are based on equations 7, 9, and 11 developed in Appendix A. It is noted that a 20-foot location of the OAO from the center of mass (nominal expected distance) results in an increase of 20% on the gravity gradient torque and a 420% increase in the aerodynamic torque disturbance. However, the combined peak torque increase would not be more than 23% over a clean configuration at 250 n. mi. orbital altitude (NOTE: from Appendix A the aerodynamic torque level at this altitude is much lower than the gravity gradient disturbance). It is estimated, however, that this increase in peak torque disturbance should have little or no effect on the controllability of the LEM/CSM vehicle.

Since the telescope experiment is floating free, with respect to the OAO, there will be differential forces acting on the telescope and the combined OAO/LEM/CSM vehicle. These forces arise from two factors. First, the two vehicles are in different orbits and, therefore, experience a different gravitational attraction, referred to as "differential gravity". Secondly, the combined OAO/LEM/CSM vehicle is exposed to aerodynamic drag while the telescope is shielded completely from the atmosphere. This creates an additional differential force referred to as "differential drag." Both differential drag and gravity tend to separate the two vehicles during the experimentation period. Figure 3.19, developed to show the combined effects of the two disturbances, shows the maximum estimated distance between the two vehicles after 30 minutes of operation in a 250 n. mi. circular orbit, and the maximum relative acceleration of the two vehicles during this same period. These results are based on a digital computer program developed at Grumman specifically for this purpose.

If the telescope has an inertia unbalance, then the gravity gradient disturbance (in addition to aerodynamic and magnetic disturbances) on the telescope must be opposed by the telescope magnetic control torquers. The magnetic torquers then transmit these disturbance forces to the OAO which must be counteracted with the OAO inertia wheel control system. If, however, the inertia unbalance of the OAO and the telescope are correctly designed, the gravity gradient torque on the two vehicles can be designed to essentially balance out and, therefore, minimize the need for OAO inertia wheel dumping during the experiment period. Figure 3.20a shows estimated elapsed time between inertia wheel

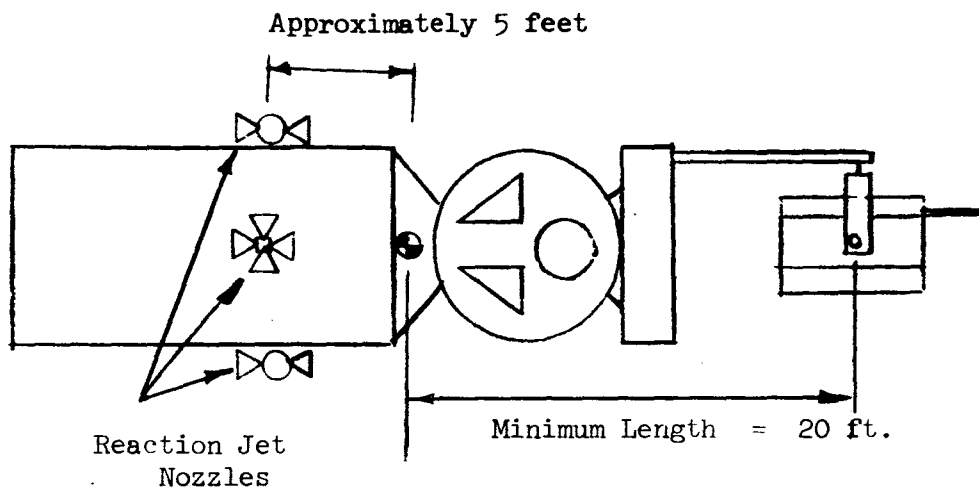


Figure 3.17a. End Mount Configuration

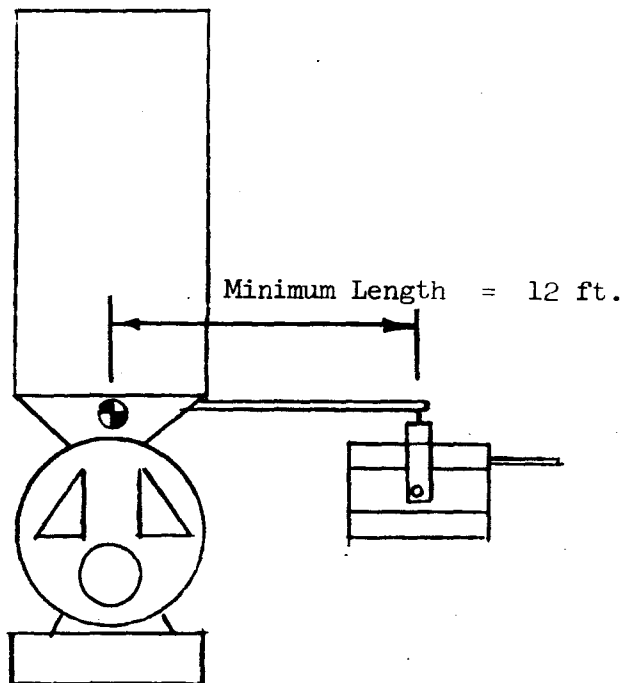


Figure 3.17b. Side Mount Configuration



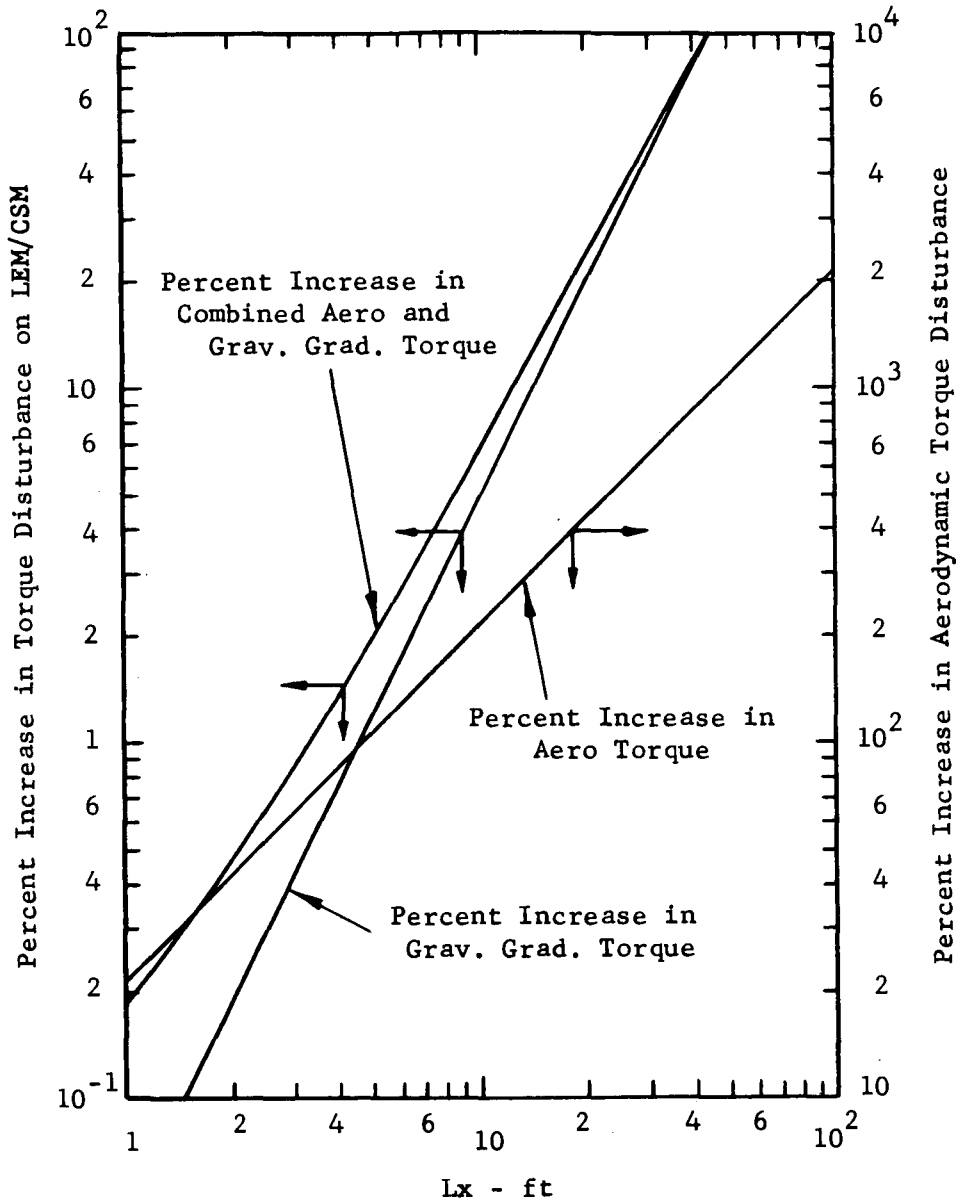


Figure 3.18. Percent Increase in Maximum Torque Disturbances on LEM/CSM Due to Grav. Grad. and Aerodynamic

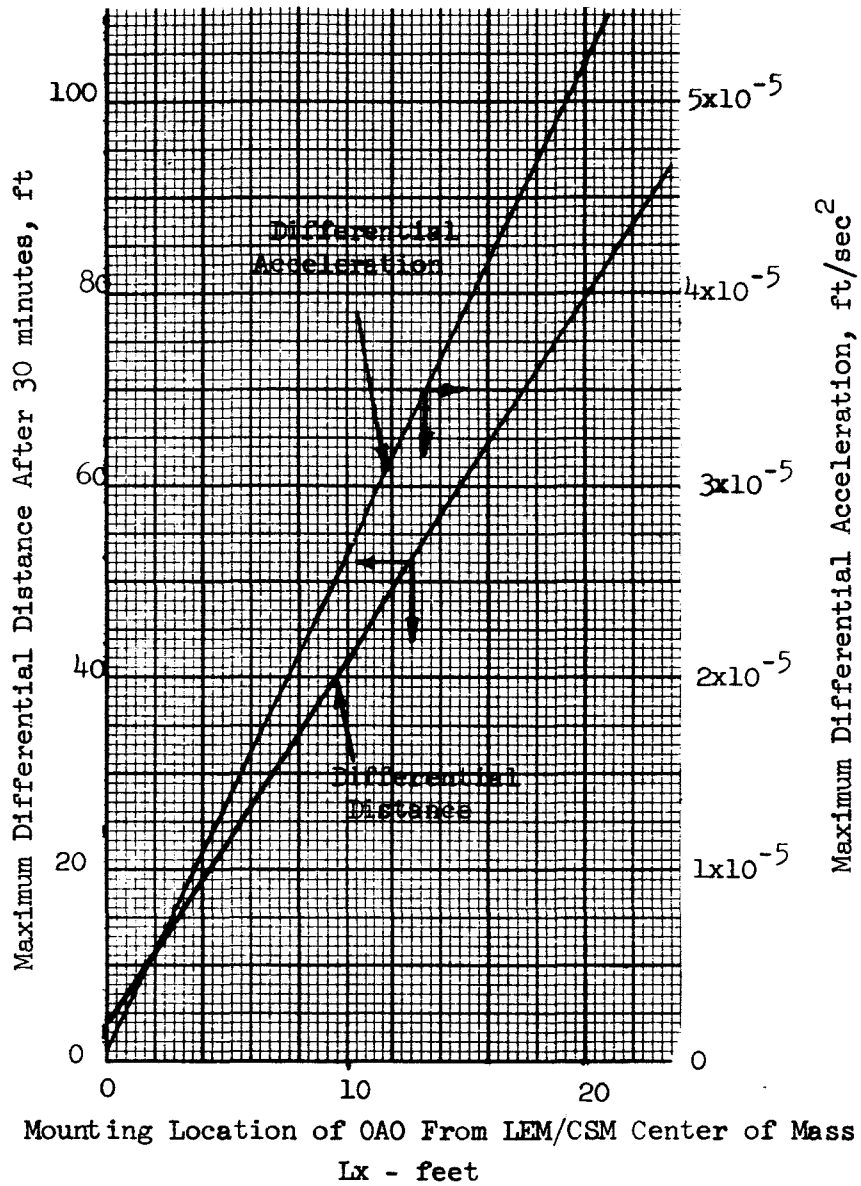


Figure 3.19. Relative Distance and Acceleration Between OAO and Telescope Due to Differential Gravity and Aero Drag

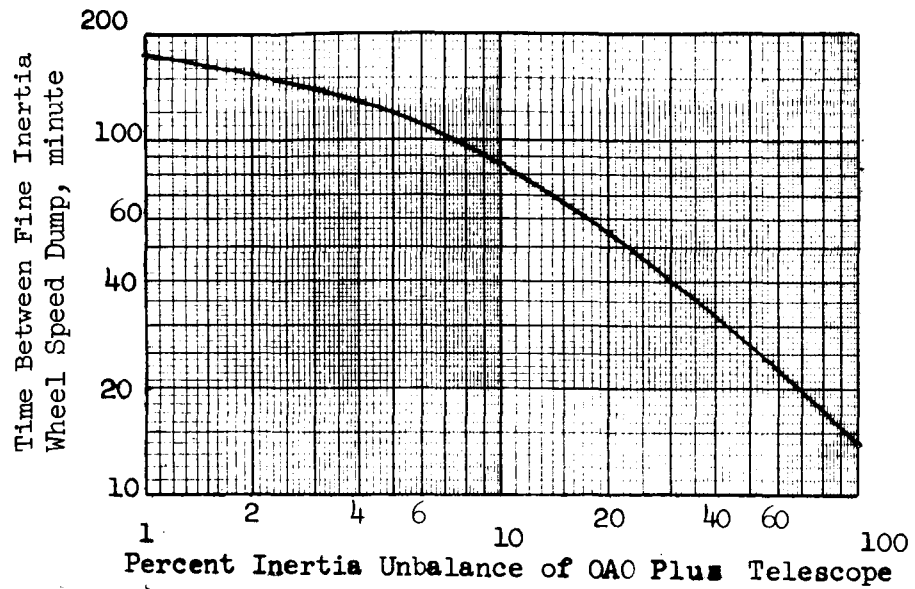


Figure 3.20a. Time Between OAO Fine Inertia Wheel Momentum Dump

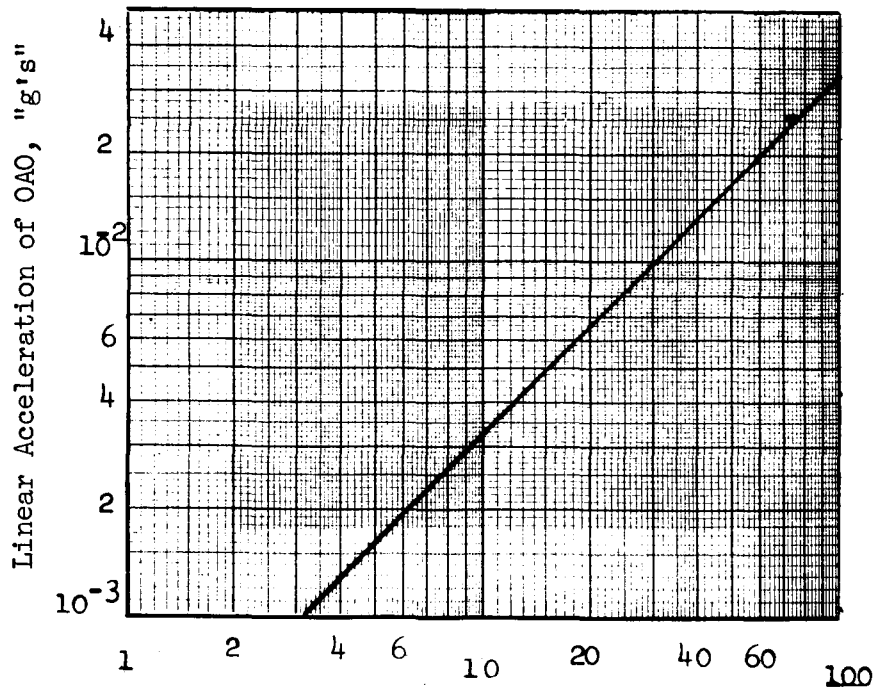


Figure 3.20b. Linear Acceleration of Rigid Mounted OAO Due to Man Motion and Jet Impulses

dump required as a function of combined OAO and telescope inertia unbalance. These results are based on Equation 14, developed in Appendix A. It is noted that an inertia unbalance of as much as 40% could be tolerated before a wheel speed dump would be required within 30 minutes of operation. It should be stated, however, that even if dumping of the OAO inertia wheel control is initiated during the experiment period it would not result in OAO attitude errors in excess of the one minute of arc specified by the experimenter. It is, therefore, concluded, that inertia unbalance of the combined OAO and telescope system should present no significant problem area.

3.2.2.3 Suspension Configurations - Stiff Pipe Rack Configuration: A schematic of the stiff pipe rack configuration is shown in Figure 3.16a. The extended boom which is attached to the LEM/CSM and the OAO gimbal is assumed to be constructed of perfectly rigid material. All rotations of the LEM/CSM vehicle about its own center of mass, must therefore result in translational motions of the OAO. The magnitude of these motions is dependent on the amount the LEM/CSM vehicle rotates and the distance the OAO is mounted from the LEM/CSM center of mass. Figure 3.15a shows the magnitude of these translations. The results of Figure 3.15a are based on Equation 11 of Appendix A. It is noted that for a  $\pm 0.20$  degree limit cycle amplitude (minimum design value for the LEM/CSM, reaction jet control system) and a location of the OAO greater than 12.5 feet from the LEM/CSM center of mass will result in translational motions in excess of the allowable  $\pm 0.50$  inches. Since 12 feet is the closest practical mounting location for the OAO, it is apparent that the stiff pipe rack configuration is marginal from the standpoint of meeting the translational requirements. As far as the OAO pointing accuracy is concerned, however, a sufficient amount of analysis has been performed (see Reference 1 and 10) to show that control errors in excess of 1 arc-second should rarely be experienced.\* A large percentage of this pointing error however, is developed because of rapid man motions in the LEM/CSM vehicle. These rapid man motions develop large rotational accelerations on the LEM/CSM vehicle which are converted into translational accelerations of the OAO and in turn, are transmitted as large disturbance torques on the OAO. Figure 3.20b shows the maximum translational acceleration that the OAO will experience when a man walks 3 feet in the LEM/CSM within 1 second time period. Figure 3.20b is based on Equation 20 developed in Appendix A. A 12.5 ft. location of the OAO from the LEM/CSM center of mass for example, yields a  $4 \times 10^{-3}$  "g" acceleration. It will be shown later that all of the other suspensions systems considered for this application significantly reduce this value and should, therefore, yield even better pointing accuracies than is predicted for the rigid pipe rack configuration.

\* This is based on the assumption that gimbal offset with respect to OAO center of mass is less than 0.10 inches.

Soft Pipe Rack Configuration: The soft pipe rack configuration is illustrated in Figure 3.16a. The extended boom attached to the LEM/CSM and the OAO gimbal is assumed to be steel tubing. The flexibility of the tube is utilized as a spring to isolate the LEM/CSM motions from being transmitted to the OAO. Figure 3.21 shows the system natural frequency as a function of the tube length and various tube diameters. Figure 3.21 is based on Equation 11, developed in Appendix B. The assumption here is that the tube thickness is one tenth of the diameter. Figure 3.22 presents the associated stress limit on the tubing\* due to man motion slewing. Figure 3.22 is based on Equation 24, developed in Appendix B. Figure 3.23 shows the maximum translational acceleration that will develop on the OAO due to a combined man motion and a jet impulse and is based on Equation 25 of Appendix B.

If the LEM/CSM vehicle is assumed to be limit cycling with a maximum amplitude ( $\theta_{lmax}$ ) of 0.20 degrees and a maximum rate of 0.02 deg/sec., the limit cycle frequency is:

$$\omega_{LC} = \frac{\pi \dot{\theta}_{lmax}}{2 \theta_{lmax}} = 0.15 \text{ rad/sec}$$

To isolate the LEM/CSM limit cycle from the OAO, the natural frequency of the system should be at least a factor of 2 below the 0.15 rad/sec value (see Figure 3.21). Cross plotting this 0.075 rad/sec frequency limit on to Figure 3.22, it can be seen that the minimum allowable stress limit on the steel boom will have to be well above the 400,000 psi level. Since steel tubing has an elastic stress limit of around 70,000 psi, it is not considered practical to use a soft pipe rack configuration to isolate LEM/CSM limit cycle motion from the OAO. It should be noted, however, from Figure 3.23 that the soft pipe rack can serve to significantly minimize the translational acceleration and velocities of the OAO. As an example, it was assumed that the maximum allowable translational acceleration is  $2 \times 10^{-4}$  g, and the tubing elastic stress limit is 70,000 psi. These two limits are cross-plotted in Figure 3.24. The intersection point of the two limits is then chosen as the design condition (tube diameter 1" and boom length 8 feet) since it results in a minimum translational rate of 0.20 in/sec. as seen from Figure 3.25. (Figure 3.25 is based on Equation 28 of Appendix B). It is concluded, therefore, that although the soft pipe rack configuration cannot be designed to minimize the translational motions of the OAO, it certainly will be able to significantly reduce the torque disturbance on the OAO to a value which is below the fine inertia wheel stall torque (see Figure 3.26).

Coil Spring Suspension: A schematic of the coil spring suspension is illustrated in Figure 3.16b. Here, the gimballed OAO is suspended within a group of coil springs designed for a low system natural frequency which cannot respond to the limit cycle motions of the LEM/CSM. The frequency, however,

\* Includes an assumed safety factor of 2.

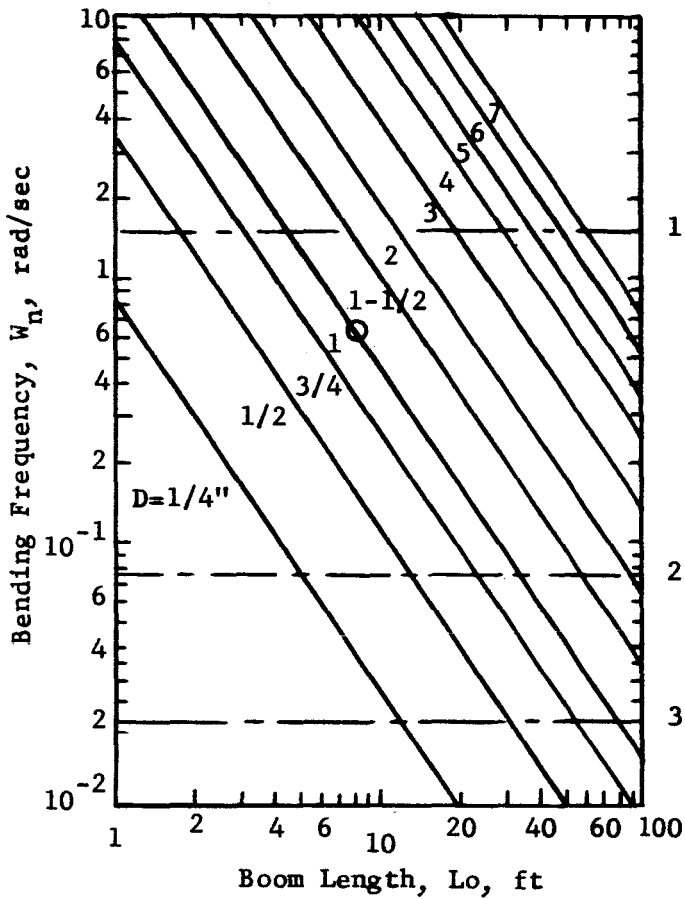


Figure 3.21. Boom Bending Frequency Assuming Steel Tubing

- 1 Max. recommended if system is not to respond to man motions in LEM/CSM.
- 2 Max. recommended if system is not to respond to LEM/CSM limit cycling.
- 3 Min. recommended to avoid interference with gravity gradient and aerodynamic disturbances.
- 4 Max. allowable for steel tubing.

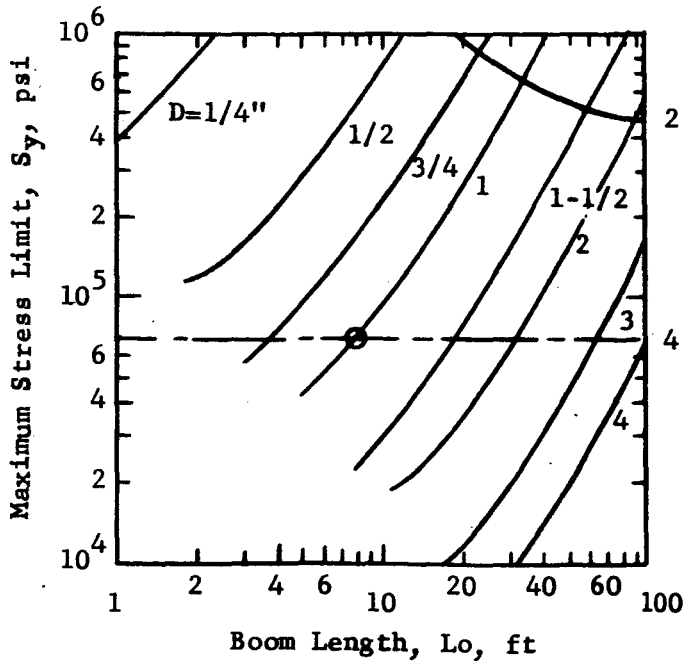


Figure 3.22. Maximum Elastic Stress Limit on Boom Resulting From Man Motion Plus Slewing Maneuver

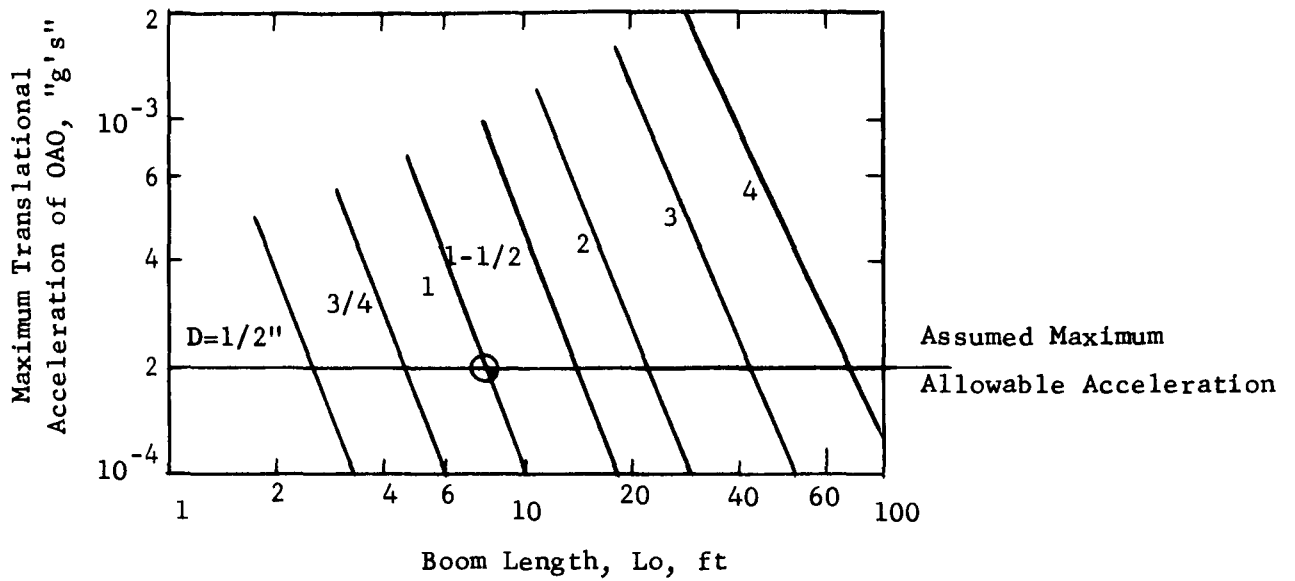


Figure 3.23. Maximum Translational Acceleration of OAO Due to Man Motion Plus Jet Impulses

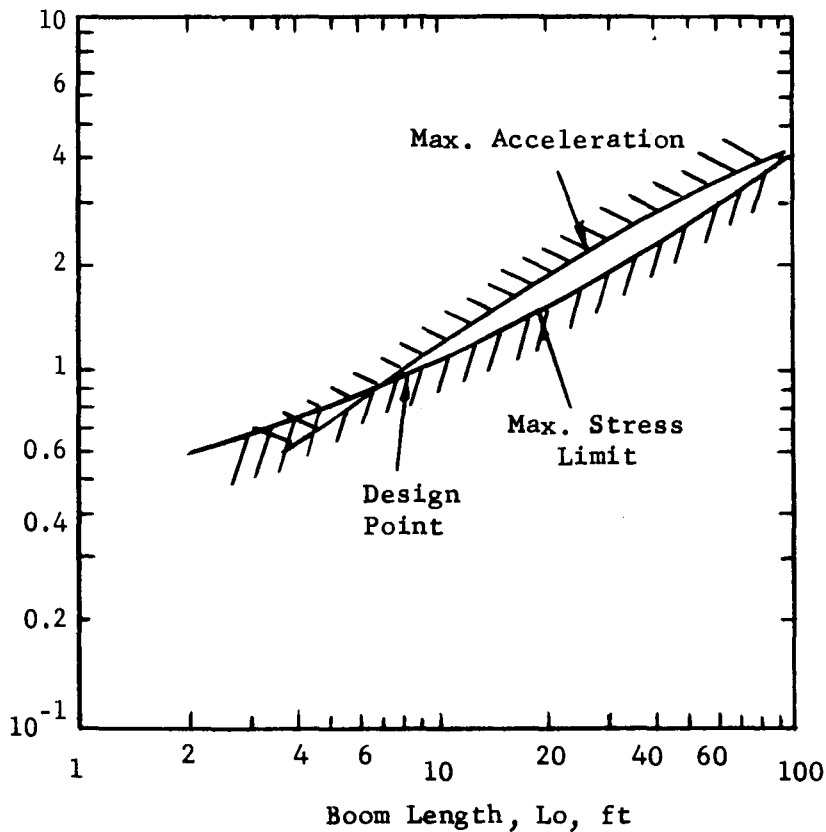


Figure 3.24. Trade-off on Maximum Allowable OAO Acceleration ( $2 \times 10^{-4}$  "g") and Boom Stress Limit (70,000 psi)

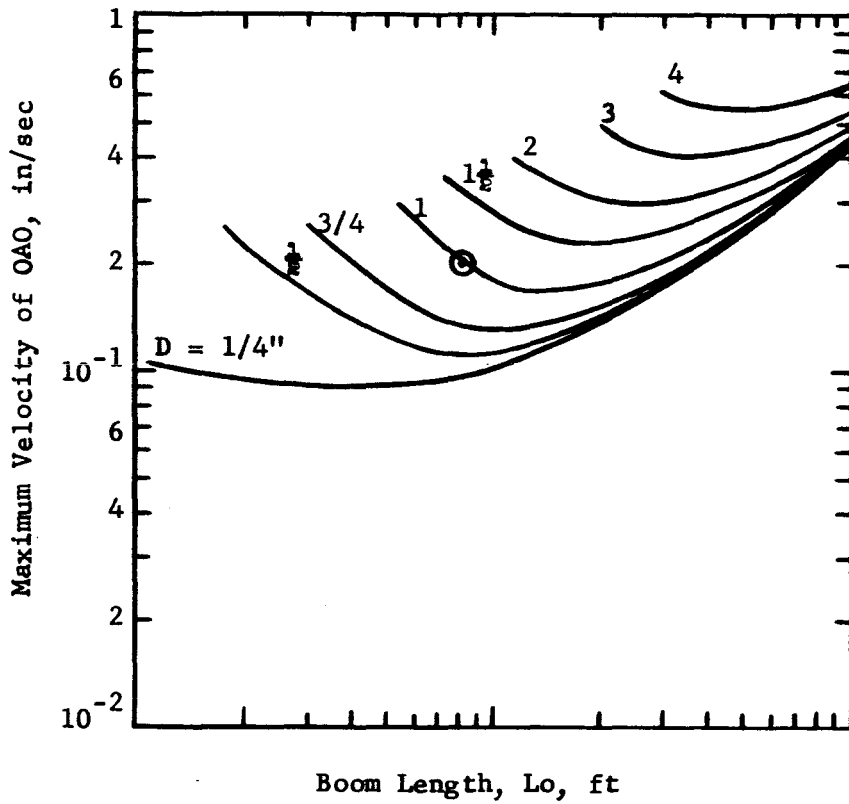


Figure 3.25. Maximum Translational Velocity of OAO Resulting From Man Motions Plus Limit Cycle in LEM/CSM



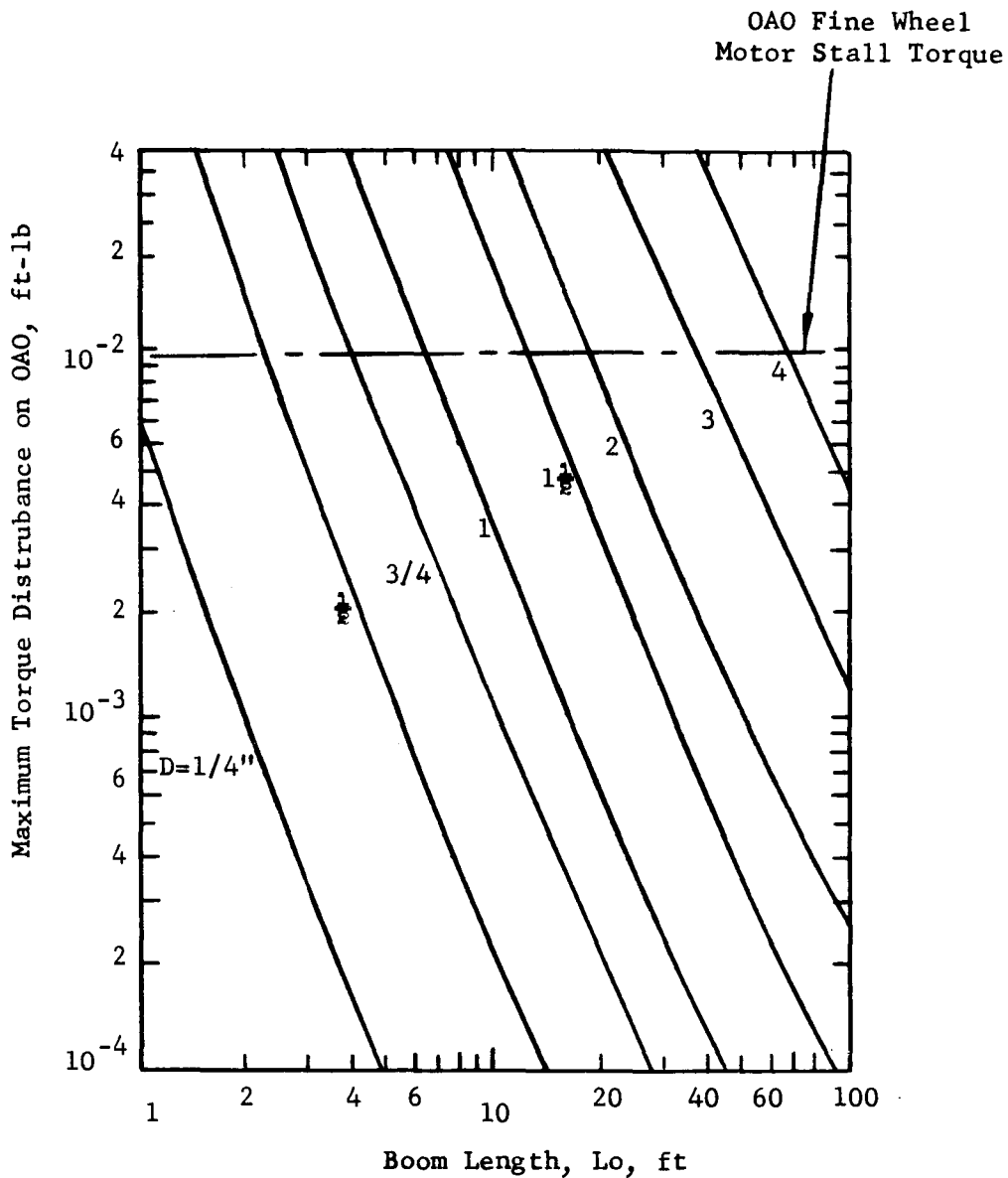


Figure 3.26. Maximum Torque Disturbance on OAO Due to Man Motion Plus Reaction Jet Impulses (Offset = 0.10 Inch)

should be high enough not to coincide with the long term disturbance torques such as gravity gradient and aerodynamic. A range of frequencies which can satisfy these conditions would be greater than 0.020 rad/sec. but less than 0.075 rad/sec. Since the upper frequency limit of 0.075 rad/sec. was based on an assumed limit cycle amplitude of 0.20 degree, developed in the previous section, it is apparent that a larger limit cycle amplitude can be tolerated without going below the minimum frequency of 0.02 rad/sec. This decrease in limit cycle frequency would result in a limit cycle amplitude of  $\pm 0.80$  degrees and a corresponding savings in fuel consumption. It should be stated, however, that the savings in fuel consumption will not be as great as might be anticipated since the limit cycle condition assumes a disturbance free vehicle. The LEM/CSM vehicle is actually under continuous loading from gravity gradient, aerodynamic and other disturbance torquers. The total fuel consumption, therefore, will approach the integrated value of the torque profile which is greater than the limit cycle fuel consumption and becomes independent of the allowable attitude error on the LEM/CSM.

A summary of the Coil Spring Suspension System performance and spring design data is presented in Table 3-VII for the two extreme frequency conditions, and locations of the OAO relative to the LEM/CSM center of mass illustrated in Figure 3.17a and 3.17b. The results shown in Table 3-VII are based on Equations 1, 4, 6, 8, 9, and 10, developed in Appendix C.

Modified Pipe Rack Configuration: The modified pipe rack configuration is illustrated in Figure 3.16c. It differs from the rigid pipe rack configuration only in that the boom is attached to the LEM/CSM with a universal joint allowing the boom to pivot in all directions. The pivoted boom is then suspended in coil springs and designed for natural frequencies very similar to the coil spring suspension system. The advantage here is that the construction of this configuration is not much more complex than the pipe rack configuration, but offers the same isolation characteristics of the coil spring configuration. The analysis for this configuration is quite similar to the coil spring configuration.

Relative Advantages and Disadvantages: Having discussed the performance of the various suspension systems, the advantages and disadvantages of each can now be summarized as follows:

The stiff pipe rack configuration has the simplest construction of all the configurations investigated but it cannot meet the maximum allowable translational limitations during limit cycling.

The soft pipe rack configuration can be designed to reduce the translational acceleration of the OAO but structural limitations prevent a design of the natural frequency low enough to minimize the translational motions of the OAO during limit cycle operation.

TABLE 3-VII  
 PERFORMANCE OF COIL SPRING SUSPENSION SYSTEM  
 AND COIL SPRING CHARACTERISTICS

L <sub>x</sub> , ft.	12	Natural Frequency - rad/sec	
	20	0.020	0.075
Maximum Trans- lation of OAO due to LEM/CSM	0.0083		0.154
Limit cycle - inches	0.0137		0.25
Maximum Trans- lation Accel- eration of OAO due to LEM/CSM	$4.5 \times 10^{-7}$		$2.7 \times 10^{-6}$
Limit cycle - "G's"	$7.5 \times 10^{-7}$		$4.5 \times 10^{-6}$
Maximum Spring Deflection - inches	1.08		0.965
	1.82		1.61
Maximum Torque Disturbance on OAO - ft. lbs.	$1.7 \times 10^{-7}$		$1.02 \times 10^{-6}$
	$2.84 \times 10^{-7}$		$1.7 \times 10^{-6}$
Spring Wire Diameter d - inches	0.065		0.127
	0.065		0.127
Solid Height of spring - inches	13		25.4
	13		25.4

Assumptions:

- Spring Diameter = 4 inches
- Number of coils = 200
- Number of spring = 6

NOTE:

L<sub>x</sub> = Distance OAO is mounted from LEM/CSM center of mass.

The coil spring configuration can be designed to minimize the translational motions (including accelerations) of the OAO, as well as the roll rotation, but is somewhat more complex in its construction since it is designed to support around the OAO. As a result the allowable gimbal rotations are limited compared to the pipe rack configuration.

The modified pipe rack configuration seems to offer the best compromise since it minimizes the translational motions of the OAO and at the same time, is not as complex in construction as the coil spring configuration, nor does it minimize the rotational travel of the gimballed OAO.

Two additional techniques were investigated for minimizing the translational motion of the OAO, that are not dependent on the suspension system design. These are discussed below:

Modified Reaction Jet Logic: The present reaction jet control system develops pure couple on the vehicle when the jets are fired. This results in a pure rotational motion of the LEM/CSM vehicle. The jets, however, can be designed to fire in pairs such that translations as well as rotation motion of the vehicle will result. If then, a point or points on the vehicle can be found whose motion due to vehicle translation is in the opposite direction of those due to vehicle rotation, the inertial translations of these points will be minimized. This effect can be achieved if the jets are offset with respect to the vehicle center of mass. Such is the case with the CSM Reaction Jets as shown in Figure 3.17a. This offset distance is approximately 5 feet depending on the distance the OAO is mounted away from the LEM/CSM. Figure 3.15b shows the translational motion of the OAO as a function of the distance the OAO is located from the combined vehicle center of mass. It is noted that a mounting distance of approximately 27 feet from the center of mass will result in no translational motion of the OAO due to jet firing. This technique is, therefore, recommended for use with the stiff pipe rack or soft pipe rack configuration and is optional with the coil spring or modified pipe rack configuration. The modified jet logic should be used only with an end mounted (Figure 3.17a) not a side mounted configuration (Figure 3.17b).

Linear Thrusters: The development of linear thrusters to minimize the motion of the LEM/CSM is not practical for this type of application since the metering of small quantities of fuel into a thrust chamber for continuous burning is not considered feasible.

### 3.2.3 Launch Environment

The purpose of phase of the study was to define the launch environment for an integrated OAO/AAP/SIB launch. The launch design conditions for the OAO are based on the environment induced by the Atlas Agena D boost vehicle. Our studies indicate that an OAO is capable of sustaining loads resulting from

an SIB launch. However, as shown in the Spacecraft Definition Studies, Section 3.3, structural modification will be required for coupling the two vehicles.

Summarized below are the accelerations used in design of the OAO, as launched by the Atlas-Agena B, and the accelerations used for design of the LEM, as launched by the SIB.

**OAO Limit Design Accelerations for Atlas-Agena D Booster Launch**

- $N_x$  9.4g forward combined with 1.9g lateral
- $N_x$  2.5g aft combined with 1.9g lateral
- shock; 6.9g longitudinal or 2.39g lateral input applied at sta 160 for 6 millisecc.
- transportation; 3.0g longitudinal with 2.0g lateral applied simultaneous at spacecraft c.g.

**LEM Limit Design Accelerations SIB Booster**

End boost cond.	$N_x$ 4.9g	$N_y$ or $N_z$ $\pm 0.1g$
Lift-off cond.	$N_x$ 1.6g	$N_y$ or $N_z$ $\pm 0.65g$
max. $q_a$	$N_x$ 2.07g	$N_y$ or $N_z$ $\pm 0.30g$
1st stage cut-off	$N_x$ 1.7g	$N_y$ or $N_z$ $\pm 0.1g$

The mission vibration environment is tabulated below:

<u>Random</u>	<u>5 min./axis</u>	<u>Sinusoidal</u>	<u>3 Oct/min.</u>
10-23	12 db/oct. rise to	5-16	0.20" D.A.
23-80	.025 $g^2/cps$	16-250	2.5g peak
80-100	12 db/oct. rise to	250-420	0.0008" D.A.
100-1000	.060 $g^2/cps$	420-1000	7g peak
1000-1200	12 db/oct. rise to	1000-2000	8g peak
1200-2000	.025 $g^2/cps$		

The acoustic environment (sound pressure levels) in db referenced in 0.0002 dynes/cm<sup>2</sup> is tabulated below:

<u>Freq. Band</u> <u>(cps)</u>	<u>Level</u> <u>(db)</u>
20-75	146
75-150	145
150-300	142
300-600	139
600-1200	135
1200-2400	131
2400-4800	125
4800-9600	120

It appears, therefore, that environment imposed by an SIB is within the capabilities of the OAO defined in the OAO design specifications. The amplification due to resonances is best evaluated by vibration testing.

#### 3.2.4 Man's Role

When one considers the role an engineer or scientist astronaut might play in regard to a complex optical instrument in space, the possibilities seem to fall into three categories: that of an analytic, systems-oriented problem-solver, an active participant in the experiment (that is, actually mounting equipment, deploying booms, etc.), and finally, a scientific interpreter of the data received. Two of these three roles depend upon an advantage which an astronaut will have that none of the planners of the experiment will have. This is the gift of "hindsight". If the planners of experiments were blessed with a perfect knowledge of how their experiments would go, there would be absolutely no need for the role of problem-solver, nor a man to interpret data and make decisions about changes in the experiment. It is this gift of hindsight that seems most important to exploit when considering the role of man in an Orbiting Astronomical Observatory.

The gift of hindsight can be distributed in various ways. If the telescope and manned vehicle are launched simultaneously, the astronaut would be present to watch the deployment of the instrument and could assist if any malfunctioning should occur. Here, the advantage of the astronaut's presence is largely determined by the ability of the sensors (including man's own sensors) to convey to the man what is going on in the experiment. If, however, a separate manned launch were to take place, then the status gathering telemetry could inform operators on the ground as to any malfunctioning components and, when the manned launch takes place, the appropriate spare parts could be launched with the astronauts. With large telemetry capability, a man on the ground may be in a more advantageous position than an unaided astronaut simply watching the

instrument unfold and commence operation. Hence, a decision about whether or not the astronauts should be launched at the same time as the instrument seemingly revolves around the telemetry capability.

Hand-in-glove with considerations of access to information about how the experiment is working is the question of accessibility of the internal parts of the experiment in the event that a malfunction should occur. Obviously, knowing all about a malfunction does no good if the man cannot get at and replace a faulty component. In the same vein, if a needed operation should not occur properly, the man must be capable of getting at and manually assisting or causing the desired operation.

To assure that the astronaut will be able to make a strong contribution to the success of the experiment, it is important that considerations of accessibility, not only to the instrument and its internal components, but also to the information necessary to reduce malfunctions must be kept in mind throughout the design of the experiment. To this end, a full-scale mockup of the telescope has been constructed. It is intended that, as the design proceeds, this mockup will be kept up-to-date and made as detailed as is feasible. A Gemini spacesuit is available to Perkin-Elmer and has already been used to perform experiments in accessibility and mobility in the telescope package. It has been found, for example, that the astronaut will be capable of moving the secondary mirror into operating position in the event of malfunction of the release mechanism. It is planned that the entire instrument section of the telescope be mounted on rails so that it can be pulled out of the aft end of the telescope cylinder so that an image mover assembly (as an example) will be accessible for examination by the astronaut. By a constant revision of this mockup and by modeling each subsystem during design, it is felt that a design goal of making the telescope repairable in orbit can be met.

It is very difficult to predict with any precision exactly what sort of in-orbit problems the astronaut would have to solve; however, his activities might be classifiable in two categories. First, there are actions which counteract the sort of failures where a bump, push, kick, or nudge would restore the component to action; secondly, replacement of a module because of a component failure (such as a burned-out resistor).

While a case can be made to show that not very many satellites fail because of the lack of deployment, there is still a record of twelve partial failures out of 118 satellite launches since 1958 of which six could very likely have gone on to successful operation if a man had been present to nudge, kick, bump, or otherwise coax a recalcitrant mechanism into operation. If one considers only the larger, more ambitious experiments, the percentage of partial failures is much larger. A specific example, though not a satellite, but very close to home is the fourth scientific flight in the Stratoscope II Program. Here, a tank of cooling liquid failed to operate as planned, and because of the unbalanced created, the telescope was unable to start operation. The presence of a man during the first ten minutes at altitude would have absolutely assured the success of this flight. In this flight, perhaps a million dollars' worth of effort was wasted. In the case of a satellite, the number of dollars would perhaps be multiplied by a factor of fifty.

There are, of course, some tasks which would be hopeless for the astronaut to attempt during an EVA. Included in these tasks would be optical alignment, electrical measurements requiring several instruments, or any other fine measurement or adjustment which the environment plus the restrictions imposed by the spacesuit would rule out. A list of possible astronaut tasks is shown in the Table.

As is shown in section 5.0 of this volume ("Photographic Systems in a Space Environment") it would be extremely difficult to provide enough shielding for UV sensitive film to permit it to survive without processing for more than approximately eight days. The UV sensitive photographic materials which are available are pressure and touch sensitive and do not lend themselves to automatic processing. Hence, the design and construction of an extremely complex processor can be avoided by having the astronaut process the film in his vehicle while still in orbit. He, then, of course, has the capability of examining the processed film and deciding whether a retake is necessary or not. As indicated earlier, the ability to use film extends the data acquisition capabilities markedly. It is simply impossible to cover the spectral range below approximately 1000A with the vidicon. Therefore, this spectral region would have to remain unexplored if it were not for the possibility of using a photographic recording media. The presence of a trained astronaut will greatly enhance the scope of the experiment and affords the possibility of new scientific discoveries which would otherwise not be possible.

As one contemplates the future of our space efforts, it is apparent that men will be able to be in the immediate vicinity of this instrument many times before the orbit decays and the telescope comes back into the atmosphere. For this reason, it is important that it be constructed in such a way that developments as yet unthought-of might later be incorporated. This sort of experience will be invaluable in learning how to modify an ultimate National Orbiting Observatory. A 120" or larger telescope will have to serve many functions and it is certain that modifications by man will be required if such an observatory is to have the expected years of life in orbit. While the 40" telescope may have rather limited justification for manned participation, the benefits accruing for future astronomical research may make the effort at this time quite worth while.

#### ASTRONAUT TASKS FOR OPTICAL PACKAGE

##### CAN BE DONE

1. Change vidicons
2. Change film cassette
3. Change secondary and drive assembly
4. Uncage from launch configuration
5. Set-up of thermal tube extension
6. Connection of test point umbilical



POSSIBLE

1. Remove instrument section
2. Insertion or removal of optical filters
3. Exchange of power supply subassemblies
4. Exchange of data processing subassemblies
5. Exchange of guidance electronics subassemblies

IMPOSSIBLE

1. Remove telescope
2. Exchange primary mirror
3. Alignment inside instrument section

3.2.4.1 Extra-Vehicular Function - An integral OAO/CSM/LEM Laboratory launch initial deployment of the OAO in its gimbal structure is shown in Figure 3.27. Assuming, however, that no LEM Laboratory exists, then the OAO and its gimbal structure may be detached from its launch position below the CSM, transposed, and attached to the front of the CSM. To obtain access to the OAO for detachment from the launch mounting, the SLA must be jettisoned. Launching the AAP without the LEM Laboratory requires the design of an adapter for supporting the OAO in the SIVB. This adapter would replace the LEM descent stage. The present mission plans for the CSM/LEM Lab launch requires jettisoning the Spacecraft Launch Adapter (SLA) which shrouds the LEM Lab and attaches the Service Module to the SIVB. This frees the CSM for transportation and docking to the LEM Lab. After docking, the LEM Lab is detached from the SIVB. To facilitate deploying the OAO, and perhaps provide structure for mounting a gimbal, this adapter should include a docking port. Also, attaching gimbal structure to the CSM should be further analyzed. Attachment at the front of the CM requires consideration of the interference with the egress/ingress hatch. Attachment at the rear of the SM would place the OAO too near the engine exhaust. The attachment of the OAO to structure on the SM should also be considered, with proper precaution given to the location with respect to the attitude thrusters.

If the initial setup is estimated at 6 man-hours and only one man operation, then, based on a crew schedule analysis discussed later, 3 days (2 hours/man/day) would be required.

Performance of adjustments and repairs in support of the Advanced Princeton Experiment have been considered in the following areas:

Deployment of solar paddles if malfunction occurs: Highly improbable as solar paddle release latches are reliable (dual redundancy and reliability of 0.9957). In addition, access to the latch mechanisms without a major redesign is very difficult if not almost impossible. However, the removal of two external nuts per paddle would free the solar paddles.

3-49

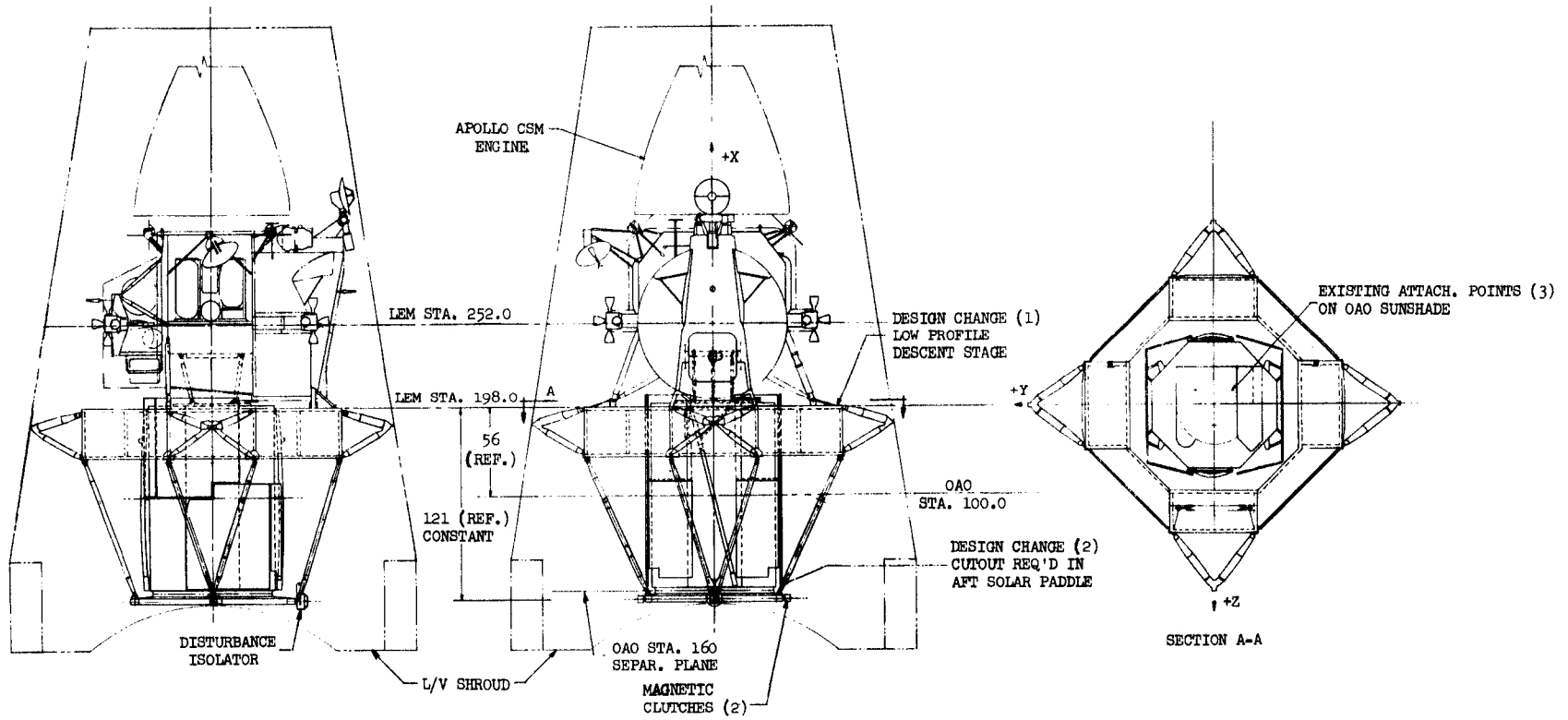


Figure 3.27. Integral Launch Configuration, S1B

Release mirrors and other delicate components from vibration isolation systems used during launch. Releasing the primary from its launch-protected position requires the design of either special tools to provide accessibility or mechanically-released remote control (wired latching pins).

Adjust optical alignment if image quality is poor and automatic control is inoperative: For this operation, one would operate the vidicon in a continuous mode. An optical alignment adjustment does not appear practical during an EVA because of the effect of man's presence (thermally) and his capability for precision adjustment in the space environment. In addition, the design of the electromechanical drive system with manual override may result in poorer total reliability as compared with redundant drive systems.

Adjust thermal environment, if necessary, with tape, foil and super-insulation: Thermal control of the structure can be accomplished by using tape or foil on the inner side of the C and G panels. Similar thermal control of the equipment packages can be accomplished by using tape on the honeycombed structure (located inside the skins) on which the equipment is mounted. The use of super-insulation is not recommended since better control of the emissivity characteristics can be obtained by removing or adding tape. There are 82 temperature sensors located throughout the OAO, and, using the data collected and a ground computation, the location and amount of tape can be determined. It should be pointed out, however, that the structure has a thermal time constant of 2-3 days and the equipment bays have a thermal time constant of 1/2-1 day.

Connect test umbilical to OAO if power or radio communication fails: Using a test umbilical implies control and diagnostic capability aboard the CSM/LEM. This is a definite requirement in event of a power or communication system failure.

Replace faulty modules, if indicated by failure diagnosis, and if spares are available: The replacement of experiment modules can be effected only at the ends of the vehicle. Support structure for the astronaut is desirable. Tether rings on the OAO or experiment package are also desirable. Storage for the replacement assemblies and the malfunction assemblies

is required. Module unlatching should be simple and modules should not be too bulky. Cold welding is probably not a problem since modules will likely be replaced only once.

The changing of detectors or film cassettes will become a routine operation during the association with the AAP vehicle. The time to actually change is estimated at 30 minutes. A suggested schedule follows:

Install cassette immediately after last pass through South Atlantic anomaly - return to spacecraft.

Take exposures for approximately 10 hr.

Remove cassette immediately before first pass through anomaly - return to spacecraft, leaving no film outside during approximately 6 hours through anomaly.

Remain inside CSM for 30 hr comprising 2 successive series of orbits through anomaly and the repeat cycle. Thus, the schedule requires two EVA some 18 hr apart and then none for 30 hr.

Film cassette changing will pose a cold welding problem. It is suggested that the interface be of dissimilar materials. It is further recommended that the camera system be designed for easy access to the film cassettes and that this assembly be replaced with a vidicon assembly at the end of the 30 day mission. It is suggested that a radiation monitoring system be included to indicate safe exit and as a warning to reenter. A similar device should also be considered for evaluating the effect of the radiation environment on the film.

The preparation of the OAO for automatic operation during the remainder of its life is estimated to take 4 man hours, during last two days. The schedule of tasks would be:

Replace camera with second image tube on next to last day when the cassette is removed for the last time.  
Make final test of all functions by ground control.

Remove gimbal structure and (cast away after operation is checked).

Release the OAO spacecraft in such a way that it is not tumbling. The spacecraft should remain in the vicinity of the free OAO for a few orbits to verify that everything is working properly after the gimbals have been removed.

If a malfunction is detected after the OAO is freed, the torque disturbances caused by an astronaut attempting a repair on a free OAO would overpower the OAO torque capability. It, therefore, appears that a rendezvous and docking capability would be highly desirable or that the Astronaut Maneuvering Unit (AMU) have sufficient capability to hold the attitude of the OAO and the astronaut during repairs.

3.2.4.2 On-Board Activities - A simplified OAO command system and data display, including a long persistence TV display can be made available in the LEM/Laboratory. The astronauts and the ground stations may both communicate with the OAO via radio link, unless a failure necessitates use of an umbilical. Because of the complexities necessary to optimize the observing program, and to avoid damaging combinations of command, normal programming of the OAO will be from the ground. The following on-board astronaut functions may be accomplished:

- Initial deployment and turn on: For this, one image tube is initially installed with the longer wavelength range microscope and spectrometer, and one film camera is installed with the shorter wavelength microscope and spectrometer.
- Following EVA set-up, prepare OAO for operation by remote-control opening of solar paddles and releasing of optical components from vibration - isolation systems (see above).
  - Turn on and check out all OAO functions by ground command. If everything is operating properly it is most efficient for the OAO to follow a stored program for these tests. An astronaut would monitor the operation with the display and be ready to stop it immediately if a failure appeared. This might prevent the serious damage which could result if the OAO continued in a failed mode until the next ground station contact. Also, if a failure appeared, an on-board astronaut could have the problem solved before the next ground station contact. If it were required to wait each time for voice link with ground command, much experimental time might be lost. To perform this function, the requirements of an on-board diagnostic system should be evaluated.
  - If image quality (as observed on a TV monitor) is below expectations, astronauts should suspend operation, check operability of automatic focusing and automatic collimation, and improve collimation and focusing by remote control, as required. (Normally, all commands by the astronaut to the OAO should be checked with the ground by voice link to reduce the possibility of a harmful combination of commands.)

- Adjust servo gains by remote control, and observe performance of guidance systems in response to controlled perturbations of the telescope pointing. Select adjustments for optimum performance.
- When systems performance seems satisfactory, return to control by ground command. Photography will then begin. Astronaut should develop film and check image quality on the photographs as soon as feasible. If quality is below expectation, further checks of optical adjustment and of guidance may be required.

#### Adjustments and Repairs:

- If malfunction is observed by astronaut or reported from ground, direct control of OAO by astronaut may be desirable for diagnosis.
- When diagnosis agreed upon by astronauts and ground control, EVA may be required. Normally, any EVA effort should be monitored at control console in AAP.

#### Routine Program:

- For each new target, orient AAP in optimum position relative to OAO within  $5^\circ$  so that gimbal functions properly.
- Put stabilization of AAP on automatic control. Check OAO gimbal angles occasionally to verify proper operation. (OAO is tracking stars and hence is fixed in inertial space.)
- Begin observing schedule alternating 18 hr. of film exposures and 30 hr of image tube recording.
- Develop exposed film and prepare cassette for next EVA.
- Note image quality on films and decide whether focus and alignment need correcting (each new target probably will require slight adjustments).
- Discuss interesting details on films with ground astronomer.

The astronaut's task will be to acquire a new target every 2 to 10 orbits. On the average, 1/2 hour of each orbit will be occulted by Earth. The occultation of the celestial sphere by the Earth does not necessarily result in restricting observations. Observations of different portions of the celestial sphere are available with reorientations throughout the orbit.

3.2.4.3 Role of Man in Data Handling - The Primary Processor and Data Storage Unit is the largest in the subsystem. It was reviewed with regard to its being repairable and maintainable in orbit by man. If no computer is available, external commands could be used for diagnostic checking, via the communications subsystem or umbilical.

Man has a dual role in this and other subsystems: he can be in the operational loop, and/or in the maintenance loop. Although he cannot completely take over the command functions in the operation loop, he can provide some inputs via typewriter/computer interface from the AAP to the OAO. And, he can monitor data received from the OAO and act as a filter for data to be transmitted to ground. New commands can be generated based on this filtered data.

In the maintenance loop, the presently designed data handling subsystem is not readily accessible or adaptable to using man. The subsystem is not packaged on a functional basis; fault isolation is difficult to accomplish, and test points are part of support equipment. Before man can begin to enhance the maintenance of the equipment, the hardware itself would have to be redesigned to off-set these deficiencies. In the redesign, state-of-the-art features such as micro-circuitry and triple modular redundancy for easier fault isolation and improved reliability would have to be considered.

The following repair considerations apply to the data handling subsystem in its present configuration. Fault diagnosis is made via ground support equipment and the communications link, and is limited to fault isolation at the black box level. With man in the loop, and if the equipment were accessible, based on ground support diagnosis, the faulty black box could be replaced. In a previous Grumman study, (Reference 1), it was shown that if the OAO-to-ground communications line broke down, the repairman would have to replace each of the following units one at a time to locate the fault:

- DC to DC Converter
- Command receiver with RF jacks and cables
- Voltage regulator - converter
- Experiment Data Handling Equipment
- Spacecraft Data Handling Equipment
- Primary Processor and Data Storage
- Data Handling power supplies
- Command Control Junction Box
- Battery charger and Sequence Controller
- Battery packs

The total time to accomplish this was estimated at 30 hours, or three 10-hour cycles.

3.2.4.4 Crew Schedule - The objective of this section is to define a CSM/LEM Lab's crew activities schedule for 30 days. The schedule's purpose is to integrate crew survivability requirements with experimental mission requirements.

Based upon the functions described in the previous section and the mission guidelines described previously, the CSM/LEM Lab housekeeping duties were established for a three- and a two-man crew. These duties were then defined as flexible and/or fixed tasks with reference to a time schedule. With this data, a sample 30-day crew schedule was prepared to indicate the expected EVA requirements, experimental time, and any allowable flexibility in the CSM/LEM Lab housekeeping tasks. When a reasonable work/experiment/sleep cycle was achieved in the crew schedule, these critical areas were then summarized for the 30-day mission.

3.2.4.4.1 Guidelines and Assumptions - The guidelines used were:

Apollo Mission Planning Task Force - Design Reference Mission  
Marshall Space Flight Center Advanced Studies for Exploration,  
Progress Report, 10/6/65.

Grumman in-house data.

Gemini 5 and 7 astronauts recommendations, specifically:

- Eating together, approximately every 6 to 8 hours
- Simultaneous sleep periods approximating normal periods on Earth. (It was stated that the low cabin noise level made any sound disturbing to sleep - even turning a page of the flight plan or notebook.)
- Housekeeping in a confined space was a major problem. More time should be allowed for general cleanup.

The assumptions used were:

All EVA Life support is provided by the Apollo PLSS which is recharged by the basic LEM Lab.

EVA is set up in 3 hr time increments equal to the nominal PLSS battery capability.

Increase in cabin atmosphere losses due to cabin dump cycles eliminates the need for additional contaminant control equipment.

Regenerable carbon dioxide removal equipment is not integrated into LEM ARS.



#### Undergarments

- Each man will be provided with one liquid cooled garment (L.C.G.) and 15 constant wear garments (C.W.G.) for the 30 days. One spare L.C.G. will be stored with the spare suit and PLSS.

LEM Lab is dumped on each EVA

If no EVA, Lab must be dumped once per day to control Lab atmosphere contamination.

The spacecraft will normally carry a three man crew, with no more than two men in the Lab at one time.

Sleeping: Two flexible, stowable bunks will be provided in the LEM Lab to allow both crewman to sleep simultaneously. The crewman will wear unpressurized suits with the helmet on.

Crew is awakened 4 hours prior to lift-off and eat 3 hours prior to lift-off.

There shall be no requirements that one crew member be in a pressure suit at all times.

28 LEM Lab LiOH canisters and 30 backpack LiOH canisters are stored outside and must be brought into the LEM Lab. 2 LiOH canisters are stored inside the LEM Lab.

#### Suits

- Four modified hard suits and 4 backpacks will be provided (backpacks assumed interchangeable). Of these, 3 suits and 3 backpacks will be worn in the CM, and 1 suit and 1 backpack will be stored in the LEM Lab.

#### Batteries

- A total of 8 rechargeable batteries will be provided, 3 in the PLSS and 5 in the LEM Lab. Battery recharge time is 10 hours with 4 recharge cycles available.

3.2.4.4.2 Two and Three Man Crew Schedules: Crew EVA depends upon the time available as well as the crew's capability to perform the required tasks in a pressure suit. Data presented have been based upon the use of the Apollo suit. NASA has established the time available for EVA with this suit to be three hours. Crew EVA time starts where the man initiates his Portable Life Support System (PLSS) in the LEM Lab prior to egress and is completed when he enters the LEM Lab and establishes the proper vehicle condition.

A summary description of the tasks of a two and three man crew is shown in Tables 3-VIII and 3-IX. Table 3-X is a tabulation of the abbreviations used throughout this section. A detailed step-by-step description of the crew activity for a three and two man crew for days 1 through 4 is presented in the Appendix as Table D-1 & D-2. By day 4, the crew has established a constant and repetitive living schedule and the remaining 26 days can be programmed from this data, as shown in Table 3-VIII. The first day of this schedule is the most difficult and a reasonable living pattern is accomplished by the fourth day. The work schedule (consecutive hours that man is awake) averages approximately 15 hours per day. The crew averages 8 hours of sleep daily, with a minimum sleep period of 7 hours and a maximum of 9 hours.

Critical data is summarized for the man and the LEM/Lab. Telescope time is defined as the time film is inserted to the time it is removed. Deducting suit-up time and EVA time, approximately 12 hours of telescope time is available on even days.

Other experimental time is defined as the time within the spacecraft that the 3-man crew can devote to various duties such as film developing, review, etc. This averages 18 hours on odd days and 9 on even days.

EVA requires 12 egresses by the system engineer-astronomer and 10 egresses each for the commanding officer and system engineer.

The Lab data of 32 PLSS recharges, 30 battery recharges indicate that batteries 1 through 6 receive the maximum of 4 recycles, while batteries 7 and 8 receive 3 recycles. Lab repressurization is required 31 times. Although the normal complement of the CSM/LEM Laboratory is three men, a crew schedule for a 2-man crew was prepared to determine the available experimental time. A reasonable cycle was also accomplished by performing the task analysis for 4 days. Table 3-IX summarizes the extrapolation for the 30 day mission with a 2-man crew. The work/sleep cycle is reasonable, but available experimental time is less. Telescope time averages to 6 hours per shift and interior experimental reduces to an average of 12 hours on odd days and 6 hours on even days.

There are 30 EVA's required and each man egresses 16 time. Other Lab data is the same as the 3-man crew.

These crew schedules illustrate that, if extensive experimental time is required, the 3-man crew can accomplish this goal. If it is possible to reduce the experimental time, a 2-man crew can meet the experimental requirements and maintain a reasonable work/rest/sleep/eat cycle.

### 3.2.5 OAD Modifications

The OAD modifications studied fall into three categories. The first is compatibility considerations imposed by associating the OAD with the LEM Lab. The second are those involved in mounting the APEP within the OAD central tube. The third is that required for malfunction detection, maintenance and repair.



TABLE 3-IX  
TWO MAN CREW SCHEDULE (30 DAYS)

CREW	HOURS																								Man				Lab																												
	1	2	3	4	5	6	7	8	9	10	11	12	13	14	15	16	17	18	19	20	21	22	23	24	Work	Sleep	Telescope	Other	EVA	PLSS	Batt	Re-p																									
	CO	SE	S	S	S	S	S	S	S	S	S	S	S	S	S	S	S	S	S	S	S	S	S	S	Hrs	Min	Hrs	Min	Hrs	Min	#	#	#	#																							
1	CO	SE		M								EVA				M	S	S	S	S	S	S	S	S	21	9			1	2	1&2	2																									
2	CO	SE	S	S	M							EVA(FI)				M	S	S	S	S	S	S	S	S	17	8	2 30		1	1	3	1																									
3	CO	SE	S	S	S	M	EVA (PR)									M	S	S	S	S	S	S	S	S	16	9	30	6 30	1	1	4	1																									
4	CO	SE	S	S	S	S	SM					EVA(FI)				M	S	S	S	S	S	S	S	S	14	9	1 30	3 00	1	1	5	1																									
5	CO	SE	S	SM			EVA (PR)									M	S	S	S	S	S	S	S	S	15	8	30	6 00	1	1	6	1																									
6	CO	SE	S	S	S	M						EVA(FI)				M	S	S	S	S	S	S	S	S	17	7	2 30	4 00	1	1	7	1																									
7	CO	SE	S	SM			EVA(FI)									M	S	S	S	S	S	S	S	S	15 30	8 30	30	2 30	1	1	8	1																									
8	CO	SE	S	S	S	M						EVA(FI)				M	S	S	S	S	S	S	S	S	18 00	7 00	3 30	4 00	1	1	1	1																									
9	CO	SE	S	S	S	SM										M	S	S	S	S	S	S	S	S	15 00	9 00	30	5 50	1	1	2	1																									
10	CO	SE	S	S	S	SM						EVA(FI)				M	S	S	S	S	S	S	S	S	16 00	7 00	3 30	3 00	1	1	3	1																									
11	CO	SE	S	S	S	SM										M	S	S	S	S	S	S	S	S	14 00	9 00	30	5 50	1	1	4	1																									
12	CO	SE	S	S	S	M						EVA(FI)				M	S	S	S	S	S	S	S	S	17 00	8 00	3 00	4 00	1	1	5	1																									
13	CO	SE	S	S	S	SM										M	S	S	S	S	S	S	S	S	15 00	9 00	30	6 00	1	1	6	1																									
14	CO	SE	S	S	S	S						EVA(FI)				M	S	S	S	S	S	S	S	S	16 00	8 00	3 00	3 00	1	1	7	1																									
15	CO	SE	S	S	S	SM										M	S	S	S	S	S	S	S	S	16 00	9 00	30	6 00	1	1	8	1																									
16	CO	SE	S	S	S	SM						EVA(FI)				M	S	S	S	S	S	S	S	S	16 00	8 00	3 00	3 00	1	1	1	1																									
17	CO	SE	S	S	S	SM										M	S	S	S	S	S	S	S	S	15 00	9 00	30	6 00	1	1	2	1																									
18	CO	SE	S	S	S	SM						EVA(FI)				M	S	S	S	S	S	S	S	S	16 00	8 00	3 00	3 00	1	1	3	1																									
19	CO	SE	S	S	S	SM										M	S	S	S	S	S	S	S	S	16 00	9 00	30	6 00	1	1	4	1																									
20	CO	SE	S	S	S	SM						EVA(FI)				M	S	S	S	S	S	S	S	S	16 00	8 00	3 00	3 00	1	1	5	1																									
21	CO	SE	S	S	S	SM										M	S	S	S	S	S	S	S	S	15 00	9 00	30	6 00	1	1	6	1																									
22	CO	SE	S	S	S	SM						EVA(FI)				M	S	S	S	S	S	S	S	S	16 00	8 00	3 00	3 00	1	1	7	1																									
23	CO	SE	S	S	S	SM										M	S	S	S	S	S	S	S	S	15 00	9 00	30	6 00	1	1	8	1																									
24	CO	SE	S	S	S	SM						EVA(FI)				M	S	S	S	S	S	S	S	S	16 00	8 00	3 00	3 00	1	1	1	1																									
25	CO	SE	S	S	S	SM										M	S	S	S	S	S	S	S	S	15 00	9 00	30	6 00	1	1	2	1																									
26	CO	SE	S	S	S	SM						EVA				M	S	S	S	S	S	S	S	S	16 00	8 00	3 00	3 00	1	1	3	1																									
27	CO	SE	S	S	S	SM										M	S	S	S	S	S	S	S	S	15 00	9 00	30	6 00	1	1	4	1																									
28	CO	SE	S	S	S	SM						EVA(FI)				M	S	S	S	S	S	S	S	S	16 00	8 00	3 00	3 00	1	1	5	1																									
29	CO	SE	S	S	S	SM										M	S	S	S	S	S	S	S	S	15 00	8 00	30	6 00	1	1	6	1																									
30	CO	SE	S	S	S	SM						EVA																				1																									
Totals																											30	32	30	31																											

M = MEALS  
S = SLEEP  
EVA = Extra Vehicular Activity  
(FI) = Film Inserted  
(PR) = Film Removed

TABLE 3-X  
LIST OF ABBREVIATIONS FOR MAN'S ROLE

ARS	Atmosphere Revitalization Section
CM	Command Module
CSM	Command and Service Module
CM-RCS	Command Module-Reaction Control System
C&I	Communication & Instrumentation System
GWG	Constant Wear Garment
ECS	Environmental Control System
EMS	Entry Monitor System
EOS	Emergency Oxygen Supply
EPS	Electrical Power Supply
EVA	Extra-Vehicular Activity
GOX	Gaseous Oxygen
G&C	Guidance & Control
G&N	Guidance & Navigation System
IMU	Inertial Measurement Unit
LCG	Liquid Cooled Garment
LEM	Lunar Excursion Module
LIOH	Lithium Hydroxide
PLSS	Portable Life Support System
RCS	Reaction Control System
S/C	Spacecraft
SCS	Stabilization and Control System
SM-RCS	Service Module-Reaction Control System
SPS	Service Propulsion System

These modifications are based on a "minimum modification" consideration since ultimate unattended free mode separation is desired.

3.2.5.1 OA0/AAP Compatibility - An integral LEM Lab and OA0 launch and operation of the OA0, in orbit, gimballed to the LEM Lab are being considered. A layout of the mechanical interfaces is shown in Figure 3.27.

The OA0 is mounted for launch by its existing adapter mounting fittings (6) on a dual purpose adapter ring/bridle which is suspended by truss work from a modified LEM descent stage structure. A circumferential wedging clamp which can be pyro-technically or manually detached secures the OA0 to the mounting ring. The second purpose of half of the mounting ring is used as a portion of the "pipe rack" gimbal structure. For deploying the OA0 and engaging the "pipe rack" gimbal system, a trio of extendable arms are attached to the LEM at the former location of the LEM ascent stage engine hatch cover. This permits lowering the OA0 while still attached to the LEM Lab to a position where the gimbal engagement can be accomplished.

3.2.5.2 APEP/OA0 Compatibility - An examination of the OA0 modification for mounting the APEP to the OA0 such that the experiment floats free of the OA0 requires the use of an RF window for communication between the floating experiment and the OA0 and providing the necessary mounting of the magnetic torques.

3.2.5.3 Maintenance and Repair - To permit accessibility to equipment within the OA0 compartments, a minimal modification would require the redesign of the outer structure to allow simple removal of the outer skins. Hinged operation and quick release fasteners with captured hardware is desirable. Without further modifications the following equipments would become accessible and replaceable.

<u>Equipment</u>	<u>Compartment</u>	<u>Reliability</u>
Inertia Packages	D-3, F-3, H-3	0.9940
Radio Tracking Equipment	A-4	0.9980
Narrow Band Telem. Equipment	A-4	0.9992
Command Receiver	A-4	0.9801
Diplexers	A-4	0.9989
Battery Charger and Sequence Cont.	E-2	0.9800
Magnetometer, Processor & Elect.	H-3	0.9983
Coarse Wheel Cont.	F-3	0.9962
Fine Wheel & Jet Controllers	D-3, F-3	0.9154 Pitch, Yaw 0.9426 Roll
Digitizer Logic Unit	B-3	0.9940
Command Control Junction Box	H-5	0.9990
High Torque Controller	H-3	0.9561
Experimenters Electronics	E-4, E-5, A-5, D-5 and E-6	---

To obtain a completely repairable/maintainable OA0 would require major redesign with accessibility and removability in orbit in mind. However, certain minimal modifications have been identified. This is shown in Table 3-XI.

TABLE XI  
OAO MODIFICATIONS

Modification	Method	Reliability
1.Solar Array Detachment	Nut retention in attachment fittings	Gain access to C-3, C-4, G-3 and G-4
2.Relocation of Gas Supply System	Repackaging of system in present location	0.8535
3.Battery Pack Mounting Revision	Change short bolts to long bolts and minor fitting rework.	0.9800
4.Primary Processor and Data Storage Mounting Revision	Replace short in-board mounting bolts (2) by long tapered bolts into in-board fittings.	0.6941
5.Spacecraft Data Handling Equipment Mounting Revision	Revise to mount from below rather than above.	0.9732
6.Star Tracker Assembly Accessibility	Add access covers in existing structure and modify mounting adapter for out-board installation of bolts into trapped caps.	0.8867
7.Boresight Star Tracker	Same as #6	0.9680
8.Stellar TV Camera	Same as #6	0.9890

A diagnostic umbilical would be used when the OAO's communication system has become inoperative. Modular replacement of all suspected components to isolate the cause of failures (particularly of a communication failure) would minimize trouble shoot time. The umbilical would consist of a 61-pin disconnect receptacle installed under the compartment A-6 skin and connected to critical power, communications and command points within the OAO. In the LEM Lab the umbilical would connect to a control/display/diagnosis panel.

A representative set of basic hand tools which the repairman must carry in an integral suit harness would include the following:

Straight and/or Right angle ratchet wrenches for #10 and 1/4 and 5/16 Hex bolts.

Set of various size Allen Head screw drivers.

Electrical wire splicing tool.

Coaxial elect. plug pliers.

Long handled quick release pliers.

Cutting pliers for wire and thermal insulation.

Pneumatic or electrical wrench drive handle for stiff, recalcitrant or multiple bolt patterns.

To these basic tools, spare bolts, washers, quick release pins or other special use tools peculiar to specific components must be provided the repairman/adjuster in a convenient, easily accessible harness or container. A gun belt or bandolier type device is indicated for this purpose.

### 3.3 SPACECRAFT DEFINITION

#### 3.3.1 General Configuration

For an integral launch, the general arrangement of the OAO/APEP and the LEM Laboratory is shown on Figure 3.27. For launch the OAO is supported in a modified descent stage. The design changes from a standard LEM required are a low profile descent stage (which is being considered in the AAP and if adopted may be utilized as shown) and a new support structure for the OAO. The pallet which is part of this structure is utilized as part of the bridle, shown in Figure 3.30. This concept does not require alteration of the mounting provisions in the shroud and maintains the spatial relationship of the Apollo CSM above the LEM spacecraft.

For orbital operation of the gimballed OAO to the AAP vehicle, two concepts were considered.



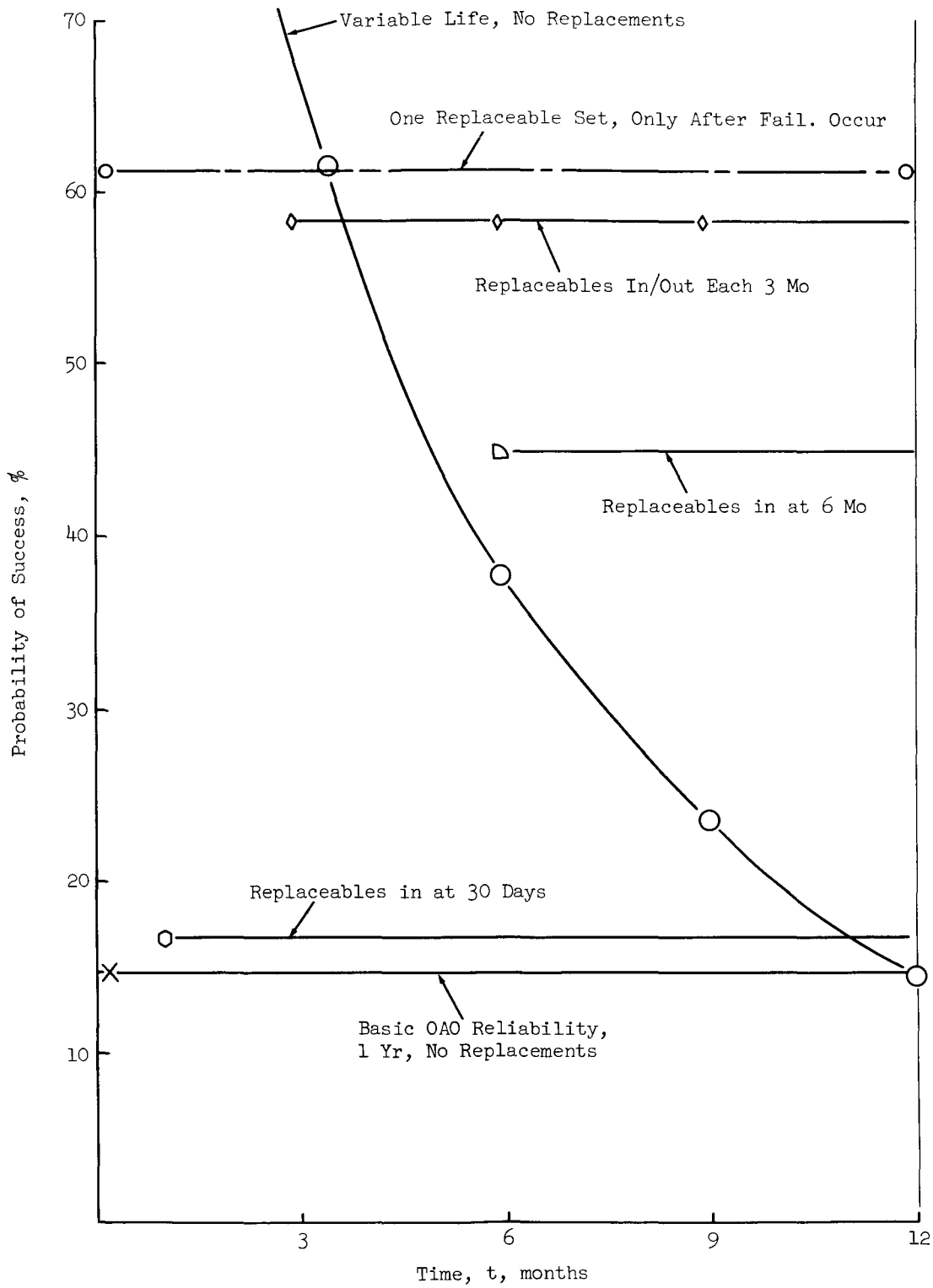


Figure 3.30. Reliability of OAO Equipment

The first, shown on Figure 3.28, represents gimbaling the OAO in an "end-mounted" position (below the descent stage), the Apollo CSM is also shown docked to the LEM ascent stage. The deployment sequence of the optical laboratory from stowed to operating state is also illustrated. This method requires extra vehicular activity of a crew man in the manipulation of the laboratory and its mounting structure.

The second configuration considered is shown on Figure 3.29. In this configuration the OAO's operating position is forward of the LEM ascent module. This design concept was a boom deployment system which also requires extra vehicular activity. The location of the gimbal structure permits direct visual observation of the operating laboratory from both manned modules.

The disturbance isolators indicated on Figures 3.27 through 3.29 must perform two damping functions as well as providing positive structural attachment of the gimbal mechanism to the spacecraft during earth launch and gross spacecraft maneuvering. The attenuation of vibratory disturbances from the spacecraft can be accomplished by recourse to gas bladder, resilient solids, or wire mesh damping materials in the design. The gross motion disturbances from the spacecraft require the more sophisticated solution of friction buildup or spring limited, soft stop mechanisms within the isolator. Combining these capabilities with a positive structural lockup mechanism presents a formidable but not impossible design problem. Conceding a reasonable design solution, full scale testing of such a device requires perhaps at least one low earth orbital flight. This development testing could be significantly reduced if model systems could be accurately scaled for parabolic flight testing in research aircraft or if the scale loads could be magnetically suspended in the laboratory to simulate weightlessness. Considering these factors, the development of the disturbance isolator hardware is considered to be a major design and testing problem.

An integrated and detailed weight statement of the CSM/LEM laboratory and the OAO/APEP spacecrafts are shown on Tables 3-XII and 3-XIII, respectively. Also shown is the allowable payload weight of the SIVB. The source of CM, SM and retro propellant weights is the "NASA LEM for AES Blue Book" Reference 9.

### 3.3.2 Reliability Assessment

System reliability improvements under various replacement concepts were made by investigating a basic OAO system associated with a space station for replenishment of selected components (Table 3-XIV). All calculations were based on free mode OAO spacecraft whose equipment configurations are the same as the current OAO spacecraft and with either regularly scheduled or required maintenance action after failure within the one year life span. All operating transmission would be accomplished through an RF link and not via hardware to the spacecraft. Basic observatory equipment, and associated one year space life

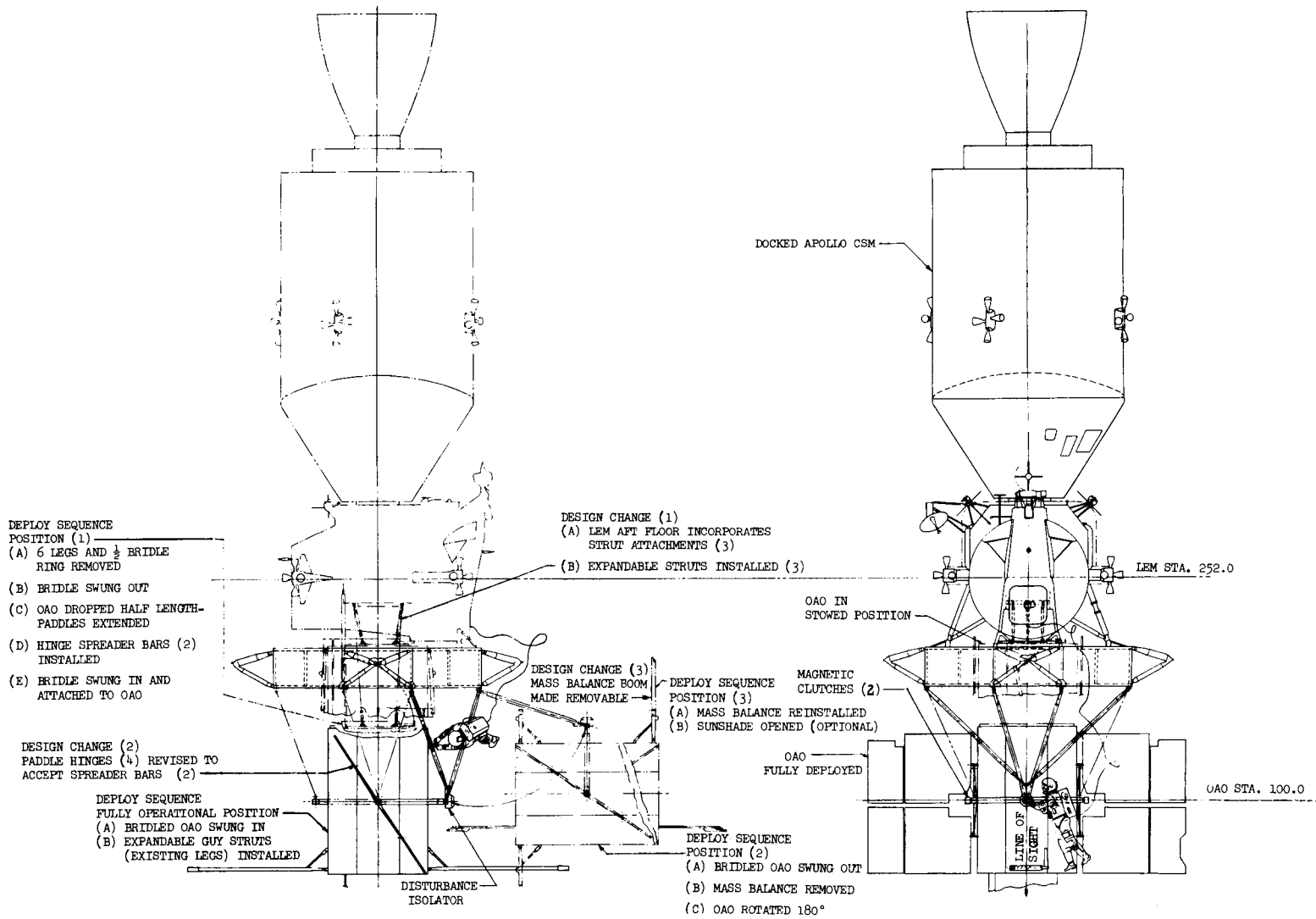


Figure 3.28. Configuration A (End Mount)

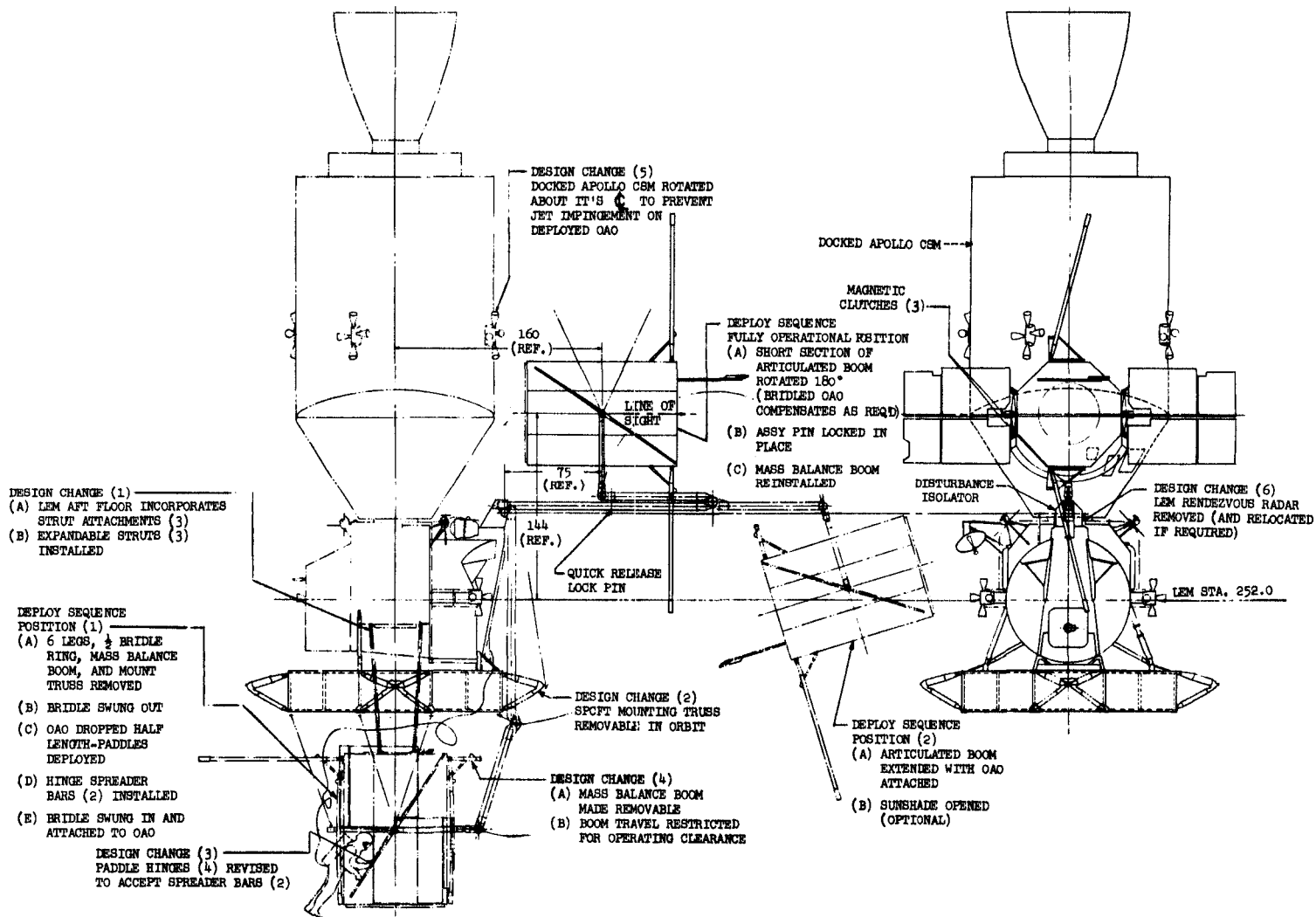


Figure 3.29. Configuration B (Side Mount)

TABLE 3-XII  
 INTEGRATED WEIGHT STATEMENT (CONFIGURATION A)

COMMAND MODULE	BASIC WT.	10,300
SERVICE MODULE	BASIC WT.	13,400
SM RETRO-PROP.		1400
TOTAL LAB WT		8954
<ul style="list-style-type: none"> <li>● Basic Structure (1987)</li> <li>● Subsys't's Dry Wt. (3613)</li> <li>● Trapped Residuals ( 517)</li> <li>● Expendables (2837)</li> </ul>		
TOTAL EXPT		4548
<ul style="list-style-type: none"> <li>● OAO-C, booms (4043)</li> <li>● Expt. Dep Wts. ( 505)</li> <li>● Spares ( 400)*</li> </ul>		
TOTAL ORBITING WT (ALLOWABLE)		38,602 (33,800)
SM ASCENT PROP (To 250 n mi.)		2370
SLA ADAPTER		3800
TOTAL LAUNCH VEH. PAYLOAD		44,772

\*Spares for OAO & APEP maintenance are not included in totals.

TABLE 3-XIII

DETAILED LAB AND EXPERIMENT WEIGHT STATEMENT

STANDARDIZED PHASE 2 LEM (DRY)	(5600)
● Ascent Structure	1363
● Descent Structure	624
● S & G	113
● Crew Provisions	119
● Environment Control	417
● Instrumentation	283
● Electric Power	1889
● Propulsion & RCS	520
● Communications	119
● Displays & Controls	153
TRAPPED & RESIDUAL	(517)
● Crew Provisions	180
● ECS	177
● Elect. Power Supply	78
● Reaction Control	82
ORBITING EXPENDABLES	(2387)
● Crew Provisions	102
● Electric Power Supply	1585
● Reaction Control	1150
TOTAL LEM ORBITING	8954
EXPERIMENT WEIGHT	(4548)
● OAO	(4043)
- Structure	898
- S & C (New Raps)	809
- Data Proc. & Instr.	346
- Communications	39
- Power Supply (W.O. Extensions)	764
- Experiment (PEP)	1000
- Balance & Booms	133
- Thermal Control	54
○ ● Spares	(400)*
- OAO	150
- APEP	250
● Experiment Dependant Weights	(505)
- Gimbal System	139
- Command Control	346
- Film & Processing	20
TOTAL ORBITING WEIGHT	38602

\*NOT INCLUDED IN TOTALS

TABLE XIV  
RELIABILITY OF REPLACEABLE COMPONENTS

ITEM NO	EQUIPMENT	BASIC RELIABILITY (ONE YR)	WEIGHT
26	Inertia Package-Pitch	.9940	31.1#s
27	Inertia Package-Yaw	.9940	31.1
28	Inertia Package-Roll	.9940	31.1
78	Radio Tracking Equip.	.9980	2.1
79	Narrow Band Telem. Eq	.9992	10.8
77	Command Receiver Eq	.9801	9.7
80	Diplexers	.9989	10.2
93	Battery Chgr. & Seqc. Cont.	.9800	25.7
60	Magnetometer, Processor & Elec.	.9983	15.9
29	Coarse Wheel Cont	.9962	11.3
31	Fine Wheel & Jet Cont. Pitch	.9154	13.0
32	Fine Wheel & Jet Cont. Yaw	.9154	13.0
33	Fine Wheel & Jet Cont. Roll	.9426	10.5
34	Digitizer Logic Unit	.9940	46.0
74	Command Control Junction Box	.9990	36.1
35	High Torque Controller	.9561	5.2
51	Gas Supply System	.8535	55.4
68	PPDS	.6941	239.8
69	SDHE	.9732	23.4
30	Boresight Stab Tracker	.9680	24.8
38	Stellar TV Camera	.9890	8.1
17-22	Six (6) ST	.8867 each	51.8 (6)

reliability numbers (System = .144) are shown in Table 3-XV. This data is from Reference 1.

Based on selected equipment replenishment programs the effect on overall system reliability has been computed.

Basic OAO system reliability for an observatory on a one year life mission with no replacements;  $R_1 = 14.4\%$ , one month,  $R = 85.1\%$ .

OAO available for first 30 days of operation -- Replacement with each spare component;  $R_2 = 16.5\%$ .

OAO available during the sixth month and all replaceable spare components are exchanged with those which have been active  $R_3 = 44.7\%$ .

OAO available during the 3rd, 6th, and 9th months and a replacement each quarter with an entire set of spare components  $R_4 = 58.4\%$ .

OAO available after each failure occurrence and replaceable units installed  $R_5 = 61.3\%$ .

These calculations versus the reliability with no repair have been superimposed on Figure 3.30 to permit a direct graphical comparison. It is recommended that replacement be accomplished after 3-6 month of operation.

Since one of the critical system requirements is for six star tracker operation, a further detailed analysis was made of these components and the results shown in Figure 3.31. and Table 3-XVI are presented below:

The reliability of a single star tracker ST is  $R_{ST} = 88.7\%$  (for one year life span).

Reliability of six (6) ST in series configuration (since all six are required for ultimate success through a year life span)  $R_{6ST} = 48.6\%$ .

Reliability of six ST plus one (1) spare ST which can be interchangeably employed in any one of six positions after a failure has occurred;  $R_{(6+1)ST} = 81.6\%$ .

Reliability of six ST plus three (3) spare ST's which can be interchangeably employed in any of six positions, after failure occurrences;  $R_{(6+3)ST} = 98.4\%$ .

Reliability of six ST plus six (6) spare ST's which can be interchangeably employed in any of six positions, after failure occurrences;  $R_{(6+6)ST} = 99.1\%$ .



TABLE 3-XV  
 OAO/SS RELIABILITY DATA (Sheet 1 of 3)

Item No.	Item Equipments	Subsyst	Basic Observatory	
			Reliability	Weight
1	Paddle Erection Mechanism	Struct	.9957	
2	Sun Shutter Mechanism & Protective Eye	Struct	.9870	
3	Structure & Thermal Control	Struct	.9990	
4	Alignment Mechanism	Struct	.9990	
5	Gimbal Mechanism	Struct	-	-
6	Tether Mechanism	Struct	-	-
7	Hangar Clean Room	Struct	-	-
8	Hangar Thermal Control	Struct	-	-
9	Structure Subsystem Reliability		.9808	-
10				
11				
12				
13				
14	Coarse Sun Sensor Assemblies (2)	S & C	.9992	0.5
15	Fine Sun & Disabling Sensor Assy	S & C	.9998	2.3
16	3 Sensor Signal Processors (Pitch, Yaw, Roll), 2 Batteries	S&C, PS	.9884	198.6
17	Star Tracker, Star Tracker Controller, Phasolver Electronics (1)	S & C	.8867	51.8
18	Star Tracker, Star Tracker Controller, Phasolver Electronics (2)	S & C	.8867	51.8
19	Star Tracker, Star Tracker Controller, Phasolver Electronics (3)	S & C	.8867	51.8
20	Star Tracker, Star Tracker Controller, Phasolver Electronics (4)	S & C	.8867	51.8
21	Star Tracker, Star Tracker Controller, Phasolver Electronics (5)	S & C	.8867	51.8
22	Star Tracker, Star Tracker Controller, Phasolver Electronics (6)	S & C	.8867	51.8
23	Improved Rate Gyro - Pitch	S & C	-	-
24	Improved Rate Gyro - Yaw	S & C	-	-
25	Improved Rate Gyro - Roll	S & C	-	-
26	Rate Gyro, Coarse & Fine Wheels, Pitch	S & C	.9940	31.1
27	Rate Gyro, Coarse & Fine Wheels, Yaw	S & C	.9940	31.1
28	Rate Gyro, Coarse & Fine Wheels, Roll	S & C	.9940	31.1
29	Coarse Wheel Controller	S & C	.9962	11.3
30	Boresighted Stab Tracker & Electronics	S & C	.9680	24.8
31	Fine Wheel & Vet Controller, Pitch	S & C	.9154	13.0
32	Fine Wheel & Vet Controller, Yaw	S & C	.9154	13.0
33	Fine Wheel & Vet Controller, Roll	S & C	.9426	10.5
34	Digitizer Logic Unit	S & C	.9940	46.0
35	High Torque Controller	S & C	.9561	5.2
36	Star Tracker Signal Processor	S & C	.9241	15.5
37	Stellar TV Electronics	S & C	.9480	9.7
38	TV Camera	S & C	.9890	8.1
39	Primary High Thrust Solenoid Valve +P	S & C	.9935	0.4
40	Primary High Thrust Solenoid Valve -P	S & C	.9935	0.4

TABLE 3-XV  
 OAO/SS RELIABILITY DATA (Sheet 2 of 3)

Item No.	Item Equipments	Subsyst	Basic Observatory	
			Reliability	Weight
41	Primary High Thrust Solenoid Valve +Y	S & C	.9935	0.4
42	Primary High Thrust Solenoid Valve -Y	S & C	.9935	0.4
43	Primary High Thrust Solenoid Valve +R	S & C	.9935	0.4
44	Primary High Thrust Solenoid Valve -R	S & C	.9935	0.4
45	Primary Low Thrust Solenoid Valve +P	S & C	.9999	0.3
46	Primary Low Thrust Solenoid Valve -P	S & C	.9999	0.3
47	Primary Low Thrust Solenoid Valve +Y	S & C	.9999	0.3
48	Primary Low Thrust Solenoid Valve -Y	S & C	.9999	0.3
49	Primary Low Thrust Solenoid Valve +R	S & C	.9999	0.3
50	Primary Low Thrust Solenoid Valve -R	S & C	.9999	0.3
51	Primary: 2N <sub>2</sub> Tanks, 2 Rel Valves, Filter, 3 S O Valves 2 Regulators, Check Valve 2 transducers	S & C	.8535	55.4
52	Secondary High Thrust Solenoid Valve +P	S & C	.9978	0.4
53	Secondary High Thrust Solenoid Valve -P	S & C	.9978	0.4
54	Secondary High Thrust Solenoid Valve +Y	S & C	.9978	0.4
55	Secondary High Thrust Solenoid Valve -Y	S & C	.9978	0.4
56	Secondary High Thrust Solenoid Valve +R	S & C	.9978	0.4
57	Secondary High Thrust Solenoid Valve -R	S & C	.9978	0.4
58	Second: 2N <sub>2</sub> Tanks, 2 Rel Valves, Filter, 2 S O Valves 2 Regulators, check Valve, 2 Transducers	S & C	.9807	49.4
59	Magnetometer Probe Assy	S & C	.9999	1.0
60	Magnetometer, Magnet Signal Processor, Torquer Electronics	S & C	.9983	15.9
61	Capacitor Boxes (3)	S & C	x	x
62	Gas Jet Fittings & Joints (Primary & Secondary)	S & C	.9995	-
63	Stabilization & Control Subsystem Reliability		.234	-
64				
65				
66				
67				
68	PPDS/PSSC	DP	.6941	239.8
69	SDHE	DP	.9732	23.4
70	EDHE	DP	1.0	-
71	Signal Conditioning Unit	DP	1.0	-
72	Spacecraft Instrumentation	DP	1.0	-
73	Maintenance Checkout Umbilical	DP	-	-
74	Command Control Junction Box	DP	.9990	36.1
75	Data Processing Subsystem Reliability		.6748	-
76				
77	Command Receiver Equip (4 Receivers, Video Signal Combiner & Detector, 2 RF Junctions)	COMM	.9801	9.7
78	Radio Tracking Equip (2 Beacon Transmitters, RF Switch)	COMM	.9980	2.1
79	Narrow Band Telem Equip (2 Transmitters, RF Switch, 2 Wide Band Transmitters, DC-DC Converter)	COMM	.9992	10.8
80	2 Diplexers, Hybrid Junctions	COMM	.9989	10.2

TABLE 3-XV  
 OAO/SS RELIABILITY DATA (Sheet 3 of 3)

Item No.	Item Equipments	Subsyst	Basic Observatory	
			Reliability	Weight
81	DC-DC Converter	COMM		1.8
82	VHF Slot Antenna	COMM	.9997	-
83	UHF Pitchfork Antenna	COMM	.9997	-
84	Communications Subsystem Reliability	COMM	.9757	-
85				
86				
87				
88				
89	Solar Array (1)	Pwr. Sup	.9963	61.6
90	Solar Array (2)	Pwr. Sup	.9963	61.1
91	Regulator Converter	Pwr. Sup	.9898	36.6
92	Inverter	Pwr. Sup	.9882	34.8
93	Battery Charger & Sequence Controller	Pwr. Sup	.9800	25.7
94	Distribution Panel	Pwr. Sup	.9990	-
95	Transformer-Rectifier	Pwr. Sup	-	-
96	Power Supply Subsystem Reliability		.951	-

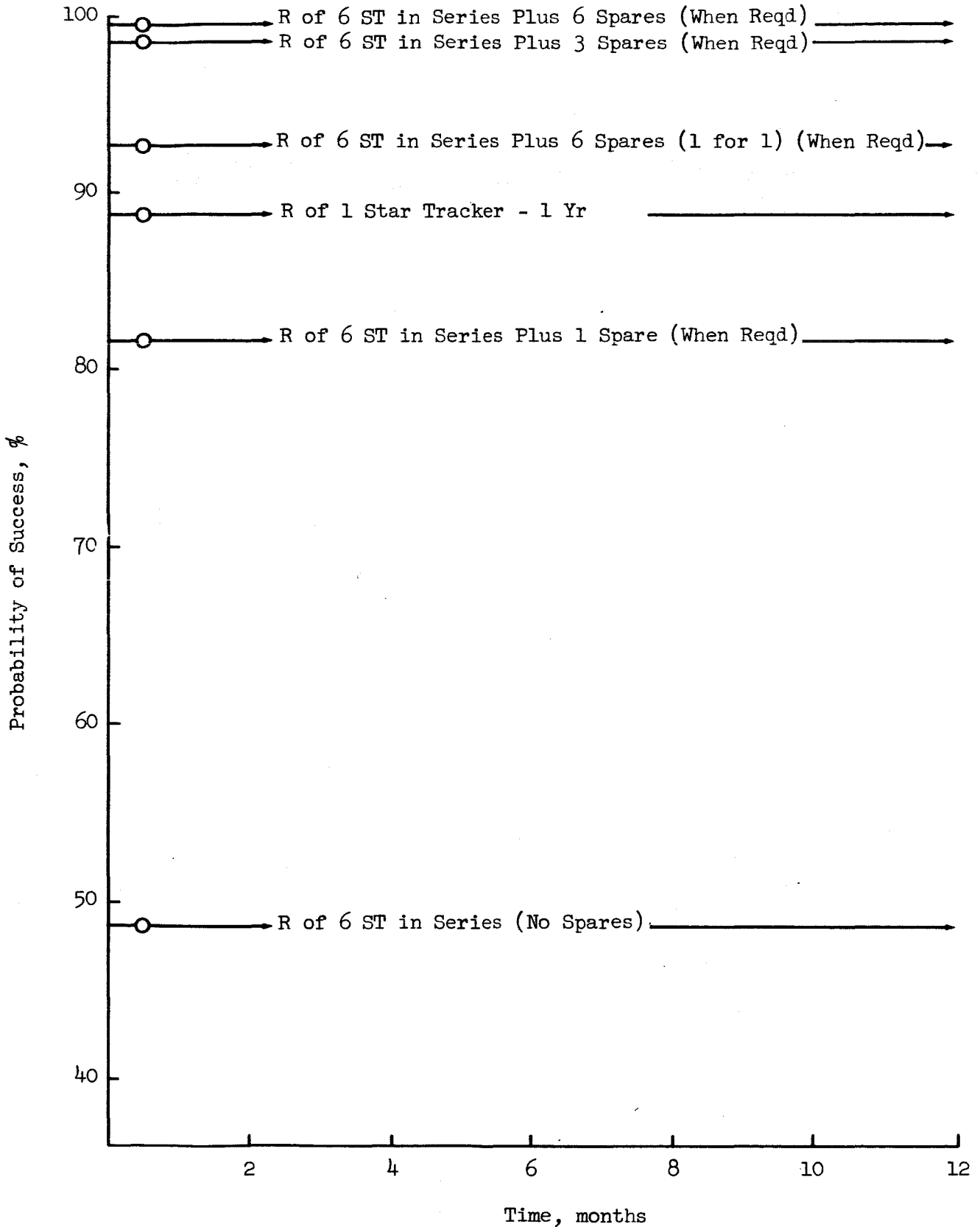


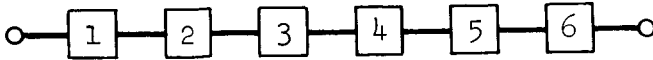
Figure 3.31. Startracker Reliability

TABLE XVI  
STAR TRACKER RELIABILITY CONFIGURATIONS

1) Single Star Tracker Package

$R = 0.8867$

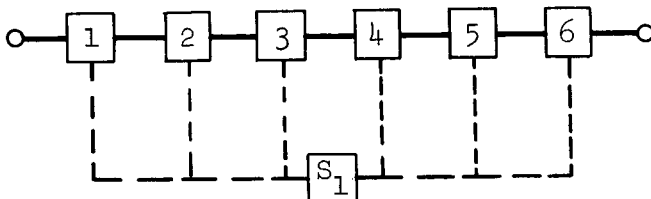
2) Six Star Trackers in Series



3) Six Star Trackers Plus One Spare

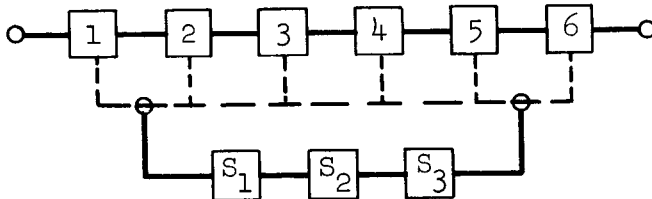
(\*Utilized after Failure Occurs)

$R_{(6 + 1)} = 0.8163$



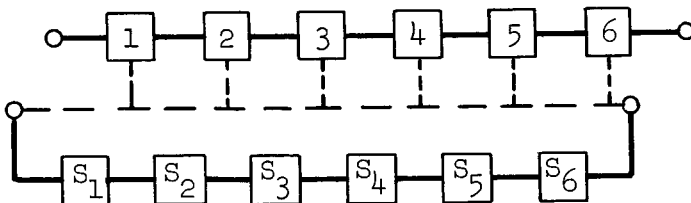
4) Six Star Trackers Plus Three Spares

$R_{(6 + 3)} = 0.9843$



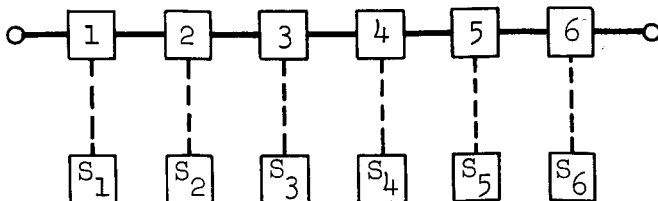
5) Six Star Trackers Plus Six Spares

$R_{(6 + 6)} = 0.9912$



6) Six Star Trackers Individualized Spares

$R_{(6 - 1/1)} = 0.9256$



Reliability of six ST plus six (6) spare ST's which are individualized, one for one, after failure occurrences;  
 $R_{(6-1/1)ST} = 92.6\%$ .

It is recommended that 3 star trackers be carried aboard the AAP spacecraft as spares.

### 3.3.3 Subsystem Analysis

3.3.3.1 Reaction Control of LEM Lab - The Reaction Control Subsystem (RCS) provides small rocket thrust impulses to maintain Laboratory attitude as commanded by the GNC subsystem. In general, changes in attitude or slewing will be provided by the CSM reaction control subsystem. The LEM Lab RCS will provide slewing for experiments performed from the Lab.

The RCS consists basically of 16 thrust chambers supplied by two separate propellant supply sections. The chambers and the dual propellant supply sections make up two parallel, independent, and redundant systems. The 16 thrust chambers are arranged in clusters of four and are mounted on four outriggers that are equally spaced around the LEM Lab. In each cluster, two thrust chambers are mounted parallel to the vehicle x-axis, and face in opposite directions; the other two are spaced 90° apart, in a plane normal to the x-axis. Two of the thrust chambers are supplied by system A, the other two by system B. Normally, both systems are operated together, but the arrangement of the thrust chambers allows complete control about all axes despite a failure in either system.

The RCS hypergolic propellants that consist of a 50-50 fuel mixture of hydrazine ( $N_2H_4$ ) and unsymmetrical dimethylhydrazine (UDMH), with nitrogen tetroxide ( $N_2O_4$ ) as the oxidizer.

The propellant supply sections in each of the systems (A and B) include all of the propellant storage, pressurization and feed components necessary for the delivery of fuel and oxidizer to the thrust chamber assemblies. Each system has two cylindrical tanks, one for fuel and one for oxidizer. The liquid propellants are contained in positive expulsion bladders supported by standpipes that run lengthwise through each tank. This insures the liquid-pressurant interface even in zero g. Both tanks in each of the dual supply sections are pressurized by an individual helium supply that acts upon the tank bladders to force fuel and oxidizer into a manifold that supplies the eight thrust chambers for that system.

A propellant quantity gaging system is provided which continuously indicates the propellant quantity remaining.

The ascent and descent propulsion subsystems of the LEM have been removed except for the descent propellant tanks. These tanks, which are four in number, spherical ended and cylindrical in shape, are available to the experimenter. By special modification, they can be converted into bladder tanks for containing non-reactive liquids. Each tank has an internal volume of 63 cu. ft.

Experimental Capability: Figures 3.32 and 3.33 indicate the Reaction Control System propellant quantity required to hold a prescribed vehicle attitude in the absence of disturbance torques, to within  $\pm 0.3$  and  $\pm 5.0$  degrees, respectively. The curves are plotted over a range of attitude hold durations and for various combinations of vehicle moments of inertia.

When the vehicle has disturbance torques acting upon it (e.g., aerodynamic, gravity gradient, or internal torques), Figure 3.36 may be used to estimate RCS propellant quantities for holding attitude about each axis. It should be noted that for the attitude deadbands available ( $\pm 0.3$  and  $\pm 5.0$  degrees) and the vehicle moments of inertia of interest, the propellant required is solely dependent upon the magnitude of the disturbance torque. Figure 3.34 presents propellant requirements for time averaged disturbance torques of 0.2 and 0.3 ft. lb.

3.3.3.2 Diagnostic and Control - A requirement exists to have complete real-time control of an OAO via an operator in an AAP vehicle independent from the manned space flight network. It is desired that the AAP vehicle be capable of performing essentially the same functional operations and commands for the OAO as does the existing OAO tracking network. The control will be accomplished via an RF link between the AAP vehicle and the OAO. All equipment additions, modifications, etc., will be made to the AAP vehicle only (no modifications or additions are to be made to the OAO). It is intended that the OAO be under control of the AAP vehicle for at least 30 days, at which time the OAO will resume "normal" operation from its earth based tracking facilities.

OAO Tracking Network Background: Presently the OAO network consists of three remote tracking stations and one central station located at GSFC. The primary function of the remote stations are:

Convert OAO commands received from GSFC into satellite language and store all predicted status and command rate.

Compare current OAO status with predicted status and transmit stored commands if acceptable.

Verify commands received by the OAO and continue to retransmit commands until verification is received.

Convert OAO status data into teletype language and transmit it to the central station.

Record experimental data and other pertinent data and mail recording to GSFC for evaluation.

It is apparent that the remote stations are strictly used for word forming and relaying of data developed at GSFC, to the OAO. The primary control of the entire OAO network, and also the OAO, is an IMB 7090 computer at GSFC. During normal operation the 7090 computer generates the satellite commands automatically based upon stored status data and continuously updated

.001 deg/sec Rate Threshold

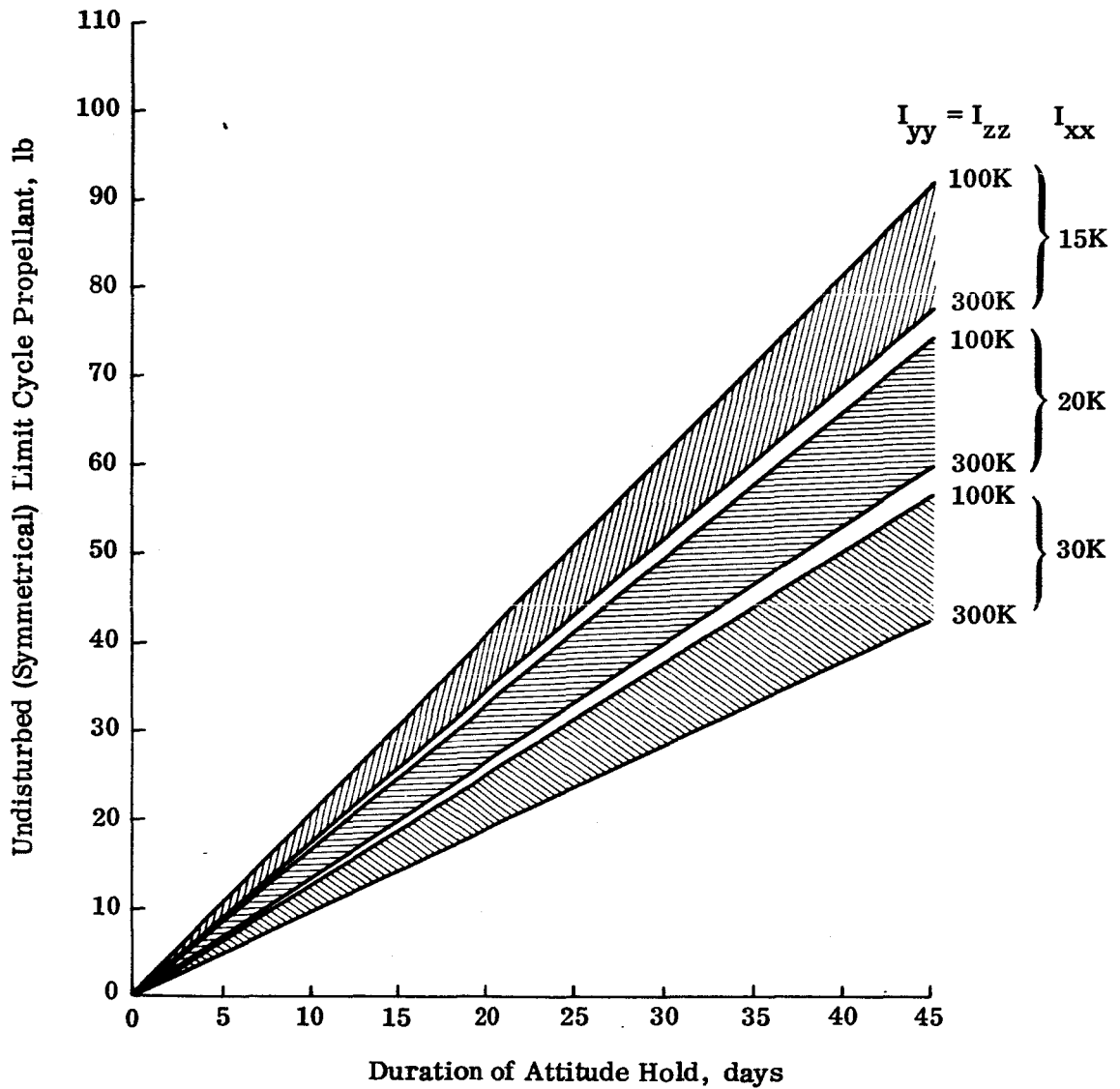


Figure 3.32. Undisturbed Limit Cycle Propellant Requirements at ±5 Degrees Deadband



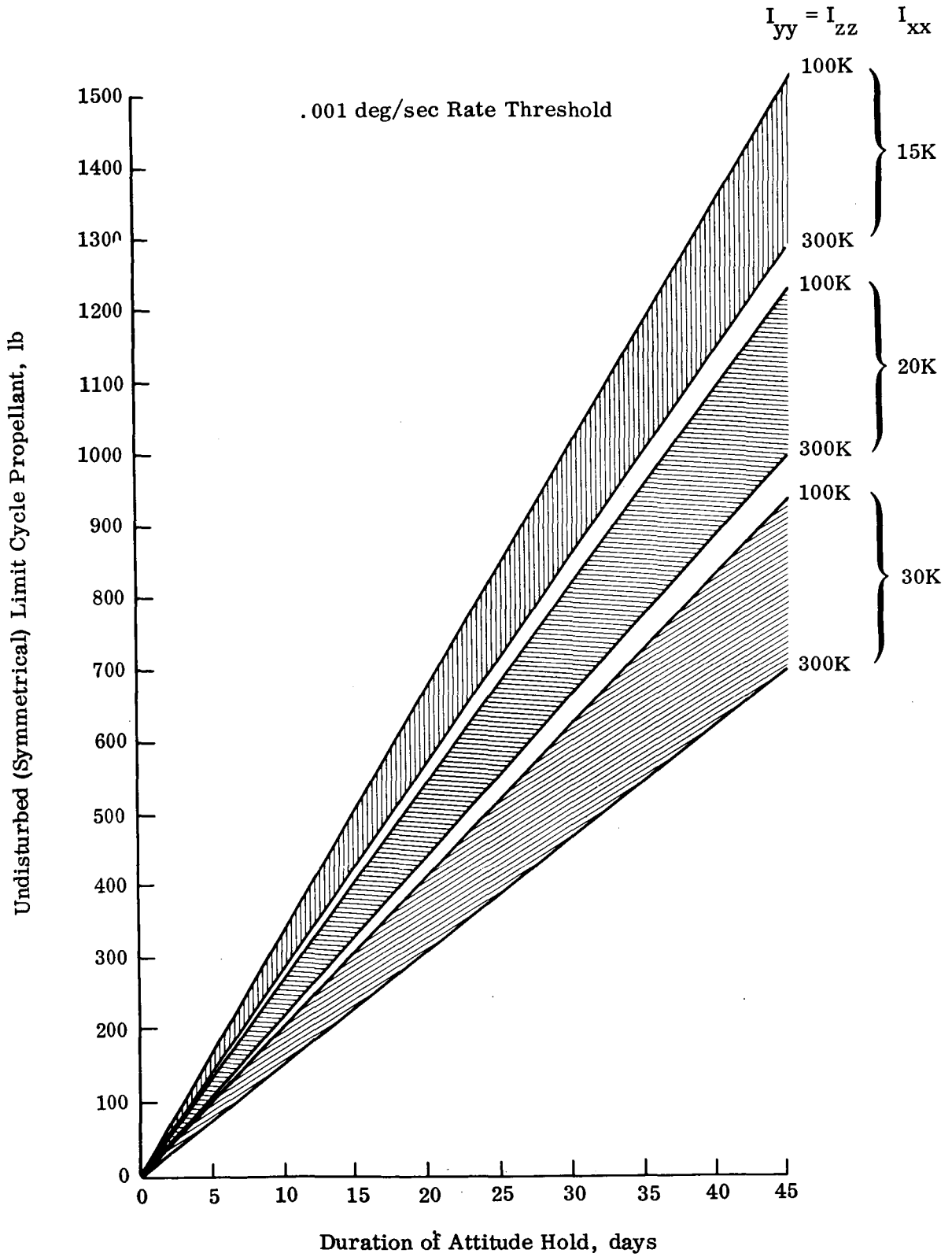


Figure 3.33. Undisturbed Limit Cycle Propellant Requirements at  $\pm 0.3$  Degree Deadband

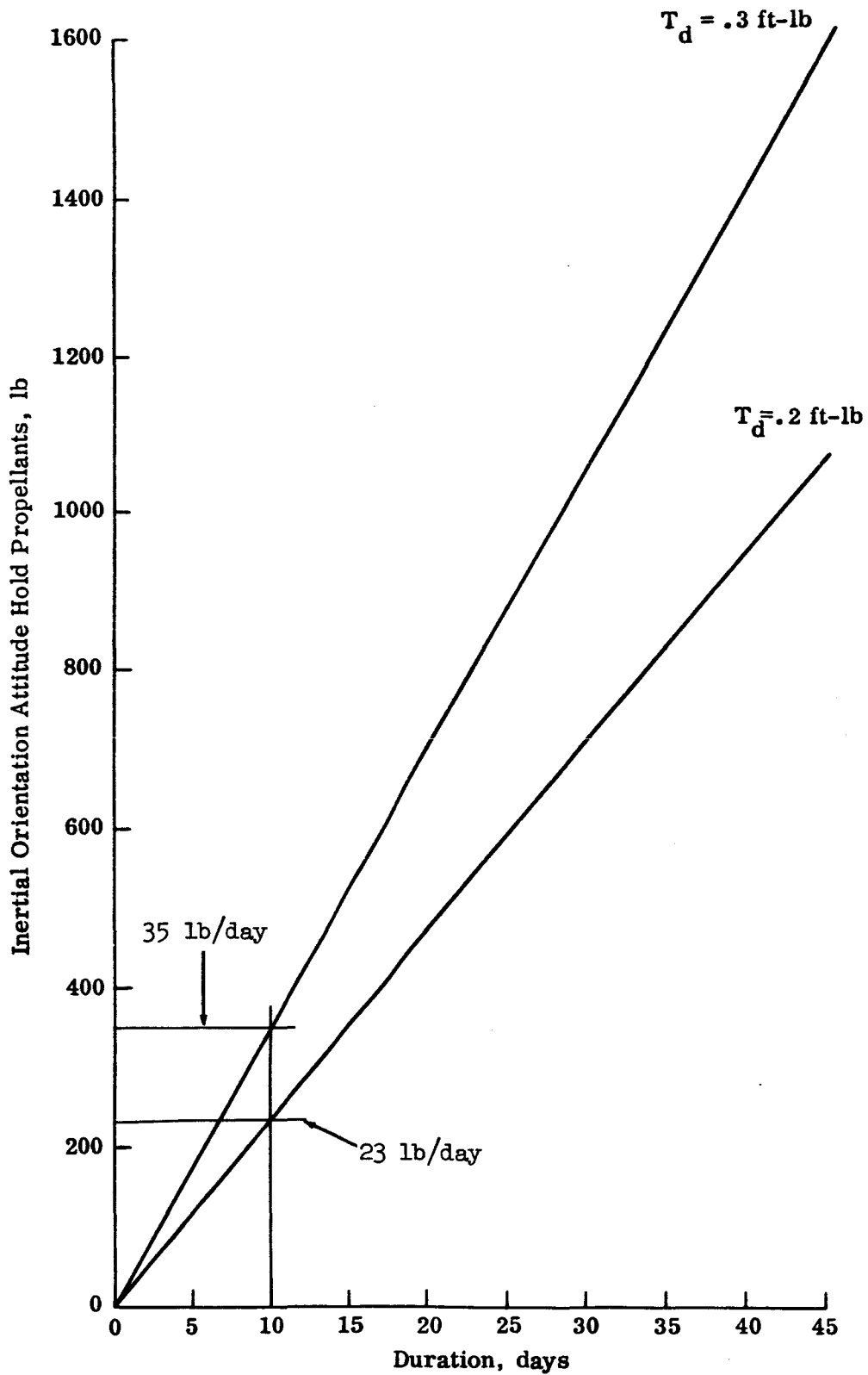


Figure 3.34. Disturbed Limit Cycle Attitude Hold Propellant Requirements

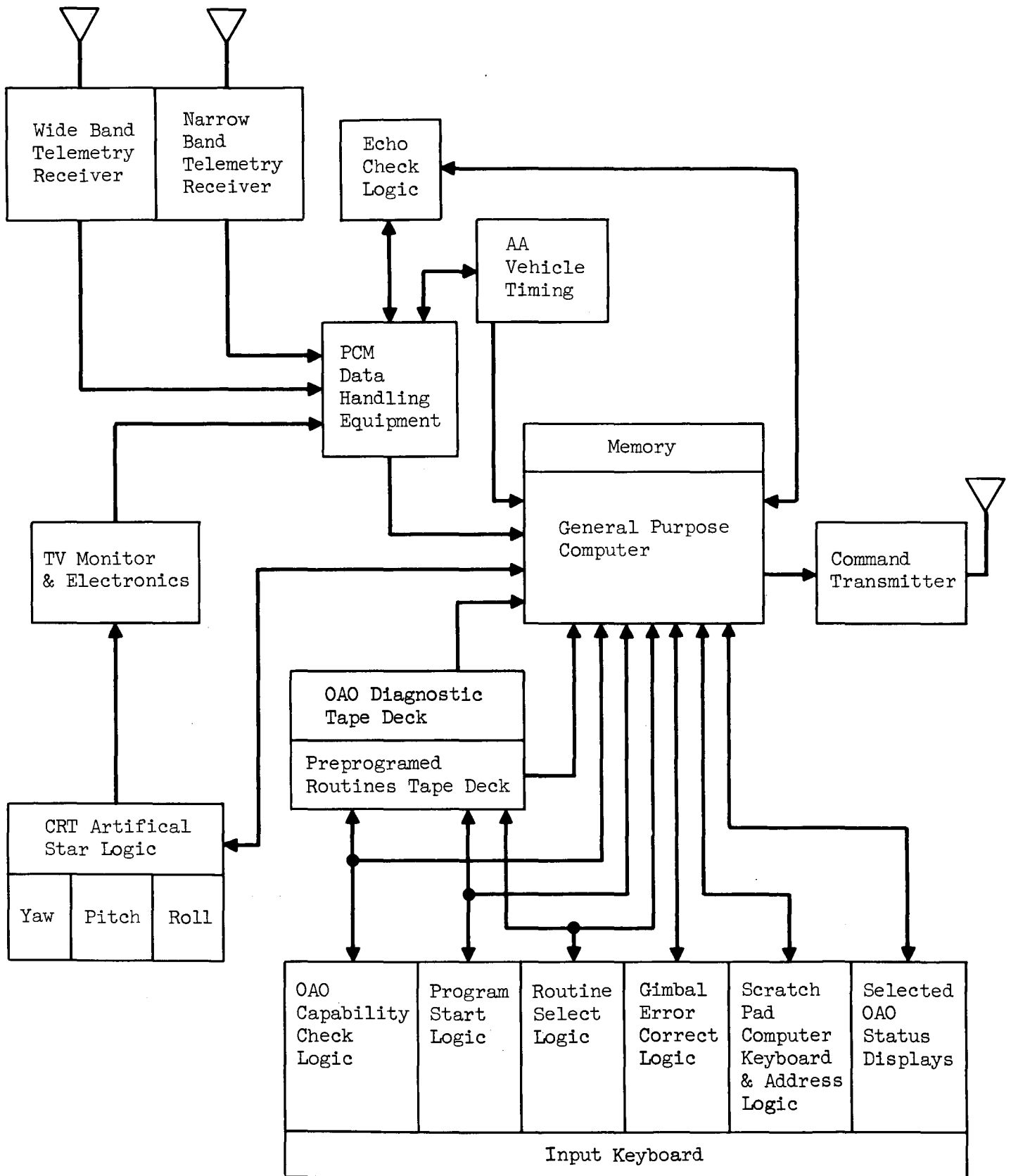


Figure 3.35. Control System Block Diagram

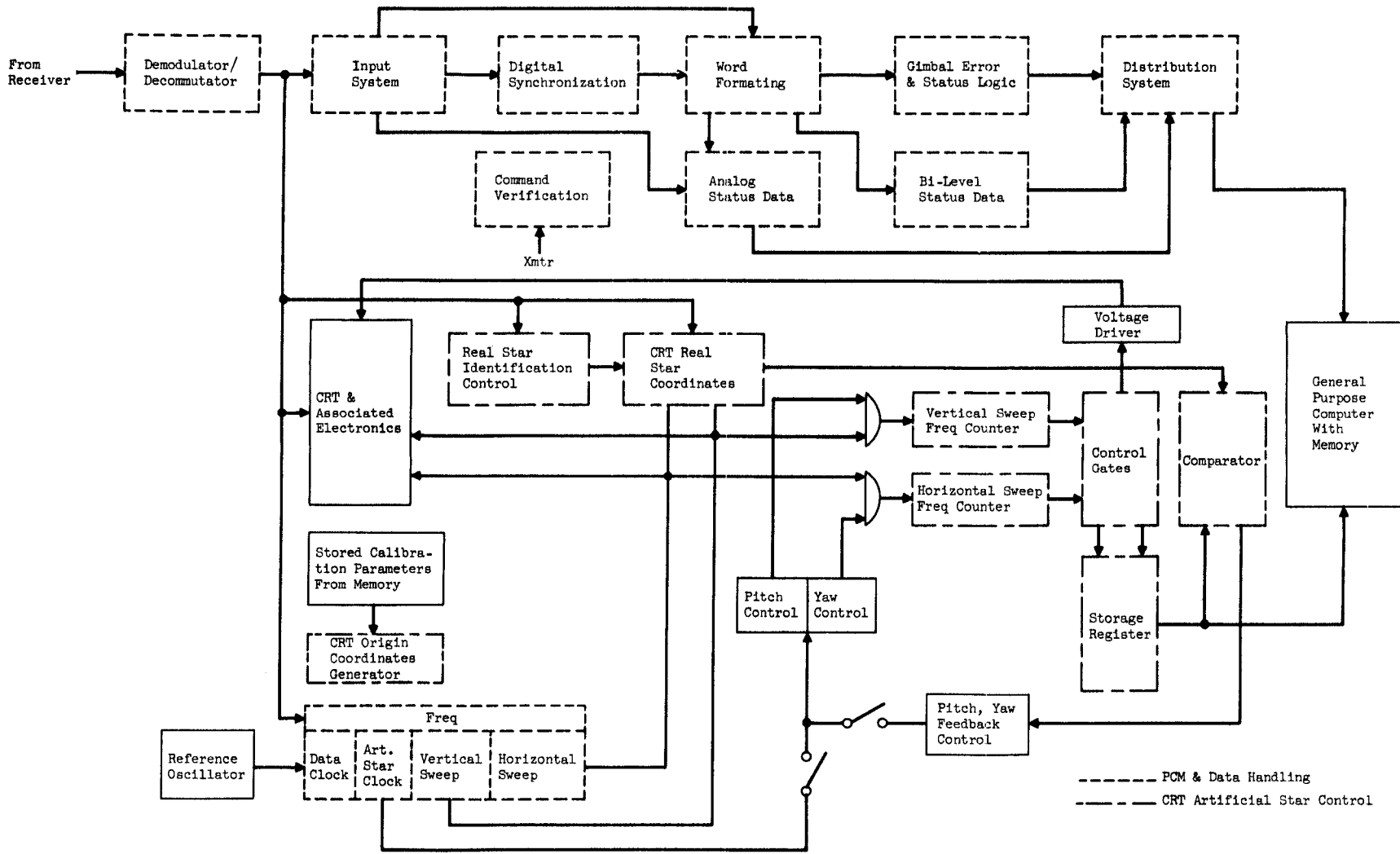


Figure 3.36. Control System Detailed Block Diagram

tolerance limits; provides prediction data based on OAO history, determine which station will interrogate the OAO and its contact time, etc. In order to perform these functions quickly and accurately, the computer requires several stored programs and a large computer memory storage. If control of the OAO is transferred from the ground to the AAP vehicle, a great deal of the information stored and generated is not required since the OAO will be operating in real-time all the time and under constant surveillance. Therefore, the equipment necessary in the AAP vehicle to provide the control required will not be equivalent to a remote ground station.

OAO Control: Two methods of OAO control from the AAP vehicle were considered: (a) complete joy stick control (immediate OAO response to a manual operated instrument in the AAP vehicle) and (b) man/computer programmed control (pre-programmed tape control). During the course of investigating the two methods, it was determined the complete joy stick control method was unacceptable because:

The power profile of the OAO must be known before any maneuver can be executed. Therefore, if the operator "overshot" his target, he may have expended more power than allotted for the maneuver. This could drain the OAO battery system to a point where any existing error or control signals may be removed for a period of time and allow the OAO to begin a random tumble. Once random tumbling occurs the OAO leaves the sun line and the solar paddles receiver energy randomly and what little energy that is received to charge the batteries may be lost because of subsystems left on when power was initially lost. Once this happens, the OAO can be considered a "dead Satellite".

In the process of "steering" the OAO to the desired target, it is quite possible to expend the RC gas which is used to prevent tumbling. This could also shorten the life of the OAO.

To slew from one target to the next is not necessarily accomplished via a straight line between the two points. Therefore, this imposes a requirement upon the AAP operator to calculate the pitch-yaw, yaw-pitch slewing angles, which star tracker can be released from its star to acquire a new guide star, etc.

The most practical method to control the OAO from an AAP vehicle while maintaining man in the loop and still have an operating OAO is via the man/computer program (MACOP) control as illustrated in Figure 3.1. The philosophy of the MACOP control is to provide the AAP operator with a set of taped pre-programmed routines for the entire time the OAO will be under control of the AAP vehicle. This will require an on board general purpose computer with a memory of approximately 8K words. The AAP operator calls up the desired routine

from the computer input keyboard. The computer will then establish the right commands, as instructed from the tape, and determine if the OAO is capable of executing the desired maneuver. If everything is "Go" the computer initiates the proper command.

The computer, based on instructions from the tape in this mode of operation, generates commands to "turn on" the OAO and determines the status of all the subsystems. Once the subsystems have been determined ready to execute a maneuver, the computer calculates the slewing angles and path of travel based on the subsystem status. When the operator observes everything in a "Go" condition, he initiates an execute command and the computer sequences the required commands to the OAO via the command transmitter. This maneuver provides coarse OAO positioning and continues until the target is in the field of the OAO bore sight star tracker, at this point fine pointing is accomplished via the OAO.

In addition to the pre-programmed routines, there will be taped diagnostic routines which will provide isolation of a fault to the subsystem level in the count of a "No Go" indication anywhere along the line.

The wide band and narrow band telemetry receiver, the command transmitter and the general purpose computers are off-the-shelf commercial units and need no further delineation. However, the PCM and data handling and the CRT artificial star logic blocks of Figure 3.35 are further delineated in Figure 3.36. Figure 3.37 shows this block diagram for the PPDS. Table 3-XVIII outlines the functional operations of each block.

If the ground rules permitted time sharing of the AAP lab equipment and integrated the Apollo MSFN into OAO update procedure (MSFN/AAP Lab/OAO), the additional equipment shown in Table 3-XVII may be reduced as shown in Table 3-XIX.

**3.3.3.3 Propulsion** - The task for this phase of the study was to determine the volume and weight of a cold gas system which may be used on the OAO vehicle for adjusting the orbit from 300 n. mi. to 490 n. mi. and to compare the cold gas system to a monopropellant system having the same total impulse of 9200 lb-sec ( $\Delta v \approx 70$  ft/sec for OAO).

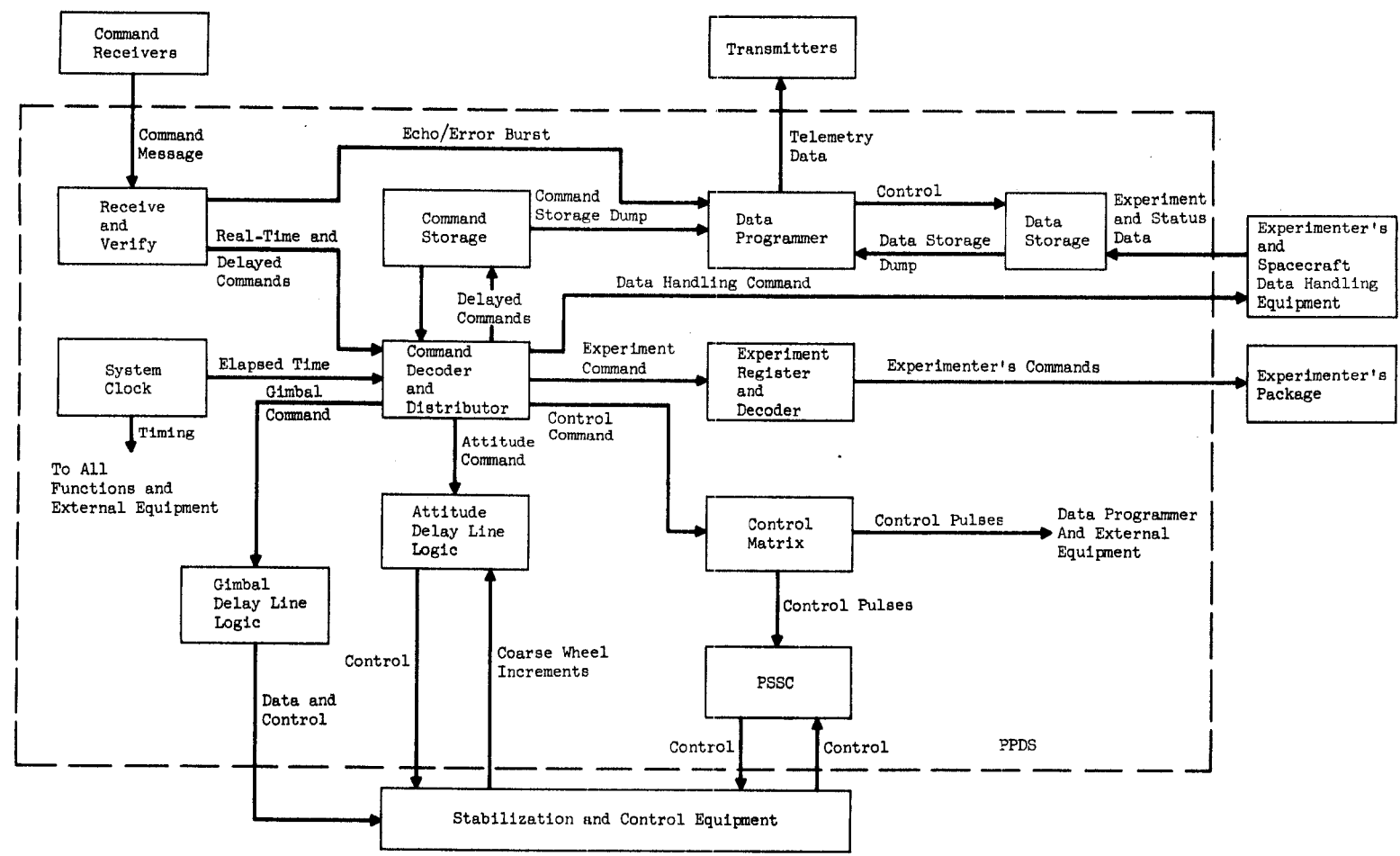
The cold system is at least 3.5 times the weight of the hydrazine monopropellant system. The cold gas  $N_2$  system and the monopropellant hydrazine system have approximately equal reliability and simplicity. Experience to date in deep space with cold gas systems and monopropellant hydrazine systems has demonstrated reliability. The calculations upon which these conclusions are based are contained in Appendix E.

The possible effects of hydrazine engine's exhaust products on the OAO will have to be evaluated.

Based on the inability of the OAO to hold attitude during thrusting due to misalignment and the modifications required to locate and mount the propulsion system, a separate propulsion system for increasing the altitude of operation after manned operation is not recommended.

TABLE XVII  
MAJOR EQUIPMENT CHARACTERISTICS

ITEM	WEIGHT lb.	VOLUME IN <sup>3</sup>	POWER WATTS
Wide Band Telemetry Receiver	14	295	15
Narrow Band Telemetry Receiver	14	295	15
PCM Data Handling Equipment	155		120
General Purpose Computer with Memory	50	812	80
Program Tape Deck	11	388	75
Diagnostic Tape Deck	5	170	50
TV Monitor and Electronics	45	2400	100
Command Transmitter	12	270	10
Input Keyboard and Logic	40	4000	40
Totals	346	8630	505



3-87

Figure 3.37. Simplified PPDS Block Diagram



TABLE 3-XVIII

## FUNCTIONAL CONTROL OPERATIONS (Sheet 1 of 2)

ITEM	FUNCTIONAL DESCRIPTION
1. Demodulator/Decommutator	Extract the data from the RF carrier and decommutate the data as required
2. Input System	Accept & condition PCM and analog data and perform various word separation operations
3. Digital Synchronization	Generates timing signals that synchronize the system operation with the incoming data
4. Word Formating	Perform serial/parallel conversion when necessary, add parity and control bits (word, frame subframe identification)
5. Gimble Error & Status Logic	Decode gimble information from data
6. Analog Status Data	Interpret analog information and condition it for distribution systems
7. Bi-level Status Data	Separate the spacecraft bi-level signals and the experiments bi-level signals and process them for the distribution system.
8. Distribution System	Perform the matching and distribution of the processed PCM data to the required subsystem.
9. Command Verification	Performs echo check on outgoing instructions
10. Frequency Divider	Provide the clock rates for the artificial star logic
11. CRT Origin coordinates generator	Establish a reference for comparing the new star location
12. Real star identification control	Determine where in the video signal the new star occurs
13. CRT Real star coordinates	Establish the new star position on the CRT
14. Pitch/Yaw Control	Provides gating for positioning of the artificial star
15. Vertical sweep frequency counter	Counts the number of cycles gated by the pitch control.
16. Horizontal sweep frequency counter	Count the number of cycles gated by the yaw control
17. Control gates	
18. Storage Register	Hold the vertical & horizontal sweep counts for comparison with real star coordinates

TABLE 3-XVIII

## FUNCTIONAL CONTROL OPERATIONS (Sheet 2 of 2)

ITEM	FUNCTIONAL DESCRIPTION
19. Comparator	Generate error signal for difference between real & artificial star coordinates
20. Pitch/Yaw feedback control	Update pitch/yaw control gating as a function of real star coordinates
21. Voltage driver	Position artificial star as required

TABLE XIX  
MAJOR EQUIPMENT CHARACTERISTICS (TIME SHARING)

ITEM	WEIGHT lb.	VOLUME IN <sup>3</sup>	POWER Watts
Wide band telemetry receiver	14	295	15
Narrow band telemetry receiver	14	295	15
PCM data handling equipment	100		80
CRT Artificial star logic	55		40
General purpose computer with memory (AA lab time shared)	-	-	-
TV monitor and electronics (AA lab time shared)	-	-	-
Command transmitter	12	270	10
Input keyboard & logic	25	2500	20
Totals	220	3360 +	180

#### 4.0 RECOMMENDATIONS FOR FUTURE STUDIES

##### 4.1 INTRODUCTION

In carrying out Project Apollo, the objectives of NASA are to land two men on the lunar surface, conduct limited observations and analyses of the lunar surface, and return the crew to earth. The Apollo Application Program (AAP) would also utilize the Apollo hardware for extended lunar surface explorations, lunar orbital survey missions, and for earth orbiting missions. For the earth orbiting missions, one of the primary categories of experiments is astronomical observations. The Orbiting Astronomical Observatory (OAO) has been developed to perform unmanned astronomical observations. The association of the OAO with AAP is an extension of the philosophy of making maximum use of developed hardware.

The purpose of this study was to identify the design criteria and benefits of associating the OAO carrying an Advanced Experiment Package (APEP) with AAP. These have been described in the previous sections. To further support the effort, additional studies have been identified. These studies have been grouped into three major areas:

- Mission Analysis
- Systems Analysis
- Preliminary Design Studies

##### 4.2 MISSION ANALYSIS

The main purpose of this study is to provide data to be used to determine the "best way" to accomplish the mission goals tentatively identified as follows:

Astronomical observations in the visible and ultraviolet spectrum using the APEP in the OAO.

1972 launch.

Evaluate man's role in astronomical observations including deployment of critical optical elements, maintenance and repair, control and diagnosis.

Establishment of stepping stones to "larger" and more "sophisticated" orbiting observatories.

A number of mission alternatives should be evaluated:

Determination of the optimal combination of spacecrafts (CSM, LEM Lab and OAO) and launch vehicles (SIB and Atlas Agena D) for a 300 n. mi. altitude. For example, performance of the mission without a LEM Lab would be attractive

based on the cost savings in using only one SIB. Similarly, the launching of an OAO separately on an Atlas-Agena D with a follow-up launch after 6 months of an AAP spacecraft and a rendezvous maneuver might improve the OAO probability of mission success for a one year mission duration.

Comparison of operation at 300 n. mi. versus synchronous altitude. Operation at synchronous altitude results in a continuous communication capability, considerably less occultation of the celestial sphere by the earth and smaller effect of earth albedo. However, the problems of the radiation environment, the near continuous sun bathing, and increased communication power requirements should be further studied.

Determination of mode of operation. The feasibility of operating the OAO in a gimbal mode with fine pointing capability provided by a free floating experiment was proven in this study. A comparison between the free mode and the gimbal mode should be made. The free mode would eliminate some of the constraints, imposed by the gimbal mode, to the operation of the OAO. It would require a rendezvous maneuver of the AAP space station at the cost of approximately one pound of fuel per maneuver. A hard docking maneuver could be eliminated by using an Astronaut Maneuvering Unit (AMU) which had the capability of locking on to the OAO and providing attitude control of the OAO during film removal or insertion, modification and maintenance.

#### 4.3 SYSTEMS ANALYSIS

The systems analysis studies described in the following paragraphs are recommended to explore in greater depth various implementation techniques and environmental constraints identified during the study.

**OAO Control and Diagnostic System** - A control and diagnostic capability on-board the manned spacecraft for the OAO and the experiment is desirable to minimize the time delay between successive orbit contacts and for use in case of failure in the power/communication subsystems of the OAO. The study should review the control and diagnostic capability of the ground control station and identify minimum and maximum requirements for the on-board equipments. Umbilical requirements and test point requirements for diagnosis in the presence of power/communication failures should also be defined.

**Occultation Effects** - A study is recommended to define the effect on the experiment, the star trackers, and the solar paddles of the occultation of the celestial sphere as a

consequence of the proximity of the manned spacecraft and the gimbal structure.

Radiation Effect on Film - The necessity for daily EVA's to insert and remove film to minimize the effect of the South Atlantic anomaly, could be obviated if the environment at the time of launch could be protected against by the choice of film or the use of shielding. Therefore, this study should result in a better prediction of the anticipated environment, an evaluation of the radiation environment on film and an identification of the shielding requirements.

Thermal Analysis - A study is recommended to evaluate the affect on the passive thermal control technique due to proximity of the manned spacecraft. It is also recognized that the thermal control of the experiment's optics is a very critical area and an integrated experimenter/OAO study is also recommended.

Sun/Earth Shield - To minimize thermal gradients and background illumination into the experimental tube, an additional shield extending along the optical axis at the perimeter of the OAO has been suggested. A study should be performed to determine the increased aerodynamic torque disturbances and new requirements for mass balance booms caused by the use of the proposed shield. In addition, the occultation of the sun sensors and the star tracker by this shield should also be evaluated.

#### 4.4 PRELIMINARY DESIGN

To assure feasibility of this mission, the following preliminary design studies are recommended:

Gimbal Design - A two axis "soft" gimbal structure, identified as a requirement to minimize the spacecraft induced torque disturbances and translations, should be designed.

OAO Mounting Structure - To accomplish an integral launch the structural system for mounting the OAO to the LEM descent stage should be designed. For a launch without the LEM Lab, OAO support structure to the SIVB stage should be designed. A docking attachment must be included to provide for withdrawal of the OAO from the SIVB and transfer of the spacecraft on the Command Module from the 80 mile parking orbit to the 300 nautical mile operating orbit.

OAO Modifications - The modifications for supporting the APEP and for maintenance of the OAO in orbit should be designed. The soft gimbals and mounts should be designed.

REFERENCES

- <sup>1</sup>GAEC, NASA Contract No. NASW-1143, The OAO in Association with a Manned Space Station, June 1965.
- <sup>2</sup>GAEC, NASA Contract No. NAS5-3124, Repair in Orbit of the OAO, April 1963.
- <sup>3</sup>GAEC, NASA Contract No. NAS9-4983, Apollo Extension Systems-Lunar Excursion Module, December 1965.
- <sup>4</sup>Zee, C-H, Trajectories of Satellites Under the Influence of Air Drag, Progress in Astronautics and Aeronautics, Vol. 26, pp. 101-112, 1964.
- <sup>5</sup>Poetzold, H.K. Solar Activity Effects on the Upper Atmosphere After Satellite Observations, Institute of Geophysics and Meteorology, University of Cologne, 1962.
- <sup>6</sup>U.S. Standard Atmosphere, 1962; Sponsored by NASA, USAF, U.S. Weather Bureau.
- <sup>7</sup>Van Allen, J.A., A Brief Note on the Radiation Belts of the Earth, Paper A-1, pp. 1-11, Proceedings of the Symposium on the Protection Against Radiation Hazards in Space, TID 7652, Gatlingburg, Tennessee, November 1962.
- <sup>8</sup>Pizzella, G., Laughlin, C.D., and O'Brien, B.J., Note on the Electron Energy Spectrum in the Inner Van Allen Belt, Journal of Geophysical Research, Vol. 67, No. 9, pp. 3281-3287, August 1962.
- <sup>9</sup>NASA LEM for AES (AAP) Blue Book, June 1965.
- <sup>10</sup>Proise, M., The Effects of Man Motions on the Precision Point Performance of a Gimballed Telescope Mounted on a LEM/CSM Vehicle. GCM-65-13, November 1965.

## 5.0 PHOTOGRAPHIC SYSTEMS IN SPACE ENVIRONMENT

### 5.1 INTRODUCTION

The use of a photographic data recording subsystem is included in this study for two reasons. Photographic systems offer a larger field coverage than the vidicon and afford the possibility of extending the range of the spectrometer coverage down to 800Å whereas the vidicon coverage diminishes rapidly beyond 1100Å. The presence of an astronaut who is trained in engineering or astronomy affords in-orbit analysis and decision-making capability after the photographic material is processed and examined. Subsidiary advantages made possible by the use of photographic recording are larger field coverage, higher resolution of low-contrast objects, continued operation in the event of TV data link failure (or if power available becomes marginal), and increased knowledge of potentialities of photographic systems in larger orbiting telescopes.

These advantages will not be realized without solving certain problems, however. Foremost among these is the requirement to shield the photographic media from the effects of Van Allen Belt radiation. Not studied here but perhaps equally important are the effects of Van Allen Belt radiation on the SEC Vidicon. The effect of the radiation environment on the photographic system are discussed in parts 5.4 and 5.6 of this section.

Also included in this section is an exploration of the available photographic systems, from the standpoint of the spectral coverage desired and the resolution capabilities of the optical system. Recommendations for photographic systems to be used with the spectrometer and image camera are made.

### 5.2 SCOPE OF PHOTSENSITIVE RECORDING MATERIALS STUDY

The consideration of permanent recording materials will be limited to Eastman Kodak silver halide systems in this report. Silver halide systems have already enjoyed considerable success as recording medium for outer space applications. A search for other systems, which might functionally replace silver halide systems and possibly afford performance improvements, may be conducted in a future phase of this program.

No photographic medium is known which competes with silver halides for sensitivity, although many have higher resolving powers.<sup>1</sup> However, the sensitivity of silver halide systems to Van Allen Belt radiation may force a search for other recording media.

### 5.3 SIMPLIFIED NATURE OF SILVER HALIDE PHOTOCHEMICAL REACTIONS<sup>2</sup>

The following is a discussion of the mechanism by which radiation exposures lead to silver deposits in the photographic process. The final step of image production in the silver halide photographic process consists of



reducing silver ions to metallic silver by a developing solution via the reaction,



The metallic silver deposits form the opaque part of the recording (or negative) while the remaining constituents of the emulsion (after it has been processed) form the transparent part of the recording.

Most unprocessed photographic emulsions consist mainly of silver halide crystals, sensitizing dyes, and gelatin (which keeps the other components colloiddally suspended). At normal temperatures some of the silver ions in the silver halide crystal lattice are bounced out of their positions by molecular kinetic energy and may be regarded to behave like a "gas" of ions wandering about with thermal energies within the lattice structure.

This "gas" of ions plays an important role in the deposit of metallic silver. At low temperature extremes the molecular kinetic energies are too low to liberate silver ions from the lattice structure and the "gas" of ions is virtually nonexistent.

The primary function of light in the production of metallic silver deposits (which constitute the image) is to generate free electrons. These free electrons drift about the lattice structure until they are captured by a loose silver ion or until they find a silver deposit or a silver sulfide impurity, in which they tend to become trapped. The electric field produced by this negatively charged deposit (or impurity) attracts loose silver atoms. Under low temperature extremes there is a shortage of free silver ions and the growth of silver deposits is inhibited. Although the generation of free electrons via the photoelectric effect still proceeds under low temperatures, the electrons are repelled by the existing negatively charged silver deposits, thus making their future union with a silver ion unlikely even when the emulsion is later returned to normal temperatures.

The role of the sensitizing dyes is to absorb light quanta at wavelengths not easily absorbed by silver halides. The energy absorbed by the dyes is transferred to the silver halides by thermal means. Silver halides are photosensitive primarily to ultraviolet light; but, with an appropriate choice of sensitizing dyes, the emulsion can be made equally photosensitive in a combination of spectral regions. This is how emulsions are made panchromatic.

The production of silver deposits solely by light exposures is a very slow process because it requires at least one photon to produce at least one free electron for each silver atom deposited; and there can be light absorption inefficiencies as well as other inefficiencies along the way. For this reason, the emulsion is attacked by a reducing solution, or developer, for a controlled period of time. If the developing time is sufficiently long, all the silver halide in even an unexposed emulsion can be reduced to silver deposits.

In emulsion areas exposed by light, the larger silver deposits in exposed silver halide grains serve as more attractive traps for the free electrons liberated by the reduction process of the developer. Thus the attraction of loose silver ions to the silver deposits and their conversion into metallic silver is accelerated. Because the emulsion transmittance depends on the fraction of its silver deposited, the reduction process (development) is intentionally stopped before most of the unexposed (by light) silver halide grains have been reduced to silver. Thus, a degree of opacity dependent on the light exposure is produced in the emulsion and unexposed emulsion areas are very transparent while exposed areas take on an opacity which increases with exposure. This explains why the adjustment of development time to exposure is a common practice in photographic processing.

The increase in graininess with development time can be explained by the nonlinear increase or acceleration with time of the reduction process within a single silver halide grain. This acceleration exaggerates small differences between adjacent unexposed silver halide grains so that one may be almost fully reduced while the reduction process in the adjacent one has only begun.

The fixer arrests the reduction process, absorbs the unreduced silver halide and sensitizing dyes from the emulsion which causes transparency in unexposed areas.

#### 5.4 PHOTOGRAPHIC EMULSION FOGGING BY VAN ALLEN BELT RADIATION<sup>3,4</sup>

A solution to the problem of radiation damage to film is reduced to one of design of adequate shielding. Since the protection needed varies with the optical performance requirements imposed on the film, radiation protection must consider vulnerability of photographic film as well as sources of radiation. In some applications, for example, the increase in graininess will impose a greater restriction on the permissible radiation exposure than will the increase in density.

The high energy trapped protons appear to present the most serious hazard with respect to photographic film. Depending on the shield thickness, protons having energies below a given value will be completely stopped while higher energy protons will be degraded in energy as they traverse the shield. To provide adequate shielding, one must not only consider the exposure dose but also, because of the spectral sensitivity of the photographic film, the emergent proton spectrum. For example, for sufficiently low specific ionization the grains will not develop whereas for sufficiently high specific ionization all grains along the path of the particle are developable and the grain density reaches a saturation value independent of particle energy. For thick shields ( $> 20 \text{ gm/cm}^2$ ) the production of secondary particles must also be considered.

The most frequent result of the interaction between high energy particles and matter is the liberation of electrons. When a charged particle traverses matter, it can produce large electric and magnetic field fluctuations

in the vicinity of its path. These field fluctuations can, in turn, cause considerable excitation and ionization in nearby molecules.

The electrons liberated by this interaction (between fast particles and a photographic emulsion) can find their way to silver deposit nuclei within silver halide crystals. Also, the molecular excitations produced by fast particles can tear a larger than usual supply of silver ions loose from their crystal lattice positions. With this increase in liberated electrons and loose silver ions, the size of silver deposits is increased within the silver halide crystals hit by fast particles. It is not surprising, then, that continued exposure to radiation from the Van Allen Belt can fog films.

The proportional silver halide content is of great importance in judging the sensitivity of a given emulsion to fast charged particles. This is because

- a. A relatively high number of electrons per unit volume makes silver halides more vulnerable to excitation by charged particles than other emulsion components with lower electron densities.
- b. Larger silver halide concentrations provide more silver ions to be knocked out of their crystal lattice positions by charged particles.

Larger loose silver ion concentrations in the presence of larger free electron concentrations build silver deposits. Sensitizing dyes, although more sensitive than silver halides to light in certain spectral regions, are less sensitive than silver halides to charged particles. The reciprocal of the silver halide concentration is a factor of merit by which different films can be compared for resistance to Van Allen Belt radiation fogging.

#### 5.5 BALANCING THE RESOLUTION, EXPOSURE, AND SPECTRAL SENSITIVITY REQUIREMENTS OF PHOTOGRAPHIC MATERIALS

According to the Rayleigh criterion for the resolution of point sources, the angular resolving power ( $\theta$ ) of an optical system is given by

$$\theta = 1.22 \frac{\lambda}{D} \quad (5-1)$$

where  $\lambda$  is the wavelength of light and where  $D$  is the diameter of the optical system entrance pupil. The linear separation ( $\delta$ ) of two star images in the focal plane (which are separated by the angle,  $\theta$ , in object space) is obtained by multiplying equation (5-1) by focal length ( $f$ ) as follows:

$$\begin{aligned} \delta &= f\theta \\ \delta &= 1.22\lambda \frac{f}{D} = 1.22\lambda F \end{aligned} \quad (5-2)$$

where,  $F = \frac{f}{D} = f\text{-number}$ .

The Rayleigh criterion for the resolution of line images is similarly given by  $\theta = \lambda/D$  and  $\delta = \lambda F$ . Thus, the approximate number of lines per millimeter resolving power at the image plane is given by,

$$\frac{1}{\delta} = \frac{1}{\lambda F} \quad (5-3)$$

The telescope f-number is 200 and its spectral range is the 4000Å band from 2000Å to 6000Å. Future designs may permit an all-reflective microscope which would afford coverage down to 800Å. Substituting these values into equation (5-3) gives a resolving power of  $\frac{1}{1.22 \times 0.4 \times 10^{-3} \times 200}$ , or about 10 l/mm. Because the limiting resolving power of the telescope is somewhat higher than the Rayleigh criterion resolving power, and because the emulsion should not limit the system resolution, at least 20 l/mm resolving power is required in recording the telescope output--preferably even under low contrast operating conditions. Low contrast resolving powers exceeding 20 l/mm should not be accepted for the telescope operational mode at the expense of light sensitivity. Although the resolving power design goal for the spectrometer calls for more than a 50% modulation transfer function at 20 l/mm (which is sufficient to obtain a system essentially limited by the vidicon), it is hoped that a higher resolving power will eventually be achieved in order to utilize the higher resolving powers attainable with photographic emulsions.

Exposure time may be long, frequently exceeding 2000 seconds, in order to make recordings of dim celestial details at f/200 with the telescope, or of weak spectral lines at f/20 with the spectrometer. Because the sensitivity to light of most emulsions falls off quite rapidly as exposure times exceed ten seconds (Table 5-I, A1), the use of emulsions specially treated against reciprocity failure at long exposures is highly desirable. Emulsion cooling is another way of arresting reciprocity failure, since low temperatures shift reciprocity failure properties toward long exposure.<sup>5</sup> This technique will not be explored at this time.

The required spectral ranges of operation are 800Å to 3000Å for the spectrometer and 2000Å to 6000Å for the telescope. The gelatin present in ordinary photographic emulsions is highly light-absorbing below about 2200Å (Table 5-I, A4). Two methods of sensitizing emulsions below this wavelength are:

- a) Using emulsions with practically no gelatin. (These are called "Schumann" emulsions).
- b) Coating the emulsion with a fluorescent substance, which converts the light into longer wavelengths which expose the emulsion.

These categories of Kodak emulsions will be examined for use with the instrument package: plates and films (103a and IIa), UV coated spectroscopic plates and films (103a and IIa), and "Schumann" emulsions (SWR, DC-3, SC-5, and SC-7). Advantages and disadvantages of these emulsion categories are presented in Tables 5-I, 5-II, and 5-III, with comments and explanations of each advantage and disadvantage given after each table.

TABLE 5-I

ADVANTAGES AND DISADVANTAGES OF SPECTROSCOPIC PLATES  
AND FILMS (103a and 11a)

<u>Advantages</u>	<u>Disadvantages</u>
A1) Relatively low reciprocity failure	A6) Relatively high sensitivity to Van Allen Belt radiation
A2) Relatively high abrasion tolerance	A7) Diminishing spectral sensitivity below 2500Å
A3) Available in quite convenient forms	A8) Bimat processing not recommended
A4) Good spectral sensitivity available between 2500Å and 7000Å	A9) Should not be in hard vacuum environment for long time periods
A5) Acceptable resolving power	

A1) At present 103a and IIa are the only Kodak emulsions specially designed for long exposure times. Most other emulsions have considerable reciprocity failure at exposure times above ten seconds. (See reciprocity characteristics of 103, 103a, II, and IIa plates given on page 18d of the handbook, "Kodak Plates and Films for Science and Industry." See, also, the reciprocity failure curves for various aerial films in the "Manual of Physical Properties of Kodak Aerial and Special Sensitized Materials.")

A2) 103a and IIa are normal emulsions which are protected by suspension in gelatin. By comparison, "Schumann" emulsions are highly abrasion sensitive because they have almost no gelatin. See C6.

A3) 103a and IIa are supplied on a large variety of plates and on 35mm and 70mm film. Although some of the IIa spectral sensitivity classes are not normally supplied in film, discussion with staff members of Eastman Kodak, Rochester, New York, indicates that some might be made on special order. (Ref. "Kodak Plates and Films" handbook.)

A4) Spectral sensitivity curves for 103 and 103a in the handbook, "Kodak Plates and Films for Science and Industry," show that about 0.03 ergs per square centimeter are required to produce a density of 0.6 above gross fog in 103a film between 2500Å and 7000Å. Below 2200Å, gelatin is highly light absorbing. (See "UV Sensitization of Photographic Plates with Sodium Salicylate" by Rinda Allison and Jay Burns, JOSA, May, 1965, Volume 55, page 574.) Beyond 7000Å good emulsions sensitivity is not available for 103a. From page 18d of the "Kodak Plates and Films" handbook, IIa has practically the same sensitivity as 103a. But because, from page 22d of the handbook, IIa is not available in the U spectral sensitivity class, the high spectral sensitivity range of IIa is 2500Å to about 6700Å. The telescope spectral range of interest is 2000Å to 6000Å.

Multiple Pages Missing from Available  
Version

TABLE 5-III

ADVANTAGES AND DISADVANTAGES OF "SCHUMANN" EMULSIONS  
(SWR, DC-3, SC-5, AND SC-7)

<u>Advantages</u>	<u>Disadvantages</u>
C1) Relatively low sensitivity to Van Allen Belt radiation	C4) Resolving power may be slightly lower than desired
C2) Higher tolerance to vacuum	C5) Reciprocity failure at long exposures
C3) Relatively high sensitivity in UV	C6) Very low abrasion tolerance. Handling is very difficult. Bimat processing not recommended.
	C7) Available in very limited forms.

C1) During the March 14 visit of the Eastman Kodak research laboratories by Perkin-Elmer, it was found that because silver halides are highly absorbing in the UV, all UV light absorption takes place in a very thin surface emulsion layer. For this reason "Schumann" emulsions are very thin layers of silver halide with a very low total silver content. Part 5.4 of this section discusses the increase in sensitivity to Van Allen Belt radiation caused by a high total silver content. Staff members of Eastman Kodak supplied information about thin emulsion properties of SWR, DC-3, SC-5, and SC-7.

C2) Because of the thinness of "Schumann" emulsions (see item C1), curling and shrinkage problems are less severe than in the case of ordinary emulsions. Soaking in water for a few seconds prior to development is still advisable in order to preclude fogging.

C3) The following data were obtained from the Kodak research laboratories:

DC-3 Type: "Medium grain size emulsions giving good definition and high contrast. UV sensitivity is close to that of SWR film. Sensitivity to visible light is slightly higher."

SC-5 Type: "High sensitivity (about 8 times that of DC-3 film above 170A). Fills a need for very high sensitivity requirements at an acceptable graininess."

SC-7 Type: "Very high sensitivity (at least 10 times that of DC-3 above 170A). Average contrast. Long development."

A relative comparison of SWR film and 103-0, coated UV plates is given on page 10d of the "Kodak Plates and Films" handbook. The comparison shows SWR to be more sensitive below about 1200Å and 103-0 UV plates to be more sensitive above 1200Å.

C4) No formally published resolving power data was found for "Schumann" emulsions; however, some pertinent data was obtained from some of Perkin-Elmer's work connected with Aerobee sounding rocket probes during the past two years. 20-micron-diameter high-density spot images were produced on SWR film in the laboratory. This suggests a high contrast resolving power of about 50  $\mu$ /mm for SWR. Also, 10-micron-diameter line images were produced in flight on SC-5 film from star track images. This suggests approximately 100  $\mu$ /mm high contrast resolving power for SC-5. GAEC measured the resolving power of SC-7 film at roughly 50 cycles per millimeter. Van Allen Belt radiation may increase granularity and reduce resolving power (see part 5.6). Spectrometer resolution demands are discussed in part 5.5 and exceed the resolution demands of the telescope.

C5) Kodak "Schumann" emulsions are not specially treated against reciprocity failure at long exposure times like 103a and IIa. If reciprocity failure characteristics of these "Schumann" emulsions turn out to be similar to most films (item A1, Table 5-I), then the sensitivity advantage of "Schumann" emulsions over UV coated 103a and IIa may disappear at long exposure times. According to Fowler<sup>13</sup>, the reciprocity failure of SWR and SC-5 should be insignificant. But according to Kodak, an indication of the reciprocity failure characteristics of SWR appears in the following table:

RECIPROCITY FAILURE OF SWR

<u>Exposure Time</u>	<u>Ixt</u> <u>(Relative)</u>	<u>Density</u>	<u>Density</u> <u>Decrease</u>
1/2 sec	64	0.52	0.28
64 sec	64	0.24	
1 sec	128	0.72	0.32
128 sec	128	0.40	

Reciprocity failure of SWR at 2000 seconds exposure time is likely to be much more pronounced than the failure shown in the table. The values in the table were deduced from unpublished "Time Scale Curves on SWR Film" obtained from Eastman Kodak during a visit by Perkin-Elmer in August, 1963. The investigation of reciprocity failure curve shifts toward long exposures with temperature reductions might be a very important step in deciding whether "Schumann" emulsions should be used rather than UV coated IIa films or plates.

C6) Low abrasion tolerance exists because of the absence of gelatin in "Schumann" emulsions. Bimat processing was discouraged by Kodak for this reason during the recent Perkin-Elmer visit.



C7) SWR is available only on plates and on 35mm by 25 foot 3 inch unperforated rolls. Ref: "Kodak Plates and Films" handbook, pp. 3d and 23d. DC-3, SC-5, and SC-7 are supplied only in unperforated 35mm by 180mm film strips.

The use of these films to record the spectrometer output will require bulky holding devices in addition to those used to handle the emulsions which record the direct telescope imagery. The design of separate processing equipment may also be required.

## 5.6 RADIATION ENVIRONMENT

High energy particles and the accompanying secondary emission not only fog film, but also increase granularity by exposing individual film grains in a random fashion. This increase in granularity is more severe than the increase normally associated with higher densities. A reduction in resolving power should, therefore, be expected with increased fast particle exposures. The use of IIA film is, therefore, recommended because it has a higher resolving power than 103a film.

The rise in total fog with particle exposures decreases the gamma of the characteristic curve. (See Figure 5.1.)<sup>7</sup> This gamma reduction, in turn decreases contrast and reduces the relative sensitivity of the film. (Relative sensitivity is the reciprocal of exposure in  $\text{ergs/cm}^2$  required to produce a density of 0.6 above gross fog.)

Figure 5.2 is a plot (for two films) of relative graininess and total fog as a function of exposure in roentgens of 1 mev gamma rays.<sup>7</sup> Note that, regardless of the gamma ray exposure, graininess was measured at a 0.80 density above gross fog, so that the indicated graininess increases with gamma ray exposure is independent of graininess increases due to density increases alone. The required 0.80 density was attained by the superposition of gamma ray exposure and exposures by 3000°K illumination.

According to Figure 5.2, the inherent film graininess is a rough measure of film sensitivity to gamma rays. The same conclusion can be reached for other films.<sup>8,9,10</sup> Type ID<sub>2</sub> Spectroscopic film was chosen for presentation in Figure 5.1 because its reaction to fast particles is likely to be greater than that of IIA-D spectroscopic film, for which suitable data was not found. (Although IIA-D is not normally available in film, discussion with staff members of Eastman Kodak, Rochester, New York, indicates that some might be made on special order). Under standard developments, the granularity of ID<sub>2</sub> film is about 0.14, whereas the granularity of IIA-D film is about 0.076.<sup>11</sup> As a result of a visit by Perkin-Elmer to Eastman Kodak, Kodak will try to obtain suitable data for 103a and IIA films.

Figure 5.3 gives a very crude relationship between granularity and resolving power obtained by comparing the granularity data of various Kodak aerial films. The resolving power in Figure 5.3 falls off at the approximate rate of 0.64  $\ell/\text{mm}$  per 0.001 increase in granularity at low contrast

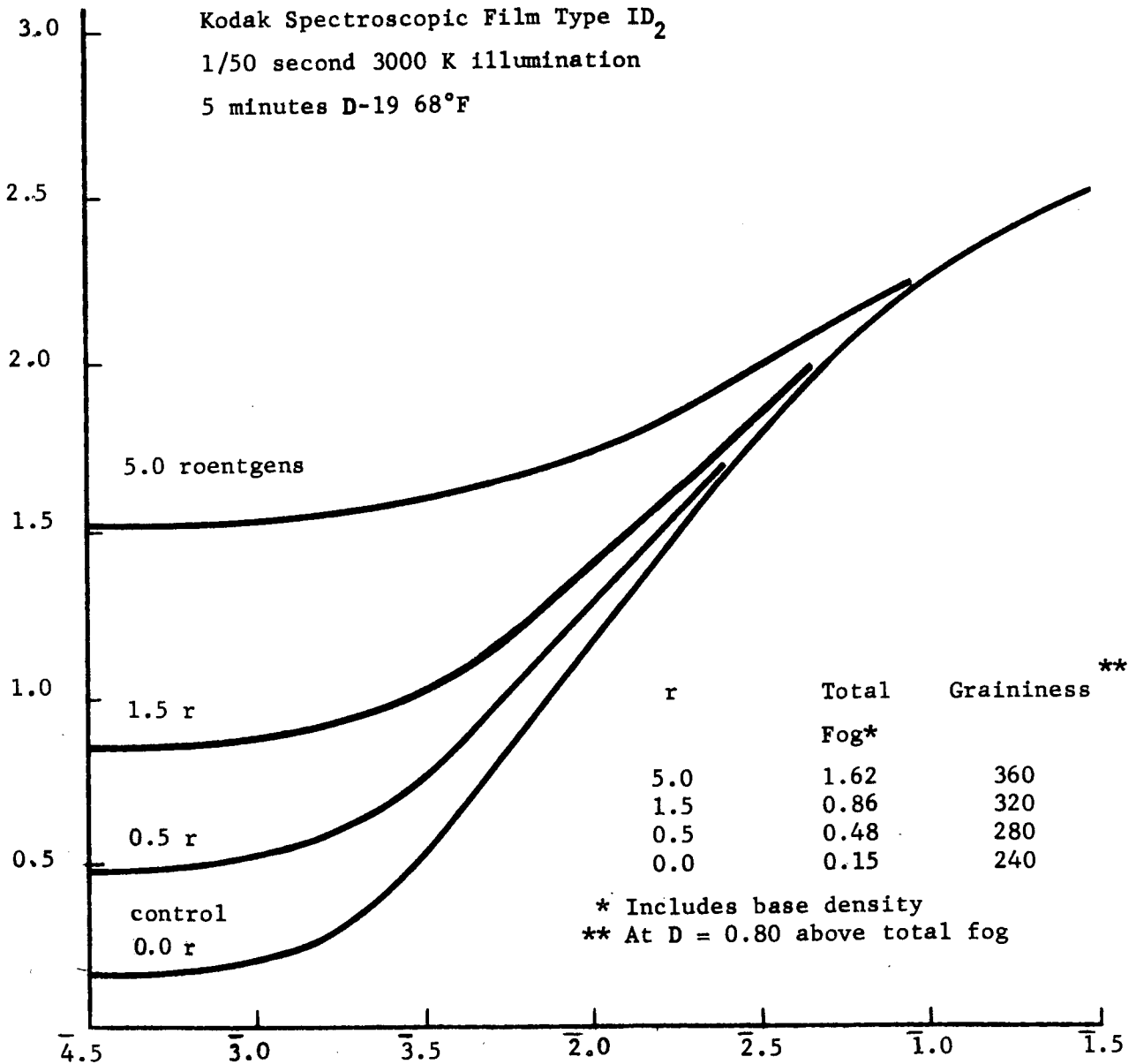


Figure 5.1 Log Exposure (meter-candle-seconds)

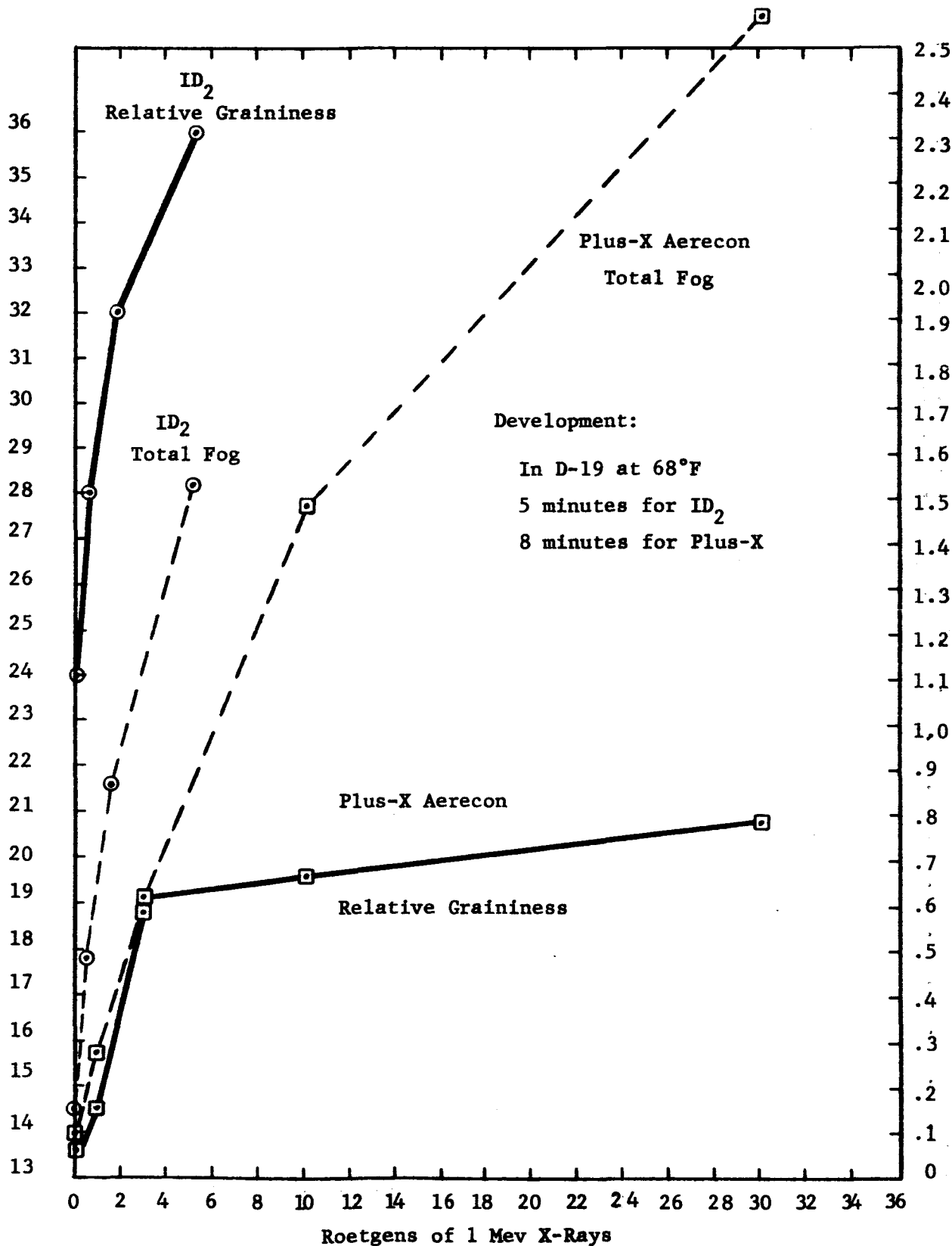


Figure 5.2 Relative Graininess and Total Fog as a Function of X-Ray Dose

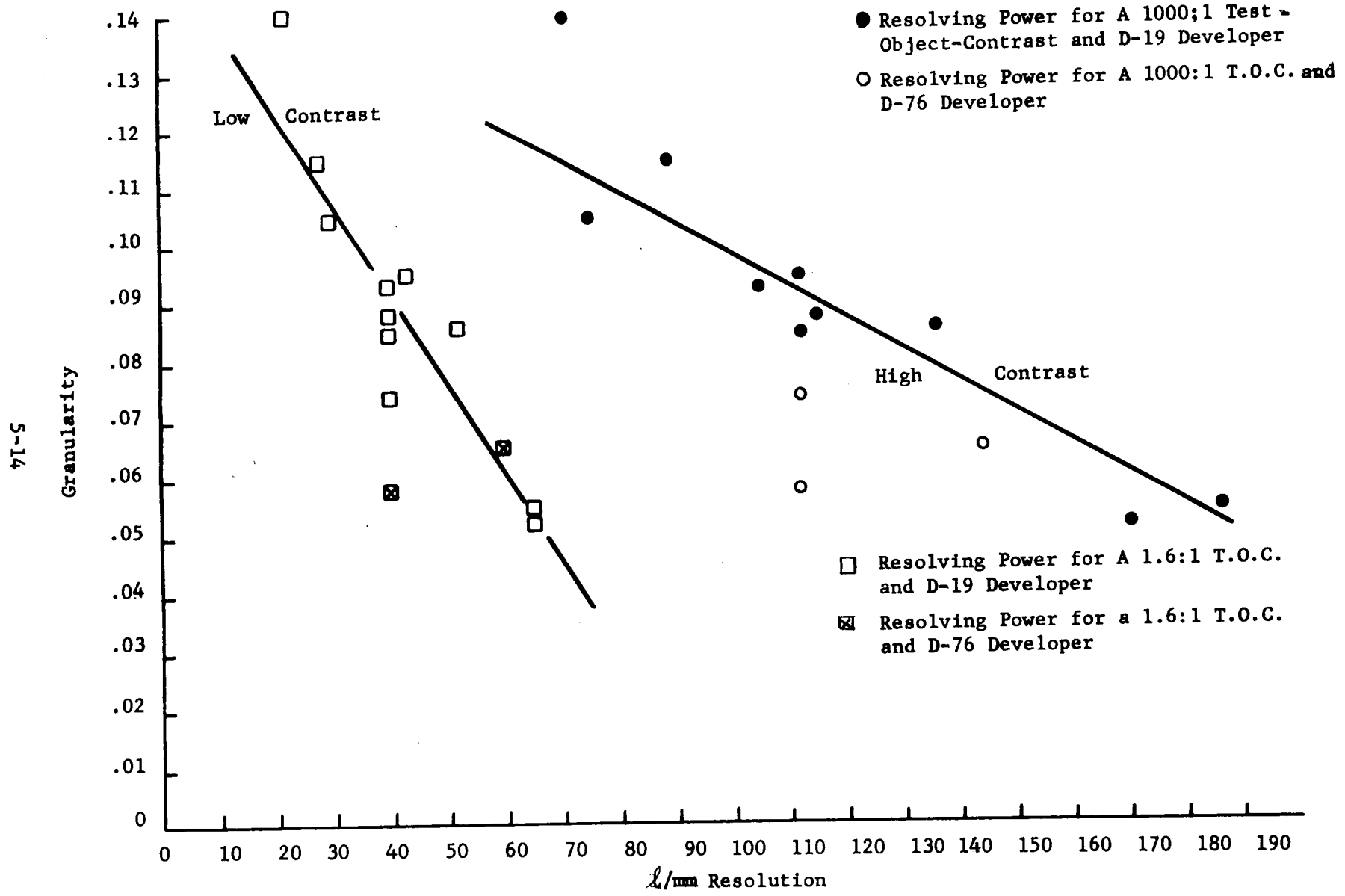


Figure 5.3 Granularity Vs. Resolving Power for Various Aerial Films From the "Manual of Physical Properties of Kodak Aerial and Special Sensitized Materials"

conditions, and at approximately 1.5  $\mu$ /mm per 0.001 increase in granularity at high contrast conditions.

As can be seen in Figure 5.2, apart from the increase in graininess directly due to the roentgen dose, there is an additional increase in graininess due to the increase in image gross density needed to produce the density above gross fog required for image detection.

A thorough study of the radiation environment and shielding requirements in a 300 nautical mile altitude satellite with a 30 degree orbital inclination has been conducted by the Grumman Aircraft Engineering Corporation (GAEC). Results of this study indicate that the artificial radiation belt in the region of the South Atlantic anomaly is responsible for nearly all of the radiation dose. This is true in spite of the fact that only about 16 minutes of the 96 minute orbital period is spent in this region, and that only about half of the orbital passes made by the satellite pass through the anomaly.

Based on calculations of the average number of silver halide grains per unit area and the average grain size, the sensitivity of some typical Eastman Kodak photographic films is expressed below in terms of the number of rads of 1 Mev gamma rays to produce a density change of 0.20 above background fog.

Type SC-7	1.0 rad
Type 649-0 and 649-F	200 rads
Type I-N, M and Z	0.50 rad

The first type is a UV ( $7\text{\AA}$  to  $5000\text{\AA}$ ) film used in rocket experiments. It is fast relative to spectrographic films; the exposure index is 1.6 and has a resolution of 50 cycles/mm at high contrast. It can be used in a hard vacuum at zero degrees centigrade. The second type is a standard UV to visible spectrographic film ( $2500\text{\AA}$  to  $6500\text{\AA}$ ) which cuts off due to gelatin absorption of UV at about  $2500\text{\AA}$  to  $2000\text{\AA}$ . It is very slow - about 600 times the first the first film exposure time in the UV. It has a very high resolution of 2000 cycles/mm. The third is a standard IR film, with 75 cycles/mm resolution and is quite fast. It must not be allowed to get much above freezing temperatures or else a high fog level results. This is a very rough agreement with Figure 5.1 (an unpublished Kodak data sheet) which shows that a 0.5 roentgen (0.42 rad) 1 mev gamma ray exposure raises the background fog level of type ID<sub>2</sub> spectroscopic film by 0.33 density units.

According to the "Kodak Plates and Films" handbook, type I film is almost twice as grainy as type IIa under recommended development. Kodak published data on SC-7 film indicates that it is grainier than SC-5 and DC-3 films. Because gamma ray sensitivity of film rises with inherent granularity (see Figure 5.2), the gamma ray sensitivities of IIa and SC-5 should be less than type I and SC-7, respectively. For the purpose of estimating shielding

requirements, a one rad radiation dose will be considered to be the maximum gamma ray tolerance level of film.

The artificial radiation belt consists of charged particles (mostly protons and electrons) "trapped" by the earth's magnetic field. Neutrons are unaffected by magnetic fields and cannot be trapped; mesons are unstable and short lived; and heavy atomic nuclei are very few in number by comparison with protons and electrons. A given number of rads of gamma ray exposure will be assumed to be equivalent to the same number of rads of proton or electron exposure.<sup>12</sup> Cobalt 60 gamma rays have been found<sup>6</sup> to have practically the same effect on film as any gamma rays having a 1 mev energy or greater.

Figure 5.4, plotted from results of the Grumman study, (see Figures 3.6 and 3.9, Section 3.0) gives the shielding requirements as a function of the number of days to acquire a one rad dose from protons or electrons (including secondary emission from the shielding). Figure 5.5 translates points from Figure 5.4 into the shielding weight needed to shield a cylindrical volume eight inches in diameter and four inches high. The film is assumed to remain within this volume and within the spacecraft. This assumption is valid if the film is removed only when away from the vicinity of the South Atlantic anomaly. The spacecraft is assumed to provide about 4 grams per square centimeter of aluminum shielding. This corresponds to an aluminum thickness of about 1.5 centimeters. It is possible that a place in the spacecraft exists (such as between cryogenic supply bottles) where the equivalent shielding is greater than 4 grams per square centimeter. Film storage in such a place could considerably reduce the required weight of the additional shielding needed.

The inflection in the curves of Figure 5.4 at about 4 grams per square centimeter of shielding marks a change in the predominant source of the accumulated radiation dose. When the shielding is less than about 4 grams per square centimeter, the radiation dose rate from electrons predominates because the number of electrons trapped in the radiation belt exceeds the number of trapped protons. When the shielding exceeds about 4 grams per square centimeter, the radiation dose rate from protons predominates because, in the Van Allen Belt, the penetrating power of protons generally exceeds that of electrons. This higher proton penetrating power exists in spite of the relatively large collision cross-section of trapped protons because they generally have much higher kinetic energy than trapped electrons.

Alternate means of protection of photographic film from the effects of ionizing radiation should be studied for their practicality and feasibility. For example, it is known that the latent image produced by charged particles fades in time. Latent image fading depends on many parameters including emulsion composition, flux type and specific ionization of the exposing particles and storage conditions of atmosphere, humidity and temperature. Exposure produced by high specific ionization particles are more stable than those by low. Thus, techniques for latent image eradication must account for the differential fading between various types of charged particles. Fading rate appears to be enhanced by storage in an atmosphere containing increased amounts of oxygen or hydrogen peroxide. Perhaps the greatest influence on fading is exerted by

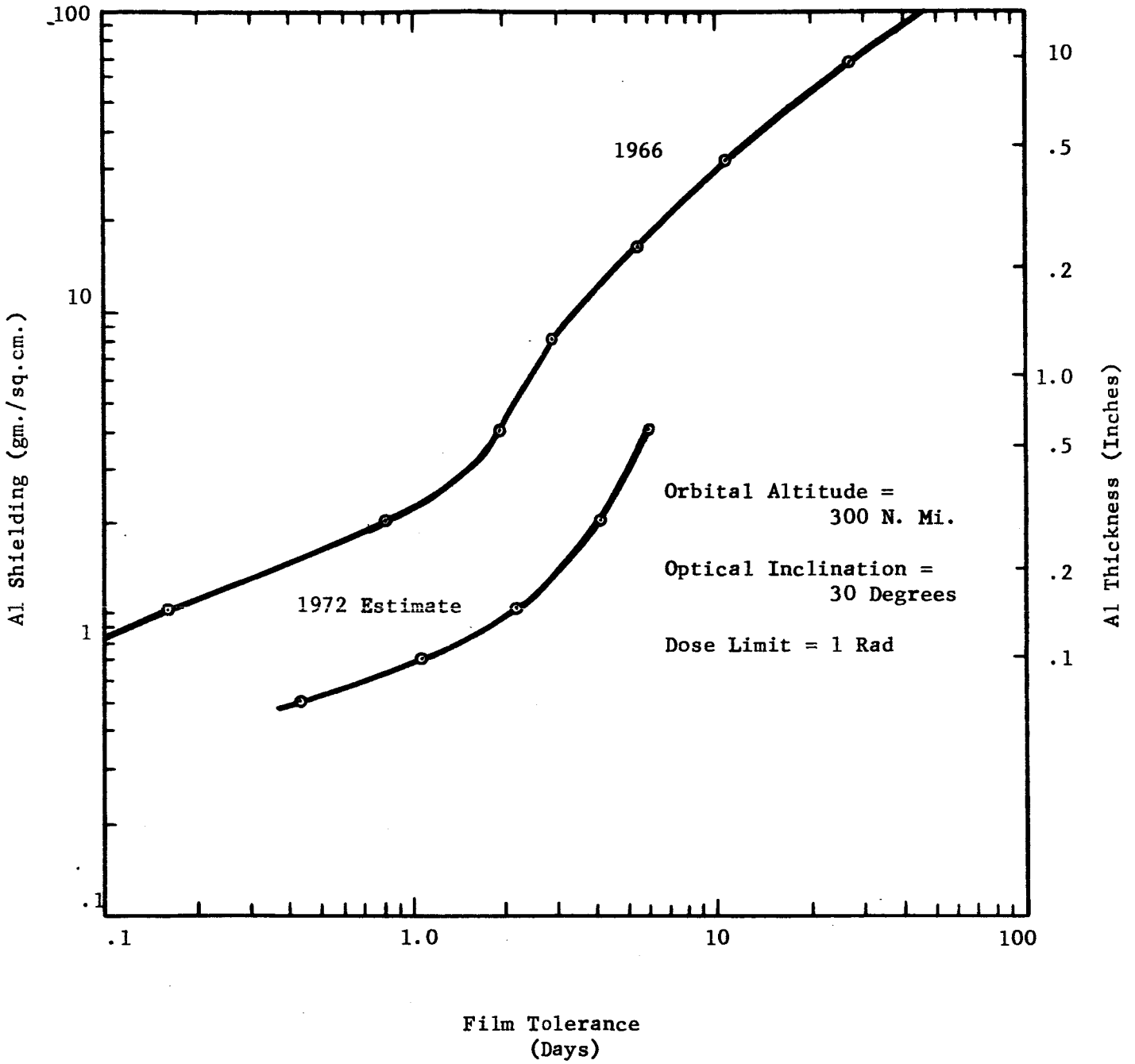


Figure 5.4. Shielding Requirements as a Function of Number of Days Exposure

emulsion moisture content, which in turn depends on atmospheric humidity. Other methods to minimize the formation of a latent image include low temperature storage prior to use.

## 5.7 SUMMARY AND CONCLUSIONS

The main problems of using photographic emulsions in space are the deleterious effects of Van Allen Belt radiation and reciprocity failure (low light sensitivity) at long exposure times. Both problems are indirectly aggravated by the telescope's F/200 convergence cone-imagery. Because the image light intensity is inversely proportional to the square of the f-number, the intensity at F/200 is 100 times dimmer than that at F/20. In order to record images at very low light levels, it is necessary to use fast emulsions (which are, unfortunately, most sensitive to Van Allen Belt radiation) at very long exposure times (sometimes exceeding 2000 seconds). Although the spectrometer operates at F/20, it also suffers from low light level recording problems due to high dispersion and deteriorating surface reflectivity of reflective optical elements in the far UV spectral region.

Kodak type IIa spectroscopic emulsion is recommended for recording imagery with the telescope because of its high light sensitivity at long exposure times and its adequate resolving power. Kodak 103a has slightly higher sensitivity at long exposure times but a lower resolving power. Other Kodak emulsions suffer from severe reciprocity failure at long exposure times.

The two kinds of photographic systems considered for recording the spectrometer output are special UV sensitive "Schumann" emulsions with practically no gelatin (gelatin isopaque to UV light below 2000Å), and regular IIa-0 emulsion coated with a special fluorescent material which converts UV light into light which penetrates gelatin and sensitizes the emulsion. The advantages and disadvantages of these films are summarized in Tables 5-II and 5-III.

The primary advantages of IIa coated emulsions are that they have a fairly uniform spectral response and that they are available in the same forms as uncoated IIa. This makes it possible to use the same processing, transport, and other handling mechanisms for both the telescope and spectrometer. If "Schumann" emulsions are used with the spectrometer, then the extra weight and bulk of additional handling mechanisms must be considered because of the limited forms of availability of "Schumann" emulsions. Also, coated IIa-0 is likely to be more light sensitive at very long exposure times than "Schumann" emulsions — unless special techniques (such as refrigeration during exposure, which will be the natural environment of film in space anyway) are proven and used to arrest reciprocity failure in "Schumann" emulsions.

The chief advantage of "Schumann" emulsions are a higher (if the reciprocity failure problem is solved) light sensitivity than coated IIa-0 especially in the far UV spectral range and a lower sensitivity Van Allen Belt radiation. A possible disadvantage is the necessity of refrigerating Kodak "Schumann" emulsions (i.e., SWR, DC-3, SC-5, and SC-7) during storage.



Assume the usable telescope format dimensions to be 70 by 70 millimeters, and the usable spectrometer format to be 70 by 80 millimeters. The use of 70 millimeter film for both applications appears to be an attractive possibility because film handling mechanisms are lighter and less bulky than plate handling mechanisms. Unfortunately, Kodak DC-3, SC-5, and SC-7 are supplied only in 35 millimeter by 180 millimeter unperforated film strips. Kodak SWR is supplied only on plates and in 35 millimeter by 25 feet, 3 inch unperforated film rolls. Kodak IIA film (coated and uncoated) can, however, be made available in 70 millimeter film rolls.

Bimat processing is not recommended by Kodak for either "Schumann" emulsions or IIA emulsions. The use of wet processing equipment in orbit is, therefore, indicated.

It is desirable that the system resolving power not be lowered by the recording emulsion. The resolving powers of UV coated IIA film and "Schumann" emulsions might be a bit lower than desired in the case of the spectrometer, especially since Van Allen Belt radiation increases granularity, and if optimistic estimates of the spectrometer resolving power are realized. The use of less grainy (and, unfortunately, less light sensitive) emulsions than IIA might be considered if the reciprocity failure problem can be solved.

Practically all the radiation dose in a 300 nautical mile altitude, 30 degree inclination orbit comes from the trapped high speed protons and electrons in the Van Allen Belt. The radiation dose is sufficiently severe to make a 30 day survival in orbit of unprocessed 103a, IIA, SWR, DC-3, SC-5, or SC-7 emulsions unfeasible. Figure 5.5 shows that 3 days survival requires about 12 pounds of aluminum shielding and that 7 days survival requires about 80 pounds of aluminum shielding. The volume shielded was assumed to be cylindrical (8 inch diameter by 4 inches). It should be pointed out that these figures are crude estimates based on a 1966 space radiation environment. On the basis of the estimated 1972 space radiation environment, only 8 pounds of shielding will be required for 8 days survival in space. This estimated dose decrease is partly due to an expected leakage of high speed protons and electrons from the Van Allen Belt and partly due to higher solar activity expected in 1972. High solar activity heats the atmosphere and raises the trapped radiation belt partly away from the 300 nautical mile altitude orbit thus, decreasing the dose rate.

Van Allen Belt radiation not only fogs film, but also increases granularity and reduces resolving power. The latter effect is especially deleterious because of the marginal resolution of emulsions considered for use in the spectrometer.

The use of finer grain emulsions would both increase resolving power and reduce the required shielding weight for a given survival time. Associated with finer grain emulsions are reduced inherent light sensitivity and severe reciprocity failure at long exposure times by comparison with 103a and IIA.

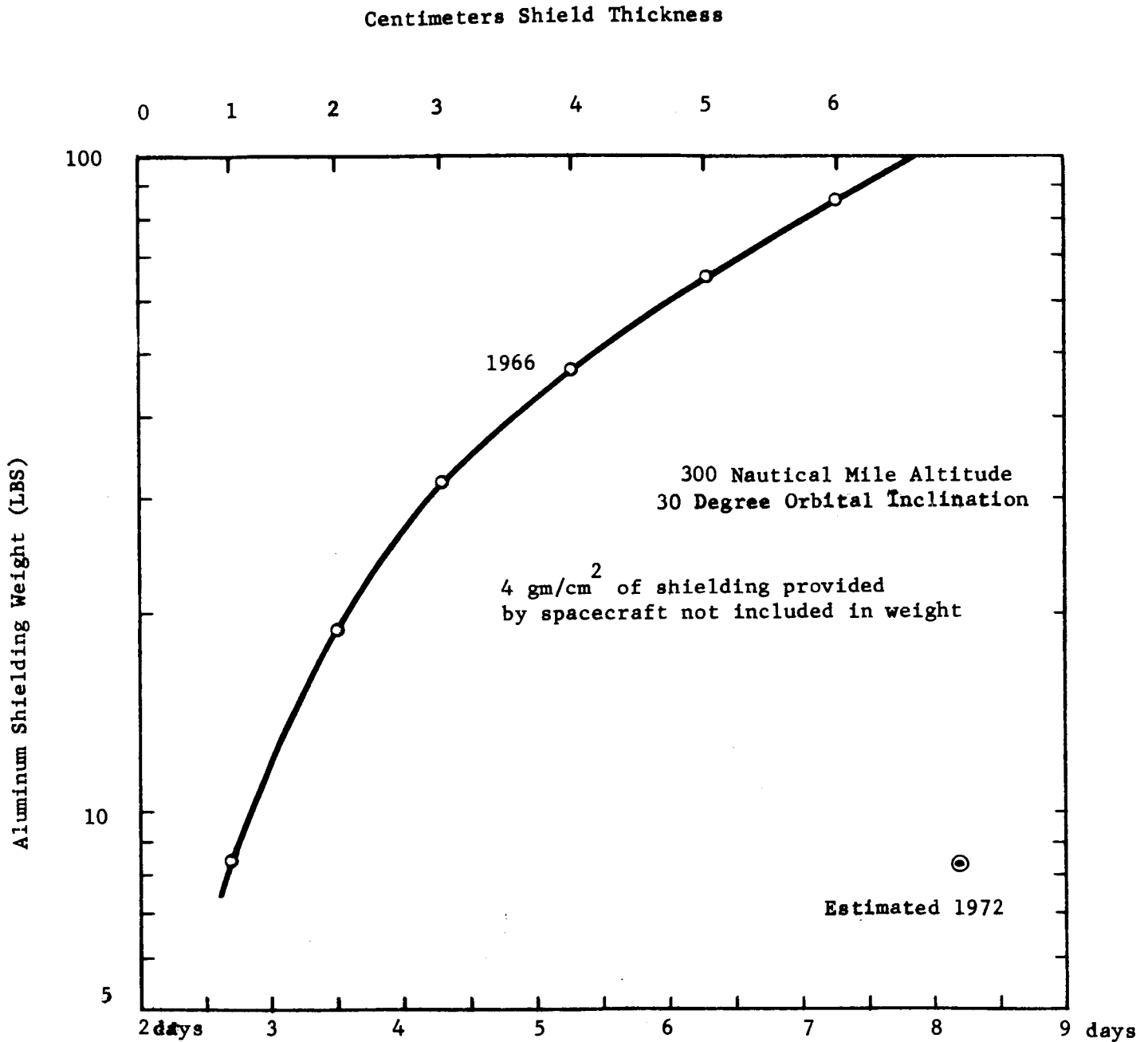


Figure 5.5. Shielding Weight Needed to Shield a Cylindrical Volume (8 inch Diameter by 4 inches) from Doses Exceeding one Rad as a Function of Days Exposure.

REFERENCES

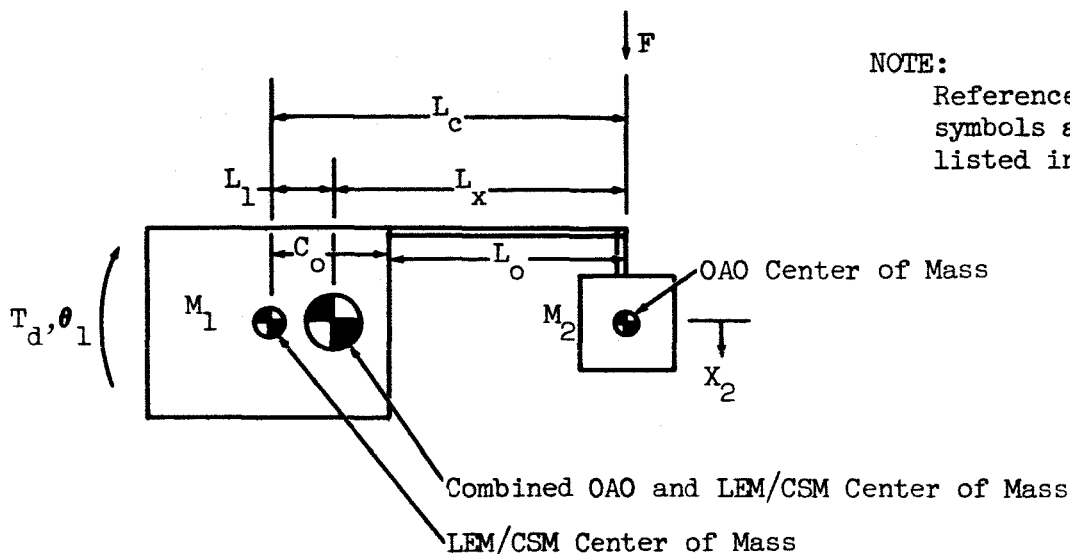
- <sup>1</sup>Perkin-Elmer Report 7173, Photographic Processing State of Art, July 27, 1962
- <sup>2</sup>Mees, C.E. Kenneth, The Theory of the Photographic Process, Revised Edition, The Macmillan Company, 1954
- <sup>3</sup>Rossi, Bruno, High Energy Particles, Prentiss-Hall, 1952
- <sup>4</sup>Mees, C.E. Kenneth, The Theory of the Photographic Process, Revised Edition, The Macmillan Company, 1954
- <sup>5</sup>Hiltner, W.A., edit., Astronomical Techniques, University of Chicago Press, 1962, p.392
- <sup>6</sup>Corney, G.M., The Effect of Gamma-Ray Exposure on Camera Films, Photographic Science and Engineering, Vol. 4, No. 5, September-October, 1960, pp.291-296
- <sup>7</sup>Corney, G.M., Effective Characteristic Curves of Certain Gamma-Ray-Fogged Aerial Photographic Films, (Unpublished), Eastman Kodak Research Library, Kodak Park, Rochester, New York
- <sup>8</sup>Corney, G.M., Effective Characteristic Curves of Certain Gamma-Ray-Fogged Aerial Photographic Films, Eastman Kodak Library
- <sup>9</sup>Corney, G.M., Gamma-Ray Sensitivity of Several Black and White Negative Photographic Films, Photographic Science and Technique, Series II, Vol. 2, No. 14, November 1955, pp.146-148
- <sup>10</sup>Lewis, Jack C., and Harold V. Watts, Effects of Nuclear Radiation on the Sensitometric Properties of Reconnaissance Films, Technical Report AFAL-TR-65-113, April 1965, Air Force Avionics Laboratory Research and Technology Division, Air Force Systems Command, Wright-Patterson AFB, Ohio, U.S.A.
- <sup>11</sup>Kodak Plates and Films for Science and Industry, handbook
- <sup>12</sup>Lewis, Jack C., and Harold V. Watts, Effects of Nuclear Radiation on the Sensitometric Properties of Reconnaissance Films, Technical Report AFAL-TR-65-113, April 1965, Air Force Avionics Laboratory Research and Technology Division, Air Force Systems Command, Wright-Patterson AFB
- <sup>13</sup>Fowler, W.K., W.A. Rense, and W.R. Simmons, Film Calibration for Rocket UV Spectrographs, Applied Optics, Vol. 4, No. 12, December 1965, p.1597

APPENDIX A

RIGID MOUNT CONFIGURATION

APPENDIX A

RIGID MOUNT CONFIGURATION



Shift in Combined OAO and LEM/CSM Center of Mass

Combining  $M_1 L_1 = L_x M_2$  (A-1)

with  $L_c = L_1 + L_x$  (A-2)

yields  $L_1 = \frac{L_c M_2}{M_1 + M_2}$

Assuming  $M_1 = 1500$  slugs,  $M_2 = 140$  slugs

then  $L_1 = 0.085 L_c$  (A-3)

It can also be show that

$$L_x = \frac{M_1}{(M_1 + M_2)} (L_o + C_o)$$
 (A-4)

Assuming  $C_o = 15$  ft

then  $L_x = 0.915 (L_o + 15)$  (A-5)

Percent Increase in Gravity Gradient Torque on LEM/CSM Vehicle

Since 
$$I_T = I_1 + M_1 L_1^2 + I_2 + M_2 (L_c - L_1)^2 \tag{A-6}$$

with 
$$I_v = I_1 + I_2$$

and substituting Equation A-3 into A-6, then

$$I_T = I_v + 127 L_c^2$$

Assuming 
$$I_v = 2.5 \times 10^5 \text{ slug ft}^2$$

then 
$$\% \Delta I_v = 5.06 \times 10^{-2} L_c^2 \tag{A-7}$$

The results of Equation A-7 are plotted in Figure 19.

Percent Increase in Aerodynamic Torque Disturbance on LEM/CSM Vehicle

Since 
$$F_{\text{aero}} = C_d A \bar{q}$$

then assume 
$$\left. \frac{W_{\text{OAO}}}{C_d A} \right|_{\text{min}} = 10 \text{ lb/ft}^2$$

and 
$$\bar{q} \approx 10^{11} / h^7$$

results in 
$$T_{\text{aero OAO}} = \frac{10^{10} L_x W_{\text{OAO}}}{h^7}$$

For 
$$W_{\text{OAO}} = 4500 \text{ lb}, h = 250 \text{ n mi}$$

then 
$$T_{\text{aero OAO}} = 6.8 \times 10^{-4} L_c \tag{A-8}$$

At 250 n mi, aerodynamic torque on a clean LEM/CSM is

$$T_{\text{aero LEM/CSM}} = 0.00315 \text{ ft lb}$$

then 
$$\% \Delta T_{\text{aero LEM/CSM}} = 21.6 L_c \tag{A-9}$$

The results of Equation A-9 are plotted in Figure 19.

At 250 n mi, gravity gradient torque on a clean LEM/CSM is

$$T_{\text{grav LEM/CSM}} = 0.48 \text{ ft lb}$$

Total Percentage Increased Torque Disturbance on LEM/CSM Vehicle

Since 
$$\% \Delta T_T = \left[ \% \Delta I_V + \frac{T_{aero}}{T_{grav}} \right]_{LEM/CSM} \left( \% \Delta T_{aero}^{LEM/CSM} \right)$$

Then 
$$\% \Delta T_T = 0.0506 L_c^2 + 0.142 L_c \tag{A-10}$$

The results of Equation A-9 are plotted in Figure 19.

Translational Motion of OAO Due to LEM/CSM Limit Cycle

Since 
$$X_2 = L_x \theta_{1LC}$$

then 
$$X_2 = 0.190 \theta_{1LC} L_c$$

where  $\theta_{1LC}$  is in degrees, and  $X_2$  in inches (A-11)

The results of Equation A-11 are plotted in Figure 20.

Time Between Inertia Wheel Dump Due to Combined OAO/Telescope Inertia Unbalance

Since 
$$T_{avg} = T_{avg} \text{ (grav. grad.)} + T_{avg} \text{ (aero)} + T_{arg} \text{ (magn + solar)}$$

and from data presented in Reference 1 for a 250 n mi orbit and assuming inertia of combined OAO/Telescope is,

$$I = 1500 \text{ slug ft}^2$$

then 
$$T_{avg} = (1.5 \times 10^{-5}) \left( \frac{\Delta I}{I} \right) \% + (0.8 \times 10^{-4}) + (4.3 \times 10^{-5}) \tag{A-12}$$

Assuming average torque can be stored for 70 percent of inertia wheel capacity, then

$$T_{avg} T = 0.70 H \tag{A-13}$$

Since OAO fine inertia wheel capacity is

$$H = 2 \text{ ft lb sec}$$

then

$$T = \frac{1.4}{60 \left[ (1.5 \times 10^{-5}) \left( \frac{\Delta I}{I} \right) \% + (1.23 \times 10^{-4}) \right]} \tag{A-14}$$

where T is expressed in minutes. The results of Equation A-14 are plotted in Figure 21A.

Translational acceleration of OAO Due to Man Motion and Jet Impulse

Since  $T_d = I_1 \ddot{\theta}_1$  and  $X_z = L_x \theta_1$

then  $T_d = \frac{I_1 \ddot{X}_2}{L_x}$  (A-15)

The torque profile (Reference 10) for a man weighing 5 slugs, located 18 ft from LEM/CSM center of mass, and walking a distance of 3 ft in the LEM/CSM is assumed to be

$$T_d = \frac{180 s}{\left(\frac{s}{\omega_f} + 1\right)^3}$$
 (A-16)

Substituting Equation A-16 into A-15 yields

$$\ddot{X}_2 = \frac{180 L_x s}{I_1 \left(\frac{s}{\omega_f} + 1\right)^3}$$
 (A-17)

From Equation A-17 it can be shown that

$$\ddot{X}_{2_{max}} = \frac{0.23 (180) L_x \omega_f^2}{I_1}$$
 (A-18)

For four jet impulse firings

$$\ddot{X}_{2_{max}} = \frac{4 L_x (T_d t_1)}{I_1}$$
 (A-19)

Assuming

$$I_1 = 2.5 \times 10^5 \text{ slug ft}^2, (T_d t_1) = 13 \text{ ft lb sec, and } \omega_f = 8 \text{ rad/sec}$$

and summing Equations A-18 and A-19, yields

$$\ddot{X}_{T_{max}} = (1.05 \times 10^{-2} + 2.08 \times 10^{-4}) L_x$$

which when divided through by 32.2 ft/sec<sup>2</sup> results in

$$\ddot{X}_{T_{max}} = 3.3 \times 10^{-4} L_x$$
 (A-20)

where  $\ddot{X}_{T_{max}}$  is expressed in "g's".

The results of Equation A-20 are plotted in Figure 21b.



TABLE A-1

SYMBOLS AND UNITS, RIGID MOUNT CONFIGURATION

$F$	- Disturbance force on OAO acting through its center of mass	lb
$h$	- Orbital altitude	n mi
$I_1$	- Moment of inertia of LEM/CSM vehicle	slug ft <sup>2</sup>
$I_2$	- Moment of inertia of OAO	slug ft <sup>2</sup>
$L_o$	- Boom length	ft
$L_x$	- Distance between OAO and LEM/CSM center of masses	ft
$M_1$	- Mass of LEM/CSM	slugs
$M_2$	- Mass of OAO	slugs
$X_2$	- Translational motion of OAO	in.
$\bar{q}$	- Dynamic pressure	lb/ft <sup>2</sup>
$s$	- Laplace operator	1/sec
$T_d$	- Disturbance torque applied to LEM/CSM	ft lb
$t_1$	- Duration of LEM/CSM reaction jet pulse	sec
$W_{OAO}$	- Weight of OAO	lb
$\theta_1$	- Angular rotation of LEM/CSM vehicle	radians

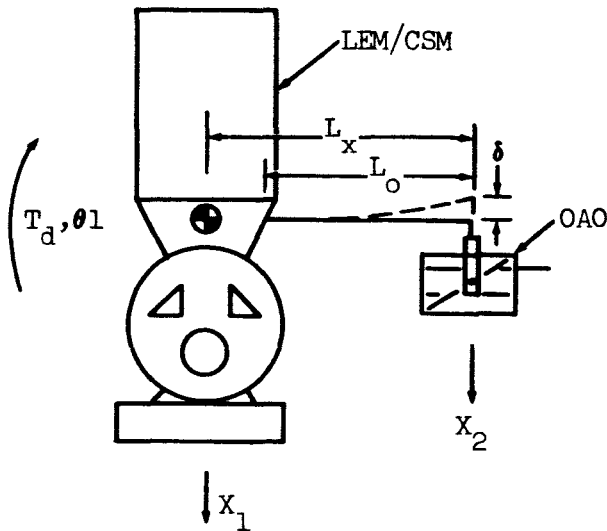
NOTE: Velocities are normally given in in./sec and accelerations in ft/sec<sup>2</sup> unless otherwise specified.

APPENDIX B

SOFT PIPE RACK CONFIGURATION

APPENDIX B

SOFT PIPE RACK CONFIGURATION



NOTE:

- Reference is made to symbols and units listed in Table B-1.
- Motions, forces, and torques are positive in direction shown.

Equations of Motion

$$(X_2 - X_1 - \theta_1 L_x) = \delta \tag{B-1}$$

$$M_1 \ddot{X}_1 - K (X_2 - X_1 - \theta_1 L_x) = 0 \tag{B-2}$$

$$M_2 \ddot{X}_2 + K (X_2 - X_1 - \theta_1 L_x) = 0 \tag{B-3}$$

$$I_1 \ddot{\theta}_1 - KL_x (X_2 - X_1 - \theta_1 L_x) = T_d \tag{B-4}$$

The Characteristic equation is

$$\Delta = I_1 M_1 M_2 S^4 (S^2 + \omega_n^2) \tag{B-5}$$

where

$$\omega_n^2 = K \left[ \frac{1}{M_2} \left( 1 + \frac{M_2}{M_1} \right) + \frac{L_x^2}{I_1} \right] \approx K \frac{(M_1 + M_2)}{M_1 M_2} \tag{E-5a}$$

Based on Equations B-1 through B-5 the following transfer functions were developed:

$$\frac{\theta_1(s)}{T_d(s)} = \frac{\left[ s^2 + \frac{K(M_1 + M_2)}{M_1 M_2} \right]}{I_1 s^2 (s^2 + \omega_n^2)} \tag{B-6}$$

$$\frac{X_2(s)}{T_d(s)} = \frac{KL_x}{I_1 M_2 s^2 (s^2 + \omega_n^2)} \tag{B-7}$$

For a weightless cantilever beam

$$K = \frac{36 EI}{L_o^3}$$

where  $L_o$  is expressed in inches.

Assuming a thin walled tube

$$I = \pi R^3 T \tag{B-8}$$

and  $T = \frac{R}{5} = \frac{D}{10}$

then 
$$K = \frac{8.2 \times 10^{-4} ED^4}{L_o^3} \tag{B-9}$$

where  $L_o$  is expressed in ft.

Substituting Equation B-9 into B-5a, yields

$$\omega_n^2 = \frac{8.2 \times 10^{-4} ED^4 (M_1 + M_2)}{L_o^3 M_1 M_2} \tag{B-10}$$

Assuming  $M_1 = 1500$  slugs  
 $M_2 = 140$  slugs  
 $E = 3 \times 10^7$  psi (steel tubing)

then 
$$\omega_n = \frac{13.8D^2}{L_o^{3/2}} \tag{B-11}$$

The results of Equation B-11 are plotted in Figure 23.

Translational Motion of OAO Due to Turning on Jet in LEM/CSM for Slewing

Substituting  $T_d(s) = \frac{T_d}{s}$

into Equation B-7 yields

$$\ddot{X}_2(s) = \frac{T_d K L_x}{I_1 M_2 \omega_n^2 s \left( \frac{s^2}{\omega_n^2} + 1 \right)}$$

and in the time domain

$$\ddot{X}_2(t) = \frac{T_d K L_x}{I_1 M_2 \omega_n^2} (1 - \cos \omega_n t)$$

which have a maximum value of

$$\ddot{X}_{2 \max} = \frac{2 T_d K L_x}{I_1 M_2 \omega_n^2} \tag{B-12}$$

Assuming  $T_d = 1300 \text{ ft lb}$   
 $I_1 = 2.5 \times 10^5 \text{ slug ft}^2$   
 $L_x = 0.91 (L_o + 15)$

and substituting Equation B-5a into B-12 yields

$$\ddot{X}_{2 \max} \text{ (Slewing)} = 2.70 \times 10^{-4} (L_o + 15), \text{ in "g's"} \tag{B-13}$$

Translational Motion of OAO Due to Jet Impulse on LEM/CSM Vehicle

From Equation B-7

$$\ddot{X}_2(s) = \frac{(T_d t_1) K L_x}{I_1 M_2 \omega_n^2 \left( \frac{s^2}{\omega_n^2} + 1 \right)}$$

and in the time domain

$$\ddot{X}_2(t) = \frac{(T_d t_1) K L_x}{I_1 M_2 \omega_n} \sin \omega_n t$$

which has a maximum value of

$$\ddot{X}_{2 \max} = \frac{(T_d t_1) K L_x}{I_1 M_2 \omega_n} \tag{B-14}$$

Assuming a 10-ms impulse duration

then  $(T_d t_1) = 1300 (0.01) = 13 \text{ ft lb sec}$

and substituting Equations B-9 and B-11 into B-14 yields

$$\ddot{X}_{2 \max} \text{ (Jet Impulse)} = \frac{6.0 \times 10^{-4} D^2 (L_o + 15)}{L_o^{3/2}}, \text{ in ft/sec}^2 \tag{B-15}$$

or 
$$\ddot{X}_{2\max} \text{ (Jet Impulse)} = \frac{1.93 \times 10^{-5} D^2 (L_o + 15)}{L_o^{3/2}}, \text{ in "g's"}$$
 (B-15a)

Translational Motion of OAO Due to Man Motion in LEM/CSM Vehicle

From Reference 1 and the following assumptions:

- Mass of man = 5 slugs
- Distance he walks = 3 ft
- Distance man is located from LEM/CSM c.m. = 12 ft
- Time required to walk 3 ft = 1 sec ( $\omega_f = 8 \text{ rad/sec.}$ )

then 
$$T_d(s) = \frac{5 (3) (12) s}{\left(\frac{s}{\omega_f} + 1\right)^3}$$
 (B-16)

Substituting Equation B-16 into B-7 yields

$$\ddot{X}_2(s) = \frac{180 K L_x s}{I_1 M_2 \omega_n^2 \left(\frac{s^2}{\omega_n^2} + 1\right) \left(\frac{s}{\omega_f} + 1\right)^3}$$
 (B-17)

Assume  $\omega_f \gg \omega_n$

then 
$$\ddot{X}_2(t) = \frac{180 K L_x}{I_1 M_2} \cos \omega_n t$$
 (B-18)

which has a maximum value of

$$\ddot{X}_{2\max} = \frac{180 K L_x}{I_1 M_2}$$
 (B-19)

Substituting Equation B-9 into B-19 yields

$$\ddot{X}_{2\max} \text{ (man motion)} = \frac{3.6 \times 10^{-3} D^4 (L_o + 15)}{L_o^3}, \text{ in "g's"}$$
 (B-20)

Development of Structural Stress Limit on Boom Due to Man Motion Plus Jet Slewing.

Since 
$$S_T = \frac{Mc}{I}$$

where  $M = F_{\max} L_o$

$$I = \frac{\pi D^4}{80}$$

$c = D/2$

then  $S_T = \frac{153 F_{\max} L_o}{D^3}$

Assuming  $S_T = \frac{S_y}{2}$

and  $S_y = \frac{305 F_{\max} L_o}{D^3}$  (B-21)

where  $F_{\max} = M_2 [\ddot{X}_{2\max} \text{ (slewing)} + \ddot{X}_{2\max} \text{ (man motion)}]$  (B-22)

and substituting Equations B-13 and B-20 into B-22 yields

$$F_{\max} = \frac{1.22 (L_o + 15) (L_o^3 + 13.3 D^4)}{L_o^3}$$
 (B-23)

Substituting Equation B-23 into B-21 yields

$$S_y = \frac{372 (L_o + 15) (L_o^3 + 13.3 D^4)}{L_o^2 D^3}$$
 (B-24)

The results of Equation B-24 are plotted in Figure 24.

Translational Acceleration of OAO Due to Man Motion Plus Four Jet Impulses

Since  $\ddot{X}_{2\max} = \ddot{X}_{2\max} \text{ (man motion)} + 4 \ddot{X}_{2\max} \text{ (jet impulse)}$

then  $\ddot{X}_{2\max} = \frac{7.45 \times 10^{-5} D^2 (L_o + 15) (48.4 D^2 L_o^{1/2} + 1)}{L_o^{7/2}}$ , in "g's" (B-25)

The results of Equation B-25 are plotted in Figure 25.

Translational Velocity of OAO Due to Limit Cycling of LEM/CSM

Since  $\dot{X}_{2\max} = L_x \dot{\theta}_{1\max}$

and  $\dot{\theta}_{1\max} = 0.02 \text{ deg/sec}$

then  $\dot{X}_{2\max}$  (Limit cycle) =  $3.83 \times 10^{-3} (L_o + 15)$  (B-26)

Translational Velocity of OAO Due to Man Motion

Integrating Equation B-18 yields

$$\dot{X}_2(t) = \frac{180 K L_x}{I_1 M_2 \omega_n} \sin \omega_n t$$

which have a maximum value of

$$\dot{X}_{2\max} = \frac{180 K L_x}{I_1 M_2 \omega_n}$$

Substituting Equations, B-9 and B-11 into above yields

$$\dot{X}_{2\max} \text{ (man motion)} = \frac{0.10 D^2 (L_o + 15)}{L_o^{3/2}} \text{ (B-27)}$$

Translational Velocity of OAO Due to Man Motions Plus Limit Cycling

Substituting Equations B-26 and B-27 into

$$\begin{aligned} \dot{X}_{2\max} &= \dot{X}_{2\max} \text{ (man motion)} + \dot{X}_{2\max} \text{ (limit cycle)} \\ \text{yields } \dot{X}_{\max} &= \frac{3.83 \times 10^{-3} (L_o + 15)(L_o^{3/2} + 26.1D^2)}{L_o^{3/2}} \text{ (B-28)} \end{aligned}$$

The results of Equation B-28 are plotted in Figure B-27.



TABLE B-1SYMBOLS AND UNITS, SOFT PIPE RACK CONFIGURATION

D	- Tube diameter	in.
E	- Modules of Elasticity	psi
I	- Moment of inertia of tube crossection	in. <sup>4</sup>
I <sub>1</sub>	- Moment of inertia of LEM/CSM Vehicle	slug ft <sup>2</sup>
K	- Tube spring constant (in bending)	lb/ft
L <sub>0</sub>	- Boom length	ft
L <sub>x</sub>	- Distance between OAO and LEM/CSM center of masses	ft
M <sub>1</sub>	- Mass of LEM/CSM	slugs
M <sub>2</sub>	- Mass of OAO	slugs
X <sub>1</sub>	- Translational motion of LEM/CSM	in.
X <sub>2</sub>	- Translational motion of OAO	in.
R	- Tube radius	in.
s	- Laplace operator	1/sec
S <sub>y</sub>	- Maximum allowable elastic limit in boom	psi
S <sub>T</sub>	- Maximum stress limit developed in boom	psi
T	- Tube thickness	in.
T <sub>d</sub>	- Disturbance torque applied to LEM/CSM	ft lb
t <sub>1</sub>	- Duration of LEM/CSM reaction jet pulse	sec
δ	- Translational motion of OAO due to boom bending	in.
θ <sub>1</sub>	- Angular rotation of LEM/CSM vehicle	radians
ω <sub>n</sub>	- Natural frequency of system	rad/sec

NOTE: Velocities are normally given in in./sec and accelerations in ft/sec<sup>2</sup> unless otherwise specified.

APPENDIX C

COIL SPRING CONFIGURATION

APPENDIX CCOIL SPRING CONFIGURATION

## NOTE:

- Equations used in Appendix B are applicable to this configuration where the spring constant,  $K$ , is replaced with an equivalent constant  $K_e$ .
- Reference is made to symbols and units listed in Table C-1.

Maximum Translation of OAO Due to LEM/CSM Limit Cycle

Combining Equations B-6 and B-7 yields

$$\frac{X_2(s)}{\theta_1(s)} = \frac{K_e L_x}{M_2 (s^2 + \omega_n^2)}$$

From Equation B-5a

$$K_e = \omega_n^2 \left( \frac{M_1 M_2}{M_1 + M_2} \right)$$

then

$$\frac{X_2(s)}{\theta_1(s)} = \frac{M_1 L_x}{(M_1 + M_2) \left( \frac{s^2}{\omega_n^2} + 1 \right)}$$

For a sinusoidal forcing function (limit cycle in  $\theta_1$ ),

where

$$s = j\omega_{Lc}$$

then

$$X_{2\max} = 0.915 \frac{L_x \theta_{1\max}}{\left[ -\left( \frac{\omega_{Lc}}{\omega_n} \right)^2 + 1 \right]}$$

(C-1)

Maximum Translational Acceleration of OAO

Due to man motion, Equation B-19,

$$\ddot{X}_{2\max} = \frac{180 K_e L_x}{I_1 M_2}$$

$$= 5.14 \times 10^{-6} K_e L_x = \frac{5.14 \times 10^{-6} M_1 M_2 \omega_n^2 L_x}{(M_1 + M_2)}$$

$$\ddot{X}_{2\max} = 6.6 \times 10^{-4} \omega_n^2 L_x \tag{C-2}$$

Due to jet impulse, Equation B-14,

$$\ddot{X}_{2\max} = \frac{(T_d t_1) K_e L_x}{I_1 M_2 \omega_n} = \frac{(T_d t_1) M_1 \omega_n L_x}{I_1 (M_1 + M_2)}$$

resulting in

$$\ddot{X}_{2\max} = 4.75 \times 10^{-5} \omega_n L_x \tag{C-3}$$

Combining Equations C-2 and C-3 yields

$$\ddot{X}_{2\max T} = \frac{\omega_n L_x}{32.2} (6.6 \times 10^{-4} \omega_n + 4.75 \times 10^{-5}), \text{ expressed in "g's"}$$

(C-4)

Maximum Spring Deflection

Due to Man Motion, Equation B-18, integrating and evaluating for maximum value yields

$$X_{2\max} = \frac{360 K_e L_x}{I_1 M_2 \omega_n^2} = \frac{360 M_1 L_x}{I_1 (M_1 + M_2)} = 1.58 \times 10^{-2} L_x$$

(C-5)

Combining Equations C-1, C-4, and C-5 and assuming  $\omega_{LC} = 0.15$  rad/sec yields

$$X_{2s\max} = X_{2\max} \text{ (Man Motion)} + X_{2\max} \text{ (Limit Cycle)} + X_{2\max} \text{ (OAO Motion)}$$

$$= 1.58 \times 10^{-2} L_x + 3.85 \times 10^{-2} L_x + \frac{\ddot{X}_{\max}}{\omega_n^2}$$

$$X_{2s_{\max}} = L_x \left[ 0.0545 + \frac{12 (6.6 \times 10^{-4} \omega_n + 4.75 \times 10^{-5})}{\omega_n} \right] \quad (C-6)$$

Maximum Torque Disturbance on OAO

Since

$$T_{\text{OAO}_{\max}} = M_2 \ddot{X}_{\max} \epsilon \quad (C-7)$$

with  $\epsilon = 0.10$  inches

and substituting Equation C-4 into C-7 yields

$$T_{\text{OAO}_{\max}} = 1.17 \omega_n L_x (6.6 \times 10^{-4} \omega_n + 4.75 \times 10^{-5}) \quad (C-8)$$

Spring Design

For the spring suspension system considered, it can be shown that

$$K = \frac{K_e}{2} = \frac{\omega_n^2}{2} \left( \frac{M_1 M_2}{M_1 + M_2} \right) = \frac{G d^4}{1.8 R^3 N}$$

or

$$d = \left[ \frac{1.8 M_1 M_2 \omega_n^2 R^3 N}{2 (M_1 + M_2) G} \right]^{1/4}$$

Assuming

$$R = 2 \text{ inches, } N = 200, G = 3.95 \times 10^6 \text{ psi}$$

then

$$d = 0.464 \sqrt{\omega_n} \quad (C-9)$$

and

$$L_s = N d = 200 d \quad (C-10)$$

TABLE C-1SYMBOLS AND UNITS, COIL SPRING CONFIGURATION

$d$	- Spring wire diameter	in.
$G$	- Shear modulus of spring material	psi
$I_1$	- LEM/CSM moment of inertia	slug ft <sup>2</sup>
$K$	- Individual spring constant	lb/ft
$K_e$	- Equivilant suspension system spring constant	lb/ft
$L_x$	- Distance between OAO gimbal mount and LEM/CSM center of mass	ft
$M_1$	- Mass of LEM/CSM vehicle	slugs
$M_2$	- Mass of OAO	slugs
$N$	- Number of coil springs	-
$R$	- Radius of coil springs	in.
$s$	- Laplace operator	1/sec
$t$	- Duration of jet impulse	sec
$T_d$	- Torque level of jet thrusters	ft lb
$X_2$	- Displacement of OAO	in.
$X_{2s}$	- Deflection of spring	in.
$\epsilon$	- Offset between gimbal moment and OAO center of mass	ft
$\theta_1$	- Rotation of LEM/CSM	deg
$\omega_n$	- Suspension system natural system	rad/sec
$\omega_{LC}$	- LEM/CSM limit cycle frequency	rad/sec

NOTE: Velocities are normally given in in./sec and accelerations in ft/sec<sup>2</sup> unless otherwise specified.

APPENDIX D

CREW SCHEDULE

APPENDIX DCREW SCHEDULE

Based upon the astronauts' functions and mission guidelines described in Section 3.2.4 of the final report, a detailed step-by-step description of the crew activity for a three- and two-man crew in the CSM/LEM Lab was prepared. The crew schedules for days 1 through 4 are presented in Table D-1 and D-2. By day 4, the crew has established a constant and repetitive living schedule, and the remaining 26 days can be programmed from this data. The work schedule (consecutive hours that a man is awake) averages approximately 15 hours per day. The crew averages 8 hours of sleep daily, with a minimum sleep period of 7 hours and a maximum of 9 hours.



TABLE D-1  
THREE-MAN CREW SCHEDULE

DAY 1	CREW ACTIVITIES			L A B	REMARKS
	Commander	System Engineer	System Engineer - Astronomer		
0000	Monitor ECS, caution warning	Monitor ascent parameters	Monitor EPS maintain radio comm		
	LIFT OFF				
	Start Earth Orbit Coast				
0012	Set controls and displays for Earth orbit phase				
0018					Canary Is comm.
0020	Perform G&C system status check, SM-RCS, check	Perform G&C system status check, EMS status check	Perform ECS, EPS, SPS system status check		
0023					Lose Canary Is comm.
0038	IMU alignment & check	IMU alignment (10 min)	IMU alignment		
0044					Evening terminator
0047					Space Craft in darkness
0054			Communications		Comm with Carnarvon
0057					Lose Carnarvon
0111					Coasting
0124					Enter sunshine
0128	Perform navigation sighting	Navigation sighting			Morning terminator
0130			Communications		Comm Guaymas
0131			Communications		Comm White Sands
0133	Communications		Communications		Comm Corpus Christi
0134					Lose Guaymas
0135	Communications		Communications		Comm Eglin
0136					Lose White Sands
0137	Communications		Communications		Comm Cape Kennedy
0138					Lose Corpus Christi
0140	Communications		Communications		Comm Bermuda
0141					Lose Eglin
0144	Communications		Communications		Lose Kennedy
0145					Comm Atlantic
0148	Navigation sighting	Navigation sighting			Lose Bermuda
0149					Lose Atlantic ship
0152	Communications		Communications		Comm Canary Is
0154					Lose Canary Is
0155		Perform SM-RCS check, end nav sighting	Perform ECS operational check, end nav sighting		
0211	End navigation sighting				

TABLE D-1  
THREE-MAN CREW SCHEDULE (Cont)

DAY 1	CREW ACTIVITIES			L A B	REMARKS
	Commander	System Engineer	System Engineer - Astronomer		
0212					Evening terminator
0213	Trajectory & Ephemeris Computation				S/C enter darkness
0215					
0218		Begin orbit enlargement for rendezvous			
0227	Communications		Communications		Comm Carnarvon
0247	Eat	Eat	Eat		
0302		Final orbital maneuvers for rendezvous			
0317		Systems status checks			
0327		Begin closure on LEM Lab			
0427		Begin performance of transposition; visually monitor CSM alignment with LEM, maneuver S/C to engage drogue and complete soft docking			
0447	Perform hard docking procedures				
0456	Communicate status	Doff pressure suit	Doff pressure suit		
0502	Start interlock and LEM cabin pressurization	Monitor LEM pressure build-up	EPS, SPS, system status check		
0512	Doff pressure suit	ECS, SM-RCS, CM-RCS status check			
0522	Check LEM cabin pressure for leakage, equalize CSM & interlock pressure.	Remove & stow CM pressure hatch & thermal hatch.	Assist	P R E S S U R I Z E D	
0542	Don LCG and pressure suit	Don LCG and pressure suit	LEM cabin equalization		
0557	Perform suit pressure suit	Perform suit pressure check			
0600					Enter SA anomaly
0602	Open LEM hatch, transfer to LEM, inspect, take umbilical	Transfer umbilical to commander	System status check		
0607	Establish initial habitability conditions in the LEM Lab	Remove PLSS units 1 & 2 from storage	LEM communications check		
0625	Stow PLSS units	Transfer PLSS units to CO.			
0627	Give SE umbilical	Transfer to LEM			
0630	Checkout LEM subsystems	Assist	Synchronize LEM clock, LEM communications check		
0705	Communicate with earth	Take biomedical readings			
0725	Take biomedical readings	Review EVA plan	Take biomedical readings		

TABLE D-1  
THREE-MAN CREW SCHEDULE (Cont)

DAY 1	CREW ACTIVITIES			L A B	REMARKS
	Commander	System Engineer	System Engineer - Astronomer		
0755	Review EVA plan		Review EVA plan	↓ P R E S S U R E I Z E D  ↓ D U M P  ↓ P R E S S U R E I Z E D  ↓	
0815	Communicate plans	System status check	System status check		
0835	Rest period - personal hygiene	Rest period - personal hygiene	Rest period - personal hygiene		
0852					S/C in darkness
0900	Eat	Eat			
0930	Doff CWG, d on LCG	Erect donning station	Communications		
0932					S/C in darkness
0935	Checkout suit & PLSS 1	Assist CO			
0953	Put suit on standby	Collect tools, lights, etc.	Eat		
1008	Assist SE	Check out suit & PLSS 2			
1030	Establish communications		System status check		
1032					S/C darkness
1040	Review deployment procedures, earth communication for anomaly data, prepare to egress		Monitor		
1110	Close face plate, close CM hatch	Close face plate, dump Lab			On PLSS
1112					S/C in sunshine
1118	Open hatch, prepare to egress	Assist			
1125	Egress, hook to tether	Assist			
1132	Assist	Egress, hook to tether			
1139	Maneuver to OAO and prepare for deployment and operation		Communication		Exit SA anomaly
1212					S/C in darkness
1252					S/C in darkness
1335	Collect tools, 2 PLSS Lich cannisters, unhook tether, ingress	Collect tools, 1 Lab Lich, Assist CO		28 PLSS Lich & 27 Lab Lich remain outside	
1345	Erect donning station	Ingress, close hatch			
1352	Establish "two men in vehicle condition"				
		OPEN FACE PLATES			
1410	Continue vehicle condition, recharge PLSS 1 & 2, initiate battery recharge & GOX recharge; place Lab Lich & used PLSS in CM, don CWG's		Prepare suit & PLSS 3 for transfer to Lab	2 PLSS recharges 1st recharge batteries 1 & 2	
1450	Communications report	Biomedical reading - complete GOX recharge	System status check		
1510	Biomedical reading				
1530	Transfer suit & PLSS 1 to CM	Transfer suit & PLSS 2 to CM	Transfer suit & PLSS 3 to Lab		
1550	Eat - Rest period	Eat - Rest period	Checkout experimental console		

TABLE D-1  
THREE-MAN CREW SCHEDULE (Cont)

DAY 1	CREW ACTIVITIES			L A B	REMARKS
	Commander	System Engineer	System Engineer - Astronomer		
1630	Prepare for sleep communications	Prepare for sleep; system status check	Communications, erect sleep	↓ P R E S S U R I Z E D	
1700	Sleep	Sleep	Eat		
1730			System status check, final communications		
1800			Sleep		

TABLE D-1  
THREE-MAN CREW SCHEDULE (Cont)

DAY 2	CREW ACTIVITIES			L A B	REMARKS	
	Commander	System Engineer	System Engineer - Astronomer			
0200	Communications	System status check		I P R E S S U R I Z E D		
0220	Biomedical readings	Biomedical readings				
0240	Eat	Eat	Remove sleep station, communications, system status check			
0310	Personal hygiene - general housecleaning-doff CWG's & don new CWG's.	Personal hygiene - general housecleaning-doff CWG's, don new CWG's.				
0350	Communications	System status check	Eat			
0410	Transfer to LEM Lab		Personal hygiene - general housecleaning			
0440			Biomedical reading			
0500	Insert Lab Lich cannister	Communications	Remove recharged batteries			Lab Lich should be inserted at this approximate time
RECREATION PERIOD						
0600	Communications	System status check	System status check			Enter SA anomaly
0620	Review next EVA plan,	experimental requirements & internal set-up				
0720	Communications	System status check	System status check			
0740	Remove auxiliary suit & PLSS 4 from storage and check	Inspect suit & PLSS 2	Inspect suit & PLSS 3			
0810	Collect tools, cannisters, lights etc. for EVA	Communications	Assist CO			
0830	System status check	System status check	System status check			
0850	Eat	Eat	Erect donning station doff CWG, don LCG			
0920	Doff CWG, don LCG, checkout suit & PLSS 4	Communications	Eat			
0950	Put suit on standby, assist SE		Checkout suit & PLSS 3			
1010	Establish communications, anomaly data, review EVA	System status check	System status check, review EVA			
1100	Close face plate & CM hatch	Monitor	Collect equipment, close face plate			
1110	Open hatch, dump Lab		Prepare to egress	D U M P		
1116	Assist		Egress, hook to tether			
1123	Monitor - biomedical & EVA	Communications	Insert used Lab Lich & PLSS Lich			
1133	Observe and prepare experiment		Insert film cassette, operation check		Exit SA anomaly	

TABLE D-1  
THREE-MAN CREW SCHEDULE (Cont)

DAY 2	CREW ACTIVITIES			L A B	REMARKS
	Commander	System Engineer	System Engineer - Astronomer		
1333	Monitor		Collect tools, 1 Lab. LiOH 1 PLSS LiOH & ingress	↓ P R E S S U R I Z E D	27 PLSS LiOH & 26 Lab LiOH remain outside
1343	Erect donning station		Ingress, close hatch		
1350	Establish "two men in vehicle condition" Open face plate		Assist CO  Open face plate		
1408	Continue vehicle con- dition, initiate GOX recharge		Recharge PLSS 3, initiate battery recharge		
1448	Biomedical, communi- cations report, don CWG	System status check	Transfer suit, PLSS 3 to CM, dry out		
1558	Experiment monitor				
1700	Eat	Eat	Experiment monitor		
1730	Erect sleep station, experiment monitor	Prepare for sleep	Eat		
1800	Sleep	Sleep	Final check		
1900			Sleep		

TABLE D-1  
THREE-MAN CREW SCHEDULE (Cont)

DAY 3	CREW ACTIVITIES			L A B	REMARKS
	Commander	System Engineer	System Engineer - Astronomer		
0200	Check experiment, communicate, remove sleep station	Transfer to LEM Lab with suit & PLSS 2			
0230	Eat - Hygiene	Eat - Hygiene			
0300	Biomedical readings	Experiment monitor			
0320	Don suit, checkout PLSS 4	Biomedical readings			
0340	Collect tools, light, etc.	Don suit, checkout PLSS 2			
0400	Prepare to egress, close face plate & CM hatch	Close face plate, dump lab	Awaken - personal hygiene Biomedical reading	D U M P	
0407	Egress, hook to tether	Assist	Housecleaning		
0415	Perform operations check, insert used LiOH		System status check		
0500	Cannisters, remove film cassette	Insert Lab LiOH remove recharged battery			
0550	Collect tools, Lab & PLSS LiOH & Ingress	Monitor	Eat - Hygiene		26 PLSS LiOH & 25 Lab LiOH remain outside Enter SA anomaly
0600	Ingress, close hatch	Erect donning station	Communications		
0607	Establish "two men in vehicle condition" OPEN FACE PLATES	Assist CO		P R E S S U R I Z E D	
0625	Recharge PLSS 4, initiate battery recharge	Continue vehicle condition, initiate GOX recharge	System status check		1 PLSS recharge battery 4 1st recharge
0705	Communication	Biomedical reading			
0725	Biomedical	Complete GOX recharge			
0745	Housecleaning	Housecleaning			
0815	Transfer suit to CM - dry out	Transfer suit to CM - dry out	Transfer suit to Lab		
0900	Eat	Eat	System status check		
0930	Communication	System status check	Experimental time		
1000	Remove suit & PLSS 4 from CM and stow in LEM Lab	Stow suit & PLSS 2	Experimental time		
1020	RECREATION PERIOD				
1120	Experimental time	Communications System status check	Experimental time		
1200					Leave SA anomaly
1220	Return to CM Experimental review, plans		System status check		
1240			Eat - Hygiene		

TABLE D-1  
THREE-MAN CREW SCHEDULE (Cont)

DAY	CREW ACTIVITIES			L A B	REMARKS
	Commander	System Engineer	System Engineer - Astronomer		
3					
1315	Communications	System status check	Exercise		
1335	Experimental time	Exercise			
1405		Experimental time	Experimental time		
1600	Eat	Eat			
1630	Communications, prepare for sleep	System status check, prepare for sleep			
1700	Sleep	Sleep	System status check		
1720			Communications		
1740			Experimental time		
2000			Eat		
2030			Erect sleeping station; final communications		
2100			Sleep		





TABLE D-1  
THREE-MAN CREW SCHEDULE (Cont)

DAY 4	CREW ACTIVITIES			L A B	REMARKS
	Commander	System Engineer	System Engineer - Astronomer		
1545		Transfer to CM, dry out suit	Experiment monitor	↓	
1600	Eat	Eat			
1630	Communications, pre- pare for sleep	System status check, prepare for sleep			
1700	Sleep	Sleep			
2200			Eat		
2400	Awaken, system status check, communica- tions, transfer to LEM Lab	Awaken, transfer to LEM Lab - experiment monitor	Transfer to CM		
0100	Eat	Experiment monitor	Sleep		

TABLE D-2  
TWO-MAN CREW SCHEDULE

DAY	CREW ACTIVITIES		L A B	REMARKS
	Commander	System Engineer-Astronomer		
0000	LIFT OFF			
	Monitor ascent parameter EPS, maintain radio communi- cations	Monitor ECS, Caution & Warning		
	Start Earth orbit coast			
0012	Set controls & displays for Earth orbit phase			
0018				Canary Is. Comm.
0020	Perform G&C, SM-RCS, CM-RCS, EMS system status check	Perform ECS, EPS, SPS, system status check		
0023				Lose Canary Is.
0038	IMU alignment & check sequence	IMU		
0044				Evening terminator
0054	Communications	System monitor		S/C in darkness
0124				Enter sunshine
0128	Navigation sighting	Navigation sighting		Morning terminator
0133	Communications	Communications		
0148	Navigation sighting	Navigation sighting		
0155	Perform SM-RCS check	Perform ECS operational check		
0211	End navigation sighting	End navigation sighting		
0212				Evening terminator
0213	Trajectory and Ephemeris computation			S/C in darkness
0218	Communications	Communications		
0228	Roll C/M to desired attitude and perform SCS attitude alignment for transposition & docking	Monitor system status Communications		
0240	Prepare for separation			
0242	Initiate separation and perform transposition; visually monitor CSM			
0252	Alignment with LEM, maneuver S/C to engage drogue and complete soft docking			S/C enters sunshine
0302	Perform hard docking procedures			
0314	Communicate S/C status	Doff pressure suit		
0319	Start interlock and LEM Lab pressurization (1 hr. 12 min.)	Monitor pressure buildup		
0324	Doff pressure suit	System status check		
0330	EAT and REST			
0352				S/C in darkness
0415	Check LEM Lab pressure for leakage, equalize CSM & interlock pressure. Re- move & stow CM pressure, thermal hatch	Don LCG & pressure suit, perform suit pressure check	P R E S S U R I Z E D ↓	

TABLE D-2  
TWO-MAN CREW SCHEDULE (Cont)

DAY	CREW ACTIVITIES		L A B	REMARKS
	Commander	System Engineer-Astronomer		
1				
0430	Don LCG, pressure suit & perform suit pressure check	LEM Lab equalization		
0440	System status check, transfer umbilical to SE	Open LEM hatch, transfer to LEM, inspect, take umbilical		
0432				S/C in sunshine
0445	LEM communications check	Establish initial habitability		
0503	Remove PLSS units #1 & #2 from storage and transfer to SE	Stow PLSS units, give CO ECS umbilical		
0510	Transfer to LEM	Assist		
0512	Synchronize LEM clock, LEM communications check	Check out LEM subsystems		
0532				S/C in darkness
0542	Doff pressure suit & LCG, don CWG	Doff suit, LCG, don CWG		
0557	Dry suits on CM couch, communications, system status check			
0600				Enter SA anomaly
0612				S/C in sunshine
0620	Record biomedical readings			
0640	Communications	System status check		
0700	REST PERIOD - Personal Hygiene			
0712				S/C in darkness
0720	Review OAO deployment plan, prepare tools, lights, suits for EVA; perform			
0752	General housecleaning, check tethers & tool belts, suit waste disposal			
0830	Communications	System status check		
0850	Remove suits from CM to donning station			
0852	In Lab			S/C in darkness
0915	Communications, anomaly data			
0932				S/C in sunshine
0945	EAT			
1015	Erect donning station	Doff CWG, don LCG		
1020	Assist SE	Checkout suit & PLSS 2		
1032				S/C in darkness
1048	Prepare equipment	Prepare PLSS 2 for standby - leave donning station		
1052	Checkout suit & PLSS 1	Assist CO		
1112				S/C in sunshine
1120	Prepare for egress - close face plates, close hatch, dump lab			
1127	Egress, hook to tether	Open hatch, monitor, assist	D U M P	On PLSS

TABLE D-2  
TWO-MAN CREW SCHEDULE (Cont)

DAY	CREW ACTIVITIES		L A B	REMARKS
	Commander	System Engineer-Astronomer		
1130	Assist	Egress, hook to tether	↓ P R E S S U R E D	Leave SA anomaly S/C in darkness S/C in sunshine S/C in darkness 28 PLSS LiOH 27 Lab LiOH remain outside On PLSS 3 hrs. and 4 mins. 2 PLSS recharges 1st recharge batteries 1 & 2 S/C in sunshine S/C in darkness S/C in sunshine
1133	Maneuver to OAO and prepare for deployment and operation			
1220				
1300				
1403	Collect tools, 2 PLSS LiOH collect tools, 1 Lab LiOH cannister, remove tether LiOH and ingress			
1413	Erect donning station, establish "two men in vehicle condition"	Ingress, secure forward hatch		
	OPEN FACE PLATES			
1431	Continue Vehicle condition, recharge PLSS 1 & 2, place Lab LiOH, PLSS LiOH in CM; don CWG's, initiate GOX recharge, initiate battery recharge			
1443				
1511	Communications report	Complete GOX recharge, system checkout		
1531	Take biomedical readings			
1543				
1551	EAT - REST PERIOD			
1623				
1636	Final communications, erect sleep stations	Experimental console checkout, erect sleep stations,		
	system status check	system status check		
1706	SLEEP	SLEEP		

TABLE D-2  
TWO-MAN CREW SCHEDULE (Cont)

DAY	CREW ACTIVITIES		L A B	REMARKS	
	Commander	System Engineer-Astronomer			
2					
0206	Remove sleep stations		P R E S S U R I Z E D	28 CWG's remain	
0212	Personal hygiene - don new CWG's				
0237	Communications	System status check			
0243					S/C in darkness
0257	EAT				
0323					S/C in sunshine
0327	Insert Lab LiOH	Remove recharged batteries and stow			
	Biomedical check	Biomedical check			
0352	General housecleaning				
0423	System status check	System status check			S/C in darkness
0453	Communications	Communications			
0503					S/C in sunshine
0513	Remove auxiliary suit & PLSS 3 from storage - inspect	Inspect suit & PLSS 2 - put used Lab LiOH & 2 PLSS LiOH near exit hatch			
0543	RECREATION PERIOD				
0600					Enter SA anomaly
0643	Communications	System status check			S/C in sunshine
0703	Review of next EVA plan, experimental requirements & set-up of internal experiment data				
0743					S/C in darkness
0803	Communications & system status check				
0823	Collect tools, lights, film cassettes for next EVA, prepare food				S/C in sunshine
0923	EAT				S/C in darkness
0953	Communications	System status check			
1003			S/C in sunshine		
1013	Erect donning station	Doff CWG, don LCG			
1019	Doff CWG, don LCG; assist SE	Checkout suit & PLSS 2			
1037	Checkout suit & PLSS 3	Prepare for standby			
1100	Collect tools, films and LiOH cannisters	Assist CO			
1103			S/C in darkness		
1130	Prepare for egress, close face plates, hatch & dump Lab		D U M P		
1138	Egress, hook tether	Plug into Lab ECS			
1143			S/C in sunshine		
1146	Insert used LiOH, complete deployment, insert film cassette, malfunction detection & repair	Monitor EVA, biomedical readings of EVA. Check out telescope and begin experiment	Exit SA anomaly		
1243			S/C in darkness		
1303			S/C in sunshine		

TABLE D-2  
TWO-MAN CREW SCHEDULE (Cont)

DAY	CREW ACTIVITIES		L A B	REMARKS
	Commander	System Engineer-Astronomer		
2				
1346	Collect tools, Lab LiOH & 1 PLSS LiOH & ingress	Assist CO, erect donning station, establish "two men in vehicle condition"	P R E S S U R I Z E D	26 Lab LiOH 27 PLSS LiOH remain outside
	OPEN FACE PLATES			
1404	Continue Vehicle condition, recharge PLSS 1, initiate GOX recharge & battery, don CWG's			S/C in darkness 1st recharge battery 3
1444	Biomedical readings			
1504	Communication report	Complete GOX recharge system status check		
1524	General house cleaning Personal hygiene, suit inspection	Experiment Monitor		
1554	Experiment monitor	General housecleaning, Suit insp., personal hygiene		
1624	Communications	Experiment monitor		
1644	Experiment Monitor	System status check		
1704	EAT	Experiment monitor		
1724	Experiment monitor Erect sleep stations	EAT		
1754	Final communications	Experiment monitor		
1814	Final experimental check	SLEEP		
1844	SLEEP			
2303				S/C in darkness

TABLE D-2  
TWO-MAN CREW SCHEDULE (Cont)

DAY	CREW ACTIVITIES		L A B	REMARKS	
	Commander	System Engineer-Astronomer			
3					
0244		Experiment check	P R E S S U R I Z E D ↓ D U M P ↓ P R E S S U R I Z E D ↓		
0314	Remove sleep stations				
0320	Personal hygiene, communications, experiment monitor	Personal hygiene, system status check, prepare food			
0350	EAT				
0405	Remove, recharge battery, stow; biomedical check, checkout suit & PLSS 1, collect tools, LiOH etc.	Experiment monitor, insert Lab LiOH; biomedical check, doff CWG, don LCG; checkout suit & PLSS 2			
0505	Close face plates, prepare for egress,				
0511	Plug into ECS, monitor EVA Communications	Egress, hook tether, insert used LiOH; maintenance & repair; remove film cassettes, bring in Film; Lab LiOH, PLSS LiOH; ingress			25 Lab LiOH 26 PLSS LiOH remain outside S/C in darkness Enter SA anomaly
0543					S/C in sunshine
0600					
0623					
0641	Assist SE, establish "two men in vehicle condition"	Erect doffing station			
	OPEN FACE PLATES				
0659	Continue Vehicle condition, recharge PLSS 2, initiate battery & GOX recharge				1 PLSS recharge 1st recharge battery 4
0740	Biomedical readings				
0800	Communication report	System status check			
0820	RECREATION PERIOD				
0920	Experimental review, film developing, etc.				
1120	EAT				
1150	General housecleaning				
1200					Exit SA anomaly
1220	Communications	Systems status check			
1240	Inspect all suits, PLSS LiOH, Lab LiOH				
1340	Experimental work, communications, system status check				
1800	EAT				
1820	Biomedical readings				
1840	Erect sleep stations				
1846	Final communications, system status check, experimental console check				
1904	SLEEP				



TABLE D-2  
TWO-MAN CREW SCHEDULE (Cont)

DAY	CREW ACTIVITIES		L A B	REMARKS
	Commander	System Engineer-Astronomer		
4				
0400	REMOVE SLEEP STATIONS - EAT			Insert Lab LiOH
0406	Personal hygiene, don new CWG's, biomedical readings, communications, system status check, prepare food, remove recharge battery			26 CWG's remain
0600				Enter SA anomaly
0700	Communications and system status check			
0725	Review next EVA, experimental requirements			
0830	Collect tools, lights, film cassettes for next EVA			
0900	Communications	System status check		
0925	Erect donning station	Doff CWG, don LCG		
0935	Doff CWG, don LCG, assist SE	Checkout suit & PLSS 2		
1000	Checkout suit & PLSS 1 EAT	Prepare suit for standby Assist C.O. EAT		
1056	Attach tool, lights, film, LiOH to suit	Assist C.O.		
1120	Experimental console check & review			
1150	Prepare to egress	Close CM hatch, dump	D	
1200	Egress, hook tether, insert used LiOH, operations check; insert film cassette, malfunction detection, repair or modular replacement	Plug into Lab ECS Monitor, coordinate experiment	U M P	Exit SA anomaly
1350	Collect tools, Lab LiOH, PLSS LiOH & ingress	Assist C.O. erect donning Station, establish "two men in vehicle condition"	P R E S S	24 Lab LiOH 25 PLSS LiOH remain outside
	OPEN FACE PLATES			
1418	Continue vehicle condition, recharge PLSS 1, battery, don CWG's, GOX recharge		U R I Z E D	1 PLSS recharge 1st cycle recharge battery 5
1450	Biomedical readings			
1510	EAT			
1525	Communications	Experiment monitor		
1545	Experiment monitor	System status check		
1605		Erect sleep stations		
1625	Final communications, system status check, experiment check, personal hygiene			
1715	SLEEP			

APPENDIX E

PROPULSION SIZING FOR  
ORBITAL ALTITUDE CHANGE

APPENDIX EPROPULSION SIZING FOR ORBITAL ALTITUDE CHANGEGENERAL

This appendix delineates the volume and weight of a cold gas nitrogen system for orbital altitude adjustments of the OAO, and compares this system to a hydrazine nonpropellant system, having the same total impulse.

SUMMARY

The result of this analyses indicates that the cold gas system is at least 3.5 times heavier and 3 times larger than a hydrazine nonpropellant system.

COLD GAS NITROGEN SYSTEMNitrogen Tank Sizing

$$N_2 \text{ gas weight} \sim W_{g_{\text{used}}} = \frac{I_T}{I_{sp}} = \frac{9200}{60} = 153 \text{ lb}$$

$$N_2 \text{ flow rate} \sim \omega = \frac{T}{I_{sp}} = \frac{50}{60} = .833 \text{ lbs/sec}$$

$$N_2 \text{ tank final pressure} = 500 \text{ psia}$$

$$\text{Pressure Ratio } P_{no}/P_{nf} = 3600/500 = 7.2$$

$$\text{Operating time} = 184 \text{ sec}$$

$$\text{Volume of gas/Flow area} = 77 \times 10^4 \text{ in.}$$

$$\text{Flow area} = .024 \text{ in.}^2$$

$$N_2 \text{ Volume (Isentropic Expansion)} = 18,500 \text{ in.}^3$$

$$\text{Volume of } N_2 \text{ gas in tanks(4)} = 4625 \text{ in.}^3$$

$$N_2 \text{ tank diameter} = 20.7 \text{ in.}$$

$$N_2 \text{ tank weight each} = 15.7 \text{ lb}$$

System envelope (estimated)

$$\begin{array}{ll} \text{Diameter} & 46.8 \text{ in.} \\ \text{Length} & 24.0 \text{ in.} \end{array}$$

Cold Gas N<sub>2</sub> System Weights

	<u>each</u>	<u>Weights</u> <u>total</u>
Thrust Chamber	6.0	6.0
Jet vane assembly	2.4	2.4
N <sub>2</sub> gas tanks (4)	15.7	62.8
Hardware		
• Fill/Vent	.1	.1
• Explosive valve (gas) (2)	.4	.8
• Pressure regulator	1.4	1.4
• Filter	.5	.5
• Control valve	.5	.5
• Explosive valve (2)	.6	1.2
Structure		40.0
N <sub>2</sub> gas weight (total)		<u>190.0</u>
Total Weight		305.7 lb

MONO-PROPELLANT SYSTEM

Parameters

Engine thrust	50 lb (force)
Specific impulse	230 sec
Nozzle expansion	45:1
Flow rate	.2157 lb/sec
Chamber pressure	190 psia
Thrust vector angle	± 4.5 deg
Fuel tank pressure	440 psia
Gas tank pressure	3600 psia

Fuel Tank Sizing

$$\text{Propellant Weight} \sim W_p = \frac{I_T}{I_{sp}} = \frac{9200}{230} = 40 \text{ lbs of } N_2H_4$$

$$\text{Tank Volume} \sim V_p = 1118 \text{ in}^3$$

$$\text{Tank Diameter} \sim D_p = 12.90 \text{ in}$$

$$\text{Tank Weight} \sim W_{TF} = 3.2 \text{ lbs}$$

Pressurant Tank Sizing

Tank Volume  $\sim V_G = 314 \text{ in}^3$

Tank Diameter  $\sim D_G = 8.44 \text{ in}$

Tank Weight  $\sim W_{TG} = 5 \text{ lbs}$

Engine Envelope

Length from oxidizer inlet to nozzle exit = 10.26 in.  
 Nozzle exit diameter = 2.904 in.  
 Chamber outside diameter  $\approx$  2.70 in.

System envelope (estimated)

Diameter 31 in.  
 Length 18 in.

Note: The envelope is very conservative.

Mono-Propellant System Weights

	<u>Weights</u>	
	<u>each</u>	<u>total</u>
Thrust chamber	5.3	5.3
Jet vane assembly	2.4	2.4
Propellant tank	3.2	3.2
Propellant tank bladder	1.5	1.5
Pressurant tank	5.0	5.0
Hardware		
• Fill/Vent	.1	.1
• Explosive valve (gas) (2)	.4	.8
• Pressure regulator	1.4	1.4
• Filter (gas)	.5	.5
• Propellant filter	.7	.7
• Control valve	.5	.5
• Explosive valve (prop) (2)	.6	1.2
Structure	20.0	20.0
Propellant weight $\sim N_2H_4$		40.0
Pressurant weight $\sim N_2$	3.0	3.0
Total Weight		85.6 lb

**APPENDIX F**

**REPRODUCTION OF LETTER (EX3/L1-66)**

**TO: DR. LYMAN SPITZER, JR.  
PRINCETON UNIVERSITY**

**FROM: NATIONAL AERONAUTICS AND  
SPACE ADMINISTRATION  
MANNED SPACECRAFT CENTER  
HOUSTON, TEXAS**



NATIONAL AERONAUTICS AND SPACE ADMINISTRATION  
MANNED SPACECRAFT CENTER  
HOUSTON, TEXAS 77058

EX3/L1-66

IN REPLY REFER TO: EX3/L1-66

March 9, 1966

Dr. Lyman Spitzer, Jr.  
Princeton University Observatory  
265 FitzRandolph Road  
Princeton, New Jersey 08540

Dear Dr. Spitzer:

We apologize for the extreme tardiness of our response to the questions left with us at the December meeting. The group which examined the feasibility was occupied with some pressing work. Any questions that you might care to ask us in the future will receive a more prompt reply.

1. Mission Feasibility

The Saturn IB mission feasibility was investigated. The mission studied consists of the delivery of a manned Apollo Applications Program (AAP) spacecraft and a 5,000 pound modified Orbital Astronomical Observatory (OAO) into a 300 nautical mile circular orbit inclined at 28.5 degrees. The AAP spacecraft would remain in orbit for 30 days. It would be necessary to perform one Extra Vehicular Activity (EVA) per day to attend the OAO. The desired orbit is achieved by first launching into a 100 nautical mile parking orbit and subsequently employing a Service Module Hohmann transfer to 300 nautical miles. Performance calculations for this mode have been carried out based on use of an Apollo Block II CSM and indicate that a maximum of 31,600 pounds may be placed in the desired orbit.

a. Environmental Control

Any EVA requires subsequent repressurization of the Command Module to 5 psi, and each such repressurization requires 8.5 pounds of oxygen. The amount of oxygen consumed by a crew member is a function of the metabolic rate, but 5.4 pounds for three crewmen or 1.8 pounds per man per 24 hours is normally used in determining oxygen requirements. A cabin leakage rate of 4.8 pounds per 24 hours must also be added to these requirements. Consequently, the oxygen requirements for a 30-day mission with one EVA per day would be as follows:

Repressurization: 30 days x 8.5 lb/day	255 pounds
Environmental Consumption and Leakage*	300 pounds
	<hr/>
Total	555 pounds

The basic Block II CSM contains only 170 pounds of oxygen for ECS purposes. (This corresponds to sufficient oxygen for six Portable Lift Support System refills and two cabin repressurizations.) Since this is obviously far short of the requirement for the 30-day mission, and since space does not exist in the Command Module for the additional oxygen needed to meet the requirements, it would be necessary to carry additional oxygen containers in the Service Module.

An airlock of minimum dimensions could result in a saving of about seven pounds of oxygen per repressurization, or 210 pounds for a 30-day mission. At least half of this saving would be offset by the weight of the airlock, so that the new weight saving might extend the mission by about one day. However, no airlock for this application is presently planned.

#### b. Attitude Control

It is our present opinion that the restrictions on spacecraft attitude imposed by thermal requirements in earth orbit at 300 nautical miles are insignificant. Thus, Reaction Control System expenditures need only allow for the retrograde maneuver and whatever is required for the experimental program. Because of the light load of the Apollo CSM, its attitude limit cycling rates are increased; thus the RCS fuel for attitude limit cycling is higher than usual computing out at .20 pounds/hour when in  $\pm 5^\circ$  attitude hold.

Asymmetries in the RCS pulse widths result in translational forces being imposed on the CSM while in attitude hold. With the maximum tolerance  $\pm 20\%$  pulse width and the most unfavorable balance, 0.80 pound seconds of impulse will be applied in translation for each cycle of attitude from a single axis. (The roll axis period is approximately 10.7 minutes. The pitch and yaw axes have 47-minute periods.) No apparent way exists other than a drastic redesign of the RCS system to avoid the asymmetry applying translational forces. The roll axis asymmetry could apply a maximum net change in velocity of .0057 feet/second during an hour with the pitch and yaw axes each supplying a maximum change of .0013 feet/second in the same period. These translational changes are of the same order of magnitude as those from aerodynamic drag. Their neutralization could require as much as a 20% increase in RCS fuel expenditure. This would bring the  $\pm 5^\circ$  attitude hold mode up to .3 pound/hour in the worst case.

---

\* This assumes that the EVA's would average out to one hour each and that the cabin would not be repressurized during EVA. Thus, for one hour per day for thirty days, there would be no leakage.



A three axis orientation maneuver in manual mode at .2 degree/second will require nominally .57 pound of RCS fuel.

The rendezvous maneuver according to the Grumman OAO Study (Control NASW-1143) requires extremely small changes in velocity on the order of 0.01 feet/second for a rendezvous. The fuel estimate in the weight breakdown is based on the Grumman findings. If it has not already been performed, a full man-in-the-loop analog simulation of the rendezvous should be implemented with an out-the-window scene for the pilot. The simulation would confirm the analytical work and reveal how much extra fuel, if any, the human factor adds to the operation.

The operations requiring RCS fuel are as follows:

(1) Attitude orientation prior to each rendezvous using the manual mode.

(2) Attitude hold two hours a day. This should cover the EVA period and the rendezvous operation.

(3) Rendezvous twice a day. This should keep the maximum separation under a mile according to the Grumman study.

(4) Retrofire sequence.

(5) A generous reserve of RCS fuel is desirable for contingencies; 100 pounds is thought to be adequate.

c. Weight Breakdown

The weight breakdown that follows indicates that the mission is feasible with a weight margin of 117 pounds. In the past space vehicles have had a tendency to grow in weight with time. The 117 pounds margin will not permit significant growth. This feasibility is predicated on a standard Apollo Applications spacecraft with no changes to accommodate this particular mission other than consumable storage in the Service Module and incorporation of the control panel and telemetry gear. Reduction to a two-man crew would save about 250 pounds. Approximately 70 pounds a day could be saved by a reduction in mission time.

SATURN IB MISSION CARRYING AN OAO  
AND APOLLO CSM TO 300 NAUTICAL MILE  
ORBIT AT 28.5° INCLINATION

## ESTIMATED WEIGHT BREAKDOWN

		<u>POUNDS</u>
CSM (3 man configuration)		22,268
<u>Consumables</u>		
Oxygen:		
a. Metabolic	5.4 lb/day x 30 days	162
b. Leakage	4.8 lb/day x 30 days	144
c. Repressurization	8.5 lb/day x 30 days	255
Fuel cell reactants (1.5KW)	34.2 lb/day x 30 days	1026
LiOH:		
a. Command Module	9.0 lb/day x 30 days	270
b. Portable Life Support	3.5 lb/day x 30 days	105
Food for crew	5.0 lb/day x 30 days	150
RCS fuel:		
a. Orientation maneuver	.57 lb/day x 60 cycles	34
b. Attitude hold ( $\pm 5^\circ$ )	.30 lb/hr x 60 hrs	18
c. Rendezvous operations	.05 lb x 60 cycles	3
d. Retrofire sequence		48
e. Reserve RCS fuel		100
Service Propulsion System Retro		<u>1400</u>
Consumables Total		3715
<u>OAO</u>		5,000
<u>OAO Structural Support Structure in SLA</u>		<u>500</u>
Grand Total		31,483
Maximum Orbiting Weight		<u>31,600</u>
Margin		117

## 2. CM Waste Management

In the basic Block II CM operated by Apollo ground rules, all waste is retained in sealed bags, except for the water produced by the fuel cells and the urine which is dumped overboard through the waste control system outlet. This outlet is located in the steam vent, which is mounted just aft of the lefthand edge of the side hatch. In longer duration missions, such as those required for the OAO, it may be desirable to dump other waste. This will be done by placing the sealed bag in a liner and ejecting it by means of the scientific airlock which is located in the main (side) hatch. Considering the locations and methods by which waste generated in the spacecraft is released, no trouble should be experienced in handling and scheduling the dumping of waste so as to not contaminate the OAO.

No difficulty is thought to ensue from the combustion products of the Reaction Control and propulsion systems which utilize  $N_2O_4$  as the oxidizer and a fuel of 50%  $N_2H_4$  and 50% UDMH. The combustion products are:

$H_2O$	37%	NO	1%
$N_2$	33%	$O_2$	2%
CO	7%	(O)	1%
(OH)	4.5%	$H_2$	0.7%
$CO_2$	5%	(H)	2.4%

## 3. Crew Exposure to External Radiation

The CSM generally provides the crew with adequate protection from external radiation sources within low earth orbit. However, at the given altitude and inclination, radiation levels in the South Atlantic anomaly are expected to prohibit EVA for approximately six consecutive orbits per day. This should not be an operational problem, but radiation effects on the film must be taken into account. The weight breakdown has assumed that any necessary shielding, and on-board developing equipment, if required, is included in the 5,000 pounds assigned to the OAO.

## 4. Control and Displays

Any experiment located external to the CM and requiring inside controls should plan on locating these controls in the lower forward equipment bay on an individually negotiated basis. Maximum permissible panel size is 100 square inches.

5. Work Space

No areas are specifically designated as work space for repair, etc.. The lower equipment bay area could be used if no other experiments are carried internally and if consumables are stored externally. An airlock, if installed, could also be used for this purpose.

6. Crew Exit and Entrance

The forward access tunnel has a clear opening 29 inches in diameter. This is the normal means of crew transfer to and from the CM. The side hatch is trapezoidal in shape, approximately 30 x 40 inches, but is intended only for emergency use in space, not for repeated operation.

7. Film Storage Space

The Block II CM incorporates 1.8 cubic feet of storage for return samples. Data return provisions are not yet defined for the AAP configuration to be flown in the 1970's, but some space will undoubtedly be available. Block II allocates 80 pounds for samples. For planning purposes, 300 pounds could be taken as a preliminary figure subject to substantial change as spacecraft definition becomes more firm. The food container storage space could be utilized as it becomes available.

8. Equipment Delivery Schedules

The equipment to be incorporated into the Apollo vehicle would be expected to be incorporated into the spacecraft six months prior to launch. This would require delivery of the gear to North American Aviation nine months prior to launch. Training equipment should be available at least six months prior to launch. It is estimated that the hardware contracts would have to be let at least thirty months prior to launch to meet the above schedule. The structural adapter for supporting the OAO in the SLA would probably be built by NAA and would require approximately 18 months to construct with installation to begin six months prior to launch.

Sincerely yours,

Fred T. Pearce, Jr.

cc:  
NASA Hq, SG, Dixon Ashworth

APPENDIX G

REPRODUCTION OF LETTER (66MA4844)

TO: DR. LYMAN SPITZER, JR.  
PRINCETON UNIVERSITY

FROM: NORTH AMERICAN AVIATION, INC.  
SPACE AND INFORMATION SYSTEMS  
DIVISION

NORTH AMERICAN AVIATION, INC. In reply refer to:  
66MA4844

April 6, 1966

Dr. Lyman Spitzer, Jr.  
Director  
Princeton University Observatory  
Princeton, New Jersey

Dear Dr. Spitzer:

Subject: Request for Information Concerning Installation of the  
Princeton High Resolution Optical Telescope in Apollo  
Spacecraft

- Reference: (a) Princeton University Observatory letter to NAA/S&ID,  
dated 18 February 1966
- (b) Telecon, March 15, 1966, between Dr. Don Morton of  
Princeton Observatory and J. A. Moran of S&ID
- (c) Telecon, March 24, 1966, between Dr. Lyman Spitzer, Jr.  
of Princeton Observatory and J. A. Moran of S&ID

Your letter of February 18, 1966, reference (a), has been received  
and the information requested is incorporated herein.

We have reviewed the questions posed relative to the Apollo spacecraft  
and the S-IB booster in conjunction with your proposed project of  
designing and operating an orbital high resolution optical telescope,  
as discussed in the reference (b) and (c) telecons. As indicated in  
your letter, NAA/S&ID has submitted a proposal and is currently nego-  
tiating a contract with the Office of Space Sciences and Applications,  
NASA Headquarters for a feasibility study of a Manned Orbital Solar  
Telescope. While there are similarities between these programs, there  
are also major differences between the operational systems approaches.  
Consequently, we will concern ourselves with answers to the questions  
posed by your program, without regard to any limitations which might be  
established by the NASA (Harvard) program.

Enclosure 1 is a sketch in general conformance with your concept of  
launching the Apollo CSM (Command and Service Module) and a modified  
SLA (Spacecraft LEM Adapter) housing the OAO equipped with your new  
high resolution telescope, an airlock mounting a gimbal support, and  
a removable stabilizing structure between the airlock and the OAO to  
take the orbit transfer loads. This assembly would be launched by the  
Saturn IB booster into a 105 n. mi. parking orbit where the CSM would  
perform a transposition maneuver and dock with the airlock and the

Dr. Lyman Spitzer, Jr.  
 Princeton University Observatory  
 Page 2.

stabilized OAO. This operational assembly would then transfer to the 300 n. mi. circular orbit where the OAO stabilizing structure would be removed and the system placed in operation.

The MSFC 1965 Saturn IB baseline capability states that a payload of 37,500 lbs can be placed into a 105 n. mi. near circular orbit in a due east launch. Based on this Saturn IB payload capability, a preliminary estimate of performance and weights follows:

Saturn IB Payload to 105 n. mi.	37,500 lb.
Existing SLA (LEM Adapter)	3,900 lb.
Estimated New SLA (shown in sketch)	2,500 lb.
Apollo Command Module, Weight Total	10,800 lb.
Apollo Service Module, Weight Empty	8,000 lb.
SPS Propellants (orbit transfer, maneuver and deorbit)	3,600 lb.
Orbiting Astronomical Observatory, without telescope	2,600 lb.
Telescope (estimated)	1,000 lb.
Estimated Airlock Structure, OAO, Gimbal and Orbit Transfer Stabilizing Structure	800 lb.

The above weights are based on a 3-man crew, so that they are comparable to other AES missions. The Apollo Command Module total weight allows for the addition of up to 300 lbs of scientific or experiment equipment.

In order to provide for extra vehicular activity (EVA) missions, it was deemed appropriate to suggest the development of a simple external airlock and integrated OAO gimbal structure. By the use of the airlock, the pressurized command module compartment can be maintained at nominal operating pressure, while an EVA mission is in progress. The airlock not only minimizes the requirements on the Environmental Control System and EVA mission dependent usable load but also provides for mounting the gimbal support structure without difficult rework to the Command Module while providing additional usable pressurized volume for the crew as well as additional storage and working area. Even with use of the airlock, it is suggested that the EVA missions be kept down to one per day, to minimize the weight requirements imposed upon the useful load of the Apollo Service Module. For the 30-day and 45-day missions, part of the usable load may be stored in and about the airlock and OAO gimbal structure. The airlock volume could be utilized by a crew member as an isolated area for tasks such as the film developing process to minimize chemical contamination of the Command Module crew compartment and Environmental Control System.

Dr. Lyman Spitzer, Jr.  
Princeton University Observatory  
Page 3.

Table 1 presents preliminary estimates for the accomplishment of the 15-day, 30-day and 45-day missions in a 300 n. mi. near circular orbit and  $28\frac{1}{2}^{\circ}$  orbit inclination.

The drawings of Enclosure 2 show blocked in areas of equipment location and space available for location of additional equipment and return cargo. While it is extremely difficult without a detailed study to state exactly what volume and weight allowances can be tolerated considering the critical reentry CG problems, it is estimated that up to 6 cubic feet total will be available in various locations in the command module and that about 300 lbs could be reasonably placed there. Only light equipment such as switches and small gages might be installed in the consoles and if a monitoring scope is required, it might be necessary to stow it in the equipment bay prior to reentry. However, during boost and orbital operation, its location on one of the consoles would be acceptable.

From inspection of the Table 1 estimates, it would appear that if the weight of the newly designed telescope did not exceed 2000 lbs, it would be possible to perform all of the missions even with the existing SLA within the Saturn IB performance and spacecraft weight limits.

We trust that the preliminary estimates and information contained in this letter will assist you in determining the suitability of the described orbital system to accomplish the desired mission. For a more comprehensive and accurate evaluation of the subject missions, we would be pleased to conduct under contract, and in cooperation with your staff, a detailed study and analysis of the modifications required to the Apollo spacecraft to perform the desired missions.

If we can be of further assistance in your task of developing systems for scientific space exploration, please do not hesitate to contact us.

Very truly yours,

NORTH AMERICAN AVIATION, INC.

J. A. Moran, Project Manager  
Manned Space  
Space and Information Systems Division

egf

- Encl. (1) 1 copy of sketch entitled "Orbital Astronomical Observatory - OAO System"
- (2) 1 copy of marked up NAA Drawing 5254-303, sheets 1 and 2, entitled "AES Command Module Internal Arrangement - Block II"



Dr. Lyman Spitzer, Jr.  
Princeton University Observatory  
Page 4.

System	15-Day Mission (lb)	30 <sup>4</sup> -Day Mission (lb)	45-Day Mission (lb)
Service Module Wt. Empty	8,000	8,000	8,000
<u>S/M Est. Useful Load</u>			
E.C.S.	315	850	1,390
Elect. Power System	503	1,072	1,492
Propulsion System (Propellants-DeOrbit & Maneuver)	1,000	1,000	1,000
Reaction Control System (Propellants)	682	972	1,322
Crew System	-0-	100	296
Total S/M Useful Load	2,500	4,000	5,500
Command Module Wt. Empty	9,034	9,034	9,034
<u>C/M Useful Load</u>			
Crew System	992	992	992
E.C.S.	153	153	153
Reaction Control System	270	270	270
Experiment Equipment	351	351	351
Total C/M Useful Load	10,800	10,800	10,800
<u>Total Spacecraft</u>			
(GSM, SPS, New SLA, OAO, Airlock, Gimbal and Stabili- zation Structure and S/M Useful Load - without tele- scope)	30,800	32,300	33,800
Saturn IB Payload Capability	37,500	37,500	37,500
Available for Telescope, Scientific and Misc. Equipment	6,700	5,200	3,700

Table 1.